

**NMR Methods to Characterise Arginine  
Side-Chains in Proteins using  $^{13}\text{C}$  Detection**

*Harold Wallace Mackenzie*



A thesis submitted for the degree

of

**Doctor of Philosophy**

in

**Protein NMR Spectroscopy**

Institute of Structural and Molecular Biology

University College London

**November 2021**



# Declaration

I, Harold Wallace Mackenzie confirm that the work presented within this thesis is my own. Where information has been derived from other sources, I confirm that this has been indicated in the thesis.



# Abstract

An understanding of the behaviour of biomolecules in their native physiological environment is the cornerstone of drug discovery and is crucial in the fight to address the unmet medical needs of a growing population. Whilst the flexible and dynamic nature of proteins has long been known to play an important role in human biology, these molecular motions often significantly hamper efforts to study the most interesting systems. The research presented in this thesis discusses the development of several new pulse sequences and aims to demonstrate the utility of NMR spectroscopy to the study of dynamic systems, with a particular focus on  $^{13}\text{C}$ -detected techniques. Historically eschewed in favour of the more sensitive nuclei, recent hardware developments have enabled the exploitation of the favourable relaxation properties of  $^{13}\text{C}$  to design novel pulse sequences that overcome some of the inherent limitations of  $^1\text{H}$ -detection.

A significant section of this research is devoted to the arginine side-chain, an amino acid that is routinely implicated in a wide range of intramolecular interactions within proteins. Firstly, a pair of pulse sequences is presented, in which  $^{15}\text{N}^n$  double-quantum magnetisation is generated and evolved to provide high-resolution correlation spectra of the functional guanidinium group, the part of the amino acid that is most often obscured by motions within the side-chain. Secondly, the development of the ASHDEX experiment – an arginine-specific method to monitor hydrogen exchange – is discussed. Data obtained using the novel experiment shows that the rate with which hydrogen nuclei undergo chemical exchange with neighbouring solvent molecules correlates with the presence of intramolecular interactions observed in the crystal structure of T4 lysozyme. A final application to arginine interrogates the atom-specific deuterium isotope shifts and illustrates that this easily measured parameter is a powerful indicator of intramolecular salt-bridge formation. The utility of the method is exemplified by application to T4 lysozyme and bacterial ribonuclease.

The final part of this thesis concerns the study of hydrogen exchange in intrinsically disordered proteins. IDPs have become the focus of many research groups owing to their implication in numerous disease models but the lack of a stable three-dimensional structure challenges the long-held view of a structure-activity relationship. Whilst the absence of tertiary structure hampers traditional  $^1\text{H}$  NMR observation, the switch to  $^{13}\text{C}$ -detection provides increased signal dispersion and enables the collection of high-resolution NMR spectra. The development of the CARBEX pulse sequence is presented and successfully demonstrated on human  $\alpha\text{Synuclein}$ , the molecule implicated in Parkinson's Disease.



# Impact Statement

The rise of NMR spectroscopy over the last 50 years has allowed scientists to study proteins, nuclei acids and other biologically important molecules in unprecedented atomic detail, ultimately uncovering new and important molecular insights. In recent years, the NMR community has begun to move away from exclusive detection of the  $^1\text{H}$  nucleus and explore the wealth of spectral information available through  $^{13}\text{C}$ -detection. The research presented in this thesis contributes to the ongoing development of  $^{13}\text{C}$ -detected NMR spectroscopy and has significant implications both within and beyond the academic scientific community.

As much of the research into novel NMR techniques and applications initially takes place in academic settings, it is anticipated that the impact of the presented research will first be felt in research groups with a similar focus to our own. An article based on the first experimental chapter of this thesis – *Double-Quantum Coherences in Arginine* – was published in 2017 and at the time of writing has been cited 10 times. A second publication based on Chapter 3 – *Side-Chain Hydrogen Exchange in Arginine* – was made available in 2019 and has been cited 3 times. It is anticipated that the remaining experimental work in this thesis will be published in the near future and thus contribute to the continuing development of NMR spectroscopy. Although the primary focus of this thesis is the functionally important arginine side-chain, the ideas that underpin the presented experiments can be extended to other amino acids and it is likely that such research will be undertaken by future students within the Hansen laboratory at UCL. Further afield, the idea behind the HDQC experiment developed in Chapter 2 has since been extended to the study of nucleic acids by a research group in Germany and our pulse sequences have been shared with scientists as far as China and the United States.

Whilst academic research groups typically take on the initial development of new spectroscopic methods, the scientific impact of such a development can be far-reaching. At the core of the pharmaceutical industry is the discovery of new or improved medical interventions that seek to prolong or improve the quality of the life of patients suffering from debilitating disease. It has long been known that the progression of disease is linked with changes within protein signalling pathways that are in turn linked with the structure and dynamics of the proteins themselves. It is therefore critical that scientists have access to state-of-the-art techniques that enable the interrogation of these important properties. To this end, NMR spectroscopy has quickly become fully integrated into Pharma and Bio-Tech companies, finding use in functions ranging from Medicinal Chemistry to Fragment-Based Drug Discovery. Arginine is found in the active site of numerous enzymes and is often of interest to drug-hunting scientists. However, properties

intrinsic to the side-chain make it difficult to observe using traditional  $^1\text{H}$  NMR techniques. The  $^{13}\text{C}$ -detected experiments developed herein provide a number of ways of detecting arginine-mediated interactions and are therefore expected to prove useful in a wide-range of drug discovery settings.

# Acknowledgements

Whilst the declaration I have just signed asserts that all of the work presented herein is my own, it would of course not have been possible without the support and guidance of numerous others. First and foremost, I would like to thank my supervisor, Professor Flemming Hansen, for his never-ending supply of enthusiasm towards NMR research and science in general. This enthusiasm, clearly evident in his habit of frequently bounding into the office or laboratory with cries of *“How’s it going?”* or *“Any new ideas?”*, is one of the many reasons that his group continues to be so successful and makes it a very pleasant place to work.

As a part-time student, my time at UCL spanned nearly half a decade and I therefore had the pleasure of meeting and working with a large number of students and post-doctoral researchers. I owe a great debt of thanks to Dr. Angelo Figueiredo, Dr. Lisbeth Andersen, Dr. Somnath Mondal, Dr. Vaibhav Shukla, Dr. Gogulan Karunanithy, Dr. Ruth Pritchard, Dr. Lucas Siemons, Martin Rosellen and Harrison O’Brien. Each of them has helped in their own way but I would particularly like to thank Lucas for his prowess with python programming and Harrison, not only for his invaluable guidance in the wet-lab but also the willingness he showed to down tools, grab a beer and discuss anything other than magnetic resonance.

I am immensely grateful to my colleagues at UCB, without whom this chapter of my life would remain unwritten. I would particularly like to thank Dr. Richard Taylor, whose unwavering support since I first joined his group in 2008 has been a source of great comfort to me. I have Richard’s ability to write exceptionally persuasive proposals to thank for getting the deal that allowed me to undertake my PhD research alongside my workplace duties over the line. On that note, it would be remiss of me not to thank my manager Dr. Rachel Davies and the analytical team at UCB, particularly Dr. Christine Prosser, Justin Staniforth, Adam Hold, Sarah Taylor and Jordan Haran for mucking in and picking up the slack when I was inconveniently entranced by nuclear spin choreography. I am lucky enough to work alongside some fantastic people and I am looking forward to re-joining the group full-time.

A PhD is a stressful enough undertaking at the best of times and the current COVID-19 pandemic has hardly helped. Fortunately, I am blessed enough to be surrounded by a supportive network of friends and family and I thank them all for their love and guidance over the years, especially during these challenging times. A special nod must go to my oldest friends, John and Henry, who have enthusiastically ensured that if we are all doomed to descend into video-chat mediated alcoholism, we will do so together.

Finally, I thank my wonderfully patient and kind wife, Helen. As successful as this PhD project has been, the absolute highlight of the last five years for me was the day I married you in the Winter of 2018. It was your encouragement that originally led me to apply for this degree program and as usual, I was wise to follow your advice. Thank you for your continued love and support, I simply could not have got here without you.

Now then, let's get some rest - the next adventure is just around the corner!

*Success is not final.*

*Failure is not fatal.*

*It is the courage to continue that counts.*

**SIR WINSTON CHURCHILL**



# Contents

<b>1</b>	<b>Introduction</b>	<b>23</b>
1.1	Preamble	23
1.2	Introduction to NMR Theory	25
1.2.1	The Vector Model	25
1.2.2	The Product Operator Formalism	27
1.2.3	Evolution of the Density Operator	29
1.2.4	Relaxation and X-Detection	32
1.2.5	Fourier Transform and Frequency Discrimination	34
1.3	Pulse Sequence Building Blocks	36
1.3.1	The Spin-Echo	36
1.3.2	INEPT	41
1.3.3	Indirect Chemical Shift Evolution	42
1.3.4	Composite Pulse Decoupling	43
1.3.5	The HSQC Experiment	44
1.3.6	Frequency-Selective Pulses	47
1.3.7	Pulsed Field Gradients	48
1.4	Introduction to Arginine	51
1.4.1	Importance of Protein Side-Chains	51
1.4.2	Structure and NMR Parameters of Arginine	52
1.4.3	Guanidinium Resonance Assignment	52
<b>2</b>	<b>Double-Quantum Coherences in Arginine</b>	<b>59</b>
2.1	Introduction	59
2.1.1	Chemical Exchange of $^1\text{H}^{\epsilon/\eta}$ with Bulk Solvent	59
2.1.2	Effect of the Restricted Rotation of the $\text{N}^{\epsilon}\text{-C}^{\zeta}$ Bond	60
2.2	Theory and Method Development	63
2.2.1	Generation of Single-Quantum Coherences	63
2.2.2	Generation of Double-Quantum Coherences	65
2.2.3	Chemical Shift Evolution of Double-Quantum Coherence	66
2.2.4	$^{13}\text{C}^{\zeta}\text{-}^{15}\text{N}^{\eta}$ HDQC Pulse Sequence	68
2.2.5	$^{13}\text{C}^{\zeta}\text{-}^{15}\text{N}^{\epsilon}\text{-}^{15}\text{N}^{\eta}$ Pulse Sequence	70
2.3	Results and Discussion	71
2.3.1	Application to Free Arginine	71
2.3.2	Application to T4 Lysozyme	72
2.3.3	Generation of Zero-Quantum Coherences	74
2.4	Conclusions	77
		13

<b>3</b>	<b>Hydrogen Exchange in Arginine</b>	<b>79</b>
3.1	<b>Introduction</b>	<b>79</b>
3.1.1	Hydrogen Exchange and Intramolecular Interactions	80
3.1.2	Established NMR Techniques for Quantifying HX Rates	82
3.1.3	Quantifying HX Rates in Arginine Side-Chains	85
3.2	<b>Theory and Method Development</b>	<b>85</b>
3.2.1	Longitudinal zz-Exchange	86
3.2.2	Improving Signal-to-Noise	92
3.2.3	Resolution of Isotope-Shifted Signals	101
3.2.4	pseudo-4D ASHDEX Pulse Sequence	107
3.3	<b>Results and Discussion</b>	<b>108</b>
3.3.1	Application to Free Arginine	108
3.3.2	Application to T4 Lysozyme	110
3.4	<b>Conclusions</b>	<b>114</b>
<b>4</b>	<b>Deuterium Isotope Shifts: Detection of Salt-Bridges</b>	<b>117</b>
4.1	<b>Introduction</b>	<b>117</b>
4.2	<b>Theory and Method Development</b>	<b>118</b>
4.2.1	Deuterium Isotope Shifts in the Guanidinium Group	118
4.2.2	Quantification by NMR Spectroscopy	119
4.2.3	Free Arginine Reference Compounds	127
4.2.4	Complexed Arginine Reference Compound	128
4.3	<b>Results and Discussion</b>	<b>129</b>
4.3.1	Application to Arginine Reference Compounds	129
4.3.2	Application to T4 Lysozyme	135
4.3.3	Application to Barnase	136
4.4	<b>Conclusions</b>	<b>138</b>
<b>5</b>	<b>HX in Intrinsically Disordered Proteins</b>	<b>141</b>
5.1	<b>Introduction</b>	<b>141</b>
5.1.1	Intrinsically Disordered Proteins	142
5.2	<b>Theory and Method Development</b>	<b>144</b>
5.2.1	Frequency-Selective $^{13}\text{C}$ Refocussing Pulses	145
5.2.2	$^{13}\text{C}^{\alpha}$ Decoupling During Acquisition	147
5.2.3	pseudo-5D CARBEX Pulse Sequence	156
5.2.4	Further Considerations	159
5.3	<b>Results and Discussion</b>	<b>162</b>

5.3.1	$^{13}\text{C}$ Longitudinal Relaxation in $\alpha$ Synuclein	162
5.3.2	Fractionation Factors in $\alpha$ Synuclein	164
5.3.3	Hydrogen Exchange Rates in $\alpha$ Synuclein	165
<b>5.4</b>	<b>Conclusions</b>	<b>167</b>
<b>5.5</b>	<b>Appendices</b>	<b>168</b>
5.5.1	$\alpha$ Synuclein Raw Data	168
<b>6</b>	<b>Conclusions</b>	<b>171</b>
6.1	Concluding Remarks	171
6.2	Future Work	174
6.2.1	Double-Quantum Coherences in Histidine and Tyrosine	174
6.2.2	Outlook	175
<b>7</b>	<b>Experimental</b>	<b>177</b>
7.1	General Procedures	177
7.2	Protein Expression and Purification	178
7.2.1	T4 Lysozyme	178
7.2.2	Bacterial Ribonuclease	179
7.2.3	Ubiquitin	179
7.2.4	$\alpha$ Synuclein	179
7.3	Synthetic Chemistry	180
7.3.1	Arginine Methyl Ester	180
7.3.2	<i>Capped</i> Arginine	180
7.3.3	<i>Complexed</i> Arginine	181
7.4	NMR Spectroscopy	183
7.4.1	NMR Hardware	183
7.4.2	Small Molecule NMR	183
7.4.3	Protein NMR	184
7.4.4	NMR Parameters	184
7.5	Pulse Sequences for Bruker Spectrometers	187
7.5.1	Arginine $^{13}\text{C}^{\zeta}$ - $^{15}\text{N}^{\epsilon}$ HSQC	188
7.5.2	Arginine $^{13}\text{C}^{\zeta}$ - $^{15}\text{N}^{\eta}$ HDQC	192
7.5.3	Arginine $^{13}\text{C}^{\zeta}$ - $^{15}\text{N}^{\epsilon}$ - $^{15}\text{N}^{\eta}$ Correlation	196
7.5.4	Arginine $^{15}\text{N}^{\epsilon}$ ( $^1\text{H}/^2\text{H}$ ) zz-Exchange (pseudo-3D)	201
7.5.5	Arginine $^{15}\text{N}^{\epsilon}$ ( $^1\text{H}/^2\text{H}$ ) zz-Exchange (pseudo-4D)	204
7.5.6	Arginine $^{13}\text{C}^{\zeta}$ - $^{15}\text{N}^{\epsilon}$ PEP-HSQC	208
7.5.7	Selective $^{13}\text{C}^{\zeta}$ Excitation	212
7.5.8	HetCP $^{13}\text{C}^{\zeta}$ Excitation	213

7.5.9	ASHDEX Experiment	217
7.5.10	Arginine $^{13}\text{C}^{\alpha}$ - $^{15}\text{N}^{\epsilon}$ HSQC (pseudo-3D)	222
7.5.11	$(^1\text{H})^{13}\text{C}'$ - $^{15}\text{N}$ HSQC (coupled)	225
7.5.12	$(^1\text{H})^{13}\text{C}'$ - $^{15}\text{N}$ HSQC (BASH decoupled)	229
7.5.13	$(^1\text{H})^{13}\text{C}'$ - $^{15}\text{N}$ HSQC (IPAP decoupled)	234
7.5.14	CARBEX Experiment	238
7.5.15	$^{13}\text{C}'(^1\text{H}/^2\text{H}) T_1$ Measurement	243
7.5.16	Fractionation Factor Measurement	247
<b>7.6</b>	<b>Data Processing Scripts</b>	<b>252</b>
7.6.1	Conversion Script (nmrPipe) for ASHDEX Experiment	252
7.6.2	Processing Script (nmrPipe) for ASHDEX Experiment	252
7.6.3	Conversion Script (nmrPipe) for CARBEX Experiment	253
7.6.4	Fitting Script (Python) for Extraction of HX Rates	256
<b>8</b>	<b>References</b>	<b>259</b>

# List of Figures

<b>Fig. 1.1</b>	Energy Levels and the Bulk Magnetisation Vector	26
<b>Fig. 1.2</b>	The Vector Model: RF Pulses	26
<b>Fig. 1.3</b>	The Vector Model: Larmor Frequency	27
<b>Fig. 1.4</b>	The Vector Model: Product Operators	28
<b>Fig. 1.5</b>	The Vector Model: Relaxation	33
<b>Fig. 1.6</b>	Fourier Transform and Frequency Discrimination	35
<b>Fig. 1.7</b>	The Spin-Echo	36
<b>Fig. 1.8</b>	The Second Frequency Dimension	43
<b>Fig. 1.9</b>	Composite Pulse Decoupling	43
<b>Fig. 1.10</b>	The HSQC Pulse Sequence	44
<b>Fig. 1.11</b>	Frequency-Selective Pulses	48
<b>Fig. 1.12</b>	Pulsed Field Gradients	49
<b>Fig. 1.13</b>	Interactions of the Arginine Side-Chain	51
<b>Fig. 1.14</b>	Scalar Couplings in the Arginine Side-Chain	52
<b>Fig. 1.15</b>	Scalar Couplings in the Protein Backbone	53
<b>Fig. 1.16</b>	Guanidinium Resonance Assignment	57
<b>Fig. 2.1</b>	$^{13}\text{C}^{\zeta}\text{-}^{15}\text{N}^{\epsilon}$ HSQC Spectrum of T4L99A	60
<b>Fig. 2.2</b>	$^1\text{H}\text{-}^{15}\text{N}^{\epsilon/\eta}$ HSQC Spectrum of T4L99A	61
<b>Fig. 2.3</b>	Rotational Exchange Broadening in $^{13}\text{C}^{\zeta}\text{-}^{15}\text{N}^{\eta}$ HSQC Spectra	62
<b>Fig. 2.4</b>	Generation of SQ Magnetisation using INEPT	64
<b>Fig. 2.5</b>	Generation of MQ Magnetisation using INEPT	64
<b>Fig. 2.6</b>	Arginine $^{13}\text{C}^{\zeta}\text{-}^{15}\text{N}^{\eta}$ HDQC Pulse Sequence	69
<b>Fig. 2.7</b>	Arginine $^{13}\text{C}^{\zeta}\text{-}^{15}\text{N}^{\epsilon}\text{-}^{15}\text{N}^{\eta}$ Pulse Sequence	71
<b>Fig. 2.8</b>	Double-Quantum Spectra of <i>Free</i> Arginine	72
<b>Fig. 2.9</b>	$^{13}\text{C}^{\zeta}\text{-}^{15}\text{N}^{\eta}$ HDQC Spectrum of T4L99A	73
<b>Fig. 2.10</b>	Assignment of $^{13}\text{C}^{\zeta}\text{-}^{15}\text{N}^{\eta}$ DQ Resonances in T4L99A	74
<b>Fig. 2.11</b>	Zero-Quantum Spectra of <i>Free</i> Arginine	76
<b>Fig. 3.1</b>	Model for Hydrogen Exchange of Amide Protons	80
<b>Fig. 3.2</b>	Example HX Reaction Profiles	83
<b>Fig. 3.3</b>	$^{13}\text{C}^{\zeta}\text{-}^{15}\text{N}^{\epsilon}$ HSQC Pulse Sequence with $^2\text{H}$ Decoupling	86
<b>Fig. 3.4</b>	Simulated Evolution of $N_x(^1\text{H})$ and $N_x(^2\text{H})$ Operators during HX Reaction	88
<b>Fig. 3.5</b>	Arginine $^{15}\text{N}^{\epsilon}(^1\text{H}/^2\text{H})$ pseudo-3D zz-Exchange Pulse Sequence	90
<b>Fig. 3.6</b>	Arginine $^{15}\text{N}^{\epsilon}(^1\text{H}/^2\text{H})$ pseudo-4D zz-Exchange Pulse Sequence	91
<b>Fig. 3.7</b>	Arginine $^{13}\text{C}^{\zeta}\text{-}^{15}\text{N}^{\epsilon}$ PEP-HSQC Pulse Sequence	92
<b>Fig. 3.8</b>	Quadrature Artefacts in PEP-HSQC	94
<b>Fig. 3.9</b>	Sensitivity Improvement from Pep-HSQC	97
<b>Fig. 3.10</b>	Simulated Evolution During HetCP (DIPSI)	98
<b>Fig. 3.11</b>	Sensitivity Improvement from HetCP	99
<b>Fig. 3.12</b>	$^1\text{H}\text{-}^{15}\text{N}$ Refocussed INEPT	100
<b>Fig. 3.13</b>	Semi-Constant-Time Chemical Shift Evolution	102

<b>Fig. 3.14</b>	Semi-Constant-Time FID Distortion	105
<b>Fig. 3.15</b>	The Sign-Coding Filter	106
<b>Fig. 3.16</b>	ASHDEX Pulse Sequence	108
<b>Fig. 3.17</b>	Effect of Deuterium Concentration on HX Rate	109
<b>Fig. 3.18</b>	Effect of pH and Temperature on HX Rate	110
<b>Fig. 3.19</b>	HX Measurement of T4L at pH 5.5	111
<b>Fig. 3.20</b>	HX Build-up and Decay Plots of T4L	111
<b>Fig. 3.21</b>	HX Measurement of T4L at pH 7.4	112
<b>Fig. 3.22</b>	HX Rate of Arg95 of T4L	113
<b>Fig. 3.23</b>	Intramolecular Interactions in T4L	114
<b>Fig. 4.1</b>	Detection of Isotope Shifts in Arginine	120
<b>Fig. 4.2</b>	Simulation of Guanidinium Deuterium Distribution	122
<b>Fig. 4.3</b>	pseudo-3D Arginine $^{13}\text{C}^{\zeta}$ - $^{15}\text{N}^{\epsilon}$ HSQC Pulse Sequence	123
<b>Fig. 4.4</b>	Application of Sign-Coding to $^{13}\text{C}^{\zeta}$ - $^{15}\text{N}^{\eta}$ DQ Resonances	125
<b>Fig. 4.5</b>	Effect of HX Rate on Observed Isotope Shift	126
<b>Fig. 4.6</b>	Dimerisation of <i>Free</i> Arginine	127
<b>Fig. 4.7</b>	Low Energy Structure of <i>Complexed</i> Arginine	129
<b>Fig. 4.8</b>	MQ-CEST Profiles of <i>Complexed</i> Arginine	131
<b>Fig. 4.9</b>	Comparison of Isotope Shifts Measured in <i>Free</i> and <i>Complexed</i> Arginine	133
<b>Fig. 4.10</b>	Isotope Shifts Measured in T4L99A	136
<b>Fig. 4.11</b>	$^{13}\text{C}^{\zeta}$ - $^{15}\text{N}^{\epsilon}$ HSQC Spectrum of Barnase	137
<b>Fig. 4.12</b>	Isotope Shifts Measured in Barnase	137
<b>Fig. 5.1</b>	$^1\text{H}$ - and $^{13}\text{C}$ -detected HSQC Spectra of T4L	142
<b>Fig. 5.2</b>	$^1\text{H}$ - and $^{13}\text{C}$ -detected HSQC Spectra of $\alpha\text{S}$	143
<b>Fig. 5.3</b>	Spin-System Comparison of Arg Guanidinium and Backbone	144
<b>Fig. 5.4</b>	Selective $^{13}\text{C}$ 180° RF Pulses	146
<b>Fig. 5.5</b>	Modifications to Retro-INEPT Block	147
<b>Fig. 5.6</b>	$^{13}\text{C}'$ - $^{13}\text{C}^{\alpha}$ Coupled CON Spectrum of Ubiquitin (In-Phase)	147
<b>Fig. 5.7</b>	Band-Selective Homonuclear Decoupling	149
<b>Fig. 5.8</b>	BASH Decoupled CON Spectrum of Ubiquitin	150
<b>Fig. 5.9</b>	Simultaneous $^{13}\text{C}'$ and $^{13}\text{C}^{\alpha}$ Refocussing	151
<b>Fig. 5.10</b>	IPAP Decoupling: Processing	153
<b>Fig. 5.11</b>	IPAP Decoupling: Pulse Sequence Blocks	154
<b>Fig. 5.12</b>	$^{13}\text{C}'$ - $^{13}\text{C}^{\alpha}$ Coupled CON Spectrum of Ubiquitin (Anti-Phase)	155
<b>Fig. 5.13</b>	CARBEX Pulse Sequence	157
<b>Fig. 5.14</b>	Pre-Processing of pseudo-5D Dataset	158
<b>Fig. 5.15</b>	CARBEX Setup Experiments	160
<b>Fig. 5.16</b>	$^{13}\text{C}'$ Longitudinal Relaxation Rates in $\alpha\text{S}$	163
<b>Fig. 5.17</b>	Fractionation Factors in $\alpha\text{S}$	164
<b>Fig. 5.18</b>	HX Rates and Protection Factors in $\alpha\text{S}$	165
<b>Fig. 5.19</b>	CARBEX HX Rate Comparison with SOLEXY Dataset	166
<b>Fig. 6.1</b>	Scalar Couplings in Histidine and Tyrosine	175

# List of Tables

<b>Table 1.1</b>	Effect of RF Pulses on $I_x$ , $I_y$ and $I_z$ Magnetisation	30
<b>Table 2.1</b>	Phase Cycle for $^{13}\text{C}^{\zeta}$ - $^{15}\text{N}^{\eta}$ HDQC Experiment	69
<b>Table 2.2</b>	Phase Cycle for $^{13}\text{C}^{\zeta}$ - $^{15}\text{N}^{\epsilon}$ - $^{15}\text{N}^{\eta}$ Correlation Experiment	70
<b>Table 3.1</b>	Effect of Deuterium Concentration on HX Rates in <i>Free</i> Arginine	108
<b>Table 3.2</b>	Effect of pH and Temperature on HX Rates in <i>Free</i> Arginine	109
<b>Table 3.3</b>	HX Rates Measured in T4L	113
<b>Table 4.1</b>	Deuterium Isotope Shifts Expected for Guanidinium Nuclei	119
<b>Table 4.2</b>	Intensity of Isotope-Shifted Signals in $^{15}\text{N}^{\eta}$ HDQC Spectra	122
<b>Table 4.3</b>	Deuterium Isotope Shifts Measured in <i>Free</i> and <i>Complexed</i> Arginine	130
<b>Table 4.4</b>	Rotational Exchange Rates of <i>Complexed</i> Arginine Measured by MQ-CEST	131
<b>Table 4.5</b>	Residue-Specific Deviation of $^1\Delta^{15}\text{N}^{\epsilon}(\text{H}^{\epsilon})$ Isotope Shifts in T4L99A	135
<b>Table 4.6</b>	Residue-Specific Deviation of $^1\Delta^{15}\text{N}^{\epsilon}(\text{H}^{\epsilon})$ Isotope Shifts in Barnase	137
<b>Table 5.1</b>	Chemical Shift, Relaxation, Fractionation and HX Data for $\alpha\text{S}$	168
<b>Table 7.1</b>	Specification of Available NMR Spectrometers	181
<b>Table 7.2</b>	Acquisition Parameters for Example NMR Spectra	182



# Abbreviations

<b>ASHDEX</b>	Arginine Side-chain Hydrogen Deuterium EXchange
<b>BASH</b>	BAnd-Selective Homonuclear
<b>BMRB</b>	Biological Magnetic Resonance data Bank
<b>BURP</b>	Band-selective, Uniform-Response, Pure-phase
<b>CARBEX</b>	CARbon-detected Backbone EXchange
<b>CEST</b>	Chemical Exchange Saturation Transfer
<b>CPD</b>	Composite Pulse Decoupling
<b>Cryo-EM</b>	Cryogenic-Electron Microscopy
<b>CS</b>	Chemical Shift
<b>CSA</b>	Chemical Shift Anisotropy
<b>CT</b>	Constant-Time
<b>CTP</b>	Coherence Transfer Pathway
<b>DFT</b>	Density Functional Theory
<b>DIPSI</b>	Decoupling In the Presence of Scalar Interactions
<b>DMSO</b>	DiMethyl SulfOxide
<b>DQ</b>	Double-Quantum
<b>EM</b>	Electron Microscopy
<b>FID</b>	Free Induction Decay
<b>FLOPSY</b>	FLip-flOP SpectroscopY
<b>FPLC</b>	Fast Protein Liquid Chromatography
<b>FT</b>	Fourier Transform
<b>GARP</b>	Globally-optimised, Alternating-phase, Rectangular Pulses
<b>HATU</b>	Hexafluorophosphate Azabenzotriazole Tetramethyl Uronium
<b>HDQC</b>	Heteronuclear Double-Quantum Correlation
<b>HDX</b>	Hydrogen-Deuterium EXchange
<b>het-CP</b>	Heteronuclear Cross-Polarisation
<b>HILIC</b>	Hydrophobic Interaction Liquid Chromatography
<b>HMQC</b>	Heteronuclear Multi-Quantum Correlation
<b>HPLC</b>	High-Performance Liquid Chromatography
<b>HSQC</b>	Heteronuclear Single-Quantum Correlation
<b>HX</b>	Hydrogen EXchange
<b>HZQC</b>	Heteronuclear Zero-Quantum Correlation
<b>IDP</b>	Intrinsically Disordered Protein
<b>INEPT</b>	Insensitive Nuclei Enhanced by Polarisation Transfer
<b>IPAP</b>	In-Phase/Anti-Phase
<b>IR</b>	Infrared
<b>LB</b>	Lysogeny Broth
<b>MQ</b>	Multi-Quantum
<b>MRI</b>	Magnetic Resonance Imaging
<b>Nat. Ab.</b>	Natural Abundance

## *1. Introduction*

<b>NMR</b>	Nuclear Magnetic Resonance
<b>PEP</b>	Preservation of Equivalent Pathways
<b>PF</b>	Protection Factor
<b>PFG</b>	Pulsed Field Gradient
<b>RADAR</b>	Radio Detection and Ranging
<b>RF</b>	Radio Frequency
<b>SAR</b>	Structure-Activity Relationship
<b>SEC</b>	Size Exclusion Chromatography
<b>SHR</b>	States-Haberkorn-Ruben
<b>SNOB</b>	Selective excitatiON fOr Biochemical applications
<b>SOLEXY</b>	SOLvent-EXchange SpectroscopY
<b>SPHERE</b>	Server Program for Hydrogen Exchange Rate Estimation
<b>SQ</b>	Single-Quantum
<b>T4L99A</b>	L99A Mutant of T4 Lysozyme
<b>T4WT</b>	Wild-Type T4 Lysozyme
<b>TOCSY</b>	TOfal Correlation SpectroscopY
<b>TPPI</b>	Time Proportional Phase Increment
<b>TROSY</b>	Transverse Relaxation Optimised SpectroscopY
<b>UPLC</b>	Ultra-Performace Liquid Chromatography
<b>UV-vis</b>	Ultraviolet-visible
<b>VHF</b>	Very High Frequency
<b>WALTZ</b>	Wideband, Alternating-phase, Low-power Technique for Residual Splitting
<b>ZQ</b>	Zero-Quantum

# 1

## Introduction

### 1.1 Preamble

As scientists across the globe rush to release a world gripped by the COVID-19 pandemic, never before has the relationship between the structure and function of biological entities been in sharper focus. The connection between the chemical make-up of a substance and its physiological activity has been known since the mid-19<sup>th</sup> Century<sup>[1]</sup> and the premise continues to guide medicinal chemistry efforts today.<sup>[2]</sup> The goal of any drug discovery program is typically to disrupt, induce or otherwise modulate the interaction between a ligand and its receptor and therefore produce some sort of physiological response. Simple models for such interactions include the *lock and key*<sup>[3]</sup> and *induced-fit*<sup>[4]</sup> hypotheses whereby the receptor acts like a *lock* and only *keys* with the correct three-dimensional structure will be able to bind efficiently. The modulation of the ligand-receptor interaction is typically achieved by designing an alternative ligand that can compete with the natural ligand. Clearly, this approach demands that the synthetic ligand has the correct structure and physical shape in order to effectively compete for the receptor binding. A successful drug discovery program therefore involves the meticulous structural modification of potential ligands and the elucidation of any effect these changes may have on biological activity.

A fundamental hurdle to the investigation of this crucial structure-activity relationship (SAR) is one of scale. The physical size of even a relatively large molecule is minute – a 200 kDa protein measures less than 8 nm across<sup>[5]</sup>, less than 1/10,000<sup>th</sup> of the width of a human hair – and for decades, scientists have turned to spectroscopy to explore this microscopic world. The precise nature of the spectroscopic technique a scientist chooses to employ will depend upon the investigation at hand, but it will involve the interaction of electromagnetic radiation with the sample. Techniques involving X-rays, ultraviolet-visible (UV-vis) or infrared (IR) light are amongst the most commonly used, but the observation of Nuclear Magnetic Resonance (NMR) in molecular beams in the late 1930s,<sup>[6]</sup> soon brought very high frequency (VHF) radio waves into play.

## 1. Introduction

The advances in Radio Detection and Ranging (RADAR) technology brought about by the Second World War meant that sources of radiofrequency (RF) radiation were freely available and shortly after the conclusion of the War in the mid-1940s, NMR spectroscopy was demonstrated on water<sup>[7,8]</sup> and paraffin<sup>[9]</sup> by two independent research groups. They observed that the nuclear magnetic moments of a solid or liquid substance, when placed in a constant magnet field would induce a voltage in a pick-up coil following the application of a second, perpendicular field oscillating at an appropriate frequency. The following decades saw numerous landmark developments in this emerging field including the development of Fourier-transform NMR spectroscopy (FT-NMR) in the 1960s,<sup>[10]</sup> multi-dimensional NMR spectroscopy in the 1970s,<sup>[11]</sup> and the successful application of NMR spectroscopy to biomolecules in the 1980s.<sup>[12–14]</sup> Today, NMR spectroscopy is routinely deployed within Chemistry<sup>[15]</sup>, Biology<sup>[16]</sup> and Material Sciences<sup>[17]</sup> departments and is considered to be the *gold-standard*<sup>[18]</sup> analytical technique for the characterisation of small organic molecules. In the field of structural biology, together with X-ray crystallography<sup>[19]</sup> and more recently cryogenic-electron microscopy (cryo-EM),<sup>[20]</sup> NMR spectroscopy is one of the few techniques capable of determining the three-dimensional structure of biological macromolecules with atomic level detail. Crucially, it is currently the only technique with the ability to do so in the native solution state. The exploitation of the NMR phenomenon has also proven to be invaluable in medical settings where, under the name Magnetic Resonance Imaging (MRI) to avoid unwelcome and anxiety-inducing associations with nuclear war, clinicians use it to obtain detailed three-dimensional images of living patients in a non-invasive manner.<sup>[21]</sup> Such is the versatility of magnetic resonance and the considerable scientific impact the various incarnations of the technique have had, it is of little surprise that no fewer than five Nobel Prizes in Physics<sup>[22,23]</sup>, Chemistry<sup>[24,25]</sup> and Medicine<sup>[26]</sup> have been awarded to the pioneering scientists responsible for the rapid growth of the field.

Owing to inherent sensitivity limits imposed by the hardware available at the time, NMR experiments have traditionally relied on the detection of the more sensitive nuclei such as hydrogen and fluorine. However, recent advances in cryoprobe technology have at least partially mitigated this limitation and NMR spectroscopy has been successfully extended to less sensitive nuclei such as carbon and nitrogen. The work presented in this thesis introduces several carbon-detected NMR experiments that exploit properties of the nucleus that more than make up for the intrinsic sensitivity penalty. In acknowledgment of the particular importance of this amino acid, Chapters 2-4 are devoted to the study of the Arginine side-chain with a novel double-quantum experiment (Chapter 2), the study of side-chain hydrogen exchange rates (Chapter 3) and the detection of intramolecular salt-bridges using the deuterium isotope shift (Chapter 4). Chapter 5 builds on the arginine hydrogen exchange work and describes a carbon-detected experiment for the quantification of backbone amide exchange particularly suited to the study

of intrinsically disordered proteins. The remainder of this Chapter will seek to introduce some key concepts concerning the theory and application of NMR spectroscopy and the biology of the arginine residue.

## 1.2 Introduction to NMR Theory

In quantum mechanics, the nucleus of an atom is characterised by a *nuclear spin quantum number*  $I$  that may take values of or above zero in half-integer steps. Nuclei with *odd* mass numbers have half-integer spin quantum numbers ( $^1\text{H}$ ,  $I = \frac{1}{2}$ ;  $^{17}\text{O}$ ,  $I = \frac{5}{2}$ ), nuclei with *even* mass and *odd* atomic numbers have integer spin quantum numbers ( $^2\text{H}$ ,  $I = 1$ ;  $^{10}\text{B}$ ,  $I = 3$ ) and nuclei with both *even* mass and atomic numbers have spin quantum numbers of zero ( $^{12}\text{C}$ ,  $^{16}\text{O}$ ). A nucleus with a non-zero spin quantum number possesses angular momentum, the z-component of which can exist in  $2I + 1$  states, each denoted by the *magnetic quantum number*,  $m$ . For spin-half nuclei this results in two possible states ( $m = +\frac{1}{2}$ ,  $-\frac{1}{2}$ ) whilst for a spin-one nucleus such as  $^2\text{H}$ , three states are possible:  $m = -1, 0, +1$ . The most useful nuclei encountered in biological NMR spectroscopy ( $^1\text{H}$ ,  $^{13}\text{C}$ ,  $^{15}\text{N}$ ) are all spin-half and so the remainder of this section will exclusively focus on these. It is important to note that whilst the NMR-active isotope of hydrogen is also the most naturally abundant<sup>[27]</sup> ( $^1\text{H} = 99.99\%$  nat. ab.), the same is not true for carbon ( $^{13}\text{C} = 1.1\%$  nat. ab.) or nitrogen ( $^{15}\text{N} = 0.36\%$  nat. ab.) and as such biological molecules are often isotopically-labelled in the laboratory<sup>[28]</sup> prior to analysis by NMR spectroscopy.

### 1.2.1 The Vector Model

In the absence of an external magnetic field, the two energy states of a spin-half nucleus ( $m = \pm\frac{1}{2}$ ) are degenerate. However, when placed in a magnetic field the nucleus undergoes Zeeman splitting into two partially-aligned states either parallel ( $\alpha$ ,  $m = +\frac{1}{2}$ ) or anti-parallel ( $\beta$ ,  $m = -\frac{1}{2}$ ) with respect to the external field (Figure 1.1a). The difference in energy,  $\Delta E$ , between these two states is proportional to the strength of the external magnetic field ( $B_0$ ):

$$\Delta E = (E_\beta - E_\alpha) = \frac{h\gamma B_0}{2\pi} \quad (1.1)$$

where  $h$  is Planck's constant and  $\gamma$  is the gyromagnetic ratio of the nucleus in question.

The energy gap is rather small (for a  $^1\text{H}$  nucleus in an 18.8 T field,  $\Delta E \approx 8.4 \times 10^{-26}$  J) and at thermal equilibrium the lower energy state ( $E_\alpha$ ) is only very slightly more energetically favourable: at 298 K, the energy difference above corresponds to approximately one spin in every 50,000. Nevertheless, the tiny excess of lower energy states results in a *Bulk Magnetisation Vector* ( $M_0$ ) that for convenience is usually visualised superimposed upon a right-handed set of cartesian axis with the  $B_0$  field aligned with the z-axis (Figure 1.1b).

## 1. Introduction

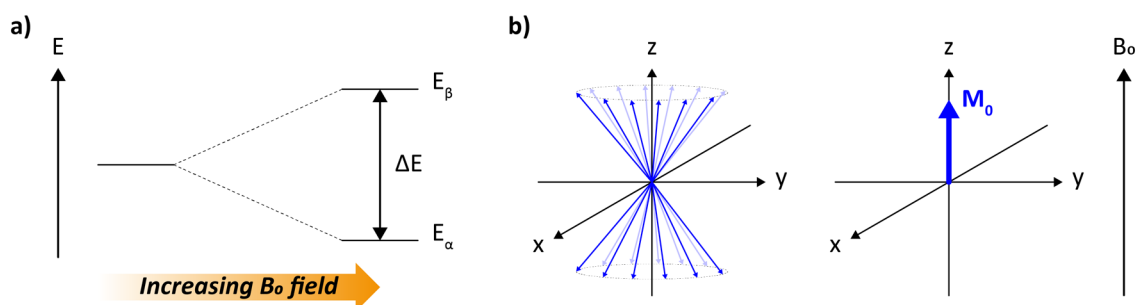


**Figure 1.1** a) Zeeman splitting of a spin-half nucleus occurs when placed in an external magnetic field ( $B_0$ ). The difference in energy between the two energy levels increases with magnetic field and corresponds to the ultra-high radiofrequency range of the electromagnetic spectrum. b) The small difference in energy between the two available spin states results in a very slight preference for the  $E_\alpha$  state leading to a bulk magnetisation vector ( $M_0$ ) aligned with the external field.

The bulk vector  $M_0$  can be manipulated using an RF field ( $B_1$ ) temporarily applied orthogonal to the  $B_0$  field, known as a *pulse*. Figure 1.2 shows the effect of an on-resonance pulse applied along the  $x$ -axis on the  $M_0$  vector. When the  $B_1$  field is applied, the magnetisation rotates about the new field towards the  $y$ -axis. Immediately following the application of the  $B_1$  field, the  $M_0$  vector has been rotated through *flip angle*  $\alpha$  and is no longer aligned with the  $z$ -axis. Similarly, if the  $B_1$  field were applied along the  $y$ -axis, the resulting rotation of the  $M_0$  vector is towards the  $x$ -axis.

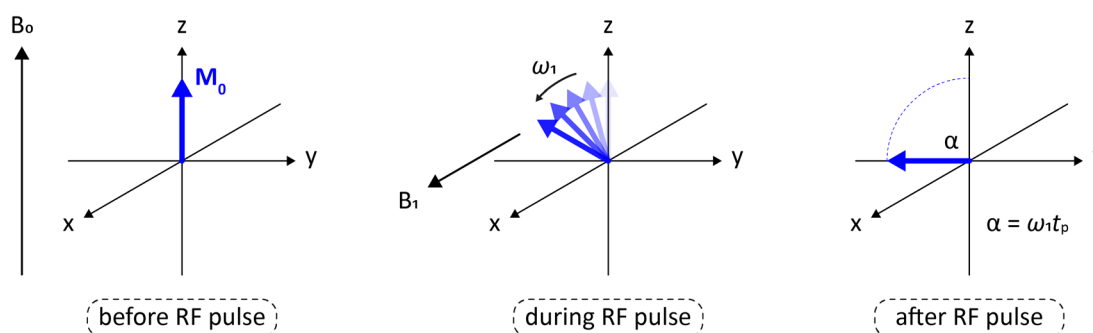


**Figure 1.2** The application of an orthogonal RF-field ( $B_1$ ) rotates the  $M_0$  vector away from the  $z$ -axis and into the  $xy$ -plane. The *flip angle*  $\alpha$  is proportional to the strength and applied duration of the  $B_1$  field.

When tipped away from the equilibrium state by the action of an RF pulse,  $M_0$  vector rotates about the  $z$ -axis at the *Larmor frequency*  $\omega_0$  in a process known as *free precession* where:

$$\omega_0 = -\gamma B_0 \quad (\text{and similarly, for the RF pulse above, } \omega_1 = -\gamma B_1) \quad (1.2)$$

The circular motion of the magnetisation vector in the  $xy$  (transverse) plane (Figure 1.3a) induces an oscillating voltage in a detection coil wound around the  $x$ - or  $y$ -axis and the intensity in each is recorded as a function of time. The time-dependent intensity of the magnetisation aligned with the  $x$ - ( $M_x$ ) and  $y$ -axes ( $M_y$ ) follows a cosine or sine function (Figure 1.3b), and subsequent Fourier transformation of the data allows the extraction of the underlying frequency. Owing to tiny differences in their local environment, nuclei in different parts of the molecule experience a very slightly different external field and therefore give rise to signals at different frequencies. This atom-specific frequency is known as the *Chemical Shift* when quoted relative to a reference.

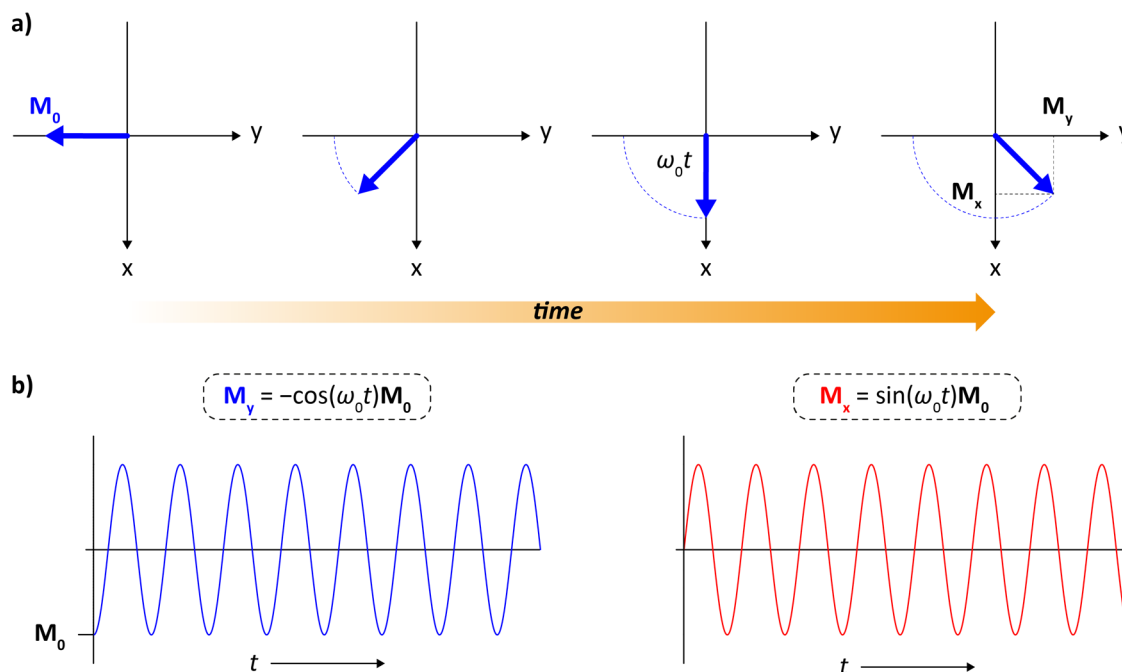


**Figure 1.3** a) After tipping into the transverse plane, the  $M_0$  vector rotates about the  $z$ -axis at the Larmor frequency  $\omega_0$ . b) The  $M_y$  and  $M_x$  components of the oscillating vector are detected as cosine and sine functions, respectively. The plots assume that the equilibrium  $M_0$  magnetisation has experienced a  $90^\circ$  RF pulse along the  $x$ -axis and was therefore aligned with  $-y$  at the start of the free precession.

### 1.2.2 The Product Operator Formalism

The Vector Model described above is a popular and intuitive model for the behaviour of magnetically active nuclei in an external field, but it is too simplistic and only holds when considering the behaviour of uncoupled spins. To adequately describe the evolution of magnetisation over the course of even the simplest multi-pulse NMR experiments, a more rigorous, quantum mechanical treatment is required.

The evolution of magnetisation during any NMR experiment can be described analytically using the *Liouville-von Neumann* equation:

$$\frac{d\sigma(t)}{dt} = -i[\mathcal{H}, \sigma(t)] \quad (1.3)$$

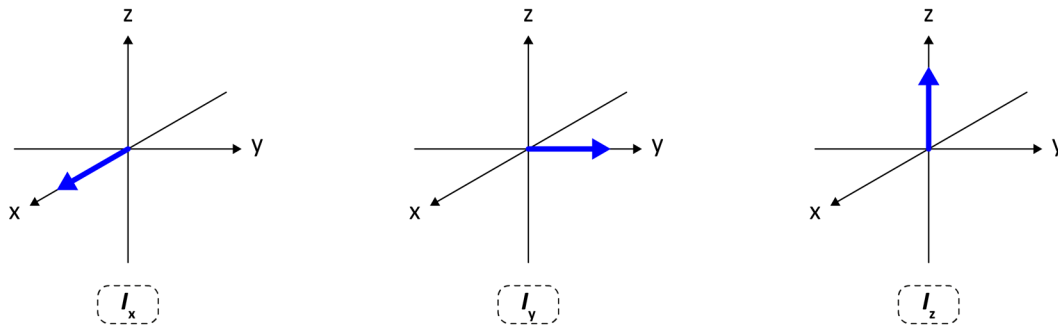
where  $\sigma(t)$  represents the *density operator* fully describing the state of the system at time  $t$  and  $\mathcal{H}$  is the Hamiltonian under which the system is evolving. However, a full solution to the equation above is unnecessary to support the work presented in this thesis. The more accessible product operator formalism<sup>[29]</sup> provides a sufficient description of the system and asserts that the density operator  $\sigma(t)$  can be expressed as a linear combination of the  $I_x$ ,  $I_y$  and  $I_z$  operators and products thereof. For a one-spin system, the density operator is given by:

$$\sigma(t) = M_x(t)I_x + M_y(t)I_y + M_z(t)I_z \quad (1.4)$$

## 1. Introduction

where the  $I_x$ ,  $I_y$  and  $I_z$  operators represent the x-, y- and z-components of the spin angular momentum and  $M_x$ ,  $M_y$  and  $M_z$  the amounts of x-, y- and z-magnetisation.  $I_x$  and  $I_y$  are often referred to as *transverse* and  $I_z$  as *longitudinal* magnetisation. This description of a single spin can be easily related back to the vector model as shown in Figure 1.4a.

### a) one-spin



### b) two-spins

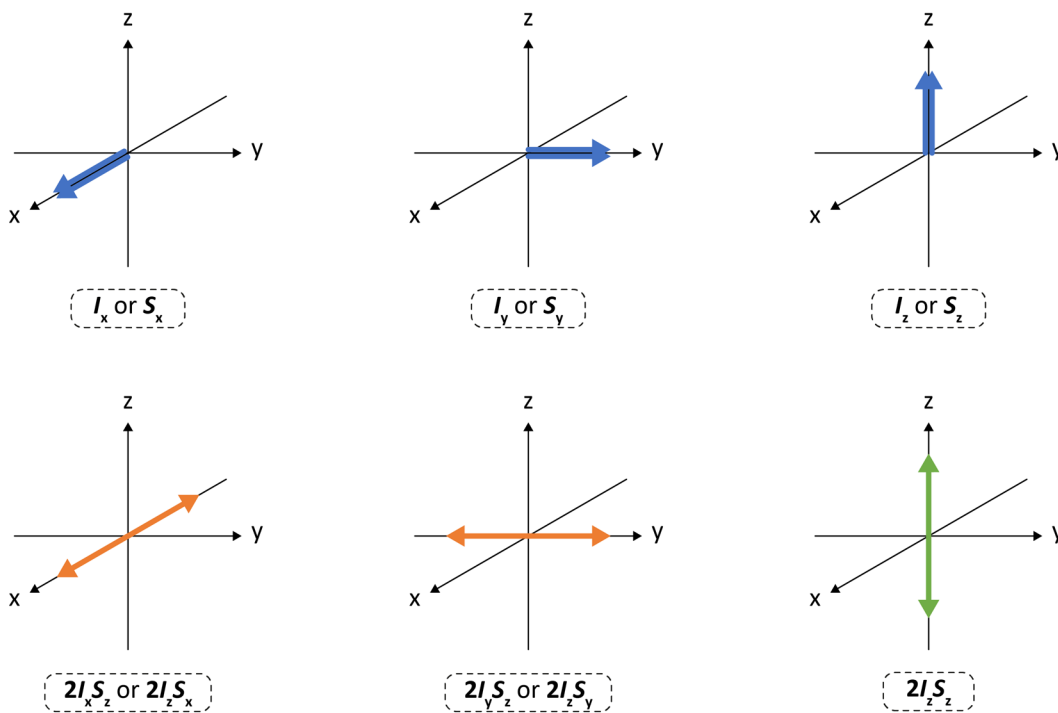


**Figure 1.4** Pictorial representation of selected product operators for a) one-spin and b) two-spin systems.

For a coupled two-spin system ( $I_S$ ), a total of 16 ( $4^2$ ) operators are required to fully describe the density operator. They are constructed from the  $I$ -spin operators above and the  $S$ -spin operators that represent the x-, y- and z-components of the second spin:

	$E_1$	$I_x$	$I_y$	$I_z$
$E_2$		$I_x$	$I_y$	$I_z$
$S_x$	$S_x$	$2I_x S_x$	$2I_y S_x$	$2I_z S_x$
$S_y$	$S_y$	$2I_x S_y$	$2I_y S_y$	$2I_z S_y$
$S_z$	$S_z$	$2I_x S_z$	$2I_y S_z$	$2I_z S_z$

where  $E_1$  and  $E_2$  represent the identity operators for spins one and two, respectively.

The two-spin operators describing *in-phase* and *anti-phase* magnetisation as well as the *longitudinal two-spin order* term can be related to the vector model and are shown graphically in Figure 1.4b. The remaining operators represent unobservable *multiple-quantum* (MQ) magnetisation and are discussed in more detail in Chapter 2.

### 1.2.3 Evolution of the Density Operator

As any NMR experiment can be deconstructed into one or more discrete *blocks* that occur sequentially (for example, an RF pulse followed by a delay can be treated as two separate events), the precise form of the Hamiltonian required to describe the evolution of the system will depend upon which block of the pulse sequence is to be analysed. The time-dependent evolution of the density operator  $\sigma$  is given by:

$$\sigma(t) = e^{-i\mathcal{H}t} \sigma(0) e^{i\mathcal{H}t} \quad (1.5)$$

where  $\sigma(0)$  is the density operator at  $t=0$ ,  $\sigma(t)$  is the density operator at time  $t$  and  $\mathcal{H}$  is the Hamiltonian relevant for time period between 0 and  $t$ . In order to facilitate the discussion of the pulse sequences introduced in this thesis, only the three forms of the Hamiltonian described below need be considered. It is important to note that the evolutions of the density operator described here only hold for Hamiltonians which are themselves *time-independent*. This is known as the *rotating-frame* and corresponds to the popular analogy of observing the up-and-down motion of a wooden horse on a fairground carousel. From the outside (the so-called *laboratory-frame*), the horse simultaneously moves up-and-down whilst rotating around the carousel, thereby tracing an oscillating path. If one were to step onto the carousel instead (and into the *rotating-frame*), the observer rotates with the carousel and the horse's motion is revealed to be simply up-and-down and is much easier to quantify.

#### a. RF pulse Hamiltonian $\mathcal{H}_{\text{pulse}}$

The Hamiltonian that describes the evolution of magnetisation during the application of a hard RF pulse is given by:

$$\mathcal{H}_{\text{pulse}} = \omega_1 [I_x \cos\theta + I_y \sin\theta] \quad (1.6)$$

where  $\theta$  indicates the *phase* of the applied RF pulse. Therefore, using Equation 1.5 above for the evolution of the density operator, the effect of an RF pulse applied about the x-axis ( $\theta = 0$ ) to  $I_z$  magnetisation (shown in Figure 1.2) is found by:

$$\begin{aligned} \sigma(t_p) &= e^{-i\omega_1\tau_p I_x} I_z e^{i\omega_1\tau_p I_x} \\ &= I_z \cos(\omega_1\tau_p) - I_y \sin(\omega_1\tau_p) \end{aligned}$$

where  $\tau_p$  is the duration of the RF pulse about the x-axis.

## 1. Introduction

As the flip angle  $\alpha$  of a pulse is given by  $\alpha = \omega_1 \tau_p$ , the evolution above can be written more succinctly as:

$$I_z \xrightarrow{\alpha I_x} I_z \cos \alpha - I_y \sin \alpha$$

Using the expression above, it is straightforward to see that a  $90^\circ$  x-pulse applied to the equilibrium magnetisation generates  $-I_y$ :

$$I_z \xrightarrow{90^\circ I_x} I_z \cos\left(\frac{\pi}{2}\right) - I_y \sin\left(\frac{\pi}{2}\right) = -I_y$$

During the course of a multi-pulse NMR experiment, RF fields are applied with different phases that affect the  $x$ -,  $y$ - and  $z$ -magnetisation operators present differently. A summary of the important transformations due to RF pulses is shown in Table 1.1. It is important to note that a pulse applied with a phase of  $\pm x$  has no effect on the  $I_x$  magnetisation and similarly, a  $\pm y$ -pulse has no effect on the  $I_y$  magnetisation.

$\mathcal{H}_{pulse}$	$\sigma(0)$	$\sigma(t)$
$\alpha I_x$	$I_x$	$I_x$
$\alpha I_{-x}$	$I_x$	$I_x$
$\alpha I_y$	$I_x$	$I_x \cos \alpha - I_z \sin \alpha$
$\alpha I_{-y}$	$I_x$	$I_x \cos \alpha + I_z \sin \alpha$
$\alpha I_x$	$I_y$	$I_y \cos \alpha + I_z \sin \alpha$
$\alpha I_{-x}$	$I_y$	$I_y \cos \alpha - I_z \sin \alpha$
$\alpha I_y$	$I_y$	$I_y$
$\alpha I_{-y}$	$I_y$	$I_y$
$\alpha I_x$	$I_z$	$I_z \cos \alpha - I_y \sin \alpha$
$\alpha I_{-x}$	$I_z$	$I_z \cos \alpha + I_y \sin \alpha$
$\alpha I_y$	$I_z$	$I_z \cos \alpha + I_x \sin \alpha$
$\alpha I_{-y}$	$I_z$	$I_z \cos \alpha - I_x \sin \alpha$

**Table 1.1** The effect of various RF pulses with flip angle  $\alpha$  on  $I_x$ ,  $I_y$  and  $I_z$  magnetisation.

## b. Chemical Shift Hamiltonian $\mathcal{H}_{cs}$

As noted previously, magnetisation that has been tipped away from the  $z$ -axis by an RF pulse rotates about the  $B_0$  field at the Larmor frequency  $\omega_0$ . For hardware reasons, the Larmor frequency of the magnetisation vector is actually detected *relative* to the RF transmitter frequency  $\omega_{tx}$  which is usually set to the midpoint of the expected frequency range. Therefore, the Hamiltonian that describes the chemical shift (CS) evolution of magnetisation in an NMR experiment is given by:

$$\mathcal{H}_{cs} = \Omega I_z \tag{1.7}$$

where the  $\Omega$  is the *offset frequency* ( $\Omega = \omega_0 - \omega_{tx}$ ).

The form of this Hamiltonian is identical to  $\mathcal{H}_{\text{pulse}}$  above and so the  $I_x$  and  $I_y$  operators evolve during time  $t$  (assuming that  $\gamma > 0$ ) as:

$$\begin{aligned} I_x &\xrightarrow{\Omega t I_z} I_x \cos(\Omega t) + I_y \sin(\Omega t) \\ I_y &\xrightarrow{\Omega t I_z} I_y \cos(\Omega t) - I_x \sin(\Omega t) \end{aligned}$$

If the gyromagnetic ratio of the evolving nucleus is negative (eg.  $^{15}\text{N}$ ), the evolution proceeds in the opposite direction and the sign of the sine-modulated component in the above is inverted. In the same way that an RF pulse with  $x$ -phase has no effect on  $I_x$ ,  $I_z$  is unaffected by the  $\mathcal{H}_{\text{CS}}$  Hamiltonian and therefore longitudinal magnetisation experiences no chemical shift evolution:

$$I_z \xrightarrow{\Omega t I_z} I_z$$

### c. Scalar Coupling Hamiltonian $\mathcal{H}_{J\text{-coupling}}$

Neighbouring spin-active nuclei often share a mutual connection known as scalar (or  $J$ ) coupling mediated by the electrons that form chemical bonds.<sup>[30]</sup> Scalar coupling can be active over a number of bonds with the size of the coupling typically decreasing as the number of bonds between the nuclei increases. The interaction is characterised by a *coupling constant* ( $J$ ) and is routinely used to elucidate the bonding network of the molecule or to investigate dihedral angles.<sup>[31–33]</sup> The evolution of the coupling in an  $IS$  spin system is described by the Hamiltonian:

$$\mathcal{H}_{J\text{-coupling}} = 2\pi J_{IS} I_z S_z \quad (1.8)$$

where  $J_{IS}$  is the coupling constant between the  $I$  and  $S$  spins. Note that this expression only holds for a *weakly-coupled* system, where  $J_{IS} \ll |\omega_I - \omega_S|$ . The evolution of *in-phase*  $I_x$  or  $I_y$  magnetisation during a delay  $\tau$  generates the *anti-phase*  $2I_y S_z$  and  $2I_x S_z$  terms, and vice versa:

$$\begin{aligned} I_x &\xrightarrow{2\pi J_{IS}\tau I_z S_z} I_x \cos(\pi J_{IS}\tau) + 2I_y S_z \sin(\pi J_{IS}\tau) \\ I_y &\xrightarrow{2\pi J_{IS}\tau I_z S_z} I_y \cos(\pi J_{IS}\tau) - 2I_x S_z \sin(\pi J_{IS}\tau) \\ 2I_x S_z &\xrightarrow{2\pi J_{IS}\tau I_z S_z} 2I_x S_z \cos(\pi J_{IS}\tau) + I_y \sin(\pi J_{IS}\tau) \\ 2I_y S_z &\xrightarrow{2\pi J_{IS}\tau I_z S_z} 2I_y S_z \cos(\pi J_{IS}\tau) - I_x \sin(\pi J_{IS}\tau) \end{aligned}$$

Whilst the above transformations assume a *positive* coupling constant, it is important to realise that a *negative* coupling constant will result in the same evolutions, but with the sign of the sine-modulated component inverted. As for the chemical shift evolution described by the  $\mathcal{H}_{\text{CS}}$  Hamiltonian, the scalar coupling is only active for transverse terms and therefore both equilibrium  $I_z$  magnetisation and the longitudinal two-spin  $2I_z S_z$  are unaffected:

$$I_z \xrightarrow{2\pi J_{IS}\tau I_z S_z} I_z \quad 2I_z S_z \xrightarrow{2\pi J_{IS}\tau I_z S_z} 2I_z S_z$$

## 1. Introduction

The coupling constant  $J$  is fixed for a given pair of spins and so the amount of anti-phase magnetisation generated from an in-phase term is dependent only upon the delay  $\tau$ . A delay equal to  $1/(2J)$  will therefore result in complete conversion of in-phase to anti-phase (and vice versa):

$$\begin{aligned} I_x &\xrightarrow{2\pi J_{IS} \tau I_S S_z} I_x \cos\left(\pi J_{IS} \frac{1}{2J_{IS}}\right) + 2I_y S_z \sin\left(\pi J_{IS} \frac{1}{2J_{IS}}\right) \\ &= I_x \cos\left(\frac{\pi}{2}\right) + 2I_y S_z \sin\left(\frac{\pi}{2}\right) \\ &= 2I_y S_z \end{aligned}$$

It will be shown during Section 1.3 that controlling the evolution of scalar couplings during fixed delays allows the crucial transfer of magnetisation between different nuclei in pulse sequences.

### 1.2.4 Relaxation and X-Detection

The product operator description of NMR experiments described above has an important omission: *relaxation*. Relaxation refers to the processes by which a system returns to equilibrium following a perturbation and in NMR spectroscopy, the return of the different components of the magnetisation ( $M_x$ ,  $M_y$  and  $M_z$ ) in Equation 1.4 can be described using the Bloch<sup>[7]</sup> equations:

$$\frac{d}{dt} \begin{bmatrix} M_x \\ M_y \\ M_z \end{bmatrix} = \begin{bmatrix} -R_2 & \gamma B_z & -\gamma B_y \\ -\gamma B_z & -R_2 & \gamma B_x \\ \gamma B_y & -\gamma B_x & -R_1 \end{bmatrix} \begin{bmatrix} M_x \\ M_y \\ M_z \end{bmatrix} + \begin{bmatrix} 0 \\ 0 \\ M_0 R_1 \end{bmatrix} \quad (1.9)$$

In an NMR experiment, a perturbation is the application of one or more RF pulses and the relaxation that follows is essentially restricted to two classes: *longitudinal* and *transverse*. Longitudinal relaxation is easily visualised using the vector model by considering what happens after the application of a  $180^\circ$  RF pulse, as shown in Figure 1.5a. The RF pulse inverts the equilibrium  $I_z$  magnetisation and causes it to become aligned with the  $-z$ -axis. Following this inversion, the magnetisation gradually shrinks back towards the origin and begins to return to the  $+z$ -axis. A plot of  $z$ -intensity against time reveals the process follows a single exponential function from  $-1$  to  $+1$  with rate constant  $R_1$ . The practical consequence of longitudinal relaxation is that one must wait for sufficient recovery of equilibrium  $I_z$  prior to the collection of each scan of an NMR experiment. Failure to allow the recovery of  $I_z$  between scans will result in attenuated intensity and in severe cases, complete suppression of the NMR signal. Transverse relaxation is the analogous process occurring in the  $xy$ -plane and describes the loss of coherent magnetisation (Figure 1.5b). Following a  $90^\circ$  RF pulse to  $I_z$ , the magnetisation vector becomes aligned with the  $x$ - or  $y$ -axis depending on the phase of the applied pulse. The magnetisation then begins to shrink back to the origin (whilst also precessing) until no net magnetisation remains. A plot of  $x$ - or  $y$ -intensity against time reveals the process follows a single exponential function tending towards zero with rate constant  $R_2$ .

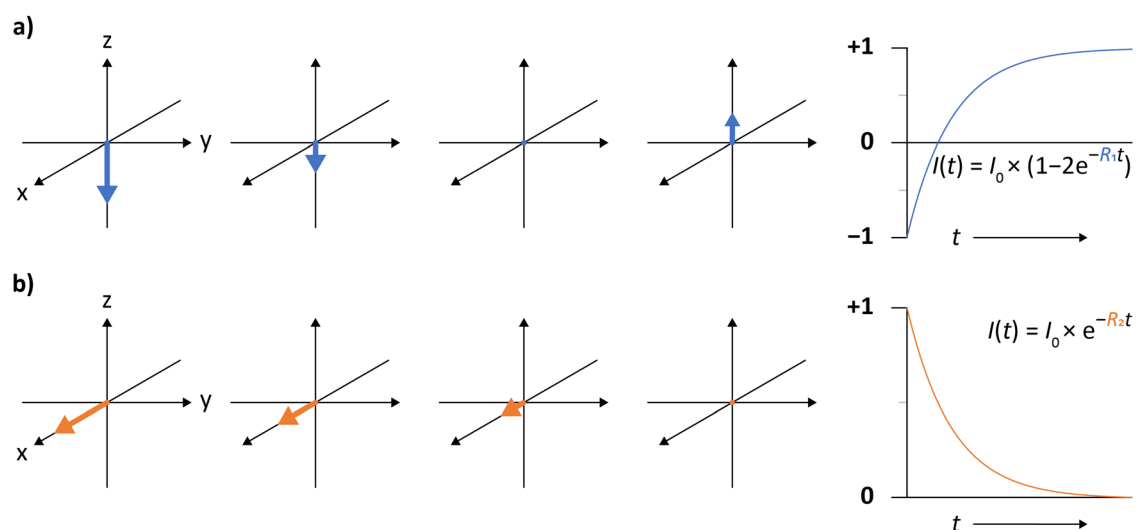


**Figure 1.5** Pictorial representation of a) longitudinal and b) transverse relaxation of magnetisation with  $\Omega = 0$ .

The practical consequence of transverse relaxation is two-fold: the first concerns the linewidth of the detected NMR signal with rapid relaxation resulting in broader peaks (see Section 1.2.5 below) whilst the second concerns magnetisation transfer. It was shown in Section 1.2.3c that the evolution of in-phase to anti-phase magnetisation depends only upon the coupling constant  $J$  and delay time  $\tau$ . However, as the magnetisation must be transverse during the evolution it will also be subject to relaxation with rate constant  $R_2$ . The relaxation of the nuclei therefore imposes a limit upon how long magnetisation can practically be kept transverse and still result in a detectable signal at the end of the experiment.

A full discussion of the theory<sup>[34]</sup> that describes the relaxation of NMR signals is beyond the scope of this thesis, but a general appreciation of the process is useful. The relaxation of a given nucleus is caused by fluctuations in the local magnetic field and for spin-half nuclei in solution-state NMR, one need only consider the two dominant mechanisms: *Chemical Shift Anisotropy* (CSA) and the *Dipole-Dipole*<sup>[35]</sup> mechanism. In the CSA mechanism, local magnetic field fluctuations are caused by the interaction of the asymmetric electron cloud of the molecule with the applied  $B_0$  field, whilst the requisite field fluctuations in the dipole-dipole mechanism are caused by the local magnetic field of a neighbouring spin within the same molecule. Both mechanisms are dependent on the relative orientation with the applied  $B_0$  field and are thus highly sensitive to the tumbling of the molecule in solution. This tumbling is characterised by the rotational correlation time ( $\tau_c$ ) of the molecule and is related to size and flexibility as well as solvent viscosity and temperature. A quantitative assessment of the relaxation of nuclei in NMR experiments is therefore routinely used to study protein motion and dynamics.<sup>[36]</sup> The dipole-dipole mechanism is additionally dependent upon the distance between the two spins ( $r$ ), an interaction that drops off quickly ( $1/r^3$ ), and their gyromagnetic ratios. The substitution of one

## 1. Introduction

half of a dipole-dipole spin pair with a low- $\gamma$  nucleus is commonly used to improve the relaxation properties of biomolecules in NMR.<sup>[37]</sup>

When considering the design and implementation of new NMR experiments, the slower relaxation of lower- $\gamma$  nuclei such as  $^{13}\text{C}$  and  $^{15}\text{N}$  has two significant consequences, one that can be considered *advantageous* and the other *disadvantageous*:

- i. **Reduced transverse relaxation** retains more signal intensity throughout periods where the magnetisation of interest is in a transverse state. This enables magnetisation transfer across coupling constants that demand longer delays for the anti-phase terms to build-up as well as allowing longer acquisition times during which the chemical shift evolution is encoded.
- ii. **Reduced longitudinal relaxation** increases the time required for the recovery of equilibrium  $I_z$  magnetisation between scans and serves to increase the overall experiment time.

However, an increased experimental time is often considered a *price worth paying* for the ability to exploit the slower relaxing nuclei for magnetisation transfer, especially when considered alongside the other advantages of X-detection such as higher digital resolution and a reduced dependence on solvent suppression.

### 1.2.5 Fourier Transform and Frequency Discrimination

As shown in Figure 1.3, the NMR signal is detected as a pair of oscillating intensities at the x- and y-axis with one component having a cosine-modulation whilst the other is sine-modulated:

$$-I_y \xrightarrow{\Omega t I_z} -I_y \cos(\Omega t) + I_x \sin(\Omega t)$$

It is convenient to express the combination of the cosine- and sine-modulated datasets as the complex time-domain *signal*  $S(t)$ :

$$S(t) = e^{i\Omega t} \times e^{-R_2 t} \quad (1.10)$$

where  $e^{i\Omega t} = \cos(\Omega t) + i \sin(\Omega t)$  and the additional  $e^{-R_2 t}$  term accounts for the transverse relaxation experienced during the detection period. This decaying time-domain signal is usually referred to as a free induction decay (FID). In order to obtain an NMR *spectrum*, the time-domain data must be converted to the frequency-domain through a mathematical process known as the Fourier transform (FT):

$$s(\omega) = \int_0^\infty S(t) e^{i2\pi\omega t} dt = \frac{R_2}{R_2^2 + (\omega - \Omega)^2} + i \frac{-(\omega - \Omega)}{R_2^2 + (\omega - \Omega)^2} \quad (1.11)$$

The complex Fourier transform is usually handled by a computer and the resulting spectral data contains both real and imaginary parts with the real part providing the desired absorption mode peaks centred at the offset  $\Omega$ .

The transmitter frequency, from which the measurement of the offset is made, is usually placed in the centre of the spectrum and both positive and negative values of  $\Omega$  are to be expected. There is therefore a need to discriminate a frequency at  $+\Omega$  from one at  $-\Omega$  and to do so requires that *both* the cosine- and sine-modulated intensities are recorded. Figure 1.6a shows the spectra resulting from Fourier transformations of only **cosine-modulated** data describing a single resonance at an offset frequency of  $\pm 50$  Hz. As  $\cos(x) = \cos(-x)$ , the frequency-domain data from both FIDs is identical with each spectrum contain a peak at  $\pm 50$  Hz. Similarly, Figure 1.6b shows the spectra resulting from the Fourier transformation of only **sine-modulated** data describing the same frequencies. As  $\sin(x) = -\sin(-x)$ , the frequency-domain data from both FIDs each contains two peaks that differ only in sign. As the absolute phase of the receiver coil is essentially arbitrary, one cannot be sure of the true frequency of a signal based on the sine-modulated data alone. Figure 1.6c shows the spectra resulting from the **complex** time-domain signal that contains both the cosine- and sine-modulated components as described above. For each of the  $\pm 50$  Hz signals, a single peak is returned by the Fourier transform that accurately reports the underlying frequency.

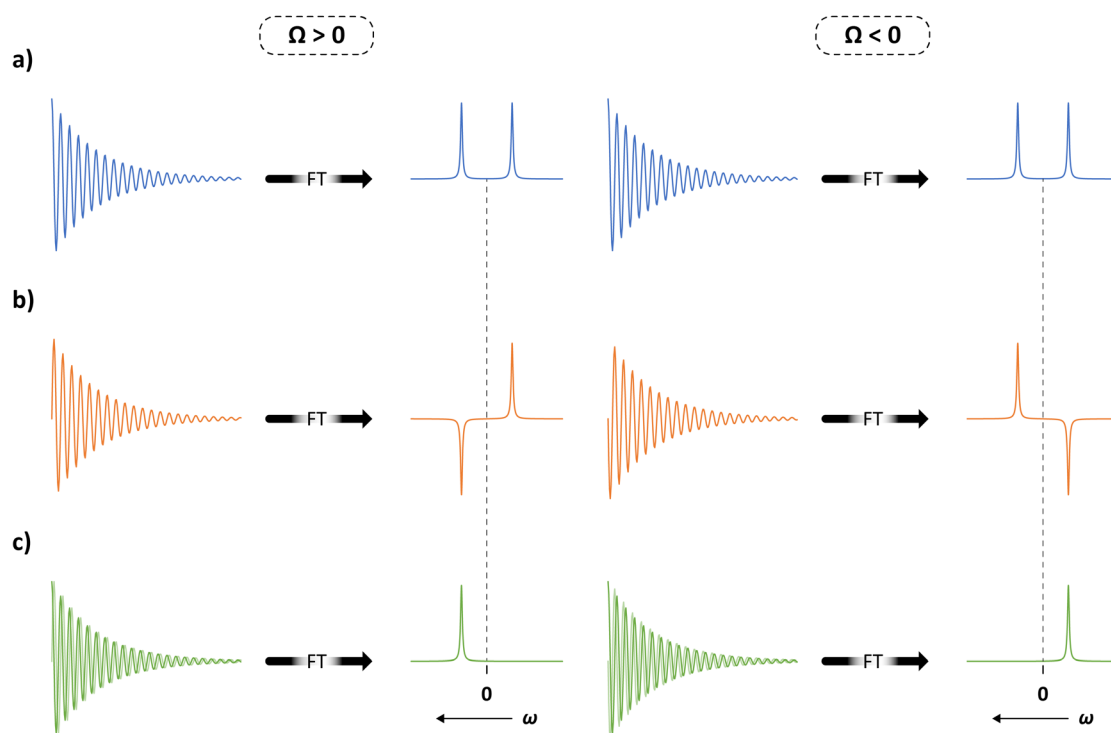


**Figure 1.6** Simulated FIDs and spectra following Fourier transformation of a) only **cosine-modulated** time-domain data, b) only **sine-modulated** time-domain data and c) **complex** time-domain data containing both the cosine- and sine-modulated components. Complex time-domain data is required to obtain both the sign and frequency of the signal. Simulations were performed using Python and used values of  $\pm 50$  Hz,  $10 \text{ s}^{-1}$  and  $0.4 \text{ s}$  for  $\Omega$ ,  $R_2$  and  $t$  respectively.

### 1.3 Pulse Sequence Building Blocks

The implementation of any NMR experiment requires a sequence of RF pulses and delays be applied to the sample in a precisely timed manner. The success or failure of the so-called *pulse sequence* depends upon the magnetisation being manipulated such that only desired coherences exist at the right moment and that any subsequent evolutions only proceed under the chosen Hamiltonian during the delay(s). Fortunately, when designing a new experiment or seeking to understand an existing one, the pulse sequence can usually be broken down into several discrete *blocks* that each perform a specific function and can be described using the product operator formalism introduced in the previous section. The following section will introduce some of the most common building blocks encountered in NMR spectroscopy and how they can be linked together to control the state of the magnetisation present during detection. Each of the building blocks introduced will feature heavily in the novel experiments discussed in the following Chapters.

#### 1.3.1 The Spin-Echo

Following the initial excitation of equilibrium magnetisation, the most common pulse sequence element found in NMR experiments is the spin echo.<sup>[38]</sup> The spin echo is used to refocus the chemical shift and/or scalar coupling evolutions during a part of the pulse sequence, usually to allow the evolution of something else, and consists of a  $180^\circ$  RF pulse applied to transverse magnetisation between two equal delays. Figure 1.7 shows the three variations of the spin echo for a heteronuclear  $IS$  spin system that differ only by which spin the  $180^\circ$  (often referred to as *refocussing*) pulse is applied to. In the pulse sequence notation used throughout this thesis,  $90^\circ$  and  $180^\circ$  RF pulses are indicated by the narrow and wide black bars respectively and are applied at maximum power with  $x$ -phase unless specified otherwise.

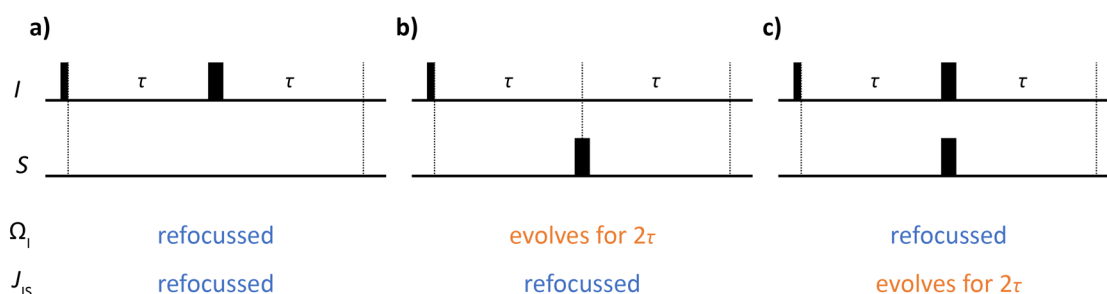


**Figure 1.7** Pulse sequence diagrams for the heteronuclear spin echo experiments described in the main text. The configuration of the  $180^\circ$  RF pulse(s) determines which chemical shift and scalar coupling evolutions are refocussed during the delays: a) a  $180^\circ I_x$  pulse refocusses both the chemical shift of the  $I$  spin and  $IS$  scalar coupling; b) a  $180^\circ S_x$  pulse allows the chemical shift of  $I$  to evolve whilst refocussing the scalar coupling and c) simultaneous  $180^\circ I_x$  and  $S_x$  pulses refocus the chemical shift and allows only the scalar coupling to evolve. The absence of any  $180^\circ$  pulse allows both the chemical shift and scalar coupling to evolve throughout the sequence.

Each spin echo sequence begins with the excitement of equilibrium  $I_z$  magnetisation:

$$I_z \xrightarrow{90^\circ I_x} -I_y$$

Following the  $90^\circ$  pulse, the transverse  $I_y$  magnetisation evolves during the first delay  $\tau$  under both the chemical shift and scalar coupling Hamiltonians:

$$\mathcal{H} = \Omega I_z + 2\pi J_{IS} I_z S_z$$

Note that the offset of the  $S$  spin does not evolve during the delay owing to the fact that it remains as  $S_z$  following the RF pulse to  $I_z$ . The chemical shift and scalar coupling parts of the Hamiltonian can be treated separately:

$$\begin{aligned} -I_y &\xrightarrow{\Omega\tau I_z} -I_y \cos(\Omega\tau) + I_x \sin(\Omega\tau) \\ &\xrightarrow{2\pi J_{IS}\tau I_z S_z} -I_y \cos(\Omega\tau)\cos(\pi J_{IS}\tau) + 2I_x S_z \cos(\Omega\tau)\sin(\pi J_{IS}\tau) \\ &\quad + I_x \sin(\Omega\tau)\cos(\pi J_{IS}\tau) + 2I_y S_z \sin(\Omega\tau)\sin(\pi J_{IS}\tau) \end{aligned}$$

The three spin echo sequences diverge at this point and subsequent evolution of the magnetisation depends upon the application of the  $180^\circ$  refocussing pulse.

### Spin Echo 1: $180^\circ I_x$ Pulse

For the spin echo experiment shown in Figure 1.7a, the  $180^\circ$  refocussing pulse is applied to the  $I$ -spin causing the inversion of only the  $I_y$  and  $2I_y S_z$  terms:

$$\begin{aligned} &\xrightarrow{180^\circ I_x} I_y \cos(\Omega\tau)\cos(\pi J_{IS}\tau) + 2I_x S_z \cos(\Omega\tau)\sin(\pi J_{IS}\tau) \\ &\quad + I_x \sin(\Omega\tau)\cos(\pi J_{IS}\tau) - 2I_y S_z \sin(\Omega\tau)\sin(\pi J_{IS}\tau) \end{aligned}$$

During the second delay  $\tau$ , chemical shift evolution leads to:

$$\begin{aligned} &\xrightarrow{\Omega\tau I_z} I_y \cos^2(\Omega\tau)\cos(\pi J_{IS}\tau) - I_x \cos(\Omega\tau)\cos(\pi J_{IS}\tau)\sin(\Omega\tau) \\ &\quad + 2I_x S_z \cos^2(\Omega\tau)\sin(\pi J_{IS}\tau) + 2I_y S_z \cos(\Omega\tau)\sin(\pi J_{IS}\tau)\sin(\Omega\tau) \\ &\quad + I_x \sin(\Omega\tau)\cos(\pi J_{IS}\tau)\cos(\Omega\tau) + I_y \sin^2(\Omega\tau)\cos(\pi J_{IS}\tau) \\ &\quad - 2I_y S_z \sin(\Omega\tau)\sin(\pi J_{IS}\tau)\cos(\Omega\tau) + 2I_x S_z \sin^2(\Omega\tau)\sin(\pi J_{IS}\tau) \end{aligned}$$

It is prudent to remove the terms that have already cancelled each other out (in grey, above) before considering the evolution due to the  $IS$  scalar coupling:

$$\begin{aligned} &\xrightarrow{2\pi J_{IS}\tau I_z S_z} I_y \cos^2(\Omega\tau)\cos^2(\pi J_{IS}\tau) - 2I_x S_z \cos^2(\Omega\tau)\cos(\pi J_{IS}\tau)\sin(\pi J_{IS}\tau) \\ &\quad + 2I_x S_z \cos^2(\Omega\tau)\sin(\pi J_{IS}\tau)\cos(\pi J_{IS}\tau) + I_y \cos^2(\Omega\tau)\sin^2(\pi J_{IS}\tau) \\ &\quad + I_y \sin^2(\Omega\tau)\cos^2(\pi J_{IS}\tau) - 2I_x S_z \sin^2(\Omega\tau)\cos(\pi J_{IS}\tau)\sin(\pi J_{IS}\tau) \\ &\quad + 2I_x S_z \sin^2(\Omega\tau)\sin(\pi J_{IS}\tau)\cos(\pi J_{IS}\tau) + I_y \sin^2(\Omega\tau)\sin^2(\pi J_{IS}\tau) \end{aligned}$$

## 1. Introduction

After removal of the cancelling terms, factorising the remaining expression and using the identity:<sup>[39]</sup>

$$\cos^2\theta + \sin^2\theta \equiv 1 \quad (1.12)$$

one can see that both the chemical shift and scalar coupling evolutions have been completely refocused and the only net effect of the spin echo sequence was the action of the  $180^\circ I_x$  pulse to invert the initial  $-I_y$  magnetisation:

$$\begin{aligned} -I_y \xrightarrow{\text{Spin Echo 1}} I_y & \left( [\cos^2(\Omega\tau) + \sin^2(\Omega\tau)] [\cos^2(\pi J_{IS}\tau) + \sin^2(\pi J_{IS}\tau)] \right) \\ & = I_y \end{aligned} \quad (1.13)$$

### Spin Echo 2: $180^\circ S_x$ Pulse

For the spin echo experiment shown in Figure 1.7b, the  $180^\circ$  refocussing pulse is applied to the S-spin causing the inversion of only the  $2I_x S_z$  and  $2I_y S_z$  terms:

$$\begin{aligned} \xrightarrow{180^\circ S_x} & -I_y \cos(\Omega\tau) \cos(\pi J_{IS}\tau) - 2I_x S_z \cos(\Omega\tau) \sin(\pi J_{IS}\tau) \\ & + I_x \sin(\Omega\tau) \cos(\pi J_{IS}\tau) - 2I_y S_z \sin(\Omega\tau) \sin(\pi J_{IS}\tau) \end{aligned}$$

During the second delay  $\tau$ , chemical shift evolution leads to:

$$\begin{aligned} \xrightarrow{\Omega\tau I_z} & -I_y \cos^2(\Omega\tau) \cos(\pi J_{IS}\tau) + I_x \cos(\Omega\tau) \cos(\pi J_{IS}\tau) \sin(\Omega\tau) \\ & - 2I_x S_z \cos^2(\Omega\tau) \sin(\pi J_{IS}\tau) - 2I_y S_z \cos(\Omega\tau) \sin(\pi J_{IS}\tau) \sin(\Omega\tau) \\ & + I_x \sin(\Omega\tau) \cos(\pi J_{IS}\tau) \cos(\Omega\tau) + I_y \sin^2(\Omega\tau) \cos(\pi J_{IS}\tau) \\ & - 2I_y S_z \sin(\Omega\tau) \sin(\pi J_{IS}\tau) \cos(\Omega\tau) + 2I_x S_z \sin^2(\Omega\tau) \sin(\pi J_{IS}\tau) \end{aligned}$$

The subsequent evolution due to the  $IS$  scalar coupling results in:

$$\begin{aligned} \xrightarrow{2\pi J_{IS}\tau I_z S_z} & -I_y \cos^2(\Omega\tau) \cos^2(\pi J_{IS}\tau) + 2I_x S_z \cos^2(\Omega\tau) \cos(\pi J_{IS}\tau) \sin(\pi J_{IS}\tau) \\ & + I_x \cos(\Omega\tau) \cos^2(\pi J_{IS}\tau) \sin(\Omega\tau) + 2I_y S_z \cos(\Omega\tau) \cos(\pi J_{IS}\tau) \sin(\Omega\tau) \sin(\pi J_{IS}\tau) \\ & - 2I_x S_z \cos^2(\Omega\tau) \sin(\pi J_{IS}\tau) \cos(\pi J_{IS}\tau) - I_y \cos^2(\Omega\tau) \sin^2(\pi J_{IS}\tau) \\ & - 2I_y S_z \cos(\Omega\tau) \sin(\pi J_{IS}\tau) \sin(\Omega\tau) \cos(\pi J_{IS}\tau) + I_x \cos(\Omega\tau) \sin^2(\pi J_{IS}\tau) \sin(\Omega\tau) \\ & + I_x \sin(\Omega\tau) \cos^2(\pi J_{IS}\tau) \cos(\Omega\tau) + 2I_y S_z \sin(\Omega\tau) \cos(\pi J_{IS}\tau) \cos(\Omega\tau) \sin(\pi J_{IS}\tau) \\ & + I_y \sin^2(\Omega\tau) \cos^2(\pi J_{IS}\tau) - 2I_x S_z \sin^2(\Omega\tau) \cos(\pi J_{IS}\tau) \sin(\pi J_{IS}\tau) \\ & - 2I_y S_z \sin(\Omega\tau) \sin(\pi J_{IS}\tau) \cos(\Omega\tau) \cos(\pi J_{IS}\tau) + I_x \sin(\Omega\tau) \sin^2(\pi J_{IS}\tau) \cos(\Omega\tau) \\ & + 2I_x S_z \sin^2(\Omega\tau) \sin(\pi J_{IS}\tau) \cos(\pi J_{IS}\tau) + I_y \sin^2(\Omega\tau) \sin^2(\pi J_{IS}\tau) \end{aligned}$$

After removal of the cancelling terms, factorising the  $I_y$  terms and using Equation 1.12 and the identity:<sup>[39]</sup>

$$\cos^2\theta - \sin^2\theta \equiv \cos 2\theta \quad (1.14)$$

the expression for  $I_y$  simplifies to:

$$\begin{aligned} &= -I_y \left( [\cos^2(\Omega\tau) - \sin^2(\Omega\tau)] [\cos^2(\pi J_{IS}\tau) + \sin^2(\pi J_{IS}\tau)] \right) \\ &= -I_y \cos(\Omega 2\tau) \end{aligned}$$

Similarly, collecting the  $I_y$  terms and using the identity:

$$2\cos\theta\sin\theta \equiv \sin 2\theta \quad (1.15)$$

the expression for  $I_x$  simplifies to:

$$\begin{aligned} &= I_x \cos(\Omega\tau)\sin(\Omega\tau) \left( \cos^2(\pi J_{IS}\tau) + \sin^2(\pi J_{IS}\tau) + \cos^2(\pi J_{IS}\tau) + \sin^2(\pi J_{IS}\tau) \right) \\ &= I_x 2\cos(\Omega\tau)\sin(\Omega\tau) \\ &= I_x \sin(\Omega 2\tau) \end{aligned}$$

Therefore, the only evolution over the spin echo sequence corresponds to the evolution of the  $I$ -spin chemical shift for a period equal to  $2\tau$  whilst the  $IS$  scalar coupling is refocussed:

$$-I_y \xrightarrow{\text{Spin Echo 2}} -I_y \cos(\Omega 2\tau) + I_x \sin(\Omega 2\tau) \quad (1.16)$$

Unlike the previous spin echo, the sign of the magnetisation is not inverted during this sequence as there was no  $180^\circ$  pulse applied to the  $I$ -spin.

### Spin Echo 3: Simultaneous $180^\circ I_x$ and $S_x$ Pulses

For the spin echo experiment shown in Figure 1.7c, the  $180^\circ$  refocussing pulse is applied to both  $I$ - and  $S$ -spins: the  $I_y$  magnetisation is inverted by the  $180^\circ I_x$  pulse; the  $2I_x S_z$  term is inverted by the  $180^\circ S_x$  pulse; the  $I_x$  magnetisation is unaffected by either  $180^\circ$  pulse and the  $2I_y S_z$  is affected by both and thus experiences no net inversion. Therefore, following the simultaneous  $180^\circ I_x$  and  $S_x$  pulses, the state of the system is described by:

$$\begin{aligned} \xrightarrow{180^\circ I_x + S_x} & I_y \cos(\Omega\tau)\cos(\pi J_{IS}\tau) - 2I_x S_z \cos(\Omega\tau)\sin(\pi J_{IS}\tau) \\ & + I_x \sin(\Omega\tau)\cos(\pi J_{IS}\tau) + 2I_y S_z \sin(\Omega\tau)\sin(\pi J_{IS}\tau) \end{aligned}$$

During the second delay  $\tau$ , chemical shift evolution leads to:

$$\begin{aligned} \xrightarrow{\Omega\tau I_z} & I_y \cos^2(\Omega\tau)\cos(\pi J_{IS}\tau) - I_x \cos(\Omega\tau)\cos(\pi J_{IS}\tau)\sin(\Omega\tau) \\ & - 2I_x S_z \cos^2(\Omega\tau)\sin(\pi J_{IS}\tau) - 2I_y S_z \cos(\Omega\tau)\sin(\pi J_{IS}\tau)\sin(\Omega\tau) \\ & + I_x \sin(\Omega\tau)\cos(\pi J_{IS}\tau)\cos(\Omega\tau) + I_y \sin^2(\Omega\tau)\cos(\pi J_{IS}\tau) \\ & + 2I_y S_z \sin(\Omega\tau)\sin(\pi J_{IS}\tau)\cos(\Omega\tau) - 2I_x S_z \sin^2(\Omega\tau)\sin(\pi J_{IS}\tau) \end{aligned}$$

## 1. Introduction

The subsequent evolution due to the  $IS$  scalar coupling results in:

$$\begin{aligned} \xrightarrow{2\pi J_{IS} I_z S_z} & I_y \cos^2(\Omega\tau) \cos^2(\pi J_{IS}\tau) - 2I_x S_z \cos^2(\Omega\tau) \cos(\pi J_{IS}\tau) \sin(\pi J_{IS}\tau) \\ & - 2I_x S_z \cos^2(\Omega\tau) \sin(\pi J_{IS}\tau) \cos(\pi J_{IS}\tau) - I_y \cos^2(\Omega\tau) \sin^2(\pi J_{IS}\tau) \\ & + I_y \sin^2(\Omega\tau) \cos^2(\pi J_{IS}\tau) - 2I_x S_z \sin^2(\Omega\tau) \cos(\pi J_{IS}\tau) \sin(\pi J_{IS}\tau) \\ & - 2I_x S_z \sin^2(\Omega\tau) \sin(\pi J_{IS}\tau) \cos(\pi J_{IS}\tau) - I_y \sin^2(\Omega\tau) \sin^2(\pi J_{IS}\tau) \end{aligned}$$

Collection of the  $I_y$  terms and using Equations 1.12 and 1.14, the expression for  $I_y$  simplifies to:

$$\begin{aligned} &= I_y \left( [\cos^2(\Omega\tau) + \sin^2(\Omega\tau)] [\cos^2(\pi J_{IS}\tau) - \sin^2(\pi J_{IS}\tau)] \right) \\ &= I_y \cos(\pi J_{IS}2\tau) \end{aligned}$$

Similarly, collecting the  $2I_x S_y$  terms and using Equation 1.15, the expression for  $I_x$  simplifies to:

$$\begin{aligned} &= -2I_x S_z \cos(\pi J_{IS}\tau) \sin(\pi J_{IS}\tau) \left( \cos^2(\Omega\tau) + \cos^2(\Omega\tau) + \sin^2(\Omega\tau) + \sin^2(\Omega\tau) \right) \\ &= -2I_x S_z 2\cos(\pi J_{IS}\tau) \sin(\pi J_{IS}\tau) \\ &= -2I_x S_z \sin(\pi J_{IS}2\tau) \end{aligned}$$

Therefore, the only evolution over the spin echo sequence corresponds to the evolution of the  $IS$  scalar coupling for a period equal to  $2\tau$  whilst the  $I$ -spin chemical shift is refocussed. It is important to note that as for Spin Echo 1, the action of the  $180^\circ$  pulse also serves to invert the signs of the in-phase and anti-phase components:

$$-I_y \xrightarrow{\text{Spin Echo 3}} I_y \cos(\pi J_{IS}2\tau) - 2I_x S_z \sin(\pi J_{IS}2\tau) \quad (1.17)$$

The spin echoes described above will be used extensively when discussing the pulse sequences developed in this thesis and for clarity, only the evolutions that result in a change in the magnetisation at the end of the delay(s) will be considered. In summary, during a spin echo element applied to an  $IS$  spin system where the  $I$ -magnetisation is transverse:

- i.* A  $180^\circ$  refocussing pulse applied to only the  $I$ -spin will refocus both the chemical shift and  $IS$  scalar coupling. Only the effect of the pulse itself need be considered.
- ii.* A  $180^\circ$  refocussing pulse applied to only the  $S$ -spin will refocus the  $IS$  scalar coupling and allow the  $I$ -spin chemical shift to evolve. No inversion of  $I$ -magnetisation occurs.
- iii.*  $180^\circ$  refocussing pulses applied simultaneously to the  $I$ - and  $S$ -spins refocus the  $I$ -spin chemical shift and allow the scalar coupling to evolve. The effect of the pulses on the sign of the operators must also be considered.

It is important to note that in order for the refocussing to be effective, the duration of the delays either side of the refocussing pulse(s) must be equal. However, asymmetric delays can be

implemented to selectively evolve different scalar couplings and/or chemical shifts in suitable spin systems. This is discussed in more detail during the development of the pulse sequences for measuring hydrogen exchange in Chapters 3 and 5.

### 1.3.2 INEPT

The evolution of the  $IS$  scalar coupling during the Spin Echo 3 sequence described above forms the basis of the most commonly used magnetisation transfer methods: the INEPT<sup>[40]</sup> block. The Insensitive Nuclei Enhanced by Polarisation Transfer sequence consists of the Spin Echo 3 (Figure 1.7c) followed by simultaneous  $90^\circ I_y$  and  $S_x$  pulses and is used to increase the generation of low- $\gamma$  magnetisation by using the greater polarisation afforded by a higher- $\gamma$  nucleus. For example, an  $IS$  spin-system at equilibrium can be described as:

$$aI_z + bS_z \quad (1.18)$$

where  $a$  and  $b$  are coefficients that stem from the gyromagnetic ratios of  $I$  and  $S$ . For an  $IS$  system where  $I = {}^1\text{H}$  and  $S = {}^{13}\text{C}$ ,  $\gamma_{\text{H}}/\gamma_{\text{C}} \approx 4$  and therefore at equilibrium the approximate state of the system is:

$$4H_z + C_z$$

If one wished to generate  ${}^{13}\text{C}$  magnetisation from this spin-system, a simple  $90^\circ C_x$  pulse would be sufficient:

$$C_z \xrightarrow{90^\circ C_x} -C_y$$

However, the lower gyromagnetic ratio of the  ${}^{13}\text{C}$  ultimately results in lower signal intensity when compared to a higher- $\gamma$  nucleus such as  ${}^1\text{H}$  or  ${}^{19}\text{F}$ . The INEPT sequence provides an alternate route to transverse  ${}^{13}\text{C}$  magnetisation that retains the polarisation coefficient initially associated with the  ${}^1\text{H}$  nucleus. Following the application of Spin Echo 3 to the  ${}^1\text{H}$ - ${}^{13}\text{C}$  spin system above, the magnetisation is proportional to:

$$4H_z + C_z \xrightarrow{\text{Spin Echo 3, } \tau = \frac{1}{4J_{\text{HC}}}} -4[2H_x C_z] - C_z$$

The INEPT sequence is completed by the application of  $90^\circ$  RF pulses to both spins:

$$\begin{aligned} &\xrightarrow{90^\circ H_y} 4[2H_z C_z] - C_z \\ &\xrightarrow{90^\circ C_x} -4[2H_z C_y] + C_y \end{aligned}$$

The  $90^\circ H_y$  pulse converts the anti-phase  ${}^1\text{H}$  magnetisation to the longitudinal two-spin order  $2H_z C_z$  before the  $90^\circ C_x$  pulse generates the anti-phase  $2H_z C_y$ . Although anti-phase in nature, the  $2H_z C_y$  term represents  ${}^{13}\text{C}$  magnetisation that would evolve according to the chemical shift

## 1. Introduction

Hamiltonian with the same frequency as the in-phase  $C_y$ . Crucially, the intensity of the anti-phase magnetisation is four-fold greater than the directly excited in-phase magnetisation and will result in a greater signal to noise ratio in the final spectrum.

The *extra*  $C_y$  magnetisation resulting from the equilibrium  $C_z$  can be suppressed using a simple two-step phase cycle to yield pure anti-phase magnetisation:

$$\text{Step one: } 4H_z + C_z \xrightarrow{\text{Spin Echo 3, } 90^\circ H_y, 90^\circ C_x} -4[2H_z C_y] + C_y$$

$$\text{Step two: } 4H_z + C_z \xrightarrow{\text{Spin Echo 3, } 90^\circ H_{-y}, 90^\circ C_x} 4[2H_z C_y] + C_y$$

$$\text{Step one} - \text{Step two} = -8[2H_z C_y]$$

### 1.3.3 Indirect Chemical Shift Evolution

In a typical one-dimensional NMR experiment, the chemical shifts of the excited nuclei are detected as an FID as a function of time and subjected to Fourier transformation as shown in Figure 1.6. This is known as *direct detection* and results in a one-dimensional NMR spectrum where each signal is characterised by a single frequency. If two different nuclei in the analyte happen to have the same chemical shift, then the resulting peaks will be overlapped in the transformed spectrum. The likelihood of signal overlap dramatically increases with molecular size and particularly in biological NMR spectroscopy, a second (or even third) chemical shift dimension is often required to resolve the individual peaks.

In order to record a second frequency dimension, one needs to have a suitable delay in the pulse sequence during which an additional chemical shift evolution can be encoded. The spin echo sequence described in Section 1.3.1 and Figure 1.7b (Equation 1.16) provides a means of incorporating such a delay:

$$-I_y \xrightarrow{\text{Spin Echo 2, } \tau = \frac{t_1}{2}} -I_y \cos(\Omega t_1) + I_x \sin(\Omega t_1)$$

In contrast to the directly detected dimension where the evolution is sampled repeatedly as a function of time, the delay  $t_1$  is fixed for each spin echo and therefore results in only a single point describing the second chemical shift. In order to construct an FID that describes the additional chemical shift evolution, the experiment must be repeated several times with increasing values of  $t_1$ . This results in an interferogram with the two chemical shift evolutions encoded in separate dimensions (Figure 1.8a). The directly detected dimension is now labelled  $t_2$  whilst the dimension constructed from the sequential experiments conducted with increasing  $t_1$  delays is referred to as the *indirect* dimension.

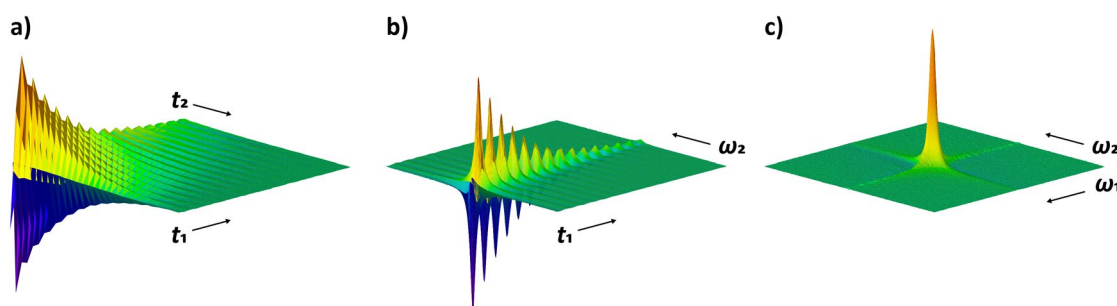


**Figure 1.8** The inclusion of a second delay for chemical shift evolution allows the collection of two-dimensional datasets. a) Chemical shift evolution during two delays (labelled  $t_1$  and  $t_2$ ) results in a two-dimensional interferogram. b) Fourier transformation with respect to the direct dimension ( $t_2$ ) delivers a frequency dimension ( $\omega_2$ ) in which the modulation due to the chemical shift during  $t_1$  is easily observed. c) A second Fourier transformation, this time with respect to the indirect dimension ( $t_1$ ), results in a cross peak ( $\omega_1, \omega_2$ ) centred at the offset frequencies in both dimensions. The data shown was recorded on a sample of  $\text{CHCl}_3$  at 16.1 T using the COSY<sup>[11]</sup> pulse sequence where both chemical shift dimensions report the  $^1\text{H}$  frequency.

### 1.3.4 Composite Pulse Decoupling

Exquisite control over which scalar coupling pathways evolve and when is at the heart of all NMR spectroscopy and there are often times when one wishes to suppress a particular interaction. This section will briefly introduce the concept of heteronuclear Composite Pulse Decoupling (CPD), a powerful technique that is routinely used to simplify the appearance of NMR spectra.

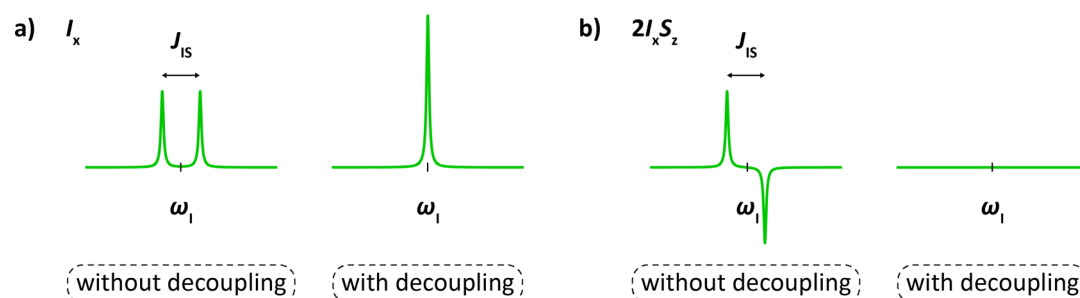


**Figure 1.9** The effect of a decoupling field applied to the  $S$ -spin of an  $IS$  spin-system on a) in-phase and b) anti-phase  $I$ -magnetisation.

In order to record the chemical shift of a nucleus, the magnetisation of interest must be transverse as otherwise there is no evolution under the  $\mathcal{H}_{CS}$  Hamiltonian. For the indirect chemical shift evolution described above, the spin echo is designed such that *only* the chemical shift evolves during the incremented delay  $t_1$ . This is not the case during the directly detected FID where the evolution of the  $J_{IS}$  scalar coupling with the chemical shift results in a splitting of the detected  $I_{xy}$  magnetisation (Figure 1.9a, left). The origin of the peak splitting of the  $I$ -spin signal is easily understood by considering the two states of the coupled  $S$ -spin: the first component of the doublet corresponds to the  $E_\alpha$  state and the second component to the  $E_\beta$  state. The doublet is centred at the  $I$ -spin frequency with the magnitude of the peak splitting equal to the coupling constant  $J_{IS}$ . The practical consequence of this peak splitting is two-fold: a doubling of the number of signals in the spectrum and the resultant halving of the absolute

## 1. Introduction

intensity of each. Both of these consequences are considered to be problematic to the spectroscopist and as such a lot of work has focussed on the development of *decoupling* strategies.

A spin echo where the  $180^\circ$  pulse is applied only to the *passive* spin (Figure 1.7b) effectively refocuses the scalar coupling whilst allowing the chemical shift evolution to continue. Accordingly, composite pulse decoupling can be thought of a series of very tightly spaced spin echoes applied during the detection of the  $I_{xy}$  magnetisation. The effect of an *S*-spin decoupling field applied during the detection of the *I*-spin is the collapse of the doublet to a singlet, thereby simplifying the spectrum and restoring maximum signal intensity. It is important to note that the desired decoupling is only achieved when the field is applied to in-phase magnetisation. Figure 1.9b shows the effect a decoupling field has on anti-phase magnetisation: the positive and negative components of the anti-phase doublet cancel each other out and the entire signal is suppressed. Numerous decoupling sequences have been developed over the years that each seek to optimise the effective bandwidth whilst simultaneously reducing spectral artefacts and the presence of unwanted side-bands. Amongst the most common are the WALTZ<sup>[41-43]</sup> and GARP<sup>[44]</sup> families that will be used to decouple  $^1\text{H}/^2\text{H}$  and  $^{15}\text{N}$  scalar couplings with  $^{13}\text{C}$  in the work that follows.

### 1.3.5 HSQC Experiment

The building blocks described thus far represent only a fraction of those available to the NMR spectroscopist, but are sufficient to implement one of the most common experiments applied to the study of biomolecules: the HSQC.<sup>[45]</sup> The Heteronuclear Single Quantum Coherence (HSQC) experiment is a two-dimensional spectrum that reports the correlated chemical shifts of an *IS* spin pair where *I* is usually a high- $\gamma$  nucleus such as  $^1\text{H}$  and *S* is a low- $\gamma$  nucleus such as  $^{13}\text{C}$  or  $^{15}\text{N}$ .<sup>[46,47]</sup> As described below, the pulse sequence begins and ends with INEPT transfers and is thus often referred to as an *inverse* or *out-and-back* type experiment.

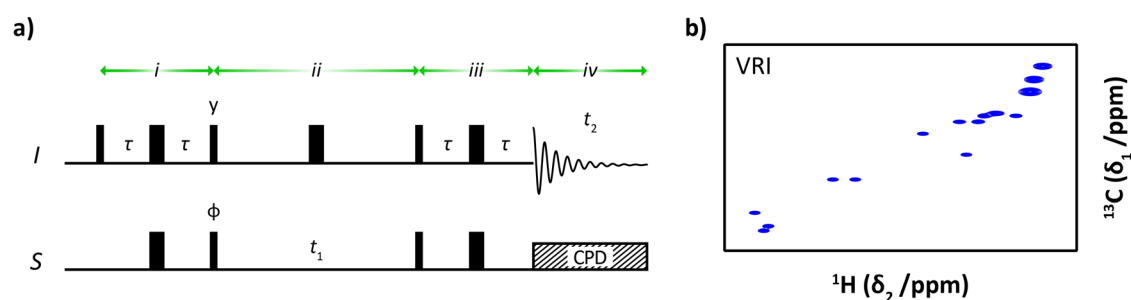


**Figure 1.10** a) The HSQC pulse sequence. The phase of the pulse marked with  $\phi$  is used to select either the cosine- or sine-modulated component of *S*-spin chemical shift for transfer back to the *I*-spin. b) Predicted  $^1\text{H}$ - $^{13}\text{C}$  HSQC spectrum of the tri-peptide Val-Arg-Ile (MestReNova 14.1, Mestrelab 2019).

The basic HSQC pulse sequence is shown in Figure 1.10a and consists of four parts:

- i. **INEPT**: Makes use of the higher- $\gamma$   $I$ -spin polarisation to generate anti-phase  $2I_zS_y$  magnetisation with high intensity as discussed in Section 1.3.2:

$$I_z \xrightarrow{\text{INEPT}, \phi = x} -2I_zS_y$$

- ii. **Indirect Chemical shift evolution**: The chemical shift of the  $S$ -spin is encoded during an incremented evolution period as discussed in Section 1.3.3.

$$-2I_zS_y \xrightarrow{\Omega_S t_1 S_z} -2I_zS_y \cos(\Omega_S t_1) + 2I_zS_x \sin(\Omega_S t_1)$$

- iii. **retro-INEPT**: a second INEPT block transfers the anti-phase  $S$ -spin magnetisation (now modulated according to the  $S$ -spin chemical shift evolution during  $t_1$ ) back to the higher- $\gamma$   $I$ -spin.

$$-2I_zS_y \cos(\Omega_S t_1) \xrightarrow{\text{retro-INEPT}} -I_x \cos(\Omega_S t_1)$$

- iv. **Detection**: Quadrature detection of the  $I$ -spin chemical shift with composite pulse decoupling of the  $S$ -spin.

$$-I_x \cos(\Omega_S t_1) \xrightarrow{\Omega_I t_2 I_z} -I_x \cos(\Omega_S t_1) \cos(\Omega_I t_2) - I_y \cos(\Omega_S t_1) \sin(\Omega_I t_2)$$

In Section 1.2.5 it was shown that *both* the cosine- and sine-modulated components of the chemical shift evolution are required for the complex Fourier transformation to correctly determine the sign of the offset frequency  $\Omega$ . However, as the cosine- and sine-modulated components of the  $S$ -spin chemical shift evolution are orthogonal, the retro-INEPT block can only select one over the other. This is easily seen when analysing the retro-INEPT block in more detail below. Following the indirect chemical shift evolution period, the anti-phase  $S$ -spin magnetisation has evolved according to the offset frequency  $\Omega_S$ :

$$\xrightarrow{\Omega_S t_1 S_z} -2I_zS_y \cos(\Omega_S t_1) + 2I_zS_x \sin(\Omega_S t_1)$$

The retro-INEPT block begins with  $90^\circ$   $x$ -pulses applied to both the  $I$ - and  $S$ -spins:

$$\xrightarrow{90^\circ I_x} 2I_yS_y \cos(\Omega_S t_1) - 2I_yS_x \sin(\Omega_S t_1)$$

$$\xrightarrow{90^\circ S_x} 2I_yS_z \cos(\Omega_S t_1) - 2I_yS_x \sin(\Omega_S t_1)$$

after which the **cosine-modulated** component is anti-phase  $I$ -spin magnetisation and the sine-modulated component has been converted into unobservable multiple-quantum (MQ) magnetisation. During the spin echo that follows, the **cosine-modulated** anti-phase  $I$ -spin

## 1. Introduction

magnetisation is refocussed to in-phase whilst the **sine-modulated** MQ magnetisation does not evolve under the scalar coupling Hamiltonian and remains unobservable:

$$\xrightarrow{2\pi I_S t I_Z S_Z, 180^\circ (I_X + S_X)} -I_X \cos(\Omega_S t_1) + 2I_Y S_X \sin(\Omega_S t_1)$$

In order to access the **sine-modulated** component of the *S*-spin chemical shift required for the complex Fourier transform, the experiment must be repeated using a  $90^\circ S_y$  pulse in place of the first  $90^\circ S_x$  pulse (identified by  $\phi$  in Figure 1.10a). The use of a *y*-pulse during the first INEPT block results in a phase shift of the resulting anti-phase magnetisation:

$$I_Z \xrightarrow{\text{INEPT, } \phi = y} 2I_Z S_X$$

During the subsequent indirect evolution period, the **cosine-** and **sine-modulated** components evolve according to the offset frequency  $\Omega_S$  as usual:

$$\xrightarrow{\Omega_S t_1 S_Z} 2I_Z S_X \cos(\Omega_S t_1) + 2I_Z S_Y \sin(\Omega_S t_1)$$

When the retro-INEPT is applied to this system, it is the **sine-modulated** component that is refocussed to in-phase *I*-spin magnetisation whilst the **cosine-modulated** component is rendered unobservable as MQ magnetisation:

$$\xrightarrow{90^\circ I_X} -2I_Y S_X \cos(\Omega_S t_1) - 2I_Y S_Y \sin(\Omega_S t_1)$$

$$\xrightarrow{90^\circ S_X} -2I_Y S_X \cos(\Omega_S t_1) - 2I_Y S_Z \sin(\Omega_S t_1)$$

$$\xrightarrow{2\pi I_S t I_Z S_Z, 180^\circ (I_X + S_X)} 2I_Y S_X \cos(\Omega_S t_1) + I_X \sin(\Omega_S t_1)$$

The collection of these two datasets therefore provides the cosine- and sine-modulated components required for frequency discrimination of the indirectly measured offset frequencies  $\Omega_S$  and are combined in accordance with the States-Haberhorn-Ruben (SHR)<sup>[48]</sup> or Time Proportional Phase Increment (TPPI)<sup>[49]</sup> schemes, a combination of the two (States-TPPI)<sup>[50]</sup> or by using the echo/anti-echo<sup>[51]</sup> procedure. Following Fourier transformation of the interferogram, a two-dimensional spectrum containing an absorption mode peak for each *IS* spin-pair is obtained (Figure 1.10b). Together with the conceptually similar Heteronuclear Multi-Quantum Coherence (HMQC)<sup>[52]</sup> and Transverse Relaxation Optimised Spectroscopy (TROSY)<sup>[53]</sup> experiments, the HSQC sequence is routinely applied to the  $^1\text{H}$ - $^{15}\text{N}$  spin pair of the peptide bonds that form the protein backbone where each amino acid (apart from proline) in the sequence gives rise to a separate cross-peak.

### 1.3.6 Frequency-Selective Pulses

The RF pulses used to manipulate the magnetisation in the experiments described up to this point are termed *hard* or *non-selective*. Practically speaking, a hard pulse is a very short high-power pulse that has a wide excitation bandwidth and is therefore used to target all the nuclei simultaneously: a hard  $90^\circ$   $^1\text{H}$  or  $^{13}\text{C}$  pulse is typically around  $10\ \mu\text{s}$  and is effective for offset frequencies of  $\pm 12.5\ \text{kHz}$  ( $\pm 20\ \text{ppm}$   $^1\text{H}$ ,  $\pm 80\ \text{ppm}$   $^{13}\text{C}$  at 14.1 T). Whilst the simultaneous excitation of all Larmor frequencies within a spectrum is crucial to the FT-NMR technique, there are numerous applications where one may want to target individual resonances *selectively* in order to manipulate a particular scalar coupling or chemical shift evolution. A commonly encountered example is found within the peptide bond of the protein backbone where the  $^{15}\text{N}$  nucleus is covalently bound to two  $^{13}\text{C}$  nuclei ( $\text{C}'$  and  $\text{C}^\alpha$ ) with a one-bond coupling constant of approximately 15 Hz in both cases. However, the large chemical shift difference between  $^{13}\text{C}'$  and  $^{13}\text{C}^\alpha$  allows them to be manipulated independently. This ultimately determines the success of many triple-resonance NMR experiments<sup>[54–56]</sup> and is discussed in more detail in Chapter 5. Figure 1.11a shows that a modified INEPT block can be applied to an  $I S_2$  spin-system to selectively evolve either or both of the  $I-S'$  or  $I-S''$  scalar couplings. To achieve this selectivity, many different *shaped* pulses during which the RF power and phase properties are carefully varied have been designed<sup>[57]</sup> to achieve narrower excitation bandwidths. Modern shaped pulses, including the Gaussian cascade<sup>[58]</sup> and SNOB<sup>[59]</sup> (Selective excitation fOr Biochemical applications) families, have been specifically designed to achieve the desired selection in a shorter time.

Figure 1.11b shows the amplitude and phase properties of a  $90^\circ$  excitation pulse from the BURP<sup>[60]</sup> (Band-selective, Uniform Response, Pure-phase) family and demonstrates the narrow excitation window achievable using this pulse. Assuming that the pulse is applied to equilibrium  $I_z$  magnetisation, efficient conversion to transverse  $I_x$  or  $I_y$  (depending on the phase of the pulse) only occurs for frequencies that are close to the carrier position whilst distant frequencies are unperturbed. Such a pulse could be used to only excite the aromatic region of a spectrum and thereby avoid the detection of signals associated with solvent molecules.

Figure 1.11c shows the amplitude and phase properties of the related Reburp shape, a selective  $180^\circ$  refocussing pulse. Assuming that the pulse is again applied to equilibrium  $I_z$  magnetisation, efficient inversion only occurs for frequencies that are close to the carrier position whilst distant frequencies are unaffected. Selective INEPT blocks that use the BURP pulses will be used extensively to direct magnetisation transfer steps in the Chapters that follow.

## 1. Introduction

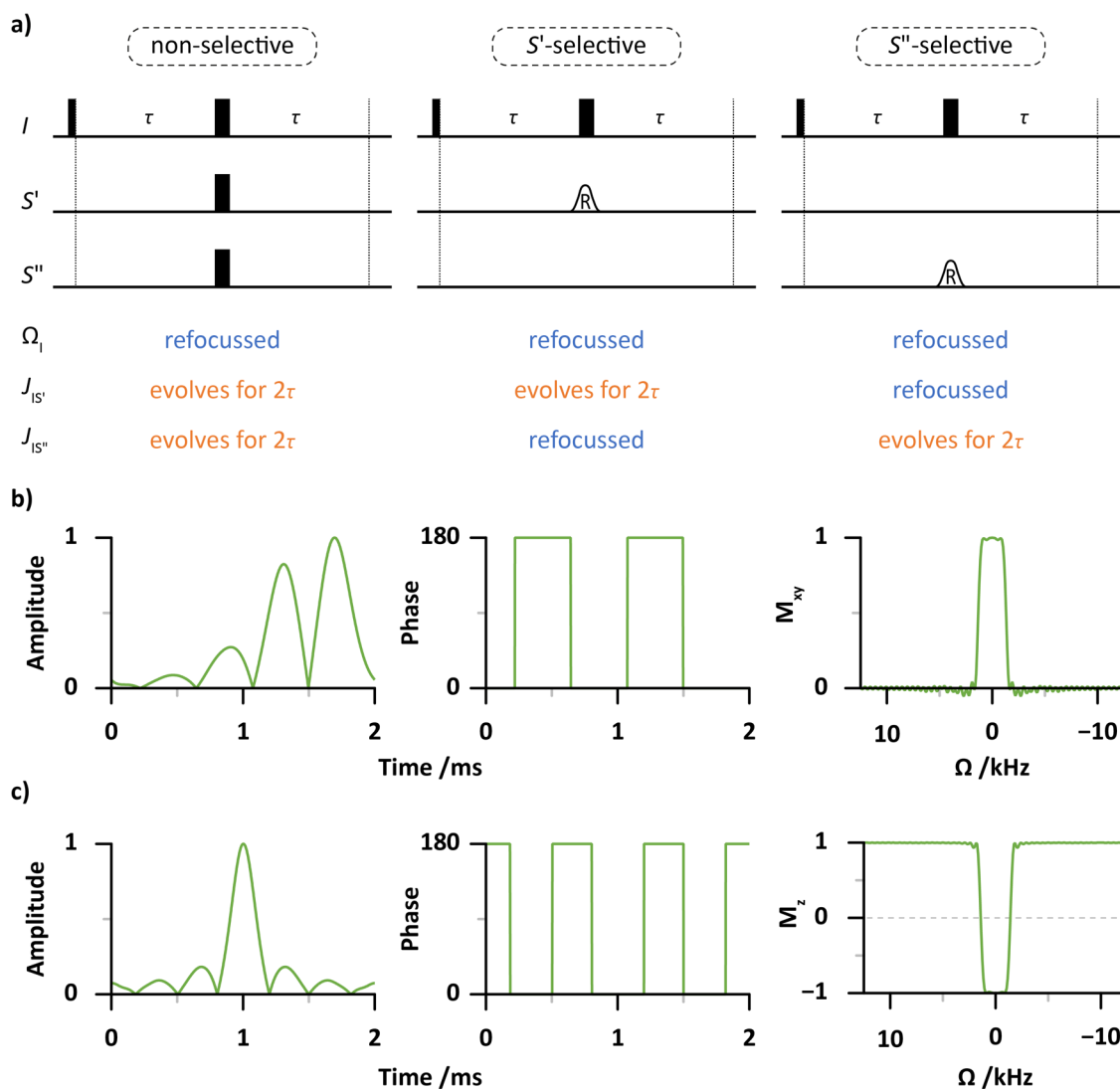


**Figure 1.11** a) The evolution/refocussing effect produced by the INEPT block can be tuned for an  $IS_2$  spin system by using selective refocussing pulses. b) Amplitude, phase and excitation properties of a 2ms Eburp-2 excitation pulse. c) Amplitude, phase and excitation properties of a 2ms Reburp refocussing pulse.

### 1.3.7 Pulsed Field Gradients

In order to collect useful NMR data, the static field ( $B_0$ ) must be uniform across the sample to ensure that the Larmor frequency of any given spin is independent from its physical location within the sample. A sufficiently homogeneous static field will therefore result in the detection of a bulk signal with a sharp and narrow peak as each spin contributes to the same detected frequency (Figure 1.12a). However, whilst one of the first tasks facing a spectroscopist is the optimisation of the field homogeneity through a process known as *shimming*, there are times where it is useful to deliberately vary the effective magnetic field along the sample.

Modern NMR probes are designed to include an additional coil that can induce a magnetic field that varies linearly along the  $z$ -axis, known as a *field gradient*. By varying the electrical current flowing through the gradient coil, the spectroscopist is able to apply Pulsed Field Gradients

(PFGs, or gradient pulses) in order carefully manipulate the effective magnetic field during a pulse sequence. During a PFG, the magnetic field along  $z$ ,  $B_z$ , is given by:

$$B_z = B_0 + G_z z \quad (1.19)$$

where  $G_z$  is the magnetic field gradient along  $z$ . The variation in the magnetic field across the sample results in a *spatially dependent* Larmor frequency,  $\omega(z)$ :

$$\omega(z) = \omega_0 - \gamma G_z z \quad (1.20)$$

The consequence of the variation of  $B_z$  during a PFG is that at each  $z$ -coordinate along the NMR sample, the nuclei have slightly different Larmor frequencies and would therefore result in slightly shifted peaks in the transformed spectrum. As shown in Figure 1.12b, all of these peaks merge together in the bulk sample and result in a very broad signal. If the gradient pulse is sufficiently strong or applied for long enough, the magnetisation can be broadened beyond detection.

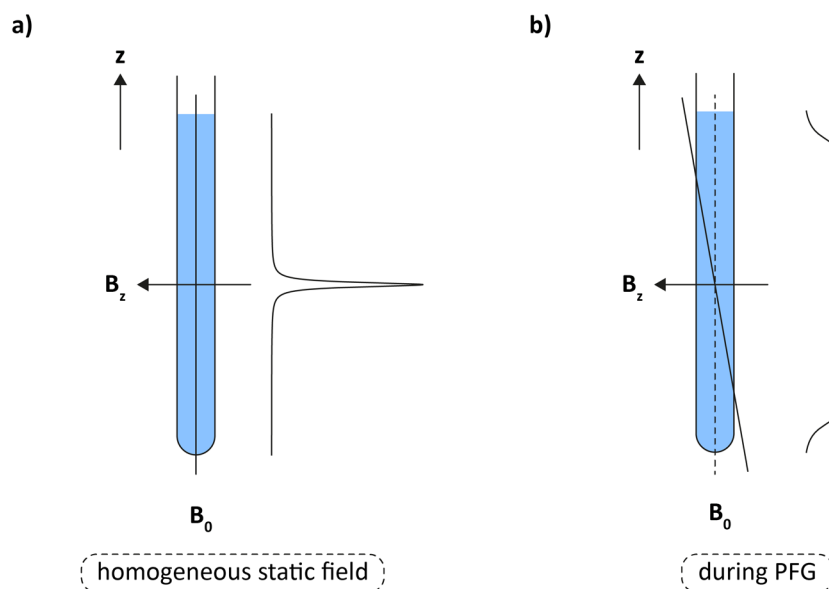


**Figure 1.12** a) The nuclei in a well-shimmed NMR sample experience a homogeneous magnetic field ( $B_z = B_0$  throughout the sample) and result in the detection of a sharp and narrow signal. b) During a PFG, the  $B_z$  field varies linearly with  $z$  and therefore spins at different positions in the sample have different Larmor frequencies, resulting in a very broad signal.

During a gradient pulse, the evolution of the magnetisation at this spatially dependent frequency results in the acquisition of a spatially dependent phase  $\theta(z)$ :

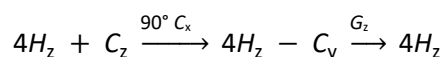
$$\theta(z) = -\rho\gamma G_z \tau_p \quad (1.21)$$

where  $\rho$  is the coherence order of the magnetisation and  $\tau_p$  is the length of the applied gradient pulse. Following a gradient pulse, any *transverse* magnetisation will have acquired the additional phase and is therefore said to be *dephased*. Typically, any desired magnetisation is *rephased* at a

## 1. Introduction

point later in the pulse sequence, prior to detection. Whilst there are a number of possible applications for pulsed field gradients in NMR spectroscopy, the work presented herein only requires them in two specific scenarios: the selection of pure z-magnetisation and the ‘cleaning up’ of imperfect 180° refocussing pulses.

Firstly, by recognising that z-magnetisation has a coherence order of zero and thus, according to Equation 1.21, acquires no additional phase during a gradient pulse, a *spoiling gradient* or *homospoil* pulse, can be used to dephase any unwanted transverse terms and retain only the desired z-magnetisation. For example, a simple *purge* block consisting of a 90°  $C_x$  pulse followed by a gradient pulse prior to the start of the INEPT block in Section 1.3.2 can be used to suppress the undesired equilibrium  $C_z$  magnetisation directly and avoid the need for the two-step phase cycle:



Whilst the selection of the desired z-magnetisation is achieved with a single gradient pulse, it is important to realise that the unwanted transverse terms have not been removed from the sample – only dephased – and therefore care must be taken to not accidentally rephase them later in the pulse sequence. Spoiling gradients will be applied throughout the pulse sequences developed in this work wherever pure z-magnetisation is required.

The second application of gradient pulses addresses phase errors introduced by the use of imperfectly calibrated 180° pulses in a pulse sequence. When power levels are even slightly mis-set, refocussing pulses can cause the transfer of magnetisation to other coherences as well as the desired inversion ( $\rho \rightarrow -\rho$ ) and would usually require a time-consuming phase cycle<sup>[61]</sup> to correct. However, flanking the 180° pulse with a pair of equal gradient pulses negates the need for such a phase cycle and selects the desired inversion directly.

The phase acquired during the first gradient pulse (when coherence order =  $\rho$ ) is:

$$\theta^1(z) = -\rho\gamma G_z \tau_p$$

The 180° pulse then changes the sign of the coherence order ( $\rho \rightarrow -\rho$ ) and therefore the phase acquired during the second gradient pulse is:

$$\theta^2(z) = +\rho\gamma G_z \tau_p$$

The two gradient pulses result in equal and opposite phases such that the total phase acquired over the pair is zero and therefore the desired  $\rho \rightarrow -\rho$  pathway is refocussed. Transfer to other coherences caused by pulse imperfections would not be refocussed and thus no additional phase cycling is required.

## 1.4 Introduction to Arginine

### 1.4.1 Importance of Protein Side-Chains

The early work in biological NMR spectroscopy focussed specifically on the nuclei that form the polypeptide backbone of the protein and since then chemical shift, NOE and RDC data has been routinely used to calculate<sup>[62–67]</sup> structural ensembles of a wide range of biomolecules. The study of the time-dependant behaviour of these nuclei by NMR spectroscopy<sup>[68–70]</sup> has subsequently confirmed that proteins are not static entities, but rather each molecule transiently samples a number of different backbone conformations in solution, some of which are invisible<sup>[71]</sup> to other biophysical techniques. Whilst the resonances of the backbone nuclei are often the first to be studied and assigned, it is the side-chain nuclei that are most often implicated in the numerous protein-protein<sup>[72]</sup> and protein-ligand<sup>[73]</sup> interactions that provide biological function and ultimately guide drug discovery efforts.<sup>[74]</sup>

Together with lysine and histidine, arginine is one of three positively charged amino acids that feature in the standard genetic code<sup>[75]</sup> and plays an important role in many key intra- and intermolecular interactions including at protein interaction surfaces,<sup>[76,77]</sup> in enzymatic active sites<sup>[78–80]</sup> and substrate binding pockets<sup>[81,82]</sup> and in phase-separation.<sup>[83,84]</sup> Figure 1.13 shows that these arginine-mediated interactions are very diverse in nature and can involve bidentate salt-bridges with carboxylates or negatively charged amino acids aspartic and glutamic acid;  $\pi$ -stacking and cation- $\pi$  interactions with aromatic rings; and hydrogen bonds with backbone carbonyl oxygen atoms or the phosphates of nucleic acids.

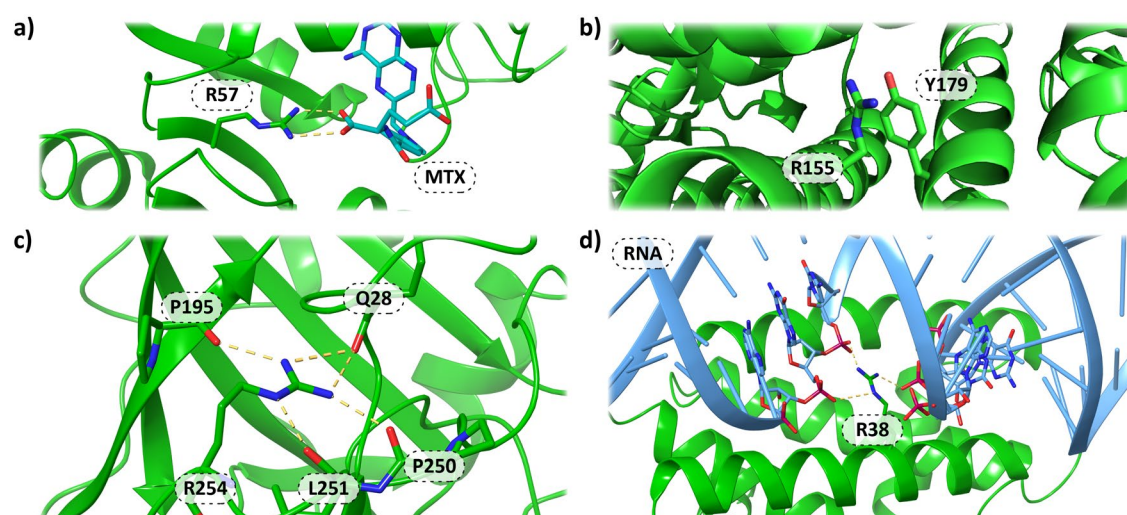


**Figure 1.13** Interactions involving the arginine side-chain. a) A salt-bridge is formed between an arginine residue of dihydrofolate reductase (DHFR) and the ligand methotrexate (MTX), PDB ID: 1RG7.<sup>[85]</sup> b) A cation- $\pi$  interaction between an arginine and tyrosine residue in the homodimer of farnesyl diphosphate synthase, PDB ID: 1UBY.<sup>[86]</sup> c) An arginine residue in carbonic anhydrase II engaged in hydrogen bonds with the carbonyl oxygen of several other residues, PDB ID: 1CA2.<sup>[87]</sup> d) The binding of RNA to the NS1 protein of the influenza A virus is mediated by the interaction of arginine residues with the phosphate backbone of the nucleic acid, PDB ID: 2ZKO.<sup>[88]</sup>

## 1. Introduction

### 1.4.2 Structure and NMR Parameters of Arginine

The structure of the arginine side-chain is shown in Figure 1.14 and consists of a flexible, four-carbon chain with a terminal guanidinium group. Owing to the number of atoms available for the delocalisation of a positive charge, the guanidinium group is a highly basic moiety with a  $pK_a$  of approximately 14.<sup>[89]</sup> The high  $pK_a$  causes the side-chain to become protonated at all physiologically relevant conditions<sup>[90]</sup> and thereby allows nature to place a positive charge at virtually any point within a protein structure. As shown in the previous Section, this perpetual state of ionisation not only allows the side-chain to participate in ionic interactions, but also increases the number of donor atoms available to engage in hydrogen bonding networks.

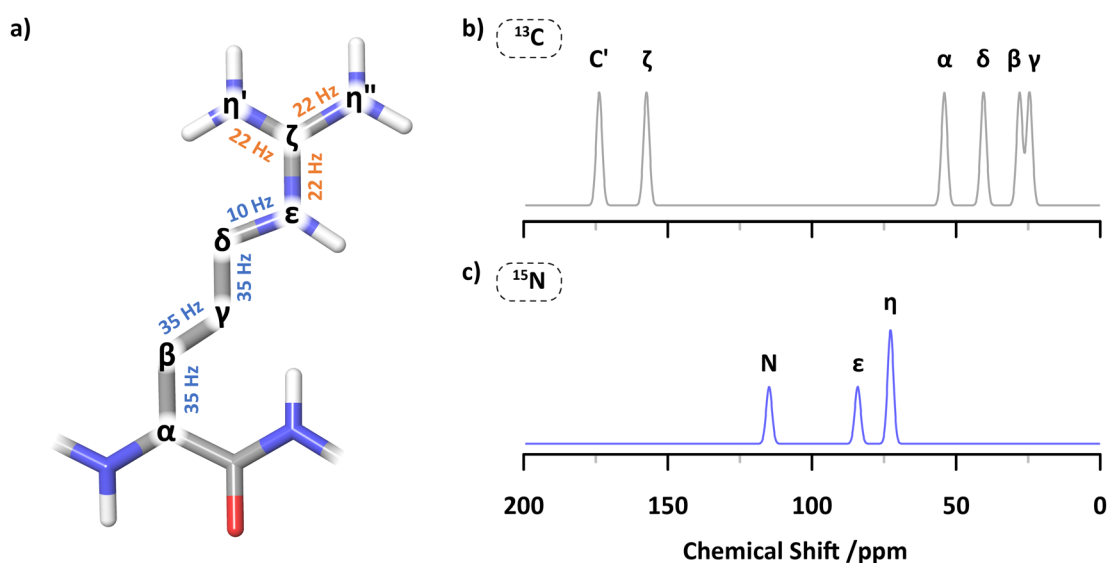


**Figure 1.14** a) The chemical structure of the arginine side-chain in the positively charged form. The one-bond **carbon-carbon** and **carbon-nitrogen** scalar couplings are indicated next to the relevant bond. b) Average  $^{13}\text{C}$  chemical shifts of proteinaceous arginine residues as taken from the Biological Magnetic Resonance Data Bank (BMRB). C' indicates the carbonyl carbon atom of the peptide backbone. c) Average  $^{15}\text{N}$  chemical shifts of proteinaceous arginine residues as taken from the Biological Magnetic Resonance Data Bank (BMRB). The N notation indicates the backbone  $^{15}\text{N}$  nucleus.

Figure 1.14 also shows the typical values for the  $^{13}\text{C}$  and  $^{15}\text{N}$  chemical shifts as well as the magnitude of the one-bond **carbon-carbon** and **carbon-nitrogen** scalar couplings. It is important to note that the heavy nuclei that make up the guanidinium group ( $^{13}\text{C}^{\zeta}$ ,  $^{15}\text{N}^{\epsilon}$ ,  $^{15}\text{N}^{\eta}$ ) exhibit significantly different chemical shifts from the  $^{13}\text{C}'$  and  $^{15}\text{N}$  nuclei of the protein backbone. These differences, combined with the ca. 20 Hz scalar couplings, can be exploited to design NMR experiments that directly probe the guanidinium group.<sup>[91–93]</sup>

### 1.4.3 Guanidinium Resonance Assignment

In favourable circumstances, the five  $^1\text{H}$ - $^{15}\text{N}$  pairs present on the guanidinium group can be detected using the standard HSQC experiment described in Section 1.3.5. However, for reasons discussed in more detail in Chapter 2, this is often not a practical approach and  $^{13}\text{C}$ -detection is

more appropriate. Regardless of the detection strategy, a crucial step in the characterisation of these side-chains is the residue-specific assignment of the observed resonances. This process can be achieved by site-directed mutagenesis<sup>[94,95]</sup> or by correlation of the guanidinium signals with previously assigned resonances. The latter typically begins with the assignment of the backbone signals observed in the  $^1\text{H}$ - $^{15}\text{N}$  HSQC spectrum: the ubiquitous one-bond  $^1J_{\text{HN}}$  scalar coupling of approximately 92 Hz is used to generate anti-phase  $^{15}\text{N}$  magnetisation proportional to  $2H_zN_y$ , that is allowed to evolve according to the  $^{15}\text{N}$  chemical shift before retro-INEPT transfer back to in-phase  $^1\text{H}$  magnetisation for detection. Figure 1.15 shows that as well as the  $^1J_{\text{HN}}$  scalar coupling, the peptide bond contains several additional coupling pathways that enable the controlled transfer of magnetisation throughout the backbone nuclei. There are numerous strategies for tackling the assignment process, but the most common approaches use pairs of three-dimensional  $^1\text{H}$ - $^{13}\text{C}$ - $^{15}\text{N}$  (so-called triple resonance) experiments to link the  $^1\text{H}$  and  $^{15}\text{N}$  resonances with the  $^{13}\text{C}$  nuclei of the adjacent amino acid(s) using the carbon-nitrogen and carbon-carbon scalar couplings. The measured  $^{13}\text{C}$  chemical shifts of the side-chain atoms can often be used to determine the amino acid type and the observed correlations can therefore be interpreted alongside the amino acid sequence to *walk through* the molecule.

The remainder of this section describes the most common approach to resonance assignment in biological NMR spectroscopy and is in no way intended to be an exhaustive summary of the available techniques. Each of the experiments described below was used to support the work in this thesis and whilst a full discussion of the pulse sequences is unnecessary, the information obtained using each experiment can be readily understood by interrogating the flow of magnetisation over several scalar couplings.

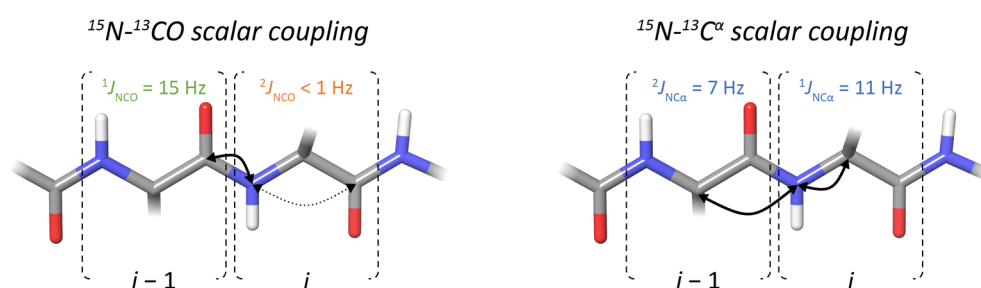


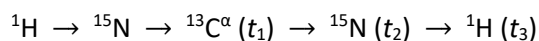
**Figure 1.15** The magnitude of the carbon-nitrogen scalar couplings present in the polypeptide backbone of proteins. The  $^{15}\text{N}$ - $^{13}\text{CO}$  coupling is used to transfer  $^{15}\text{N}$  magnetisation to the carbonyl  $^{13}\text{C}$  of only the preceding amino acid whilst the  $^{15}\text{N}$ - $^{13}\text{C}\alpha$  pathway is used to transfer magnetisation to the  $^{13}\text{C}\alpha$  nucleus within the same residue *and* the preceding amino acid.

### Correlating $^1\text{H}$ - $^{15}\text{N}$ with $^{13}\text{C}\alpha$

The  $J_{\text{NC}\alpha}$  coupling can be used to correlate a  $^1\text{H}$ - $^{15}\text{N}$  cross peak with the  $^{13}\text{C}\alpha$  chemical shift in an HNCA experiment.<sup>[55,96,97]</sup> The HNCA relies on the sequential evolution of proton-nitrogen and

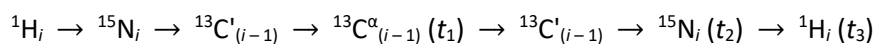
## 1. Introduction

nitrogen-carbon scalar couplings to guide the magnetisation through the peptide bond as follows:



where  $t_1$ ,  $t_2$  and  $t_3$  represent the three chemical shift evolutions. The two indirect chemical shift evolutions are made up from sequential acquisitions with increasing values of  $t_1$  and  $t_2$ . The data is Fourier transformed in a manner analogous to the two-dimensional dataset described in Section 1.3.3 and results in a three-dimensional spectrum, often visualised as a cube with the  ${}^1\text{H}$ ,  ${}^{15}\text{N}$  and  ${}^{13}\text{C}^\alpha$  frequencies of each amino acid as the  $x$ -,  $y$ - and  $z$ -axes, respectively.

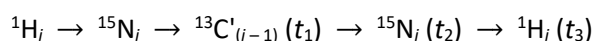
As a consequence of the similar magnitude of the one- and two-bond  ${}^{15}\text{N}$ - ${}^{13}\text{C}^\alpha$  scalar couplings (Figure 1.15, right), the HNCA experiment also provides a correlation from each  ${}^1\text{H}$ - ${}^{15}\text{N}$  cross peak ( $i$ ) to the  ${}^{13}\text{C}^\alpha$  nucleus of the preceding residue ( $i-1$ ), thereby allowing one to identify the  ${}^1\text{H}$ - ${}^{15}\text{N}$  HSQC cross peaks that arise from adjacent amino acids. Often, the  ${}^{13}\text{C}^\alpha$  intensity can be used to determine which of the two  ${}^1\text{H}$ - ${}^{15}\text{N}$ - ${}^{13}\text{C}^\alpha$  resonances belongs to the parent residue, but extra certainty can be provided by using the  ${}^{15}\text{N}$ - ${}^{13}\text{C}'$  scalar coupling. Fortunately for the NMR spectroscopist, the two-bond  ${}^2J_{\text{NC}'}$  coupling is negligible and magnetisation transfer only occurs to the  ${}^{13}\text{C}'$  nucleus of the preceding residue. By sequential evolution of the  ${}^1J_{\text{NC}'}$  and one-bond carbon-carbon  ${}^1J_{\text{C}'\text{C}\alpha}$  couplings, magnetisation can therefore be selectively transferred from  ${}^{15}\text{N}$  of one residue to the  ${}^{13}\text{C}^\alpha$  nucleus of the preceding residue in an HN(CO)CA<sup>[97,98]</sup> experiment:



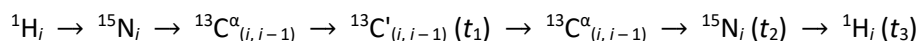
A combination of these two datasets will therefore allow one to unambiguously assign a single  ${}^{13}\text{C}^\alpha$  chemical shift to each  ${}^1\text{H}$ - ${}^{15}\text{N}$  cross peak whilst the HNCA correlations allow adjacent signals to be linked together.

### Correlating ${}^1\text{H}$ - ${}^{15}\text{N}$ with ${}^{13}\text{C}'$

The  ${}^{13}\text{C}'$  chemical shifts of each amino acid can be obtained from two additional experiments that are very closely related to the HNCA/HN(CO)CA described above: the HNCO and HN(CA)CO. As the names suggest, the HNCO<sup>[55,97,99]</sup> experiment uses the  ${}^1J_{\text{NC}'}$  coupling to provide the chemical shift of only the preceding residue:



whilst the HN(CA)CO<sup>[100]</sup> uses the  $J_{\text{NC}\alpha}$  and  ${}^1J_{\text{C}'\text{C}\alpha}$  couplings to provide the chemical shift for both the parent and preceding amino acid:

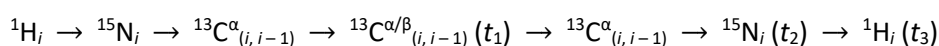


These two datasets provide an unambiguous assignment of the  $^{13}\text{C}'$  chemical shifts for each amino acid and provide an alternate means of correlating adjacent resonances. For example, the connectivity identified using the  $^{13}\text{C}^\alpha$  chemical shifts becomes ambiguous in instances where two (or more) residues are overlapped in each of the three chemical shift dimensions. Switching focus to the  $^{13}\text{C}'$  correlations in such cases may allow the elucidation of the connections between resonances to continue.

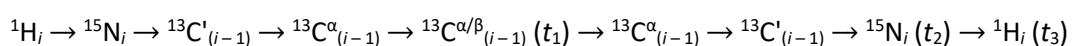
### Correlating $^1\text{H}$ - $^{15}\text{N}$ with $^{13}\text{C}^\alpha$ and $^{13}\text{C}^\beta$

In the HN(CO)CA and HN(CA)CO experiments above, the one-bond homonuclear  $J_{\text{C}^\alpha\text{C}'}$  coupling is used to transfer magnetisation from  $^{13}\text{C}^\alpha$  to  $^{13}\text{C}'$  and vice versa. By recognising that  $^{13}\text{C}^\alpha$  is also coupled to the  $^{13}\text{C}^\beta$  nucleus (for all residues with the exception of glycine), an alternate magnetisation transfer pathway can be exploited to provide the HNCACB/HN(CO)CACB experiments below.

HNCACB:<sup>[101,102]</sup>



HN(CO)CACB:<sup>[103,104]</sup>



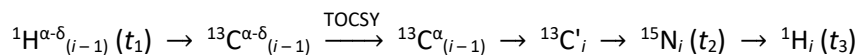
These experiments each provide three-dimensional ( $^1\text{H}$ - $^{15}\text{N}$ - $^{13}\text{C}$ ) datasets in which the  $^{13}\text{C}^{\alpha/\beta}$  chemical shifts are encoded together in a single dimension. The measurement of the  $^{13}\text{C}^\beta$  chemical shift not only provides a third  $^{13}\text{C}$  frequency to help identify correlations between adjacent residues, but also an insight into the *type* of amino acid. For example, the  $^{13}\text{C}^\beta$  chemical shift of the alanine residue ( $^{13}\text{C}^\beta = 16.3$  ppm) is very different to the  $^{13}\text{C}^\beta$  chemical shift of serine ( $^{13}\text{C}^\beta = 61.0$  ppm) and the glycine residue is notable for the absence of a  $^{13}\text{C}^\beta$  cross peak.<sup>[16]</sup> A combination of the six triple-resonance experiments above and a knowledge of the amino acid sequence is usually sufficient to complete the assignment of the  $^1\text{H}$ - $^{15}\text{N}$  HSQC spectra of small to medium sized proteins.

### Correlating $^1\text{H}$ - $^{15}\text{N}$ with Side-Chain Nuclei

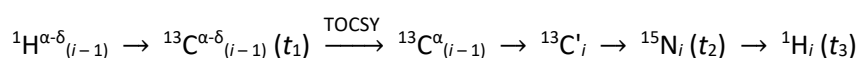
For amino acids with additional side-chain nuclei, magnetisation transfer further up the spin-system can be achieved by using various TOCSY (Total Correlation Spectroscopy) based experiments. With reference to the arginine residue, these experiments implement a  $^{13}\text{C}$  isotropic mixing scheme to transfer  $^{13}\text{C}^{\beta-\delta}$  magnetisation to  $^{13}\text{C}^\alpha$ . From  $^{13}\text{C}^\alpha$ , the magnetisation is directed through the usual carbon-carbon and carbon-nitrogen scalar couplings via  $^{15}\text{N}$  chemical shift evolution for detection on  $^1\text{H}^N$ . As the  $^1\text{H}$ - $^{15}\text{N}$  cross peaks will usually have already been

## 1. Introduction

assigned by this point, it is usual to direct the magnetisation through the  $^{13}\text{C}^{\alpha}-^{15}\text{N}$  scalar coupling such that the side-chain nuclei of only the preceding residue are recorded for each  $^1\text{H}-^{15}\text{N}$  resonance. Two major variants of this experiment are available and differentiated according to whether one wishes to record the  $^1\text{H}$  or  $^{13}\text{C}$  chemical shifts of the side-chain. For  $^1\text{H}^{\alpha-\delta}$  measurement, the H(CCO)NH-TOCSY<sup>[105,106]</sup> is used:

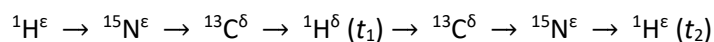


where the transfer between  $^1\text{H}$  and  $^{13}\text{C}$  is achieved using the one-bond proton-carbon scalar coupling of ca. 125 Hz. The analogous experiment for the measurement of the  $^{13}\text{C}^{\alpha-\delta}$  chemical shifts is the CC(CO)NH-TOCSY<sup>[106]</sup>:

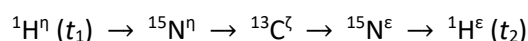
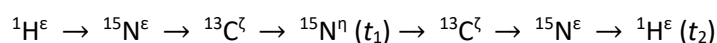


### Correlating $^1\text{H}-^{15}\text{N}$ with The Guanidinium Nuclei

The difficulty with identifying the guanidinium nuclei of each arginine residue is two-fold: firstly, the guanidinium group is separated from the backbone  $^1\text{H}^{\text{N}}$  proton by at least seven bonds and therefore many magnetisation steps would be required to detect a correlation. Secondly, the  $^{13}\text{C}$  spin-system is broken by the presence of the  $^{15}\text{N}^{\epsilon}$  and therefore the  $^{13}\text{C}^{\zeta}$  chemical shift is absent from the CC(CO)NH-TOCSY spectrum described above. To overcome this and provide a link between the known side-chain chemical shifts and the  $^1\text{H}^{\epsilon/\eta}$  and  $^{15}\text{N}^{\epsilon/\eta}$  resonances of the arginine guanidinium group, a family of two-dimensional experiments have developed.<sup>[107,108]</sup> Magnetisation is transferred between the various nuclei of the guanidinium group using the scalar couplings shown in Figure 1.14 and is correlated with the residue-specific  $^1\text{H}^{\delta}$  chemical shifts obtained using the H(CCO)NH-TOCSY experiment described above. Several variations exist, each encoding the chemical shift of a different guanidinium nuclei. For example, the  $\text{H}^{\epsilon}(\text{N}^{\epsilon}\text{C}^{\delta})\text{H}^{\delta}$  experiment correlates the  $^1\text{H}^{\epsilon}$  and  $^1\text{H}^{\delta}$  chemical shifts:



whilst the  $\text{H}^{\epsilon}(\text{N}^{\epsilon}\text{C}^{\zeta})\text{N}^{\eta}$  and  $\text{H}^{\eta}(\text{N}^{\eta}\text{C}^{\zeta}\text{N}^{\epsilon})\text{H}^{\epsilon}$  experiments correlate the  $^1\text{H}^{\epsilon}$  nuclei with the  $^{15}\text{N}^{\eta}$  and  $^1\text{H}^{\eta}$  chemical shifts, respectively:



A drawback of this approach is that successful assignment of the guanidinium resonances is predicated on an unambiguous  $^1\text{H}^{\delta}$  chemical shift for each arginine residue. Where this is not the case, an alternative means of correlating the guanidinium cross peaks with the backbone assignment is required. Figure 1.16a shows a strategy based on the collection of two

complimentary TOCSY experiments that can provide a more rigorous assignment. The first required dataset is the standard CC(CO)NH-TOCSY described above where each of the four side-chain  $^{13}\text{C}$  chemical shifts are recorded simultaneously. The second dataset is a  $\text{CCN}^{\epsilon}\text{H}^{\epsilon}$ -TOCSY where after the isotropic mixing period, the  $^{13}\text{C}^{\delta-15}\text{N}^{\epsilon}$  scalar coupling is used to transfer the  $^{13}\text{C}^{\alpha-\delta}$  magnetisation to the  $^1\text{H}^{\epsilon-15}\text{N}^{\epsilon}$  spin-pair instead of the backbone:

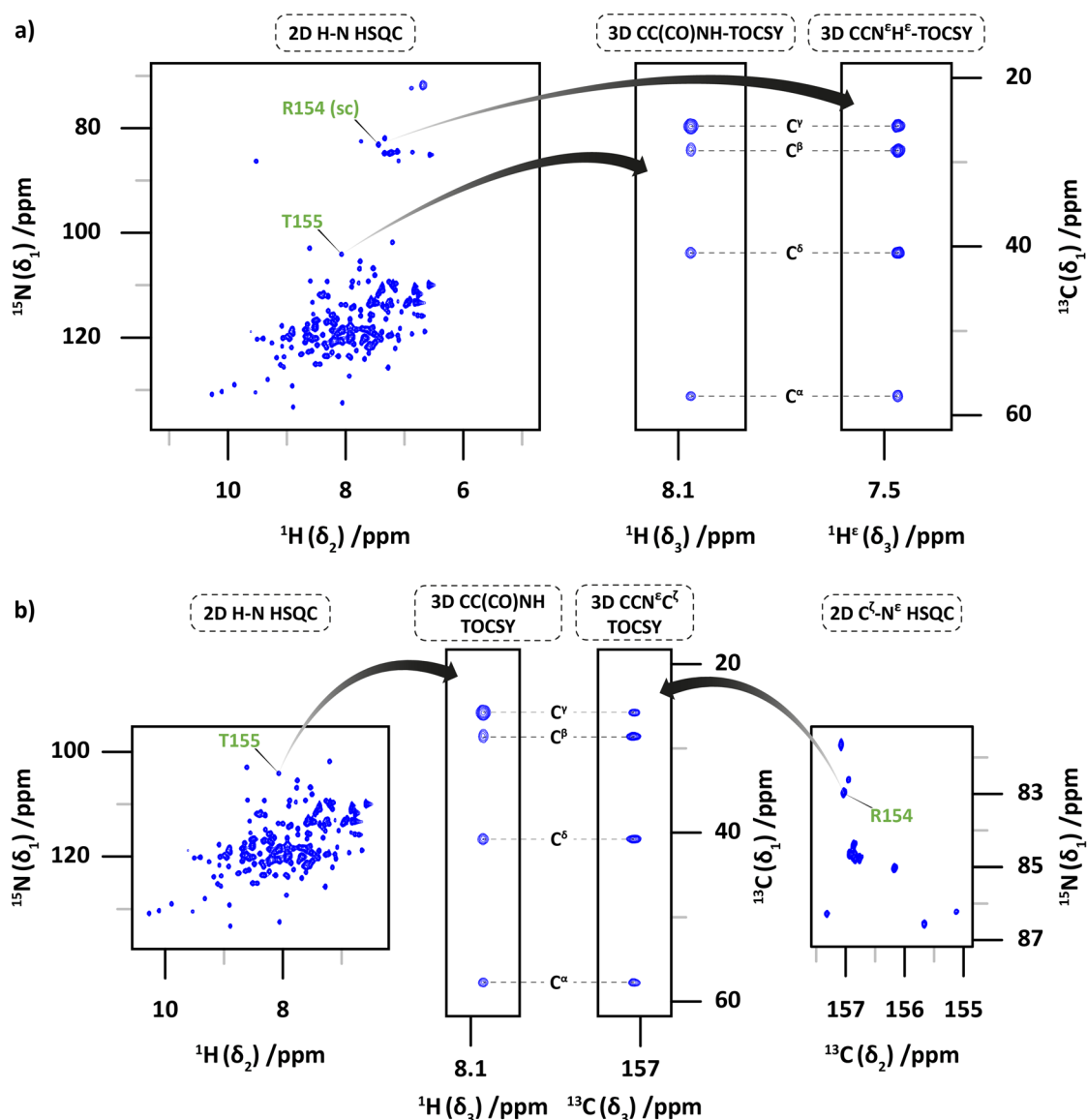
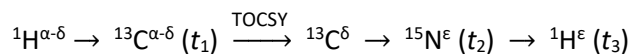


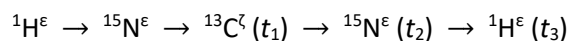
**Figure 1.16** a) A comparison of the  $^{13}\text{C}^{\alpha-\delta}$  chemical shifts obtained from the complimentary CC(CO)NH-TOCSY and  $\text{CCN}^{\epsilon}\text{H}^{\epsilon}$ -TOCSY datasets permits a high-confidence assignment of the arginine  $^1\text{H}^{\epsilon-15}\text{N}^{\epsilon}$  resonances. b) A comparison of the  $^{13}\text{C}^{\alpha-\delta}$  chemical shifts obtained from the complimentary CC(CO)NH-TOCSY and  $\text{CCN}^{\epsilon}\text{C}^{\epsilon}$ -TOCSY datasets permits a high-confidence assignment of the arginine  $^{13}\text{C}^{\epsilon-15}\text{N}^{\epsilon}$  resonances. The data shown was recorded on U- $^{13}\text{C}, ^{15}\text{N}$ ]-T4L99A at 14.1 T.

Between the two TOCSY datasets, a comparison of the four side-chain  $^{13}\text{C}$  chemical shift measurements can be made for all of the arginine residues within the protein. As a consequence of the four points of reference between backbone  $^1\text{H}-^{15}\text{N}$  and arginine  $^1\text{H}^{\epsilon-15}\text{N}^{\epsilon}$  cross peaks, a

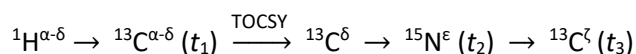
## 1. Introduction

high-confidence assignment can be made. It is worth noting that whilst this strategy is exemplified using the  $^{13}\text{C}^{\alpha-\delta}$  chemical shifts, it is equally applicable to the  $^1\text{H}^{\alpha-\delta}$  nuclei by using the analogous H(CCO)NH-TOCSY and H(CC)N $^{\epsilon}$ H $^{\epsilon}$ -TOCSY experiments.

With the  $^1\text{H}^{\epsilon}$ - $^{15}\text{N}^{\epsilon}$  resonances assigned, the  $^{13}\text{C}^{\zeta}$  nucleus of each guanidinium group can then be obtained using a variant of the HNCO experiment, the H $^{\epsilon}$ N $^{\epsilon}$ C $^{\zeta}$ .<sup>[109]</sup>



To avoid the magnetisation losses associated with the chemical exchange of the  $^1\text{H}^{\epsilon/\eta}$  nuclei with solvent and to obtain the  $^{13}\text{C}^{\zeta}$  frequencies directly, one can use a  $^{13}\text{C}$ -detected TOCSY experiment for the comparison of the  $^{13}\text{C}^{\alpha-\delta}$  chemical shifts (Figure 1.16b). The  $^{13}\text{C}$ -detected CCN $^{\epsilon}$ C $^{\zeta}$ -TOCSY<sup>[91]</sup> uses the  $^1J_{\text{CN}}$  scalar coupling to transfer magnetisation to  $^{13}\text{C}^{\zeta}$  for detection after the chemical shift evolution of  $^{15}\text{N}^{\epsilon}$ :



The switch to  $^{13}\text{C}$ -detection removes any reliance on  $^1\text{H}$ - $^{15}\text{N}$  magnetisation transfer for the assignment and is thus applicable to samples prepared at neutral to high pH. The next Chapter will further demonstrate how  $^{13}\text{C}$ -detection can be used to characterise arginine residues in proteins.

# 2

## Double-Quantum Coherences in Arginine

### 2.1 Introduction

The biological importance of the arginine side-chain stems from the properties of the terminal guanidinium group. Bearing a perpetual positive charge and five hydrogen-bond donors, arginine can form many of the key interactions that mediate enzyme catalysis and regulate protein function. However, owing to solvent exchange and the delocalised electrons of the guanidinium group, the direct observation of these key sites using standard NMR techniques can be troublesome. This chapter will describe some of the pitfalls of existing techniques and introduce a pair of novel NMR experiments that seek to address them. The generation and controlled evolution of the desired coherences is first described using the product operator formalism before an application to the 19 kDa protein T4 Lysozyme is presented.

#### 2.1.1 Chemical Exchange of $^1\text{H}^{\epsilon/\eta}$ with Bulk Solvent

The conventional approach to probe the chemical shift of an amide or amine  $^{15}\text{N}$  within a biomolecule involves the collection of one of several  $^1\text{H}$ - $^{15}\text{N}$  correlation experiments, most commonly an HSQC or HMQC. These experiments make use of the  $^1J_{\text{HN}}$  scalar coupling between the  $^{15}\text{N}$  nucleus and the directly bound proton and employ  $^1\text{H}$  detection, affording high sensitivity as well as an additional chemical shift dimension that reduces spectral crowding and subsequent signal overlap. However, for arginine side-chains, two exchange processes lead to severe broadening of the  $^1\text{H}$ - $^{15}\text{N}$  correlations, particularly at physiological pH and ambient temperature. During the first process, the directly bound  $^1\text{H}^{\epsilon}$  and  $^1\text{H}^{\eta}$  protons of the guanidinium group undergo a rapid chemical exchange with the solvent,<sup>[110]</sup> which leads to a line broadening in the  $^1\text{H}$  dimension and an attenuation of the signal intensity in the NMR experiment. In the most extreme cases, the chemical exchange proceeds so rapidly that each proton does not spend enough time on the side-chain for the required  $2H_zN_z$  coherence to build up to detectable levels, rendering these nuclei essentially invisible to the spectroscopist. This is quite often the

## 2. Double-Quantum Coherences in Arginine

case in samples prepared at neutral and high pH, unless the proton in question is involved in a strong hydrogen bond.<sup>[80,111]</sup>

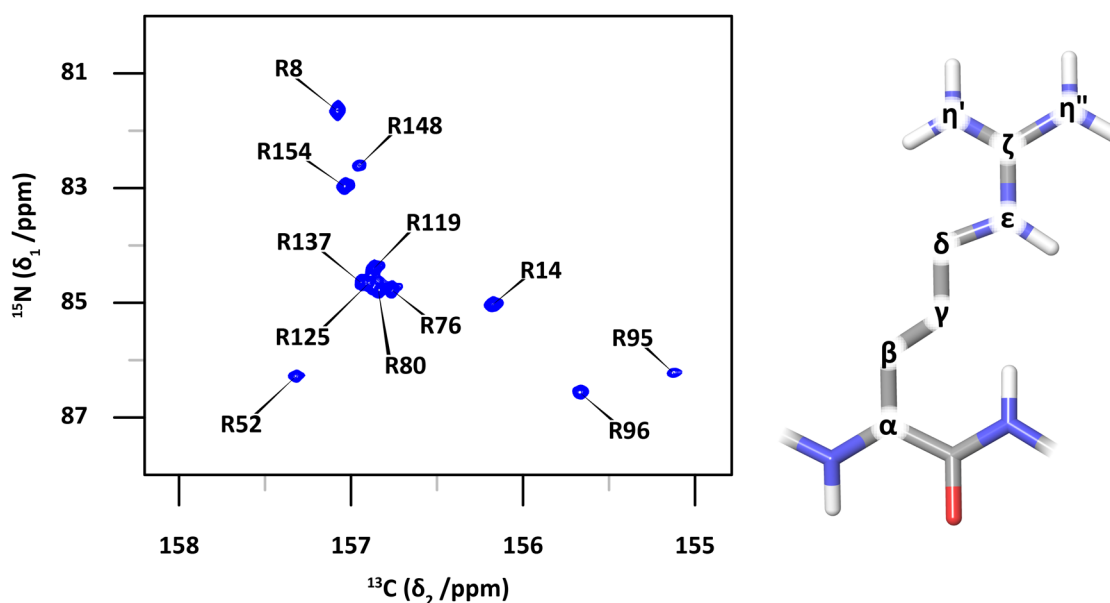


**Figure 2.1**  $^{13}\text{C}$ -detected arginine  $^{13}\text{C}^z$ - $^{15}\text{N}^\epsilon$  HSQC spectrum of T4L99A recorded at 16.4 T.

This limitation is overcome by switching the detection nucleus from  $^1\text{H}^\epsilon/{}^1\text{H}^\eta$  to  $^{13}\text{C}^z$ .<sup>[91,92]</sup> As discussed in Chapter 1, the  $^{13}\text{C}^z$  nucleus shares a  ${}^1J_{\text{CN}}$  scalar coupling with  $^{15}\text{N}^\epsilon$  of approximately 20 Hz allowing the transfer of equilibrium  $^{13}\text{C}$  magnetisation to the required antiphase term,  $2C_zN_{x/y}$ , in a reasonable amount of time. The absence of a  ${}^1\text{H}$  term in this transfer highlights the insensitivity of this pathway towards hydrogen exchange and the  $^{13}\text{C}^z$ - $^{15}\text{N}^\epsilon$  HSQC spectrum of T4L99A correspondingly shows an intense signal for each arginine residue in the protein, regardless of the exchange rate (Figure 2.1).

### 2.1.2 Effect of the Restricted Rotation of the $\text{N}^\epsilon$ - $\text{C}^z$ Bond

In samples prepared at lower pH (< 6.5), the hydrogen exchange rate is sufficiently slowed so that  ${}^1\text{H}$ -detected HSQC spectra of arginine residues can be obtained.<sup>[112–114]</sup> For example, the spectrum of T4L99A recorded at pH 5.5 and 298 K contains a cross-peak for each of the 13 arginine  ${}^1\text{H}^\epsilon$ - ${}^{15}\text{N}^\epsilon$  pairs (Figure 2.2,  $\delta_1 \sim 85$  ppm). It is clear however, that even with the favourable hydrogen exchange conditions, the  ${}^1\text{H}^\eta$ - ${}^{15}\text{N}^\eta$  correlations remain significantly broadened and difficult to identify (Figure 2.2,  $\delta_1 \sim 71$  ppm). This is a manifestation of a second exchange process, resulting from the restricted rotation about the  $\text{N}^\epsilon$ - $\text{C}^z$  bond.<sup>[115]</sup> The reduced rotational frequency of this bond is in part caused by the delocalisation of the perpetual positive charge across the three nitrogen atoms of the guanidinium group and is analogous to the well-known hindered internal rotation observed in simple amides such as dimethylformamide.<sup>[116]</sup>

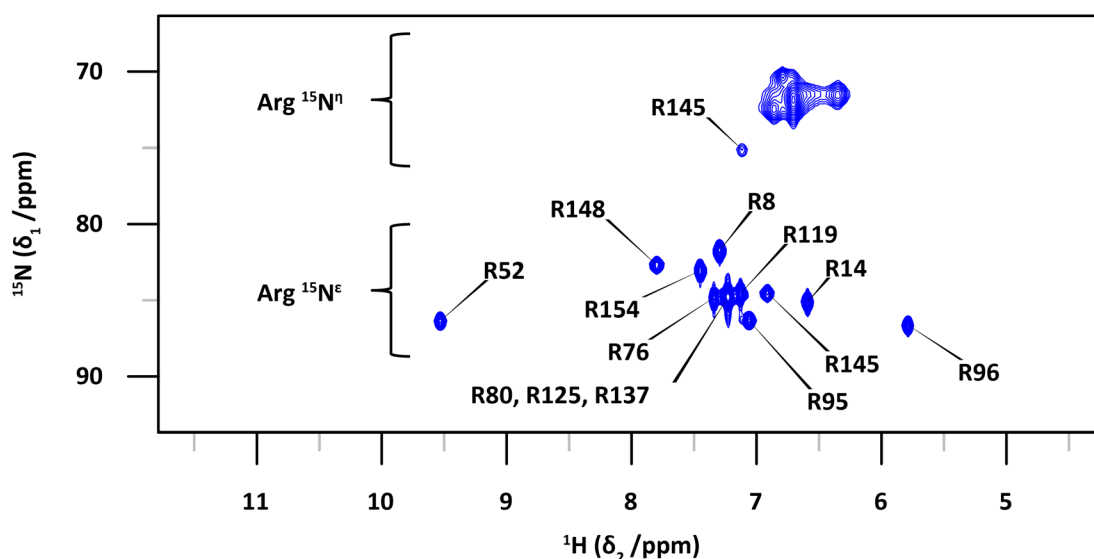


**Figure 2.2**  $^1\text{H}$ - $^{15}\text{N}$  HSQC spectrum with focus on the arginine side-chains of T4L99A at pH 5.5 recorded at 11.7 T. Whilst all the  $^{15}\text{N}^\epsilon$  resonances are detectable, the peaks associated with the amine  $^{15}\text{N}^\eta$  are broad and overlap significantly.

How exchanging nuclei manifest themselves in NMR spectra depends on both the difference in chemical shift ( $\Delta\delta$ ) of the two nuclei as well as the exchange rate ( $k_{\text{ex}}$ ) between them (Figure 2.3a).<sup>[117–119]</sup> In the slow-exchange limit, where the exchange rate is much smaller than the chemical shift difference ( $k_{\text{ex}}/\Delta\delta \rightarrow 0$ ), the two individual signals of the exchanging nuclei are observed. In the fast-exchange limit, ( $k_{\text{ex}}/\Delta\delta \rightarrow \infty$ ), a single sharp signal is observed at the average chemical shift of the two contributing nuclei. In the intermediate exchange regime, as the rate of exchange approaches the chemical shift difference ( $k_{\text{ex}} \approx \Delta\delta$ ), the two signals coalesce and result in a broad resonance that is often at or beyond the limit of detection. Whilst the chemical shift difference is essentially fixed for a given residue, numerous NMR experiments have been developed to reduce the effective shift difference spectroscopically in an effort to reduce the line broadening effect.<sup>[70,71,120–124]</sup> More intuitively, the rate of exchange can be tuned by altering the sample temperature. For example, a sample of *free* arginine recorded at 310 K will exhibit a single  $^{15}\text{N}^\eta$  signal whilst lowering the temperature to approximately 263 K will slow the exchange sufficiently to enable the detection of separate  $^{15}\text{N}^\eta$  signals. It is also interesting to note that the single-, double- and triple-quantum coherences of a spin-system exhibit different line broadenings.<sup>[125–127]</sup>

With adaptations to the previously published  $^{13}\text{C}^\zeta$ - $^{15}\text{N}^\epsilon$  experiment, a  $^{13}\text{C}^\zeta$ - $^{15}\text{N}^\eta$  HSQC<sup>[128]</sup> can be recorded in which one can clearly see the effects of different exchange regimes on the observed NMR signals (Figure 2.3b). Owing in part to the ability of the guanidinium group to form salt-bridges with negatively charged side-chains such as aspartic and glutamic acids, a wide range of  $\text{N}^\epsilon$ - $\text{C}^\zeta$  bond rotational rates are typically observed for arginine residues in proteins. In T4L99A, residues R52, R95, R96, R145 and R148 are clearly in the slow-exchange regime as a separate

## 2. Double-Quantum Coherences in Arginine

signal is observed for each of the two  $^{15}\text{N}^{\eta}$  nuclei. For R14 and several signals around 157 ppm ( $^{13}\text{C}$ ), the line broadening caused by the intermediate-exchange regime is similarly evident.

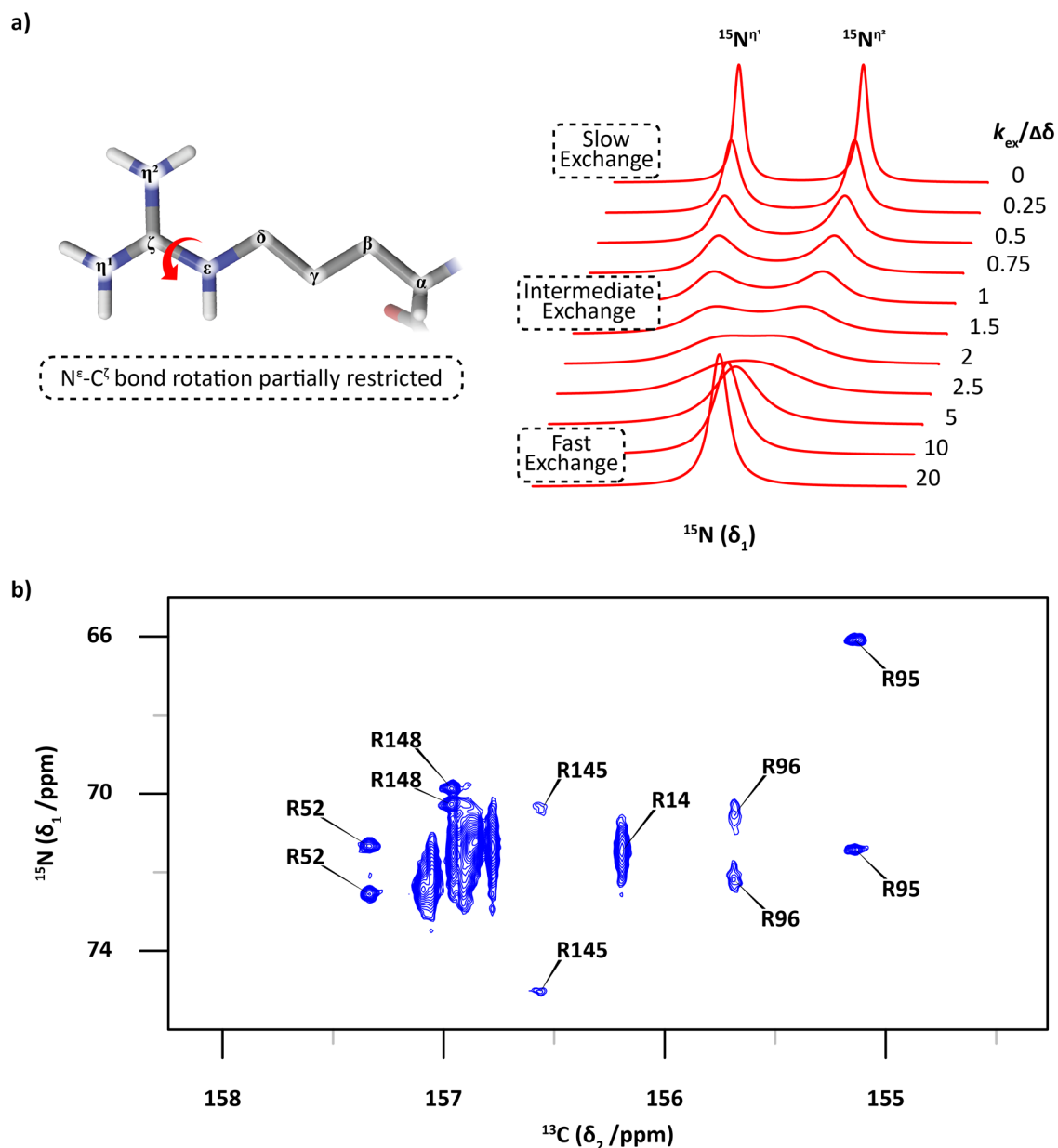


**Figure 2.3** a) Simulated NMR spectra showing two  $^{15}\text{N}^{\eta}$  nuclei in different exchange regimes.  $\Delta\omega$  is fixed at 100 Hz whilst  $k_{\text{ex}}$  is varied between 0 and 2000  $\text{s}^{-1}$ . Simulations performed using the WINDNMR-Pro software package. b)  $^{13}\text{C}^{\zeta}$ - $^{15}\text{N}^{\eta}$  HSQC spectrum of T4L99A recorded at 16.4 T. Arginine residues that exhibit slow rotation about the  $\text{N}^{\epsilon}$ - $\text{C}^{\zeta}$  bond give rise to two sharp peaks (R52, R95, R96, R145 and R148). However, for many of the arginine side-chains, the rotational frequency about the  $\text{N}^{\epsilon}$ - $\text{C}^{\zeta}$  bond approaches the chemical shift difference between the two  $^{15}\text{N}^{\eta}$  nuclei causing a substantial line broadening of the NMR signals.

As the  $^{13}\text{C}^{\zeta}$ - $^{15}\text{N}^{\eta}$  HSQC experiment relies on chemical shift evolution of  $^{13}\text{C}^{\zeta}$  and  $^{15}\text{N}^{\eta}$  and the  $^1J_{\text{CN}}$  scalar coupling between them, the exchange of  $^1\text{H}^{\eta}$  with the bulk solvent does not affect the obtained spectrum. It should be noted that because the experiment is based on  $^{13}\text{C}$ -excitation and  $^{13}\text{C}$ -detection there is an intrinsic sensitivity penalty owing to the lower gyromagnetic ratio

of  $^{13}\text{C}$  compared to  $^1\text{H}$ . However, in the case of  $^{15}\text{N}^n$  this is outweighed by the slowing of the exchange with the bulk solvent, thus resulting in a clear improvement over the  $^1\text{H}$ - $^{15}\text{N}$  spectrum. Despite that, many of the  $^{13}\text{C}^\zeta$ - $^{15}\text{N}^n$  correlations are substantially broadened in the  $^{15}\text{N}$  dimension and consequently overlapped. The line broadening observed for those residues in intermediate-exchange regimes can be removed by the generation of a double-quantum coherence that is entirely insensitive to the rotational exchange. As described in the following sections, this strategy can enable the collection of high-quality Heteronuclear Double-Quantum Correlation (HDQC) data for arginine residues over the entire range of exchange rates.

## 2.2 Theory and Method Development

Firstly, it is noted that the nature of the exchange between  $^{15}\text{N}^{\eta^1}$  and  $^{15}\text{N}^{\eta^2}$  means that the population of the two exchanging sites is identical. Secondly, the double-quantum coherences  $C_2^\zeta N_+^{\eta^1} N_+^{\eta^2}$  and  $C_2^\zeta N_-^{\eta^1} N_-^{\eta^2}$  would evolve under the free precession Hamiltonian with the sum of the two contributing  $^{15}\text{N}^n$  frequencies. An exchange process that interchanges  $^{15}\text{N}^{\eta^1}$  and  $^{15}\text{N}^{\eta^2}$  therefore leaves the double-quantum precession frequencies unchanged. Consequently, the rotation about the  $\text{N}^\epsilon$ - $\text{C}^\zeta$  bond does not affect the evolution of the double-quantum (DQ) coherences and thus no exchange-broadening arising from this rotation is expected to be observed. A thorough description of the HSQC experiment on which these novel experiments are based using the standard  $I_{xyz}$  and  $S_{xyz}$  operators can be found in Chapter 1.

### 2.2.1 Generation of Single-Quantum Coherences

In the previous  $^{13}\text{C}^\zeta$ - $^{15}\text{N}^\epsilon$  HSQC experiment (Figure 2.4a),  $^{13}\text{C}^\zeta$  equilibrium magnetisation is selectively excited using a frequency-selective pulse and transferred to the two-spin order longitudinal element,  $2C_2^\zeta N_z^\epsilon$ , at point *a* using an INEPT block with selective refocussing of  $^{15}\text{N}^\epsilon$ . The application of a  $^{15}\text{N}^\epsilon$ -selective pulse during the INEPT ensures that only the  $^{13}\text{C}^\zeta$ - $^{15}\text{N}^\epsilon$  coupling pathway is active and thus prevents any transfer to the  $^{15}\text{N}^n$  nuclei. Anti-phase transverse  $2C_2^\zeta N_{x,y}^\epsilon$  magnetisation is subsequently evolved at point *b* and transferred back to transverse  $C_x^\zeta$  for detection at point *c* using a second INEPT block. The desired *single-quantum* (SQ) coherence,  $2C_x^\zeta N_z^\epsilon$ , builds up during the first INEPT block according to the sine function shown in Figure 2.4b and is subsequently converted to  $2C_2^\zeta N_z^\epsilon$  using a  $90_y^0$   $^{13}\text{C}$  pulse. The optimal delay is therefore based on a knowledge of the coupling constant with perhaps an additional consideration being made for losses caused by transverse  $^{13}\text{C}$  relaxation during the delay. A total delay for each INEPT of approximately  $25 \text{ ms} - 1/2(J_{\text{CN}})$  - is appropriate in most cases.

## 2. Double-Quantum Coherences in Arginine

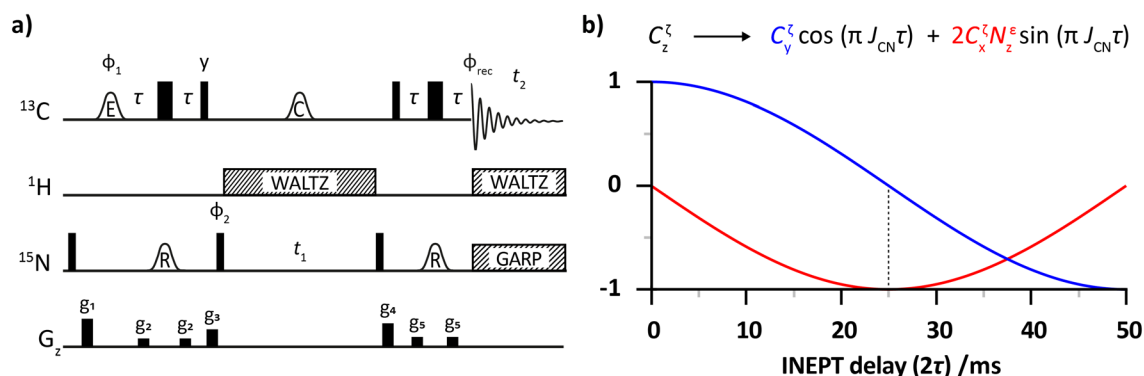


**Figure 2.4** a) Pulse sequence for obtaining  $^{13}\text{C}^{\zeta}\text{-}^{15}\text{N}^{\epsilon}$  HSQC spectra of arginine side-chains in proteins. The phase cycle used is  $\phi_1$ : x, -x;  $\phi_2$ : 2(x), 2(-x);  $\phi_{\text{rec}}$ : x, 2(-x), x. b) Simulated transfer of equilibrium  $C_z^{\zeta}$  magnetisation to the anti-phase  $2C_x^{\zeta}N_z^{\epsilon}$  coherence as a function of the INEPT delay,  $2\tau$ , using a fixed  $^1J_{\text{CN}}$  coupling constant of  $-20$  Hz. The dashed line marks the optimal delay time of  $1/2(J_{\text{CN}}) = 25$  ms.

To enable the collection of  $^{13}\text{C}^{\zeta}\text{-}^{15}\text{N}^{\eta}$  spectra instead, two simple modifications must be made:

1. The  $^{15}\text{N}$  pulse used in the INEPT blocks must be made selective for  $^{15}\text{N}^{\eta}$
2. The total length of each INEPT block must be halved to  $1/4(J_{\text{CN}})$

The first modification is to ensure that this time, only the  $^{13}\text{C}^{\zeta}\text{-}^{15}\text{N}^{\eta}$  coupling pathways are active and any transfer to the  $^{15}\text{N}^{\epsilon}$  nucleus is prevented. The second modification is due to the fact that the  $^{13}\text{C}^{\zeta}$  nucleus is now coupled to *two*  $^{15}\text{N}$  nuclei and therefore the transfer to the desired single-quantum terms proceeds twice as quickly (Figure 2.5, red line).

Coupling to the first  $^{15}\text{N}^{\eta}$  nuclei:

$$C_z^{\zeta} \xrightarrow{N^{\eta 1}} C_y^{\zeta} \cos(\pi J_{\text{CN}} \tau) + 2C_x^{\zeta} N_z^{\eta 1} \sin(\pi J_{\text{CN}} \tau)$$

Coupling to the second  $^{15}\text{N}^{\eta}$  nuclei:

$$\begin{aligned} &\xrightarrow{N^{\eta 2}} C_y^{\zeta} \cos^2(\pi J_{\text{CN}} \tau) \\ &\quad 2C_x^{\zeta} N_z^{\eta 1} \sin(\pi J_{\text{CN}} \tau) \cos(\pi J_{\text{CN}} \tau) \\ &\quad 2C_x^{\zeta} N_z^{\eta 2} \sin(\pi J_{\text{CN}} \tau) \cos(\pi J_{\text{CN}} \tau) \\ &\quad -4C_y^{\zeta} N_z^{\eta 1} N_z^{\eta 2} \sin^2(\pi J_{\text{CN}} \tau) \end{aligned}$$

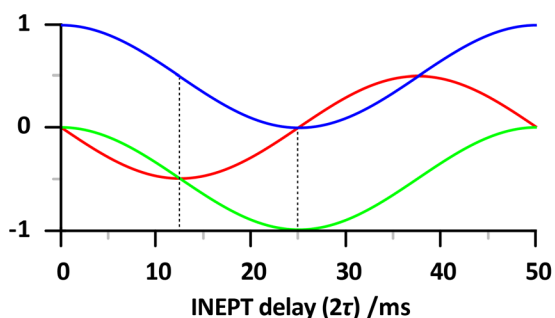


**Figure 2.5** Simulated transfer of equilibrium  $C_z^{\zeta}$  magnetisation to the single-  $2C_x^{\zeta}N_z^{\eta}$  and double-anti-phase  $4C_y^{\zeta}N_z^{\eta 1}N_z^{\eta 2}$  coherences as a function of the INEPT delay,  $2\tau$ , using a fixed  $^1J_{\text{CN}}$  coupling constant of  $-20$  Hz. The dashed lines mark the optimal delay times of  $1/4(J_{\text{CN}}) = 12.5$  ms for the single-anti-phase transfer and  $1/4(J_{\text{CN}}) = 25$  ms for the double-anti-phase transfer.

A drawback of this step is that the maximum achievable transfer to the anti-phase terms is only 50%. This means that we are forced to discard half of the excited  $^{13}\text{C}^{\zeta}$  magnetisation during the first INEPT block and similarly can only transfer half of the  $^{15}\text{N}^{\eta}$  frequency-modulated anti-phase magnetisation back to the  $^{13}\text{C}^{\zeta}$  nucleus for detection. Although this intrinsic inefficiency imposes a significant sensitivity penalty, implementation of both these simple modifications will allow the collection of arginine  $^{13}\text{C}^{\zeta}\text{-}^{15}\text{N}^{\eta}$  HSQC spectra such as the one shown in Figure 2.3c.

### 2.2.2 Generation of Double-Quantum Coherences

It is clear from Figure 2.5 that whilst a delay of 12.5 ms is appropriate for the generation of the single-anti-phase terms, a delay of 25 ms will result in the clean conversion of  $C_z^\zeta$  to the double-anti-phase  $4C_y^\zeta N_z^{\eta^1} N_z^{\eta^2}$  coherence. This term is quadrature with respect to the  $2C_x^\zeta N_z^{\eta^1}$  terms and is easily suppressed in the HSQC experiment using a suitable phase cycle or spoiling gradient pulse. However, this coherence could be converted to the highly-ordered  $4C_z^\zeta N_z^{\eta^1} N_z^{\eta^2}$  term using a  $90_x^0$   $^{13}\text{C}$  pulse with additional suppression of any residual single-quantum terms instead. A subsequent  $90_{x/y}^0$   $^{15}\text{N}$  pulse would then generate multiple-quantum  $^{15}\text{N}$  magnetisation:

$$\begin{aligned} -4C_z^\zeta N_z^{\eta^1} N_z^{\eta^2} &\xrightarrow{90_x^0 \text{ } ^{15}\text{N}} -4C_z^\zeta N_y^{\eta^1} N_y^{\eta^2} \\ -4C_z^\zeta N_z^{\eta^1} N_z^{\eta^2} &\xrightarrow{90_y^0 \text{ } ^{15}\text{N}} -4C_z^\zeta N_x^{\eta^1} N_x^{\eta^2} \end{aligned}$$

Both resulting terms,  $4C_z^\zeta N_y^{\eta^1} N_y^{\eta^2}$  and  $4C_z^\zeta N_x^{\eta^1} N_x^{\eta^2}$  are mixtures of **double-** (DQ) and **zero-**quantum (ZQ) coherences:

$$\begin{aligned} -4C_z^\zeta N_y^{\eta^1} N_y^{\eta^2} &= -4C_z^\zeta \frac{1}{2i} (N_+^{\eta^1} - N_-^{\eta^1}) \frac{1}{2i} (N_+^{\eta^2} - N_-^{\eta^2}) \\ &= C_z^\zeta (N_+^{\eta^1} N_+^{\eta^2} - N_+^{\eta^1} N_-^{\eta^2} - N_-^{\eta^1} N_+^{\eta^2} + N_-^{\eta^1} N_-^{\eta^2}) \\ &= C_z^\zeta N_+^{\eta^1} N_+^{\eta^2} + C_z^\zeta N_-^{\eta^1} N_-^{\eta^2} - C_z^\zeta N_+^{\eta^1} N_-^{\eta^2} - C_z^\zeta N_-^{\eta^1} N_+^{\eta^2} \\ -4C_z^\zeta N_x^{\eta^1} N_x^{\eta^2} &= -4C_z^\zeta \frac{1}{2} (N_+^{\eta^1} + N_-^{\eta^1}) \frac{1}{2} (N_+^{\eta^2} + N_-^{\eta^2}) \\ &= -C_z^\zeta (N_+^{\eta^1} N_+^{\eta^2} + N_+^{\eta^1} N_-^{\eta^2} + N_-^{\eta^1} N_+^{\eta^2} + N_-^{\eta^1} N_-^{\eta^2}) \\ &= -C_z^\zeta N_+^{\eta^1} N_+^{\eta^2} - C_z^\zeta N_-^{\eta^1} N_-^{\eta^2} - C_z^\zeta N_+^{\eta^1} N_-^{\eta^2} - C_z^\zeta N_-^{\eta^1} N_+^{\eta^2} \end{aligned}$$

One could therefore select only the double-quantum terms using a simple phase cycle where the  $90^\circ$   $^{15}\text{N}$  pulse is stepped from x to y with concomitant inversion of the receiver phase. This results in the cancellation of the unwanted **zero-quantum** terms and preserves only the desired **double-quantum** terms:

$$\begin{aligned} \text{Scan 1 } (90_x^0, \phi_{\text{rec.}} = x): & \quad C_z^\zeta N_+^{\eta^1} N_+^{\eta^2} + C_z^\zeta N_-^{\eta^1} N_-^{\eta^2} - C_z^\zeta N_+^{\eta^1} N_-^{\eta^2} - C_z^\zeta N_-^{\eta^1} N_+^{\eta^2} \\ \text{Scan 2 } (90_y^0, \phi_{\text{rec.}} = -x): & \quad - \left( -C_z^\zeta N_+^{\eta^1} N_+^{\eta^2} - C_z^\zeta N_-^{\eta^1} N_-^{\eta^2} - C_z^\zeta N_+^{\eta^1} N_-^{\eta^2} - C_z^\zeta N_-^{\eta^1} N_+^{\eta^2} \right) \\ \text{Scan 1} + \text{Scan 2} & \quad = 2 \left( C_z^\zeta N_+^{\eta^1} N_+^{\eta^2} + C_z^\zeta N_-^{\eta^1} N_-^{\eta^2} \right) \end{aligned}$$

## 2. Double-Quantum Coherences in Arginine

### 2.2.3 Chemical Shift Evolution of Double-Quantum Coherence

Following the generation and selection of this pure double-quantum term, evolution can proceed under the free precession Hamiltonian during an indirect chemical shift period:

$$\mathcal{H} = \mathbf{\Omega}_{\eta^1} \mathbf{N}_z^{\eta^1} + \mathbf{\Omega}_{\eta^2} \mathbf{N}_z^{\eta^2} + \left( 2\pi J_{\text{CN}} C_z^\zeta N_z^{\eta^1} + 2\pi J_{\text{CN}} C_z^\zeta N_z^{\eta^2} + 2\pi J_{\text{NN}} N_z^{\eta^1} N_z^{\eta^2} \right) \quad (2.1)$$

The Hamiltonian contains both terms relating to chemical shift and scalar coupling evolution. However, the heteronuclear  $^{13}\text{C}$ - $^{15}\text{N}$  couplings will be refocussed in the final sequence and the homonuclear  $^{15}\text{N}$ - $^{15}\text{N}$  coupling does not affect the double-quantum states so only the chemical shift terms in bold will be considered here.

To examine the effect of the free precession, it is useful to first define the double-quantum part of the magnetisation we have selected in Section 2.2.2,  $DQ_x$ , as:

$$DQ_x = 4C_z^\zeta N_x^{\eta^1} N_x^{\eta^2} - 4C_z^\zeta N_y^{\eta^1} N_y^{\eta^2} \quad (2.2)$$

The precession then proceeds as:

$$\begin{aligned} & 4C_z^\zeta N_x^{\eta^1} N_x^{\eta^2} \xrightarrow{\Omega_{\eta^1} t_1 N_z^{\eta^1} + \Omega_{\eta^2} t_1 N_z^{\eta^2}} \\ & 4C_z^\zeta \left[ N_x^{\eta^1} \cos(\Omega_{\eta^1} t_1) - N_y^{\eta^1} \sin(\Omega_{\eta^1} t_1) \right] \left[ N_x^{\eta^2} \cos(\Omega_{\eta^2} t_1) - N_y^{\eta^2} \sin(\Omega_{\eta^2} t_1) \right] \\ & - 4C_z^\zeta N_y^{\eta^1} N_y^{\eta^2} \xrightarrow{\Omega_{\eta^1} t_1 N_z^{\eta^1} + \Omega_{\eta^2} t_1 N_z^{\eta^2}} \\ & - 4C_z^\zeta \left[ N_y^{\eta^1} \cos(\Omega_{\eta^1} t_1) + N_x^{\eta^1} \sin(\Omega_{\eta^1} t_1) \right] \left[ N_y^{\eta^2} \cos(\Omega_{\eta^2} t_1) + N_x^{\eta^2} \sin(\Omega_{\eta^2} t_1) \right] \end{aligned}$$

Combining the two and expansion the brackets gives:

$$\begin{aligned} & 4C_z^\zeta N_x^{\eta^1} N_x^{\eta^2} \cos(\Omega_{\eta^1} t_1) \cos(\Omega_{\eta^2} t_1) - 4C_z^\zeta N_x^{\eta^1} N_x^{\eta^2} \sin(\Omega_{\eta^1} t_1) \sin(\Omega_{\eta^2} t_1) \\ & - 4C_z^\zeta N_y^{\eta^1} N_y^{\eta^2} \cos(\Omega_{\eta^1} t_1) \cos(\Omega_{\eta^2} t_1) + 4C_z^\zeta N_y^{\eta^1} N_y^{\eta^2} \sin(\Omega_{\eta^1} t_1) \sin(\Omega_{\eta^2} t_1) \\ & - 4C_z^\zeta N_x^{\eta^1} N_y^{\eta^2} \cos(\Omega_{\eta^1} t_1) \sin(\Omega_{\eta^2} t_1) - 4C_z^\zeta N_x^{\eta^1} N_y^{\eta^2} \sin(\Omega_{\eta^1} t_1) \cos(\Omega_{\eta^2} t_1) \\ & - 4C_z^\zeta N_y^{\eta^1} N_x^{\eta^2} \cos(\Omega_{\eta^1} t_1) \sin(\Omega_{\eta^2} t_1) - 4C_z^\zeta N_y^{\eta^1} N_x^{\eta^2} \sin(\Omega_{\eta^1} t_1) \cos(\Omega_{\eta^2} t_1) \end{aligned}$$

Now re-factorise:

$$\begin{aligned} & \left( 4C_z^\zeta N_x^{\eta^1} N_x^{\eta^2} - 4C_z^\zeta N_y^{\eta^1} N_y^{\eta^2} \right) \left[ \cos(\Omega_{\eta^1} t_1) \cos(\Omega_{\eta^2} t_1) - \sin(\Omega_{\eta^1} t_1) \sin(\Omega_{\eta^2} t_1) \right] \\ & - \left( 4C_z^\zeta N_x^{\eta^1} N_y^{\eta^2} + 4C_z^\zeta N_y^{\eta^1} N_x^{\eta^2} \right) \left[ \cos(\Omega_{\eta^1} t_1) \sin(\Omega_{\eta^2} t_1) + \sin(\Omega_{\eta^1} t_1) \cos(\Omega_{\eta^2} t_1) \right] \end{aligned}$$

Recognising that:<sup>[39]</sup>

$$\begin{aligned}\cos(\Omega_{\eta^1}t_1 + \Omega_{\eta^2}t_1) &= \cos(\Omega_{\eta^1}t_1)\cos(\Omega_{\eta^2}t_1) - \sin(\Omega_{\eta^1}t_1)\sin(\Omega_{\eta^2}t_1) \\ \sin(\Omega_{\eta^1}t_1 + \Omega_{\eta^2}t_1) &= \cos(\Omega_{\eta^1}t_1)\sin(\Omega_{\eta^2}t_1) + \sin(\Omega_{\eta^1}t_1)\cos(\Omega_{\eta^2}t_1)\end{aligned}$$

the precession can be re-written as:

$$DQ_x \xrightarrow{\Omega_{\eta^1}t_1 N_z^{\eta^1} + \Omega_{\eta^2}t_1 N_z^{\eta^2}} DQ_x \cos[(\Omega_{\eta^1} + \Omega_{\eta^2})t_1] - DQ_y \sin[(\Omega_{\eta^1} + \Omega_{\eta^2})t_1] N_x^{\eta^2} \quad (2.3)$$

where:

$$\begin{aligned}DQ_x &= 4C_z^{\zeta} N_x^{\eta^1} N_x^{\eta^2} - 4C_z^{\zeta} N_y^{\eta^1} N_y^{\eta^2} \\ DQ_y &= 4C_z^{\zeta} N_x^{\eta^1} N_y^{\eta^2} + 4C_z^{\zeta} N_y^{\eta^1} N_x^{\eta^2}\end{aligned} \quad (2.4)$$

Therefore, the double-quantum coherence generated by the initial INEPT block will evolve during an indirect chemical shift period according to the sum of the two contributing  $^{15}\text{N}^{\eta}$  frequencies,  $\Omega_{\text{DQ}} = \Omega_{\eta^1} + \Omega_{\eta^2}$ . Irrespective of the  $\text{N}^{\epsilon}\text{-C}^{\zeta}$  rotational frequency and exchange of  $^{15}\text{N}^{\eta}$ ,  $\Omega_{\text{DQ}}$  remains constant and as such the evolution of  $DQ_x$  is unaffected by the associated line-broadening.

Following the chemical shift evolution, only half of the now cosine-modulated  $DQ_x$  magnetisation can be returned to  $4C_z^{\zeta} N_z^{\eta^1} N_z^{\eta^2}$  and subsequently refocussed for detection. If a  $90_x^{\circ}$   $^{15}\text{N}$  pulse is applied at the end of the  $t_1$  evolution period, it is the y-component of  $DQ_x$  that is selected:

$$\begin{aligned}DQ_x \cos[(\Omega_{\text{DQ}})t_1] &\xrightarrow{90_x^{\circ} \text{ } ^{15}\text{N}} (4C_z^{\zeta} N_x^{\eta^1} N_x^{\eta^2} - 4C_z^{\zeta} N_z^{\eta^1} N_z^{\eta^2}) \cos[(\Omega_{\text{DQ}})t_1] \\ DQ_y \sin[(\Omega_{\text{DQ}})t_1] &\xrightarrow{90_x^{\circ} \text{ } ^{15}\text{N}} (4C_z^{\zeta} N_x^{\eta^1} N_z^{\eta^2} + 4C_z^{\zeta} N_z^{\eta^1} N_x^{\eta^2}) \sin[(\Omega_{\text{DQ}})t_1]\end{aligned}$$

The remaining terms,  $4C_z^{\zeta} N_x^{\eta^1} N_x^{\eta^2}$ ,  $4C_z^{\zeta} N_x^{\eta^1} N_z^{\eta^2}$  and  $4C_z^{\zeta} N_z^{\eta^1} N_x^{\eta^2}$ , all retain at least one x-component and are therefore removed by the spoiling gradient pulse. The  $4C_z^{\zeta} N_z^{\eta^1} N_z^{\eta^2}$  term can now be returned to in-phase  $^{13}\text{C}^{\zeta}$  magnetisation for detection via a retro-INEPT sequence analogous to that described in the previous section:

$$-4C_z^{\zeta} N_z^{\eta^1} N_z^{\eta^2} \cos[(\Omega_{\text{DQ}})t_1] \xrightarrow{\text{retro-INEPT}} C_y^{\zeta} \cos[(\Omega_{\text{DQ}})t_1]$$

This results in the detection of  $^{13}\text{C}$  magnetisation that is cosine-modulated with the DQ frequency of the  $^{15}\text{N}^{\eta}$  nuclei. In order to achieve frequency discrimination in the indirect dimension, we also require the corresponding sine-modulated magnetisation,  $C_y^{\zeta} \sin[(\Omega_{\text{DQ}})t_1]$ . As described in Chapter 1, the usual method of achieving this is to induce a  $90^{\circ}$  phase shift in

## 2. Double-Quantum Coherences in Arginine

the cosine-modulated signal by incrementing the  $^{15}\text{N}$  pulse prior to the  $t_1$  period by  $90^\circ$ . However, this will not affect the desired phase shift in this context. The phase shift induced on the coherences by changing the phase of this  $^{15}\text{N}$  pulse by  $\Delta\phi$  is proportional to the change in coherence order caused by the pulse:

$$\text{Phase shift of coherence} = -\Delta\rho \times \Delta\phi \quad (2.5)$$

Recognising that the change in coherence order,  $\Delta\rho$ , caused by the  $^{15}\text{N}$  pulse generating the  $DQ_x$  term is  $\pm 2$  one can induce the required  $90^\circ$  phase shift by incrementing the phase by  $45^\circ$  instead.<sup>[129]</sup> With this small modification, the cosine- and sine-modulated datasets can be recorded and processed according to the States-TPPI scheme. The Echo/Anti-echo detection scheme using pulsed field gradients is equally applicable to this application but lead to slightly diminished signal-to-noise when compared to the phase sensitive method described above. The Echo/Anti-echo scheme requires the incorporation of dephasing and rephasing gradient pulses and relaxation losses during these additional pulses were sufficient to degrade the sensitivity of the gradient-selected method.

### 2.2.4 $^{13}\text{C}^\zeta$ - $^{15}\text{N}^\eta$ HDQC Pulse Sequence

The pulse sequence developed to evolve the DQ coherences of arginine, referred to as the HDQC (Heteronuclear Double Quantum Coherence) experiment,<sup>[130]</sup> is shown in Figure 2.6 along with the Coherence Transfer Pathway (CTP). The sequence consists of four parts:

- i.* **Purge of  $N_z^\eta$ :** Following the relaxation delay, equilibrium  $^{15}\text{N}^\eta$  magnetisation is purged using a  $90_x^\circ$   $^{15}\text{N}$  pulse followed by gradient pulse  $g_1$ . This ensures that any  $^{15}\text{N}$  magnetisation manipulated during the rest of the pulse sequence is generated via the  $^{13}\text{C}^\zeta$ - $^{15}\text{N}^\eta$  scalar coupling.
- ii.*  **$\text{C}^\zeta$ - $\text{N}^\eta$  INEPT:** Selective  $^{13}\text{C}^\zeta$  inversion and  $^{15}\text{N}^\eta$  refocussing efficiently converts equilibrium  $^{13}\text{C}^\zeta$  magnetisation to the double-anti-phase  $4C_y^\zeta N_z^{\eta 1} N_z^{\eta 2}$  at point *a*. The optimal duration and waveform of the required selective pulses will depend on the spectrometer. The spectra presented in this chapter were typically recorded at 16.4 T using 1.5 ms Eburp2 and 4.5 ms Reburp pulses for the  $^{13}\text{C}^\zeta$  inversion and  $^{15}\text{N}^\eta$  refocussing, respectively.
- iii.* **Chemical shift evolution of  $DQ_x$ :** Pure double-quantum magnetisation, selected by the phase cycle, is allowed to evolve during the variable delay  $t_1$  between points *a* and *b* where the  ${}^n J_{\text{HN}}$  scalar couplings are suppressed with a  $^1\text{H}$  WALTZ decoupling scheme. Coupling to the  $^{13}\text{C}^\zeta$  nucleus is refocused by a  $180^\circ$   $^{13}\text{C}$  pulse in the middle of the  $t_1$  period.

- iv.  **$^{13}\text{C}$ - $^{15}\text{N}$  retro-INEPT:** The cosine-modulated y-component of  $DQ_x$  is selected and returned to in-phase carbon magnetisation,  $C_y^z$ , for detection at point c using a retro-INEPT transfer incorporating a selective  $^{15}\text{N}$  refocussing pulse. Quadrature detection of the  $^{13}\text{C}$  signal proceeds under simultaneous  $^1\text{H}$  and  $^{15}\text{N}$  decoupling schemes.

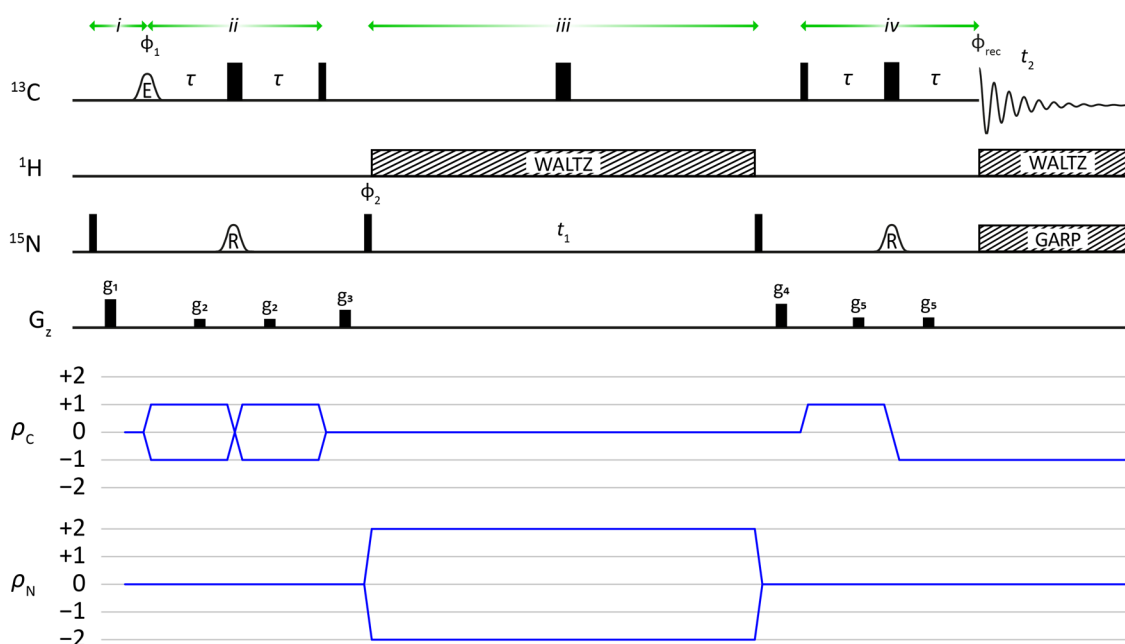


**Figure 2.6** Pulse sequence and coherence transfer pathway diagram for obtaining  $^{13}\text{C}$ - $^{15}\text{N}$  double-quantum correlation (HDQC) spectra of arginine side-chains in proteins. The phase cycle used to select the transfers in the CTP diagram is  $\phi_1: 4(x), 4(-x)$ ;  $\phi_2: x, y, -x, -y$ ;  $\phi_{\text{rec}}: x, -x$ .

From the CTP diagram, one can see that we require the  $^{15}\text{N}$  pulse prior to the  $t_1$  period to simultaneously select the  $0 \rightarrow +2$  ( $\Delta\rho^+ = 2$ ) and  $0 \rightarrow -2$  ( $\Delta\rho^- = -2$ ) pathways and thus will need a phase cycle consisting of four steps ( $\Delta\rho^+ - \Delta\rho^- = 4$ ):

Scan	$^{15}\text{N}$ pulse ( $\phi_2$ )	$-\Delta\rho \times \phi_2$	Receiver ( $\phi_{\text{rec}}$ )
1	$0^\circ$	$0^\circ$	$0^\circ$
2	$90^\circ$	$\pm 180^\circ$	$180^\circ$
3	$180^\circ$	$\pm 360^\circ$	$0^\circ$
4	$270^\circ$	$\pm 540^\circ$	$180^\circ$

**Table 2.1** Four-step phase cycle for the  $^{13}\text{C}$ - $^{15}\text{N}$  HDQC experiment. Whilst four steps are formally required for the double-quantum selection, good quality data can be obtained in only two scans.

Owing to the intrinsic insensitivity of the  $^{13}\text{C}$  nucleus, it is likely that more than four scans per  $t_1$  will be collected in which case axial peak suppression can be included by repeating the phase cycle above whilst inverting the first pulse ( $\phi_1 = -x$ ). Two-dimensional Fourier transformation of the interferogram results in a signal for each arginine residue with the  $^{13}\text{C}$  frequency along the direct dimension ( $f_2$ ) and the sum of the two coupled  $^{15}\text{N}$  frequencies,  $\Omega_{\text{N}\eta 1} + \Omega_{\text{N}\eta 2}$ , along the indirect dimension ( $f_1$ ).

## 2. Double-Quantum Coherences in Arginine

### 2.2.5 $^{13}\text{C}^{\zeta}\text{-}^{15}\text{N}^{\epsilon}\text{-}^{15}\text{N}^{\eta}$ Pulse Sequence

In favourable circumstances, an existing  $^{13}\text{C}^{\zeta}\text{-}^{15}\text{N}^{\epsilon}$  assignment can be transferred to the  $^{13}\text{C}^{\zeta}\text{-}^{15}\text{N}^{\eta}$  HDQC spectrum based on the  $^{13}\text{C}^{\zeta}$  chemical shift alone. However spectral overlap of the arginine  $^{13}\text{C}^{\zeta}$  is not uncommon in even modestly-sized proteins. The  $^{15}\text{N}^{\eta}$  double-quantum experiment described above can be combined with the existing  $^{13}\text{C}^{\zeta}\text{-}^{15}\text{N}^{\epsilon}$  HSQC sequence to provide a three-dimensional experiment suitable for chemical shift assignment. The pulse sequence, shown in Figure 2.7, can be broken down into several parts:

- i. **Purge of  $\text{N}_z^{\eta}$** : See 2D sequence, above.
- ii.  **$\text{C}^{\zeta}\text{-N}^{\epsilon}$  INEPT**: Transfer of  $^{13}\text{C}^{\zeta}$  to anti-phase  $2\text{C}_x^{\zeta}\text{N}_z^{\epsilon}$  at point *a* using selective  $^{15}\text{N}^{\epsilon}$  refocussing during the INEPT described in Figure 2.4.
- iii. **Chemical shift evolution of  $2\text{C}_z^{\zeta}\text{N}_{x,y}^{\epsilon}$** : Anti-phase  $^{15}\text{N}^{\epsilon}$  magnetisation is allowed to evolve during the variable delay  $t_1$  between points *a* and *b* where the  ${}^{\eta}J_{\text{HN}}$  scalar couplings are suppressed with a  $^1\text{H}$  WALTZ decoupling scheme. Coupling to the  $^{13}\text{C}^{\zeta}$  and  $^{13}\text{C}^{\delta}$  nuclei is refocused by an adiabatic  $^{13}\text{C}$  pulse in the middle of the  $t_1$  period. This encodes the  $^{15}\text{N}^{\epsilon}$  chemical shift.
- iv. **Non-selective  $\text{C}^{\zeta}\text{-N}^{\epsilon/\eta}$  INEPT**: The application of a non-selective  $180^\circ$   $^{15}\text{N}$  pulse during the INEPT block between *b* and *c* ensures that all  $J_{\text{CN}}$  scalar couplings are active during the transfer. This allows the refocussing of the  $^{13}\text{C}^{\zeta}\text{-}^{15}\text{N}^{\epsilon}$  coupling whilst simultaneously allowing the  $^{13}\text{C}\text{-}^{15}\text{N}^{\eta}$  couplings to evolve resulting in the clean conversion of  $2\text{C}_z^{\zeta}\text{N}_z^{\epsilon}$  to  $4\text{C}_z^{\zeta}\text{N}_z^{\eta 1}\text{N}_z^{\eta 2}$  in a single step.
- v. **Chemical shift evolution of  $\text{DQ}_x$** : The  $^{15}\text{N}^{\eta}$  DQ chemical shift is then encoded during a second variable delay,  $t_2$ , between *c* and *d*. See 2D sequence, above.
- vi.  **$\text{C}^{\zeta}\text{-N}^{\eta}$  retro-INEPT**: Transfer back to in-phase  $^{13}\text{C}^{\zeta}$  magnetisation for detection via a  $^{15}\text{N}^{\eta}$ -selective retro-INEPT between *d* and *e*, as above.

Frequency discrimination in  $f_1$  and  $f_2$  is achieved by incrementing  $\phi_1$  and  $\phi_2$  by  $90^\circ$  and  $45^\circ$ , respectively, in line with the States-TPPI scheme. An eight-step phase cycle is required to first select the  $0 \rightarrow \pm 1$  pathways prior to  $t_1$ , followed by the  $0 \rightarrow \pm 2$  pathways prior to  $t_2$ :

Scan	$\phi_1$	$\phi_2$	$\phi_{\text{rec}}$
1	$0^\circ$	$0^\circ$	$0^\circ$
2	$180^\circ$	$0^\circ$	$180^\circ$
3	$0^\circ$	$90^\circ$	$180^\circ$
4	$180^\circ$	$90^\circ$	$0^\circ$
5	$0^\circ$	$180^\circ$	$0^\circ$
6	$180^\circ$	$180^\circ$	$180^\circ$
7	$0^\circ$	$270^\circ$	$180^\circ$
8	$180^\circ$	$270^\circ$	$0^\circ$

**Table 2.2** Eight-step phase cycle required for the  $^{13}\text{C}^{\zeta}\text{-}^{15}\text{N}^{\epsilon}\text{-}^{15}\text{N}^{\eta}$  correlation experiment.

Alternate scans implement the selection of the  $\Delta\rho = \pm 1$  pathways for the  $^{15}\text{N}^{\text{E}}$  chemical shift whilst scans 1, 3, 5 and 7 select the  $\Delta\rho = \pm 2$  pathways required for the  $^{15}\text{N}^{\text{N}}$  chemical shift. Fourier transformation results in a three-dimensional spectrum containing a signal for each arginine residue encoded with the  $^{13}\text{C}^{\zeta}$ ,  $^{15}\text{N}^{\text{E}}$  and  $^{15}\text{N}^{\text{N}}$ (DQ) frequencies in  $f_3$ ,  $f_2$  and  $f_1$ , respectively.

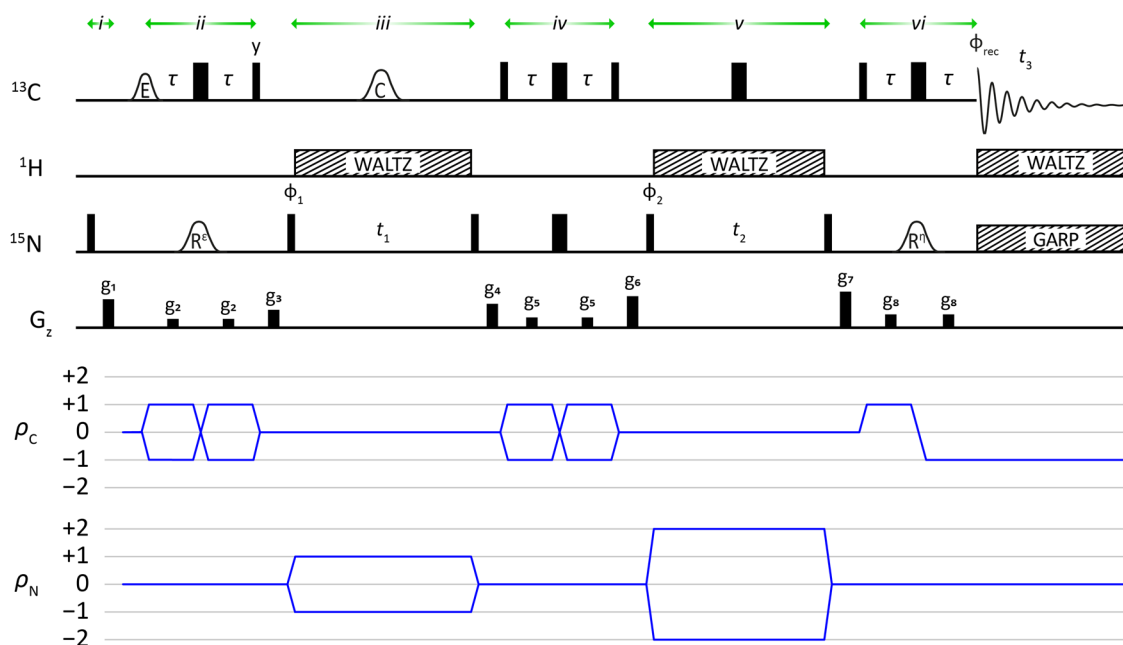


**Figure 2.7** Pulse sequence and coherence transfer pathway to obtain the intra-residue correlation between  $^{15}\text{N}^{\text{E}}$  and  $^{15}\text{N}^{\text{N}}$  double-quantum chemical shifts. The phase cycle used to select the transfers in the CTP diagram is:  $\phi_1$ :  $x, -x$ ;  $\phi_2$ :  $2(x), 2(y), 2(-x), 2(-y)$ ;  $\phi_{\text{rec}}$ :  $x, 2(-x), x$ .

## 2.3 Results and Discussion

### 2.3.1 Application to Free Arginine

As a simple proof of concept, the pulse sequences discussed above were first applied to a sample of *free* [ $^{13}\text{C}_6, ^{15}\text{N}_4$ ]-L-arginine. The free amino acid doesn't form any interactions and so at room temperature the rotational frequency approaches the fast-exchange limit,  $k_{\text{ex}} = 2000 \text{ s}^{-1}$ .<sup>[128]</sup> To demonstrate the effect of evolving the double-quantum magnetisation on the exchange-broadening, the spectra shown in Figure 2.8 were recorded at 275 K to slow the rotational exchange rate to approximately  $200 \text{ s}^{-1}$  and thus increase the associated line-broadening. Figure 2.8a shows the  $^{13}\text{C}^{\zeta}$ - $^{15}\text{N}^{\text{N}}$  HSQC spectrum of free arginine in which the two  $^{15}\text{N}^{\text{N}}$  signals result in the familiar broad resonance indicative of an intermediate-exchange regime. However, the evolution of the double-quantum coherence,  $\text{DQ}_x$ , results in a single sharp signal (Figure 2.8b). The nature of the double-quantum coherence renders it completely insensitive to the line-broadening caused by the rotation of the  $\text{N}^{\text{E}}\text{-C}^{\zeta}$  bond and a sharp signal is detected. It is worth noting that whilst the DQ frequency is the sum of the two  $^{15}\text{N}^{\text{N}}$  frequencies ( $\Omega_{\text{N}1} + \Omega_{\text{N}2}$ ), the

## 2. Double-Quantum Coherences in Arginine

data has been processed so that the peak is centred at the *average* frequency of the  $^{15}\text{N}^{\eta}$  nuclei. The spectrum resulting from the three-dimensional experiment in Figure 2.7 is shown in Figure 2.8c. As expected, the spectrum contains a single peak centred at the  $^{13}\text{C}^{\zeta}$ ,  $^{15}\text{N}^{\eta}(\text{DQ})$  and  $^{15}\text{N}^{\epsilon}$  frequencies in  $f_3$ ,  $f_2$  and  $f_1$ , respectively.

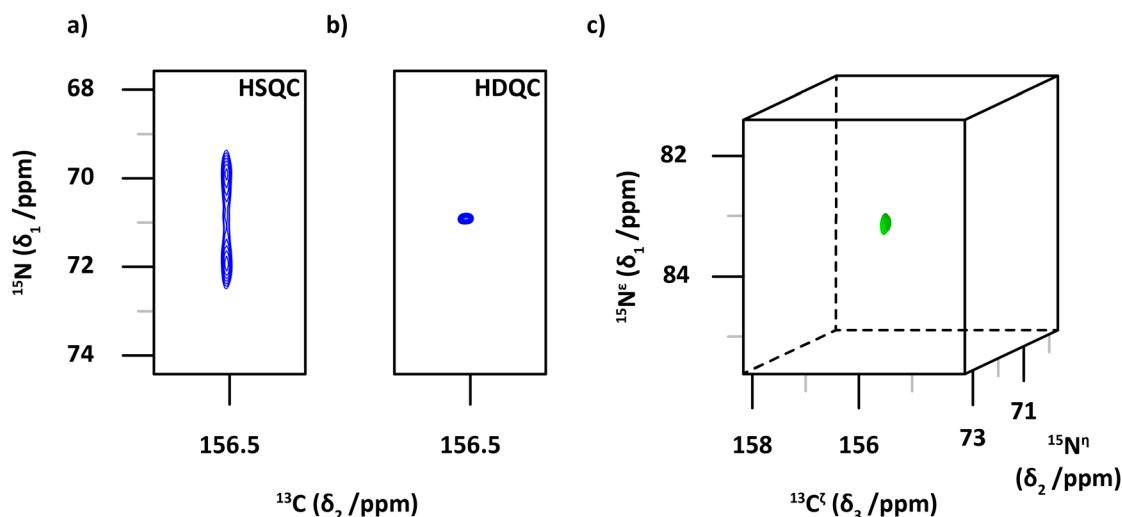


**Figure 2.8**  $^{13}\text{C}$ -detected NMR spectra of  $[^{13}\text{C}_6, ^{15}\text{N}_4]$ -arginine in  $\text{H}_2\text{O}$  recorded at 275 K and 14.1 T. a) The  $^{13}\text{C}^{\zeta}$ - $^{15}\text{N}^{\eta}$  HSQC spectrum results in the detection of a broad resonance for the two  $^{15}\text{N}^{\eta}$  nuclei owing to the partially restricted rotation of the  $\text{N}^{\epsilon}$ - $\text{C}^{\zeta}$  bond. b) The  $^{13}\text{C}^{\zeta}$ - $^{15}\text{N}^{\eta}$  HDQC results in a single sharp resonance at the average chemical shift of the two contributing  $^{15}\text{N}^{\eta}$  nuclei. The exchange broadening caused by the restricted rotation is completely removed. c) The 3D  $^{13}\text{C}^{\zeta}$ - $^{15}\text{N}^{\epsilon}$ - $^{15}\text{N}^{\eta}$  spectrum results in a resonance encoded with the  $^{13}\text{C}^{\zeta}$ ,  $^{15}\text{N}^{\epsilon}$  and  $^{15}\text{N}^{\eta}(\text{DQ})$  frequencies and can be used for chemical shift assignment.

### 2.3.2 Application to T4 Lysozyme

#### $^{13}\text{C}^{\zeta}$ - $^{15}\text{N}^{\eta}$ HDQC Pulse Sequence

The  $^{13}\text{C}^{\zeta}$ - $^{15}\text{N}^{\eta}$  HDQC spectrum recorded using the pulse sequence shown in Figure 2.6 on a sample of T4L99A is shown in Figure 2.9. When compared to the single-quantum  $^{13}\text{C}^{\zeta}$ - $^{15}\text{N}^{\eta}$  in Figure 2.3c, it is immediately apparent that the broad resonances around 157.0 ppm ( $^{13}\text{C}$ ) have sharpened considerably. The double-quantum experiment is particularly useful to probe flexible arginine side-chains, where eight signals are clearly distinguishable in the region previously containing a single broad, overlapped resonance.

A disadvantage of the double-quantum experiment to the single-quantum is the faster (ca. 2-fold) transverse relaxation during the indirect chemical shift evolution period, since the spin density matrix elements involved,  $4C_z^{\zeta}N_{x,y}^{\eta 1}N_{x,y}^{\eta 2}$ , are transverse with respect to both  $^{15}\text{N}^{\eta}$  nuclei, which in turn relax with the two directly bound protons. The faster relaxation, which ultimately leads to lower signal-to-noise, only becomes significant for arginine side-chains that are rigid and therefore experience a rotational correlation time ( $\tau_c$ ) similar to the whole protein. This is evident by the lack of signal observed for R145 in the HDQC experiment. However, the rigid side-

chains are typically less affected by the exchange process this sequence seeks to address and so the data obtained from the  $^{13}\text{C}^{\zeta}\text{-}^{15}\text{N}^{\eta}$  HSQC experiment is often useful for these residues (Figure 2.3c). The substantially better resolution provided by the double-quantum experiment adequately compensates for the associated loss of signal for less rigid and more flexible residues.

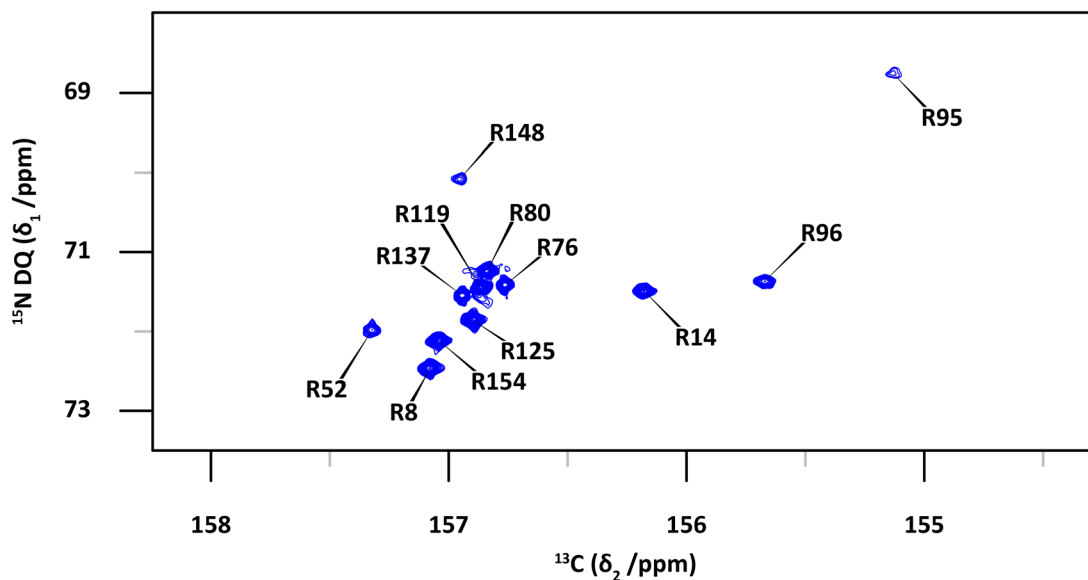


**Figure 2.9**  $^{13}\text{C}^{\zeta}\text{-}^{15}\text{N}^{\eta}$  HDQC spectrum of T4L99A recorded at 16.4 T. The indirect  $^{15}\text{N}$  chemical shift is encoded by the double-quantum components  $C_2^{\zeta}N_+^{\eta}N_+^{\eta^2}$  and  $C_2^{\zeta}N_+^{\eta}N_-^{\eta^2}$  and is processed such that the cross peaks appear at the average chemical shift of the two contributing  $^{15}\text{N}^{\eta}$  frequencies.

The rapid transverse relaxation of the  $^{15}\text{N}^{\eta}$  nuclei of rigid residues in medium-to-large proteins can be mitigated by preparing the sample in a 100%  $^2\text{H}_2\text{O}$  buffer. Substitution of the  $^1\text{H}^{\eta}$  protons with deuterium leads to slower  $^{15}\text{N}^{\eta}$  transverse relaxation and thus sharper lines in the indirect dimension of the double-quantum experiment. However, the longitudinal relaxation time of the  $^{13}\text{C}^{\zeta}$  nucleus also increases, which limits the permitted recycle rate of the experiment and increases the overall acquisition time. Whilst we have not observed a significant sensitivity gain per unit time using a 100%  $^2\text{H}_2\text{O}$  buffer, recording spectra in 100%  $^2\text{H}_2\text{O}$  could be useful in applications where experimental time is not a concern.

### $^{13}\text{C}^{\zeta}\text{-}^{15}\text{N}^{\epsilon}\text{-}^{15}\text{N}^{\eta}$ Pulse Sequence

Whilst most of the arginine residues detected in T4L99A using the HDQC sequence can be identified from the previously assigned  $^{13}\text{C}^{\zeta}\text{-}^{15}\text{N}^{\epsilon}$  spectrum, both R137 and R148 have a  $^{13}\text{C}^{\zeta}$  frequency of 156.95 ppm and thus any  $^{15}\text{N}^{\eta}$  assignment based on this alone would be ambiguous. Figure 2.10 shows how the  $^{13}\text{C}^{\zeta}\text{-}^{15}\text{N}^{\epsilon}\text{-}^{15}\text{N}^{\eta}$  pulse sequence can be used to unambiguously assign these residues. The  $^{15}\text{N}^{\epsilon}\text{-}^{15}\text{N}^{\eta}$  plane (Figure 2.10b) extracted from the three-dimensional dataset clearly demonstrates that the  $^{15}\text{N}^{\epsilon}$  and  $^{15}\text{N}^{\eta}$  (DQ) frequencies of 82.5 ppm and 70.0 ppm, respectively, are from the same residue (R148) as are the  $^{15}\text{N}^{\epsilon}$  and  $^{15}\text{N}^{\eta}$  (DQ) frequencies of 84.5 ppm and 71.5 ppm (R137).

## 2. Double-Quantum Coherences in Arginine

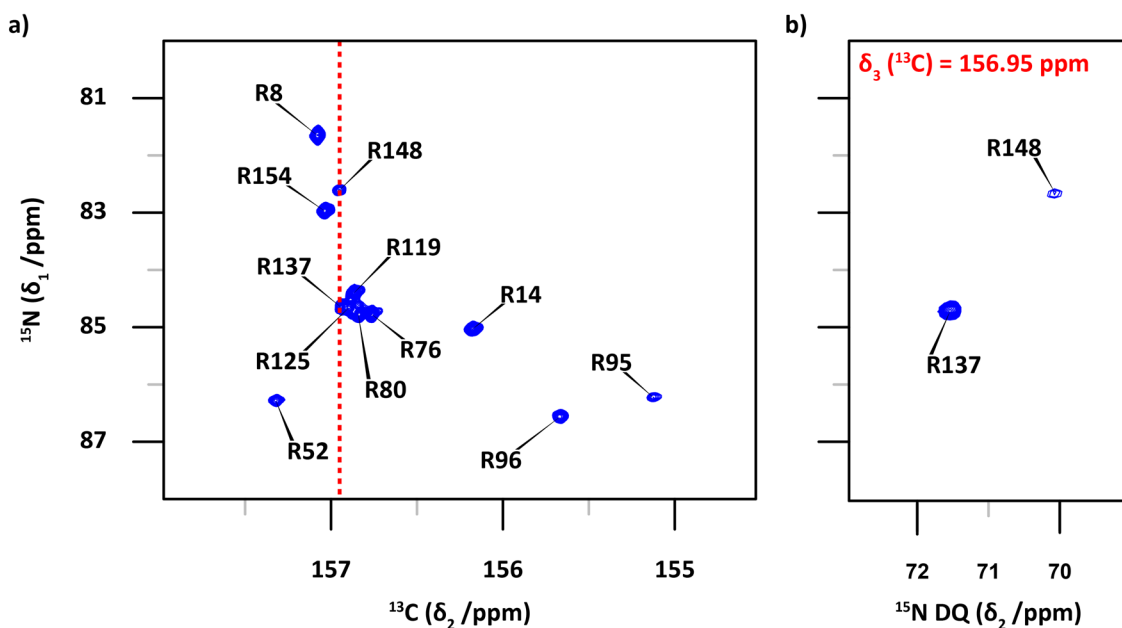


**Figure 2.10** a)  $^{13}\text{C}^{\zeta}\text{-}^{15}\text{N}^{\epsilon}$  HSQC spectrum of T4L99A recorded at 16.4 T. The overlap of R137 and R148 in the  $^{13}\text{C}$  dimension is highlighted by red dashed line. This ambiguity hampers the chemical shift assignment of the double-quantum spectrum in Figure 2.9. b)  $^{15}\text{N}^{\epsilon}\text{-}^{15}\text{N}^{\delta}$ (DQ) 2D-plane extracted at  $^{13}\text{C}^{\zeta} = 156.95$  ppm (red line in a) from the 3D experiment (Figure 2.7) recorded at 11.7 T. The 3D spectrum allows unambiguous chemical shift assignment of R137 and R148 in the  $^{15}\text{N}^{\delta}$  double-quantum spectrum.

### 2.3.3 Generation of Zero-Quantum Coherences

In Section 2.2.2, it was shown how pure  $DQ_x$  magnetisation could be extracted from the multiple-quantum terms  $4C_z^{\zeta}N_y^{\eta^1}N_y^{\eta^2}$  and  $4C_z^{\zeta}N_x^{\eta^1}N_x^{\eta^2}$  using appropriately phased pulses. In a simple extension, if one were to step the  $90^\circ$   $^{15}\text{N}$  pulse from x to y *without* inversion of the receiver phase, it is straightforward to see that the result would instead be cancellation of the **double-quantum** terms and retention of the **zero-quantum** terms:

$$\text{Scan 1 } (90_x^\circ, \phi_{\text{rec.}} = x): \quad C_z^{\zeta}N_+^{\eta^1}N_+^{\eta^2} + C_z^{\zeta}N_-^{\eta^1}N_-^{\eta^2} - C_z^{\zeta}N_+^{\eta^1}N_-^{\eta^2} - C_z^{\zeta}N_-^{\eta^1}N_+^{\eta^2}$$

$$\text{Scan 2 } (90_y^\circ, \phi_{\text{rec.}} = x): \quad -C_z^{\zeta}N_+^{\eta^1}N_+^{\eta^2} - C_z^{\zeta}N_-^{\eta^1}N_-^{\eta^2} - C_z^{\zeta}N_+^{\eta^1}N_-^{\eta^2} - C_z^{\zeta}N_-^{\eta^1}N_+^{\eta^2}$$

$$\text{Scan 1} + \text{Scan 2} = -2 \left( C_z^{\zeta}N_+^{\eta^1}N_-^{\eta^2} + C_z^{\zeta}N_-^{\eta^1}N_+^{\eta^2} \right)$$

This can be more succinctly expressed as pure  $ZQ_x$  magnetisation:

$$ZQ_x = 4C_z^{\zeta}N_x^{\eta^1}N_x^{\eta^2} + 4C_z^{\zeta}N_y^{\eta^1}N_y^{\eta^2} \quad (2.6)$$

Analysis of how this operator would evolve under the free precession Hamiltonian proceeds in an analogous fashion to that described in Section 2.2.3 for the double-quantum magnetisation  $DQ_x$  and results in:

$$ZQ_x \xrightarrow{\Omega_{\eta^1}t_1N_z^{\eta^1} + \Omega_{\eta^2}t_1N_z^{\eta^2}} ZQ_x \cos[(\Omega_{\eta^1} - \Omega_{\eta^2})t_1] - ZQ_y \sin[(\Omega_{\eta^1} - \Omega_{\eta^2})t_1] \quad (2.7)$$

where:

$$\begin{aligned} ZQ_x &= 4C_z^z N_x^{\eta^1} N_x^{\eta^2} + 4C_z^z N_y^{\eta^1} N_y^{\eta^2} \\ ZQ_y &= 4C_z^z N_y^{\eta^1} N_x^{\eta^2} - 4C_z^z N_x^{\eta^1} N_y^{\eta^2} \end{aligned} \quad (2.8)$$

The important difference here is that the zero-quantum coherences would evolve according to the *difference* between the two contributing  $^{15}\text{N}^{\eta}$  frequencies,  $\Omega_{\text{ZQ}} = \Omega_{\eta^1} - \Omega_{\eta^2}$ , rather than the sum. Whilst for the double-quantum frequency,  $\Omega_{\text{DQ}} = \Omega_{\eta^1} + \Omega_{\eta^2}$ , the exchange of  $^{15}\text{N}^{\eta^1}$  with  $^{15}\text{N}^{\eta^2}$  has no effect on the chemical shift evolution (as  $\Omega_{\eta^1} + \Omega_{\eta^2} = \Omega_{\eta^2} + \Omega_{\eta^1}$ ), the rotational exchange does affect the zero-quantum magnetisation.

This arises because the exchange of  $^{15}\text{N}^{\eta^1}$  with  $^{15}\text{N}^{\eta^2}$  (and vice versa) results in the exchange of two different zero-quantum frequencies:

$$\Omega_{\eta^1} - \Omega_{\eta^2} \neq \Omega_{\eta^2} - \Omega_{\eta^1}$$

As described previously in Figure 2.3b, the way an exchange process manifests itself in NMR spectra is dependent on both the exchange rate,  $k_{\text{ex}}$ , and the difference in frequency between the exchanging nuclei,  $\Delta\delta$ . For the single-quantum spectrum shown in Figure 2.3c,  $\Delta\delta$  for the rotational exchange in each arginine residue is:

$$\Delta\delta (\text{SQ}) = \Omega_{\eta^1} - \Omega_{\eta^2} \quad (2.9)$$

The rotational exchange experienced by the zero-quantum magnetisation described above is:

$$\begin{aligned} \Delta\delta (\text{ZQ}) &= (\Omega_{\eta^1} - \Omega_{\eta^2}) - (\Omega_{\eta^2} - \Omega_{\eta^1}) \\ &= 2(\Omega_{\eta^1} - \Omega_{\eta^2}) \end{aligned} \quad (2.10)$$

The exchange rate,  $k_{\text{ex}}$ , would remain the same for both the single- and zero-quantum magnetisation but as the apparent difference in frequencies present in the zero-quantum spectrum is twice that of those in the single-quantum spectrum, the zero-quantum resonances would be expected to be sharper.

Unfortunately, a problem is encountered when trying to obtain the sine-modulated magnetisation required for frequency discrimination in the indirect dimension. For the HDQC experiment, the required  $90^\circ$  phase shift was induced in the cosine-modulated  $DQ_x$  magnetisation by applying a  $45^\circ$  phase increment ( $\Delta\phi$ ) to the  $^{15}\text{N}^{\eta}$  pulse that begins the  $t_1$  evolution period. This was effective because that pulse causes a change in coherence order,  $\Delta\rho$ , of  $\pm 2$  and

$$\text{phase shift of coherence} = -\Delta\rho \times \Delta\phi$$

## 2. Double-Quantum Coherences in Arginine

Therefore, the cosine-modulated magnetisation is shifted by  $90^\circ$  and becomes sine-modulated, as required for the States-TPPI scheme. In the Heteronuclear Zero Quantum Coherence (HZQC) experiment, that same pulse converts the  $4C_2^z N_z^{\eta^1} N_z^{\eta^2}$  term to the zero-quantum coherences,  $C_2^z N_+^{\eta^1} N_-^{\eta^2}$  and  $C_2^z N_-^{\eta^1} N_+^{\eta^2}$ , all of which have a coherence order of zero. This means that the change in coherence order caused by the pulse,  $\Delta\rho$ , is also zero and thus there is no phase shift induced on the  $ZQ_x$  magnetisation upon the phase incrementation of this pulse. Without both the cosine- and sine-modulated components of the indirect chemical shift evolution, the phase-modulated two-dimensional HZQC spectrum cannot be recorded. Nevertheless, the cosine-modulated zero-quantum magnetisation can be obtained and subsequently treated with a real Fourier transform as discussed in Chapter 1. The data recorded on a sample of *free* [ $^{13}\text{C}_6, ^{15}\text{N}_4$ ]-L-arginine is shown below in Figure 2.11. Owing to the lack of sine-modulated magnetisation, frequency discrimination cannot be performed, and two peaks are observed symmetrically about the carrier frequency. However, the data is still useful and demonstrates how the zero-quantum magnetisation behaves in arginine side-chains. When the sample is cooled to 274 K, the rotational exchange is sufficiently slowed to reveal two resonances in the single-quantum spectrum (Figure 2.11a). It is useful to reference the HZQC data such that the middle of the  $^{15}\text{N}$  dimension is set to 0 ppm and thus the zero-quantum spectrum (Figure 2.11b) correspondingly shows a peak at a frequency equal to the difference between  $^{15}\text{N}^{\eta^1}$  and  $^{15}\text{N}^{\eta^2}$ , as expected.

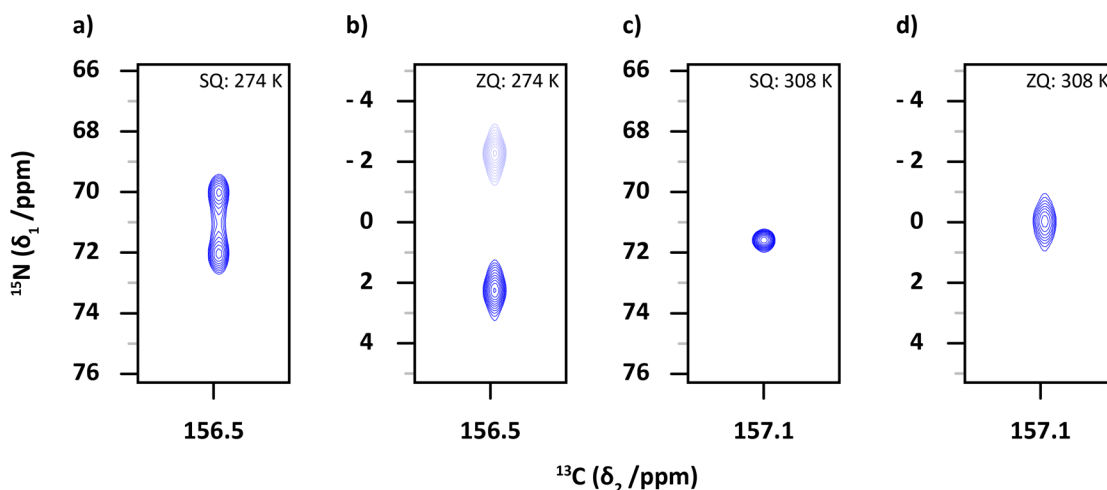


**Figure 2.11** Example  $^{13}\text{C}$ - $^{15}\text{N}^{\eta}$  HSQC (a,c) and HZQC (b,d) spectra of *free* [ $^{13}\text{C}_6, ^{15}\text{N}_4$ ]-L-arginine recorded at 14.1 T. At the slow-exchange limit (274 K), a peak corresponding to  $(\Omega_{\eta^1} - \Omega_{\eta^2})$  is observed in the HZQC spectrum. As described in the main text, frequency discrimination in the HZQC spectra cannot be achieved and so the resulting cosine-modulation artefact in b) has been rendered transparent to avoid confusion. At the fast exchange limit (308 K), the rotational exchange renders the two  $^{15}\text{N}^{\eta}$  frequencies the same and as such a single peak is observed at 0 ppm in the HZQC spectrum. Chemical shift differences observed between the 274 K and 308 K spectra are a result of the data being referenced to the temperature-sensitive water resonance.

Increasing the sample temperature to 308 K results in a rotational exchange rate sufficiently high to cause the observation of a single peak in the single-quantum spectrum at the average of

the two contributing  $^{15}\text{N}^n$  chemical shifts (Figure 2.11c). The rapid exchange between  $^{15}\text{N}^n$  nuclei causes the effective chemical shift difference between them to be negligible and the HZQC spectrum shows a peak with no chemical shift evolution (Figure 2.11d). At both temperatures, the ZQ-coherence appears to undergo rapid  $T_2$  relaxation and results in a significant broadening of the detected signal.

It is important to realise that in addition to the difficulties encountered regarding the sine-modulated magnetisation required for frequency discrimination, there is no evolution of the underlying  $^{15}\text{N}^n$  chemical shifts regardless of the exchange regime a given arginine residue is subject to. In a molecule containing several arginine side-chains, one would therefore have to rely on the  $^{13}\text{C}^\zeta$  chemical shift alone to resolve the individual residues or design a pulse sequence containing an additional  $^{15}\text{N}^{\epsilon/\eta}$  dimension to evolve the intrinsic  $^{15}\text{N}$  chemical shift. It is anticipated that the apparent rapid relaxation of the ZQ magnetisation would limit the utility of such an experiment.

## 2.4 Conclusions

Although arginine residues are often of critical importance when studying biological interactions, the nature of the side-chain renders them difficult to observe directly using established NMR-based techniques. The experiments proposed in this chapter exploit the unique properties of double-quantum magnetisation and allow the easy collection of arginine NMR spectra of the highest resolution. The strategy of generating and subsequently evolving a double-quantum coherence involving both the  $^{15}\text{N}^n$  nuclei of arginine side-chains results in spectra in which the line-broadening caused by the restricted rotation of the  $\text{N}^\epsilon\text{-C}^\zeta$  bond is completely removed. A two-dimensional implementation, HDQC, is complementary to the existing  $^{13}\text{C}^\zeta\text{-}^{15}\text{N}^n$  HSQC experiment because whilst the double-quantum experiment is ideally suited to characterise arginine side-chains whose  $^{13}\text{C}^\zeta\text{-}^{15}\text{N}^n$  single-quantum resonances are severely broadened because of exchange, the HSQC experiment provides site-specific ( $^{15}\text{N}^{\eta^1}$ ,  $^{15}\text{N}^{\eta^2}$ ) information for the well-resolved resonances. A three-dimensional implementation of the HDQC experiment, in which it is combined with the single-quantum  $^{13}\text{C}^\zeta\text{-}^{15}\text{N}^\epsilon$  experiment has been shown to be useful in the residue-specific assignment of the  $^{15}\text{N}^n$  (DQ) resonances. The presented experiments add to a growing list of methods for characterising functional protein side-chains, which ultimately will allow a quantification of the structure, dynamics, and interactions of side-chains in solution to a level where their specific contribution to enzymatic function and protein interactions can be elucidated.

## 2. Double-Quantum Coherences in Arginine

# 3

## Side-Chain Hydrogen Exchange in Arginine

### 3.1 Introduction

The previous chapter provided an example of why the rapid exchange of labile protons is often considered an obstacle to biological NMR spectroscopy: a critical step in many pulse sequences is the transfer of magnetisation from  $^1\text{H}$  to  $^{15}\text{N}$  and the rapid exchange of  $^1\text{H}$  nuclei with bulk solvent essentially prevents this process. It was shown that by switching to  $^{13}\text{C}$ -based NMR experiments, one can safely ignore the exchange of the protons. However, an accurate quantification of the rate of these sometimes-troublesome exchange processes can provide a valuable insight into the many non-covalent interactions present within proteins.<sup>[131–133]</sup> Numerous experimental strategies exist for the quantification of these processes, the most common of which follow the chemical exchange of a labile hydrogen atom with a deuterium atom, or vice versa.<sup>[134,135]</sup> Owing to the physical properties of the deuterium isotope, this exchange reaction - commonly referred to hydrogen-deuterium exchange (HDX) or more simply hydrogen exchange (HX) - is easy to follow using a variety of analytical techniques including mass spectrometry,<sup>[136]</sup> neutron crystallography<sup>[137,138]</sup> and NMR spectroscopy.<sup>[139–141]</sup> The additional neutron in deuterium provides a +1 Da mass shift compared to the protonated species that is easily detected using mass spectrometry. In neutron crystallography, as the neutrons are scattered by the nucleus of the atoms rather than the electrons responsible for the diffraction of X-rays, the difference in size of the proton and deuterium nuclei is easily detectable. As for NMR spectroscopy, the gyromagnetic ratio of deuterium,  $\gamma_{\text{D}}$ , is approximately 6.5 times smaller than that of the proton,  $\gamma_{\text{H}}$ , and as such the two isotopes have markedly different Larmor frequencies. This means that protons replaced with deuterium atoms become invisible in proton NMR spectra as the exchange reactions proceed.

A further advantage, regardless of the analytical technique chosen, is the very low natural abundance (ca. 0.02 %) of deuterium.<sup>[142]</sup> Coupled with a facile route of deuterium enrichment, by using heavy-water ( $^2\text{H}_2\text{O}$ ) as the solvent, this allows the careful control of the hydrogen-exchange process in the laboratory.

### 3. Side-Chain Hydrogen Exchange in Arginine

#### 3.1.1 Hydrogen Exchange and Intramolecular Interactions

It has been known since the early 1950s<sup>[143–145]</sup> that the exchange rates of the amide protons of the protein backbone with neighbouring solvent molecules can inform on the solvent accessibility and tertiary structure of the molecule. Firstly, the chemical reaction that affects the substitution of a proton with a deuterium requires that a source of deuterium is present at the site of exchange. For the reverse process, a proton source must be present to allow the analogous substitution of a deuteron. In aqueous systems, this requirement is met by the solvent and the reactions are thus dependent on the ability of a water molecule to penetrate the tertiary protein structure. For regions of a protein that are not solvent exposed, one would expect the exchange rate to be much lower than for regions on the protein surface, for example. Secondly, the proton to exchange must be able to physically separate from the amide nitrogen. For an amide not involved in interactions, this is not a problem and the amide proton is able to readily exchange with the solvent. However, if the proton is held in an interaction such as hydrogen bond or salt-bridge, the rate of exchange will be significantly attenuated. A measurement of the residue-specific hydrogen exchange rates followed by a comparison with the rates observed in the corresponding free and non-interacting amino acids therefore allows one to identify residues that are engaged in intra- or even intermolecular interactions.

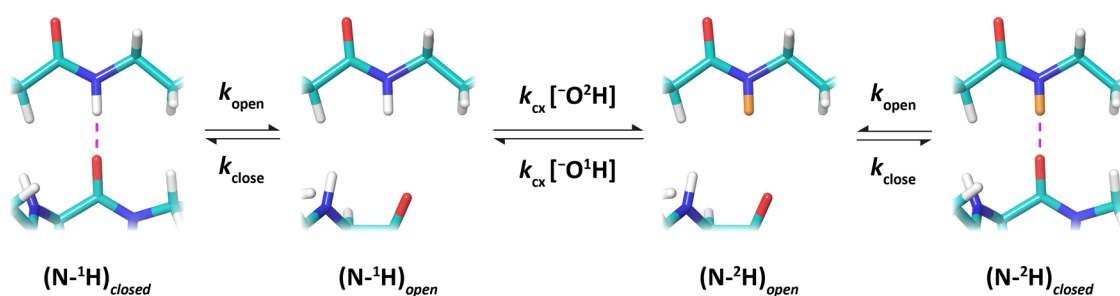


**Figure 3.1** The accepted model for the base-catalysed hydrogen exchange of amide protons in proteins. Several equilibrium processes are present, as described in the main text.

The mechanism<sup>[146,147]</sup> of the complete hydrogen exchange process is illustrated in Figure 3.1. An amide proton engaged in a hydrogen-bond or similar interaction is in a dynamic equilibrium between the (N-1H)<sub>closed</sub> and (N-1H)<sub>open</sub> forms, with associated exchange rates  $k_{\text{open}}$  and  $k_{\text{close}}$  for the opening and closing rates of the interaction, respectively. As discussed above, only the *open* form can undergo chemical exchange with deuterium to form the deuterated (N-2H)<sub>open</sub> species with the rate  $k_{\text{cx}}$ . This deuterated species is then able to re-form the interaction and generate the (N-2H)<sub>closed</sub> complex with the rates  $k_{\text{open}}$  and  $k_{\text{close}}$ . The reverse pathway is also present whereby a deuterated amide complex undergoes an opening process followed by chemical exchange with a proton-bearing solvent molecule to generate the corresponding protonated amide. As a result of the lower vibrational energy caused by the higher mass of deuterium, the

### 3. Side-Chain Hydrogen Exchange in Arginine

forward and reverse chemical exchange reactions typically differ by around 10%, in favour of the formation of the deuterated species.<sup>[148]</sup> However, using the average rate  $k_{cx}$  is an appropriate approximation for the following discussion.

Within a real system, the opening and closing of an interaction occurs together with the chemical exchange of the amide proton and thus the two competing processes cannot generally be assessed individually. Instead, one can only observe an exchange process defined as a combination of the individual rate constants:

$$k_{obs} = \frac{k_{open}k_{cx}}{k_{open} + k_{close} + k_{cx}} \quad (3.1)$$

If one were to assume that the interaction in question was sufficiently favourable such that  $k_{close} \gg k_{open}$ , the  $k_{open}$  contribution to the total denominator in the expression above can be ignored:

$$k_{obs} = \frac{k_{open}k_{cx}}{k_{close} + k_{cx}} \quad (3.2)$$

Using this expression, there are two limits to the hydrogen exchange process. The first limit, usually referred to as EX<sub>1</sub>, occurs when the intrinsic chemical exchange rate is much greater than the closing rate of the interaction ( $k_{cx} \gg k_{close}$ ). In this limit, the rate determining step is the opening of the interaction and the observed rate,  $k_{obs}$ , reports only on this process:

$$k_{obs} = \frac{k_{open}k_{cx}}{k_{close} + k_{cx}} = k_{open} \quad \text{EX}_1, \text{ when } k_{cx} \gg k_{close} \quad (3.3)$$

EX<sub>1</sub> kinetics are therefore expected for protons that require a significant (and thus slow) conformational change within the protein in order to expose them to the solvent. For example, this may be encountered for residues that are buried deep within the three-dimensional structure of the molecule.

The second limit, EX<sub>2</sub>, occurs when the closing of the interaction is much faster than the rate of chemical exchange ( $k_{close} \gg k_{cx}$ ) and is expected for protons that are either already solvent exposed or only a require small conformational change to become solvent exposed. In this limit, the opening of the interaction is no longer the rate determining step and thus  $k_{obs}$  reports directly on the equilibrium constant of the interaction,  $K_{int}$ :

$$k_{obs} = \frac{k_{open}k_{cx}}{k_{close} + k_{cx}} = k_{cx} \frac{k_{open}}{k_{close}} \quad \text{EX}_2, \text{ when } k_{close} \gg k_{cx}$$
$$k_{obs} = k_{cx}K_{int}. \quad (3.4)$$

### 3. Side-Chain Hydrogen Exchange in Arginine

However, in order to extract the equilibrium constant for the interaction from the observed exchange rate, prior knowledge of the intrinsic chemical exchange rate is required. This rate is not only highly sensitive to pH and temperature,<sup>[149–151]</sup> but also to the residue type of both the proton-bearing amino acid and its immediate neighbour ( $i + 1$ ). In recognition of the structural information available from the quantification of hydrogen exchange rates, computational tools exist that allow the prediction of these intrinsic chemical exchange rates for a poly-peptide chain at a given pH and temperature.<sup>[152]</sup> Armed with the value of  $k_{cx}$ , it is then simple to extract the equilibrium constant and therefore calculate the Gibbs Free Energy,  $\Delta G^\ddagger$  for the interaction:<sup>[153]</sup>

$$K_{int.} = \frac{k_{obs}}{k_{cx}} \quad (3.5)$$

$$\Delta G^\ddagger = -RT \ln K_{int.} \quad (3.6)$$

where R is the universal gas constant and T the temperature

It follows that an exchange rate resulting in a larger value for the Gibbs Free Energy indicates a stronger, more energetically favourable interaction within the molecule. Conversely, a small value for the Gibbs Free Energy indicates a weaker interaction that takes only a small amount of energy to overcome.

An alternative and commonly used way of expressing the strength of an interaction is by the computation of a protection factor (PF) for the exchanging nuclei:<sup>[154]</sup>

$$PF = \frac{k_{cx}}{k_{obs}} \quad (3.7)$$

This is simply the inverse of the equilibrium constant,  $K_{int.}$ , with a higher value resulting from a stronger interaction that reflects the higher degree of *protection* afforded from the chemical exchange reaction. Residues that return a protection factor of close to 1 indicate nuclei that are highly solvent exposed and not involved in any significant interactions.

#### 3.1.2 Established NMR Techniques for Quantifying HX Rates

The simplest method to quantify the exchange of the amide protons with deuterium is based on the collection of a series of  $^1\text{H}$ - $^{15}\text{N}$  HSQC spectra on a sample prepared in a fully deuterated buffer.<sup>[155–157]</sup> The protein to be studied is first lyophilised from a buffer prepared using 100%  $^1\text{H}_2\text{O}$  after a suitable incubation period. This ensures that all the amide sites are protonated prior to the start of the exchange reactions. The lyophilised sample is then dissolved in  $^2\text{H}_2\text{O}$  and the collection of  $^1\text{H}$ - $^{15}\text{N}$  HSQC spectra begins. A typical reaction profile is shown in Figure 3.2a. As

### 3. Side-Chain Hydrogen Exchange in Arginine

discussed previously, the HSQC experiment relies on the  $^1\text{H}$ - $^{15}\text{N}$  scalar coupling to transfer the magnetisation throughout the NMR experiment and with all sites initially protonated, maximum signal is obtained at  $t = 0$ . However, as time elapses residues exchange with deuterium and become  $^2\text{H}$ - $^{15}\text{N}$  instead, rendering them invisible. This results in a gradual decay of the observed signal for each amide in the protein. This decay follows a single exponential trajectory from which a simple least-squares fitting procedure allows the extraction of the residue-specific exchange rate:

$$[I] = e^{(-k_{\text{obs}}t)} [I]_0 \quad (3.8)$$

where  $[I]_0$  is the signal at  $t = 0$

Although conceptually very straightforward, the method has a couple of significant limitations. Firstly, the protein under study must tolerate the lyophilisation and subsequent dissolution processes required for the experiment. For unstable molecules or proteins that are prone to mis-folding or aggregation, this may not be possible. Secondly, whilst the exchange reactions begin the moment the lyophilised protein is solubilised, it takes some time to introduce the sample into the NMR spectrometer and to collect each spectrum. This means that the experiment is limited to the measurement of only reasonably slow exchange rates. The time between dissolution of the protein and the collection of the first spectrum is likely to be several minutes and enough for the complete exchange with deuterium for rapidly exchanging residues.

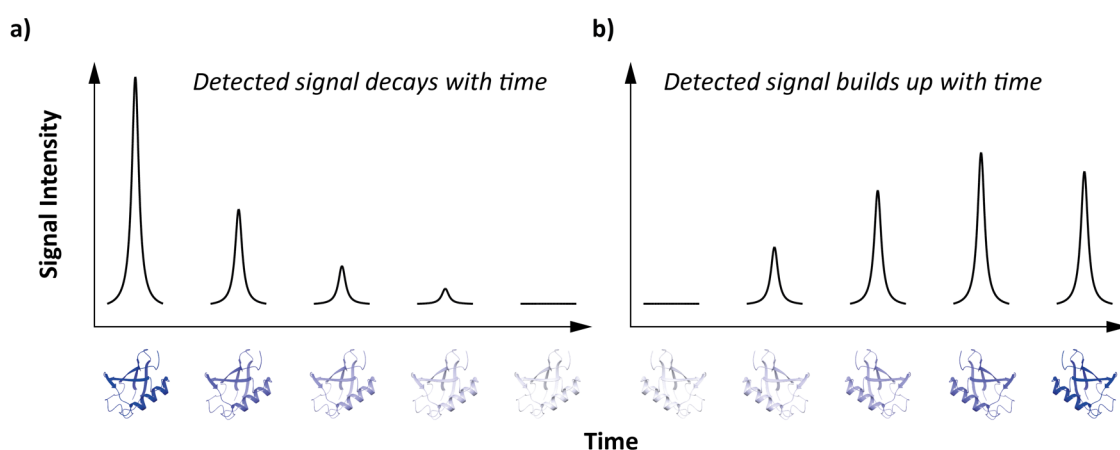


**Figure 3.2** Typical reaction profiles obtained when following the hydrogen exchange of amide protons in a protein using a)  $^1\text{H}$ - $^{15}\text{N}$  HSQC spectra recorded in  $^2\text{H}_2\text{O}$  and b) the CLEANEX-PM experiment recorded in  $^1\text{H}_2\text{O}$ .

Instead of directly exciting the protons of interest, an alternative strategy involves selectively exciting the water resonance and allowing the hydrogen exchange process to transfer magnetisation into the amide sites on the protein.<sup>[158,159]</sup> The CLEANEX-PM<sup>[160]</sup> experiment achieves this by using a selective pulse followed by a time-variable spin-locking sequence to keep the water resonance transverse during the hydrogen exchange. The experiment can be

### 3. Side-Chain Hydrogen Exchange in Arginine

acquired as a single dimension using proton detection or combined with an experiment such as the HSQC to provide an additional chemical shift dimension.<sup>[161]</sup> Figure 3.2b shows a typical reaction profile obtained using this method. When a short spin-lock is used, little to no intensity is detected at the amide chemical shift. As the spin-lock is increased in duration, magnetised protons initially bound to solvent molecules exchange into the protein and are detected at the corresponding amide chemical shifts. Integration of the detected signal with respect to time therefore allows the hydrogen exchange reaction to be followed. The fitting procedure required to extract the exchange rate is slightly more complex than the HSQC based method as whilst an increasing spin-lock duration allows the exchange reaction to proceed further and thus more signal to be detected, the signals also undergo  $R_{1\rho}$  relaxation which decreases the signal accordingly. These competing processes result in a plateau and even a decrease in the detected signal at long spin-lock times:

$$[I] = k_{\text{obs}}t \times e^{(-R_{1\rho}t)} \quad (3.9)$$

The sample requirements for this method are simply that the sample must be prepared in a buffer containing  $^1\text{H}_2\text{O}$  in order to mediate the transfer of magnetisation into the protein. A significant drawback of the CLEANEX-PM method is the implementation of the spin-locking sequence. The long and strong RF-field required to ensure that water magnetisation remains transverse can induce significant heating within the sample. This heating will affect the hydrogen exchange rate and thus lower the overall accuracy of the method. In order to mitigate this, the spin-locking period is kept as short as possible, typically < 50 ms, and thus limits the utility of the method to the quantification of the faster exchanging residues.

A more recent experiment designed to probe the hydrogen exchange rates of amide protons is found in the SOLEXY<sup>[162]</sup> (SOLvent EXchange Spectroscopy) method presented by Skrynnikov and co-workers in late 2009. The experiment is applied to samples prepared in mixed  $^1\text{H}_2\text{O}:$  $^2\text{H}_2\text{O}$  buffers and relies on the  $^{15}\text{N}$  chemical shift difference between protonated and deuterated amides to monitor the exchange reactions. The pulse sequence makes use of several transfer steps to convert equilibrium  $^1\text{H}^\alpha$  magnetisation to the antiphase coherence  $2C'_2N_x$  via the  $^1\text{H}^\alpha$ - $^{13}\text{C}^\alpha$ ,  $^{13}\text{C}^\alpha$ - $^{13}\text{C}'$  and  $^{13}\text{C}'$ - $^{15}\text{N}$  scalar couplings. The experiment begins with the excitation of the non-labile  $^1\text{H}^\alpha$  proton such that generation of antiphase  $^{15}\text{N}$  magnetisation is achieved for both the protonated and deuterated amides. An indirect chemical shift period then follows during which the  $^{15}\text{N}$  chemical shift of the amide is encoded with simultaneous refocussing of the  $^{13}\text{C}'$ - $^{15}\text{N}$  scalar coupling. Owing to the large isotope shift of  $^{15}\text{N}$ ,<sup>[163]</sup> the chemical shift difference between the protonated and deuterated species is easily resolved during this period. The resulting in-phase  $N_x$  magnetisation is then transferred to the amide  $^1\text{H}$  proton for detection using standard INEPT blocks. It is important to note that this transfer is only active for the

protonated amides and the magnetisation resulting from the deuterated sites is essentially discarded. The hydrogen exchange reactions can be followed by inserting a mixing period immediately prior to the final transfers from  $N_x$  to  $H_x$ . During this variable mixing period, the exchange reactions proceed and allows some of the deuterated  $2C'_2N_x$  coherences to become protonated, and vice versa. This protonation enables the subsequent transfer to  $H_x$  for detection but results in a cross-peak labelled with the isotope-shifted  $^{15}\text{N}(^2\text{H})$  chemical shift in the indirect dimension. The intensity of these shifted peaks relative to the cross-peaks arising from the protonated species permits the exchange reactions to be followed in a quantitative manner.

#### 3.1.3 Quantifying HX Rates in Arginine Side-Chains

The mechanism and implications for the hydrogen exchange of amide protons outlined above is easily extended to the  $^1\text{H}^\epsilon$  and  $^1\text{H}^\eta$  nuclei of the arginine side-chain where in the absence of an interaction, the exchange reaction of the typically solvent-exposed protons is expected to be very fast.<sup>[164,165]</sup> However, the guanidinium group can engage in numerous intramolecular interactions and thus an interrogation of the exchange kinetics ( $\text{EX}_2$ ) of these protons is expected to inform on the relative stability of these interactions. Several of the existing experimental approaches outlined above can be applied to arginine, albeit with their inherent limitations, with the notable exception of the SOLEXY experiment as the coupling network of a peptide bond differs significantly from that encountered in arginine's guanidinium group. The following sections describe a novel method designed to quantify the hydrogen exchange of the  $^1\text{H}^\epsilon$  proton of arginine, demonstrated on wild-type T4-lysozyme.

## 3.2 Theory and Method Development

A critical part of the first method described above to measure hydrogen exchange rates is that the deuterated sites become invisible in the  $^1\text{H}$ -detected HSQC experiment as the exchange reactions proceed. However, the use of a  $^{13}\text{C}$ -detected experiment instead would allow the simultaneous observation of both deuterated and non-deuterated sites throughout the exchange reactions. For the arginine side-chain, a suitable NMR experiment can be constructed from the standard  $^{13}\text{C}^{\zeta}\text{-}^{15}\text{N}^\epsilon$  HSQC sequence by the addition of deuterium decoupling during the  $t_1$  evolution period, as shown in Figure 3.3a. The experiment is appropriate for samples prepared in deuterium-enriched aqueous buffers, the simplest of which contains equal volumes of  $^1\text{H}_2\text{O}$  and  $^2\text{H}_2\text{O}$ . The resulting deuteration of some of the  $^1\text{H}^\epsilon$  sites necessitates the application of the additional deuterium decoupling field to suppress the  $^{15}\text{N}^\epsilon\text{-}^2\text{H}^\epsilon$  scalar couplings active during the  $t_1$  evolution period. As the deuteration of the solvent is not 100% and some sites remain protonated, the proton decoupling field remains necessary to suppress the  $^{15}\text{N}^\epsilon\text{-}^1\text{H}^\epsilon$  couplings as in the original experiment described in Section 2.2. Whilst both decoupling fields are applied

### 3. Side-Chain Hydrogen Exchange in Arginine

simultaneously, the deuterium field is flanked by orthogonal  $90^\circ$  pulses to minimise disturbances to the  $^2\text{H}_2\text{O}$  resonance used by the spectrometer as the field-frequency lock. Immediately prior to the decoupling field being activated, a  $90_y^0$  pulse converts the solvent to  $(^2\text{H}_2\text{O})_x$  magnetisation. The subsequent decoupling field, applied with x-phase, behaves as a spin-locking sequence for the solvent resonance during the  $t_1$  period before a  $90_{-y}^0$  pulse returns the solvent to the z-axis. Without these flanking pulses, the solvent resonance would be rapidly de-phased by the decoupling field and the spectrometer would be unable to maintain a strong lock signal throughout the experiment.

The spectrum recorded using this modified sequence on a sample of *free* [ $^{13}\text{C}_6, ^{15}\text{N}_4$ ]-L-arginine is shown in Figure 3.3b and demonstrates that as a result of the deuterium isotope shifts, the  $\text{N}^\epsilon(^1\text{H})$  and  $\text{N}^\epsilon(^2\text{H})$  species are easily resolved from one another. As for the SOLEXTSY experiment described above in Section 3.1.2, the methodology developed during this chapter will make use of the isotope-shifted peaks to quantify the exchange rate between the protonated and deuterated species. A more thorough discussion of the numerous deuterium isotope shifts encountered in arginine side-chains, including the notation used to describe them, is presented in Chapter 4.

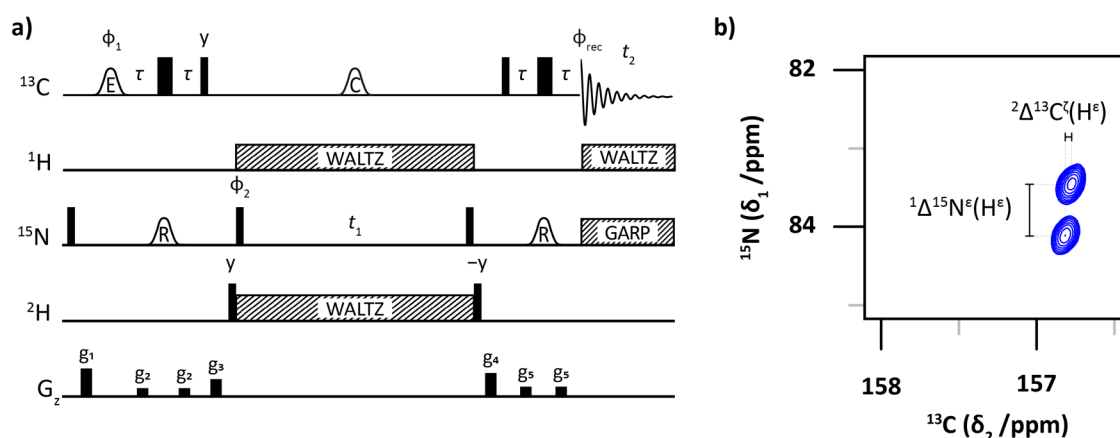


**Figure 3.3** a)  $^{13}\text{C}\text{-}^{15}\text{N}^\epsilon$  HSQC sequence modified to include  $^2\text{H}$  decoupling during the  $t_1$  evolution period. The pulses flanking the WALTZ decoupling field are to minimise disturbances to the field-frequency lock of the spectrometer caused by the  $^2\text{H}$  pulses. The rest of the sequence is identical to that discussed in Section 2.2.1. b) The  $^{13}\text{C}\text{-}^{15}\text{N}^\epsilon$  HSQC sequence of *free* [ $^{13}\text{C}_6, ^{15}\text{N}_4$ ]-L-arginine prepared in 50:50  $^1\text{H}_2\text{O}$ : $^2\text{H}_2\text{O}$  at pH 5.5 showing the two peaks easily resolved due to the one-bond isotope shift of  $^{15}\text{N}^\epsilon$ . The two-bond  $^{13}\text{C}$  isotope shift is much smaller and so the resolution in  $f_2$  is rather poor. The asymmetric properties of each peak are due to the distribution of deuterium amongst the  $^1\text{H}^\epsilon$  protons.

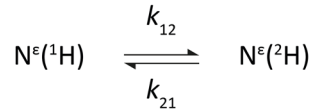
#### 3.2.1 Longitudinal zz-Exchange

One of the most commonly encountered methods for monitoring nuclei that are in exchange is the so-called zz-exchange experiment<sup>[166]</sup> whereby the magnetisation flow from one exchanging partner to the other is followed whilst the nuclei are aligned with the z-axis. This orientation ensures that no scalar coupling contributions need to be considered and avoids losses due to rapid transverse relaxation. Applied to the  $^1\text{H}^\epsilon$  exchange within the arginine side-chain, a suitable

### 3. Side-Chain Hydrogen Exchange in Arginine

zz-exchange strategy could involve the generation of longitudinal  $N_z^\epsilon(^1\text{H})$  magnetisation and a subsequent monitoring of the conversion into  $N_z^\epsilon(^2\text{H})$ . Figure 3.3b demonstrates that the protonated and deuterated sites can be easily distinguished from one another based on their chemical shift and the  $N_z^\epsilon$  magnetisation is expected to have sufficiently slow  $T_1$  relaxation to accommodate the significant duration of the mixing times without too much signal loss.

To understand the evolution of the  $N_z^\epsilon$  magnetisation during the mixing period, consider the simple exchange between the protonated and deuterated forms of an isolated  $N^\epsilon$  nucleus:



where the rate constant  $k_{12}$  reflects the change in atomic mass number of the bound hydrogen atom from 1 (proton) to 2 (deuteron). The reverse reaction proceeds with the analogous rate constant  $k_{21}$ .

During the mixing period, several processes simultaneously affect the intensity of the  $N^\epsilon(^1\text{H})$  magnetisation: a combination of longitudinal relaxation and hydrogen exchange cause the signal to **decrease** whilst back-exchange from the deuterated species works to **increase** the signal. The evolution of the  $N^\epsilon(^1\text{H})$  magnetisation during mixing period  $\tau$  can therefore be expressed as:

$$\frac{d[\text{N}^\epsilon(^1\text{H})]}{d\tau} = -R_1^{\text{N}^\epsilon(^1\text{H})} [\text{N}^\epsilon(^1\text{H})]_\tau - k_{12} [\text{N}^\epsilon(^1\text{H})]_\tau + k_{21} [\text{N}^\epsilon(^2\text{H})]_\tau \quad (3.10)$$

Similarly, the evolution of the deuterated  $N^\epsilon(^2\text{H})$  magnetisation follows:

$$\frac{d[\text{N}^\epsilon(^2\text{H})]}{d\tau} = -R_1^{\text{N}^\epsilon(^2\text{H})} [\text{N}^\epsilon(^2\text{H})]_\tau - k_{21} [\text{N}^\epsilon(^2\text{H})]_\tau + k_{12} [\text{N}^\epsilon(^1\text{H})]_\tau \quad (3.11)$$

These two expressions can be combined and expressed more succinctly using matrices:

$$\frac{d}{d\tau} \begin{pmatrix} [\text{N}^\epsilon(^1\text{H})] \\ [\text{N}^\epsilon(^2\text{H})] \end{pmatrix} = \begin{pmatrix} -R_1^{\text{N}^\epsilon(^1\text{H})} - k_{12} & k_{21} \\ k_{12} & -R_1^{\text{N}^\epsilon(^2\text{H})} - k_{21} \end{pmatrix} \begin{pmatrix} [\text{N}^\epsilon(^1\text{H})]_\tau \\ [\text{N}^\epsilon(^2\text{H})]_\tau \end{pmatrix} \quad (3.12)$$

In order to fit this expression to experimental data, it is necessary to integrate it and thereby obtain the *integrated rate equation*. This is readily achieved using the *separation of variables*<sup>[167]</sup> methodology where the rate equation above is rearranged to:

$$\frac{d}{\begin{pmatrix} [\text{N}^\epsilon(^1\text{H})]_\tau \\ [\text{N}^\epsilon(^2\text{H})]_\tau \end{pmatrix}} \begin{pmatrix} [\text{N}^\epsilon(^1\text{H})] \\ [\text{N}^\epsilon(^2\text{H})] \end{pmatrix} = \begin{pmatrix} -R_1^{\text{N}^\epsilon(^1\text{H})} - k_{12} & k_{21} \\ k_{12} & -R_1^{\text{N}^\epsilon(^2\text{H})} - k_{21} \end{pmatrix} d\tau$$

### 3. Side-Chain Hydrogen Exchange in Arginine

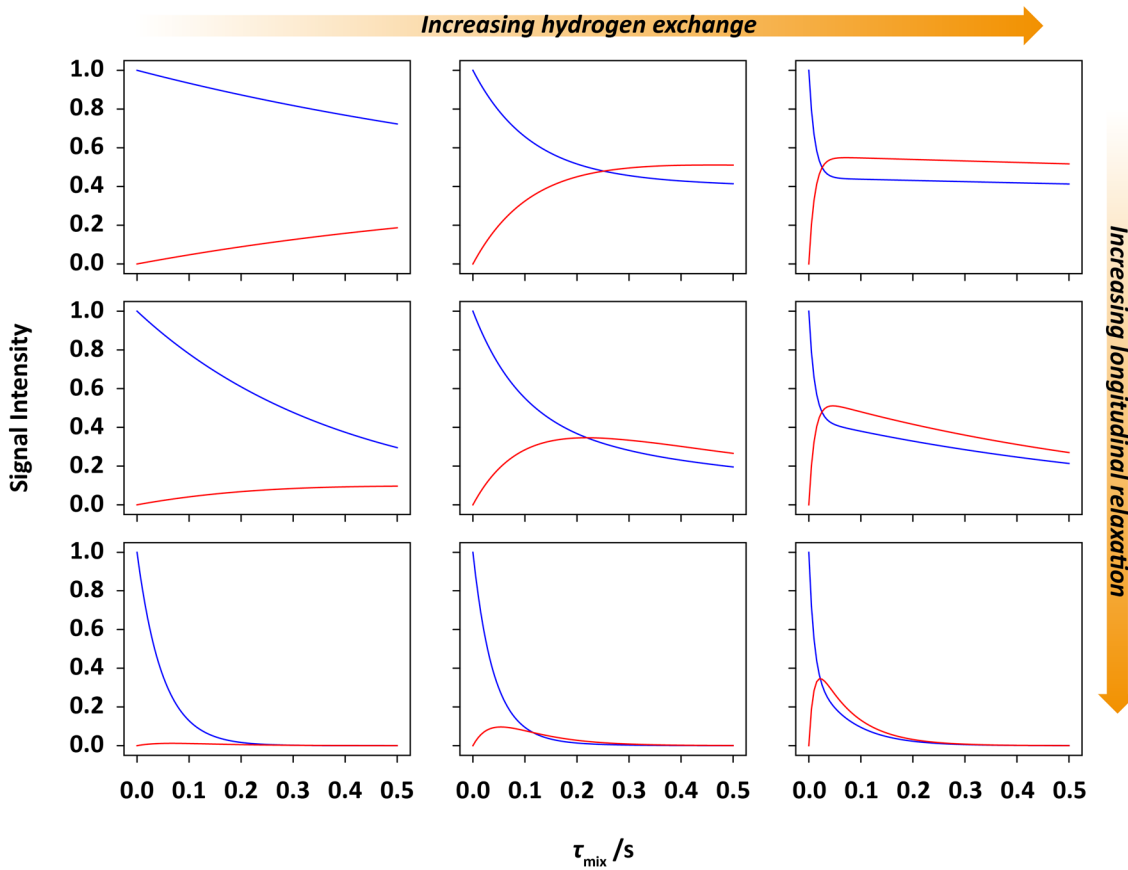


**Figure 3.4** Simulated intensity vs. time plots showing the evolution of  $N_z(^1\text{H})$  and  $N_z(^2\text{H})$  magnetisation with different hydrogen exchange and longitudinal relaxation rates. The values for  $k_{12}(k_{21})$  from left-to-right, are 0.5(0.4), 5.0(4.0) and 50(40)  $\text{s}^{-1}$  and the values for  $R_1^{N(^1\text{H})}$  ( $R_1^{N(^2\text{H})}$ ) from top-to-bottom, are 0.2(0.1), 2.0(1.0) and 20(10)  $\text{s}^{-1}$ .

followed by integration of both sides:

$$\ln \left( \begin{bmatrix} [N^\epsilon(^1\text{H})]_\tau \\ [N^\epsilon(^2\text{H})]_\tau \end{bmatrix} \right) = \int_0^\tau \begin{pmatrix} -R_1^{N(^1\text{H})} - k_{12} & k_{21} \\ k_{12} & -R_1^{N(^2\text{H})} - k_{21} \end{pmatrix} d\tau$$

$$= \left( \begin{pmatrix} -R_1^{N(^1\text{H})} - k_{12} & k_{21} \\ k_{12} & -R_1^{N(^2\text{H})} - k_{21} \end{pmatrix} \tau \right) + C$$

Taking the exponents of both sides results in:

$$\begin{bmatrix} [N^\epsilon(^1\text{H})]_\tau \\ [N^\epsilon(^2\text{H})]_\tau \end{bmatrix} = \exp \left( \begin{pmatrix} -R_1^{N(^1\text{H})} - k_{12} & k_{21} \\ k_{12} & -R_1^{N(^2\text{H})} - k_{21} \end{pmatrix} \tau \right) \cdot C$$

To find the value of C, consider the lower limit where  $\tau = 0$ :

$$\begin{bmatrix} [N^\epsilon(^1\text{H})]_0 \\ [N^\epsilon(^2\text{H})]_0 \end{bmatrix} = \exp \left( \begin{pmatrix} -R_1^{N(^1\text{H})} - k_{12} & k_{21} \\ k_{12} & -R_1^{N(^2\text{H})} - k_{21} \end{pmatrix} 0 \right) \cdot C = \exp(0) \cdot C = C$$

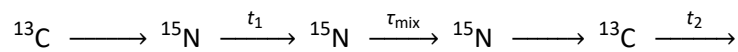
Therefore, the integrated rate equation for the evolution of the magnetisation during the mixing period of a zz-exchange experiment is:

$$\begin{pmatrix} [N^{\epsilon}(^1H)]_{\tau} \\ [N^{\epsilon}(^2H)]_{\tau} \end{pmatrix} = \exp\left(\begin{pmatrix} -R_1^{N(^1H)} - k_{12} & k_{21} \\ k_{12} & -R_1^{N(^2H)} - k_{21} \end{pmatrix} \tau\right) \cdot \begin{pmatrix} [N^{\epsilon}(^1H)]_0 \\ [N^{\epsilon}(^2H)]_0 \end{pmatrix} \quad (3.13)$$

where  $[N^{\epsilon}(^1H)]_0$  and  $[N^{\epsilon}(^2H)]_0$  represent the amount of  $^{15}N^{\epsilon}(^1H)$  and  $^{15}N^{\epsilon}(^2H)$  magnetisation present at the start of the mixing period, respectively.

From the above equations, the intensity of the  $^{15}N^{\epsilon}(^1H/^2H)$  magnetisation remaining after a given time  $\tau$ , can therefore be calculated from the initial intensities based on a knowledge of the longitudinal relaxation rates and the hydrogen exchange rates involved (Figure 3.4). More usefully, if one were to have a dataset of measured intensities at several values of  $\tau$ , the data can be fit to the equation above and the underlying rate constants extracted mathematically.

In order to obtain such a dataset, the HSQC experiment in Figure 3.3a must be modified to include a suitable mixing period. The simplest implementation of the zz-exchange methodology is achieved by inserting a mixing period in between the two chemical shift periods,  $t_1$  and  $t_2$ , of a two-dimensional experiment such that the flow of magnetisation is:



This is applied to the  $^{13}C^{\zeta}-^{15}N^{\epsilon}$  HSQC experiment in Figure 3.5a resulting in a pseudo-three-dimensional ( $\tau_{mix}$ ,  $t_1$ ,  $t_2$ ) sequence where only two of the dimensions are Fourier transformed after data collection. If the experiment is recorded with only a brief mixing time ( $\tau_{mix} \approx 0$ ), a typical  $^{13}C^{\zeta}-^{15}N^{\epsilon}$  HSQC spectrum is obtained with the two expected isotope-shifted peaks at  $(\Omega_{N(N-^1H)}, \Omega_{C(N-^1H)})$  and  $(\Omega_{N(N-^2H)}, \Omega_{C(N-^2H)})$ . However, as the mixing time increases the hydrogen exchange reaction causes some magnetisation that was protonated during the  $t_1$  evolution period and thus encoded with the  $\Omega_{N(N-^1H)}$  frequency to become deuterated prior to detection during  $t_2$  at the  $\Omega_{C(N-^2H)}$  frequency. This results in the appearance of an *extra* peak in the spectrum at  $(\Omega_{N(N-^1H)}, \Omega_{C(N-^2H)})$ , the intensity of which is proportional to the length of the mixing time,  $\tau_{mix}$ . The corresponding peak at  $(\Omega_{N(N-^2H)}, \Omega_{C(N-^1H)})$  results from the exchange of magnetisation that was deuterated during  $t_1$  to protonated magnetisation prior to detection during  $t_2$ .

Fourier transformation of the frequency domains results in a stack of two-dimensional HSQC spectra, two of which are shown in Figure 3.5b. As discussed previously, the one-bond deuterium isotope shift of  $^{15}N$  is sufficiently large to enable the easy resolution of the protonated and deuterated species in the  $^{15}N$  dimension. However, the two-bond isotope shift induced upon the  $^{13}C^{\zeta}$  nucleus is much smaller and insufficient for the clear detection of the extra

### 3. Side-Chain Hydrogen Exchange in Arginine

peaks resulting from the hydrogen exchange. A comparison of the two spectra in Figure 3.5b show just two peaks in both, but rounder peak shapes for the data collected when  $\tau_{\text{mix}} = 100$  ms. This occurs because whilst the exchange reaction proceeds during the mixing time and generates the extra peaks discussed above, the  $^{13}\text{C}^\zeta(\text{H}^\epsilon)$  isotope shift is over two bonds and much smaller so the  $^{13}\text{C}$  resolution is not sufficient to allow the complete resolution of the  $(\Omega_{\text{N}(\text{N}^{\cdot\text{H}})}, \Omega_{\text{C}(\text{N}^{\cdot\text{H}})})$  and  $(\Omega_{\text{N}(\text{N}^{\cdot\text{H}})}, \Omega_{\text{C}(\text{N}^{\cdot\text{H}})})$  peaks, nor the  $(\Omega_{\text{N}(\text{N}^{\cdot\text{H}})}, \Omega_{\text{C}(\text{N}^{\cdot\text{H}})})$  and  $(\Omega_{\text{N}(\text{N}^{\cdot\text{H}})}, \Omega_{\text{C}(\text{N}^{\cdot\text{H}})})$  peaks.

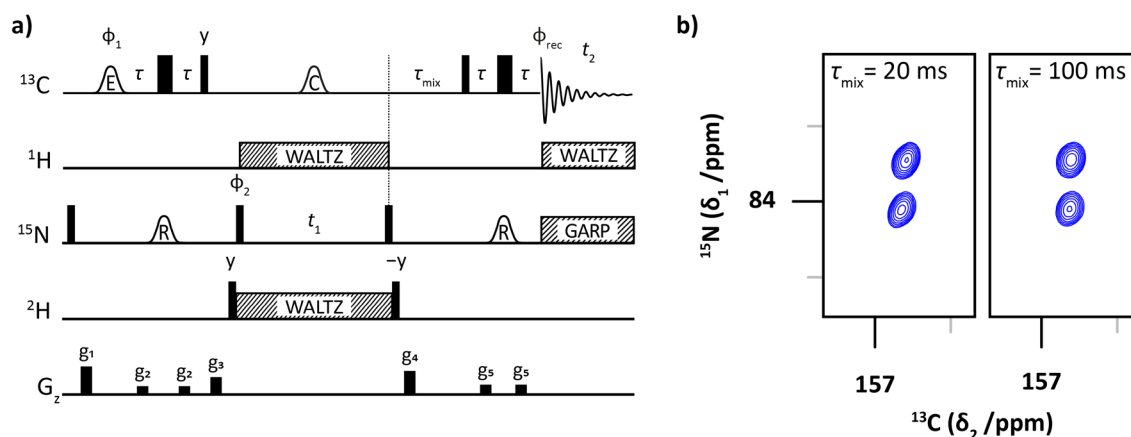
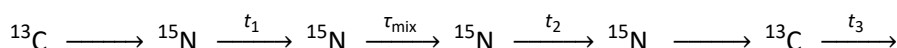


**Figure 3.5** a) The pseudo-3D  $^{13}\text{C}$ - $^{15}\text{N}$  HSQC  $zz$ -exchange sequence for measuring the hydrogen exchange of  $^1\text{H}^\epsilon$ . A variable mixing time,  $\tau_{\text{mix}}$ , is inserted between the  $t_1$  and  $t_2$  evolution periods to monitor the exchange reaction. b) A 2D HSQC spectrum is obtained for each value of  $\tau_{\text{mix}}$ : the spectra recorded when  $\tau_{\text{mix}} = 20$  ms and  $\tau_{\text{mix}} = 100$  ms demonstrate the lack of resolution in the  $^{13}\text{C}$  dimension.

The limiting  $^{13}\text{C}$  resolution can be overcome by the addition of a second  $^{15}\text{N}$  evolution period to the previous  $zz$ -exchange sequence such that the magnetisation instead flows as:



The result is the pseudo-four-dimensional ( $\tau_{\text{mix}}, t_1, t_2, t_3$ ) experiment shown in Figure 3.6a where the variable mixing time,  $\tau_{\text{mix}}$ , is now located in between two  $^{15}\text{N}$  evolutions. Following the  $^{13}\text{C}^\zeta$  detection, a three-dimensional  $(\Omega_{\text{N}^\epsilon}, \Omega_{\text{N}^\epsilon}, \Omega_{\text{C}^\zeta})$  spectrum is obtained for each value of  $\tau_{\text{mix}}$ . Although the  $^{13}\text{C}^\zeta$  frequency does not provide any useful resolution of the isotope-shifted signals, the two-dimensional  $^{15}\text{N}$ - $^{15}\text{N}$  projections of these spectra exploit the large one-bond isotope shift of  $^{15}\text{N}$  twice and thus well resolved peaks are obtained at  $(\Omega_{\text{N}^1(\text{N}^{\cdot\text{H}})}, \Omega_{\text{N}^2(\text{N}^{\cdot\text{H}})})$  and  $(\Omega_{\text{N}^1(\text{N}^{\cdot\text{H}})}, \Omega_{\text{N}^2(\text{N}^{\cdot\text{H}})})$  (Figure 3.6b;  $\tau_{\text{mix}} = 2$  ms). The mixing period behaves as for the pseudo-three-dimensional  $zz$ -exchange experiment and allows some magnetisation that was protonated during the first  $^{15}\text{N}$  evolution to become deuterated in time for the second  $^{15}\text{N}$  evolution, and vice versa. This results in the formation of two extra peaks  $(\Omega_{\text{N}^1(\text{N}^{\cdot\text{H}})}, \Omega_{\text{N}^2(\text{N}^{\cdot\text{H}})})$  and  $(\Omega_{\text{N}^1(\text{N}^{\cdot\text{H}})}, \Omega_{\text{N}^2(\text{N}^{\cdot\text{H}})})$  that are easily resolved in the  $^{15}\text{N}$ - $^{15}\text{N}$  projections (Figure 3.6b;  $\tau_{\text{mix}} = 20, 100$  ms). The intensity of these peaks as a function of  $\tau_{\text{mix}}$  can then be fitted using the equations described on the previous pages and the relevant values for the exchange extracted. It is worth noting that during

### 3. Side-Chain Hydrogen Exchange in Arginine

the mixing time in these experiments, the magnetisation is proportional to  $2C_z^z N_z^\epsilon$  rather than simply  $N_z^\epsilon$  and therefore the extracted longitudinal relaxation rate reflects the total relaxation experienced ( $R_1^{C_z} + R_1^{N^\epsilon}$ ).

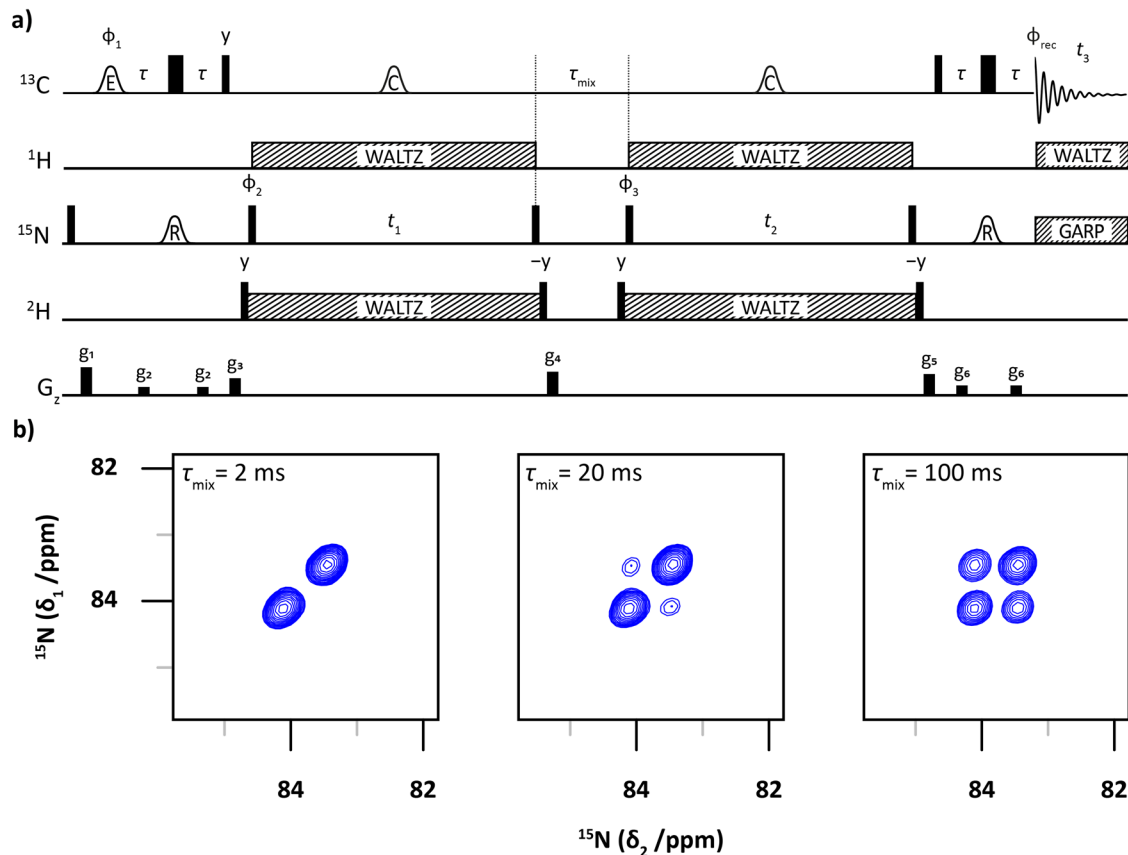


**Figure 3.6** a) The pseudo-4D  $^{13}\text{C}^z\text{-}^{15}\text{N}^\epsilon\text{-}^{15}\text{N}^\epsilon$  HSQC zz-exchange sequence for measuring the hydrogen exchange of  $^1\text{H}^\epsilon$ . A variable mixing time,  $\tau_{\text{mix}}$ , is inserted between two  $^{15}\text{N}$  chemical shift evolution periods,  $t_1$  and  $t_2$ , to monitor the exchange reaction. b) A 3D  $^{13}\text{C}^z\text{-}^{15}\text{N}^\epsilon\text{-}^{15}\text{N}^\epsilon$  spectrum is obtained for each value of  $\tau_{\text{mix}}$ , the  $^{15}\text{N}\text{-}^{15}\text{N}$  projections of which are sufficiently well resolved to monitor the exchange reaction: the spectra recorded when  $\tau_{\text{mix}} = 2, 20$  and  $100$  ms demonstrate the time-dependent intensity of the off-diagonal peaks ( $\Omega_{N^1(N^1\text{-H})}$ ,  $\Omega_{N^2(N^2\text{-H})}$ ) and ( $\Omega_{N^1(N^2\text{-H})}$ ,  $\Omega_{N^2(N^1\text{-H})}$ ).

Although clearly an improvement on the previous zz-exchange experiment, the extra resolution afforded by the additional  $^{15}\text{N}$  dimension comes at a considerable cost. Firstly, each value of  $\tau_{\text{mix}}$  to be sampled now requires the collection of a three-dimensional dataset, dramatically increasing the overall experiment time. This will have implications for both the stability of the sample under study as well as the availability of suitable spectrometer time. Secondly, each indirect chemical shift evolution period carries an intrinsic sensitivity penalty of 50% and thus the two  $^{15}\text{N}$  dimensions prevent at least 75% of the excited  $^{13}\text{C}^z$  magnetisation from contributing to the final spectrum. The first problem can be at least partially overcome using non-uniform sampling (NUS) schedules to speed up the data acquisition, but the inefficiency of the back-to-back chemical shift evolutions is far from ideal when combined with the relatively low sensitivity of the detection nucleus. The following sections will therefore explore several strategies that seek to overcome this limitation by boosting the sensitivity of the experiments.

### 3. Side-Chain Hydrogen Exchange in Arginine

#### 3.2.2 Improving Signal-to-Noise

##### a. Preservation of Equivalent Pathways

The intrinsic loss of half of the detectable signal during an HSQC experiment can in principle be addressed using the *Preservation of Equivalent Pathways* (PEP)<sup>[168]</sup> methodology now commonly embedded within the standard two- and three-dimensional triple-resonance experiments used for backbone and side-chain chemical shift assignments of proteins.<sup>[169–172]</sup> The PEP modification works by sequentially refocussing both parts of the phase-modulated signal after the  $t_1$  evolution period such that neither is discarded and results in a so-called *sensitivity enhanced* version of the parent experiment. This sequential refocussing is possible because after the chemical shift evolution during  $t_1$ , the cosine- and sine-modulated parts of the signal are orthogonal and therefore each part can be selected individually using an appropriately phased  $90^\circ$  pulse. In the non-PEP HSQC, the part of the signal not selected at this point is either dephased with a gradient pulse or converted into a multiple-quantum coherence that is not directly detectable and is therefore lost. However, this multiple-quantum coherence can instead be refocussed using an additional INEPT transfer step and therefore converted into detectable signal, avoiding the associated signal loss. One can think of the part of magnetisation not refocussed during the existing INEPT block as being *stored* as multiple-quantum magnetisation prior to subsequent refocussing in a second INEPT block. The part of the magnetisation refocused during the first INEPT is similarly *stored* during the second INEPT. This strategy is implemented for the standard  $^{13}\text{C}^{\zeta}$ - $^{15}\text{N}^{\epsilon}$  HSQC in Figure 3.7 and described in detail below. Whilst for simplicity only the protonated coherences are considered, the experiment would be equally applicable to deuterated species subject to the addition of appropriate decoupling schemes.

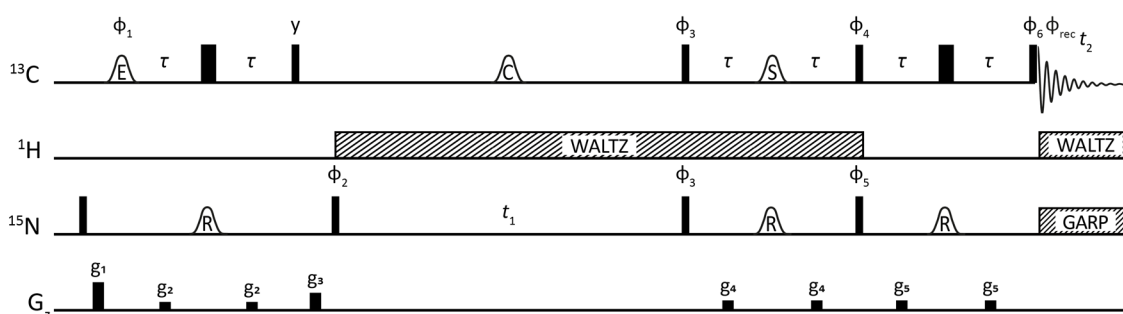


**Figure 3.7** The PEP-HSQC sequence for recording sensitivity-enhanced  $^{13}\text{C}^{\zeta}$ - $^{15}\text{N}^{\epsilon}$  spectra of arginine side-chains. The phase cycle used is  $\phi_1$ : x, -x;  $\phi_2$ : 2(x), 2(-x);  $\phi_3$ : 4(x), 4(y);  $\phi_4$ : 4(y), 4(x);  $\phi_5$ : 4(y), 4(x);  $\phi_6$ : 4(x), 4(y);  $\phi_{\text{rec}}$ : x, 2(-x), x, -x, 2(x), -x. Frequency discrimination in the indirect dimension is achieved as described in the main text.

Following the usual  $^{13}\text{C}^{\zeta}$  excitation and INEPT transfer to  $^{15}\text{N}^{\epsilon}$ , evolution under the free precession Hamiltonian during  $t_1$  proceeds, resulting in the cosine- and sine-modulated terms:

$$2C_z^{\zeta}N_y^{\epsilon} \xrightarrow{\Omega_{\epsilon}t_1N_z^{\epsilon}} -2C_z^{\zeta}N_y^{\epsilon} \cos(\Omega_{\epsilon}t_1) - 2C_z^{\zeta}N_x^{\epsilon} \sin(\Omega_{\epsilon}t_1)$$

### 3. Side-Chain Hydrogen Exchange in Arginine

If the  $^{13}\text{C}$  and  $^{15}\text{N}$   $90^\circ$  pulses that follow are both applied with x-phase, the magnetisation is converted to:

$$\xrightarrow{90_x^0 (^{13}\text{C} + ^{15}\text{N})} 2C_Y^\zeta N_Z^\epsilon \cos(\Omega_\epsilon t_1) + 2C_Y^\zeta N_X^\epsilon \sin(\Omega_\epsilon t_1)$$

It is important to note that the spoiling gradient pulse between the two  $90^\circ$  pulses ( $g_4$  in Figure 3.3) must be removed to prevent the de-phasing of the  $2C_Z^\zeta N_X^\epsilon$  coherence that is unaffected by the  $90^\circ$   $^{15}\text{N}$  pulse. A subsequent INEPT block refocuses the now anti-phase cosine-modulated signal whilst the sine-modulated signal is *stored* as multiple-quantum magnetisation that does not evolve under the scalar-coupling Hamiltonian:

$$\xrightarrow{2\pi J_{\text{CN}} C_Z^\zeta N_Z^\epsilon, 180_x^0 (^{13}\text{C} + ^{15}\text{N})} C_X^\zeta \cos(\Omega_\epsilon t_1) - 2C_Y^\zeta N_X^\epsilon \sin(\Omega_\epsilon t_1)$$

In a standard HSQC the  $2C_Y^\zeta N_X^\epsilon$  coherence does not lead to detectable signal and so it is usually safely ignored; however, in this experiment this coherence will be refocused and so all evolutions it experiences throughout the sequence must be considered. Whilst the  $J_{\text{CN}}$  scalar coupling between  $^{13}\text{C}^\zeta$  and  $^{15}\text{N}^\epsilon$  does not evolve during this INEPT block, there are the additional couplings to  $^1\text{H}^\epsilon$  and  $^{13}\text{C}^\delta$  to consider. Therefore, two minor modifications must be made to the existing INEPT block in order to mediate this transfer efficiently:

1. The  $^1\text{H}$  decoupling field applied during the  $t_1$  period is continued to refocus the couplings to  $^1\text{H}^\epsilon$  as well as to other protons in the side-chain
2. The  $180^\circ$   $^{13}\text{C}$  pulse during the INEPT is made selective only for  $^{13}\text{C}^\zeta$  resulting in the refocussing of the  $^{15}\text{N}^\epsilon$ - $^{13}\text{C}^\delta$  coupling

The subsequent  $^{13}\text{C}$  and  $^{15}\text{N}$   $90^\circ$  pulses, applied with y-phase, convert the magnetisation to:

$$\xrightarrow{90_y^0 (^{13}\text{C} + ^{15}\text{N})} -C_Z^\zeta \cos(\Omega_\epsilon t_1) + 2C_Y^\zeta N_Z^\epsilon \sin(\Omega_\epsilon t_1)$$

The sine-modulated magnetisation is now anti-phase and ready for refocussing whilst the cosine-modulated part has been *stored* longitudinally, a state that is similarly unaffected by the scalar coupling Hamiltonian. A standard  $\text{C}^\zeta$ - $\text{N}^\epsilon$  INEPT allows the refocussing of the anti-phase coherence as for the standard HSQC sequence:

$$\xrightarrow{2\pi J_{\text{CN}} C_Z^\zeta N_Z^\epsilon, 180_x^0 (^{13}\text{C} + ^{15}\text{N})} C_Z^\zeta \cos(\Omega_\epsilon t_1) + C_X^\zeta \sin(\Omega_\epsilon t_1)$$

A final  $90_{-x}^0$   $^{13}\text{C}$  read pulse prior to acquisition results in:

$$\xrightarrow{90_{-x}^0 ^{13}\text{C}} C_Y^\zeta \cos(\Omega_\epsilon t_1) + C_X^\zeta \sin(\Omega_\epsilon t_1)$$

### 3. Side-Chain Hydrogen Exchange in Arginine

Thus, the PEP modification has achieved the conversion of both the cosine- and sine-modulated parts of the magnetisation to observable, in-phase coherences; however, they require separation prior to Fourier transformation. The separation is easily achieved by repeating the experiment with inversion of the phase of the  $90^\circ$   $^{15}\text{N}$  pulse midway through the PEP block ( $\phi_5$ ):

$$\begin{array}{l}
 \xrightarrow{90^\circ_{\text{y}} \text{ } ^{13}\text{C}, 90^\circ_{\text{y}} \text{ } ^{15}\text{N}} \\
 \xrightarrow{2\pi J_{\text{CN}} C_z^\zeta N_z^\epsilon, 180^\circ_{\text{x}} ({}^{13}\text{C} + {}^{15}\text{N})} \\
 \xrightarrow{90^\circ_{\text{x}} \text{ } ^{13}\text{C}}
 \end{array}
 \quad
 \begin{array}{l}
 - C_z^\zeta \cos(\Omega_\epsilon t_1) - 2C_y^\zeta N_z^\epsilon \sin(\Omega_\epsilon t_1) \\
 C_z^\zeta \cos(\Omega_\epsilon t_1) - C_x^\zeta \sin(\Omega_\epsilon t_1) \\
 C_y^\zeta \cos(\Omega_\epsilon t_1) - C_x^\zeta \sin(\Omega_\epsilon t_1)
 \end{array}$$

The consequence of the inversion of  $\phi_5$  is the inversion of the sine-modulated component,  $C_x^\zeta$ , of the detected signal in the second experiment. Both experiments result in the simultaneous detection of orthogonal, in-phase magnetisation originating from the cosine- and sine-modulated parts of the indirect chemical shift evolution during  $t_1$ , with neither part discarded. Using the two datasets together, the individual cosine- and sine-modulated components required for frequency discrimination are easily separated by taking the linear combinations:

$$\begin{array}{l}
 \text{Experiment 1 } (\phi_5 = \gamma): \quad C_y^\zeta \cos(\Omega_\epsilon t_1) + C_x^\zeta \sin(\Omega_\epsilon t_1) \\
 \text{Experiment 2 } (\phi_5 = -\gamma): \quad C_y^\zeta \cos(\Omega_\epsilon t_1) - C_x^\zeta \sin(\Omega_\epsilon t_1) \\
 \text{Exp. 1} + \text{Exp. 2} = \quad 2C_y^\zeta \cos(\Omega_\epsilon t_1) \\
 \text{Exp. 1} - \text{Exp. 2} = \quad 2C_x^\zeta \sin(\Omega_\epsilon t_1)
 \end{array}$$

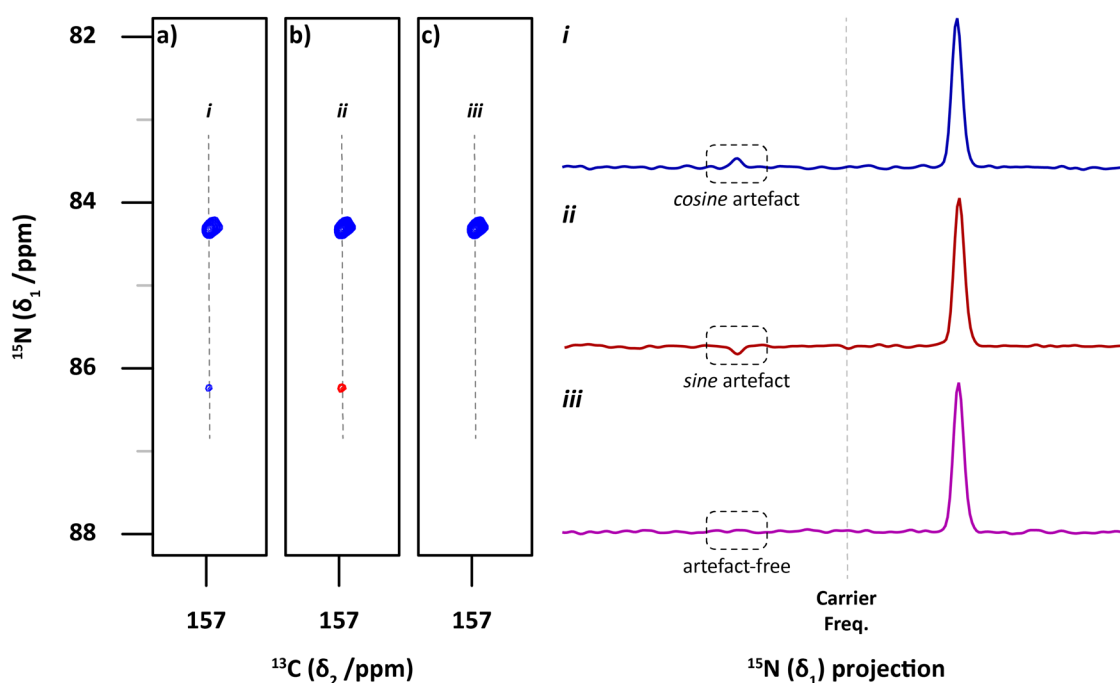


**Figure 3.8**  $^{13}\text{C}^\zeta\text{-}^{15}\text{N}^\epsilon$  PEP-HSQC spectra recorded on *free* [ $^{13}\text{C}_6, ^{15}\text{N}_4$ ]-L-arginine using different phase cycles showing typical quadrature artefacts in the indirect dimension: a) the cosine-modulated part of the signal is stored as the slower relaxing longitudinal magnetisation resulting in a small cosine-like artefact; b) the sine-modulated part of the signal is stored as longitudinal magnetisation leading to a sine-like artefact; c) the phase cycle is designed such the two relaxation pathways are balanced allowing the complete cancellation of the quadrature artefact.

### 3. Side-Chain Hydrogen Exchange in Arginine

Whilst both the longitudinal  $C_z^\zeta$  and multiple-quantum  $2C_y^\zeta N_x^\epsilon$  coherences are unaffected by the scalar coupling Hamiltonian, each of them experiences different relaxation during the delays involved in the INEPT blocks:  $C_z^\zeta$  relaxes with only the  $R_1$  rate of the  $^{13}\text{C}^\zeta$  nucleus where  $2C_y^\zeta N_x^\epsilon$  relaxes with the  $R_2$  rates of both the  $^{13}\text{C}^\zeta$  and  $^{15}\text{N}^\epsilon$  nuclei. These rates can be significantly different and result in quadrature artefacts in the indirect dimension of the processed spectra. The spectrum recorded on a sample of *free* [ $^{13}\text{C}_6, ^{15}\text{N}_4$ ]-L-arginine using the pulses discussed above contains such an artefact (Figure 3.8a). In this example, a small positive signal is observed at the mirrored frequency about the carrier. This is a direct result of the cosine-modulated part being stored as longitudinal magnetisation and therefore relaxing slower than the sine-modulated part stored as multiple-quantum. The resulting lower intensity of the sine-modulated part results in an incomplete cancellation of the mirrored frequency leading to a small cosine-type quadrature artefact.

The route by which each part of the cosine- and sine-modulated magnetisation is refocused can be reversed by changing the phase of each of the  $90^\circ$  pulses applied during the PEP block:

$$\begin{array}{l}
 2C_z^\zeta N_y^\epsilon \xrightarrow{\Omega_\epsilon t_1 N_z^\epsilon} -2C_z^\zeta N_y^\epsilon \cos(\Omega_\epsilon t_1) - 2C_z^\zeta N_x^\epsilon \sin(\Omega_\epsilon t_1) \\
 \xrightarrow{90_y^0 (^{13}\text{C} + ^{15}\text{N})} -2C_x^\zeta N_y^\epsilon \cos(\Omega_\epsilon t_1) + 2C_x^\zeta N_z^\epsilon \sin(\Omega_\epsilon t_1) \\
 \xrightarrow{2\pi J_{\text{CN}} C_z^\zeta N_z^\epsilon, 180_x^0 (^{13}\text{C} + ^{15}\text{N})} 2C_x^\zeta N_y^\epsilon \cos(\Omega_\epsilon t_1) + C_y^\zeta \sin(\Omega_\epsilon t_1) \\
 \xrightarrow{90_x^0 (^{13}\text{C} + ^{15}\text{N})} 2C_x^\zeta N_z^\epsilon \cos(\Omega_\epsilon t_1) + C_z^\zeta \sin(\Omega_\epsilon t_1) \\
 \xrightarrow{2\pi J_{\text{CN}} C_z^\zeta N_z^\epsilon, 180_x^0 (^{13}\text{C} + ^{15}\text{N})} C_y^\zeta \cos(\Omega_\epsilon t_1) - C_z^\zeta \sin(\Omega_\epsilon t_1) \\
 \xrightarrow{90_y^0 ^{13}\text{C}} C_y^\zeta \cos(\Omega_\epsilon t_1) + C_x^\zeta \sin(\Omega_\epsilon t_1)
 \end{array}$$

Separation of the orthogonal components is achieved by the collection of a second dataset with inversion of the  $^{13}\text{C}$  pulse midway through the PEP block ( $\phi_4$ ):

$$\begin{array}{l}
 90_x^0 ^{13}\text{C}, 90_x^0 ^{15}\text{N} \xrightarrow{\quad} 2C_x^\zeta N_z^\epsilon \cos(\Omega_\epsilon t_1) - C_z^\zeta \sin(\Omega_\epsilon t_1) \\
 \xrightarrow{2\pi J_{\text{CN}} C_z^\zeta N_z^\epsilon, 180_x^0 (^{13}\text{C} + ^{15}\text{N})} C_y^\zeta \cos(\Omega_\epsilon t_1) + C_z^\zeta \sin(\Omega_\epsilon t_1) \\
 \xrightarrow{90_y^0 ^{13}\text{C}} C_y^\zeta \cos(\Omega_\epsilon t_1) - C_x^\zeta \sin(\Omega_\epsilon t_1)
 \end{array}$$

Followed by treatment of the resulting two datasets as before:

$$\begin{array}{l}
 \text{Experiment 1 } (\phi_4 = x): \quad C_y^\zeta \cos(\Omega_\epsilon t_1) + C_x^\zeta \sin(\Omega_\epsilon t_1) \\
 \text{Experiment 2 } (\phi_4 = -x): \quad C_y^\zeta \cos(\Omega_\epsilon t_1) - C_x^\zeta \sin(\Omega_\epsilon t_1) \\
 \text{Exp. 1} + \text{Exp. 2} = 2C_y^\zeta \cos(\Omega_\epsilon t_1) \\
 \text{Exp. 1} - \text{Exp. 2} = 2C_x^\zeta \sin(\Omega_\epsilon t_1)
 \end{array}$$

### 3. Side-Chain Hydrogen Exchange in Arginine

Whilst the result of this alternate phase cycle is the same as it was for the previous scheme, the cosine-modulated part of the signal was stored as multiple-quantum magnetisation and the sine-part longitudinally. This results in the corresponding sine-type quadrature artefact in the indirect dimension owing to the faster relaxation of the cosine-modulated signal and thus incomplete cancellation of the mirrored frequency (Figure 3.8b).

A combination of both pathways would ultimately lead to cancellation of the quadrature artefact and result in clean, sensitivity-enhanced spectra of arginine side-chains. As for the previous HSQC experiments, a simple phase cycle is required to select the  $\Delta\rho = \pm 1$  transitions prior to the  $t_1$  period ( $\phi_2$ ) and optional axial peak suppression can be included through the cycling of the  $^{13}\text{C}$  excitation pulse ( $\phi_1$ ). Therefore, the full relaxation-optimised phase cycle is:<sup>[173]</sup>

**First FID:**  $C_Y^\zeta \cos(\Omega_\epsilon t_1) + C_X^\zeta \sin(\Omega_\epsilon t_1)$

Scan	$\phi_1$	$\phi_2$	$\phi_3$	$\phi_4$	$\phi_5$	$\phi_6$	$\phi_{\text{rec}}$
1	0°	0°	0°	90°	90°	180°	0°
2	180°	0°	0°	90°	90°	180°	180°
3	0°	180°	0°	90°	90°	180°	180°
4	180°	180°	0°	90°	90°	180°	0°
5	0°	0°	90°	0°	0°	270°	0°
6	180°	0°	90°	0°	0°	270°	180°
7	0°	180°	90°	0°	0°	270°	180°
8	180°	180°	90°	0°	0°	270°	0°

**Second FID:**  $C_Y^\zeta \cos(\Omega_\epsilon t_1) - C_X^\zeta \sin(\Omega_\epsilon t_1)$

Scan	$\phi_1$	$\phi_2$	$\phi_3$	$\phi_4$	$\phi_5$	$\phi_6$	$\phi_{\text{rec}}$
1	0°	0°	0°	90°	270°	180°	0°
2	180°	0°	0°	90°	270°	180°	180°
3	0°	180°	0°	90°	270°	180°	180°
4	180°	180°	0°	90°	270°	180°	0°
5	0°	0°	90°	180°	0°	270°	0°
6	180°	0°	90°	180°	0°	270°	180°
7	0°	180°	90°	180°	0°	270°	180°
8	180°	180°	90°	180°	0°	270°	0°

One may expect a two-fold sensitivity enhancement arising from the PEP modification; however, it is important to realise that each of the cosine- and sine-modulated parts of the signal come with their own experimental noise. This means that although the desired signal is increased by a factor of two, the noise against which the signal is detected is correspondingly increased by a factor of  $\sqrt{2}$  and thus the maximum theoretical gain in signal-to-noise is 41%.<sup>[174]</sup> The increase in signal-to-noise achieved on a real sample is further reduced by the fact that the PEP-HSQC pulse sequence is longer than the conventional HSQC due to the double-INEPT block required to refocus both parts of the modulated magnetisation. As discussed above, the coherences continue to relax during the extra delays and thus some signal is lost during the transfers. For

free arginine, the signal enhancement achieved is close to the maximum as the intrinsic relaxation rates in the small molecule are slow (Figure 3.9a). When the experiment is applied to a protein such as T4L99A, a range of enhancements are observed within the molecule (Figure 3.9b). For residues that are relatively flexible, the relaxation is not fast enough to cause significant losses during the additional delays. However, for residues that are more rigid the additional 25 ms INEPT block results in significant attenuation of the detected signal. For residues with an order parameter ( $S^2$ ) of above 0.5, the relaxation is fast enough to result in an overall *decrease* in signal-to-noise when compared to the conventional HSQC sequence. As an interrogation of the hydrogen exchange rates is likely to be of more interest for the rigid, interacting arginine residues present within a protein, the PEP modification is not a suitable means by which to increase the signal-to-noise of the experiments described in Section 3.2.1.

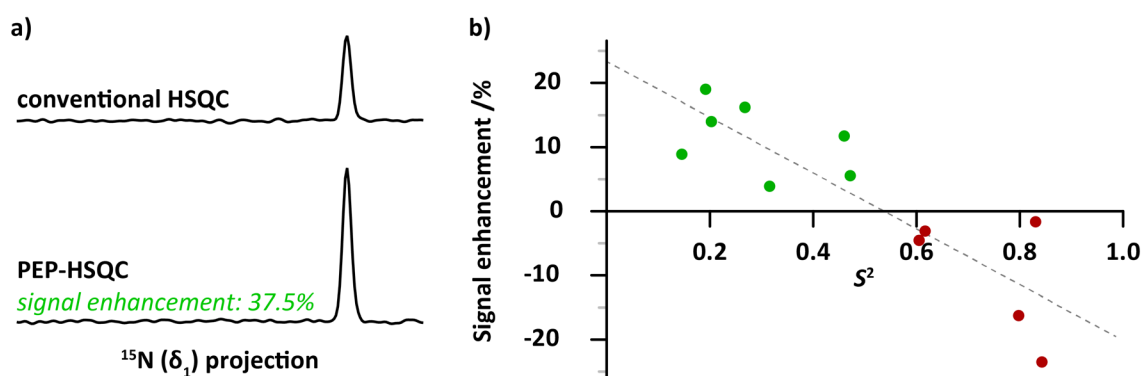


**Figure 3.9** A comparison of the signal intensity obtained using the conventional and PEP-HSQC sequences for a) free [ $^{13}\text{C}_6, ^{15}\text{N}_4$ ]-L-arginine and b) T4L99A. Whilst close to the maximum enhancement is observed for free arginine, the enhancement of the signal in T4L99A appears dependent on the flexibility of the residue in question. The more flexible residues ( $S^2 < 0.5$ ) experience a signal **enhancement** whilst more rigid residues ( $S^2 > 0.5$ ) result in signal **reduction** when using the PEP-HSQC.

### b. Heteronuclear Cross-Polarisation

One of the sources of the relatively low sensitivity of the existing  $^{13}\text{C}^{\zeta}\text{-}^{15}\text{N}^{\epsilon}$  experiments is the  $^{13}\text{C}$ -excitation- $^{13}\text{C}$ -detection strategy, stemming from the lower gyromagnetic ratio of the  $^{13}\text{C}$  nucleus. Whilst there are several advantages of this strategy, as discussed in the previous chapters, an alternative approach would make use of the higher- $\gamma$   $^1\text{H}$  nucleus for excitation whilst retaining the  $^{13}\text{C}$  nucleus for detection in a so called  $^1\text{H}$ -excitation- $^{13}\text{C}$ -detection strategy.

The experiments proposed in Chapter 2 are design using  $^{13}\text{C}^{\zeta}$  excitation in part to mitigate the signal loss arising from the hydrogen exchange of the  $^1\text{H}^{\epsilon/\eta}$  nuclei with the solvent during the  $^1\text{H}$ - $^{15}\text{N}$  INEPT transfers in a typical HSQC experiment. Heteronuclear cross-polarisation (het-CP) is an alternative technique for this magnetisation transfer that is partially resistant to the hydrogen exchange process.<sup>[92,175]</sup> Commonly found in solid-state NMR experiments, het-CP makes use of carefully designed isotropic mixing sequences to transfer magnetisation between

### 3. Side-Chain Hydrogen Exchange in Arginine

scalar coupled nuclei. There are numerous pulse sequences explicitly designed to optimise the isotropic mixing of spins including the WALTZ<sup>[41-43]</sup>, DIPSI<sup>[176,177]</sup> and FLOPSY<sup>[178]</sup> schemes. Whilst a full discussion of the characteristics of such sequences is beyond the scope of this thesis, each mixing scheme consists of a train of pulses with carefully optimised flip angles and phases. For example, the pulses applied during the DIPSI sequences are shown below:

$$\text{DIPSI-1: } 365^\circ - \overline{295^\circ} - 65^\circ - \overline{305^\circ} - 350^\circ$$

$$\text{DIPSI-2: } 320^\circ - \overline{410^\circ} - 290^\circ - \overline{285^\circ} - 30^\circ - \overline{245^\circ} - 375^\circ - \overline{265^\circ} - 370^\circ$$

$$\begin{aligned} \text{DIPSI-3: } & \overline{245^\circ} - 395^\circ - \overline{250^\circ} - 275^\circ - \overline{30^\circ} - 230^\circ - \overline{360^\circ} - 245^\circ - \overline{370^\circ} \\ & 340^\circ - \overline{350^\circ} - 260^\circ - \overline{270^\circ} - 30^\circ - \overline{225^\circ} - 365^\circ - \overline{255^\circ} - 395^\circ \end{aligned}$$

Each of the DIPSI sequences is applied as a super-cycle of  $R\overline{R}\overline{R}R$ , where  $R$  is the applicable pulse train described above and the overbar indicates a phase shift of  $180^\circ$ . When applied simultaneously to scalar-coupled nuclei, these mixing sequences effect a transfer between in-phase coherences directly, without the generation of the anti-phase coherences present during INEPT transfers. The mixing sequences are often applied to homonuclear couplings (to effect  $^1\text{H}$ - $^1\text{H}$ , or  $^{13}\text{C}$ - $^{13}\text{C}$  transfers) but are equally applicable to heteronuclear systems using matched pulses simultaneously applied on both nuclei. Furthermore, in the case of a  $^1\text{H}$ - $^{15}\text{N}$  transfer in the presence of hydrogen exchange, the solvent resonance is also affected by the isotropic mixing and thus contributes to the polarisation of the  $^{15}\text{N}$  nuclei. One can think of the het-CP in this case as *pumping* magnetisation from the solvent into the  $^{15}\text{N}$  coherence via the hydrogen exchange mechanism. Considering an application to the arginine guanidinium group, there are a total of five  $^1\text{H}^{\epsilon/\eta}$  protons available for the het-CP transfer to the directly bound  $^{15}\text{N}^{\epsilon/\eta}$  nuclei and crucially, each  $^{15}\text{N}$  nucleus is scalar coupled to the same  $^{13}\text{C}^\zeta$ . A second het-CP transfer between  $^{15}\text{N}$  and  $^{13}\text{C}$  would therefore result in the generation of in-phase  $^{13}\text{C}^\zeta$  magnetisation from which the existing HSQC experiments could begin.

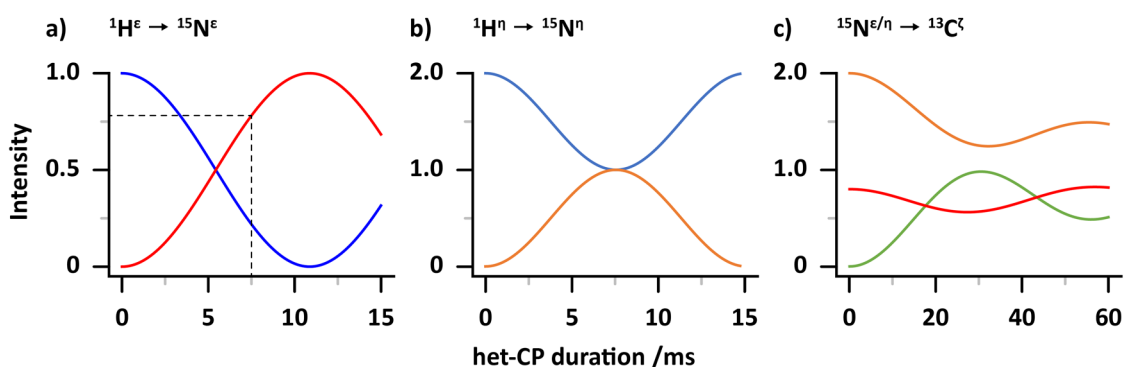


**Figure 3.10** Simulation of the het-CP mediated transfer of magnetisation between a)  $^1\text{H}^\epsilon$  and  $^{15}\text{N}^\epsilon$ , b)  $^1\text{H}^\eta$  and  $^{15}\text{N}^\eta$  and c)  $^{15}\text{N}^{\epsilon/\eta}$  and  $^{13}\text{C}^\zeta$ . As both  $^1\text{H}$ - $^{15}\text{N}$  transfers occur simultaneously, the duration is optimised for the  $^1\text{H}$ - $^{15}\text{N}^\eta$  transfer resulting in a lower conversion of  $^1\text{H}^\epsilon$  to  $^{15}\text{N}^\epsilon$  (ca. 80%, dotted line in a).

### 3. Side-Chain Hydrogen Exchange in Arginine

Much like an INEPT transfer, the optimum duration of the het-CP transfer will depend upon the coupling constant between the nuclei involved and in the simplest systems, maximum transfer is achieved using a mixing period equal to  $1/J$ . This is the case for the transfer between  $^1\text{H}^\epsilon$  and  $^{15}\text{N}^\epsilon$  (Figure 3.10a). The analogous transfer of the  $^1\text{H}^\eta$  protons is less efficient because there are two protons coupled to a single  $^{15}\text{N}^\eta$  nucleus and thus an incomplete transfer is expected (Figure 3.10b). This is very much like the generation of the single-quantum  $^{13}\text{C}^\zeta$ - $^{15}\text{N}^\eta$  coherences discussed in Chapter 2. As well as differing in efficiency, the transfers from  $^1\text{H}^\epsilon$  and  $^1\text{H}^\eta$  have different optimum durations and as such, a compromise value must be found. As the  $^1\text{H}^\eta$  nuclei outnumber  $^1\text{H}^\epsilon$  by four to one, it is sensible to optimise the transfer with respect to  $^1\text{H}^\eta$  and simply accept the lower transfer efficiency of the  $^1\text{H}^\epsilon$ - $^{15}\text{N}^\epsilon$  pathway. Similarly, the  $^{13}\text{C}^\zeta$  is directly coupled to three  $^{15}\text{N}$  nuclei and the het-CP transfer is only able to transfer approximately a third of the available magnetisation from  $^{15}\text{N}^{\epsilon/\eta}$  to  $^{13}\text{C}^\zeta$  (Figure 3.10c). As a result of the multiple coupling pathways present in the guanidinium group, the entire transfer from  $^1\text{H}^{\epsilon/\eta}$  to  $^{13}\text{C}^\zeta$  proceeds with an approximate maximum efficiency of 20%, equivalent to the transfer of the magnetisation from a single proton. However, considering the higher gyromagnetic ratio of the proton, this results in a theoretical four-fold increase in signal intensity when compared to the direct excitation of  $^{13}\text{C}^\zeta$ . Whilst relaxation during the various het-CP transfers will partially degrade the real-world enhancement, further sensitivity gains are possible due to the faster  $T_1$  relaxation of the  $^1\text{H}^{\epsilon/\eta}$  nuclei when compared with  $^{13}\text{C}^\zeta$ . Whilst the slow  $T_2$  relaxation of  $^{13}\text{C}^\zeta$  is considered an advantage as it minimises losses during the pulse sequence, the similarly slow  $T_1$  relaxation limits the repetition rate of the experiment and a relaxation delay ( $d_1$ ) on the order of several seconds is typically required between scans. Protons generally relax much faster and thus an experiment beginning with  $^1\text{H}^{\epsilon/\eta}$  excitation requires a correspondingly shorter relaxation delay to perform optimally. The combination of the gyromagnetic ratio and favourable relaxation properties is expected to result in a significant increase in the polarisation of  $^{13}\text{C}^\zeta$  when using the het-CP transfer scheme.

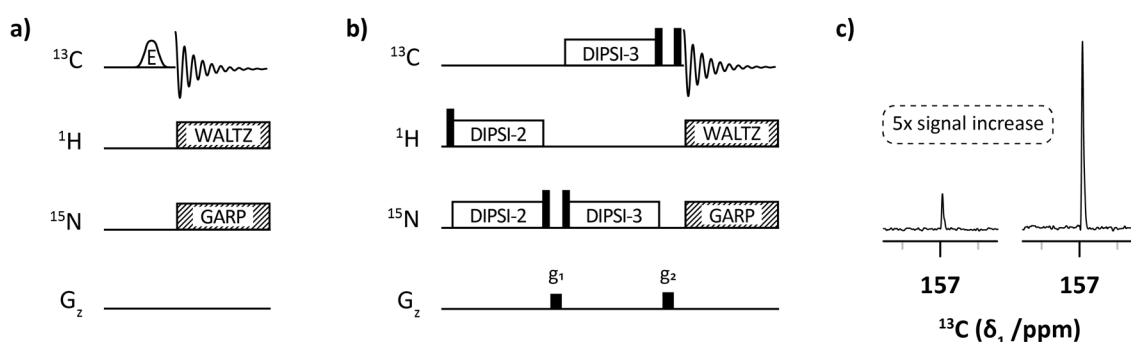


**Figure 3.11** Pulse sequences designed to test the sensitivity gains of switching to a het-CP based excitation scheme. a) Excitation of  $^{13}\text{C}^\zeta$  using a selective pulse followed by detection under the usual  $^1\text{H}$  and  $^{15}\text{N}$  schemes. b) Excitation of  $^{13}\text{C}^\zeta$  via  $^1\text{H}^{\epsilon/\eta}$  using the het-CP transfers described in the text. c) 1D  $^{13}\text{C}$  spectra obtained using pulse sequences a) and b). Each spectrum was acquired in 30s on a sample of *free* [ $^{13}\text{C}_6$ ,  $^{15}\text{N}_4$ ]-L-arginine at pH 5 and 298 K.

### 3. Side-Chain Hydrogen Exchange in Arginine

Applying the het-CP mediated excitation scheme to a sample of *free* [ $^{13}\text{C}_6, ^{15}\text{N}_4$ ]-L-arginine demonstrates a five-fold signal improvement when compared to the direct excitation of  $^{13}\text{C}^\zeta$  using a selective pulse (Figure 3.11). The recycle time was optimised for the selective  $^{13}\text{C}^\zeta$  excitation spectrum as  $1.3 \times T_1 = 2.8\text{s}$  to provide the maximum signal per unit time with 8 scans collected in 30 seconds. The het-CP sequence used a recycle time of 1.5s and so 16 scans were able to be collected in the same overall experiment time of 30 seconds. A shorter recycle time provided even higher sensitivity gains but at the cost of significant probe heating due to the high-power spinlock pulses. In proteins, the gain in sensitivity by using the het-CP sequence will vary from residue to residue based on the relative relaxation rates of the  $^{13}\text{C}^\zeta$  and  $^1\text{H}^{\epsilon/\eta}$  nuclei as well as the intrinsic hydrogen exchange rates. However, it would only be expected to perform worse than the selective  $^{13}\text{C}^\zeta$  excitation when the exchange rate of the  $^1\text{H}^{\epsilon/\eta}$  nuclei exceeds the  $^1J_{\text{HN}}$  scalar coupling of 92 Hz.

#### c. Refocused-INEPT

In favourable hydrogen exchange regimes, using the  $^1\text{H}^{\epsilon/\eta}$  nuclei for the initial excitation clearly has a positive effect on the overall sensitivity of the  $^{13}\text{C}^\zeta$ - $^{15}\text{N}^\epsilon$  experiment. However, it was noted that due to the multiple active coupling pathways in the guanidinium group, the total magnetisation transferred from the five available protons is equivalent to the complete transfer of just one of them. An alternate strategy, and one that avoids the need for high-power spinlocking pulse trains, is to optimise the transfer with respect to the single  $^1\text{H}^\epsilon$  nucleus by using a refocused-INEPT sequence.<sup>[179–181]</sup> A refocused-INEPT block consists of two back-to-back INEPT transfers and results in the efficient transfer of equilibrium  $H_z$  to  $N_z$  magnetisation, as described in Figure 3.12.

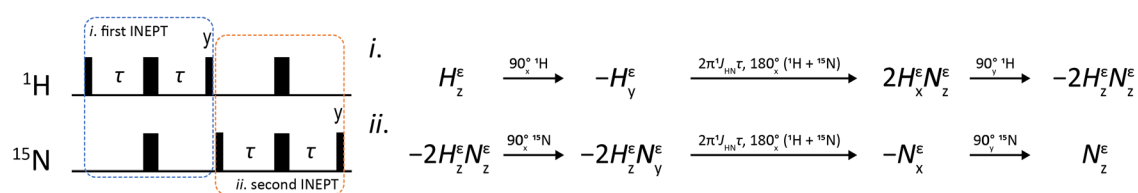


**Figure 3.12** Refocused-INEPT block used to transfer in-phase equilibrium  $^1\text{H}^\epsilon$  magnetisation to  $^{15}\text{N}^\epsilon$ . The delay  $\tau$  is set to  $1/4(^1J_{\text{HN}}) = 2.72\text{ ms}$  to maximise the transfer between nuclei.

It is important to note that unlike the het-CP experiments described above, the INEPT transfers proceed via the antiphase coherences  $2H_x N_z$  and  $2H_z N_y$  and are thus subject to the adverse effects of rapid hydrogen exchange. However, such an exchange regime would also cause the isotope shifted  $^{15}\text{N}(^1\text{H}/^2\text{H})$  resonances to merge together in the  $^{15}\text{N}$  dimension so an upper limit on the measurable exchange rates already exists within this experimental strategy.

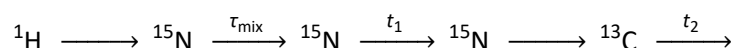
A significant advantage of this excitation scheme is that for samples prepared in mixed  $^1\text{H}_2\text{O}/^2\text{H}_2\text{O}$  buffers, only the *protonated*  $^{15}\text{N}^\epsilon$  nuclei are excited: the deuterated  $^{15}\text{N}^\epsilon$  species lack

the  $^1\text{H}^\epsilon$  nucleus required to mediate the transfer. Conversely, the het-CP transfer in partially deuterated solvent systems would result in the excitation of both protonated and deuterated residues because of the mixed deuteration of the  $\text{H}^\eta$  nuclei. The ability to excite only the protonated species is advantageous as it allows the variable mixing period – during which the hydrogen exchange will take place – to be inserted *before* the  $^{15}\text{N}$  chemical shift is evolved. Therefore, the selective excitation of  $^{15}\text{N}^\epsilon(^1\text{H})$  achievable using the refocused-INEPT completely removes the need for the additional time consuming  $^{15}\text{N}^\epsilon$  dimension present in Figure 3.6 whilst simultaneously providing a boost to the overall sensitivity of the experiment.

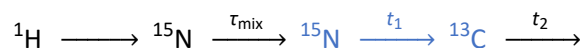
### 3.2.3 Resolution of Isotope-Shifted Signals

#### a. Semi-Constant-Time Chemical Shift Evolution

The selective generation of  $^{15}\text{N}^\epsilon(^1\text{H})$  magnetisation described above allows a rearrangement of the magnetisation flow within the pulse sequence as there is no longer a need for the initial  $^{13}\text{C}^\zeta\text{-}^{15}\text{N}^\epsilon$  INEPT transfer or additional  $^{15}\text{N}$  chemical shift dimension. The proposed scheme, starting from the  $^1\text{H}^\epsilon$  proton is as follows:



During the chemical shift evolution, multiple scalar-coupling pathways involving the  $^{15}\text{N}^\epsilon$  nucleus are active and each unwanted interaction must be addressed individually. As discussed previously, the  $^{15}\text{N}\text{-}^1\text{H}$  and  $^{15}\text{N}\text{-}^2\text{H}$  couplings are easily suppressed using composite pulse decoupling schemes whilst the  $^{15}\text{N}\text{-}^{13}\text{C}^{\zeta/\delta}$  couplings can be refocused with strategically placed  $180^\circ$   $^{13}\text{C}$  pulses. The flow of magnetisation through the pulse sequence can be optimised by recognising that the desired chemical shift evolution of  $^{15}\text{N}^\epsilon$  can proceed during  $t_1$  with the simultaneous evolution of only the  $^1J_{\text{CN}}$  scalar coupling to  $^{13}\text{C}^\zeta$  using a modified evolution period, highlighted in blue, that avoids the need for a subsequent  $^{15}\text{N}\text{-}^{13}\text{C}$  transfer:



This strategy is known as *constant-time*<sup>[182,183]</sup> (CT) chemical shift evolution and is widely used throughout biomolecular NMR spectroscopy to selectively evolve one coupling or chemical shift whilst refocussing another.<sup>[184–186]</sup> For the experiment discussed here, it is made possible by the significant difference in chemical shift between the  $^{13}\text{C}^\zeta$  (157 ppm) and  $^{13}\text{C}^\delta$  (40 ppm) nuclei, rendering them amenable to targeted refocussing using frequency selective pulses. The idea is to keep the overall duration of the evolution period constant (appropriate for the evolution of the desired coupling pathway) whilst incrementing the timing of pulses within the block to affect a gradual increase in chemical shift evolution. Several pulse sequence elements applicable to the arginine side-chain are examined in Figure 3.13.

### 3. Side-Chain Hydrogen Exchange in Arginine

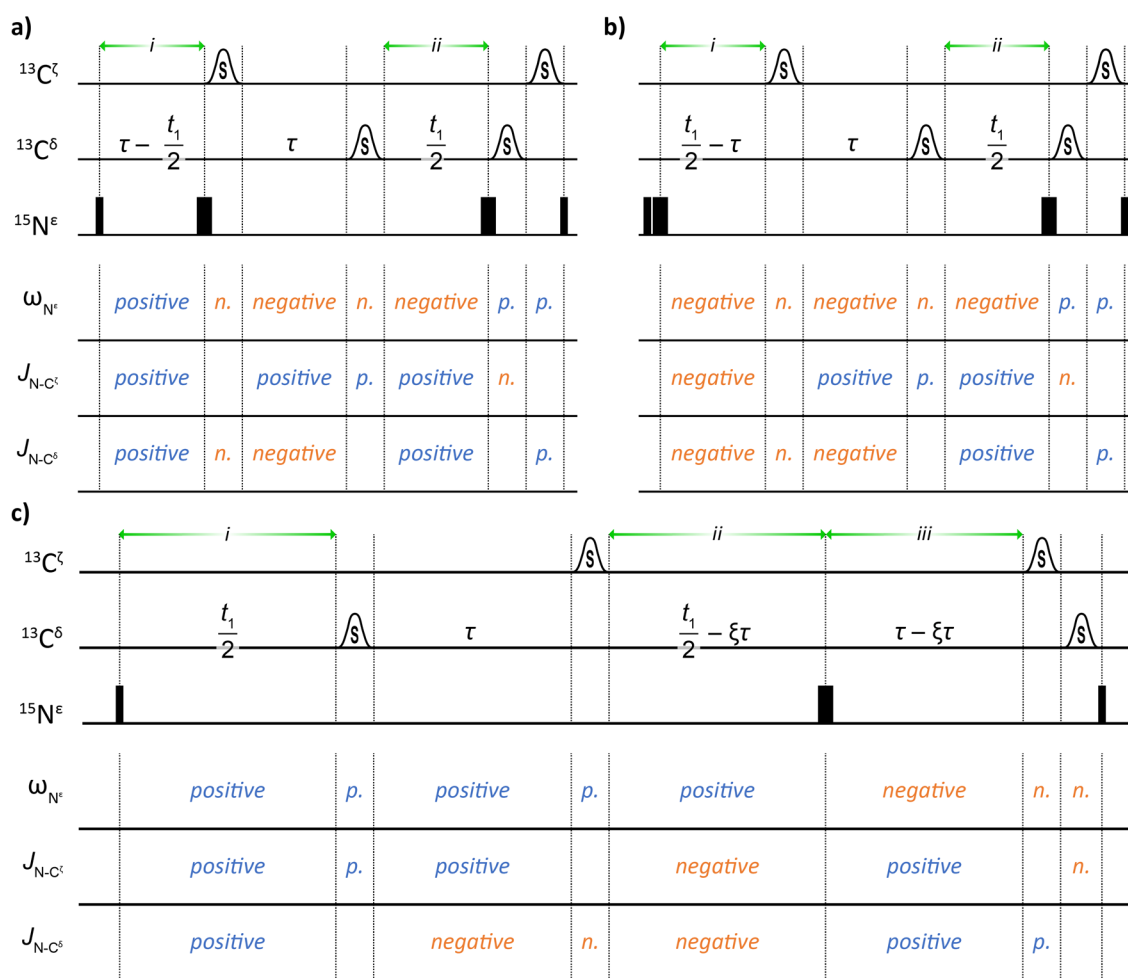


**Figure 3.13** Pulse sequence elements used to record the chemical shift of  $^{15}\text{N}^\epsilon$  of arginine whilst selectively evolving the  $^{13}\text{C}^\zeta$ - $^{15}\text{N}^\epsilon$  scalar coupling. a) A *true* constant-time evolution block: as the total delay  $ii$  increases, delay  $i$  is decreased accordingly to maintain the same total duration. The maximum duration of  $t_1$  is therefore limited by the value of  $\tau$ ,  $1/4(^1J_{\text{CN}}) = 12.5$  ms. b) A non-constant time evolution block allows the continued incrementation of  $t_1$  beyond the limit set by  $\tau$ . c) A modified evolution block that spreads the additional non-constant time part of the chemical shift evolution between all FIDs in order to improve the lineshape in the indirect dimension. The value of  $\xi$  is incremented alongside  $t_1$  between zero and the total number of FIDs recorded such that the delay  $iii$  is linearly decreased to zero during the experiment.

The coupling between  $^{15}\text{N}^\epsilon$  and  $^{13}\text{C}^\zeta$  is approximately 20 Hz and therefore the antiphase component  $2C_2^7N_V^\epsilon$  is maximised when allowed to evolve for  $1/2(^1J_{\text{CN}}) = 25$  ms. If one required a chemical shift evolution of  $^{15}\text{N}^\epsilon$  of up to 25 ms, the sequence shown in Figure 3.13a is most appropriate. The sequence is intended to follow the refocused-INEPT excitation block described in Section 3.2.2c and begins with longitudinally stored  $N_z^\epsilon$  magnetisation. The initial  $90^\circ$   $^{15}\text{N}$  pulse creates transverse magnetisation and starts the *evolution* of the  $^{15}\text{N}^\epsilon$  chemical shift and both  $^{15}\text{N}$ - $^{13}\text{C}^{\zeta/\delta}$  scalar couplings during the first variable delay period,  $i$ . A  $180^\circ$   $^{15}\text{N}$  pulse followed immediately by a  $^{13}\text{C}^\zeta$ -selective pulse inverts the sense of the  $^{15}\text{N}^\epsilon$  chemical shift and  $^{15}\text{N}$ - $^{13}\text{C}^\delta$  coupling causing them to begin to *refocus* during the fixed delay  $\tau$ . The selective pulse causes the  $^{15}\text{N}$ - $^{13}\text{C}^\zeta$  coupling to continue to evolve during  $\tau$ . It is important to note that the inversion of the chemical shift and  $^{15}\text{N}$ - $^{13}\text{C}^\delta$  coupling is caused by the  $^{15}\text{N}$  pulse and therefore they begin to refocus during the subsequent  $^{13}\text{C}^\zeta$ -selective pulse. Following the fixed delay, a  $^{13}\text{C}^\delta$ -selective

### 3. Side-Chain Hydrogen Exchange in Arginine

pulse inverts the sense of the  $^{15}\text{N}$ - $^{13}\text{C}^\delta$  coupling whilst leaving the other evolutions unaffected, prior to the second variable delay, *ii*. Finally,  $^{15}\text{N}$ ,  $^{13}\text{C}^\delta$  and  $^{13}\text{C}^\zeta$  pulses are applied to correct for unwanted evolutions during the previously applied selective pulses. The total evolution of each of the pathways during the sequence can be expressed as:

$$\begin{aligned}\omega_{\text{N}^\epsilon} &= \tau - \frac{t_1}{2} - \text{sel. } ^{13}\text{C}^\zeta - \tau - \text{sel. } ^{13}\text{C}^\delta - \frac{t_1}{2} + \text{sel. } ^{13}\text{C}^\delta + \text{sel. } ^{13}\text{C}^\zeta \\ &= -t_1\end{aligned}$$

$$\begin{aligned}J_{\text{N-C}^\zeta} &= \tau - \frac{t_1}{2} + \tau + \text{sel. } ^{13}\text{C}^\delta + \frac{t_1}{2} - \text{sel. } ^{13}\text{C}^\delta \\ &= 2\tau\end{aligned}$$

$$\begin{aligned}J_{\text{N-C}^\delta} &= \tau - \frac{t_1}{2} - \text{sel. } ^{13}\text{C}^\zeta - \tau + \frac{t_1}{2} + \text{sel. } ^{13}\text{C}^\zeta \\ &= 0\end{aligned}$$

The chemical shift of  $^{15}\text{N}^\epsilon$  evolves for the total duration of  $t_1$ , the  $^{15}\text{N}$ - $^{13}\text{C}^\zeta$  coupling for a period equal to  $2\tau$  whilst the  $^{15}\text{N}$ - $^{13}\text{C}^\delta$  coupling is completely refocussed. If the fixed delay  $\tau$  is set to  $1/4(^1J_{\text{CN}}) = 12.5$  ms, the  $N_z^\epsilon$  magnetisation evolves completely into  $2C_2^\zeta N_y^\epsilon$  whilst simultaneously being labelled with the  $^{15}\text{N}^\epsilon$  chemical shift, as desired.

The caveat when using this constant-time element is that when  $t_1/2$  is incremented above the value of  $\tau$ , the variable delay *i* becomes negative and the method stalls. In this scenario, the sequence depicted in Figure 3.13b is more appropriate. Here, the  $180^\circ$   $^{15}\text{N}$  pulse has been moved and the variable delays re-configured to accommodate the increasing duration of  $t_1/2$ , whilst ensuring that only the desired pathways evolve during the sequence:

$$\begin{aligned}\omega_{\text{N}^\epsilon} &= -\frac{t_1}{2} + \tau - \text{sel. } ^{13}\text{C}^\zeta - \tau - \text{sel. } ^{13}\text{C}^\delta - \frac{t_1}{2} + \text{sel. } ^{13}\text{C}^\delta + \text{sel. } ^{13}\text{C}^\zeta \\ &= -t_1\end{aligned}$$

$$\begin{aligned}J_{\text{N-C}^\zeta} &= -\frac{t_1}{2} + \tau + \tau + \text{sel. } ^{13}\text{C}^\delta + \frac{t_1}{2} - \text{sel. } ^{13}\text{C}^\delta \\ &= 2\tau\end{aligned}$$

$$\begin{aligned}J_{\text{N-C}^\delta} &= -\frac{t_1}{2} + \tau - \text{sel. } ^{13}\text{C}^\zeta - \tau + \frac{t_1}{2} + \text{sel. } ^{13}\text{C}^\zeta \\ &= 0\end{aligned}$$

This sequence is not constant-time and thus increases in duration as  $t_1/2$  is incremented as a typical indirect evolution period would. When used in combination with the constant-time block (Figure 3.13a), the result is a semi-constant-time experiment that does not have an inherent limit on the indirect evolution time ( $t_1$ ). However, the indirect FID constructed from the individual experiments will not have a smooth decay as the relaxation of the spins during the

### 3. Side-Chain Hydrogen Exchange in Arginine

constant- and non-constant-time parts of the evolution is different. Figure 3.14a shows the FID from a simulated semi-constant-time acquisition and the resulting spectrum following Fourier transformation. The first section of the FID does not decay with relaxation due to the constant-time period and retains a constant intensity. This causes a step-like artefact when the acquisition mode is subsequently changed to non-constant-time and the exponential relaxation decay begins. The spectrum obtained by Fourier transformation of this FID exhibits distortions around the base of the peak consistent those associated with a truncated FID. In addition to the undesirable peak shape, the non-exponential decay of the detected signal renders the FID unsuitable for treatment using linear-prediction algorithms.

An alternate strategy to acquiring the data using an indirect evolution time greater than  $1/2(^1J_{\text{CN}})$  is shown in Figure 3.13c. Here, the *extra* evolution time is spread out evenly between each of the sequential FIDs such that there is no longer a harsh transition between the constant- and non-constant-time regimes.<sup>[159]</sup> The smoothed-semi-constant-time period begins in the same way as the previous approach with a  $90^\circ$   $^{15}\text{N}$  pulse applied to the longitudinally stored  $N_z^\epsilon$  magnetisation. After the first variable delay  $i$ , a  $^{13}\text{C}^\delta$ -selective pulse inverts the sense of the  $^{15}\text{N}$ - $^{13}\text{C}^\delta$  coupling for the subsequent fixed delay  $\tau$ , before a  $^{13}\text{C}^\zeta$ -selective pulse inverts the  $^{15}\text{N}$ - $^{13}\text{C}^\zeta$  coupling. Two more variable delays,  $i$  and  $ii$ , separated by a  $180^\circ$   $^{15}\text{N}$  pulse and followed by  $^{13}\text{C}^\zeta$ - and  $^{13}\text{C}^\delta$ -selective pulses to correct for unwanted evolutions complete the evolution period:

$$\begin{aligned}\omega_{\text{N}^\epsilon} &= \frac{t_1}{2} + \text{sel. } ^{13}\text{C}^\delta + \tau + \text{sel. } ^{13}\text{C}^\zeta + \frac{t_1}{2} - \xi\tau - \tau + \xi\tau - \text{sel. } ^{13}\text{C}^\zeta - \text{sel. } ^{13}\text{C}^\delta \\ &= -t_1 \\ J_{\text{N-C}^\zeta} &= \frac{t_1}{2} + \text{sel. } ^{13}\text{C}^\delta + \tau - \frac{t_1}{2} + \xi\tau + \tau - \xi\tau - \text{sel. } ^{13}\text{C}^\delta \\ &= 2\tau \\ J_{\text{N-C}^\delta} &= \frac{t_1}{2} - \tau - \text{sel. } ^{13}\text{C}^\zeta - \frac{t_1}{2} + \xi\tau + \tau - \xi\tau + \text{sel. } ^{13}\text{C}^\zeta \\ &= 0\end{aligned}$$

As before, the fixed delay  $\tau$  is set to  $1/4(^1J_{\text{CN}}) = 12.5$  ms to ensure the complete evolution of  $N_z^\epsilon$  into  $2C_z^\zeta N_y^\epsilon$  by the end of the evolution period. As  $t_1/2$  is incremented between successive FIDs,  $\xi$  is varied linearly from zero to  $2/N$  where  $N$  is the total number of FIDs to be acquired. This results in the smooth transition of delay  $ii$  from  $t_1/2$  to  $(t_1/2 - \tau)$  and delay  $iii$  from  $\tau$  to zero by the time the last FID is recorded. The constructed FID for the indirect dimension now exhibits the usual exponential relaxation decay, free from the step-like artefact present in the non-constant-time version discussed above. Fourier transformation of this FID results in a uniform peak shape without the previously observed distortions (Figure 3.14b). The only caveat when

using the smoothed-semi-constant-time evolution period is that the indirect acquisition time ( $t_1$ ) must exceed the value of  $2\tau$ , else the variable delay period  $ii$  becomes negative during the experiment. However, for acquisitions where  $t_1$  will not exceed  $2\tau$ , the fully constant-time evolution block in Figure 3.13a is most appropriate.

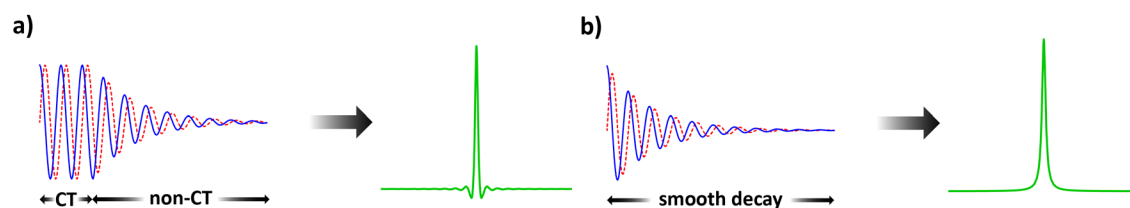


**Figure 3.14** Simulated FID and Fourier transformed spectra arising from a) semi-constant-time and b) smoothed semi-constant-time acquisitions. The FIDs are generated using a frequency of 100 Hz and a relaxation rate of  $50 \text{ s}^{-1}$  with the real and imaginary parts of the complex time-domain signal in blue and red, respectively. The FIDs were simulated for 100 ms with the constant-time period of a) fixed at 25 ms.

### b. Sign-Coding $^1\text{H}/^2\text{H}$ Filter

Whilst it has been noted in previous sections that the protonated [ $^{15}\text{N}^\epsilon(^1\text{H})$ ] and deuterated [ $^{15}\text{N}^\epsilon(^2\text{H})$ ] species are easily resolved from one another by exploiting the one-bond deuterium isotope shift, it is important to recognise that this will double the number of peaks in the resulting  $^{13}\text{C}^\zeta\text{-}^{15}\text{N}^\epsilon$  spectra. In favourable circumstances, for example the study of small proteins with only a few arginine residues, this may not be cause for concern. However, it is anticipated that signal overlap is likely to cause problems for a significant number of proteins that one may wish to study using this methodology.

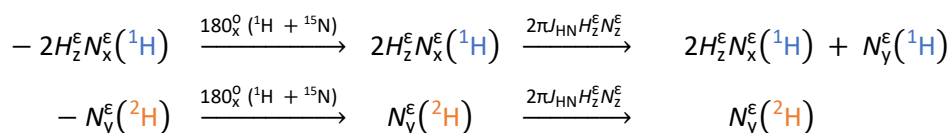
Fortunately, the spectral crowding resulting from the necessary doubling of the number of signals can be mitigated by separating the protonated and deuterated signals into different sub-spectra by using a sign-coding filter prior to the indirect chemical shift evolution period (Figure 3.15).<sup>[187]</sup> The filter consists of a  $^1\text{H}\text{-}^{15}\text{N}$  spin-echo applied with a deuterium decoupling field to selectively invert only the protonated species between alternate experiments. The filter is placed directly after the variable delay  $\tau_{\text{mix}}$  and thus begins with longitudinal  $^{15}\text{N}^\epsilon$  magnetisation. Recognising that a spin-echo containing a  $180^\circ$  pulse to the transverse nuclei ( $^{15}\text{N}^\epsilon$ ) will refocus any chemical shift evolutions it may experience, only the evolution under the scalar coupling Hamiltonian will be considered:

$$\begin{aligned}
 N_z^\epsilon &\xrightarrow{90_x^\circ \text{ } ^{15}\text{N}} -N_y^\epsilon(^1\text{H}) \xrightarrow{2\tau J_{\text{HN}} H_z^\epsilon N_z^\epsilon} -N_y^\epsilon(^1\text{H}) - 2H_z^\epsilon N_x^\epsilon(^1\text{H}) \\
 &\quad -N_y^\epsilon(^2\text{H}) \xrightarrow{2\tau J_{\text{HN}} H_z^\epsilon N_z^\epsilon} -N_y^\epsilon(^2\text{H})
 \end{aligned}$$

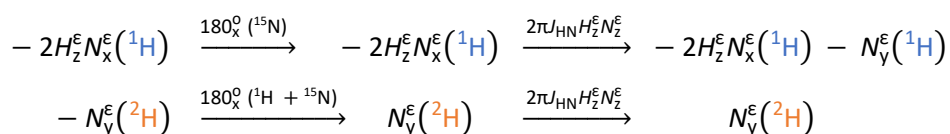
The delay  $\tau$  is optimised to  $1/2(J_{\text{HN}})$  in order to maximise the anti-phase component  $2H_z^\epsilon N_x^\epsilon$  and ensure that no in-phase  $N_y^\epsilon$  magnetisation remains. Following this delay, the usual simultaneous  $180^\circ$   $^1\text{H}$  and  $^{15}\text{N}$  pulses of the spin-echo are applied. However, the  $^1\text{H}$  pulse is applied as back-to-

### 3. Side-Chain Hydrogen Exchange in Arginine

back  $90^\circ$  pulses so that the phase properties of each can be manipulated individually. When the second  $90^\circ$   $^1\text{H}$  pulse is applied with  $x$ -phase, the back-to-back pulses serve as a standard  $180^\circ$  pulse and cause the anti-phase  $2H_z^E N_x^E$  magnetisation to continue to evolve during the subsequent delay  $\tau$ . The total evolution period of  $2\tau = 1/(J_{\text{HN}})$  results in the inversion of the  $N_y^E(^1\text{H})$  magnetisation by the end of the spin-echo:



When the experiment is repeated with  $\phi = -x$ , the second  $90^\circ$   $^1\text{H}$  pulse cancels out the first and the back-to-back pulse train has no net effect on  $^1\text{H}$ . The effective absence of a  $180^\circ$   $^1\text{H}$  pulse during the spin-echo results in the refocussing of the  $J_{\text{HN}}$  coupling over the course of the spin-echo:



Due to the lack of a  $^1\text{H}^E$  proton, the deuterated species is unaffected by the change in phase of the  $^1\text{H}$  pulse between the two experiments and is simply inverted by the  $180^\circ$   $^{15}\text{N}$  pulse in both cases. The linear combination of the resulting two datasets result in the easy separation of the protonated and deuterated signals into sub-spectra and thereby avoiding the resolution problems caused by increased spectral crowding (Figure 3.15b):

$$\begin{aligned} \text{Experiment 1 } (\phi = x): & \quad N_y^E(^1\text{H}) \quad + \quad N_y^E(^2\text{H}) \\ \text{Experiment 2 } (\phi = -x): & \quad -N_y^E(^1\text{H}) \quad + \quad N_y^E(^2\text{H}) \\ \text{Exp. 1} \quad + \quad \text{Exp. 2} & \quad = \quad 2N_y^E(^2\text{H}) \\ \text{Exp. 1} \quad - \quad \text{Exp. 2} & \quad = \quad 2N_y^E(^1\text{H}) \end{aligned}$$

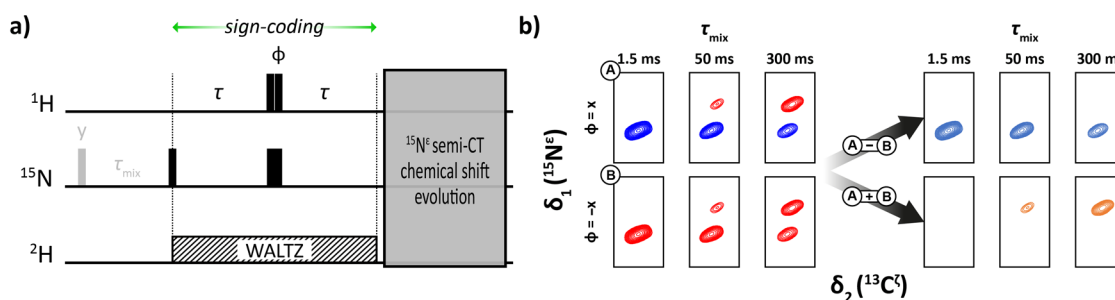


**Figure 3.15** a) The sign-coding element used to generate separated sub-spectra for the protonated and deuterated  $^{13}\text{C}^{\zeta}\text{-}^{15}\text{N}^E$  resonances is placed between the mixing delay the indirect chemical shift evolution period. Two experiments are required for the separation ( $\phi = x, -x$ ). b) The linear combination of the resulting two datasets allows the separation of the  $^{13}\text{C}^{\zeta}\text{-}^{15}\text{N}^E(^1\text{H})$  and  $^{13}\text{C}^{\zeta}\text{-}^{15}\text{N}^E(^2\text{H})$  resonances, avoiding the spectral crowding resulting from a doubling of the number of signals.

### 3.2.4 pseudo-4D ASHDEX Pulse Sequence

The full pseudo-four-dimensional ( $\phi_3$ ,  $\tau_{\text{mix}}$ ,  $t_1$ ,  $t_2$ ) pulse sequence for the quantification of the  $^1\text{H}^\epsilon$  hydrogen exchange rate of arginine side-chains is shown below in Figure 3.16. The experiment is referred to herein as the ASHDEX (Arginine Side-chain Hydrogen EXchange) experiment.<sup>[188]</sup> It is important to note that for the experiment to work correctly, two purge elements are required: a  $90_x^\circ$   $^1\text{H}$  pulse followed by gradient pulse  $g_1$  is inserted *before*  $d_1$  to ensure that the amount of  $^1\text{H}^\epsilon$  magnetisation present at the start of each scan is independent of the mixing time,  $\tau_{\text{mix}}$ . As for the previously discussed  $^{13}\text{C}^\zeta$ - $^{15}\text{N}^\epsilon$  experiments, equilibrium  $^{15}\text{N}$  magnetisation is purged using a  $90_x^\circ$   $^{15}\text{N}$  pulse followed by gradient pulse  $g_2$ . Following  $^1\text{H}$  and  $^{15}\text{N}$  purging elements, the sequence consists of the building blocks discussed above:

- i.  **$^1\text{H}$ - $^{15}\text{N}$  refocussed-INEPT:** Makes use of  $^1\text{H}$  sensitivity to generate in-phase  $^{15}\text{N}$  magnetisation using a double INEPT element. The requirement of the  $^1\text{H}$ - $^{15}\text{N}$  scalar coupling ensures that only the protonated sites [ $^{15}\text{N}(^1\text{H})$ ] are initially polarised.
- ii. **Variable mixing time,  $\tau_{\text{mix}}$ :** Incremented delay to follow the course of the hydrogen exchange reaction. When  $\tau_{\text{mix}} = 0$ , only  $^{15}\text{N}(^1\text{H})$  magnetisation is present; as  $\tau_{\text{mix}}$  increases, hydrogen exchange generates the deuterated [ $^{15}\text{N}(^2\text{H})$ ] species.
- iii. **Sign-coding filter:** Separation of  $^{15}\text{N}(^1\text{H})$  and  $^{15}\text{N}(^2\text{H})$  into sub-spectra by selective inversion using the  $^1\text{H}$ - $^{15}\text{N}$  scalar coupling.
- iv. **Chemical shift evolution of  $^{15}\text{N}$ :** The chemical shift of the  $^{15}\text{N}$  nucleus is encoded during a semi-constant-time evolution period whilst the in-phase  $N_y^\epsilon$  magnetisation is evolved into the anti-phase  $2C_2^\zeta N_x^\epsilon$  coherence. Simultaneous  $^1\text{H}$  and  $^2\text{H}$  composite pulse decoupling schemes are applied to suppress the undesired couplings.
- v.  **$\text{C}^\zeta$ - $\text{N}^\epsilon$  retro-INEPT:** an INEPT block incorporating selective  $^{13}\text{C}^\zeta$  and  $^{15}\text{N}^\epsilon$  pulses uses the  $^{13}\text{C}^\zeta$ - $^{15}\text{N}^\epsilon$  scalar coupling to convert the anti-phase  $2C_2^\zeta N_x^\epsilon$  coherence into in-phase  $C_y^\zeta$  magnetisation for detection.
- vi. **Detection:** Quadrature detection of the  $^{13}\text{C}^\zeta$  FID under simultaneous  $^1\text{H}$  and  $^{15}\text{N}$  decoupling.

Following the processing of the sign-coding filter described in Figure 3.15, Fourier transformation of the two frequency domains ( $t_1$  and  $t_2$ ) results in two *stacks* of two-dimensional  $^{13}\text{C}^\zeta$ - $^{15}\text{N}^\epsilon$  spectra. The first of these stacks contains cross-peaks corresponding to the protonated species,  $^{15}\text{N}(^1\text{H})$ , and reports on the decay of the intensity during  $\tau_{\text{mix}}$  due to a combination of hydrogen exchange and longitudinal relaxation. The second stack of spectra reports on the intensity of the deuterated species,  $^{15}\text{N}(^2\text{H})$ , initially increasing with  $\tau_{\text{mix}}$  due to the hydrogen exchange process before plateauing and beginning to decay with longitudinal relaxation (see Figure 3.4).

### 3. Side-Chain Hydrogen Exchange in Arginine

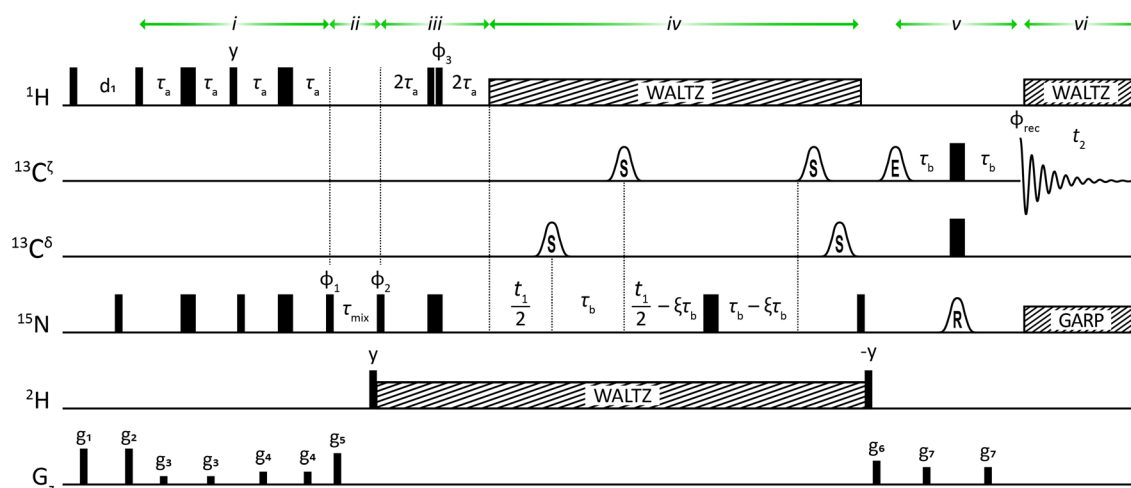


**Figure 3.16** The pseudo-4D ASHDEX pulse sequence for quantifying the  $^1\text{H}^\epsilon$  exchange rate in arginine side-chains. The phase cycle used is  $\phi_1$ :  $y$ ,  $-y$ ;  $\phi_2$ :  $2(x)$ ,  $2(-x)$ ;  $\phi_{\text{rec}}$ :  $x$ ,  $2(-x)$ ,  $x$ ;  $\phi_3$  is cycled ( $x$ ,  $-x$ ) to implement the sign-coding filter.

## 3.3 Results and Discussions

### 3.3.1 Application to Free Arginine

#### a. The Effect of Deuterium Concentration

The ASHDEX sequence developed in the previous section was first applied to samples of *free* [ $^{13}\text{C}_6$ ,  $^{15}\text{N}_4$ ]-L-arginine prepared in different amounts of  $^2\text{H}_2\text{O}$  to demonstrate the effect the concentration of deuterium has on the observed exchange rate (Figure 3.17). The course of the exchange reaction is clearly very sensitive to the relative amount of  $^1\text{H}_2\text{O}/^2\text{H}_2\text{O}$ , so it is useful to define the *total* exchange rate ( $k_{\text{ex}}$ ) as:

$$k_{\text{ex}} = k_{12} + k_{21} \quad (3.14)$$

Applying this to the data in Figure 3.17 reveals that whilst the *forward* and *reverse* exchange processes are highly dependent on the level of deuterium in the system, the *total* exchange rate remains constant:

Deuterium content (vol. %)	<i>forward</i> exchange rate ( $k_{12}$ )	<i>reverse</i> exchange rate ( $k_{21}$ )	<i>total</i> exchange rate ( $k_{\text{ex}}$ )
25	$0.97 \pm 0.01$	$2.83 \pm 0.06$	$3.80 \pm 0.06$
50	$1.98 \pm 0.05$	$1.80 \pm 0.08$	$3.78 \pm 0.09$
75	$3.00 \pm 0.06$	$0.96 \pm 0.04$	$3.96 \pm 0.07$

**Table 3.1**  $^1\text{H}^\epsilon$  hydrogen exchange rates measured for *free* [ $^{13}\text{C}_6$ ,  $^{15}\text{N}_4$ ]-L-arginine at different concentrations of deuterium at pH 5.6\*. The total exchange rate remains constant as a function of deuterium concentration. The units are  $\text{s}^{-1}$  and the errors are obtained from the least-squares fitting procedure.

Defining the total exchange rate like this removes the need to very carefully control the amount of  $^2\text{H}_2\text{O}$  in solution whilst also enabling the comparison of datasets recorded on samples in

### 3. Side-Chain Hydrogen Exchange in Arginine

different concentrations of deuterium. There are also practical difficulties in maintaining a constant pH between samples containing different levels of deuterium owing to the isotope effect on the glass electrode, as seen by the slight difference in  $k_{\text{ex}}$  at high levels of deuterium.

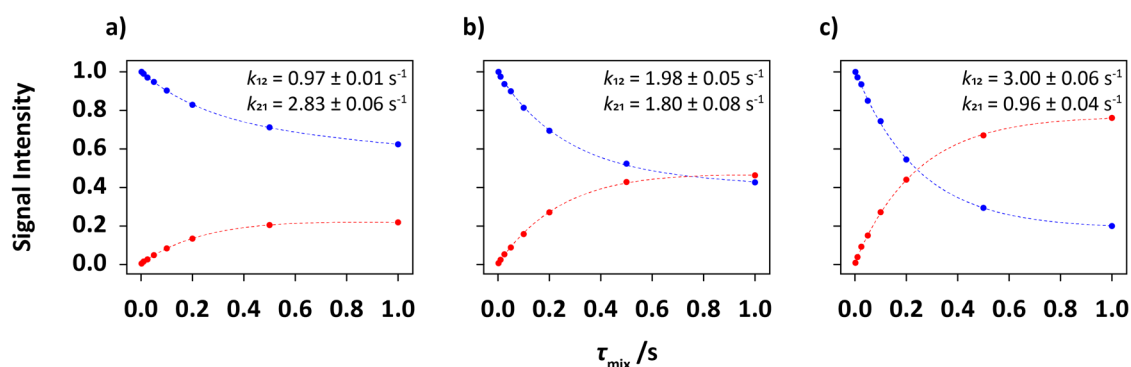


**Figure 3.17** Build-up/decay curves obtained for the  $^1\text{H}^\epsilon$  hydrogen exchange of *free* [ $^{13}\text{C}_6, ^{15}\text{N}_4$ ]-L-arginine in sodium phosphate buffer containing a) 25%, b) 50% and c) 75%  $^2\text{H}_2\text{O}$  at pH 5.6\*. The decay of  $^{15}\text{N}^\epsilon(^1\text{H})$  and build-up of  $^{15}\text{N}^\epsilon(^2\text{H})$  intensity is shown in blue and red, respectively. The dotted lines are the result of a least-squares fit to the equations discussed in Section 3.2.1.

#### b. The Effect of pH and Temperature

As well as the level of deuterium available, the rate of hydrogen exchange is also known to be highly sensitive to sample pH and temperature. For backbone hydrogen atoms, computational tools provide the intrinsic exchange rate expected at a given pH and temperature and thus permit the calculation of the protection factor for residue(s) involved. Unfortunately, this tool does not extend to the arginine side-chain and therefore the intrinsic, interaction-free exchange rate of  $^1\text{H}^\epsilon$  must be measured using a suitable model system.

To provide the required reference data at a range of different pH and temperatures, the ASHDEX experiment was applied to samples of [ $^{13}\text{C}_6, ^{15}\text{N}_4$ ]-L-arginine prepared between pH 4.5 and 7.0 and at temperatures ranging from 278 to 313 K. The total exchange rate ( $k_{\text{ex}}$ ) extracted from the resulting datasets is shown below in Table 3.2 and displayed graphically in Figure 3.18. The provided data therefore allows the quantitative assessment of interactions involving the arginine side-chain at a wide range of sample conditions.

Temp. /K	pH 4.53	pH 4.99	pH 5.54	pH 5.99	pH 6.50	pH 7.00
278.2	0.17 ± 0.02	0.50 ± 0.01	1.68 ± 0.02	4.58 ± 0.06	14.2 ± 0.3	46.9 ± 2.5
283.2	0.29 ± 0.01	0.87 ± 0.02	3.04 ± 0.03	8.25 ± 0.10	25.1 ± 0.8	
288.2	0.54 ± 0.01	1.53 ± 0.03	5.29 ± 0.05	14.5 ± 0.3	45.9 ± 3.3	
293.2	0.95 ± 0.02	2.64 ± 0.03	9.23 ± 0.15	25.5 ± 0.7		
298.2	1.64 ± 0.03	4.42 ± 0.08	15.5 ± 0.5			
303.2	2.78 ± 0.07	7.28 ± 0.30	25.0 ± 1.4			
308.2	4.58 ± 0.10	12.5 ± 0.6				
313.2	8.13 ± 0.36					

**Table 3.2**  $^1\text{H}^\epsilon$  hydrogen exchange rates ( $k_{\text{ex}}$ ) measured for *free* [ $^{13}\text{C}_6, ^{15}\text{N}_4$ ]-L-arginine at different pH and temperatures. The units are  $\text{s}^{-1}$  and the errors are obtained from the least-squares fitting procedure.

### 3. Side-Chain Hydrogen Exchange in Arginine

The pH dependence of  $\log(k_{\text{ex}})$  is linear with a slope of approximately 1.0, as would be expected for a base-catalysed reaction such as this (Figure 3.18a). The temperature dependence of the exchange rate is also linear between the temperatures studied (Figure 3.18b). As well as for conditions covered by these experiments, the two linear dependencies allow the calculation of the intrinsic exchange rate of  $^1\text{H}^\epsilon$  at sample conditions that would otherwise prevent a direct measurement. For example, the exchange rate of free arginine at physiological conditions (pH 7.4, 308 K) is calculated to be  $3100 \pm 100 \text{ s}^{-1}$ . Using these data as a reference, it ought to be possible to calculate protection factors for arginine residues within proteins at a wide range of sample conditions.

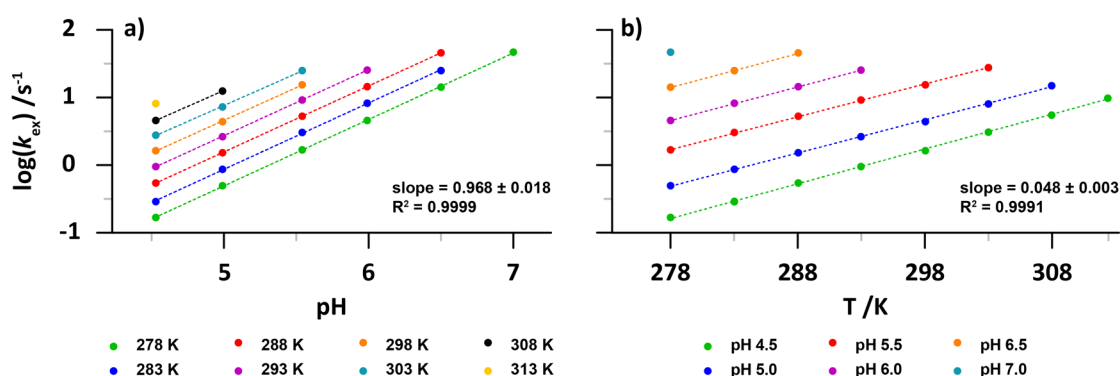


**Figure 3.18** Plots demonstrating the linear dependence of  $\log(k_{\text{ex}})$  on a) pH and b) temperature. Data was recorded on samples of free  $[^{13}\text{C}_6, ^{15}\text{N}_4]$ -L-arginine at 11.7 T. At high pH and/or temperature, the exchange rate becomes too fast to measure.

#### 3.3.2 Application to T4-Lysozyme

Armed with the high-quality reference spectra for the free amino acid discussed above, the experiment can now be applied to protein samples to investigate arginine-mediated interactions within the biomolecule. Selected spectra obtained using the ASHDEX experiment on the model protein T4 Lysozyme are shown in Figure 3.19. For clarity, the figure shows the  $^{13}\text{C}^\zeta\text{-}^{15}\text{N}^\epsilon$  planes recorded with  $\phi_3 = x$  prior to the processing of the sign-coding filter so that the protonated and deuterated species can be viewed together. As expected, the data recorded with a short mixing time ( $\tau_{\text{mix}} = 1.5 \text{ ms}$ , Figure 3.19a) shows a single peak for each arginine residue and resembles a standard  $^{13}\text{C}^\zeta\text{-}^{15}\text{N}^\epsilon$  HSQC spectrum. As the mixing time is gradually increased, the initially protonated residues become deuterated and an additional peak is observed. It is evident from the data that a range of exchange rates are present within the molecule as the deuterated cross peaks for each arginine residue becomes detectable at different mixing times (Figure 3.19b-c). The importance of the sign-coding filter discussed in Section 3.2.3b is exemplified by the spectrum shown in Figure 3.19c in which the deuterated signal of R154 coincides with the protonated signal of R148. This overlap would clearly prevent the quantitative assessment of both residues had the sign-coding filter not been implemented.

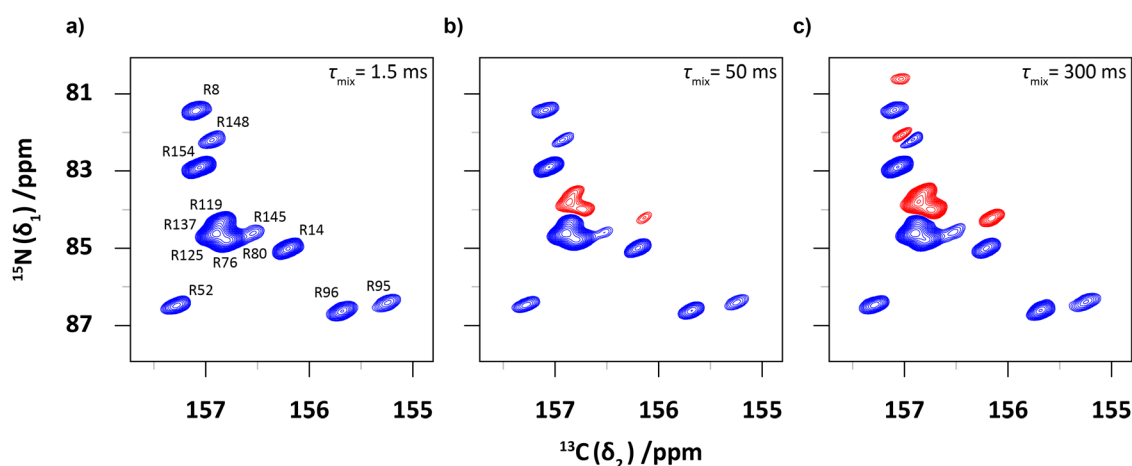


**Figure 3.19**  $^{13}\text{C}\text{-}^{15}\text{N}^{\epsilon}$  spectra of a sample of T4L at pH 5.5 and 298K recorded at 18.8 T using the ASHDEX sequence. The increasing duration of  $\tau_{\text{mix}}$  allows the build-up of the deuterated signals [ $^{15}\text{N}^{\epsilon}(^2\text{H})$ ]. Each of the spectra was recorded with  $\phi_3 = x$  causing the inversion of the [ $^{15}\text{N}^{\epsilon}(^1\text{H})$ ] signal (blue) with respect to the [ $^{15}\text{N}^{\epsilon}(^2\text{H})$ ] signal (red).

Integration of the data obtained above demonstrates the decay of the initial [ $^{15}\text{N}^{\epsilon}(^1\text{H})$ ] signal and subsequent build-up of the deuterated [ $^{15}\text{N}^{\epsilon}(^2\text{H})$ ] signal for each residue. The quality of the data is such that accurate exchange rate constants for both the forward (protium  $\rightarrow$  deuterium,  $k_{12}$ ) and reverse (deuterium  $\rightarrow$  protium,  $k_{21}$ ) processes can generally be obtained (Figure 3.20) by fitting the equations discussed in Section 3.2.1 to the experimental data. As discussed previously, the total exchange rate ( $k_{\text{ex}}$ ) can be defined as the sum of the forward and reverse processes, sidestepping the need to carefully control the amount of  $^2\text{H}_2\text{O}$  in the sample.

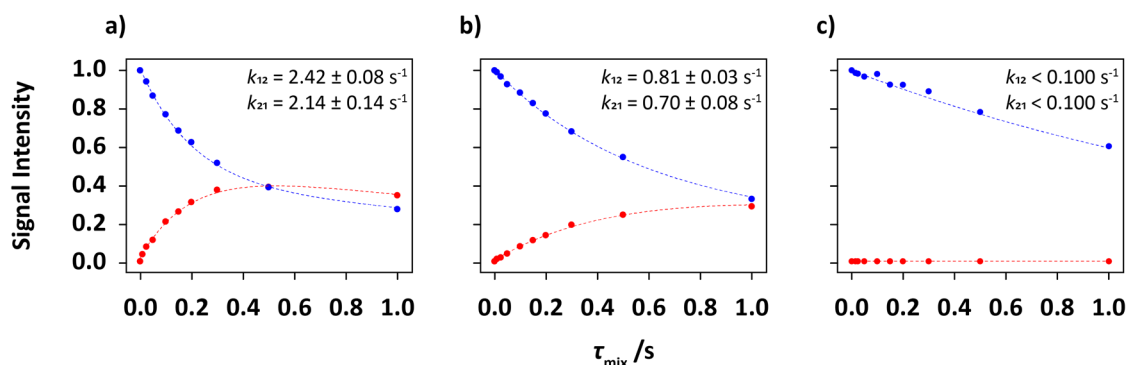


**Figure 3.20** Intensities of the [ $^{15}\text{N}^{\epsilon}(^1\text{H})$ ] (blue) and [ $^{15}\text{N}^{\epsilon}(^2\text{H})$ ] signals (red) as a function of  $\tau_{\text{mix}}$  for a) R14, b) R154 and c) R52 of T4L. The circles represent experimental measurements whilst the dotted line is the result of a least-squares fit of the equations discussed in Section 3.2.1 to the data shown.

The rate constants for 8 of the 13 arginine residues in T4L are obtainable from this dataset and are shown in Table 3.3. However, the remaining five residues appear to exchange too slowly for the deuterated signals to build-up to detectable levels. An example of one of these residues is R52, the intensity profile of which is shown in Figure 3.20c. There is no trace of the deuterated species even after a  $\tau_{\text{mix}}$  duration of 1.0 s and whilst the decay of the protonated species is

### 3. Side-Chain Hydrogen Exchange in Arginine

evident, this alone is insufficient to separate the hydrogen exchange rate from the longitudinal relaxation mechanism. One could logically infer from these data that the five arginine residues showing no hydrogen exchange are likely to be engaged in some form of intramolecular interaction however the relative strength of the five interactions cannot be assessed.

To further characterise these potentially interacting residues, the experiment is repeated at sample conditions which cause an increase in the intrinsic exchange rate of the hydrogen exchange reaction. Figure 3.21 shows the spectra recorded on T4L at pH 7.4 and 308 K where both an elevation of pH and temperature work to increase this intrinsic exchange rate. The  $^{13}\text{C}^{\zeta}\text{-}^{15}\text{N}^{\epsilon}$  plane recorded with  $\tau_{\text{mix}} = 1.5$  ms again resembles the standard HSQC spectrum however it now only contains a signal for each of the five slowly exchanging side-chains (Figure 3.21a). The  $^1\text{H}^{\epsilon}$  nuclei from the other 8 residues are now exchanging too fast to allow the transfer of magnetisation using the refocused-INEPT block that begins the pulse sequence. As before, the increasing duration of  $\tau_{\text{mix}}$  allows the build-up of the deuterated species as the hydrogen exchange reactions occur. This dataset allows the quantification of the hydrogen exchange rate of four of the five side-chains, as shown in Table 3.3.

The remaining residue R95 does not show any hydrogen exchange even at these sample conditions. For completeness, the exchange rate for this residue was determined using the traditional lyophilisation method described in Section 3.1.2. The protein was first lyophilised from 100%  $^1\text{H}_2\text{O}$  containing buffer at pH 5.5 before being re-dissolved in  $^2\text{H}_2\text{O}$ . The hydrogen exchange reaction was followed at 288 K using back-to-back  $^1\text{H}\text{-}^{15}\text{N}$  HSQC acquisitions where the signal intensity for R95 followed a simple exponential decay as the residue gradually became deuterated and undetectable (Figure 3.22).

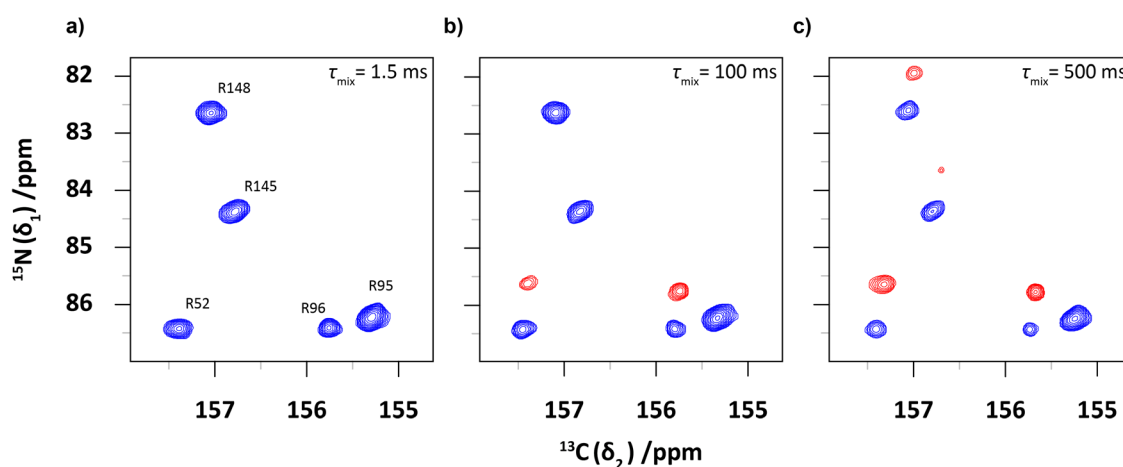


**Figure 3.21**  $^{13}\text{C}^{\zeta}\text{-}^{15}\text{N}^{\epsilon}$  spectra of a sample of T4L at pH 7.4 and 308K recorded at 18.8 T using the ASHDEX sequence. The increasing duration of  $\tau_{\text{mix}}$  allows the build-up of the deuterated signals [ $^{15}\text{N}^{\epsilon}(^2\text{H})$ ]. Each of the spectra was recorded with  $\phi_3 = x$  causing the inversion of the [ $^{15}\text{N}^{\epsilon}(^1\text{H})$ ] signal (blue) with respect to the [ $^{15}\text{N}^{\epsilon}(^2\text{H})$ ] signal (red).

Residue	$k_{\text{ex}} / \text{s}^{-1}$ pH 5.5, 298 K	$k_{\text{ex}} / \text{s}^{-1}$ pH 7.4, 308 K	PF
8	$2.58 \pm 0.20$	ND <sup>b</sup>	$6.0 \pm 0.5$
14	$4.56 \pm 0.20$	ND <sup>b</sup>	$3.4 \pm 0.2$
52	ND <sup>a</sup>	$8.98 \pm 1.8$	$343 \pm 58$
76 <sup>d</sup>	$4.00 \pm 0.10$	ND <sup>b</sup>	$3.9 \pm 0.1$
80 <sup>d</sup>	$4.00 \pm 0.10$	ND <sup>b</sup>	$3.9 \pm 0.1$
95	ND <sup>a</sup>	ND <sup>b</sup>	$1.71 \pm 0.08 \times 10^5$
96	ND <sup>a</sup>	$22.3 \pm 5.0$	$138 \pm 25$
119	$7.52 \pm 0.95$	ND <sup>b</sup>	$2.1 \pm 0.3$
125 <sup>e</sup>	$3.51 \pm 0.14$	ND <sup>b</sup>	$4.4 \pm 0.2$
137 <sup>e</sup>	$3.51 \pm 0.14$	ND <sup>b</sup>	$4.4 \pm 0.2$
145	ND <sup>a</sup>	$1.38 \pm 0.40$	$2200 \pm 470$
148	ND <sup>a</sup>	$2.64 \pm 0.40$	$1200 \pm 190$
154	$1.51 \pm 0.10$	ND <sup>b</sup>	$10.2 \pm 0.6$
<i>free arg.</i>	$15.5 \pm 0.5$	$3100 \pm 100^c$	

**Table 3.3**  $^1\text{H}^\epsilon$  hydrogen exchange rates ( $k_{\text{ex}}$ ) measured for T4L using the ASHDEX sequence. a) Exchange rate too slow to be determined. b) Exchange rate too fast to be determined. c) Extrapolated from the linear dependence in Figure 3.18. d/e) Average rate determined as signal overlap prevented residue-specific assignment. The values shown for R95 are determined from data shown in Figure 3.22.

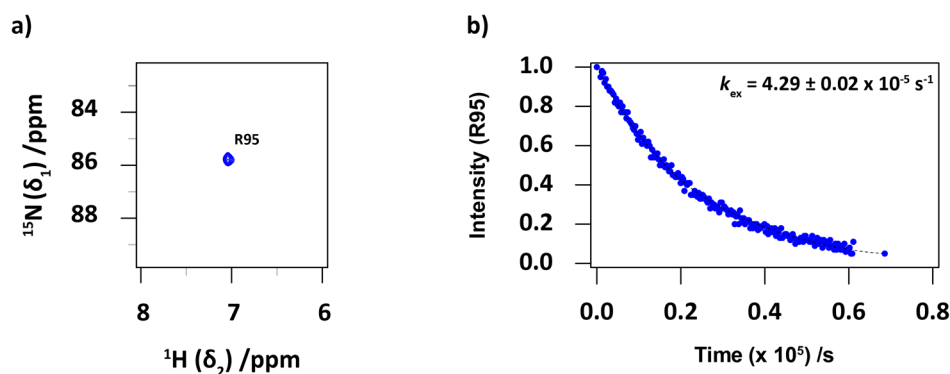


**Figure 3.22** a) Arginine side-chain region of a  $^1\text{H}$ - $^{15}\text{N}$  HSQC spectrum of T4L just after dissolution into 100%  $^2\text{H}_2\text{O}$  phosphate buffer recorded at 18.8 T at 288 K. The spectrum was acquired using an HSQC pulse sequence modified to be selective for arginine side-chains and clearly shows that R95 is exchanging much slower than the other 12 arginines in this protein. b) Plot of the intensity of R95 as a function of time, measured by repeated HSQC acquisitions over 16 hours. The intensity follows a single-exponential decay and a simple fitting procedure allows the rate constant ( $k_{\text{ex}}$ ) to be extracted.

The hydrogen exchange rates obtained for T4L using the ASHDEX experiment allow the calculation of the protection factors as described in Section 3.1.1. Five of the 13 residues display significantly elevated protection factors, a finding that is supported by inspection of the available crystal structure of the protein and is consistent with previous studies of the  $^{15}\text{N}^n$  rotational exchange using Divided-evolution<sup>[128]</sup> and Chemical Exchange Saturation Transfer (CEST).<sup>[189]</sup> Each of the five residues appears to be engaged in one or more intramolecular interactions specifically involving the  $^1\text{H}^\epsilon$  nuclei (Figure 3.23b-f) whereas the more rapidly exchanging residues are not (Figure 3.23a).

### 3. Side-Chain Hydrogen Exchange in Arginine

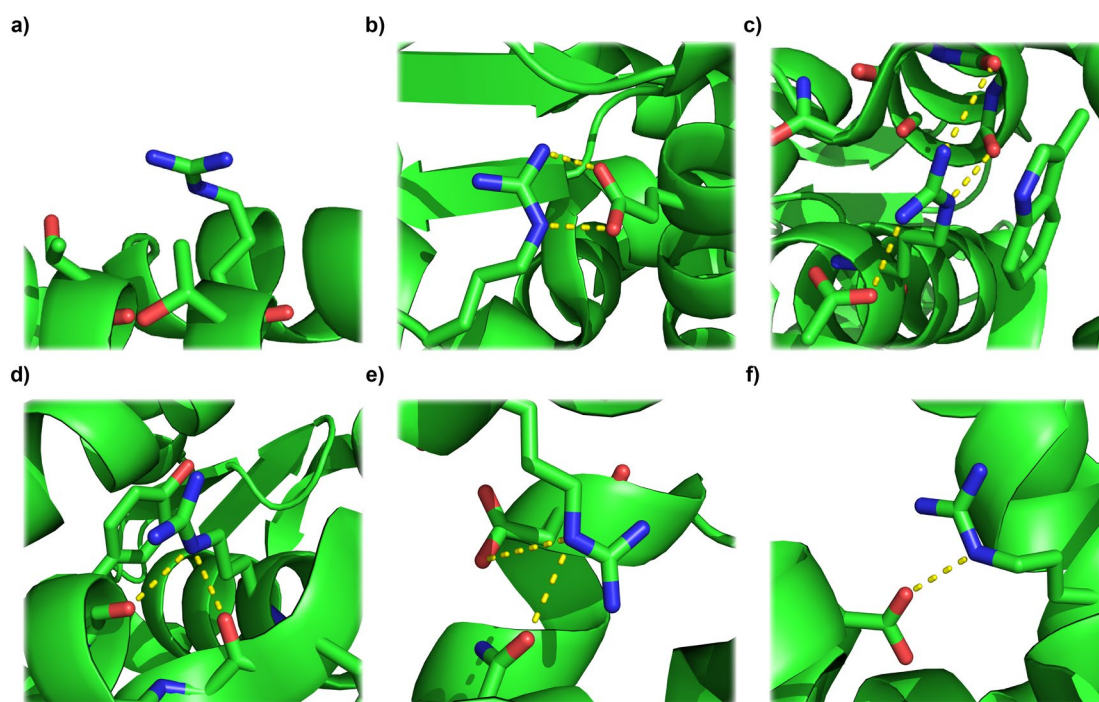


**Figure 3.23** Crystal structures (PDB: 102L)<sup>[190]</sup> of the local environments of a) R14, b) R52, c) R95, d) R96, e) R145 and f) R148. Potential hydrogen bond and/or salt-bridge interactions are shown using the dotted lines.

## 3.4 Conclusions

The ASHDEX experiment is a novel NMR approach to the quantification of arginine side-chain  $^1\text{H}^\epsilon$  exchange rates applicable to small to medium sized biomolecules that allows the study of intramolecular interactions such as hydrogen-bonds and salt-bridges. Several iterations of the experiment were explored including pseudo-three- and pseudo-four-dimensional zz-exchange strategies as well as the PEP methodology and het-CP transfers to increase the overall sensitivity. The final  $^{13}\text{C}$ -detected NMR experiment makes use of equilibrium  $^1\text{H}^\epsilon$  to selectively polarise the protonated  $^{15}\text{N}^\epsilon$  nuclei using a refocussed-INEPT block followed by a variable mixing period to follow the hydrogen exchange reactions. The resulting mix of  $^{15}\text{N}^\epsilon(^1\text{H})$  and  $^{15}\text{N}^\epsilon(^2\text{H})$  signals are resolved during a semi-constant time chemical shift evolution period using the one-bond deuterium isotope shift of the  $^{15}\text{N}^\epsilon$  nucleus before INEPT transfer to  $^{13}\text{C}^\zeta$  for detection. The protonated and deuterated resonances are separated into sub-spectra using a sign-coding filter that makes use of the  $^1J_{\text{HN}}$  scalar coupling between  $^1\text{H}^\epsilon$  and  $^{15}\text{N}^\epsilon$  to avoid additional spectral crowding. The experiment permits the measurement of the exchange rates between approximately  $0.2 \text{ s}^{-1}$  and  $50 \text{ s}^{-1}$  as demonstrated by the application to T4 Lysozyme and the free arginine amino acid. The dependence of the observed rate on the concentration of deuterium in solution as well as on pH and temperature is well characterised and therefore enables the calculation of protection factors for each arginine residue. The results presented above show that 12 of the 13 arginine residues of T4 Lysozyme are well characterised using the ASHDEX

### *3. Side-Chain Hydrogen Exchange in Arginine*

experiment and the results are consistent with previous studies and observations made on the X-ray structure of the crystallised protein. The remaining residue, R95, undergoes exceptionally slow exchange as a result of several intramolecular interactions and was therefore characterised using appropriate existing techniques. It should be stressed that arginine residues that engage in salt-bridges and medium-strong hydrogen bonds are well captured under physiological conditions (pH 7.4, 308 K) using the ASHDEX experiment. Moreover, the exchange rates are very sensitive to pH and temperature fluctuations and thus a wide range of arginine side-chains can be studied using only small changes in sample conditions. Hydrogen exchange rates have long been known to be a critical aspect of the overall dynamic behaviour of a biomolecule in solution and although traditionally confined to backbone atoms, it is envisaged that the presented ASHDEX experiment will be a useful tool to extend this focus to side-chain atoms.

### *3. Side-Chain Hydrogen Exchange in Arginine*

# 4

## Deuterium Isotope Shifts: Detection of Salt-Bridges

### 4.1 Introduction

A rigorous analysis of the exchange rate of the  $^1\text{H}^\epsilon$  proton in each arginine residue in a protein provides a quantitative insight into the many interactions formed by arginine within a biomolecule. The information is clearly very valuable to the spectroscopist but the process from which the molecular insights are extracted is fairly involved. A simpler, albeit more qualitative approach is found by measuring the small chemical shift differences induced by partially deuterating the guanidinium groups. The key to the methodology described in the previous chapter lies with the substitution of proton with a deuteron, a process that requires little other than the presence of deuterium in the sample buffer. It was noted that the one-bond deuterium isotope shift associated with the  $^{15}\text{N}$  nucleus was sufficiently large to allow the separation of the  $^{15}\text{N}(^1\text{H})$  and  $^{15}\text{N}(^2\text{H})$  species based on their chemical shift. However, the presence of one or more deuterium nuclei on the arginine side-chain induces a chemical shift difference on each atom of the guanidinium group, not just  $^{15}\text{N}^\epsilon$ . Furthermore, the magnitude of these chemical shift differences appears to vary within the same sample and has been used to infer the presence of intramolecular interactions involving lysine side-chains in proteins<sup>[191,192]</sup> as well as in numerous small molecules.<sup>[193–196]</sup> The rationale behind these observations is that the magnitude of the chemical shift difference observed upon substitution of a proton with a deuteron depends on the bond length involved.<sup>[197–199]</sup> For example, as the length of an N-H bond can vary depending on the degree of hydrogen bonding it is involved in, it could be surmised that the  $^{15}\text{N}$  chemical shift difference between the  $^{15}\text{N}-^1\text{H}$  and  $^{15}\text{N}-^2\text{H}$  species may report on the nature of the hydrogen bond.<sup>[200]</sup> Indeed, this phenomenon has been extensively studied in the protein ubiquitin.<sup>[201]</sup>

This chapter describes the extension of this methodology to the arginine side-chain as demonstrated by application to both T4 Lysozyme and Barnase proteins. The chemical shift differences induced upon the guanidinium group nuclei by deuterium, herein referred to as *Deuterium Isotope Shifts*, are easy to measure using the  $^{13}\text{C}$ -detected experiments described in the previous chapters. The use of  $^{13}\text{C}$  for detection is particularly critical for isotope shifts

#### 4. Deuterium Isotope Shifts: Detection of Salt-Bridges

involving the  $^{15}\text{N}^\epsilon$  nucleus as when the single  $^1\text{H}^\epsilon$  proton is replaced with deuterium, the  $^1\text{H}$ - $^{15}\text{N}$  coupling is lost and the resonance becomes invisible to conventional  $^1\text{H}$ - $^{15}\text{N}$  based techniques. Deuterium isotope shifts are firstly measured using synthetically derivatised arginine compounds to provide reference figures that are subsequently compared to data recorded in isotopically labelled protein samples to infer the presence of intramolecular interactions.

## 4.2 Theory and Method Development

### 4.2.1 Deuterium Isotope Shifts in the Guanidinium Group of Arginine

The high  $\text{pK}_a$  of arginine's guanidinium group renders the side-chain positively charged in all physiologically encountered conditions. This results in the guanidinium group bearing a total of five protons ( $4 \times \text{H}^\eta$ ,  $1 \times \text{H}^\epsilon$ ), each of which is available for substitution with deuterium. Subsequently, there are many substitution configurations available to each arginine residue. It is therefore prudent to define a suitable notation for when one needs to refer to an individual isotope shift.<sup>[163]</sup>

Each isotope shift can be described as:

$${}^n\Delta X(Y) \quad (4.1)$$

where  $X$  is the nucleus on which the chemical shift difference is measured,  $Y$  is the nucleus experiencing the isotope substitution and  $n$  is the number of bonds through which the chemical shift difference is detected. For example:

${}^2\Delta^{13}\text{C}^\zeta(\text{H}^\eta)$  describes the two-bond isotope shift measured on  $^{13}\text{C}^\zeta$ , caused by the substitution of a  $^1\text{H}^\eta$  proton with deuterium

${}^1\Delta^{15}\text{N}^\epsilon(\text{H}^\epsilon)$  describes the one-bond isotope shift measured on  $^{15}\text{N}^\epsilon$ , caused by the substitution of the  $^1\text{H}^\epsilon$  proton with deuterium

The isotope shift is usually calculated by subtracting the chemical shift measured for the heavier isotope from the chemical shift measured for the lighter isotope. Using the examples above:

$${}^2\Delta^{13}\text{C}^\zeta(\text{H}^\eta) = \delta_{\text{C}}[{}^{13}\text{C}^\zeta(^1\text{H}^\eta)] - \delta_{\text{C}}[{}^{13}\text{C}^\zeta(^2\text{H}^\eta)]$$

$${}^1\Delta^{15}\text{N}^\epsilon(\text{H}^\epsilon) = \delta_{\text{N}}[{}^{15}\text{N}^\epsilon(^1\text{H}^\epsilon)] - \delta_{\text{N}}[{}^{15}\text{N}^\epsilon(^2\text{H}^\epsilon)]$$

Table 4.1 below details the deuterium isotope shifts potentially available for the guanidinium group of arginine side-chains as well as the expected magnitude of each. As discussed in Chapter 3, the one-bond isotope shifts are large and easily resolved in two-dimensional NMR spectra. However, the longer range two- and three-bond isotope shifts are much smaller and thus are anticipated to be harder to measure. In the case of an isotope shift induced by the

#### 4. Deuterium Isotope Shifts: Detection of Salt-Bridges

substitution of a  $^1\text{H}^n$  proton, the effect is expected to be linearly additive for each substitution. As for the assignment of the individual resonances to each subsequent addition of deuterium, the magnitude and direction of the chemical shift change is assessed and compared to a spectrum recorded in 100%  $^1\text{H}_2\text{O}$ .

	Typical value /ppm
$^1\Delta^{15}\text{N}^\epsilon(\text{H}^\epsilon), ^1\Delta^{15}\text{N}^n(\text{H}^n)$	0.60 – 0.70
$^2\Delta^{13}\text{C}^\zeta(\text{H}^\epsilon), ^2\Delta^{13}\text{C}^\zeta(\text{H}^n)$	0.05 – 0.10
$^3\Delta^{15}\text{N}^n(\text{H}^\epsilon), ^3\Delta^{15}\text{N}^\epsilon(\text{H}^n)$	unknown (< 0.10)

**Table 4.1** The one-, two- and three-bond deuterium isotope shifts expected to be encountered in the arginine guanidinium group.

#### 4.2.2 Quantification by NMR Spectroscopy

The  $^{13}\text{C}^\zeta$ -detected experiments described in Chapter 2 allow the easy measurement of the deuterium isotope shifts described above. There are only two simple preparation steps required:

1. The sample must be prepared in a solution containing a suitable amount of deuterium to visualise the isotope shifted signals. This is most easily achieved by preparing an aqueous buffer using a mixture of  $^1\text{H}_2\text{O}$  and  $^2\text{H}_2\text{O}$ . Any amount of deuterium can be used, at the expense of sensitivity. To enable the detection of as many isotopomers as possible, most of the data reported in this chapter were recorded on samples prepared in 50:50 mixtures of  $^1\text{H}_2\text{O}$  and  $^2\text{H}_2\text{O}$ .
2. The pulse sequences must be modified to include  $^2\text{H}$  decoupling during the indirect chemical shift evolution period(s). This is described in more detail in Section 3.2.

Figure 4.1 shows typical spectra recorded using these pulse sequences on a sample of the free amino acid in 50:50  $^1\text{H}_2\text{O}$ : $^2\text{H}_2\text{O}$ . The simplest isotope shift to measure is associated with the deuteration of the  $\text{H}^\epsilon$  proton. As there is only one  $\text{H}^\epsilon$  proton in arginine, there are only two possible states:  $\text{N}^\epsilon\text{-}^1\text{H}$  and  $\text{N}^\epsilon\text{-}^2\text{H}$ . The one-bond  $^1\Delta^{15}\text{N}^\epsilon(\text{H}^\epsilon)$  shift, and the corresponding two-bond  $^2\Delta^{13}\text{C}^\zeta(\text{H}^\epsilon)$ , are easily identified and measured from the  $^{13}\text{C}^\zeta\text{-}^{15}\text{N}^\epsilon$  HSQC spectrum (Figure 4.1a). However, the situation quickly becomes more complex when considering the deuteration of the  $\text{H}^n$  protons. Arginine, in its ubiquitous protonated form, contains four  $\text{H}^n$  protons and thus up to five deuterated species are expected from the incorporation of 0, 1, 2, 3, or 4  $^2\text{H}^n$  nuclei. Coupled with the  $\text{H}^\epsilon$  atom, there are therefore up to 32 ( $2^5$ ) possible species present for each arginine residue. Whilst the rapid rotation of the two  $\text{C}^\zeta\text{-N}^n$  bonds provides some degeneracy and reduces the number of unique species to 18, the same simplification does not stem from the slower rotational exchange of the  $\text{N}^\epsilon\text{-C}^\zeta$  bond. The distribution of deuterium amongst the  $\text{H}^n$  nuclei is evident in asymmetric lineshapes of the two detected HSQC cross-peaks,  $^{13}\text{C}^\zeta\text{-}^{15}\text{N}^\epsilon(1\text{H}^\epsilon)$  and

#### 4. Deuterium Isotope Shifts: Detection of Salt-Bridges

$^{13}\text{C}^{\zeta}\text{-}^{15}\text{N}^{\epsilon}(\text{H}^{\epsilon})$ , resulting from the two-bond  ${}^2\Delta^{13}\text{C}^{\zeta}(\text{H}^{\epsilon})$  and three-bond  ${}^3\Delta^{15}\text{N}^{\epsilon}(\text{H}^{\epsilon})$  isotope shifts. These isotope shifts are much smaller than the one-bond  ${}^1\Delta^{15}\text{N}^{\epsilon}(\text{H}^{\epsilon})$  shift and are often not resolved under ambient conditions using this NMR experiment. The addition of deuterium to the system further obscures the limited information available from the  $^{13}\text{C}^{\zeta}\text{-}^{15}\text{N}^{\eta}$  HSQC spectrum (Figure 4.1b). Even the  ${}^1\Delta^{15}\text{N}^{\eta}(\text{H}^{\eta})$  shift, expected to be of a similar magnitude to the  ${}^1\Delta^{15}\text{N}^{\epsilon}(\text{H}^{\epsilon})$  shift is not measurable for *free* arginine using this experiment.

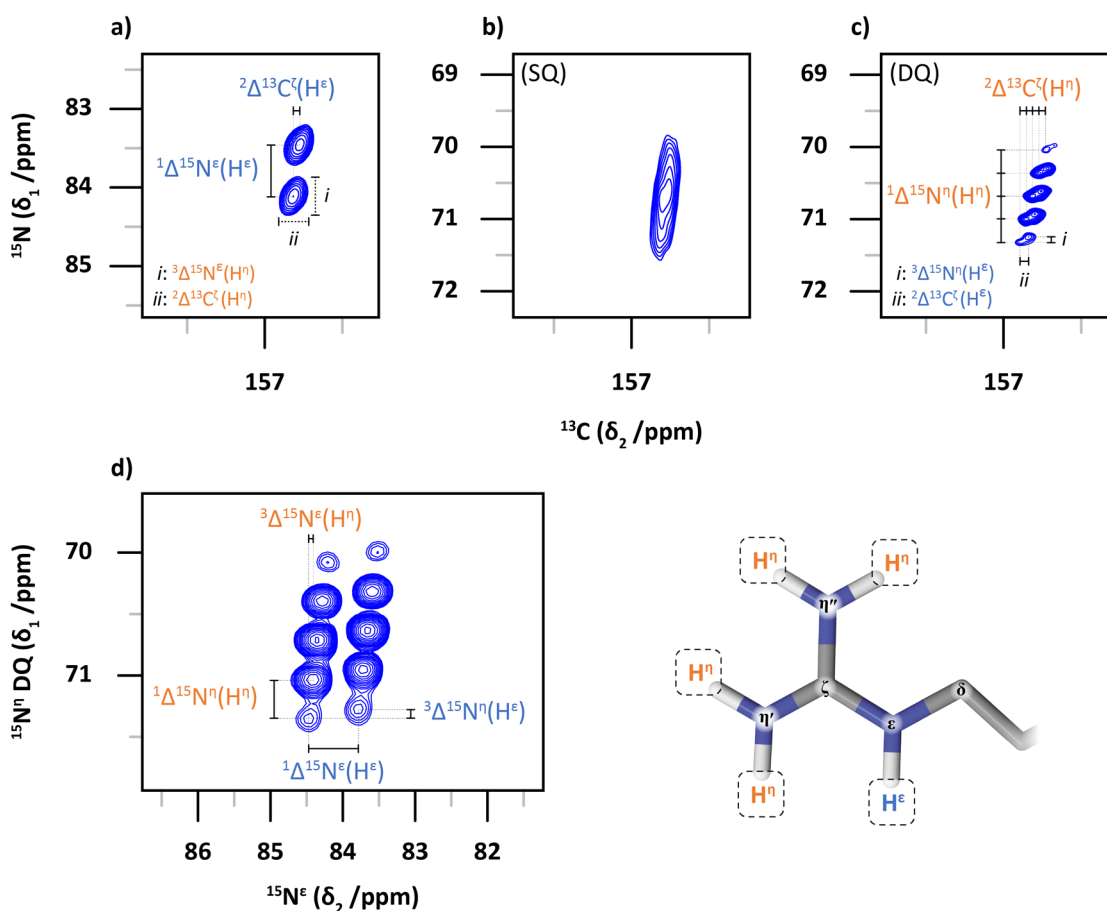


**Figure 4.1** Visualisation of the various deuterium isotope shifts using  $^{13}\text{C}^{\zeta}$ -detection: a)  $^{13}\text{C}^{\zeta}\text{-}^{15}\text{N}^{\epsilon}$  HSQC spectrum showing the large one-bond isotope shift of  $^{15}\text{N}^{\epsilon}$ . The asymmetric peak shape is a result of the two- and three-bond isotope shifts caused by the deuteration of the  $\text{H}^{\eta}$  nuclei. b) The  $^{13}\text{C}^{\zeta}\text{-}^{15}\text{N}^{\eta}$  HSQC spectrum provides limited information owing to the restricted rotation of the  $\text{N}^{\epsilon}\text{-C}^{\zeta}$  bond, as discussed in Chapter 2. c)  $^{13}\text{C}^{\zeta}\text{-}^{15}\text{N}^{\eta}$  HDQC spectrum showing the sequential one-bond isotope shifts of  $^{15}\text{N}^{\eta}$ . The fine structure of each peak reveals the two- and three-bond isotope shifts associated with the deuteration of  $\text{H}^{\epsilon}$ . d) The  $^{15}\text{N}^{\eta}\text{-}^{15}\text{N}^{\epsilon}$  projection of the three-dimensional  $^{13}\text{C}^{\zeta}\text{-}^{15}\text{N}^{\epsilon}\text{-}^{15}\text{N}^{\eta}$  experiment depicted in Figure 2.7 provides a clearer picture of each isotope-shifted peak. Each of the signals also has a unique  $^{13}\text{C}^{\zeta}$  chemical shift (not shown). All spectra were recorded on a sample of *free* [ $^{13}\text{C}_6, ^{15}\text{N}_4$ ]-L-arginine prepared in 50:50  ${}^1\text{H}_2\text{O}:$  ${}^2\text{H}_2\text{O}$ .

The  $^{13}\text{C}^{\zeta}\text{-}^{15}\text{N}^{\eta}$  HDQC spectrum developed in Chapter 2, removes the line-broadening effect of the  $\text{N}^{\epsilon}\text{-C}^{\zeta}$  rotational exchange and reveals the multiple peaks caused by the one-bond  ${}^1\Delta^{15}\text{N}^{\eta}(\text{H}^{\eta})$  and two-bond  ${}^2\Delta^{13}\text{C}^{\zeta}(\text{H}^{\eta})$  isotope shifts (Figure 4.1c). Additionally, the double-quantum methodology introduces another source of isotope shift degeneracy and reduces the number of unique chemical shifts to ten. It is important to note that owing to the double-quantum  $^{15}\text{N}^{\eta}$  chemical

#### 4. Deuterium Isotope Shifts: Detection of Salt-Bridges

shift in the HDQC reflecting the average of the two contributing  $^{15}\text{N}^n$  shifts, the distance between the detected cross-peaks ( $\Delta\delta$ ) is equal to half of the *true* isotope shift.

For example, for the first isotope shift (substitution of one  $\text{H}^n$  atom):

$$\begin{aligned}\Delta\delta &= \frac{1}{2} [\delta_{\text{N}^{15}\text{N}^n(^1\text{H}_2)} + \delta_{\text{N}^{15}\text{N}^n(^1\text{H}_2)}] - \frac{1}{2} [\delta_{\text{N}^{15}\text{N}^n(^1\text{H}_2)} + \delta_{\text{N}^{15}\text{N}^n(^1\text{H}^2\text{H})}] \\ &= \frac{1}{2} [\delta_{\text{N}^{15}\text{N}^n(^1\text{H}_2)} - \delta_{\text{N}^{15}\text{N}^n(^1\text{H}^2\text{H})}] \\ &= \frac{1}{2} [^1\Delta^{15}\text{N}^n(\text{H}^n)]\end{aligned}$$

Each of the five isotope-shifted cross-peaks detected in the  $^{13}\text{C}^{\zeta}\text{-}^{15}\text{N}^n$  HDQC spectrum is further split by the two-bond  $^2\Delta^{13}\text{C}^{\zeta}(\text{H}^{\epsilon})$  and three-bond  $^3\Delta^{15}\text{N}^n(\text{H}^{\epsilon})$  isotope shifts associated with the deuteration of the  $\text{H}^{\epsilon}$  proton. The smaller magnitude of these longer-range isotope shifts results in their only partial resolution and thus makes an accurate measurement more difficult. This limitation can be overcome using the three-dimensional  $^{13}\text{C}^{\zeta}\text{-}^{15}\text{N}^{\epsilon}\text{-}^{15}\text{N}^n$  experiment described in Figure 2.7 to exploit the large one-bond  $^1\Delta^{15}\text{N}^{\epsilon}(\text{H}^{\epsilon})$  and  $^1\Delta^{15}\text{N}^n(\text{H}^n)$  isotope shifts to adequately resolve each of the ten cross-peaks (Figure 4.1d). From the  $^{15}\text{N}^n\text{-}^{15}\text{N}^{\epsilon}$  projection of the three-dimensional dataset, all the individual isotope shifts can be visualised and quantified. Although the data is easier to view as the presented projection, each cross-peak is picked in three-dimensions to permit the calculation of the  $^2\Delta^{13}\text{C}^{\zeta}(\text{H}^{\epsilon})$  and  $^2\Delta^{13}\text{C}^{\zeta}(\text{H}^n)$  isotope shifts. The only isotope shift that cannot be directly quantified using these experiments is the three-bond  $^3\Delta^{15}\text{N}^n(\text{N}^n\text{-H}^n)$  shift experienced by one  $^{15}\text{N}^n$  upon the deuteration of the other  $^{15}\text{N}^n$  nucleus. The magnitude of this unobtainable isotope shift is expected to be quite similar to the  $^3\Delta^{15}\text{N}^{\epsilon}(\text{H}^n)$  isotope shift.

The relative intensity of the isotope-shifted peaks is dependent on the degree of deuteration of the solvent system: the higher the percentage of  $^2\text{H}_2\text{O}$  present in the buffer, the greater the population of the deuterated species and vice versa. Whilst this is simple to understand in the case of the  $\text{N}^{\epsilon}$  nucleus where there are only two possible states, the situation for the  $\text{N}^n$  nuclei is more complex. There are five possible states of deuteration for the double-quantum magnetisation and the observed intensity of each follows a binomial distribution. The relative amount of each of the individual deuterated species can be calculated as:

$$\text{Intensity} = \binom{n}{k} p^k (1-p)^{n-k} \quad (4.2)$$

where  $k$  is the total number of substituted  $^2\text{H}$  nuclei,  $n$  is the maximum possible number of substitutions (4),  $p$  is the fraction of  $^2\text{H}_2\text{O}$  in the system (0 - 1) and:

$$\binom{n}{k} = \frac{n!}{k!(n-k)!}$$

#### 4. Deuterium Isotope Shifts: Detection of Salt-Bridges

Table 4.2 shows the relative intensity ratios expected for spectra recorded in different amounts of  $^2\text{H}_2\text{O}$  as calculated using the formula above. Figure 4.2 shows the simulated ‘multiplet’ structure expected at each concentration of deuterium using the calculated populations of each species. The distribution expected for a sample prepared in 50%  $^2\text{H}_2\text{O}$  closely resembles the experimental data presented in Figure 4.1c. It is important to note that the  $^{13}\text{C}^\zeta$  nucleus of each of the deuterated species will exhibit a larger  $T_1$  relaxation rate constant as the level of deuterium increases. This means that aside from experiments that are performed with a very long recycle delay, the observed intensity ratio will not quite match the theoretical distribution discussed above due to a partial saturation of the highly deuterated species. This phenomenon is responsible for the lower intensity of the per-deuterated  $-\text{N}^{\text{n}}_2(^2\text{H}_4)$  signals ( $^{15}\text{N} = 70$  ppm) when compared to the per-protonated  $-\text{N}^{\text{n}}_2(^1\text{H}_4)$  ( $^{15}\text{N} = 71.5$  ppm) in Figure 4.1c.

$[^2\text{H}_2\text{O}]$ (p)	$-\text{N}^{\text{n}}_2(^1\text{H}_4)$ (k = 0)	$-\text{N}^{\text{n}}_2(^1\text{H}_3^2\text{H})$ (k = 1)	$-\text{N}^{\text{n}}_2(^1\text{H}_2^2\text{H}_2)$ (k = 2)	$-\text{N}^{\text{n}}_2(^1\text{H}^2\text{H}_3)$ (k = 3)	$-\text{N}^{\text{n}}_2(^2\text{H}_4)$ (k = 4)
0.1	0.66	0.29	0.05		
0.2	0.41	0.41	0.15	0.03	
0.3	0.24	0.41	0.26	0.08	0.01
0.4	0.13	0.35	0.35	0.15	0.03
0.5	0.06	0.25	0.38	0.25	0.06

**Table 4.2** Relative intensities of the five isotope-shifted signals expected for the  $^{15}\text{N}^{\text{n}}$  double-quantum coherences of arginine residues as calculated using Equation 4.2 as a function of deuterium concentration.

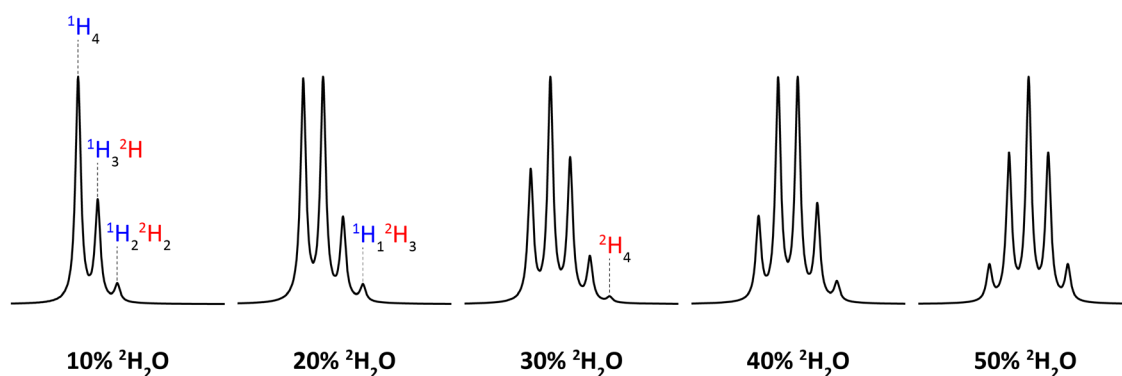


**Figure 4.2** Expected ‘multiplet’ structure of  $^{15}\text{N}^{\text{n}}$  double-quantum signals at different levels of  $^2\text{H}_2\text{O}$  simulated using the data from Table 4.2. Each isotope-shifted peak is separated by a uniform distance of 50 Hz and the spectrum is normalised to the largest peak in each case for clarity.

#### Application of the Sign-coding Filter

As noted for the ASHDEX experiment developed in Chapter 3 to measure  $^1\text{H}^\epsilon$  solvent exchange rates, the presence of the additional deuterated resonances for each arginine residue can cause problems with signal overlap in the study of even modestly sized proteins. In the case of the  $^{13}\text{C}^\zeta$ - $^{15}\text{N}^\epsilon$  experiment, this can be mitigated by implementing a sign-coding filter to separate the protonated [ $^{15}\text{N}^\epsilon(^1\text{H})$ ] and deuterated [ $^{15}\text{N}^\epsilon(^2\text{H})$ ] signals into different sub-spectra. The

#### 4. Deuterium Isotope Shifts: Detection of Salt-Bridges

pseudo-three-dimensional experiment incorporating the sign-coding filter is shown below in Figure 4.3a. The filter makes use of the  $^1J_{\text{HN}}$  coupling pathway that is active only for the protonated species to selectively invert the  $^{13}\text{C}^{\zeta}\text{-}^{15}\text{N}^{\epsilon}(\text{H})$  cross-peaks with respect to the  $^{13}\text{C}^{\zeta}\text{-}^{15}\text{N}^{\epsilon}(\text{H})$  signals. After processing of the two required datasets ( $\phi_3 = x, -x$ ), the protonated and deuterated cross-peaks appear in different spectra and thus no additional spectral crowding is encountered (Figure 4.3b). The sign-coding filter as applied to the ASHDEX experiment is described in more detail in Section 3.2.4b.

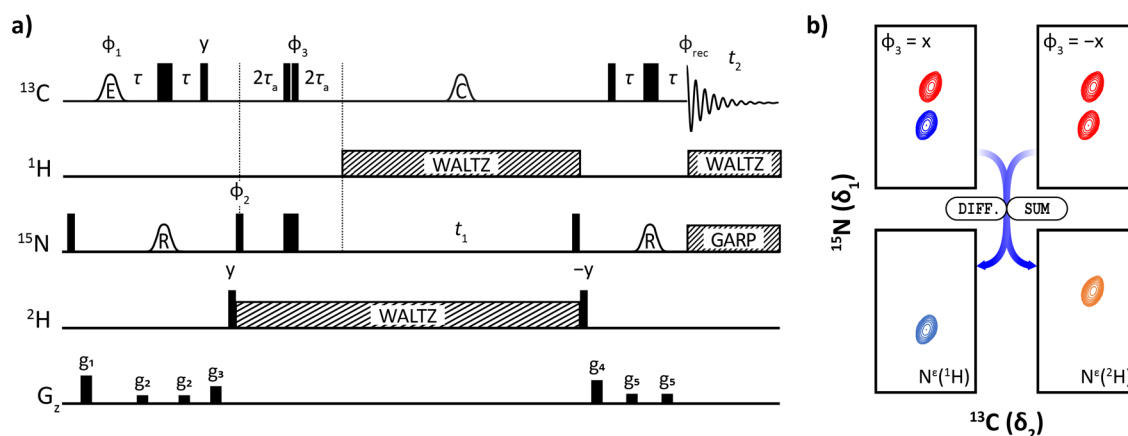


**Figure 4.3** a) The standard  $^{13}\text{C}^{\zeta}\text{-}^{15}\text{N}^{\epsilon}$  HSQC sequence can be augmented with the sign-coding filter described in Section 3.2.4b to separate the protonated and deuterated resonances into sub-spectra and avoid signal overlap. b) Two datasets are recorded ( $\phi_3 = x, -x$ ) and linearly combined to affect the separation. This process alleviates the spectral crowding caused by the additional deuterated peaks in the spectrum.

The application of the sign-coding filter to the  $^{13}\text{C}^{\zeta}\text{-}^{15}\text{N}^{\eta}$  HDQC experiment for the analysis of  $^{15}\text{N}^{\eta}$  isotope shifts is complicated by the increased number of  $^1\text{H}^{\eta}$  nuclei and their associated coupling pathways. It is impossible to selectively evolve a single  $^1\text{H}\text{-}^{15}\text{N}$  coupling whilst refocussing the others as to do so would require very selective  $^1\text{H}^{\eta}$  pulses as well as *a priori* knowledge of the precise  $^1\text{H}^{\eta}$  chemical shifts. However, it can still be implemented effectively to partially mitigate signal overlap. In the sign-coding supplemented HDQC experiment, the magnetisation is proportional to  $4C_2^{\zeta}N_2^{\eta 1}N_2^{\eta 2}$  regardless of the protonation/deuteration of the two  $^{15}\text{N}^{\eta}$  nuclei after the first INEPT transfer. As described in Chapter 2, the phase cycle of the following  $90^\circ$   $^{15}\text{N}$  pulse generates pure double-quantum magnetisation  $DQ_x$  prior to sign-coding filter. As for the  $^{15}\text{N}^{\epsilon}$  experiment, the per-deuterated species  $\text{-N}^{\eta 2}(\text{H}_4)$  is unaffected by the sign-coding filter due to the absence of an active  $^1J_{\text{HN}}$  scalar coupling. The remaining species all evolve under the scalar coupling Hamiltonian during the sign-coding filter ( $\tau$ ) depending on the number of attached  $^1\text{H}^{\eta}$  protons:

One  $^1\text{H}^{\eta}$  proton, three  $^2\text{H}^{\eta}$  deuterons:

$$DQ_x(^1\text{H}^2\text{H}_3) \xrightarrow{2\pi J_{\text{HN}}\tau H_z^1} DQ_x(^1\text{H}^2\text{H}_3) \cos(\pi J_{\text{HN}}\tau) - 2DQ_y H_z^1(^1\text{H}^2\text{H}_3) \sin(\pi J_{\text{HN}}\tau)$$

#### 4. Deuterium Isotope Shifts: Detection of Salt-Bridges

Additional  $^1\text{H}^n$  couplings simply further modulate the magnetisation as follows. For simplicity, let  $\pi J_{\text{HN}}\tau = \theta$ .

Two  $^1\text{H}^n$  protons, two  $^2\text{H}^n$  deuterons:

$$DQ_x(^1\text{H}_2^2\text{H}_2) \xrightarrow{2\pi J_{\text{HN}}\tau H_z^2 H_z^2} DQ_x(^1\text{H}_2^2\text{H}_2) \cos^2(\theta) - 2DQ_y H_z^2(^1\text{H}_2^2\text{H}_2) \cos(\theta)\sin(\theta) \\ - 2DQ_y H_z^1(^1\text{H}_2^2\text{H}_2) \sin(\theta)\cos(\theta) - 4DQ_x H_z^1 H_z^2(^1\text{H}_2^2\text{H}_2) \sin^2(\theta)$$

Three  $^1\text{H}^n$  protons, one  $^2\text{H}^n$  deuteron:

$$DQ_x(^1\text{H}_3^2\text{H}) \xrightarrow{2\pi J_{\text{HN}}\tau H_z^2 H_z^2 H_z^2} DQ_x(^1\text{H}_3^2\text{H}) \cos^3(\theta) - 2DQ_y H_z^2(^1\text{H}_3^2\text{H}) \cos^2(\theta)\sin(\theta) \\ - 2DQ_y H_z^1(^1\text{H}_3^2\text{H}) \sin(\theta)\cos^2(\theta) - 4DQ_x H_z^1 H_z^2(^1\text{H}_3^2\text{H}) \sin^2(\theta)\cos(\theta) \\ - 2DQ_y H_z^3(^1\text{H}_3^2\text{H}) \cos^2(\theta)\sin(\theta) - 4DQ_x H_z^2 H_z^3(^1\text{H}_3^2\text{H}) \cos(\theta)\sin^2(\theta) \\ - 4DQ_x H_z^1 H_z^3(^1\text{H}_3^2\text{H}) \sin^2(\theta)\cos(\theta) + 8DQ_y H_z^1 H_z^2 H_z^3(^1\text{H}_3^2\text{H}) \sin^3(\theta)$$

Four  $^1\text{H}^n$  protons:

$$DQ_x(^1\text{H}_4) \xrightarrow{2\pi J_{\text{HN}}\tau H_z^2 H_z^2 H_z^2 H_z^2} DQ_x(^1\text{H}_4) \cos^4(\theta) - 2DQ_y H_z^2(^1\text{H}_4) \cos^3(\theta)\sin(\theta) \\ - 2DQ_y H_z^1(^1\text{H}_4) \sin(\theta)\cos^3(\theta) - 4DQ_x H_z^1 H_z^2(^1\text{H}_4) \sin^2(\theta)\cos^2(\theta) \\ - 2DQ_y H_z^3(^1\text{H}_4) \cos^3(\theta)\sin(\theta) - 4DQ_x H_z^2 H_z^3(^1\text{H}_4) \cos^2(\theta)\sin^2(\theta) \\ - 4DQ_x H_z^1 H_z^3(^1\text{H}_4) \sin^2(\theta)\cos^2(\theta) + 8DQ_y H_z^1 H_z^2 H_z^3(^1\text{H}_4) \sin^3(\theta)\cos(\theta) \\ - 2DQ_y H_z^4(^1\text{H}_4) \cos^3(\theta)\sin(\theta) - 4DQ_x H_z^2 H_z^4(^1\text{H}_4) \cos^2(\theta)\sin^2(\theta) \\ - 4DQ_x H_z^1 H_z^4(^1\text{H}_4) \sin^2(\theta)\cos^2(\theta) + 8DQ_y H_z^1 H_z^2 H_z^4(^1\text{H}_4) \sin^3(\theta)\cos(\theta) \\ - 4DQ_x H_z^3 H_z^4(^1\text{H}_4) \cos^2(\theta)\sin^2(\theta) + 8DQ_y H_z^2 H_z^3 H_z^4(^1\text{H}_4) \cos(\theta)\sin^3(\theta) \\ + 8DQ_y H_z^1 H_z^3 H_z^4(^1\text{H}_4) \sin^3(\theta)\cos(\theta) + 16DQ_x H_z^1 H_z^2 H_z^3 H_z^4(^1\text{H}_4) \sin^4(\theta)$$

Particularly for the highly protonated species, many different coherences are evolving simultaneously and a thorough description of the system at any given timepoint becomes rather complicated. However, the evolution of the magnetisation follows a simple pattern according to the coherence orders involved and may be summarised as follows:

For an arginine guanidinium group bearing  $n$   $^1\text{H}^n$  protons ( $\text{NH}^n$ ):

$$DQ_x \text{ evolves as } \cos^n(\pi J_{\text{HN}}\tau) \\ 2DQ_y H_z \text{ evolves as } \sin(\pi J_{\text{HN}}\tau)\cos^{n-1}(\pi J_{\text{HN}}\tau) \\ 4DQ_x H_z H_z \text{ evolves as } \sin^2(\pi J_{\text{HN}}\tau)\cos^{n-2}(\pi J_{\text{HN}}\tau) \\ 8DQ_x H_z H_z H_z \text{ evolves as } \sin^3(\pi J_{\text{HN}}\tau)\cos^{n-3}(\pi J_{\text{HN}}\tau) \\ 16DQ_x H_z H_z H_z H_z \text{ evolves as } \sin^4(\pi J_{\text{HN}}\tau)$$

It is noted that each of the terms that are anti-phase with respect to a proton will evolve during the sign-coding filter with at least one sine-modulation whereas the desired in-phase magnetisation only ever evolves with cosine modulation(s). The consequence of this is that when the sign-coding delay,  $\tau$ , is set to  $1/J$ , each of the anti-phase terms are equal to zero. At the same time, the desired cosine-modulated in-phase magnetisations are at their maximum values. This is convenient given that a sample prepared in 50%  $^2\text{H}_2\text{O}$  contains up to 30 different coherences evolving during the sign-coding filter. The evolution of the in-phase magnetisation of each of the protonated states of  $DQ_x$  during a sign-coding filter of length  $1/J$  is shown below in Figure 4.4a. Each additional  $^1\text{H}^n$  results in the sequential inversion of the double-quantum magnetisation:  $DQ_x(^1\text{H}^2\text{H}_3)$  is inverted with respect to  $DQ_x(^2\text{H}_4)$ ;  $DQ_x(^1\text{H}^2\text{H}_2)$  with respect to  $DQ_x(^1\text{H}^2\text{H}_3)$ ;  $DQ_x(^1\text{H}_3^2\text{H})$  with respect to  $DQ_x(^1\text{H}_2^2\text{H}_2)$  and  $DQ_x(^1\text{H}_4)$  with respect to  $DQ_x(^1\text{H}_3^2\text{H})$ .

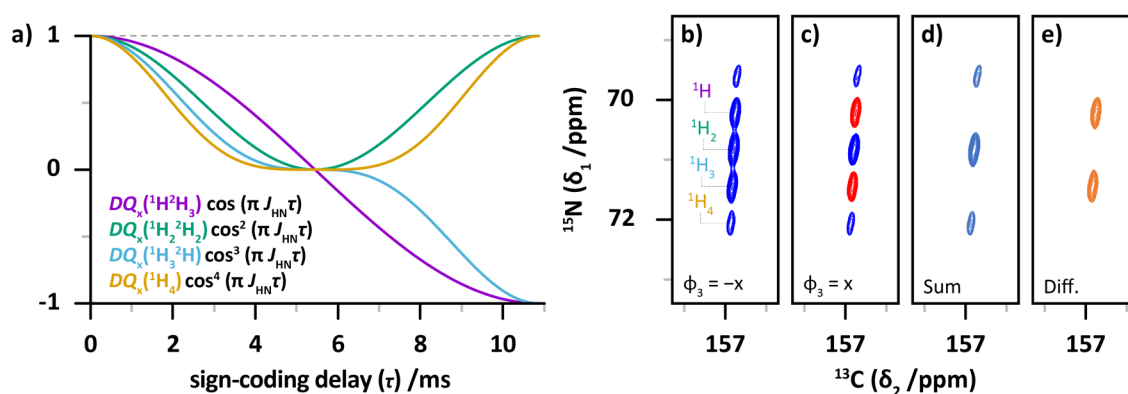


**Figure 4.4** a) Simulated evolution of the in-phase  $DQ_x$  magnetisation during the sign-coding delay as a result of the  $(^1\text{H})_n$ - $^{15}\text{N}$  scalar coupling(s). The value of  $^1J_{\text{HN}}$  was set to -92 Hz and the simulation was run up to 10.9ms ( $1/J$ ). The dashed line follows the  $DQ_x(^2\text{H}_4)$  magnetisation that does not evolve during the filter. b-e)  $^{13}\text{C}$ - $^{15}\text{N}^n$  spectra obtained using the pulse sequence in Figure 4.3a where the  $^{15}\text{N}$  refocussing pulses are made selective for  $^{15}\text{N}^n$ : b) 'in-phase' spectrum ( $\phi_3 = -x$ ) where the  $^1\text{H}$ - $^{15}\text{N}$  coupling is refocussed; c) 'anti-phase' spectrum ( $\phi_3 = x$ ) where the evolution of the  $^1\text{H}$ - $^{15}\text{N}$  coupling causes the inversion of the  $DQ_x(^1\text{H}^2\text{H}_3)$  and  $DQ_x(^1\text{H}_3^2\text{H})$  magnetisation; d) the sum; and e) difference spectra obtained following the linear combination of the two datasets.

The  $^{13}\text{C}$ - $^{15}\text{N}^n$  HDQC spectra obtained using the sign-coding filter are shown in Figure 4.4b and 4.4c. Unlike the  $^1\text{H}^e$  filter, these two datasets cannot be used to isolate each separate signal. However, the linear combinations can be used to separate alternate signals into two sub-spectra and therefore providing an avenue to at least partially mitigate increased spectra crowding. It is envisaged that the sign-coded  $^{15}\text{N}^n$  data will be of most use for samples prepared at lower concentrations of  $^2\text{H}_2\text{O}$  (10-20%) as comparatively fewer species will be present in solution (Figure 4.2).

#### Implications of Rapid Hydrogen Exchange

It is very important to realise that when taking a measurement of the deuterium isotope shifts in the manner described above, the chemical exchange process that substitutes a proton with a deuterium atom continues to occur during the indirect chemical shift evolution period. The

#### 4. Deuterium Isotope Shifts: Detection of Salt-Bridges

effect this exchange process has on the resulting spectrum is very similar to that described for the exchanging  $^{15}\text{N}^n$  nuclei in Chapter 2: at the slow exchange limit, separate peaks are observed for the protonated and deuterated species whilst at the fast exchange limit, a single peak at the average chemical shift is expected. As for the  $^{15}\text{N}^n$  exchange shown in Figure 2.3b, between these two extremes and as the hydrogen exchange rate increases, the initially separated peaks appear to move closer together and eventually coalesce into the single resonance. There is therefore the danger that a measurement of an isotope shift made on a sample undergoing hydrogen exchange on an intermediate timescale may be rendered artificially low.

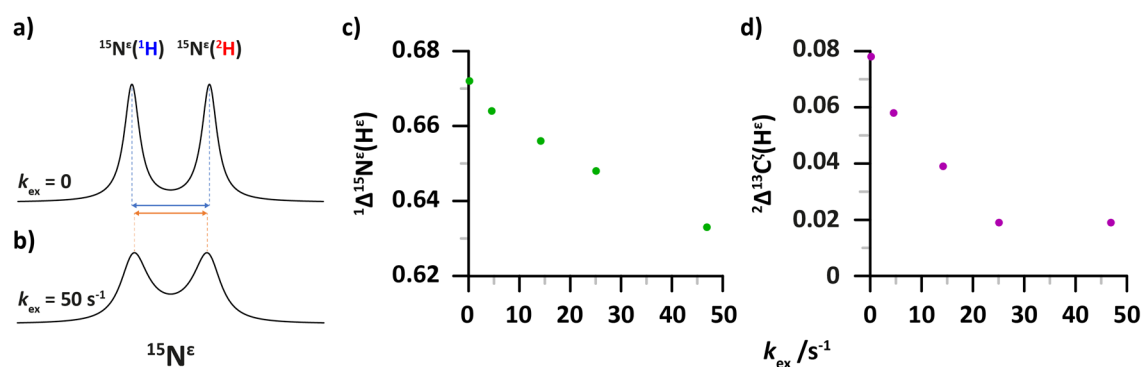


**Figure 4.5** a-b) Simulated  $^{15}\text{N}$  NMR spectra showing the apparent isotope shift in a) the absence of exchange and b) the presence of an exchange reaction with a rate constant of  $50 \text{ s}^{-1}$ . The exchange reaction causes the two peaks to appear closer together and would thus contaminate an isotope shift measurement. Both spectra were simulated using a fixed 'isotope shift' of 42 Hz (0.7 ppm at 60 MHz). c-d) Plots of the hydrogen exchange rate as a function of the apparent a) one-bond  $^{15}\text{N}^\epsilon$  and b) two-bond  $^{13}\text{C}^\zeta$  isotope shifts. Data were taken from the pH and temperature titrations of *free* arginine discussed in Chapter 4.

Figure 4.5a shows a simulated one-dimensional NMR spectrum of two  $^{15}\text{N}$  resonances separated by 42 Hz, consistent with a typical one-bond isotope shift recorded on a 14.1 T spectrometer. Figure 4.5b shows the same resonances with an additional exchange process with a rate constant of  $50 \text{ s}^{-1}$ . The two resonances are now noticeably broader, but the critical difference is that the peaks have shifted slightly closer together. Therefore, if one was to measure the isotope shift as the observed difference in the exchanging spectrum, the measurement would be inaccurate. Fortunately, the magnitude of this hydrogen exchange induced error is quite small for the relatively large one-bond isotope shift. For example, the apparent  $^1\Delta^{15}\text{N}^\epsilon(^1\text{H}^\epsilon)$  isotope shift observed during fast exchange ( $k_{\text{ex}} = 50 \text{ s}^{-1}$ ) is only 5% smaller than the same isotope shift measured at the slow exchange limit (Figure 4.5c). For the smaller isotope shifts such as the two-bond  $^{13}\text{C}^\zeta$  shift, the effect of rapid hydrogen exchange is more dramatic (Figure 4.5d). From the presented data, even a moderate hydrogen exchange rate of  $15 \text{ s}^{-1}$  caused the observed isotope shift to decrease by a factor of two. It is thus critical that isotope shift measurements are interpreted alongside hydrogen exchange data or, where such data does not exist or cannot be recorded, with reference to the data for *free* arginine presented in Chapter 3.

## 4.2.3 Free Arginine Reference Compounds

In order to investigate how the magnitude of the deuterium isotope shift is affected by the presence of an intramolecular interaction, it is important that the isotope shifts are first studied in a non-interacting molecule. Whilst the obvious choice is a sample of [ $^{13}\text{C}_6, ^{15}\text{N}_4$ ]-L-arginine used in the development of the NMR experiments in the previous chapters, the free amino acid bears a carboxylic acid group. This carboxylic acid moiety is potentially able to form an intermolecular complex with the guanidino group of a second free arginine molecule and thus not be truly representative of the non-interacting state (Figure 4.6). It is therefore prudent to chemically block the carboxylic acid and prevent the formation of the dimer (or higher multimer) complex from contaminating the reference isotope shifts.

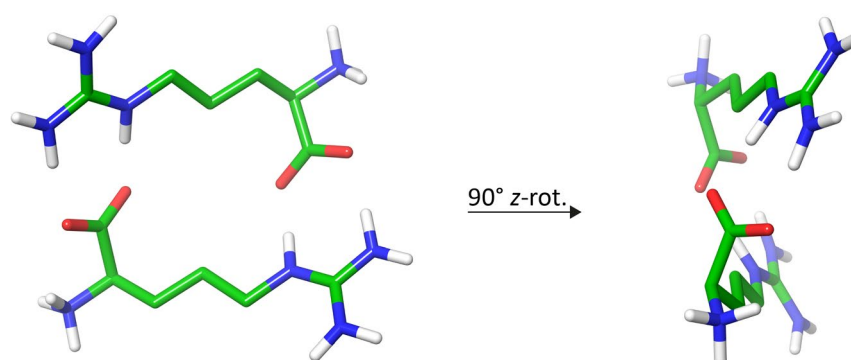
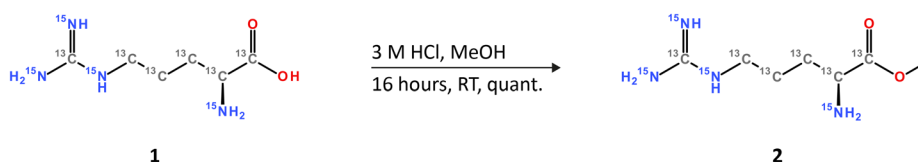


**Figure 4.6** DFT-optimised (M06-2x/6-311+G\*\*) [202,203] structure of the homo-dimer using the polarisation continuum model for water solvation. The formation of such a dimer would clearly not provide reference isotope shifts for a non-interacting arginine residue.

The simplest approach to preventing the dimer formation would be to block the carboxylic acid by preparing the methyl ester **2**. This would prevent the carboxylic acid from becoming negatively charged in solution and disrupt any potential ionic interaction with the positively charged guanidinium group. The reaction is depicted in Scheme 4.1 below and is achieved by treating [ $^{13}\text{C}_6, ^{15}\text{N}_4$ ]-L-arginine **1** with hydrochloric acid in methanol. [204] The reaction proceeds at room temperature overnight and very cleanly converts the starting material to the desired methyl ester in a quantitative yield. As the reactants are all volatile, no further purification of the material was required, aside from the removal of the reaction solvent.

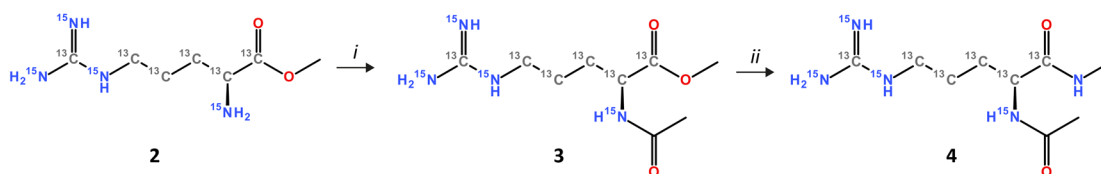


**Scheme 4.1** The preparation of L-arginine methyl ester from the free amino acid.

Whilst the synthesis of the methyl ester was successful, the utility of the resulting compound was significantly diminished by the aqueous instability of the ester protecting group. Under the

#### 4. Deuterium Isotope Shifts: Detection of Salt-Bridges

mildly acidic aqueous conditions to be employed in this study (phosphate buffer, pH 5.5), the newly formed carbon-oxygen bond was easily cleaved to re-generate the free amino acid **1** over the course of a few hours. To address this limitation, an amide-protected molecule **4** was designed and synthesised according to the Scheme 4.2 instead. Where **2** bears a labile methyl ester, this group has been replaced with the more stable methyl amide in **4**. Additionally, the free amine group - potentially capable of forming hydrogen bonds - has also been protected by acetylation. The resulting structure, referred to as *capped* arginine now closely resembles a single arginine side-chain found in the polypeptide backbone of a real protein.

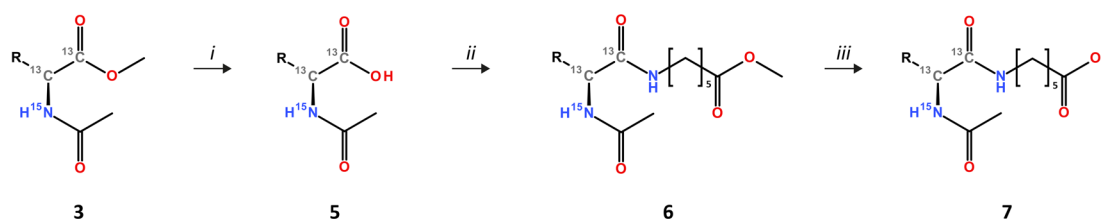


**Scheme 4.2** The preparation of *capped* L-arginine from the methyl ester synthesised in Scheme 4.1. i)  $\text{Ac}_2\text{O}$ ,  $\text{Et}_3\text{N}$  in DMF,  $0^\circ\text{C}$ , 1 hour. ii)  $\text{MeNH}_2$  in EtOH, RT, 16 hours.

The primary amine of methyl ester **2** is first acylated using acetic anhydride in *N,N*-dimethyl formamide with triethylamine serving as the base required to neutralise the positively charged amine.<sup>[205]</sup> The reaction proceeded rapidly and although only one equivalent of acetic anhydride was used, a small amount of the *bis*-acylated amine was detected. Nevertheless, the solvent was removed and the crude material re-dissolved in a solution of methylamine in ethanol to convert the methyl ester to the corresponding methyl amide.<sup>[206]</sup> Isolation of compound **4** from the reaction mixture was achieved by preparative-HPLC using a hydrophilic interaction (HILIC)<sup>[207]</sup> column.

#### 4.2.4 Complexed Arginine Reference Compound

Once the reference data has been collected for the non-interacting *capped* arginine sample, it would be ideal to investigate the effect of the intermolecular salt-bridge shown in Figure 4.6b on the magnitude of the isotope shifts. Rather than rely on the potentially transient dimer formation of *free* arginine **1**, a molecule containing an *intramolecular* salt-bridge was designed and synthesised according to Scheme 4.3.



**Scheme 4.3** The preparation of *complexed* L-arginine from the intermediate synthesised in Scheme 4.2. i)  $\text{LiOH}$  in  $\text{H}_2\text{O}$ , RT, 16 hours. ii)  $\text{NH}_2(\text{CH}_2)_5\text{CO}_2\text{CH}_3$ , HBTU, DIPEA in DMF,  $0^\circ\text{C} \rightarrow \text{RT}$ , 16 hours. iii)  $\text{LiOH}$  in  $\text{H}_2\text{O}$ , RT, 16 hours.  $\text{R} = ^{13}\text{CH}_2^{13}\text{CH}_2^{13}\text{CH}_2^{15}\text{NH}^{13}\text{C}(^{15}\text{NH})^{15}\text{NH}_2$ .

#### 4. Deuterium Isotope Shifts: Detection of Salt-Bridges

The synthesis begins by treating the *N*-acetylated methyl ester intermediate **3** from Scheme 4.2 with aqueous lithium hydroxide to give the free carboxylic acid **5**.<sup>[208]</sup> The reaction proceeded fairly cleanly with only a small amount of the *N*-acetyl group being removed. The crude material was then coupled to methyl 6-aminocaproate using the HATU procedure<sup>[209]</sup> to give the methyl ester **6**. This material was subjected to reverse-phase preparative-HPLC purification to remove any side-products or other reactants. Finally, the methyl ester was treated with aqueous lithium hydroxide and subsequently purified on the HILIC column to provide the desired compound **7** in a reasonable yield.

Compound **7**, referred to as *complexed* arginine, contains a free carboxylic acid at the end of a flexible carbon linker that permits the formation of an intramolecular salt-bridge. Extensive conformational sampling (Maestro 12.4, Schrödinger 2020) of this molecule suggests that the lowest energy conformation in solution likely contains such an interaction. The chemical shift of the <sup>1</sup>H<sup>ε</sup> proton in **7** experiences a marked downfield shift when compared to the same proton in **4**, also consistent with this hypothesis. The Density Functional Theory (DFT)-derived structure of the low energy conformation of **7** showing the intramolecular salt-bridge is shown in Figure 4.7.

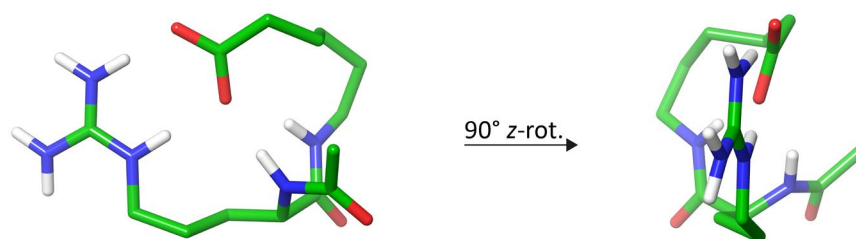


**Figure 4.7** DFT-optimised (M06-2x/6-311+G\*\*) structure of the lowest energy conformation of **7** showing the presence of an intramolecular salt-bridge. The structure is the result of an extensive conformational search using molecular modelling followed by DFT-optimisation using the polarisation continuum model for water solvation.

With access to the reference compounds **4** and **7** above and the NMR experiments laid out in Figure 4.1 for the measurement of the numerous deuterium isotope shifts expected in arginine side-chains, the stage is now set for the application of the method to protein samples.

### 4.3 Results and Discussions

#### 4.3.1 Application to Arginine Reference Compounds

In order to identify any change in the isotope shift(s) upon the formation of an arginine salt-bridge, it is first essential to determine reference measurements for both a non-interacting residue (using compound **4**) and one that forms a salt-bridge (using compound **7**). To this end, samples of **4** and **7** were prepared in an aqueous phosphate buffer containing 50 % <sup>2</sup>H<sub>2</sub>O, adjusted to pH 5.5 to slow the effect of hydrogen exchange, and analysed using the <sup>13</sup>C<sup>ζ</sup>-<sup>15</sup>N<sup>ε</sup>

#### 4. Deuterium Isotope Shifts: Detection of Salt-Bridges

HSQC and  $^{13}\text{C}^{\zeta}\text{-}^{15}\text{N}^{\eta}$  HDQC experiments discussed previously. The results are displayed below in Table 4.3.

Cpd.	$^1\Delta^{15}\text{N}^{\epsilon}(\text{H}^{\epsilon})$	$^1\Delta^{15}\text{N}^{\eta}(\text{H}^{\eta})$	$^2\Delta^{13}\text{C}^{\zeta}(\text{H}^{\epsilon})$	$^2\Delta^{13}\text{C}^{\zeta}(\text{H}^{\eta})$	$^3\Delta^{15}\text{N}^{\eta}(\text{H}^{\epsilon})$	$^3\Delta^{15}\text{N}^{\epsilon}(\text{H}^{\eta})$
<b>4</b>	$0.691 \pm 0.001$	$0.626 \pm 0.002$	$0.058 \pm 0.001$	$0.044 \pm 0.001$	$0.157 \pm 0.003$	$0.059 \pm 0.001$
<b>7</b>	$0.694 \pm 0.001$	$0.634 \pm 0.001$	$0.062 \pm 0.001$	$0.044 \pm 0.001$	$0.141 \pm 0.001$	$0.063 \pm 0.001$

**Table 4.3** Deuterium isotope shifts for *capped* arginine **4** and *complexed* arginine **7** as measured by  $^{13}\text{C}^{\zeta}$ -detected NMR experiments in phosphate buffer containing 50%  $^2\text{H}_2\text{O}$  at pH 5.5. Presented values are the average measurements of at least three signals detected in the same experiment.

It is clear that in each of the six categories – the one-, two- and three-bond isotope shifts caused by the incorporation of either  $^2\text{H}^{\epsilon}$  or  $^2\text{H}^{\eta}$  – the measurements are very similar for both the non-interacting residue **4** and compound **7** that allegedly contains an intramolecular salt-bridge. However, this initially disappointing result can potentially be explained by considering the solvent in which the system is studied. The salt-bridge hypothesised to exist in *complexed* arginine **7** is the result of a combination of an electrostatic interaction between the oppositely charged functional groups as well the hydrogen bonds between the  $\text{N-H}^{\epsilon/\eta}$  and oxygen atoms. Both processes are quite likely to be outcompeted by huge excess of solvent and buffer molecules also present within the sample. Water is capable of both accepting and donating hydrogen bonds whilst the high concentration of positively charged sodium and negatively charged phosphate ions could easily disrupt the ionic interaction of the proposed salt-bridge. Indeed, this theory is supported by the lack of observation of similar interactions on the surface of proteins - it is only within the three-dimensional core of a protein, where solvent molecules cannot penetrate, that such interactions are likely to form.

To further investigate this theory, and with confidence in the computational study that predicted the presence of the interaction, compound **7** was additionally analysed in organic solvent systems where it was hoped that the absence of water and other charged molecules would allow the internal salt-bridge to emerge. The presence, or otherwise, of the salt-bridge was identified through the measurement of the  $\text{N}^{\epsilon}\text{-C}^{\zeta}$  rotational exchange using the recently published multiple-quantum chemical exchange saturation transfer (MQ-CEST) experiment.<sup>[189]</sup> During the MQ-CEST experiment, a low-power  $^{15}\text{N}$  RF field is applied to longitudinal  $4\text{C}_z^{\zeta}\text{N}_z^{\eta 1}\text{N}_z^{\eta 2}$  magnetisation and results in a decrease in the detected  $^{13}\text{C}^{\zeta}\text{-}^{15}\text{N}^{\epsilon}$  cross peak when the applied frequency is on resonance with one of the two  $^{15}\text{N}^{\eta}$  chemical shifts. The saturation of the  $^{15}\text{N}^{\eta}$  signal when the RF field is on resonance results in a characteristic *dip* in the CEST profile centred at the underlying  $^{15}\text{N}^{\eta}$  chemical shift and can provide a quantitative assessment of chemical exchange.<sup>[210,211]</sup> The rationale was that in the absence of an interaction, the  $\text{N}^{\epsilon}\text{-C}^{\zeta}$  bond undergoes rapid rotational exchange as described in further detail in Chapter 2 and would result

in a single dip in the CEST profile, centred at the average  $^{15}\text{N}^n$  frequency. A side-on salt-bridge such as the one hypothesised for **7** in Figure 4.7 would clearly hinder this rotation and thus two equally sized dips and a significantly attenuated exchange rate ought to be detectable using the MQ-CEST experiment.

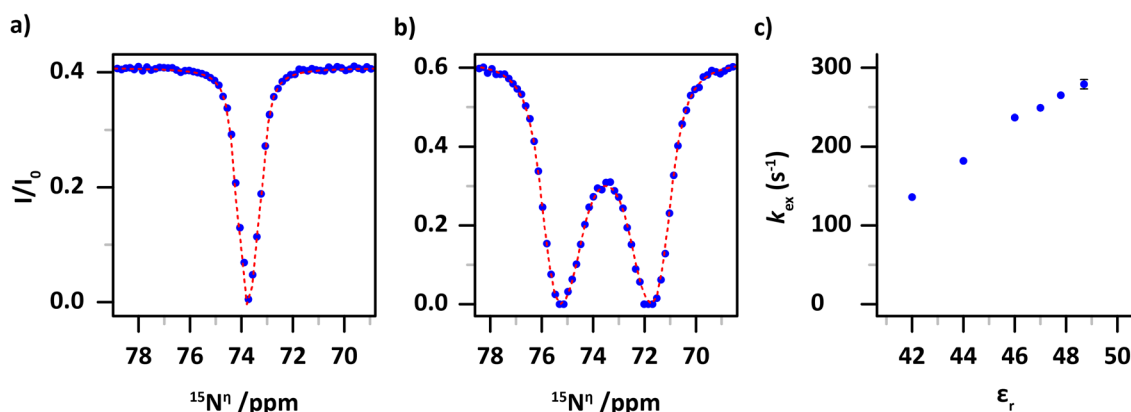


**Figure 4.8** MQ-CEST profiles obtained for *complexed* arginine **7** in a) DMSO:H<sub>2</sub>O (85:15),  $\epsilon_r = 52$ ,  $k_{\text{ex}} > 350 \text{ s}^{-1}$  and b) DMSO:MeCN (50:50),  $\epsilon_r = 42$ ,  $k_{\text{ex}} = 136 \pm 1 \text{ s}^{-1}$  showing the slowing of the  $\text{N}^{\epsilon}\text{-C}^{\zeta}$  bond rotation caused by the formation of the intra-molecular salt-bridge in solvents with decreasing polarity  $\epsilon_r$ .

$f_{\text{DMSO}}$	$f_{\text{MeCN}}$	$f_{\text{water}}$	$\epsilon_r$	$k_{\text{ex}} (\text{s}^{-1})$
0.5	0.5		42.0	$136 \pm 1$
	0.7		44.0	$182 \pm 1$
	0.9		46.0	$237 \pm 1$
	1.0		47.0	$249 \pm 2$
	0.975	0.025	47.8	$265 \pm 4$
	0.95	0.05	48.7	$279 \pm 6$
	0.9	0.1	50.3	$323 \pm 15$
	0.85	0.15	52.0	$>350$

**Table 4.4** Rotational exchange rate constant ( $k_{\text{ex}}$ ) about the  $\text{N}^{\epsilon}\text{-C}^{\zeta}$  bond of **7** as determined by MQ-CEST experiments in solvent systems of increasing polarity.

Dimethylsulphoxide (DMSO) is a common solvent in organic chemistry and is less polar ( $\epsilon_r = 47$ )<sup>[212]</sup> than water ( $\epsilon_r = 80$ )<sup>[213]</sup> therefore making it suitable for use as the 'base' solvent in the subsequent MQ-CEST experiments. The effective polarity of the base DMSO solvent was either raised through the addition of water or lowered with the addition of acetonitrile (MeCN,  $\epsilon_r = 37$ )<sup>[214]</sup> to provide a range of solvent systems with increasing polarity. Using these solvents the behaviour of the intra-molecular salt-bridge was studied between  $\epsilon_r$  values of 42 and 52. Unfortunately, the lack of solubility of **7** in non-polar solvents such as hexane ( $\epsilon_r = 1.9$ )<sup>[215]</sup> or chloroform ( $\epsilon_r = 4.8$ )<sup>[216]</sup> prevented the assessment of the interaction in solvents with even lower polarity. However, Figure 4.8 shows that even the modest range of solvent polarity available experimentally was enough to reveal the propensity of **7** to form the intra-molecular salt-bridge in the right conditions.

#### 4. Deuterium Isotope Shifts: Detection of Salt-Bridges

In solvents of higher polarity ( $\epsilon_r > 52$ ), the rotational exchange about the  $N^\epsilon-C^\zeta$  bond is sufficiently fast to coalesce the two contributing  $^{15}N^\eta$  frequencies in the MQ-CEST experiment (Figure 4.8a) indicating that there is no significant interaction present to slow the rotation. In less polar environments, the rotational exchange is dramatically slowed and the MQ-CEST profile clearly shows the two separate  $^{15}N^\eta$  frequencies (Figure 4.8b). The exchange rate constant extracted from this MQ-CEST dataset is  $136 \pm 1 \text{ s}^{-1}$ , significantly lower than the value of approximately  $2000 \text{ s}^{-1}$  expected for a non-interacting arginine residue. This is a direct result of the intramolecular salt-bridge forming as the same result is not observed for *capped* arginine **4**. Figure 4.8c shows that the observed rotational exchange rate ( $k_{ex}$ ) correlates well with the relative permittivity ( $\epsilon_r$ ) of the solvent system achieved through the binary combination of DMSO, acetonitrile and water and explains why no difference in the isotope shifts of **4** and **7** was revealed in Table 4.3.

In order to quantify the deuterium isotope shifts of arginine as a function of relative permittivity, a source of deuterium in each solvent system is required. For solvent mixtures comprising DMSO and water, this is achieved through the simple substitution of the water added to the DMSO with a 50% water/deuterium oxide mixture. However, care must be taken when adding water to the DMSO:MeCN solvent systems as Table 4.4 shows that even a few % of water can significantly alter the relative permittivity of the binary mixture. DMSO is a highly hygroscopic solvent and readily absorbs moisture from the air so it was expected that no additional  $^1H_2O$  would be required. To ensure that no excess water was added and to thus preserve the low relative permittivity of the system, small amounts of deuterium were titrated into each sample until the relative intensity of the  $^{15}N^\epsilon(^1H)$  and  $^{15}N^\epsilon(^2H)$  cross-peaks in a  $^{13}C^\zeta$ - $^{15}N^\epsilon$  HSQC spectrum were approximately equal. This led to a total concentration of water in each sample of less than 0.25%. To ensure the pH of each sample was kept low, the deuterium was introduced as a 100 mM solution of HCl and each sample subsequently demonstrated a negligible rate of hydrogen exchange. The deuterium isotope shifts measured for both *capped* and *complexed* arginine samples are shown in Figure 4.9.

#### $^1\Delta^{15}N^\epsilon(H^\epsilon)$ and $^1\Delta^{15}N^\eta(H^\eta)$

The one-bond deuterium isotope shift of the  $^{15}N^\epsilon$  nucleus is the largest of the detected shifts in the arginine side-chain and is easily extracted from a  $^{13}C^\zeta$ - $^{15}N^\epsilon$  HSQC spectrum (see Figure 4.1a). The data recorded on series of *capped* arginine **4** samples demonstrates an isotope shift of between 0.7 and 0.8 ppm for solvent systems with relative permittivity between 64 and 42 (Figure 4.9a, orange). The observed isotope shift appears to increase gradually as the relative permittivity of the solvent is lowered. The data recorded for *complexed* arginine **7** at high relative permittivity ( $\epsilon_r > 50$ ) reveals an isotope shift that is indistinguishable from that of *capped*

#### 4. Deuterium Isotope Shifts: Detection of Salt-Bridges

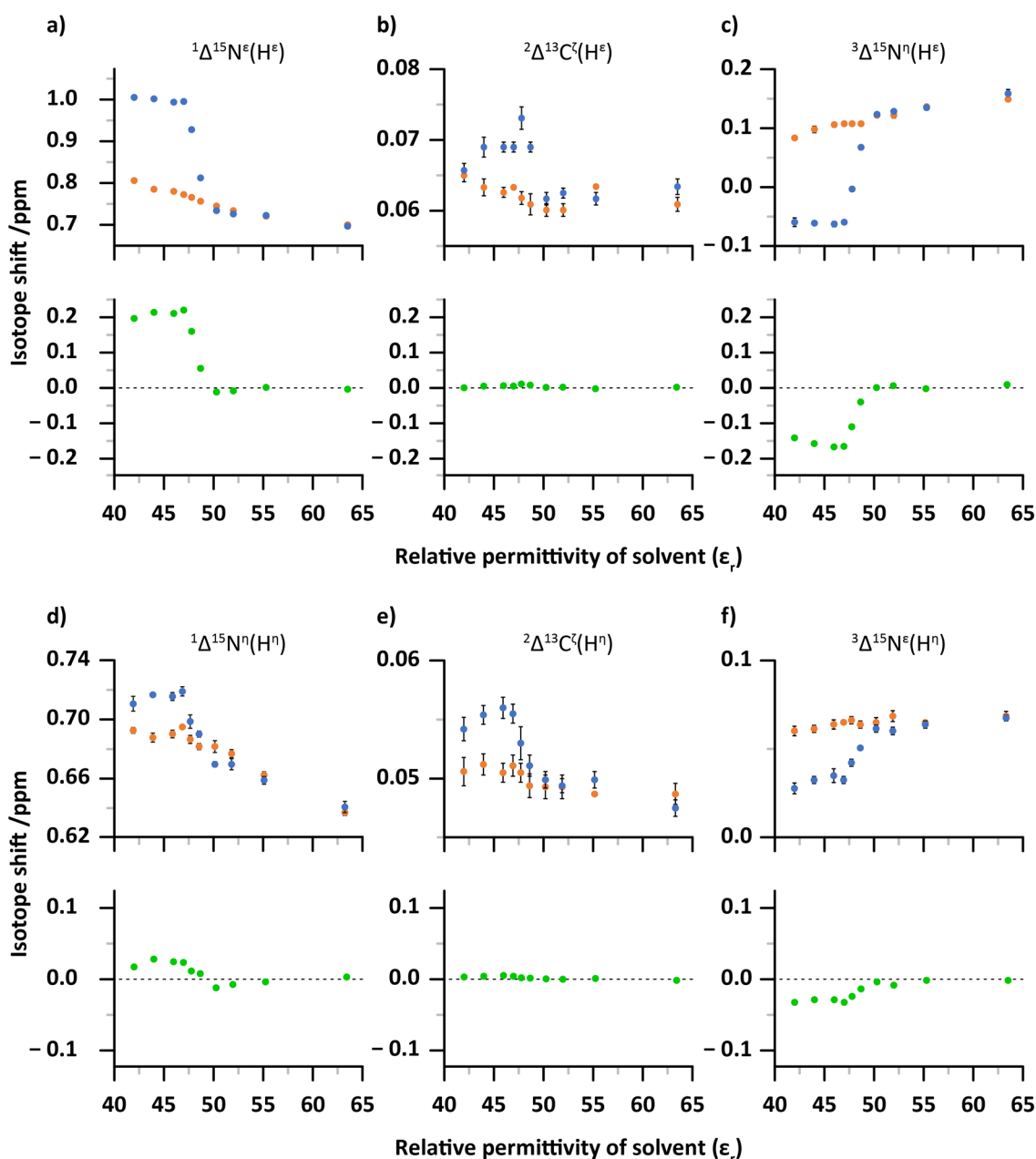


**Figure 4.9** Deuterium isotope shifts measured for *capped* and *complexed* arginine reference compounds, **4** and **7**, as a function of the relative permittivity of the solvent system. The **difference** between the measurements for **4** and **7** are shown in the lower plot for each different isotope shift. The relative permittivity of the solvent was adjusted as described in the main text.

arginine **4**, in line with the observations made above in Table 4.3. However, in samples prepared in solvent systems with lower relative permittivity ( $\epsilon_r < 50$ ), a significant change in the deuterium isotope shift is observed. Whilst the rotational exchange rate of the  $\text{N}^\epsilon\text{-C}^\zeta$  bond appears to decrease in an approximately linear fashion with the polarity of the bulk solvent, the same gradual trend is not observed in the isotope shift data. Instead, an abrupt increase in the deuterium isotope shift, from approximately 0.7 to 1.0 ppm between  $\epsilon_r$  values of 50 and 47 (Figure 4.9a, **blue**) is seen. This observation suggests that deuterium isotope shift is highly sensitive to discrete changes in the molecular composition of the solvent and the microenvironment of the intra-molecular salt-bridge present in *complexed* arginine **7**.

#### 4. Deuterium Isotope Shifts: Detection of Salt-Bridges

To correct for the intrinsic increase in isotope shift caused by the lowering of the relative permittivity required to encourage the interaction to form, it is useful to view the data as the difference between the *capped* and *complexed* measurements (Figure 4.9a, green) where the sudden increase in isotope shift can be seen even more clearly.

The equivalent one-bond isotope shift of the  $^{15}\text{N}^n$  nuclei exhibit the same trends, albeit less significantly (Figure 4.9d). The magnitude of the isotope shift measured for *capped* arginine **4** varies between 0.64 and 0.70 ppm over the range of relative permittivity values studied with the relatively large chemical shift difference easily extracted from a  $^{13}\text{C}^{\zeta}\text{-}^{15}\text{N}^n$  HDQC spectrum (Figure 4.1c). As for the  $^1\Delta^{15}\text{N}^{\epsilon}(\text{H}^{\epsilon})$  measurement, an increase in isotope shift upon the formation of the salt-bridge is observed for *complexed* arginine **7**, although the effect is less pronounced for the  $^{15}\text{N}^n$  nuclei. An explanation for this observation could be that whilst the  $\text{H}^{\epsilon}$  nucleus is always engaged in the salt-bridge, only one of the two  $\text{H}^n$  nuclei can be involved at any one time whilst the other is *free* and thus does not experience an increased isotope shift. As the HDQC experiment reports the *average*  $^{15}\text{N}^n$  chemical shift, this would result in only a partial increase in the observed  $^1\Delta^{15}\text{N}^n(\text{H}^n)$  isotope shift.

#### $^2\Delta^{13}\text{C}^{\zeta}(\text{H}^{\epsilon})$ and $^2\Delta^{13}\text{C}^{\zeta}(\text{H}^n)$

The magnitude of the two-bond isotope shift of the  $^{13}\text{C}^{\zeta}$  nucleus caused by substitution of either the  $\text{H}^{\epsilon}$  or  $\text{H}^n$  nuclei, extracted from  $^{13}\text{C}^{\zeta}\text{-}^{15}\text{N}^{\epsilon}$  HSQC or  $^{13}\text{C}^{\zeta}\text{-}^{15}\text{N}^n$  HDQC spectra, are much smaller than the one-bond isotope shifts above at 0.06-0.07 ppm for  $^2\Delta^{13}\text{C}^{\zeta}(\text{H}^{\epsilon})$  (Figure 4.9b) and slightly smaller at 0.05-0.055 for  $^2\Delta^{13}\text{C}^{\zeta}(\text{H}^n)$  (Figure 4.9e). The formation of the salt-bridge does appear to influence the  $^2\Delta^{13}\text{C}^{\zeta}(\text{H}^n)$  isotope shift but the effect is much less pronounced than for the  $^{15}\text{N}^{\epsilon/n}$  nuclei above. This only small effect, coupled with the small size of the individual  $^{13}\text{C}^{\zeta}$  isotope shifts that would hamper an accurate measurement in proteins where the linewidth is expected to be broader, limits their utility for the detection of such interactions.

#### $^3\Delta^{15}\text{N}^n(\text{H}^{\epsilon})$ and $^3\Delta^{15}\text{N}^{\epsilon}(\text{H}^n)$

The three-bond deuterium isotope shifts of the  $^{15}\text{N}^n$  and  $^{15}\text{N}^{\epsilon}$  nuclei can be extracted from the  $^{13}\text{C}^{\zeta}\text{-}^{15}\text{N}^n$  HDQC and  $^{13}\text{C}^{\zeta}\text{-}^{15}\text{N}^{\epsilon}$  HSQC, respectively and are shown in Figure 4.9c/f. As for the one-bond  $^{15}\text{N}$  isotope shifts, both measurements appear to be affected by the formation of the salt-bridge of *complexed* arginine **7**, with a larger effect observed upon the substitution of the  $\text{H}^{\epsilon}$  nucleus (Figure 4.9c). Interestingly, the three-bond isotope shifts show a *decrease* in size as the salt-bridge is formed rather than the *increase* that is observed for the one-bond measurements. Whilst the difference between the *capped* and *complexed* arginine measurements reveals that the effect of the salt-bridge on the three-bond (*interacting* – *free*  $\approx -0.2$ ) and one-bond (*interacting* – *free*  $\approx 0.2$ ) isotope shifts is similar, the three-bond isotope shifts are almost an order of magnitude smaller and correspondingly harder to extract from the NMR spectra of

proteins. This problem is exacerbated by the fact that the three-bond isotope shifts decrease further upon the formation of the interaction and in the case of the  ${}^3\Delta^{15}\text{N}^\eta(\text{H}^\epsilon)$  isotope shift goes through zero and therefore may be completely undetectable.

The results obtained for the reference compounds discussed in this section provide a clear indication that the formation of a salt-bridge has a significant effect on the magnitude of the deuterium isotope shift(s) of the different nuclei that make up the guanidinium group of arginine. Each of the one-, two- and three-bond isotope shifts are at least in principle obtainable through the combination of two NMR experiments: the  ${}^{13}\text{C}^\zeta\text{-}{}^{15}\text{N}^\epsilon$  HSQC and  ${}^{13}\text{C}^\zeta\text{-}{}^{15}\text{N}^\eta$  HDQC. The most informative isotope shift appears to be the one-bond  ${}^{15}\text{N}^\epsilon$  which, rather fortunately turns out to also be the largest and thus easiest to measure. The following section demonstrates the general utility of the proposed method to detect the presence of these side-on salt-bridges involving the arginine side-chain as applied to the proteins T4 Lysozyme and Barnase.

#### 4.3.2 Application to T4 Lysozyme

T4 Lysozyme, the model protein studied in previous Chapters contains 13 arginine residues, several of which have been shown to engage in different interactions with other parts of the protein. Table 4.5 shows the deviation of the  ${}^1\Delta^{15}\text{N}^\epsilon(\text{H}^\epsilon)$  isotope shifts extracted from the  ${}^{13}\text{C}^\zeta\text{-}{}^{15}\text{N}^\epsilon$  spectrum of the L99A mutant of T4 Lysozyme (T4L99A) recorded in phosphate buffer at pH 5.5 from the expected value for a non-interacting residue. As the isotope shift of a non-interacting arginine residue is now known to be sensitive to the relative permittivity of the solvent, the data in Table 4.5 has been calculated using the value obtained for *capped* arginine **4** in the same buffer (Table 4.3). It is worth noting that this isotope shift data is available ‘for free’ from the ASHDEX datasets discussed in Chapter 3 though of course the single two-dimension NMR spectrum required here is considerably faster to record than the full four-dimensional ASHDEX experiment.

Residue No.	$\Delta[{}^1\Delta^{15}\text{N}^\epsilon(\text{H}^\epsilon)]$	Residue No.	$\Delta[{}^1\Delta^{15}\text{N}^\epsilon(\text{H}^\epsilon)]$
8	0.022	96	- 0.031
14	- 0.002	119 <sup>b</sup>	- 0.002
52	0.114	125 <sup>b</sup>	- 0.002
76 <sup>a</sup>	- 0.012	137 <sup>b</sup>	- 0.002
80 <sup>a</sup>	- 0.012	148	- 0.021
95	0.003	154	0.007

**Table 4.5** Residue-specific deviation of the one-bond  ${}^{15}\text{N}^\epsilon$  deuterium isotope shifts recorded for T4L99A in a phosphate buffer containing 50%  ${}^2\text{H}_2\text{O}$  at pH 5.5. The measurements were extracted from a  ${}^{13}\text{C}^\zeta\text{-}{}^{15}\text{N}^\epsilon$  HSQC spectrum and calculated by subtracting the value obtained for *capped* arginine **4** in the same buffer (0.691 ppm). Residue 145 is not shown owing to the very low intensity of the associated cross-peaks. Signal overlap of a) 76 and 80 and b) 119, 125 and 137 prevented an individual measurement for these residues.

#### 4. Deuterium Isotope Shifts: Detection of Salt-Bridges

The data reveals that for most of the detectable residues in T4L99A, the deuterium isotope shifts are unremarkable. However, residue 52 clearly stands out (Figure 4.10a) and shows a positive deviation of 0.114 ppm from the value expected for a non-interacting arginine residue, indicating a salt-bridge of the type observed in *complexed* arginine **7** may be present. Crucially, this finding corresponds with the observation of such an interaction between R52 and glutamic acid E62 in the X-ray crystal structure of T4L99A (Figure 4.10b) and thus provides further evidence that this isotope shift is sensitive to the formation of a side-on salt-bridge. No other arginine residue in the crystal structure of T4L99A was also shown to be involved in a side-on salt-bridge.

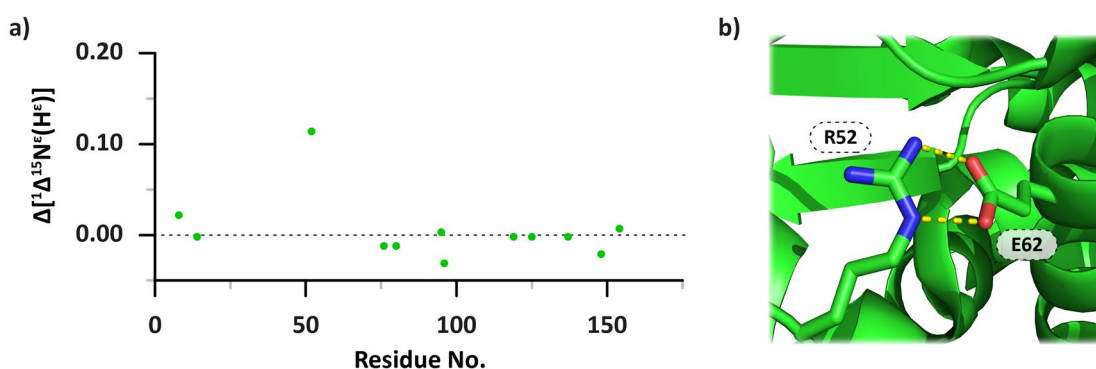


**Figure 4.10** a) Plot of the residue-specific deviation of the one-bond  $^{15}\text{N}^\epsilon$  deuterium isotope shifts recorded for T4L99A in a phosphate buffer containing 50%  $^2\text{H}_2\text{O}$  at pH 5.5. The values are taken from Table 4.5. The data indicates that R52 is significantly different from the other residues and suggest the presence of a salt-bridge. b) The X-ray crystal structure (PDB: 102L)<sup>[190]</sup> of T4L99A shows that R52 is engaged in a salt-bridge interaction with glutamic acid E62.

#### 4.3.3 Application to Barnase

To provide further evidence of the correlation between an increased deuterium isotope shift and the formation of a salt-bridge, a second model protein was studied. Bacterial ribonuclease (Barnase), a 110 amino acid protein containing a total of six arginine residues, was chosen as a suitable model system. As for T4L99A, a [ $^{13}\text{C}$ ,  $^{15}\text{N}$ ]-labelled sample was prepared in a phosphate buffer containing 50%  $^2\text{H}_2\text{O}$  at pH 5.5 and analysed by  $^{13}\text{C}^\zeta$ -detected NMR spectroscopy. The  $^{13}\text{C}^\zeta$ - $^{15}\text{N}^\epsilon$ [ $^1\text{H}^\epsilon$ ] HSQC spectrum is shown below in Figure 4.11 and shows six well resolved signals, suitable for the analysis of deuterium isotope shifts. The results from the isotope shift analysis (using the pseudo-3D experiment) are shown in Table 4.6 and Figure 4.12.

Of the six arginine residues present in Barnase, two of them exhibit an isotope shift that is significantly higher than the reference measurement made on the *capped* arginine **4** sample. Upon interrogation of the X-ray crystal structure of Barnase, it is found that both residues R69 and R83 are engaged in side-on salt-bridges with aspartic acid residues as suggested by the large  $^{15}\text{N}^\epsilon$  isotope shift measurement (Figure 4.12b/c). The remaining four arginine residues of Barnase are not shown to be involved in side-on salt bridges.

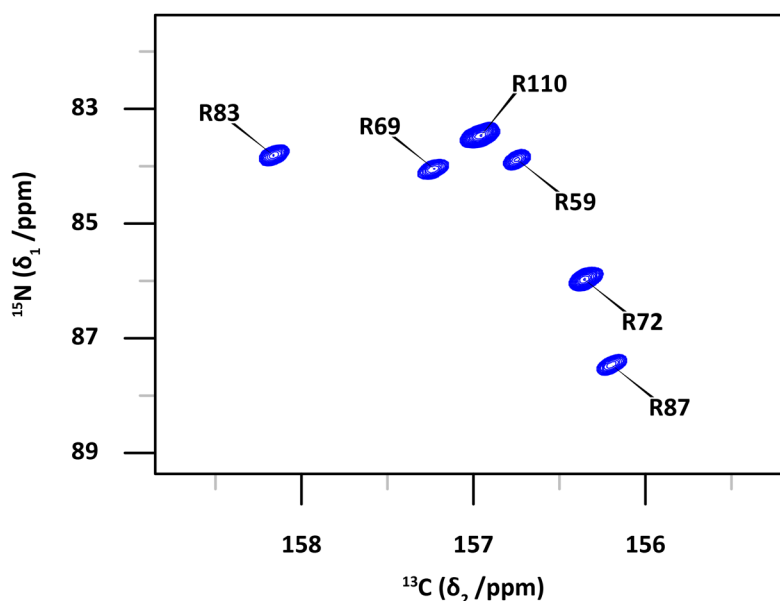


**Figure 4.11** The  $^{13}\text{C}$ - $^{15}\text{N}$   $^{\epsilon}[\text{H}^{\epsilon}]$  HSQC spectrum of Barnase recorded at 16.4 T.

Residue No.	$\Delta[{}^1\Delta^{15}\text{N}^{\epsilon}(\text{H}^{\epsilon})]$	Residue No.	$\Delta[{}^1\Delta^{15}\text{N}^{\epsilon}(\text{H}^{\epsilon})]$
59	-0.012	83	0.104
69	0.104	87	-0.011
72	-0.036	110	-0.017

**Table 4.6** Residue-specific deviation of the one-bond  $^{15}\text{N}^{\epsilon}$  deuterium isotope shifts recorded for Barnase in a phosphate buffer containing 50%  $^2\text{H}_2\text{O}$  at pH 5.5. The measurements were extracted from a  $^{13}\text{C}$ - $^{15}\text{N}^{\epsilon}$  HSQC spectrum and calculated by subtracting the value obtained for *capped* arginine **4** in the same buffer (0.691 ppm).

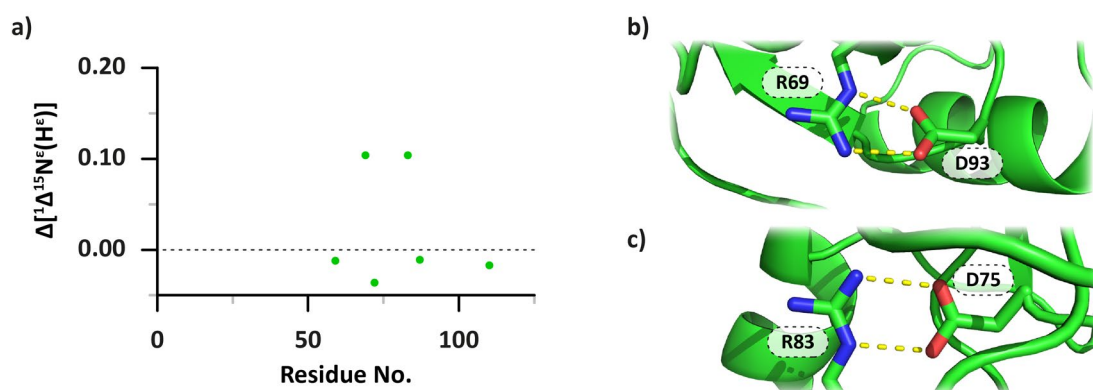


**Figure 4.12** a) Plot of the residue-specific deviation of the one-bond  $^{15}\text{N}^{\epsilon}$  deuterium isotope shifts recorded for Barnase in a phosphate buffer containing 50%  $^2\text{H}_2\text{O}$  at pH 5.5. The values are taken from Table 4.6. The data indicates that R69 and R83 are significantly different from the other residues and suggest the presence of salt-bridges. The X-ray crystal structure of Barnase (PDB: 1A2P)<sup>[217]</sup> shows that b) R69 is engaged in a salt-bridge interaction with aspartic acid D93 and c) R83 forms a similar interaction with aspartic acid D75.

## 4.4 Conclusions

The positively charged guanidinium group of the arginine side-chain contains five labile protons and can result in up to ten individual cross peaks per residue where an increased amount of deuterium is present. As the  $^1\text{H}$  nuclei themselves are not required for detection purposes,  $^{13}\text{C}^\zeta$ -detected NMR spectra are able to resolve and quantify the difference in chemical shift of each of the isotopomers, the so-called deuterium isotope shift. The isotope shift is experienced by each of the heavy atoms that make up the guanidinium group and has been shown to report on the formation of salt-bridges between arginine and the negatively charged side-chains aspartic and glutamic acid. A thorough study of the behaviour of the numerous isotope shifts of the  $^{13}\text{C}^\zeta$ ,  $^{15}\text{N}^\epsilon$  and  $^{15}\text{N}^\eta$  nuclei within the guanidinium group upon the formation a salt-bridge was achieved through the use of synthetic arginine reference compounds. Two compounds were designed and synthesised, one of which included an intra-molecular salt-bridge. The presence of the internal salt-bridge was confirmed by monitoring the rotational exchange of the  $^{15}\text{N}^\eta$  nuclei about the  $\text{N}^\epsilon\text{-C}^\zeta$  using MQ-CEST and was shown to be highly dependent on the composition of the solvent. The magnitude of the isotope shifts showed a dramatic change upon the formation of the salt-bridge with  $^1\Delta^{15}\text{N}^\epsilon(\text{H}^\epsilon)$  being the most significantly affected. Interestingly, the one-bond isotope shifts  $-^1\Delta^{15}\text{N}^\epsilon(\text{H}^\epsilon)$  and  $^1\Delta^{15}\text{N}^\eta(\text{H}^\eta)$  – showed an increase when the salt-bridge was present, whilst the longer range three-bond isotope shifts  $-^3\Delta^{15}\text{N}^\epsilon(\text{H}^\eta)$  and  $^3\Delta^{15}\text{N}^\eta(\text{H}^\epsilon)$  – showed a decrease. The two-bond isotope shifts experienced by the  $^{13}\text{C}^\zeta$  nucleus were only very slightly affected by the salt-bridge formation. It should be stressed that an appreciation of the hydrogen exchange rate of the  $^1\text{H}^{\epsilon/\eta}$  nuclei is important when extracting the isotope shift data. Particularly in the case of the small two- and three-bond isotope shifts, where even modest hydrogen exchange can obscure the true measurement. However, it was shown that the most diagnostic isotope shifts are both the largest and increase further in magnitude upon salt-bridge formation. Firstly, the large size of the one-bond  $^{15}\text{N}$  isotope shift renders the measurement intrinsically less sensitive to hydrogen exchange when compared to the smaller two- and three-bond isotope shifts. Secondly, as the salt-bridge induces an *increase* in the size of the isotope shift it is unlikely to be confused with hydrogen exchange as that would result in a *decrease* in the apparent isotope shift. Both effects combine to ensure that the observation of an increased  $^1\Delta^{15}\text{N}^\epsilon(\text{H}^\epsilon)$  isotope shift is the result of the presence of a salt-bridge.

The effect of a salt-bridge on the magnitude of the deuterium isotope shift was shown to transfer well to the study of isotopically labelled protein samples. A total of 19 arginine side-chains across two different proteins were studied using this method with three residues being identified as being engaged in side-on salt-bridges with aspartic or glutamic acid residues. Each of the three residues, two in Barnase and one in T4L99A, were shown to be involved in salt-

#### *4. Deuterium Isotope Shifts: Detection of Salt-Bridges*

bridges by X-ray crystallography whilst the remaining 16 were not. The ability to identify a specific class of interaction (here, a side-on salt-bridge) amongst several generally 'interacting' residues can provide an atomic-level 'image' of the solution-state protein and in cases where X-ray data is missing or otherwise unobtainable. The ease at which one can obtain the isotope shift measurements will allow this method of detecting interacting arginine residues to become a valuable technique, generally applicable to protein samples of biological interest.

#### *4. Deuterium Isotope Shifts: Detection of Salt-Bridges*

# 5

## HX in Intrinsically Disordered Proteins

### 5.1 Introduction

As discussed in Chapter 3, the exchange rate of the labile amide protons of the protein backbone can report on local interactions and provide an insight into the tertiary structure of the molecule. In acknowledgement of the importance of these insights, numerous experimental strategies exist to facilitate the measurement of residue-specific hydrogen exchange rates. Whilst all of the NMR based methods currently employ  $^1\text{H}$ -detection, it was shown that by using a  $^{13}\text{C}$ -detected experiment useful exchange rate data could be obtained for the  $\text{H}^\epsilon$  nucleus of arginine residues and subsequently used to identify side-chain interactions within the protein. The use of  $^{13}\text{C}$ -detection was required for the specific case of the arginine guanidinium group but it is equally applicable to the protein backbone. This Chapter describes the modification of the ASHDEX experiment described in Chapter 3 to allow the measurement of the backbone amide hydrogen exchange rates using  $^{13}\text{C}$ -detection.

The more favourable transverse relaxation properties and the removal of the requirement for solvent suppression can make the use of  $^{13}\text{C}$  over  $^1\text{H}$  for detection advantageous to the spectroscopist but a switch to  $^{13}\text{C}$ -detection can also be useful in situations where two (or more) signals of interest by chance have the same  $^1\text{H}/^{15}\text{N}$  frequency. Figure 5.1a shows the  $^1\text{H}$ - $^{15}\text{N}$  HSQC spectrum of T4 Lysozyme, a 164 amino acid protein studied extensively in the previous Chapters. Whilst the two-dimensional experiment provides sufficient peak dispersion for the majority of residues, the cross-peaks for I58, D127 and N163 are significantly overlapped in both  $^1\text{H}$  and  $^{15}\text{N}$  frequency. As the available  $^1\text{H}$ -detected NMR experiments for measuring hydrogen exchange rely on a combination of the  $^1\text{H}$  and/or  $^{15}\text{N}$  frequencies for a residue specific measurement, this overlap would make it impossible to obtain individual exchange rates for these three residues. Figure 5.1b shows the analogous  $^{13}\text{C}$ -detected HSQC spectrum (CO-N)<sup>[218]</sup> in which the three previously overlapped residues are easily resolved using the  $^{13}\text{C}$  chemical shift of the carbonyl group (C') of the preceding residue. Of course, there are now likely to be residues overlapped that were previously resolved in the  $^1\text{H}$ - $^{15}\text{N}$  HSQC spectrum so one approach is not implicitly

## 5. HX in Intrinsically Disordered Proteins

superior to the other and the most appropriate detection strategy will clearly depend on the molecule under study. The additional option of a  $^{13}\text{C}$ -detected experiment for probing hydrogen exchange is therefore expected to be useful to the NMR spectroscopist.

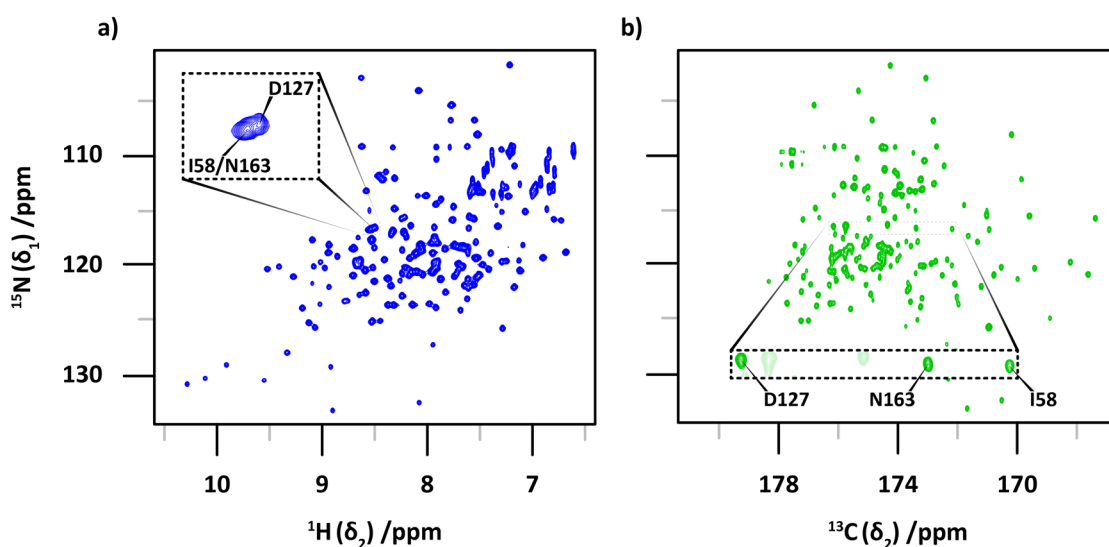


**Figure 5.1** Using  $^{13}\text{C}$ -detection to overcome signal overlap encountered in  $^1\text{H}$ -detected NMR spectra. The  $^1\text{H}$ - $^{15}\text{N}$  HSQC spectrum (a) of T4WT recorded at 14.1 T shows the almost complete overlap of residues I58, D127 and N163 whilst the  $^{13}\text{C}$ -detected CO-N spectrum (b) recorded on the same sample shows a well resolved peak for each of these three residues.

### 5.1.1 Intrinsically Disordered Proteins

Intrinsically Disordered Proteins (IDPs)<sup>[219]</sup> are a type of molecule where one is expected to run into severe signal overlap problems when studying them by  $^1\text{H}$ - $^{15}\text{N}$  HSQC spectra.<sup>[220]</sup> As the name suggests, this class of proteins lack a defined tertiary structure and instead exist in solution as highly flexible chains that transiently sample numerous different conformations. The interest in IDPs in the last few decades has significantly grown, and they have been implicated in several neurodegenerative diseases such as Alzheimer's<sup>[221]</sup> and Parkinson's.<sup>[222]</sup> Whilst the flexible nature of these unstructured proteins hampers the crystallisation process required for study by X-ray crystallography, solution-state NMR spectroscopy is well suited to the characterisation of such molecules.<sup>[223]</sup> However, the chemical shift dispersion<sup>[223]</sup> of the  $^1\text{H}$  signals in a typical  $^1\text{H}$ - $^{15}\text{N}$  HSQC spectrum of an IDP is rather poor. For example, whilst the signals in the  $^1\text{H}$  dimension of the HSQC spectrum of globular protein T4WT span over 4 ppm, they span less than 1 ppm in the spectrum of human  $\alpha$ -synuclein ( $\alpha\text{S}$ ), a 140 amino acid IDP (Figure 5.2a). The primary reason for this is that the  $^1\text{H}$  chemical shift of the backbone amides is significantly affected by their local environment and interactions with other residues as a consequence of tertiary structure have a large contribution to the observed chemical shift. As this tertiary structure is typically absent in an IDP, each amide proton presents with a very similar  $^1\text{H}$  chemical shift. The same trend in chemical shift is observed for globular proteins that have unfolded due to instability or through addition of an unfolding agent such as guanidine. In fact, when studying a new batch of

laboratory-produced protein for the first time, the dispersion of the  $^1\text{H}$  signals in an NMR spectrum is one of the first pieces of experimental data gathered in order to confirm the presence of a well folded sample.<sup>[224]</sup>

For the heavy nuclei of the backbone (particularly  $^{13}\text{C}'$  and  $^{15}\text{N}$ ), the observed chemical shift is more dependent on the primary structure of the molecule than on the local environment of the nucleus or on intramolecular interactions with neighbouring residues.<sup>[225–227]</sup> For the amide  $^{15}\text{N}$ , a wide range of chemical shifts is observed in both folded proteins (T4WT,  $\sim 30$  ppm) and IDPs ( $\alpha\text{S}$ ,  $\sim 25$  ppm). For the  $^{13}\text{C}'$  nuclei, the range of chemical shifts observed in IDPs is narrower ( $\alpha\text{S}$ ,  $\sim 6$  ppm) than for folded proteins (T4WT,  $\sim 10$  ppm) but the narrowing effect of unfolding is less pronounced than it is for the  $^1\text{H}$  chemical shift (Figure 5.2). The  $^{13}\text{C}'$  nuclei, whilst less affected than the  $^1\text{H}$  nuclei, are known to be sensitive to local environment and are often used to determine the presence of secondary structure elements such as  $\alpha$ -helices or  $\beta$ -sheets.<sup>[228,229]</sup>

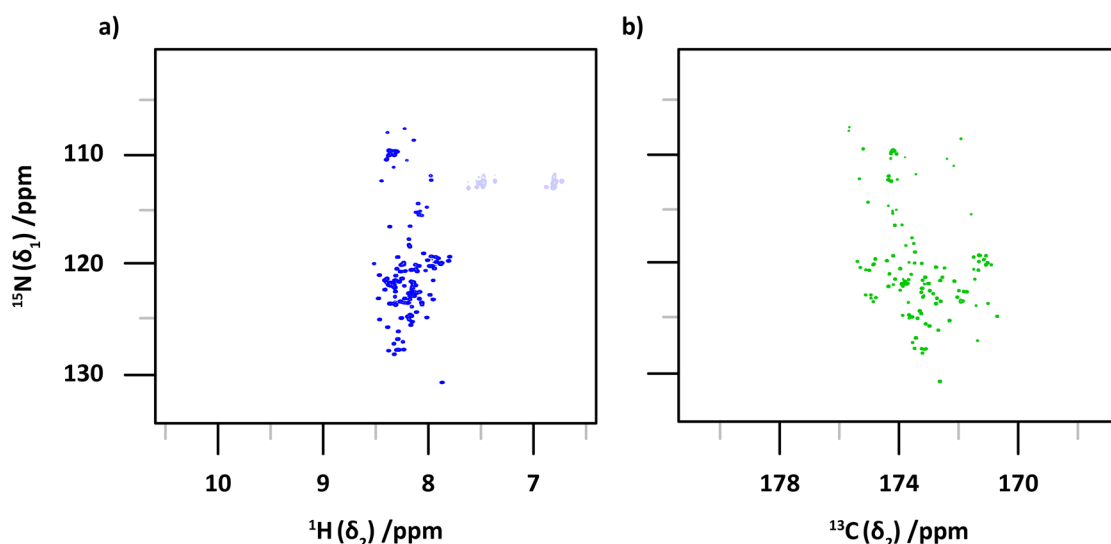


**Figure 5.2**  $^1\text{H}$ - $^{15}\text{N}$  HSQC (a) and CO-N (b) spectra of  $\alpha\text{S}$  recorded at 14.1 T. The absence of tertiary structure of the IDP causes significant overlap of the  $^1\text{H}$  frequencies. The  $^{13}\text{C}'$  and  $^{15}\text{N}$  are less affected and so the CON spectrum often provides superior resolution to the  $^1\text{H}$ - $^{15}\text{N}$  HSQC. For clarity, the spectra in this Figure have been plotted on the same scale as for Figure 5.1.

As well as the poor  $^1\text{H}$  signal dispersion, a second complication encountered during the study of IDPs concerns the hydrogen exchange rate of the amide protons. The absence of a stable tertiary structure allows the facile chemical exchange of the amide protons with solvent molecules and so not only are the  $^1\text{H}$ -detected cross-peaks highly overlapped, they are often of low intensity unless the data is acquired at a low pH or temperature. This is not a problem when using the  $^{13}\text{C}'$  nucleus for excitation and detection as the exchange of the  $^1\text{H}$  nuclei have no bearing on the amount of available magnetisation. However, as demonstrated for the arginine residues investigated in Chapter 3, the residue-specific hydrogen exchange rates can provide valuable insights into intramolecular interactions present within the protein.

## 5. HX in Intrinsically Disordered Proteins

In recent years, the favourable dispersion of the  $^{13}\text{C}'$  signals of IDPs compared to the corresponding  $^1\text{H}$  signals has resulted in the development of entire families of  $^{13}\text{C}$ - $^{15}\text{N}$  detected NMR pulse sequences specifically designed to probe unstructured proteins. Among the first sequences to be reported were the CBCACON<sup>[236]</sup> and COCON experiments that allow the chemical shift assignment of the  $^{15}\text{N}$ ,  $^{13}\text{C}'$ ,  $^{13}\text{C}^\alpha$  and  $^{13}\text{C}^\beta$  nuclei of IDPs without the need for any  $^1\text{H}$  detection. Further experiments have been developed to measure residue-specific relaxation rates and thus provide an insight into local dynamics. Despite the growing interest in IDPs and the utility of  $^{13}\text{C}$ -detection, no NMR experiments explicitly designed to probe the hydrogen exchange reactions using  $^{13}\text{C}$ -detection have currently been reported.

## 5.2 Theory and Method Development

Although it is not directly applicable to the study of backbone hydrogen exchange, the ASHDEX experiment described in Chapter 3 can be made so with only a few simple modifications. This is possible by recognising that the spin-system that makes up the arginine guanidinium group is reminiscent of the spin-system found in the peptide bonds that make up the protein backbone (Figure 5.3). The  $^{13}\text{C}^\zeta$  nucleus of arginine is analogous to the backbone  $^{13}\text{C}'$  atom whilst the  $^1\text{H}^\epsilon$  and  $^{15}\text{N}^\epsilon$  nuclei are similar to the amide  $^1\text{H}$  and  $^{15}\text{N}$  nuclei. In both spin systems, the  $^{15}\text{N}^{(\epsilon)}$  nucleus is additionally bonded to an aliphatic carbon atom:  $^{13}\text{C}^\delta$  in arginine and  $^{13}\text{C}^\alpha$  in the protein backbone.

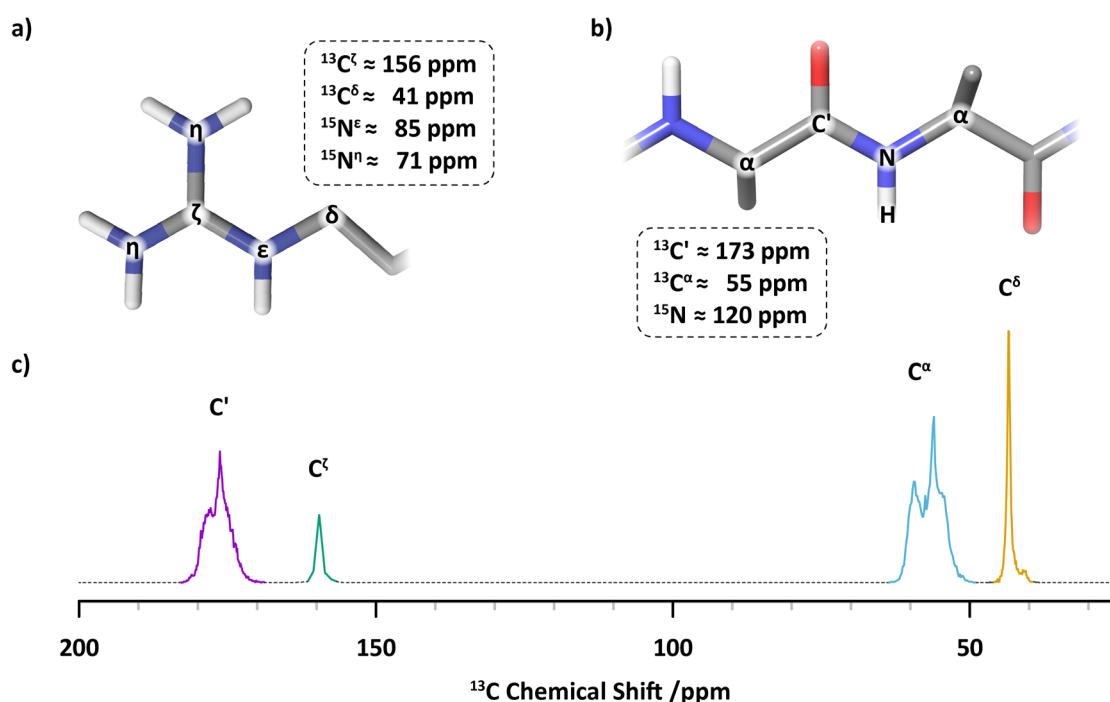


**Figure 5.3** The structure and typical chemical shifts observed in a) the guanidinium group of the arginine side-chain and b) the peptide bond that makes up the protein backbone. c) The range of  $^{13}\text{C}$  chemical shifts reported in the Biological Magnetic Resonance Data Bank (BMRB) for the  $\text{C}'$ ,  $\text{C}^\zeta$ ,  $\text{C}^\alpha$  and  $\text{C}^\delta$  nuclei of arginine. The chemical shifts are binned in steps of 0.1 ppm and comprise 35,533  $\text{C}'$ , 750  $\text{C}^\zeta$ , 50,313  $\text{C}^\alpha$  and 28,000  $\text{C}^\delta$  shifts.

The one-bond  $^1\text{H}$ - $^{15}\text{N}$  and  $^{15}\text{N}$ - $^{13}\text{C}'$  scalar couplings that mediate the transfer of magnetisation throughout the NMR experiment are also of similar magnitude to the  $^1\text{H}^\epsilon$ - $^{15}\text{N}^\epsilon$  and  $^{15}\text{N}^\epsilon$ - $^{13}\text{C}^\zeta$  couplings in arginine. These similarities make it possible to design an NMR experiment that starts by selectively polarising the protonated backbone  $^{15}\text{N}[\text{H}]$  nuclei using the  $^1\text{H}$ - $^{15}\text{N}$  scalar coupling before an incremented mixing time allows the chemical exchange with  $^2\text{H}_2\text{O}$  to proceed. As with the ASHDEX experiment, a semi-constant time chemical shift evolution period will then encode the  $^{15}\text{N}$  frequency, resolving the  $^{15}\text{N}[\text{H}]$  and  $^{15}\text{N}[\text{H}]$  species followed by transfer to the  $^{13}\text{C}'$  for detection via the  $^{15}\text{N}$ - $^{13}\text{C}'$  scalar coupling. A slight difference is encountered here as where the  $^{13}\text{C}^\zeta$  nucleus of arginine is bonded to the two  $^{15}\text{N}^\eta$  nuclei, the backbone  $^{13}\text{C}'$  nucleus is bonded to oxygen (NMR-silent) and a second  $^{13}\text{C}^\alpha$  atom. This difference has implications for the decoupling strategy used during detection, as discussed later in this Chapter.

### 5.2.1 Frequency-Selective $^{13}\text{C}$ Refocussing Pulses

A critical part of the ASHDEX experiment is the semi-constant time chemical shift evolution period discussed in detail in Section 3.2.3 during which in-phase  $N_y^\epsilon$  is transferred to anti-phase  $2C_z^\zeta N_x^\epsilon$  magnetisation whilst the  $^{15}\text{N}^\epsilon$  shift is simultaneously encoded. The selective evolution of the  $^{15}\text{N}^\epsilon$ - $^{13}\text{C}^\zeta$  coupling rather than  $^{15}\text{N}^\epsilon$ - $^{13}\text{C}^\delta$  is made possible by exploiting the large chemical shift difference between  $^{13}\text{C}^\zeta$  and  $^{13}\text{C}^\delta$  (approx. 115 ppm) using frequency selective refocussing pulses. To adapt the experiment to the protein backbone, these refocussing pulses must be made selective for the  $\text{C}'$  and  $\text{C}^\alpha$  nuclei instead. Figure 5.3c shows the range of  $^{13}\text{C}$  chemical shifts reported in the Biological Magnetic Resonance Data Bank (BMRB) for the  $\text{C}'$ ,  $\text{C}^\zeta$ ,  $\text{C}^\alpha$  and  $\text{C}^\delta$  nuclei of arginine, revealing a similarly large chemical shift difference between the  $^{13}\text{C}'$  and  $^{13}\text{C}^\alpha$  nuclei (approx. 118 ppm) that enables the application of the semi-constant time strategy to the backbone atoms.

Aside from the difference in chemical shift, it is also evident from Figure 5.3c that the range of shifts exhibited by the  $\text{C}'$  and  $\text{C}^\alpha$  nuclei is greater than for the  $\text{C}^\zeta$  and  $\text{C}^\delta$  nuclei. This results in a need for selective pulses with a slightly increased bandwidth for the semi-constant time block to function correctly. For the original ASHDEX sequence,  $180^\circ$  SEDUCE pulses of  $300\ \mu\text{s}$  (at 14.1 T) provided sufficient bandwidth for the effective manipulation of the  $\text{C}^\zeta$  and  $\text{C}^\delta$  scalar couplings owing to the relatively narrow chemical shift range of these nuclei. However, the same pulses do not provide sufficient bandwidth to adequately cover the full chemical shift range of the  $\text{C}'$  and  $\text{C}^\alpha$  nuclei (Figure 5.4a). To provide the required bandwidth, the SEDUCE pulses were replaced with REBURP pulses (1.25 ms for  $\text{C}'$  and 0.75 ms for  $\text{C}^\alpha$  at 14.1 T, Figure 5.4b). The flatter excitation profile of the REBURP (or SNOB) pulses provide very good refocussing over a much wider chemical shift than the corresponding SEDUCE pulses. It is important to note that Figures

## 5. HX in Intrinsically Disordered Proteins

5.3 and 5.4 were generated using experimental data from only the arginine side-chain and whilst it is true that the chemical shift ranges of C' and C $\alpha$  in arginine are representative of most other amino acids, glycine is a notable exception. Glycine is the only amino acid that lacks a C $\beta$  atom and as such the C $\alpha$  chemical shift is significantly lower than usual (around 45 ppm). This low chemical shift is well outside of the bandwidth of the SEDUCE pulse but is adequately covered by the REBURP pulse.

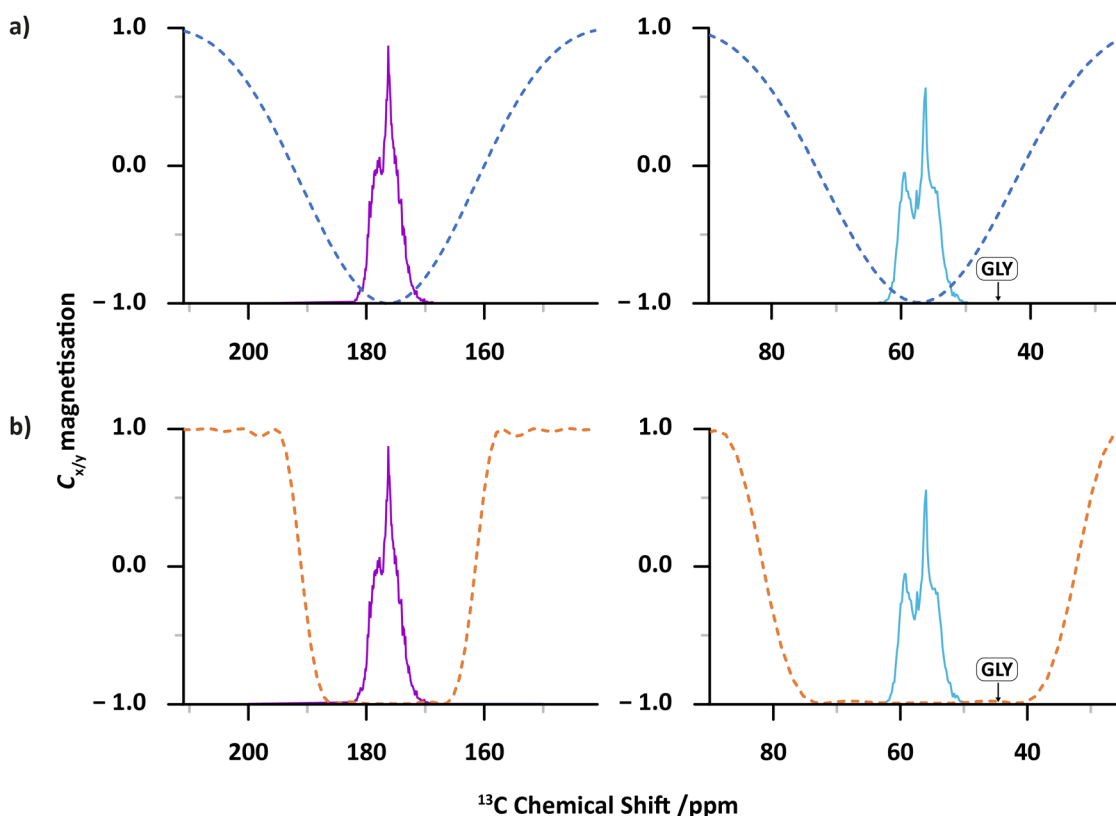


**Figure 5.4** The effective bandwidth of  $^{13}\text{C}$  refocussing pulses using a) SEDUCE or b) REBURP shapes on the C' (left) and C $\alpha$  (right) nuclei. The dashed lines indicate the frequency dependent inversion caused by the pulse with a value of 1.0 indicating no inversion and a value of -1.0 indicating complete inversion. The excitation profiles were calculated using TopSpin 4.0.9 (Bruker, 2020): C' and C $\alpha$  SEDUCE pulses had a duration of 300  $\mu\text{s}$  and a power level of 1.8 kHz; the REBURP pulses were 1.25 ms at a power level of 4.9 kHz (C') and 0.75 ms at a power level of 8.0 kHz (C $\alpha$ ). The chemical shift scale is calculated for a 14.1 T instrument (150 MHz  $^{13}\text{C}$  frequency). The chemical shift data is taken from Figure 5.3.

The final step in the experiment concerns the refocussing of the  $^{15}\text{N}$ -chemical shift encoded anti-phase  $2C_zN_x$  coherences into in-phase carbon magnetisation for detection. The selective  $^{15}\text{N}^{\epsilon}$  refocussing pulse in the retro-INEPT of the ASHDEX experiment (used to suppress the C $^{\zeta}$ -N $^{\delta}$  scalar coupling pathways) is not required and can be replaced with a non-selective  $180^\circ$   $^{15}\text{N}$  pulse. However, a selective  $^{13}\text{C}'$  pulse is required to suppress the homonuclear C'-C $\alpha$  coupling during the retro-INEPT (Figure 5.5). This will ensure that only the C'-N scalar coupling is active and will allow the correct refocussing of the  $2C_zN_x$  magnetisation for detection. The reason a hard  $180^\circ$   $^{13}\text{C}$  pulse is sufficient at this point in the ASHDEX experiment is because the two-bond C $^{\zeta}$ -C $\delta$  scalar coupling is negligible.

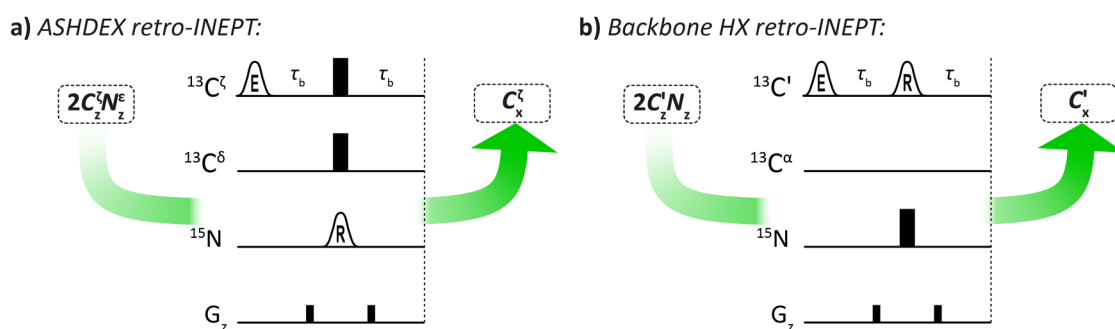


**Figure 5.5** a) The retro-INEPT used in the ASHDEX sequence utilises a selective  $^{15}\text{N}^E$  pulse in conjunction with a hard  $^{13}\text{C}$  pulse that allows only the desired  $\text{C}^z\text{-N}^E$  coupling to evolve. The selective  $^{15}\text{N}$  pulse prevents the competing heteronuclear  $\text{C}^z\text{-N}^H$  couplings from evolving. b) The retro-INEPT suitable for the backbone peptide spin-system requires a selective  $^{13}\text{C}$  pulse and a hard  $^{15}\text{N}$  to allow only the desired  $\text{C}^z\text{-N}$  coupling to evolve. The selective  $^{13}\text{C}$  pulse prevents the competing homonuclear  $\text{C}^z\text{-C}^\alpha$  coupling from evolving.

### 5.2.2 $^{13}\text{C}^\alpha$ Decoupling During Acquisition

Following the modifications to the ASHDEX sequence discussed above, the experiment was applied to a sample of human U- $^{13}\text{C}, ^{15}\text{N}$ -ubiquitin (Ubq, 76 amino acids) with the in-phase  $\text{C}^z$  magnetisation generated by the modified retro-INEPT detected under the usual  $^1\text{H}$  and  $^{15}\text{N}$  decoupling schemes. The resulting  $^{13}\text{C}^z\text{-}^{15}\text{N}$  spectrum (CON) is shown below in Figure 5.6. Immediately apparent in the data is the undesired effect of the  $^1J_{\text{C}^z\text{C}^\alpha}$  scalar coupling on the detected cross-peaks. The problem caused by evolution of the  $\text{C}^z\text{-C}^\alpha$  coupling during acquisition is two-fold: the number of cross-peaks in the spectrum is doubled and consequently the signal-to-noise of each is halved. These are clearly undesirable features and work to complicate the final spectrum and thus hinder any subsequent analysis.

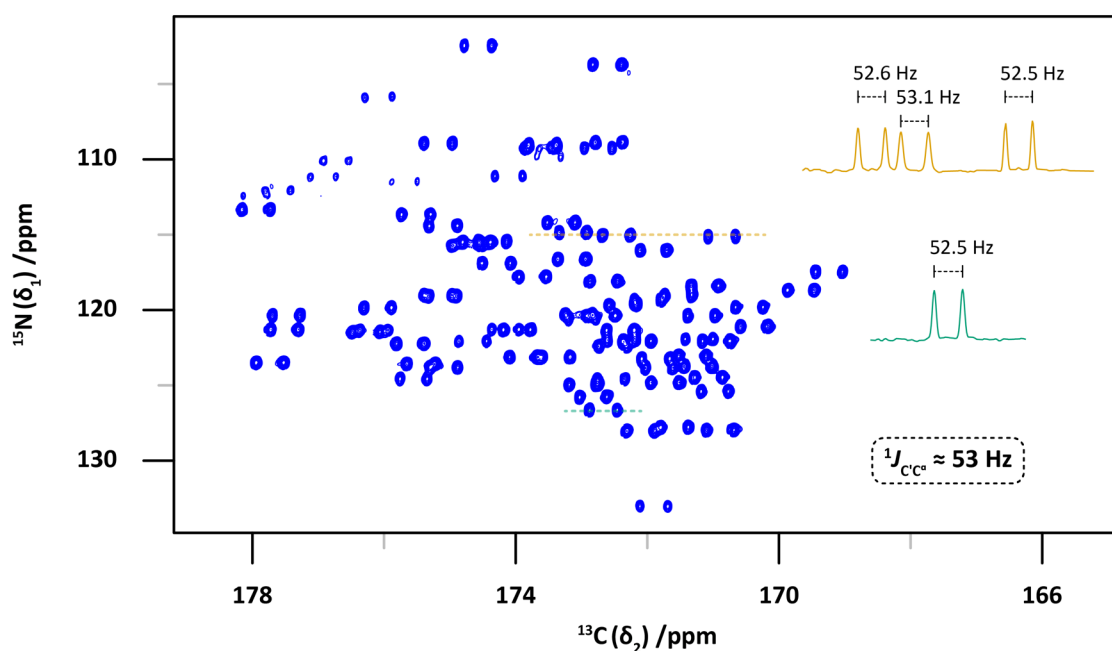


**Figure 5.6**  $^{13}\text{C}^z\text{-}^{15}\text{N}$  spectrum recorded on a sample of U- $^{13}\text{C}, ^{15}\text{N}$ -ubiquitin at 11.7 T using the ASHDEX sequence with the modifications described above. Each cross-peak appears as a doublet due to the evolution of the  $^1J_{\text{C}^z\text{C}^\alpha}$  scalar coupling during acquisition consequently doubling the number of peaks whilst halving the signal-to-noise.

## 5. HX in Intrinsically Disordered Proteins

The difficulty with the C'-C $\alpha$  coupling is that it is *homonuclear* and therefore one is not simply able to turn on  $^{13}\text{C}$  decoupling during the acquisition period as doing so would also suppress the desired  $^{13}\text{C}'$  signals. Fortunately, there are a number of alternate decoupling strategies available that enable the suppression of this particular scalar coupling.

### a. Band-Selective Homonuclear Decoupling (BASH)

Whilst it is true that the spectrometer cannot deliver a  $^{13}\text{C}$  RF pulse and simultaneously detect the decay of the  $^{13}\text{C}$  magnetisation, it is possible to achieve the required homonuclear decoupling in real time. In a Band-Selective Homonuclear Decoupling (BASH)<sup>[237,238]</sup> scheme, rather than the detection of a single continuous FID, the acquisition period is split up into a series of smaller *chunks* in between which the evolution of the undesired scalar coupling is manipulated in a controlled fashion. The technique is based on the idea that the sense of the coupling can be reversed using a selective RF pulse in between successive chunks so that any *J*-evolution during one chunk is refocused during the following chunk. The individual chunks are then stitched together to form the 'decoupled' FID and provided that the duration of each chunk is kept short enough, the C'-C $\alpha$  coupling is not observed in the transformed spectrum.

Figure 5.7 shows how a BASH decoupling scheme could be implemented to suppress the C'-C $\alpha$  coupling in  $^{13}\text{C}'$ -detected experiments. During the initial experimental setup, the number and duration of the data chunks must be considered bearing in mind the size of the coupling to be suppressed and the total acquisition time to be collected. In order to efficiently remove the impact of the homonuclear coupling has on the final NMR spectrum, each data chunk must be kept shorter than  $\sim 1/5J$  which for the 53 Hz C'-C $\alpha$  coupling corresponds to 3.8 ms. The individual chunks are collected as many times as necessary to build up the desired FID. For a typical acquisition time (Aq.) of 95 ms, 25 chunks of 3.8 ms are to be collected:

$$\tau_{\text{chunk}} = \frac{1}{5J} \quad n = \frac{\text{Aq.}}{\tau_{\text{chunk}}}$$

When the acquisition period begins, the receiver is opened and the FID is detected for a period equal to half a *chunk* before the receiver is blanked and the dwell timer paused. Two spin echo blocks are then used to manipulate the magnetisation: the first, a *non-selective* spin echo with  $180^\circ$  pulses applied to both  $^{13}\text{C}'$  and  $^{13}\text{C}^\alpha$  inverts only the evolving  $^{13}\text{C}'$  chemical shift (the homonuclear C'-C $\alpha$  scalar coupling continues to evolve); the second, *selective* spin echo with the  $180^\circ$  pulse only applied to  $^{13}\text{C}'$  inverts the C'-C $\alpha$  scalar coupling *and* the C' chemical shift. The cumulative effect of the successive spin echoes is therefore the inversion of the C'-C $\alpha$  scalar coupling with the evolution of the  $^{13}\text{C}'$  chemical shift unaffected.

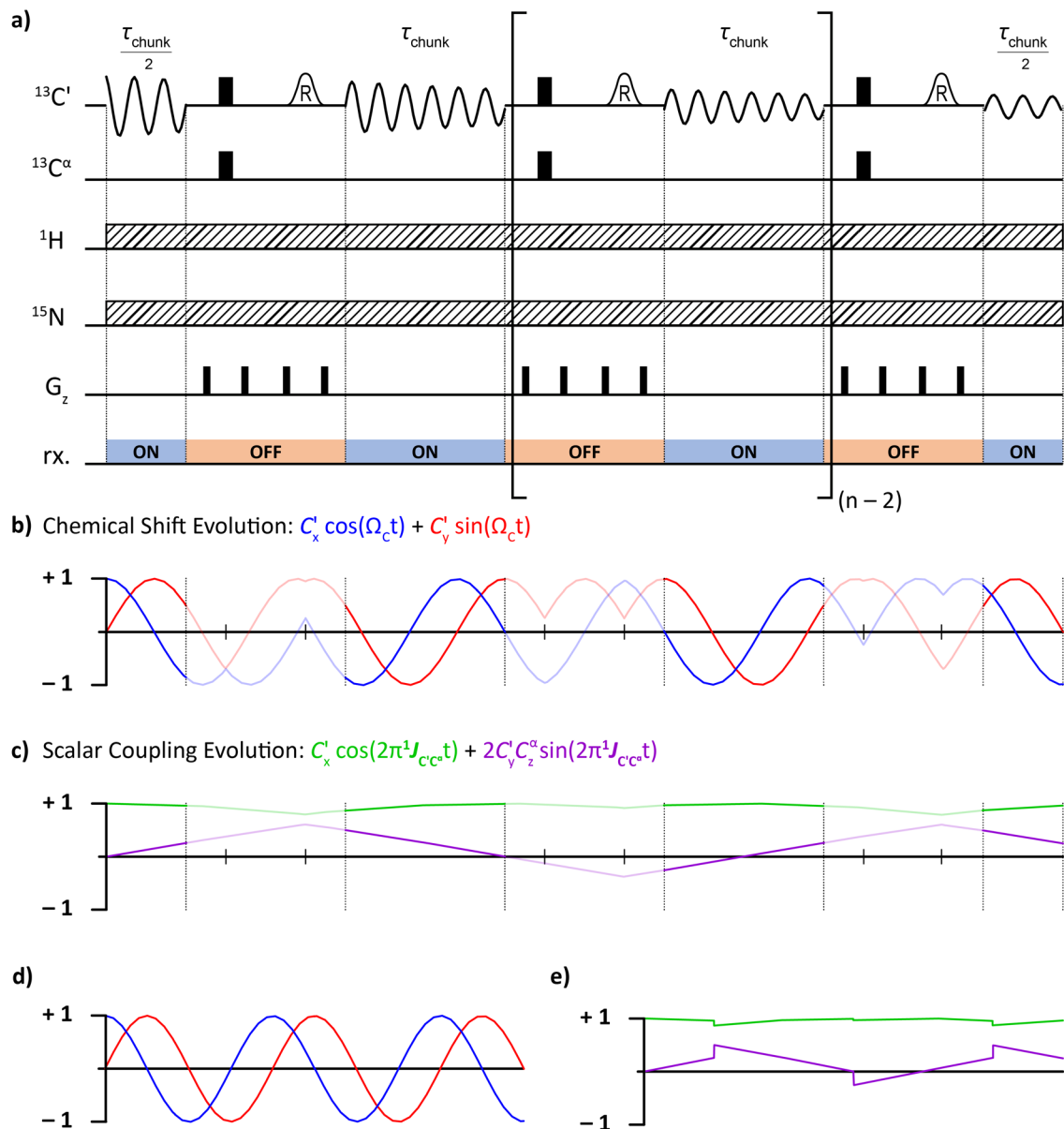


**Figure 5.7** Band-Selective Homonuclear Decoupling. a) Pulse sequence showing how the undesired  $\text{C}'\text{-C}^\alpha$  coupling can be inverted in between successive chunks of data acquisition to effectively decouple the resulting spectrum. Between each chunk, a selective  $180^\circ$   $^{13}\text{C}'$  pulse inverts the coupling so that the evolution during the previous chunk is refocussed in the next chunk. The non-selective  $180^\circ$  pulses undo the inversion of the  $^{13}\text{C}'$  chemical shift also caused by the selective  $^{13}\text{C}'$  pulse. b,c) The evolution of the cosine- and sine-modulated parts of the chemical shift and scalar coupling, respectively. d) The receiver is blanked in between data chunks so that the chemical shift evolution actually collected resembles an uninterrupted FID. e) The evolution of the scalar coupling observed by the receiver is suppressed and thus does not affect the transformed spectrum. Rather than evolving into the anti-phase component, the magnetisation remains in-phase with respect to  $^{13}\text{C}^\alpha$ . The size of the data chunk in this example was chosen to illustrate the effect of the refocussing pulses, a much shorter data chunk would be required to provide efficient decoupling (see main text). For clarity, the effect of relaxation during the sequence is omitted.

The receiver is now re-opened, the dwell timer restarted and data collection resumes for another chunk. The process is then repeated until the total duration of the collected chunks is equal to the desired acquisition time. Note that like the first one, the final acquisition is also half a chunk in duration. The *decoupled* FID is then constructed by stitching together each successive

## 5. HX in Intrinsically Disordered Proteins

data chunk. The result of this process is the smooth chemical shift evolution of the  $^{13}\text{C}'$  magnetisation (Figure 5.7d) whilst the evolution of the  $\text{C}'\text{-C}^\alpha$  scalar coupling is suppressed (Figure 5.7e). The sequential inversion of the  $\text{C}'\text{-C}^\alpha$  coupling throughout the acquisition period mimics a conventional heteronuclear decoupling scheme although it is achieved without having to simultaneously pulse and detect the same nucleus. The BASH decoupled spectrum of Ubq is shown in Figure 5.8 and clearly demonstrates the successful suppression of the  $\text{C}'\text{-C}^\alpha$  doublets.

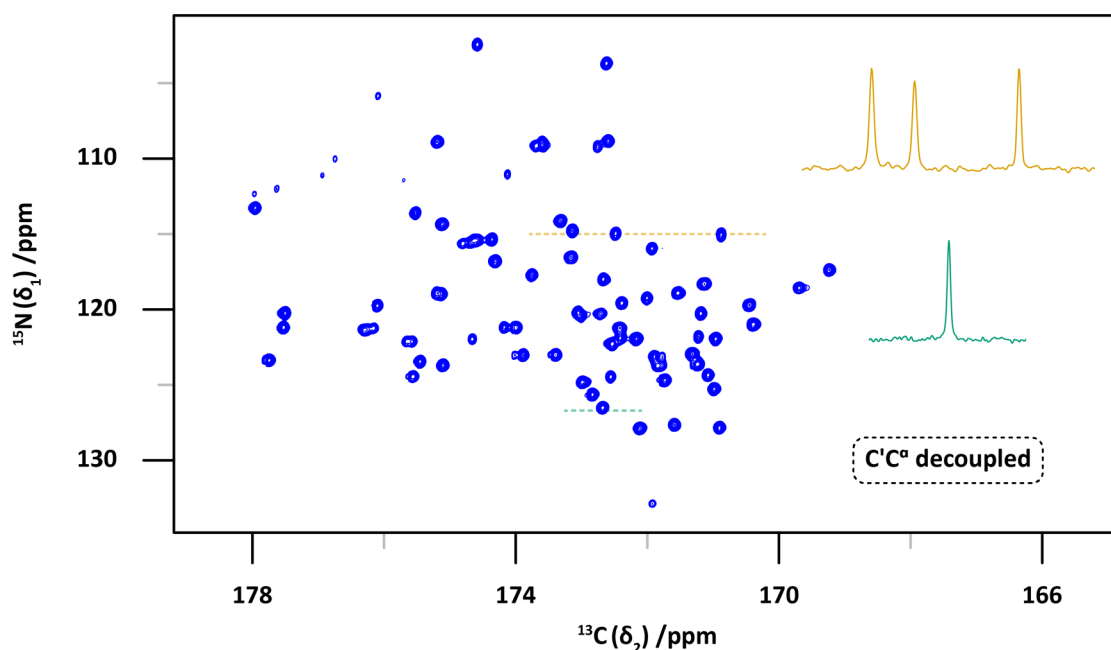


**Figure 5.8**  $^{13}\text{C}'\text{-}^{15}\text{N}$  spectrum recorded on a sample of U- $^{13}\text{C},^{15}\text{N}$ -ubiquitin at 11.7 T with BASH decoupling. Each doublet seen in Figure 5.6 has collapsed to a singlet due to the effective suppression of the  $^1J_{\text{C}'\text{C}^\alpha}$  scalar coupling.

A significant drawback inherent in the BASH decoupling scheme applied above is the requirement for the simultaneous inversion of the  $^{13}\text{C}'$  and  $^{13}\text{C}^\alpha$  frequencies. This is an essential step in order to observe the smooth chemical shift evolution of the  $^{13}\text{C}'$  magnetisation of interest. Unfortunately, where the large chemical shift difference between the  $^{13}\text{C}'$  and  $^{13}\text{C}^\alpha$  nuclei is an advantage when trying to selectively target one over the other, it becomes a considerable disadvantage when trying to target both, particularly on higher field spectrometers. Figure 5.9a shows the effective bandwidth of hard  $180^\circ$   $^{13}\text{C}$  RF-pulse on a 14.1 T (150 MHz  $^{13}\text{C}$  frequency) spectrometer. It is clear from the purple line that even if the  $180^\circ$  pulse is applied between the  $^{13}\text{C}'$  and  $^{13}\text{C}^\alpha$  frequencies ( $\sim 118$  ppm), the effectiveness of the inversion drops below 70% for both nuclei. This would result in a significant loss of detectable magnetisation and result in considerable phase distortions in the final NMR spectrum.

This problem is set to continue, particularly as the magnetic fields available to NMR spectroscopists become larger and larger. For example, 118 ppm ( $^{13}\text{C}$ ) corresponds to  $\sim 18$  kHz at 14.1 T (600 MHz spectrometer) but is  $\sim 30$  kHz at 23.5 T (1.0 GHz). As the bandwidth of a hard

RF-pulse is inversely proportional to the pulse duration and current hardware already delivers the required power in as little as 10  $\mu$ s, there isn't much scope for the required bandwidth increase to be provided by shorter pulses. In order to achieve the required broadband inversion, one must move away from the standard high-power RF-pulses and into the field of *adiabatic* pulses. Figure 5.9b shows the excitation profile of a 2.0 ms composite CHIRP pulse as applied to the  $^{13}\text{C}'$  and  $^{13}\text{C}^\alpha$  nuclei. The **green** line shows very good inversion over a wide chemical shift range indicating that this pulse would be appropriate for the BASH decoupling application.

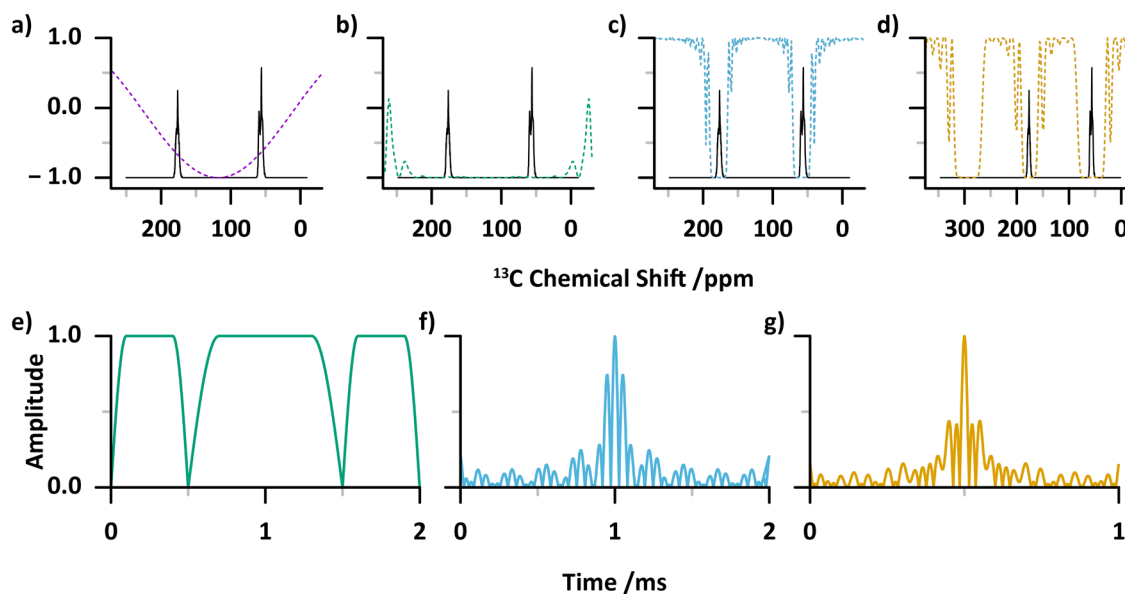


**Figure 5.9** The effective bandwidths of different pulses designed to simultaneously invert the  $^{13}\text{C}'$  and  $^{13}\text{C}^\alpha$  resonances during the BASH decoupling scheme: a) 24  $\mu$ s 20.8 kHz **rectangular** pulse; b) 2.0 ms 9.8 kHz **composite CHIRP** pulse; c) 2.0 ms 8.4 kHz **double-selective  $\text{C}'/\text{C}^\alpha$**  pulse; d) 1.0 ms 20.3 kHz **symmetrical double-selective  $\text{C}'/\text{C}^\alpha$**  pulse. The chemical shift scale is calculated for a 14.1 T instrument (150 MHz  $^{13}\text{C}$  frequency). e-f) The amplitude vs. time profile for the **composite CHIRP**, **double-selective  $\text{C}'/\text{C}^\alpha$**  and **symmetrical double-selective  $\text{C}'/\text{C}^\alpha$**  pulses. Both of the double-selective  $\text{C}'/\text{C}^\alpha$  pulses were optimised using the GRAPE<sup>[239]</sup> algorithm.

However, one must be very wary of the amount of RF power that is being applied. The CHIRP pulses achieve the required wide inversion bandwidths by *sweeping* through the different frequencies rather than by being an intrinsically wide bandwidth pulse. Figure 5.9e shows that the power level (amplitude) applied during the CHIRP pulse is relatively high for most of the 2 ms duration. Integration of Figure 5.9e shows that the power applied during the 2 ms CHIRP pulse is equivalent to a 1.7 ms (84%) rectangular pulse at the same power level. Whilst the peak power (9.8 kHz) is lower than the peak power of the hard pulse (20.8 kHz), it is applied for considerably longer (2 ms vs. 24  $\mu$ s). Considering that this refocussing pulse must be applied in each *decoupling block* described in Figure 5.7a to be effective and they are to be separated by at most 3.8 ms, this would represent a duty cycle of  $\sim$ 45%. This is much too high for an NMR probe to handle at the power levels required and would likely result in hardware damage.

## 5. HX in Intrinsically Disordered Proteins

Recognising that our application only requires the inversion of the two distant frequencies rather than inversion of every frequency *in between* two distant values, one can design *doubly-selective pulses* that specifically invert only the C' and C $\alpha$  nuclei. Figure 5.9c shows the excitation bandwidth of such a pulse (blue line). The double-selective C'/C $\alpha$  pulse shows uniform inversion around both the  $^{13}\text{C}'$  and  $^{13}\text{C}^\alpha$  nuclei whilst causes no inversion at frequencies in between. Crucially, the RF-power required for this pulse is considerably lower. The duration of this pulse is the same as the CHIRP pulse (2 ms) and is applied with a slightly lower peak power level (8.4 kHz). However, the major difference is seen when considering how the power is applied during the pulse. Figure 5.9f shows that the amplitude throughout the pulse is relatively low and only very briefly is the peak power applied. Integration of this profile indicates that the power applied is approximately equivalent to a 200  $\mu\text{s}$  (11%) rectangular pulse and represents a much lower duty cycle of ~5%.

The power requirement of the double-selective C'/C $\alpha$  pulse makes it more suitable for use in the BASH decoupling but it has a different drawback. Owing to the non-symmetrical nature of the pulse with respect to the carrier frequency ( $^{13}\text{C}'$ , 173 ppm), the  $^{13}\text{C}^\alpha$  part of the excitation profile can affect the apparent  $^{13}\text{C}'$  frequency that is detected, a phenomenon known as a *Bloch-Siegert shift*.<sup>[240]</sup> This can cause the  $^{13}\text{C}'$  chemical shifts observed with and without  $^{13}\text{C}^\alpha$  decoupling to differ. To ensure the collection of high-quality data, Bloch-Siegert shifts must be carefully refocussed within a pulse sequence or prevented from arising in the first place. Figure 5.9d shows an alternative inversion pulse suitable for BASH decoupling that directly compensates for any induced Bloch-Siegert shift. The symmetrical double-selective C'/C $\alpha$  pulse results in an excitation profile (yellow) with three effective frequencies. Similar to the pulse described in Figure 5.9c, the pulse targets both the  $^{13}\text{C}'$  and  $^{13}\text{C}^\alpha$  frequency with no inversion in between. However, this new pulse is applied on-resonance with  $^{13}\text{C}'$  and features two symmetrical bands of off-resonance inversion: the first, as discussed provides the required inversion of  $^{13}\text{C}^\alpha$  118 ppm upfield; the second band would invert any  $^{13}\text{C}$  nuclei 118 ppm downfield at around ~290 ppm. Clearly there are no  $^{13}\text{C}$  nuclei within this spin-system at such high frequencies to invert; however, the second off-resonance inversion band (~290 ppm) also induces a Bloch-Siegert shift that *cancels out* any induced by the first band (~118 ppm). The net result of this symmetrical pulse is the inversion of both  $^{13}\text{C}'$  and  $^{13}\text{C}^\alpha$  without the introduction of any distortion of the  $^{13}\text{C}'$  chemical shift. The pulse is applied with a duration of 1.0 ms and a peak power level of 20.3 kHz. Whilst this peak power level is considerably higher than the CHIRP, the pulse is half the length of the CHIRP and as the amplitude profile shows (Figure 5.9g), is much less demanding of the probe in terms of total applied power. Integration of this profile indicates that the pulse is equivalent to a ~100  $\mu\text{s}$  (10%) rectangular pulse and thus represents a duty cycle of ~2.5%.

Although these bespoke selective  $C'/C^\alpha$  pulses are demonstrably superior to the conventional CHIRP pulses as applied to BASH decoupling, even the reduced power levels involved are likely to be pushing the limits of what current NMR probes are designed to withstand. The next section details an alternate means of decoupling the CON spectra that does not place such high power demands on the spectrometer hardware.

### b. Virtual Decoupling (IPAP)

An alternate means of achieving the required homonuclear decoupling is by means of the In-Phase/Anti-Phase (IPAP)<sup>[241]</sup> technique, a form of *virtual decoupling*. Where the BASH approach described above seeks to remove the effect of the  $C'-C^\alpha$  scalar coupling from the detected FID, the IPAP technique actually allows the evolution to proceed before ‘decoupling’ the spectrum in a post-acquisition processing step. The virtual decoupling process requires that *two* complimentary datasets be recorded: the first containing *In-Phase* doublets with respect to the  $C'-C^\alpha$  coupling and the second containing *Anti-Phase* doublets. With these two datasets available, the data can be processed as shown in Figure 5.10 to ‘decouple’ each signal.

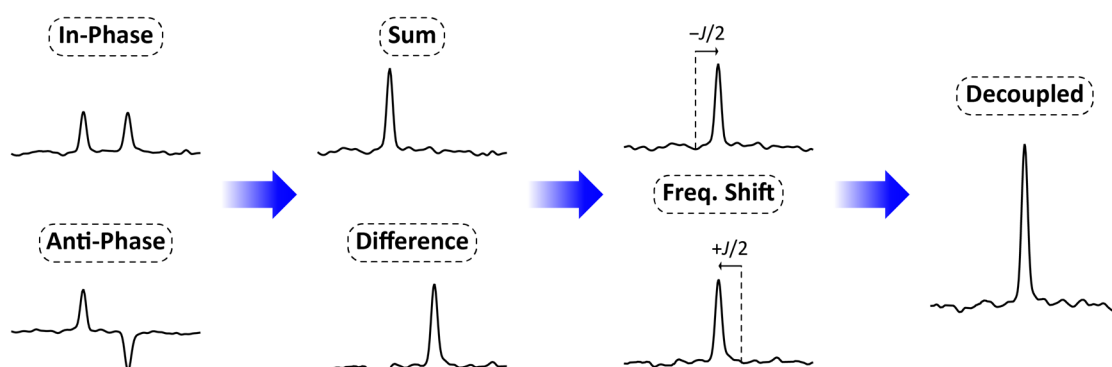


**Figure 5.10** The IPAP decoupling scheme. Linear combinations of in-phase (IP) and anti-phase (AP) datasets isolate each component of the doublet. Each component is then frequency-shifted and summed to provide the ‘decoupled’ signal.

The individual components of each doublet are first isolated by taking the sum and difference of the IP and AP datasets. This results in two new spectra, both containing only singlets. Each spectrum is then subjected to a frequency shift equal to half of the active coupling constant (53 Hz) so that the two components coincide. Finally, the frequency-shifted spectra are combined to provide the decoupled singlet.

The coupled spectrum shown in Figure 5.6 is an example of a suitable in-phase dataset where the  $C'-C^\alpha$  scalar coupling has been refocused during the retro-INEPT transfer. In order to obtain the analogous anti-phase dataset required for the virtual decoupling process, the  $C'-C^\alpha$  scalar coupling must be allowed to evolve such that when the receiver is opened, the magnetisation

## 5. HX in Intrinsically Disordered Proteins

present is proportional to  $2C_\gamma C_z^\alpha$  (anti-phase with respect to  $^{13}\text{C}^\alpha$ ). To avoid additional delays and associated losses due to relaxation, it is prudent to manipulate the  $\text{C}'\text{-C}^\alpha$  coupling during the existing retro-INEPT period. Figure 5.11a shows how the retro-INEPT can be modified to allow the evolution of the  $\text{C}'\text{-C}^\alpha$  coupling and thus the detection of the anti-phase magnetisation.

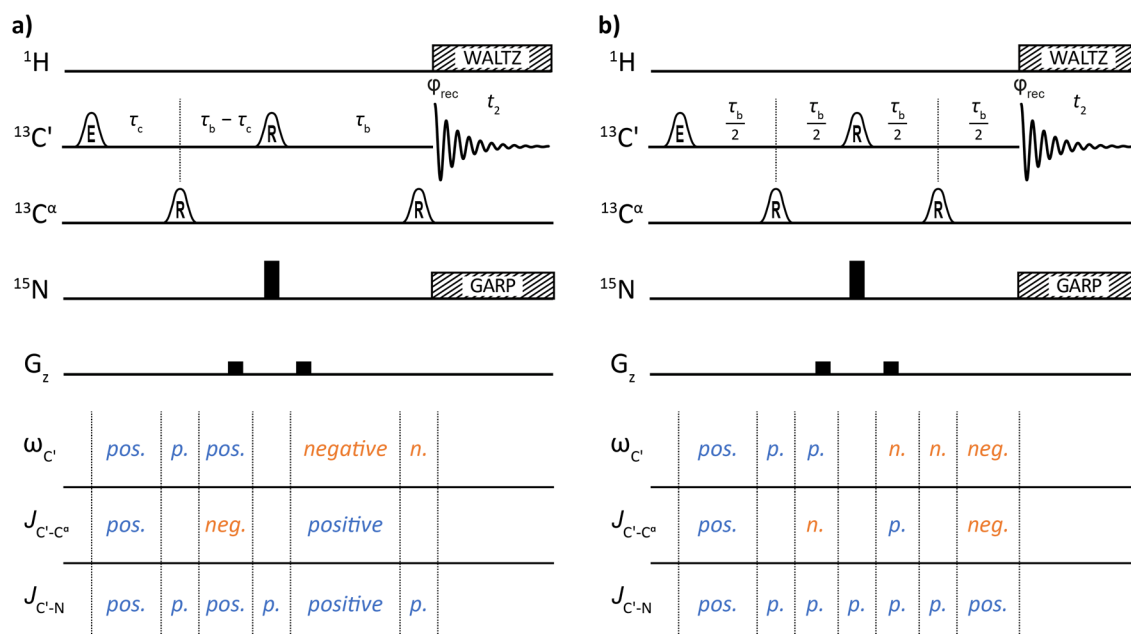


**Figure 5.11** Retro-INEPT blocks suitable for the implementation of the IPAP decoupling scheme. a) Anti-phase (AP) block results in the detection of  $2C_\gamma C_z^\alpha$  magnetisation. b) In-phase (IP) block results in the detection of  $C_x$  magnetisation.

Following the application of the  $^{13}\text{C}'$  excitation pulse to the  $2C_z N_z$  coherence present after the semi-constant time evolution period, the magnetisation evolves under the scalar coupling and free precession Hamiltonians for a fixed delay,  $\tau_c$ . A  $^{13}\text{C}^\alpha$  refocussing pulse then inverts only the  $\text{C}'\text{-C}^\alpha$  coupling before a second fixed delay, calculated as  $\tau_b - \tau_c$ . Simultaneous  $^{13}\text{C}'$  and  $^{15}\text{N}$  pulses then invert the  $\text{C}'\text{-C}^\alpha$  coupling again, this time along with the chemical shift evolution of  $^{13}\text{C}'$ , whilst allowing the  $\text{C}'\text{-N}$  coupling to continue for a third fixed delay,  $\tau_b$ . A final  $^{13}\text{C}^\alpha$  pulse is applied immediately prior to acquisition to account for the chemical shift evolution occurring during the first  $^{13}\text{C}^\alpha$  pulse. The total evolution of each of the pathways during the modified retro-INEPT block can be expressed as:

$$\begin{aligned} \omega_{\text{C}'} &= \tau_c + \text{sel.}^{13}\text{C}^\alpha + \tau_b - \tau_c - \tau_b - \text{sel.}^{13}\text{C}^\alpha \\ &= \mathbf{0} \end{aligned}$$

$$\begin{aligned} J_{\text{C}'\text{-C}^\alpha} &= \tau_c - \tau_b + \tau_c + \tau_b \\ &= \mathbf{2\tau_c} \end{aligned}$$

$$\begin{aligned} J_{\text{C}'\text{-N}} &= \tau_c + \text{sel.}^{13}\text{C}^\alpha + \tau_b - \tau_c + \text{sel.}^{13}\text{C}' + \tau_c + \tau_b + \text{sel.}^{13}\text{C}^\alpha \\ &= \mathbf{2\tau_b} + (\text{sel.}^{13}\text{C}' + 2\text{sel.}^{13}\text{C}^\alpha) \end{aligned}$$

So, during the retro-INEPT chemical shift evolution of the  $^{13}\text{C}'$  magnetisation is completely refocussed whilst the homonuclear  $\text{C}'\text{-C}^\alpha$  coupling evolves for a period of  $2\tau_c$ . Setting the duration of the delay  $\tau_c$  to  $1/4J$  ( $J = 53 \text{ Hz}$ ,  $\tau_c = 4.72 \text{ ms}$ ) maximises the desired anti-phase component:

$$C_x \xrightarrow{2\pi J_{CC} C_2 C_2^\alpha \tau_c} C_x \cos(2\pi J_{CC} \tau_c) - 2C_y C_2^\alpha \sin(2\pi J_{CC} \tau_c)$$

$$\text{Let } \tau_c = \frac{1}{4J}$$

$$C_x \xrightarrow{2\pi J_{CC} C_2 C_2^\alpha \tau_c} C_x \cos\left(\frac{\pi}{2}\right) - 2C_y C_2^\alpha \sin\left(\frac{\pi}{2}\right) = -2C_y C_2^\alpha$$

As discussed previously, the retro-INEPT must also ensure that the  $\text{C}'\text{-N}$  coupling evolves for a period of  $2\tau_b$ . This is achieved by the anti-phase INEPT block in Figure 5.11a though it is important to note that as the  $\text{C}'\text{-N}$  also evolves during the selective  $^{13}\text{C}$  pulses, it is necessary to account for the *extra* evolution when computing the delays. The anti-phase CON spectrum of Ubq recorded using this retro-INEPT block is shown in Figure 5.12, clearly showing the anti-phase doublets. As the detected magnetisation,  $2C_y C_2^\alpha$ , is orthogonal to the in-phase magnetisation ( $C_x$ ) shown in Figure 5.6, a  $90^\circ$  phase correction has been applied

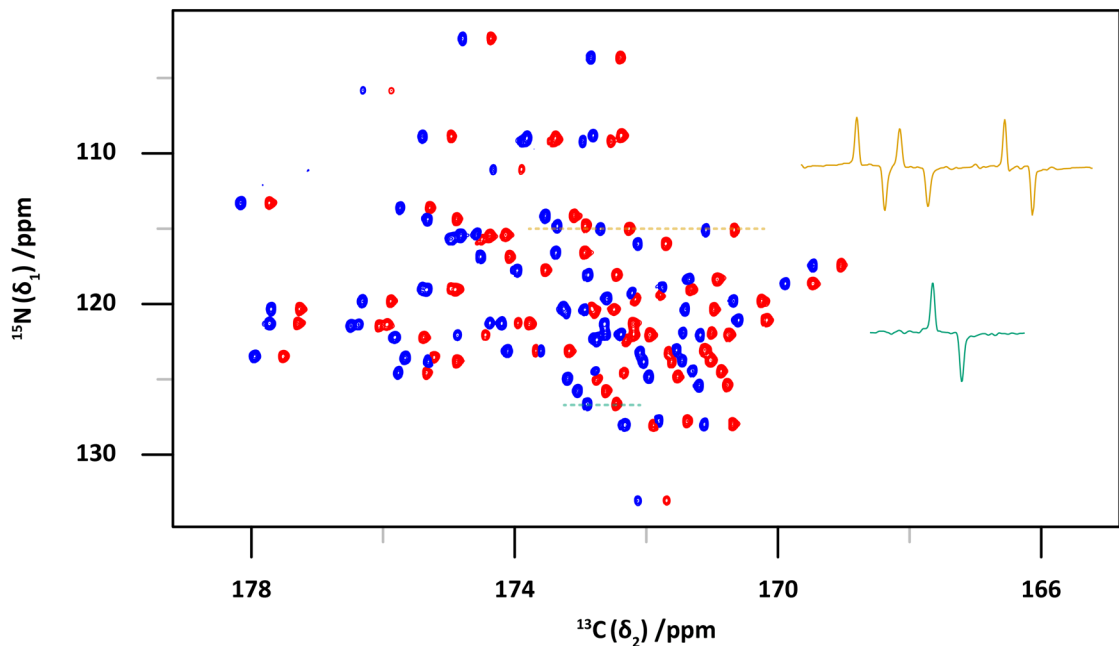


**Figure 5.12** Anti-phase  $^{13}\text{C}'\text{-}^{15}\text{N}$  spectrum recorded on a sample of U- $^{13}\text{C},^{15}\text{N}$ -ubiquitin at 11.7 T. A  $90^\circ$  phase correction has been applied compared to the in-phase data shown in Figure 5.6.

Whilst the retro-INEPT block described in Figure 5.5b does provide in-phase data suitable for IPAP decoupling, it does not contain the selective  $^{13}\text{C}^\alpha$  pulses applied during the anti-phase INEPT. In order to preserve the RF load on the sample between the in-phase and anti-phase

## 5. HX in Intrinsically Disordered Proteins

datasets, the in-phase retro-INEPT block shown in Figure 5.11b is considered more appropriate as it contains exactly the same pulses as the anti-phase block. This ensures that any artefacts arising from pulse imperfections or sample heating are identical between the in-phase and anti-phase datasets and ultimately leads to higher quality spectral data after the decoupling process is applied. As for the anti-phase sequence, the in-phase element begins with a selective  $^{13}\text{C}'$  excitation pulse applied to the  $2C_2N_2$  magnetisation. Selective  $^{13}\text{C}$  refocussing pulses, alternating between  $^{13}\text{C}'$  and  $^{13}\text{C}^\alpha$ , are then applied between equal delays of  $\tau_b/2$ . As before, the  $^{13}\text{C}'$  refocussing pulse is applied simultaneously with a  $^{15}\text{N}$  pulse. The total evolution of each of the pathways during the modified retro-INEPT block can be expressed as:

$$\begin{aligned}\omega_{\text{C}'} &= \frac{\tau_b}{2} + \text{sel. } ^{13}\text{C}^\alpha + \frac{\tau_b}{2} - \frac{\tau_b}{2} - \text{sel. } ^{13}\text{C}^\alpha - \frac{\tau_b}{2} \\ &= \mathbf{0} \\ J_{\text{C}'-\text{C}^\alpha} &= \frac{\tau_b}{2} - \frac{\tau_b}{2} + \frac{\tau_b}{2} - \frac{\tau_b}{2} \\ &= \mathbf{0} \\ J_{\text{C}'-\text{N}} &= \frac{\tau_b}{2} + \text{sel. } ^{13}\text{C}^\alpha + \frac{\tau_b}{2} + \text{sel. } ^{13}\text{C}' + \frac{\tau_b}{2} + \text{sel. } ^{13}\text{C}^\alpha + \frac{\tau_b}{2} \\ &= \mathbf{2\tau_b} + (\text{sel. } ^{13}\text{C}' + 2\text{sel. } ^{13}\text{C}^\alpha)\end{aligned}$$

Both the  $^{13}\text{C}'$  chemical shift and  $\text{C}'-\text{C}^\alpha$  coupling evolutions have been refocussed whilst the important  $\text{C}'-\text{N}$  coupling evolves for a period of  $2\tau_b$ . As with the anti-phase INEPT block, the extra evolution of the  $\text{C}'-\text{N}$  coupling during the selective  $^{13}\text{C}$  pulses must be accounted for by reducing the applied delay accordingly. With these two complementary datasets now available, the virtual decoupling process can be applied to provide a  $^{13}\text{C}^\alpha$ -decoupled CON spectrum analogous to the BASH decoupled spectrum shown in Figure 5.8 without the need for the potentially damaging high-power refocussing pulses.

### 5.2.3 pseudo-5D CARBEX Pulse Sequence

With the modifications described in the previous section, the ASHDEX experiment for the arginine side-chain can be converted into an NMR experiment suitable for application to backbone amide hydrogen exchange. The CARbon-detected Backbone EXchange (CARBEX) pulse sequence is shown in Figure 5.13. The additional IPAP decoupling scheme renders the full experiment pseudo-5D (IPAP,  $\phi_3$ ,  $\tau_{\text{mix}}$ ,  $t_1$ ,  $t_2$ ) and consists of building blocks *i-vi* below. As with the ASHDEX experiment, it is important that the sequence begins with purging pulses to the equilibrium  $^1\text{H}$  and  $^{15}\text{N}$  magnetisation to ensure that a) the detected signal has passed through the pulse sequence as expected and b) the level of initial polarisation is independent of the



## 5. HX in Intrinsically Disordered Proteins

generate the two pseudo-3D datasets (the time-dependent decay of the protonated and deuterated  $^{13}\text{C}'\text{-}^{15}\text{N}$  cross-peaks) is outlined in Figure 5.14. It is important to note that for clarity, Figure 5.14 shows the pre-processing steps applied to the  $^{13}\text{C}'\text{-}^{15}\text{N}$  spectral data following Fourier-transformation of the time-domain data. In reality, the virtual decoupling of the  $\text{C}'\text{-C}^\alpha$  scalar couplings and the separation of the protonated and deuterated signals into two sub-spectra is performed directly on the time-domain data prior to the normal spectral processing steps.

For each of the 8-12  $\tau_{\text{mix}}$  increments typically used in the CARBEX experiment, four  $^{13}\text{C}'\text{-}^{15}\text{N}$  planes are recorded:

- i. **IP(+)**:  $\text{C}'\text{-C}^\alpha$  coupling is *in-phase* with  $^{13}\text{C}'\text{-}^{15}\text{N}(^1\text{H})$  cross-peaks *positive*
- ii. **AP(+)**:  $\text{C}'\text{-C}^\alpha$  coupling is *anti-phase* with  $^{13}\text{C}'\text{-}^{15}\text{N}(^1\text{H})$  cross-peaks *positive*
- iii. **IP(-)**:  $\text{C}'\text{-C}^\alpha$  coupling is *in-phase* with  $^{13}\text{C}'\text{-}^{15}\text{N}(^1\text{H})$  cross-peaks *negative*
- iv. **AP(-)**:  $\text{C}'\text{-C}^\alpha$  coupling is *anti-phase* with  $^{13}\text{C}'\text{-}^{15}\text{N}(^1\text{H})$  cross-peaks *negative*

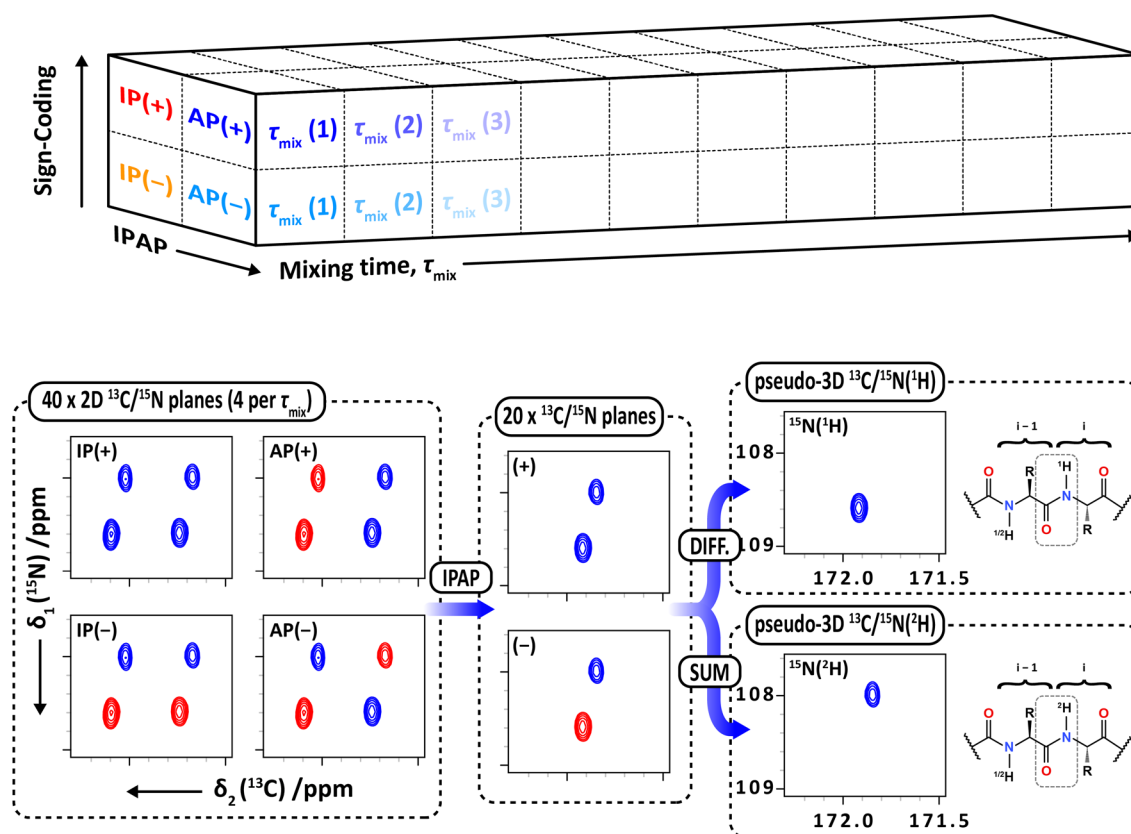


**Figure 5.14** Generation of pseudo-3D spectra reporting selectively on the intensity of the  $^{13}\text{C}'\text{-}^{15}\text{N}(^1\text{H})$  and  $^{13}\text{C}'\text{-}^{15}\text{N}(^2\text{H})$  cross-peaks. Four planes are generated for each mixing time,  $\tau_{\text{mix}}$  and the in-phase (IP) and anti-phase (AP) planes are combined first to remove the  $^1J_{\text{CC}}$  splitting. The protonated and deuterated species are then separated into two pseudo-3D datasets for further processing. The example shown is G68 in  $\alpha\text{S}$  at 14.1 T, pH 7.1 and 298 K. The mixing time,  $\tau_{\text{mix}}$ , for the four planes shown is 100 ms. Note that whilst the IPAP and sign-coding processing steps are illustrated using the Fourier-transformed data, the process is actually performed on the unprocessed FIDs.

To achieve the requisite IPAP decoupling, alternate AP and IP planes are combined in the manner described in Figure 5.10 to generate a pair of  $^{13}\text{C}'\text{-}^{15}\text{N}$  planes for each  $\tau_{\text{mix}}$  increments:

- i. (+):  $^{13}\text{C}'\text{-}^{15}\text{N}(^1\text{H})$  cross-peaks *positive* ( $\text{C}^\alpha$  decoupled)
- ii. (-):  $^{13}\text{C}'\text{-}^{15}\text{N}(^1\text{H})$  cross-peaks *negative* ( $\text{C}^\alpha$  decoupled)

To implement the sign-coding filter, alternate (+) and (-) planes are combined in the manner described in Figure 3.15 to separate the protonated and deuterated  $^{13}\text{C}'\text{-}^{15}\text{N}$  cross-peaks into sub-spectra and thus avoid the spectral crowding caused by the doubling of the number of detected peaks. The result of this pre-processing routine is two pseudo-3D datasets that are then subjected to the usual NMR processing steps: window-function, Fourier-transform, phase correction etc. The first dataset contains  $^{13}\text{C}'\text{-}^{15}\text{N}$  cross-peaks corresponding to the protonated species  $^{15}\text{N}(^1\text{H})$  and reports on the intensity decay during  $\tau_{\text{mix}}$  due to the combination of hydrogen exchange and longitudinal relaxation. The second dataset contains  $^{13}\text{C}'\text{-}^{15}\text{N}$  cross-peaks corresponding to the deuterated species  $^{15}\text{N}(^2\text{H})$ , initially increasing in intensity during  $\tau_{\text{mix}}$  due to hydrogen exchange before plateauing and beginning to decay with longitudinal relaxation.

#### 5.2.4 Further Considerations

It was noted in Chapter 3 that the observed ratio of the forward (protium  $\rightarrow$  deuterium,  $k_{12}$ ) and reverse (deuterium  $\rightarrow$  protium,  $k_{21}$ ) chemical exchanges processes is highly dependent on the concentration of  $^2\text{H}_2\text{O}$  in the sample. However, an interesting phenomenon is observed in samples containing 50%  $^2\text{H}_2\text{O}$ . Rather than the two exchange rates being equal and the equilibrium populations of  $^{15}\text{N}(^1\text{H})$ : $^{15}\text{N}(^2\text{H})$  the same, there appears to be a slight preference for the deuteration of the amide sites resulting in overpopulation of the  $^{15}\text{N}(^2\text{H})$  species by  $\sim 10\%$ . This *fractionation factor* of 1.1 has been reported previously and is the result of a lower vibrational energy level for a deuterium nucleus compared to a protium nucleus due to its larger mass. A knowledge of the residue-specific fractionation factor can help in the least-square fitting routine used to extract the exchange rates from the decay/build-up of the NMR intensities by constraining the forward and reverse fitting parameters to  $k_{12} = 1.1 \times k_{21}$  as in the original SOLEXY experiment. However, the value of 1.1 is approximate and the true fractionation factor differs slightly between residues. Therefore, it is useful to determine the residue-specific fractionation factor experimentally prior to recording the full CARBEX experiment. A pair of  $^{13}\text{C}'$ -detected NMR experiments suitable for this purpose are shown in Figure 5.15. The first experiment (Figure 5.15a) is used to determine the fractionation factor by directly exciting the  $^{13}\text{C}'$  nuclei of both the protonated and deuterated species and omitting the mixing time. The sign-coding filter is used to separate the resonances into the protonated and deuterated sub-

## 5. HX in Intrinsically Disordered Proteins

spectra and aid the subsequent interpretation. The second NMR experiment will be used to determine the longitudinal relaxation rate ( $R_1$ ) of the  $^{13}\text{C}$  nuclei to ensure that any difference in the relaxation of the protonated and deuterated species during the initial recycle delay can be accounted for when measuring the fractionation factors.

A further advantage of measuring the fractionation factors directly is that by careful choreography of the magnetisation during the pulse sequence used, the slight intensity distortions caused by the differential transverse relaxation ( $R_2$ ) of the protonated and deuterated species during the sign-coding filter and semi-constant time chemical shift evolution can be compensated for in the CARBEX datasets.

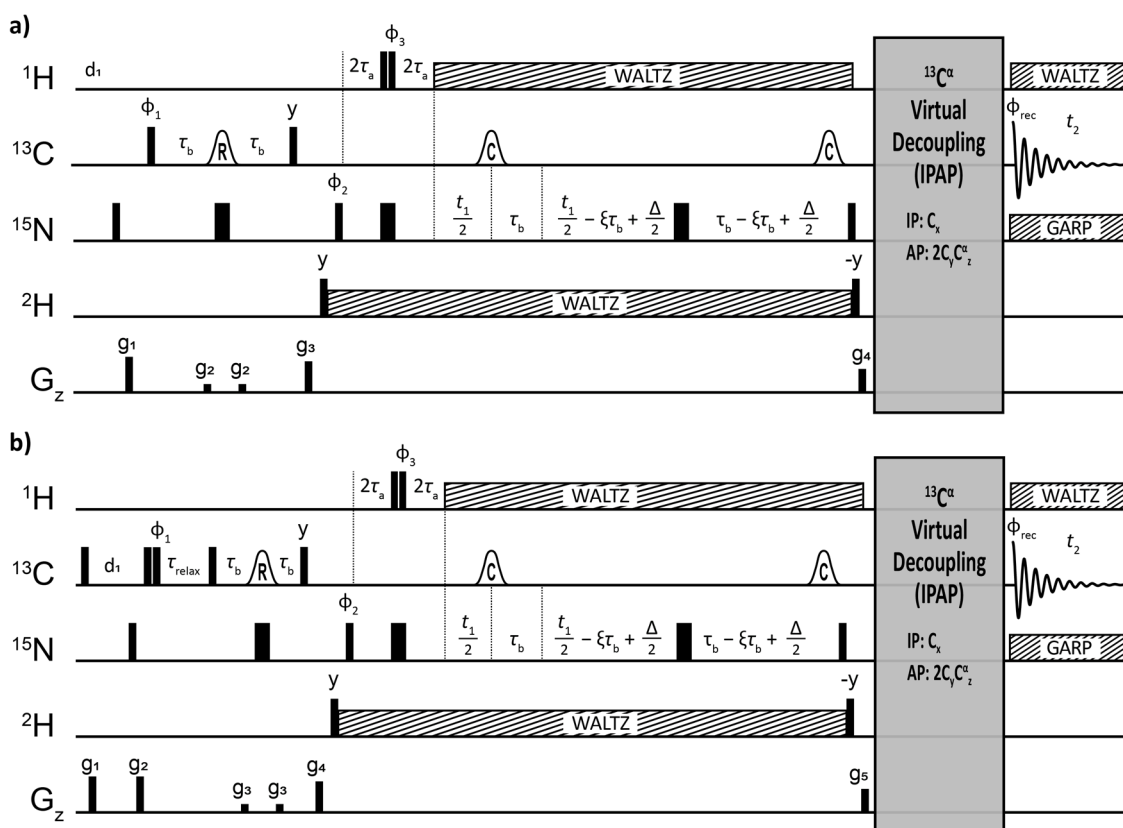


**Figure 5.15**  $^{13}\text{C}$ -detected pulse sequences suitable for the measurement of a) equilibrium fractionation factors in samples prepared in mixed  $^1\text{H}_2\text{O}$ : $^2\text{H}_2\text{O}$  solutions and b) the  $^{13}\text{C}$   $R_1$  relaxation rates of the protonated ( $2C_2N_z[^1\text{H}]$ ) and deuterated ( $2C_2N_z[^2\text{H}]$ ) species. The phase cycle used for both sequences is  $\phi_1$ :  $x$ ,  $-x$ ;  $\phi_2$ :  $2(x)$ ,  $2(-x)$ ;  $\phi_{\text{rec}}$ :  $x$ ,  $2(-x)$ ,  $x$ ;  $\phi_3$  is cycled ( $x$ ,  $-x$ ) to implement the sign-coding filter.  $^{13}\text{C}$  decoupling is achieved using the IPAP technique (see Figure 5.11).

When comparing the magnetisation transfer pathways, there are some slight differences between the CARBEX experiment (Figure 5.13) and the experiment used to measure the fractionation factors (Figure 5.15a) stemming from how the initial magnetisation is excited. Where the CARBEX sequence uses a  $^1\text{H}$ - $^{15}\text{N}$  refocused INEPT block to transfer equilibrium  $^1\text{H}$  magnetisation selectively to the protonated amides  $N_z(^1\text{H})$ , the magnetisation present after the initial INEPT in Figure 5.15a is proportional to  $2C_2N_z(^1\text{H})$  and  $2C_2N_z(^2\text{H})$  for the protonated and deuterated species, respectively. Following the sign-coding filter that serves to selectively invert

the protonated species in alternate experiments, the  $^{15}\text{N}$  chemical shift is encoded during a semi-constant time evolution period. It is important to note that the RF-pulses applied during the semi-constant time evolution period of this pulse sequence differ from those applied during the CARBEX experiment. Whilst the semi-constant time block of the CARBEX experiment is designed to take in-phase  $N_y$  magnetisation and allow the evolution into anti-phase  $2C_zN_x$  during the chemical shift evolution, the magnetisation reaching the  $^{15}\text{N}$  chemical shift evolution period of the  $^{13}\text{C}$ -excitation experiment is already anti-phase with respect to  $^{13}\text{C}'$ :  $2C_zN_y$ . As there is no longer a need to simultaneously evolve a scalar coupling, one could simply use a typical incremented chemical shift evolution period here to encode the  $^{15}\text{N}$  chemical shift before retro-INEPT transfer back to  $^{13}\text{C}$  for detection. However, in order to prevent the different transverse relaxation rates of the protonated and deuterated magnetisation from affecting the hydrogen exchange rate measurement, it is prudent to keep the two experiments as similar as possible in terms of time that the magnetisation spends transverse during the pulse sequence. In order to achieve this, the semi-constant time block is designed to track the duration of the CARBEX sequence whilst *refocussing* the  $\text{C}'\text{-N}$  and  $\text{C}^\alpha\text{-N}$  scalar couplings throughout:

$$\begin{aligned}\omega_{\text{N}} &= \frac{t_1}{2} + {}^{13}\text{C chirp} + \tau_b + \frac{t_1}{2} - \xi\tau_b + \frac{\Delta}{2} - \tau_b + \xi\tau_b - \frac{\Delta}{2} - {}^{13}\text{C chirp} \\ &= -t_1 \\ J_{\text{N-C}'} &= \frac{t_1}{2} - \tau_b - \frac{t_1}{2} + \xi\tau_b - \frac{\Delta}{2} + \tau_b - \xi\tau_b + \frac{\Delta}{2} \\ &= \mathbf{0} \\ J_{\text{N-C}^\alpha} &= \frac{t_1}{2} - \tau_b - \frac{t_1}{2} + \xi\tau_b - \frac{\Delta}{2} + \tau_b - \xi\tau_b + \frac{\Delta}{2} \\ &= \mathbf{0}\end{aligned}$$

As there is no longer the need to selectively target the  $^{13}\text{C}'$  or  $^{13}\text{C}^\alpha$  nuclei, an adiabatic *chirp* pulse is used to invert both resonances simultaneously. To compensate for the difference in duration of the applied  $^{13}\text{C}$  pulses between the experiments, an additional delay  $\Delta$  has been introduced. The actual duration of the semi-constant time evolution period can be easily compared by summing all of the delays and pulses applied:

$$\begin{aligned}time &= \frac{t_1}{2} + {}^{13}\text{C chirp} + \tau_b + \frac{t_1}{2} - \xi\tau_b + \frac{\Delta}{2} + \tau_b - \xi\tau_b + \frac{\Delta}{2} + {}^{13}\text{C chirp} \\ &= t_1 + 2({}^{13}\text{C chirp} + \tau_b - \xi\tau_b) + \Delta\end{aligned}$$

and compared with the CARBEX experiment:

$$\begin{aligned}time &= \frac{t_1}{2} + \text{sel. } {}^{13}\text{C}^\alpha + \tau_b + \text{sel. } {}^{13}\text{C}' + \frac{t_1}{2} - \xi\tau_b + \tau_b - \xi\tau_b + \text{sel. } {}^{13}\text{C}' + \text{sel. } {}^{13}\text{C}^\alpha \\ &= t_1 + 2(\text{sel. } {}^{13}\text{C}^\alpha + \text{sel. } {}^{13}\text{C}' + \tau_b - \xi\tau_b)\end{aligned}$$

## 5. HX in Intrinsically Disordered Proteins

The delay to compensate for the different  $^{13}\text{C}$  pulse lengths between experiments can therefore be calculated as:

$$\begin{aligned}t_1 + 2(^{13}\text{C chirp} + \tau_b - \xi\tau_b) + \Delta &= t_1 + 2(\text{sel. } ^{13}\text{C}^\alpha + \text{sel. } ^{13}\text{C}' + \tau_b - \xi\tau_b) \\2(^{13}\text{C chirp}) + \Delta &= 2(\text{sel. } ^{13}\text{C}^\alpha + \text{sel. } ^{13}\text{C}') \\ \Delta &= 2(\text{sel. } ^{13}\text{C}^\alpha + \text{sel. } ^{13}\text{C}') - 2(^{13}\text{C chirp})\end{aligned}$$

The duration of the selective  $^{13}\text{C}'$  and  $^{13}\text{C}^\alpha$  pulses shown in Figure 5.4 are 1.25 ms and 0.75 ms respectively and so considering a duration of 0.5 ms for a typical  $^{13}\text{C}$  chirp pulse, the compensation delay  $\Delta$  becomes 3 ms. To ensure that the  $^{15}\text{N}$  chemical shift is refocused during this additional delay, it is divided in half and placed around the  $^{15}\text{N}$  refocussing pulse.

Following the processing of the sign-coding filter to separate the protonated and deuterated species, the relative intensities of the  $^{13}\text{C}'\text{-}^{15}\text{N}(^1\text{H})$  and  $^{13}\text{C}'\text{-}^{15}\text{N}(^2\text{H})$  cross-peaks can be calculated for each residue from the resulting pair of spectra. The experiment shown in Figure 5.15b has been modified to include a standard pulse sequence element to measure the longitudinal relaxation rate ( $R_1$ ) of  $^{13}\text{C}'$ . A pair of  $^{13}\text{C}'\text{-}^{15}\text{N}(^1\text{H})$  and  $^{13}\text{C}'\text{-}^{15}\text{N}(^2\text{H})$  spectra is obtained for each increment of the relaxation delay  $\tau_{\text{relax}}$  showing the intensity decay of each cross-peak due to longitudinal relaxation.

## 5.3 Results and Discussion

### 5.3.1 $^{13}\text{C}'$ Longitudinal Relaxation in $\alpha\text{Synuclein}$

The experiment described in Figure 5.15b was first applied to a sample of human U- $[^{13}\text{C}, ^{15}\text{N}]$ - $\alpha\text{S}$  prepared in 50%  $^2\text{H}_2\text{O}$  in order to determine a suitable recycle delay ( $d_1$ ) to allow an accurate measurement of the fractionation factors using the experiment in Figure 5.15a. For a quantitative study of relative NMR intensities, it is important to have a delay of at least  $5 \times T_1$  ( $T_1 = R_1^{-1}$ ) of the signal that *relaxes the slowest* between each scan for the system to reach equilibrium. If one wanted to assess the ratio of two signals where one signal relaxes significantly faster than the other, an insufficiently long recycle delay would cause the slower relaxing signal to become partially saturated as the number of scans collected increases. The signal intensity of the slower relaxing signal would become attenuated and therefore result in a distorted ratio when compared to the faster relaxing signal.

In the present application, the fractionation factor is measured as the ratio of a protonated species against a deuterated species. As the incorporation of deuterium is well known to affect the relaxation properties of adjacent nuclei, it is important to understand the isotope-specific  $T_1$  rates prior to attempting to measure the fractionation factors. Figure 5.16 shows the  $^{13}\text{C}'$   $T_1$  rates

obtained for the protonated and deuterated residues in  $\alpha$ S. The method is exemplified using the  $^{13}\text{C}'(^1\text{H})$  intensity decay of residue A124 as a function of the relaxation time,  $\tau_{\text{relax}}$ . The decay follows a simple exponential decay and can be fitted to:

$$[I] = e^{\left(\frac{-\tau_{\text{relax}}}{T_1}\right)} [I]_0$$

where  $[I]_0$  is the signal intensity at  $\tau_{\text{relax}} = 0$ , to allow the extraction of the  $T_1$  relaxation time. It is evident from the data that there is little variation in the longitudinal relaxation of the  $^{13}\text{C}'$  nuclei either between different residues or between the protonated and deuterated forms of each residue. This finding means that provided the recycle delay is long enough to allow enough magnetisation to return to equilibrium between scans to provide sufficient signal-to-noise in the final spectrum, there is no need to wait the full  $5 \times T_1$  for a quantitative measurement.

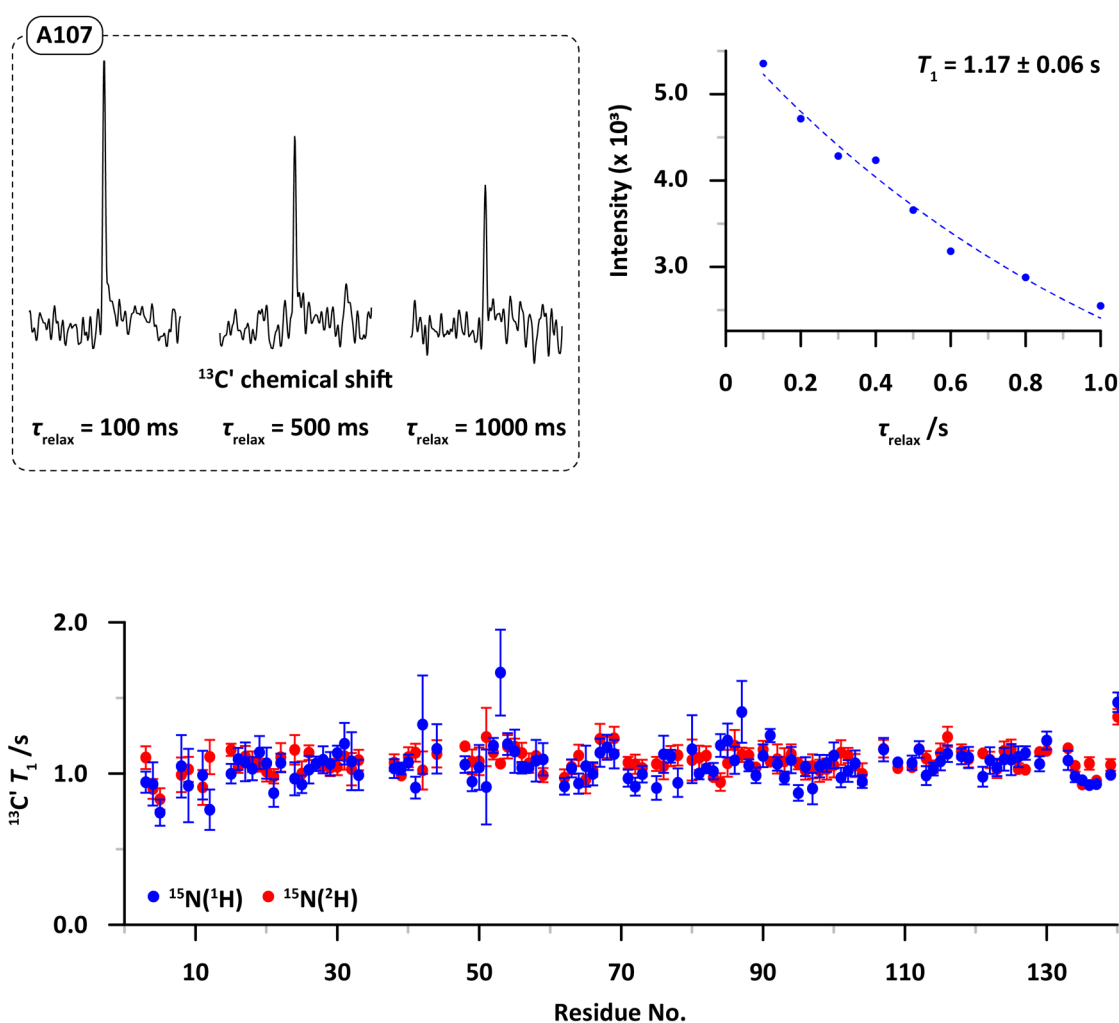


**Figure 5.16** The measurement of  $^{13}\text{C}'$  longitudinal relaxation times ( $T_1$ ) for protonated and deuterated residues in  $\alpha$ S using the pulse sequence shown in Figure 5.15b. The decay of the cross-peak intensity as a function of the relaxation delay,  $\tau_{\text{relax}}$ , is fitted to a single exponential function to extract the value of  $T_1$  for each residue.

## 5. HX in Intrinsically Disordered Proteins

### 5.3.2 Fractionation Factors in $\alpha$ Synuclein

Following the interrogation of the  $^{13}\text{C}'$  longitudinal relaxation data recorded on  $\alpha\text{S}$ , the pulse sequence to quantify the residue-specific fractionation factor was applied. As described previously, the experiment provides two  $^{13}\text{C}'$ - $^{15}\text{N}$  NMR spectra: the first containing cross-peaks pertaining to the protonated species; the second containing the deuterated cross-peaks. The fractionation factors were computed as the ratio of the deuterated to protonated cross-peak areas:

$$\text{fractionation factor} = \frac{I_{2\text{H}}}{I_{1\text{H}}}$$

where  $I_{2\text{H}}$  and  $I_{1\text{H}}$  represent the peak areas of the deuterated and protonated cross-peaks, respectively.

The data reveals the expected small overpopulation of the deuterated species due to the energetic stability conferred by the heavier deuterium nucleus (Figure 5.17). The average fractionation factor measured in  $\alpha\text{S}$  was approximately 1.3 and residue-specific measurements appear to vary only slightly throughout the molecule. The value of 1.3 is slightly higher than the value of 1.1 reported in previously studies owing to the fact that the data reported here is uncorrected for differential relaxation losses between the protonated and deuterated species. As the deuterated species would be expected to experience slower  $^{15}\text{N}$  transverse relaxation ( $R_2$ ) during the INEPT transfers and chemical shift evolution period, the apparent fractionation factor is skewed to the higher value. As an accurate measurement of the fractionation factors in  $\alpha\text{S}$  is not the objective of this study - this pulse sequence was carefully designed to mimic the magnetisation flow of the CARBEX experiment - correction of this dataset is unnecessary. Instead, this data will be used to assist the fitting routine used to extract the hydrogen exchange rates from data collected using the CARBEX experiment.

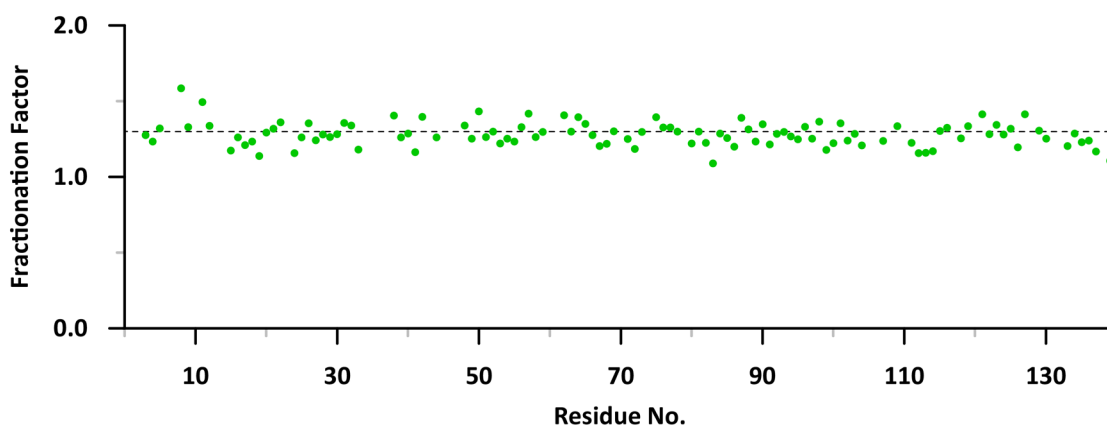


**Figure 5.17** Residue-specific fractionation factors for  $\alpha\text{S}$  as measured using the pulse sequence described in Figure 5.15a. The dashed line indicated the molecular average of 1.3.

### 5.3.3 Hydrogen Exchange Rates in $\alpha$ Synuclein

The full CARBEX experiment was successfully applied to  $\alpha$ S and resulted in the extraction of hydrogen exchange rates for 109 of the available residues (Figure 5.18a). This equates to a coverage of 81% of the molecule once the N-terminus and five prolines are accounted for: Neither proline nor the N-terminus of the molecule has an amide  $^1\text{H}$  nucleus to undergo chemical exchange with the solvent. The data reveals that despite the apparent lack of a tertiary structure for  $\alpha$ S, a wide range of hydrogen exchange rates is observed ( $0.2 - 20 \text{ s}^{-1}$ ). Using the computed reference exchange rates, one can calculate the protection factor of each residue (Figure 5.19b).

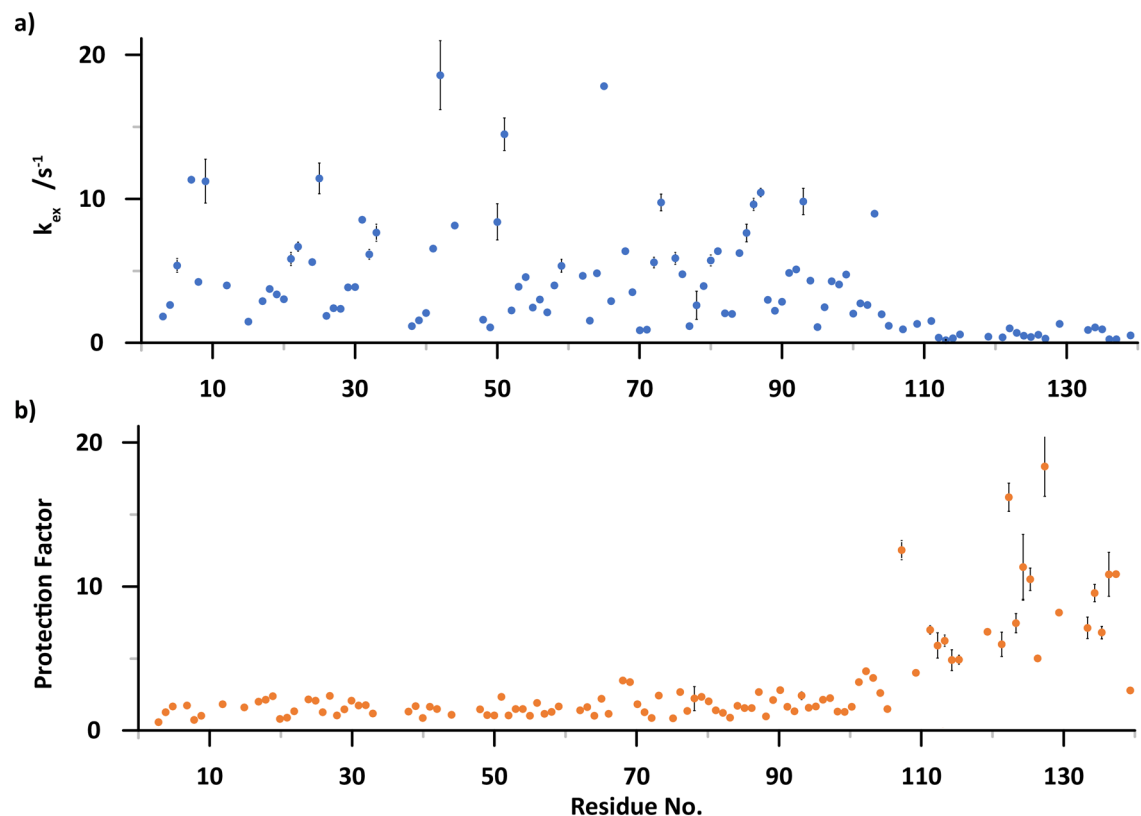


**Figure 5.18** a) Residue-specific hydrogen exchange rates of the backbone amide  $^1\text{H}$  nuclei of  $\alpha$ S measured at pH 7.3, 288 K and 14.1 T. b) Protection factors calculated using reference data obtained from SPHERE.

The protection factors obtained for the majority of residues in  $\alpha$ S are around 1.0 and typical of an unstructured molecule. It is interesting to note that the data for the C-terminus residues shows much more variation and generally higher protection factors than for the rest of the molecule. This observation highlights the importance of obtaining reference exchange rates from a source such as SPHERE (Server Program for Hydrogen Exchange Rate Estimation) before interpreting the data as the exchange rate of each residue is highly dependent on not only itself but also the amino acid immediately adjacent to it. Whilst a thorough discussion of the behaviour of  $\alpha$ S in solution is beyond the scope of this thesis, this observation appears to mirror

## 5. HX in Intrinsically Disordered Proteins

a similar trend observed during the interaction of the C-terminus with  $\text{Ca}^{2+}$  ions<sup>[242]</sup> and may suggest that there is a similar structural organisation in order to interact with the  $\text{Na}^+$  ions from the sodium phosphate buffer. However, it seems more likely to be an artefact resulting from an inaccurate calculation of the reference chemical exchange rates. The raw hydrogen exchange data indicates a marked decrease in exchange rate for the C-terminus when compared to the result of the molecule:  $0.7 \text{ s}^{-1}$  for the last 35 residues compared with  $4.9 \text{ s}^{-1}$  for residues 3 - 105. This can be rationalised by considering that of the 24 acidic residues in the molecule (six aspartic acid and 18 glutamic acid), half of them (four aspartic acid and eight glutamic acid) are located in the final 35 amino acids of the protein sequence. The prevalence of these acidic residues in the C-terminus of  $\alpha\text{S}$  results in a high degree of localised negative charge. This negative charge is thought to be responsible for the metal ion affinity mentioned above but is also likely to repel the negatively charged hydroxide ions known to catalyse the hydrogen exchange process. The reference exchange rates obtained from SPHERE are derived using only binary combinations of amino acids and are thus likely to miss an effect brought on by the combination of the many local negative charges. This would cause that the reference exchange rates predicted by the algorithm to be overestimated for the residues in the unusually negatively charged part of the molecule. The resulting over estimation of the C-terminus exchange rates by SPHERE manifests itself as erroneously high protection factors for these residues.

A comparison of the hydrogen exchange rates obtained using the CARBEX experiment with those measured on the same sample using the  $^1\text{H}$ -detected SOLEXY experiment reveals an excellent overall correlation between the two datasets (Figure 5.19). However, owing to the lack of  $^1\text{H}$  signal dispersion in the SOLEXY experiment measurement was only possible for 59 (44%) of the residues, even when using an ultra-high-field 22.3 T (950 MHz  $^1\text{H}$  frequency) spectrometer.

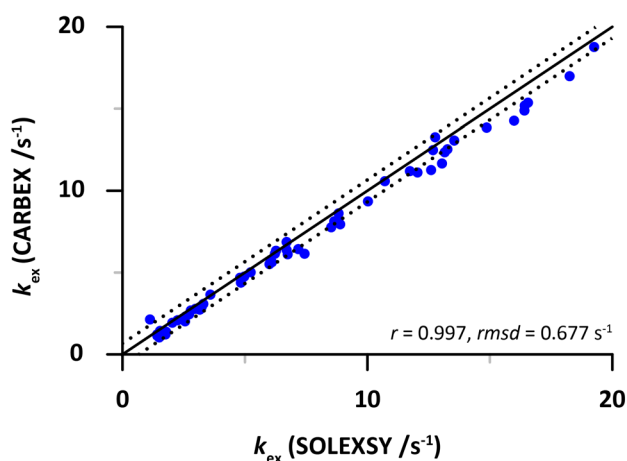


**Figure 5.19** Comparison of the hydrogen exchange rates for  $\alpha\text{S}$  as determined by  $^1\text{H}$ -detected SOLEXY and  $^{13}\text{C}$ -detected CARBEX. Measurements were made at pH 7.1, 298 K and 14.1 T (CARBEX), 22.3 T (SOLEXY)

## 5.4 Conclusions

The general utility of  $^{13}\text{C}$ -detected NMR experiments to the study of proteins is exemplified through the demonstration of the novel CARBEX technique for measuring hydrogen exchange. With the modifications discussed above, the ASHDEX experiment described in Chapter 3 can be successfully applied to uniformly [ $^{13}\text{C}$ ,  $^{15}\text{N}$ ]-labelled proteins in partially deuterated aqueous buffers to quantify the rate of amide hydrogen exchange with the bulk solvent. The modifications stem from the inherent differences between the guanidinium spin system of arginine and the peptide bonds that form the protein backbone and demand alternate  $^{13}\text{C}$ -selective refocussing pulses as well as a suitable decoupling strategy for suppressing the homonuclear  $\text{C}'\text{-C}^\alpha$  splitting during acquisition. Both BASH and IPAP decoupling schemes were explored and found to be equally applicable with the optimum choice ultimately being determined by the hardware available to the spectroscopist. The use of  $^{13}\text{C}$ -detection provides an alternate frequency dimension for signal dispersion and is an important feature where spectral overlap in  $^1\text{H}\text{-}^{15}\text{N}$  is problematic. This problem is particularly prevalent in the study of IDPs where a lack of tertiary structure causes the  $^1\text{H}$  signals to occupy a rather narrow chemical shift range.

The CARBEX-IPAP experiment is a pseudo-five-dimensional NMR experiment that enables the interrogation of the residue-specific hydrogen exchange rates by monitoring the intensity of  $^{13}\text{C}\text{-}^{15}\text{N}$  cross peaks as a function of an incremented mixing time. In-phase  $^{15}\text{N}$  magnetisation is initially generated from the amide  $^1\text{H}$  nuclei using the  $^1\text{H}\text{-}^{15}\text{N}$  scalar coupling to provide a sensitivity boost compared to direct  $^{13}\text{C}$  excitation as well as a means to polarise only the protonated species. During the subsequent mixing time, hydrogen exchange results in the build-up of the deuterated species. The resulting mix of  $^{15}\text{N}(^1\text{H})$  and  $^{15}\text{N}(^2\text{H})$  signals are resolved during a semi-constant chemical shift period whilst the evolution of the one-bond  $^{13}\text{C}'\text{-}^{15}\text{N}$  scalar coupling generates anti-phase  $2\text{C}_z\text{N}_y$  magnetisation. A final retro-INEPT block completes the transfer to  $^{13}\text{C}'$  for detection under  $^1\text{H}$  and  $^{15}\text{N}$  decoupling. Virtual decoupling of  $^{13}\text{C}^\alpha$  is achieved by recording interleaved in-phase (IP) and anti-phase (AP) experiments and combining them in a specific manner to remove the homonuclear splitting. Two additional NMR experiments were described: the first to measure the effect of deuteration of the longitudinal relaxation time of  $^{13}\text{C}'$  and the second to provide a measurement of the residue-specific fractionation factor. Both measurements are useful to have when extracting the hydrogen exchange rates using a least-squares fitting routine.

The CARBEX experiment allows access to hydrogen exchange rates between  $0.2\text{ s}^{-1}$  and  $20\text{ s}^{-1}$  as demonstrated on the IDP  $\alpha\text{Synuclein}$ . A comparison with hydrogen exchange data obtained

## 5. HX in Intrinsically Disordered Proteins

using the  $^1\text{H}$ -detected SOLEXY experiment showed a high level of agreement between the two techniques. In the case of  $\alpha\text{S}$  however, many more residues were accessible using the  $^{13}\text{C}$ -detected CARBEX experiment (109 vs. 59) highlighting the practicality of an additional frequency dimension. It is envisaged that the CARBEX experiment will serve as a complimentary technique to established NMR methods to study hydrogen exchange and will prove invaluable in cases where the  $^1\text{H}$  and  $^{15}\text{N}$  dimensions provide insufficient signal dispersion for a molecule of interest.

## 5.5 Appendices

### 5.5.1 $\alpha\text{Synuclein}$ Raw Data

Res. No.	Amino Acid	$^{13}\text{C}'(\text{i} - 1)$ /ppm	$^{15}\text{N}$ /ppm	$T_1(^{13}\text{C}')$ /s	Fractionation Factor	$k_{\text{ex}}$ /s $^{-1}$	$R_1(^{15}\text{N})$ /s $^{-1}$
3	Val	173.106	120.155	0.944	1.276	1.843	1.421
4	Phe	173.117	123.206	0.932	1.235	2.641	1.553
5	Met	173.039	122.038	0.743	1.320	5.378	1.443
7	Gly	174.323	109.637	1.049	1.586	11.333	1.612
8	Leu	171.352	121.348	0.921	1.329	4.241	1.636
9	Ser	174.821	116.502	0.990	1.495	11.229	1.538
12	Lys	175.087	120.664	0.762	1.337	4.004	1.681
15	Val	171.213	119.937	0.999	1.175	1.475	1.446
17	Ala	173.184	128.237	1.097	1.262	2.903	1.355
18	Ala	174.856	123.483	1.078	1.210	3.756	1.270
19	Ala	175.096	122.881	1.033	1.235	3.360	1.478
20	Glu	175.390	119.888	1.140	1.139	3.039	1.371
21	Lys	174.134	122.053	1.069	1.293	5.831	1.367
22	Thr	174.338	115.012	0.873	1.319	6.687	1.448
24	Gln	173.865	121.500	1.071	1.361	5.615	1.603
25	Gly	173.771	110.324	0.966	1.157	11.424	1.556
26	Val	171.434	119.552	0.930	1.262	1.871	1.399
27	Ala	173.554	127.172	1.027	1.355	2.420	1.523
28	Glu	175.317	120.373	1.066	1.242	2.363	1.427
29	Ala	173.859	124.724	1.092	1.281	3.851	1.503
30	Ala	174.927	122.826	1.065	1.264	3.878	1.461
31	Gly	175.644	107.571	1.137	1.283	8.563	1.467
32	Lys	171.382	120.480	1.198	1.358	6.144	1.689
33	Thr	174.185	115.382	1.082	1.340	7.659	1.232
38	Leu	173.078	125.626	0.991	1.181	1.158	1.554
39	Tyr	173.813	122.246	1.034	1.406	1.566	1.579
40	Val	172.755	123.105	1.035	1.261	2.071	1.563
41	Gly	173.315	111.910	1.075	1.288	6.554	1.540
42	Ser	171.116	115.425	0.908	1.164	18.596	1.284
44	Thr	174.038	115.288	1.324	1.397	8.156	1.404
48	Val	171.033	119.730	1.165	1.262	1.621	1.330
49	Val	173.185	124.863	1.060	1.341	1.081	1.462
50	His	173.036	124.335	0.947	1.253	8.403	1.722
51	Gly	172.806	110.379	1.041	1.433	14.491	1.824
52	Val	170.957	119.361	0.912	1.264	2.267	1.460
53	Ala	173.108	127.989	1.186	1.30†	3.901	1.545
54	Thr	175.005	114.659	1.668	1.222	4.565	1.327
55	Val	171.714	122.856	1.195	1.254	2.456	1.338
56	Ala	173.036	127.903	1.148	1.234	3.023	1.368
57	Glu	174.957	120.703	1.039	1.329	2.123	1.533
58	Lys	173.892	122.608	1.036	1.418	3.983	1.603
59	Thr	174.154	115.723	1.086	1.263	5.353	1.473
62	Gln	173.612	121.566	1.094	1.297	4.670	1.639
63	Val	173.143	121.723	0.916	1.408	1.552	1.608

5. HX in Intrinsically Disordered Proteins

Res. No.	Amino Acid	$^{13}\text{C}'(i-1)$ /ppm	$^{15}\text{N}$ /ppm	$T_1(^{13}\text{C}')$ /s	Fractionation Factor	$k_{\text{ex}}$ /s $^{-1}$	$R_1(^{15}\text{N})$ /s $^{-1}$
64	Thr	173.524	117.884	1.035	1.300	4.837	1.583
65	Asn	171.221	121.625	0.935	1.395	17.839	1.170
66	Val	172.422	120.543	1.050	1.350	2.900	1.510
67	Gly	174.038	112.417	0.999	1.276	1.941	1.867
68	Gly	171.837	108.599	1.139	1.205	6.365	1.595
69	Ala	170.900	123.558	1.175	1.219	3.527	1.416
70	Val	174.824	120.292	1.129	1.302	0.875	1.290
71	Val	173.513	125.211	0.970	1.252	0.916	1.525
72	Thr	173.458	118.449	0.915	1.185	5.592	1.587
73	Gly	172.073	111.133	0.997	1.297	9.745	1.551
75	Thr	173.731	118.743	0.905	1.395	5.873	1.283
76	Ala	171.247	127.204	1.128	1.328	4.774	1.597
77	Val	174.739	119.870	1.115	1.328	1.175	1.338
78	Ala	173.186	127.978	0.940	1.30 <sup>†</sup>	2.615	1.577
79	Gln	174.800	120.165	1.162	1.222	3.957	1.705
80	Lys	173.113	123.100	1.001	1.30 <sup>†</sup>	5.723	1.806
81	Thr	173.854	116.721	1.036	1.226	6.383	1.495
82	Val	171.616	122.825	1.017	1.091	2.048	1.383
83	Glu	173.325	125.137	1.187	1.287	2.015	1.517
84	Gly	174.211	110.494	1.219	1.258	6.241	1.641
85	Ala	171.324	123.755	1.089	1.201	7.637	1.434
86	Gly	175.672	107.955	1.409	1.391	9.625	1.411
87	Ser	171.474	115.484	1.055	1.315	10.454	1.217
88	Ile	171.884	122.564	0.988	1.234	3.002	1.379
89	Ala	173.437	127.872	1.118	1.348	2.234	1.440
90	Ala	174.731	123.159	1.252	1.216	2.869	1.320
91	Ala	174.901	123.224	1.064	1.285	4.861	1.411
92	Thr	175.303	112.423	0.971	1.298	5.111	1.461
93	Gly	172.318	110.483	1.090	1.268	9.815	1.355
94	Phe	170.777	120.114	0.873	1.248	4.332	1.583
95	Val	172.646	123.545	1.047	1.332	1.096	1.507
96	Lys	172.561	126.230	0.901	1.254	2.473	1.497
97	Lys	173.624	123.602	1.050	1.366	4.292	1.642
98	Asp	173.524	121.038	1.069	1.179	4.052	1.604
99	Gln	173.390	119.990	1.120	1.223	4.740	1.475
100	Leu	173.193	122.638	0.974	1.355	2.031	1.517
101	Gly	175.162	109.581	1.018	1.240	2.745	1.604
102	Lys	171.236	120.557	1.069	1.284	2.637	1.608
103	Asn	173.616	119.814	0.948	1.208	8.971	1.393
104	Glu	172.482	121.196	1.159	1.238	1.993	1.660
105	Glu	173.742	121.627	1.075	1.336	1.187	1.568
107	Ala	170.604	124.751	1.071	1.225	0.949	1.377
109	Gln	174.225	121.008	1.161	1.158	1.326	1.395
111	Gly	174.010	110.062	0.988	1.159	1.530	1.517
112	Ile	170.904	119.992	1.031	1.171	0.375	1.333
113	Leu	173.410	126.937	1.081	1.305	0.200	1.471
114	Glu	174.301	122.136	1.132	1.326	0.315	1.439
115	Asp	173.042	121.296	1.115	1.256	0.587	1.381
118	Val	173.886	120.664	1.107	1.335	0.085	1.374
119	Asp	172.944	125.898	0.980	1.414	0.430	1.396
121	Asp	174.089	119.219	1.087	1.282	0.390	1.432
122	Asn	173.356	118.955	1.042	1.345	1.018	1.368
123	Glu	172.536	121.563	1.095	1.280	0.701	1.404
124	Ala	173.216	124.345	1.093	1.318	0.505	1.324
125	Tyr	174.338	119.896	1.111	1.195	0.412	1.343
126	Glu	172.492	123.667	1.137	1.415	0.560	1.366
127	Met	172.598	123.803	1.065	1.307	0.305	1.456
129	Ser	174.051	116.614	1.219	1.253	1.330	1.337
133	Tyr	170.971	120.119	1.088	1.205	0.899	1.380
134	Gln	172.883	122.602	0.981	1.287	1.087	1.458
135	Asp	171.990	121.579	0.957	1.230	0.945	1.439

## 5. HX in Intrinsically Disordered Proteins

Res. No.	Amino Acid	$^{13}\text{C}(i-1)$ /ppm	$^{15}\text{N}$ /ppm	$T_1(^{13}\text{C})$ /s	Fractionation Factor	$k_{\text{ex}}$ /s <sup>-1</sup>	$R_1(^{15}\text{N})$ /s <sup>-1</sup>
136	Tyr	172.678	120.328	0.926	1.240	0.265	1.416
137	Glu	172.238	125.261	0.932	1.168	0.259	1.486
139	Glu	174.042	121.427	0.993	1.107	0.515	1.245
140	Ala	172.574	130.774	1.472	1.156	0.039	0.980

**Table 5.1** Chemical shift, relaxation, fractionation factor and hydrogen exchange data as measured for  $\alpha\text{S}$ . Chemical shift and relaxation data is shown for the protonated species ( $^{15}\text{N}[^1\text{H}]$ ) only. †Signal-to-noise insufficient to make accurate determination so the average value across the molecule (1.3) is used.

# 6

## Conclusion

### 6.1 Concluding Remarks

The latter half of the 20<sup>th</sup> Century saw the discovery and continued development of magnetic resonance into one of the most powerful analytical techniques available to the scientist wishing to study the microscopic world. Since then, innumerable NMR methods have been developed and published, only serving to increase the general utility of the technique. Early experimentation focussed on the polypeptide backbone of the protein with the behaviour of the side-chain nuclei more or less ignored. This oversight is beginning to be addressed as evidenced by the increasing number of NMR experiments specifically designed to probe the amino acid side-chains and their critical interactions with ligands, metal ions and each other. Along with novel applications, iterative improvements in hardware design have also fuelled the rapid evolution of modern NMR spectroscopy. The introduction of ultra-high field magnets (now exceeding 1 GHz <sup>1</sup>H frequency) and the invention of cryogenically-cooled probes at the turn of the Century, has dramatically reduced the demand on both experimental time and sample concentration. More recently, the development of NMR probes specifically optimised for the direct detection of <sup>13</sup>C or <sup>15</sup>N magnetisation has ushered in an era of *X-detected* NMR with more and more applications moving away from the traditionally detected high- $\gamma$  nuclei. The work presented in this thesis describes the development and application of several novel <sup>13</sup>C-detected NMR experiments, most of which are explicitly designed to characterise the important arginine side-chain.

In 2013, the unique nature of the guanidinium spin system found in the arginine side-chain was recognised and used to develop a <sup>13</sup>C-detected experiment that overcame the problems associated with rapid <sup>1</sup>H<sup>ε</sup> hydrogen exchange. Prior to publication of this experiment, the observation of arginine side-chains in proteins was limited to the typical <sup>1</sup>H-<sup>15</sup>N HSQC-type experiments and consequently suffered from poor signal to noise caused by exchange-mediated coherence loss during the INEPT magnetisation transfer steps. Using frequency-selective RF-pulses to directly target the <sup>13</sup>C<sup>ζ</sup>-<sup>15</sup>N<sup>ε</sup> spin system and the <sup>1</sup>J<sub>CN</sub> scalar coupling to transfer the

## 6. Conclusions

magnetisation, intense  $^{13}\text{C}$ - $^{15}\text{N}$  cross-peaks were observed even for residues undergoing rapid hydrogen exchange. Chapter 2 built on this early work and explored the terminal  $^{15}\text{N}^n$  amines of the guanidinium group. By changing the  $^{15}\text{N}$ -selective refocussing pulses and re-optimising the delay for the  $^{13}\text{C}^\zeta$ -( $^{15}\text{N}^n$ )<sub>2</sub> scalar coupling, a  $^{13}\text{C}^\zeta$ - $^{15}\text{N}^n$  HSQC spectrum was successfully obtained. However, whilst this overcame the hydrogen exchange problem, a further difficulty unique to the  $^{15}\text{N}^n$  nuclei was encountered. Owing to the delocalisation of the  $\text{N}^\epsilon$  lone pair into the  $\text{N}^\epsilon$ - $\text{C}^\zeta$  bond, exchange broadening of the  $^{13}\text{C}^\zeta$ - $^{15}\text{N}^n$  resonances is often observed due to the rate of the restricted rotational exchange about this bond. The degree to which the signals are broadened depends upon the exchange rate with the most severe broadening occurring when the rate is approximately equal to the chemical shift difference (rad/s) between the two  $^{15}\text{N}^n$  nuclei. At the two extremes, rapid exchange results in the detection of a single averaged  $^{15}\text{N}^n$  chemical shift whilst only slow exchange allows the individual frequencies of the two  $^{15}\text{N}^n$  nuclei to be accurately recorded. By recognising that the two  $^{15}\text{N}^n$  nuclei are coupled to the same  $^{13}\text{C}^\zeta$  nucleus, a double-quantum coherence can be generated and selected using a suitable phase cycle. During a subsequent indirect chemical shift evolution period, the pure double-quantum magnetisation evolves at the sum of the two  $^{15}\text{N}^n$  frequencies. This double-quantum coherence is insensitive to the rotational exchange about the  $\text{N}^\epsilon$ - $\text{C}^\zeta$  bond and sharp cross-peaks are detected for all residues within the model protein T4 Lysozyme. The double-quantum approach to the  $^{15}\text{N}^n$  is expected to be generally applicable to biomolecules and was successfully embedded within the existing  $^{13}\text{C}^\zeta$ - $^{15}\text{N}^\epsilon$  experiment to provide a three-dimensional NMR experiment suitable for resonance assignment of arginine  $^{15}\text{N}^n$  nuclei.

Since the late 1950s, following the pioneering work of the *father of hydrogen-deuterium exchange* Linderstrøm-Lang, hydrogen exchange rates have been used to study the tertiary structure and interactions of proteins in solution. Whilst Chapter 2 briefly discussed the problem that rapid hydrogen exchange causes for traditional  $^1\text{H}$ - $^{15}\text{N}$  experiments, Chapter 3 explored the underlying hydrogen exchange process in more detail. The theory behind hydrogen exchange in the presence of non-covalent interactions has been well studied and is often applied to the backbone amide  $^1\text{H}$  nuclei where high degrees of protection are used to infer the presence of secondary and tertiary structure. Arginine residues are often found in active sites and stemming from the presence of five N-H pairs, the potential for hydrogen-bond formation is extensive. Using the  $^{13}\text{C}^\zeta$ - $^{15}\text{N}^\epsilon$  HSQC experiment as a starting point, this Chapter discussed the successful development of the ASHDEX pulse sequence. The ASHDEX sequence is a  $^{13}\text{C}$ -detected pseudo-four-dimensional NMR experiment that allows the measurement of the residue-specific  $^1\text{H}^\epsilon$  exchange rates and is demonstrated on wild-type T4 Lysozyme. Five residues were identified as being engaged in intramolecular interactions, a finding that correlated well with observations

made using D-evolution and MQ-CEST NMR experiments as well as by interrogation of the available X-ray crystallography data.

Together with the  $^{13}\text{C}^{\zeta}\text{-}^{15}\text{N}^{\epsilon}$  HSQC, the novel double-quantum  $^{15}\text{N}^{\eta}$  experiment was used to quantify the small chemical shift differences between protonated and deuterated arginine nuclei in Chapter 4. The guanidinium group of arginine is highly basic, existing purely as a positively charged moiety bearing five exchangeable hydrogen atoms, and preparation of a sample in a deuterium-enriched buffer results in the detection of up to ten separate signals for each residue. The deuterium isotope shifts measured using  $^{13}\text{C}$ -detected NMR were shown, particularly for the  $^{15}\text{N}$  nuclei, to correlate well with the formation of intramolecular salt-bridges with negatively charged residues aspartic or glutamic acid. Reference isotope shifts were measured in synthetic arginine derivatives designed to allow the control of salt-bridge formation. Firstly, a molecule incapable of forming inter- or intramolecular interactions was obtained by blocking the free amine and carboxylic acid functional groups of the free amino acid with additional peptide bonds. A second molecule containing an intramolecular salt-bridge was designed and synthesised with the presence of the interaction confirmed experimentally through a measurement of the decreased rotation of the  $\text{N}^{\epsilon}\text{-C}^{\zeta}$  bond. An application to two proteins containing 19 arginine residues between them identified three salt-bridges from a large increase in the one-bond  $^{15}\text{N}^{\epsilon}$  deuterium isotope shift. The ease at which the isotope shift measurements can be obtained using  $^{13}\text{C}$ -detected NMR ought to provide the spectroscopist with a powerful additional tool for gaining an atomic-level insight into the behaviour of arginine residues within the active site of biomolecules.

Chapter 5 saw a departure from the arginine side-chain and described the development of the CARBEX pulse sequence. Closely related to the ASHDEX sequence of Chapter 3, the CARBEX experiment is designed to be applied to intrinsically disordered proteins and was demonstrated on human  $\alpha$ Synuclein. The backbone spin system is conceptually similar to the one found in the arginine guanidinium group and only a few important modifications needed to be made. The most significant difference between the two spin systems results in the need to decouple the homonuclear  $^1J_{\text{CC}}$  scalar coupling between  $^{13}\text{C}'$  and  $^{13}\text{C}^{\alpha}$  during acquisition. Two alternate approaches are discussed, BASH and IPAP, with the latter being ultimately selected due to hardware reasons. The IPAP decoupling procedure demands that two complimentary datasets are collected: the first with the  $^{13}\text{C}'\text{-}^{13}\text{C}^{\alpha}$  coupling refocussed at the point of detection and the second after evolution to the anti-phase state. This adds an additional dimension to the ASHDEX experiment and results in a pseudo-five-dimension NMR experiment. As for the ASHDEX experiment, post-acquisition processing of the CARBEX dataset results in two pseudo-three-dimensional spectra from which the time-dependent intensity of the protonated and deuterated

## 6. Conclusions

cross-peaks can be used to extract the hydrogen exchange rates. The obtained rates were compared with data obtained using the  $^1\text{H}$ -detected SOLEXY experiment and were found to correlate well. Crucially, the  $^{13}\text{C}$ -detected experiment allowed the measurement of almost twice as many exchange rates than were obtainable by using the SOLEXY pulse sequence. This is a consequence of the superior signal dispersion of  $^{13}\text{C}$  over  $^1\text{H}$  that is typically observed for IDPs and highlights the need for a hydrogen exchange experiment using an alternate detection nucleus.

It is hoped that the methods and applications described herein will further equip the NMR spectroscopist with the necessary tools to study the important relationship between the structure and function of biological entities and ultimately lead to the development of new or improved medical interventions that our continued survival will clearly demand. As has been shown over the last few decades, method development is a gradual process and whilst it remains to be seen what the true impact of this work will be, it is clear that the future of biological NMR spectroscopy will not revolve simply around the proton.

## 6.2 Future Work

### 6.2.1 Double-Quantum Coherences in Histidine and Tyrosine

Much of the work described in this thesis focusses on the functionally important arginine residue and in Chapter 2 the double-quantum experiment exploits the unique spin system found in the guanidinium head group. The significant scalar coupling of arginine  $^{13}\text{C}^\zeta$  with two  $^{15}\text{N}^\eta$  nuclei mediates this magnetisation transfer and based upon DFT calculations, the generation of similar double-quantum coherences for the histidine and tyrosine side chains ought to be possible.

For the histidine side-chain, the  $^{13}\text{C}^{\epsilon 1}$  nucleus is coupled to two nitrogen atoms ( $^{15}\text{N}^{\delta 1}$  and  $^{15}\text{N}^{\epsilon 2}$ ) with a coupling constant that appears to vary significantly upon the tautomer and ionisation state of the imidazole ring (Figure 6.1a). For the  $\text{N}^{\delta 1}\text{-H}$  and  $\text{N}^{\epsilon 2}\text{-H}$  tautomers, a  $^1J_{\text{CN}}$  coupling of around  $-11$  Hz is expected between  $^{13}\text{C}^{\epsilon 1}$  and the *protonated* nitrogen atom whilst the coupling to the non-protonated nitrogen is negligible. As the exchange rate between the two tautomers is likely to be quite fast, the effective coupling constant would be halved to around  $-6$  Hz. This would demand an INEPT delay ( $1/2J$ ) of over 80 ms for each transfer, clearly impractical for all but the smallest of proteins. However, the imidazole ring is basic ( $\text{pK}_a$  6-7) and is able to pick up a proton in suitably acidic solutions. This renders both nitrogen atoms protonated and the two  $^{13}\text{C}\text{-}^{15}\text{N}$  couplings in the positively-charged ring are expected to be equally large ( $-19$  Hz). The size of these couplings would only demand an INEPT delay of 26 ms, similar to the guanidinium group of arginine, and so may provide a framework for a histidine-selective  $^{13}\text{C}\text{-}^{15}\text{N}$  HDQC-type

experiment. Histidine residues have long been known to engage in salt-bridges and other intramolecular interactions and so it is anticipated that such an experiment could provide a useful tool for their continued investigation.

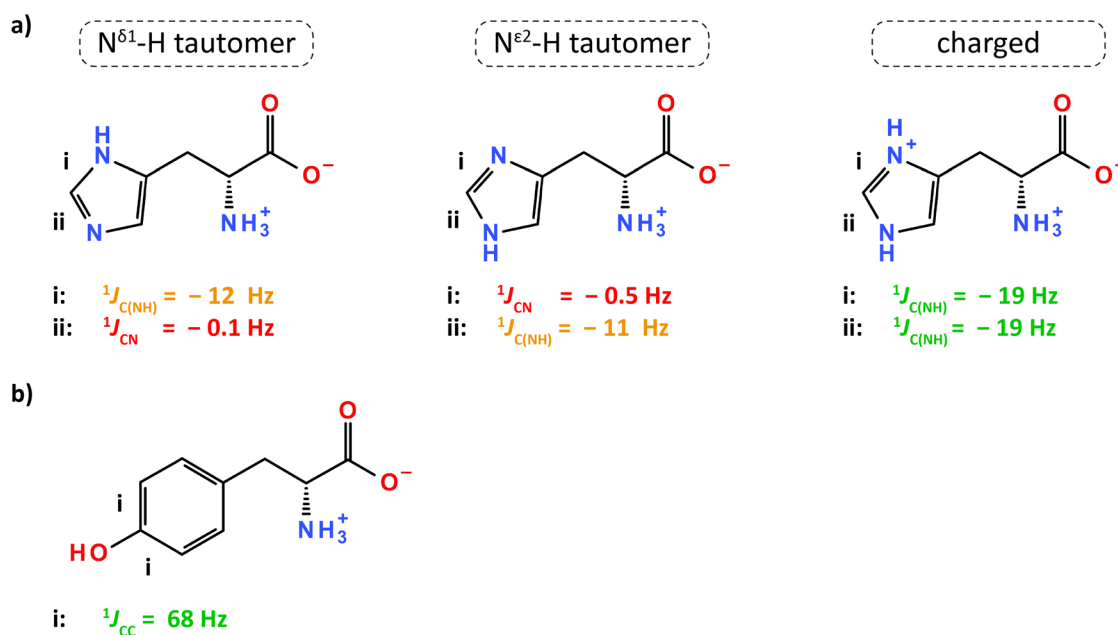


**Figure 6.1** One-bond  $^{13}\text{C}$ - $^{15}\text{N}$  scalar couplings in a) histidine and b) tyrosine side-chains as computed using DFT at the B3LYP/6-311+G(2d,2p)//M06-2X/6-31+G(d,p) level of theory. The ionisation state of histidine directs the magnitude of the scalar coupling and a spin-system suitable for the double-quantum experiment is only found in the charged state. For tyrosine, a suitable spin system exists at all physiological conditions.

For tyrosine, no similar variation of the coupling constants based on side-chain ionisation is expected (Figure 6.1b). The  $^{13}\text{C}^\zeta$  nucleus is directly bonded to oxygen and shares two homonuclear scalar couplings with the two neighbouring  $^{13}\text{C}^\epsilon$  nuclei. The  $^1J_{\text{CC}}$  is large (68 Hz) and would therefore allow an INEPT based magnetisation transfer in approximately 7.4 ms. Complications are expected due to the additional homonuclear scalar couplings around the phenyl ring ( $^3J_{\text{CC}}[^{13}\text{C}^\zeta\text{-}^{13}\text{C}^\nu] = 10 \text{ Hz}$ ,  $^3J_{\text{CC}}[^{13}\text{C}^\epsilon\text{-}^{13}\text{C}^\delta] = 7 \text{ Hz}$ ), although it is anticipated that these could be mitigated through judicious use of frequency-selective pulses to provide a tyrosine  $^{13}\text{C}^\zeta\text{-}^{13}\text{C}^\epsilon$  HDQC experiment. Potential applications could include a quantitative assessment of the ring-flipping rate and therefore contribute to the understanding of *protein breathing* as mediated by hydrophobic residues.

## 6.2.2 Outlook

The importance of protein side-chains cannot be overstated: the side-chain atoms provide the diversity between different amino acids and mediate much of the chemistry on which the function of a biomolecule depends. An intimate knowledge of side-chain behaviour can therefore be invaluable to the scientist wishing to understand or modulate a protein's activity *in vivo* during the search for new or differentiated medicines. Whilst the last few years has seen

## 6. Conclusions

the dramatic rise of cryo-EM as a biophysical technique to rival X-ray crystallography for the determination of protein structure, the side-chain atoms are typically absent from these datasets. NMR spectroscopy therefore remains the principle technique for side-chain analysis, particularly in the native solution state, and it is envisaged that the complementary fields of magnetic resonance and cryo-EM will grow together. Indeed, the incremental hardware developments that have enabled the use of X-detected NMR methods in recent years look set to continue both through cutting-edge probehead design and the availability of  $^1\text{H}$  operating frequencies well beyond 1 GHz. Together with recent computational advances including optimal control theory<sup>[243]</sup> and on-the-fly parameter optimisation,<sup>[244]</sup> such improvements are expected to bring non- $^1\text{H}$  detected NMR experiments to the fore and usher in a new era of biological spectroscopy.

# 7

## Experimental

### 7.1 General Procedures

All chemicals and solvents were purchased from Alfa Aesar, Apollo Scientific Ltd., Fisher Scientific UK Ltd., Merck KGaA or VWR International Ltd. and used without further purification. Lysogeny broth (LB)/Agar plates were freshly prepared in house using the appropriate antibiotic prior to each protein expression. The pH of aqueous samples was determined using a Thermo Scientific Orion Star pH meter and is quoted uncorrected for the isotope effect for partially deuterated solutions. Unless stated otherwise, all cell cultures were agitated at 200 rpm using a Healthcare Equipment ES-20 Compact Shaker or New Brunswick Innova Incubators. The optical density of growing cell cultures was measured at 600 nm ( $OD_{600}$ ) using a Thermo Scientific Biomate 3 UV-vis spectrophotometer. Centrifugation of large volumes was performed on a Beckman Avanti J25 centrifuge. Where required, NMR samples were centrifuged using an Eppendorf 5415R Refrigerated Centrifuge. Samples were loaded onto FPLC columns using a GE Healthcare P-1 peristaltic pump. Column chromatography of protein samples was performed on an GE Healthcare AKTA FPLC system equipped with a UV detector operating at 280 nm. Analysis of the resulting fractions was performed by SDS-PAGE using NuPAGE 4-12% Bis-Tris gels. The concentration of proteinaceous samples was determined using the UV absorbance at 280 nm ( $A_{280}$ ) as measured on a Thermo Scientific Nanodrop 2000 spectrophotometer in combination with the molar attenuation coefficient ( $\epsilon$ ) calculated using the protein sequence. The derivatised arginine samples were purified on a Waters Autopurification LC system equipped with an SQD2 mass spectrometer. Binary solvent gradients were applied over the course of 11 min and the retention times are quoted uncorrected for the intrinsic 2.5 min dead time of the system. Analysis of the resulting fractions was performed on a Waters I-Class UPLC system equipped with a QDa mass detector. Separation was achieved using a 5-15% gradient of solvent A (100 mM ammonium formate, pH 3) in solvent B (95% acetonitrile) over the course of 2.6 min. UPLC retention times are quoted uncorrected for the intrinsic 0.1 min dead time of the system.

## 7.2 Protein Expression and Purification

### 7.2.1 T4 Lysozyme<sup>[245]</sup>

The two different constructs of the T4-Lysozyme protein used in this work were prepared using the general procedure as outlined below. The initial plasmids were kindly provided by Prof. L. Kay the University of Toronto, Canada.

#### C54TC97A Mutant (T4WT)

MNIFEMLRIDEGLRLKIYKDTEGYTYTIGIGHLLTKSPSLNAAKSELDKAI GRNTNGVITKDEA  
EKLFNQDVDAAVRGILRNAKLKPVYDSLDAVRRAAAINMVFQMGETGVAGFTNSLRMLQQKRW  
DEAAVNLAKSRYNQTPNRAKRVIITTFRTGTW DAYKNL

**No. of amino acids:** 164      **Molecular weight:** 18559.3      **Theoretical pI:** 9.76

#### C54TC97AL99A Mutant (T4L99A)

MNIFEMLRIDEGLRLKIYKDTEGYTYTIGIGHLLTKSPSLNAAKSELDKAI GRNTNGVITKDEA  
EKLFNQDVDAAVRGILRNAKLKPVYDSLDAVRRAAALINMVFQMGETGVAGFTNSLRMLQQKRW  
DEAAVNLAKSRYNQTPNRAKRVIITTFRTGTW DAYKNL

**No. of amino acids:** 164      **Molecular weight:** 18601.4      **Theoretical pI:** 9.76

The gene for either T4WT or T4L99A in the kanamycin resistant pET-29b (+) vector was transformed into BL21 (DE3) chemically competent *E. coli* cells using standard techniques. A single colony was used to inoculate a 50 mL LB culture, which was grown overnight at 37 °C. This was used to inoculate 2 L of minimal M9 media supplemented with 1 g L<sup>-1</sup> [<sup>15</sup>N]-ammonium chloride and 3 g L<sup>-1</sup> [<sup>13</sup>C]-glucose as the sole nitrogen and carbon sources, respectively. The M9 culture was grown to OD<sub>600</sub> ≈ 0.7 before an overnight induction with 1 mM IPTG at 16 °C. The cells were harvested by centrifugation at 4,000 xg and 4 °C for 20 min. Cells were resuspended in 80 mL NaP-1 buffer (50 mM NaPO<sub>4</sub>, 2 mM EDTA, pH 6.5) with 1 cComplete™ Mini Protease Inhibitor Cocktail tablet and lysed by sonication. Cell debris was pelleted (20,000 xg, 20 min) and the soluble fraction was loaded onto a 5 mL HiTrap SF FF column (GE Healthcare). Protein was eluted from the column using a linear gradient (0-100%) of NaP-2 buffer (50 mM NaPO<sub>4</sub>, 2 mM EDTA, 1 mM NaCl, pH 6.5). T4WT/T4L99A eluted at ~300 mM NaCl. Fractions containing T4WT/T4L99A were pooled and further purified by size exclusion chromatography (SEC) using a Superdex S75 gel filtration column (GE Healthcare) (50 mM NaPO<sub>4</sub>, 25 mM NaCl, 2 mM EDTA, pH 5.5). T4WT/T4L99A eluted at ~75 mL. Fractions were pooled and concentrated using a 10 kDa MWCO concentrator to a final concentration of ~2.0 mM. NMR samples were buffer exchanged as appropriate to provide samples at different pHs or <sup>2</sup>H<sub>2</sub>O concentrations and briefly centrifuged at 15,000 xg immediately prior to use to remove any insoluble particulates.

**7.2.2 Bacterial Ribonuclease (Barnase)**

AQVINTFDGVADYLLTYHKLDPDNYITKSEAQALGWVASKGNLADVAPGKSIGGDIFSNREGKL  
PAKSGRTWREADINYTSGFRNSDRILYSSDWLIYKTTDHYKTFTKIR

**No. of amino acids:** 110      **Molecular weight:** 12381.9      **Theoretical pI:** 9.16

A sample of 0.5 mM U-[<sup>13</sup>C,<sup>15</sup>N]-barnase (kindly provided by Prof. M. Williamson at the University of Sheffield, UK) was buffer exchanged into 50 mM NaPO<sub>4</sub>, 25 mM NaCl, 2 mM EDTA, pH 5.5, 50% <sup>2</sup>H<sub>2</sub>O prior to use.

**7.2.3 Ubiquitin (Ubq)**

MQIFVKTLTGKTTITLEVEPSDTIENVKAKIQDKEGIPPDQQRLLIFAGKQLEDGRTLSDYNIQK  
ESTLHLVLRLRGG

**No. of amino acids:** 76      **Molecular weight:** 8564.8      **Theoretical pI:** 6.56

A 1.0 mM NMR sample of U-[<sup>13</sup>C,<sup>15</sup>N]-human ubiquitin prepared in 50 mM NaPO<sub>4</sub>, pH 7.0, 10% <sup>2</sup>H<sub>2</sub>O was purchased from CortecNet, France and used without further purification.

**7.2.4 αSynuclein (αS)<sup>[246]</sup>**

MDVFMKGLSKAKEGVVAAAEEKTKQGVAEAAAGKTKEGVLYVGSKTKEGVVHGVATVAEKTKEQV  
TNVGGAVVTGVTAVAQKTVEGAGSIAAATGFVKKDQLGKNEEGAPQEGILEDMFVDPDNEAYE  
MPSEEGYQDYEPEA

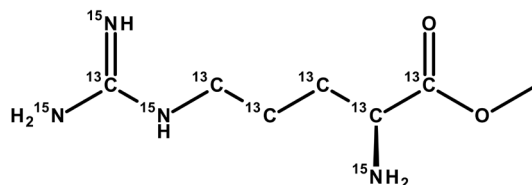
**No. of amino acids:** 140      **Molecular weight:** 14460.2      **Theoretical pI:** 4.67

The gene for αS in the ampicillin-resistant pT7-7 vector (kindly provided by Prof. P. Selenko at the Weizmann Institute of Science, Israel) was transformed into BL21 (DE3) chemically competent *E. coli* cells using standard techniques. A single colony was used to inoculate a 3 mL LB culture, which was grown for 6 h at 37 °C. This was used to inoculate 100 mL of minimal M9 media supplemented with 1 g L<sup>-1</sup> [<sup>15</sup>N]-ammonium chloride and 3 g L<sup>-1</sup> [<sup>13</sup>C]-glucose as the sole nitrogen and carbon sources, respectively. This culture was grown overnight at 37 °C and used to inoculate a final 1 L M9 culture. The final culture was grown to OD<sub>600</sub> ≈ 0.7 before a 3 h induction with 1 mM IPTG at 37 °C. The cells were harvested by centrifugation at 4,000 xg and 4 °C for 20 min. Cells were resuspended in 15 mL lysis buffer (20 mM Tris, 2 mM EDTA, pH 7 and 1 cOmplete™ Mini Protease Inhibitor Cocktail tablet) and heated to 90 °C for 10 min. After pelleting of the cell debris (20,000 xg, 20 min) the soluble fraction was loaded onto a 5 mL HiTrap Q FF column (GE Healthcare) (20 mM Tris, 2 mM EDTA, pH 7.0). αS was eluted from the column using a gradient of 1 M NaCl at ~250 mM NaCl. Pooled fractions were buffer exchanged into H<sub>2</sub>O and stored at -80 °C. NMR samples were made by first thawing the frozen samples and passing through a 100 kDa filter before buffer exchanging into NMR buffer (20 mM NaPO<sub>4</sub>, 10 mM NaCl, 1 mM EDTA, pH 7.0) using a 10 kDa MWCO concentrator. NMR samples were passed through a 30 kDa filter to remove any aggregated protein and contained 0.6 - 1.0 mM αS.

## 7.3 Synthetic Chemistry

### 7.3.1 Arginine Methyl Ester

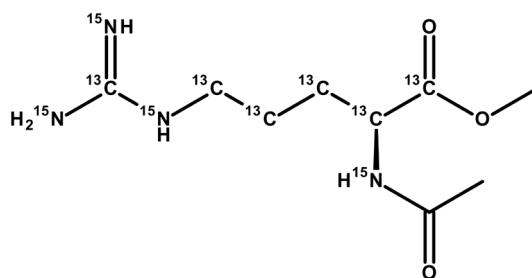
#### Methyl (2S)-2-[<sup>15</sup>N]amino-5-[<sup>13</sup>C,<sup>15</sup>N<sub>3</sub>]guanidino-[1,2,3,4,5-<sup>13</sup>C<sub>5</sub>]pentanoate **2**



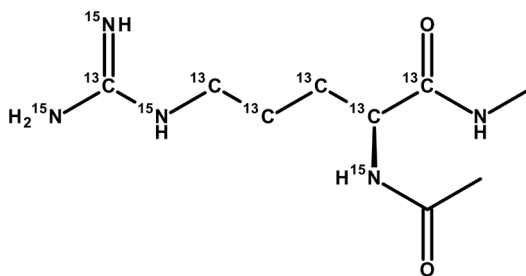
[<sup>13</sup>C<sub>6</sub>,<sup>15</sup>N<sub>4</sub>]-L-arginine hydrochloride **1** (104 mg, 0.472 mmol) was dissolved in hydrochloric acid (3 M) in methanol (1 mL, 3 mmol) and stirred overnight at room temperature. The solution was concentrated *in vacuo* to give the desired product di-hydrochloride salt as a white solid (134 mg, 100%). UPLC (HILIC, pH 3) 2.25 min. ESI-MS (pos. *m/z*) 199.2 (100% [M+H]<sup>+</sup>). TOF-MS (pos. *m/z*) [M+H]<sup>+</sup> calcd. for [<sup>13</sup>C]<sub>6</sub>CH<sub>17</sub>[<sup>15</sup>N]<sub>4</sub>O<sub>2</sub>: 199.1434; found: 199.1437. <sup>1</sup>H NMR (400 MHz, DMSO-*d*<sub>6</sub>) δ 8.57 (d, *J* = 71.8 Hz, 3H, NH<sub>3</sub>), 7.79 (d, *J* = 92.4 Hz, 1H, H<sup>ε</sup>), 7.20 (br. s, 4H, H<sup>n</sup>), 4.07 (d, *J* = 146.9 Hz, 1H, H<sup>α</sup>), 3.77 (d, *J* = 3.8 Hz, 3H, CH<sub>3</sub>), 3.13 (d, *J* = 137.7 Hz, 2H, H<sup>δ</sup>), 1.82 (d, *J* = 125.3 Hz, 2H, H<sup>γ</sup>), 1.61 (d, *J* = 130.6 Hz, 1H, H<sup>β'</sup>), 1.52 (d, *J* = 128.8 Hz, 1H, H<sup>β''</sup>). <sup>13</sup>C NMR (101 MHz, DMSO-*d*<sub>6</sub>) δ 170.30 (d, *J* = 61.7 Hz, C<sup>i</sup>), 157.32 (q, *J* = 20.6 Hz, C<sup>j</sup>), 53.34 (CH<sub>3</sub>), 51.97 (ddt, *J* = 62.1, 33.8, 5.8 Hz, C<sup>a</sup>), 40.43 (ddd, *J* = 35.8, 9.5, 5.8 Hz, C<sup>δ</sup>), 27.63 (t, *J* = 34.1 Hz, C<sup>γ</sup>), 24.67 (t, *J* = 35.1 Hz, C<sup>β</sup>).

### 7.3.2 Capped Arginine

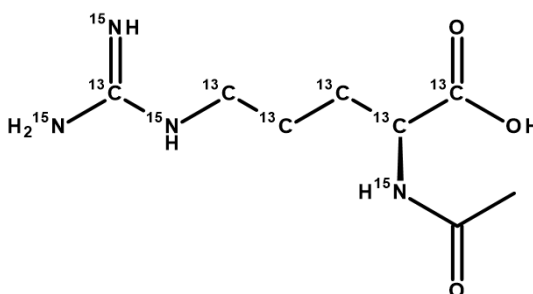
#### Methyl (2S)-2-[<sup>15</sup>N]acetamido-5-[<sup>13</sup>C,<sup>15</sup>N<sub>3</sub>]guanidino-[1,2,3,4,5-<sup>13</sup>C<sub>5</sub>]pentanoate **3**



Methyl (2S)-2-[<sup>15</sup>N]amino-5-[<sup>13</sup>C,<sup>15</sup>N<sub>3</sub>]guanidino-[1,2,3,4,5-<sup>13</sup>C<sub>5</sub>]pentanoate **2** (134 mg, 0.494 mmol) was dissolved in *N,N*-dimethyl formamide (2.5 mL) at 0 °C in an ice/water bath before triethylamine (150 μL, 1.08 mmol, 2.2 eq.) was added. Acetic anhydride (47 μL, 0.497 mmol, 1 equiv.) was added dropwise and the reaction stirred on ice for 1 hour. The solution was concentrated *in vacuo* and the crude residue was taken onto the subsequent step without further purification. UPLC (HILIC, pH 3) 0.97 min. ESI-MS (pos. *m/z*) 241.2 (100% [M+H]<sup>+</sup>).

**(2S)-2-[<sup>15</sup>N]acetamido-5-[<sup>13</sup>C,<sup>15</sup>N<sub>3</sub>]guanidino-*N*-methyl-[1,2,3,4,5-<sup>13</sup>C<sub>5</sub>]pentanamide 4**

Crude methyl (2S)-2-[<sup>15</sup>N]acetamido-5-[<sup>13</sup>C,<sup>15</sup>N<sub>3</sub>]guanidino-[1,2,3,4,5-<sup>13</sup>C<sub>5</sub>]pentanoate **3** was dissolved in methylamine (33%) in ethanol (3 mL, 27 mmol, 50 equiv.) before the reaction was stirred overnight at room temperature. The solution was concentrated *in vacuo* and the residue purified over a 19 x 150 mm 5 μm HILIC prep-HPLC column (Waters) using a 10 - 20% gradient of solvent A (100 mM ammonium formate, pH 3) in solvent B (95% acetonitrile). The desired compound eluted at 10.3 min as confirmed by mass spectrometry. Fractions containing **4** were pooled and concentrated *in vacuo* to give the desired product as a gummy solid (65 mg, 46% over two steps, formate salt). UPLC (HILIC, pH 3) 1.58 min. ESI-MS (pos. *m/z*) 240.2 (100% [M+H]<sup>+</sup>). TOF-MS (pos. *m/z*) [M+H]<sup>+</sup> calcd. for [<sup>13</sup>C]<sub>6</sub>C<sub>3</sub>H<sub>20</sub>[<sup>15</sup>N]<sub>4</sub>NO<sub>2</sub>: 240.1700; found: 240.1703. <sup>1</sup>H NMR (400 MHz, DMSO-d<sub>6</sub>) δ 8.68 (d, *J* = 91.4 Hz, 1H, H<sup>ε</sup>), 8.14 (dd, *J* = 91.8, 7.5 Hz, 1H, NH), 7.96 (p, *J* = 4.5 Hz, 1H, NH), 7.66 (d, *J* = 88.2 Hz, 4H, H<sup>η</sup>), 4.16 (d, *J* = 140.2 Hz, 1H, H<sup>α</sup>), 3.04 (d, *J* = 138.0 Hz, 2H, H<sup>δ</sup>), 2.57 (dd, *J* = 4.6, 3.4 Hz, 3H, *N*-CH<sub>3</sub>), 1.85 (d, *J* = 1.3 Hz, 3H, CH<sub>3</sub>), 1.66 (d, *J* = 139.6 Hz, 1H, H<sup>β'</sup>), 1.46 (d, *J* = 127.9 Hz, 3H, H<sup>β''</sup> + H<sup>γ</sup>). <sup>13</sup>C NMR (101 MHz, DMSO-d<sub>6</sub>) δ 172.44 (dd, *J* = 53.1, 2.3 Hz, C<sup>γ</sup>), 169.75 (d, *J* = 13.6 Hz, C<sup>γ</sup>), 157.72 (q, *J* = 20.3 Hz, C<sup>ε</sup>), 52.53 (dddd, *J* = 52.5, 35.4, 11.0, 4.1 Hz, C<sup>α</sup>), 40.50 (ddd, *J* = 35.7, 9.8, 4.5 Hz, C<sup>δ</sup>), 29.56 (t, *J* = 35.2 Hz, C<sup>β</sup>), 25.96 (*N*-CH<sub>3</sub>), 25.49 (t, *J* = 35.3 Hz, C<sup>γ</sup>), 22.96 (d, *J* = 8.6 Hz, CH<sub>3</sub>).

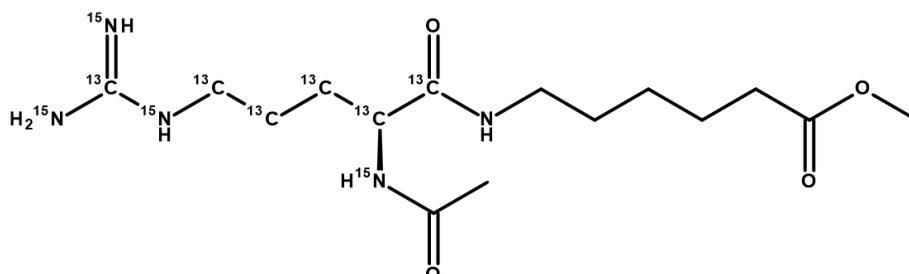
**7.3.3 Complexed Arginine****(2S)-2-[<sup>15</sup>N]acetamido-5-[<sup>13</sup>C,<sup>15</sup>N<sub>3</sub>]guanidino-*N*-methyl-[1,2,3,4,5-<sup>13</sup>C<sub>5</sub>]pentanoic acid 5**

Crude methyl (2S)-2-[<sup>15</sup>N]acetamido-5-[<sup>13</sup>C,<sup>15</sup>N<sub>3</sub>]guanidino-[1,2,3,4,5-<sup>13</sup>C<sub>5</sub>]pentanoate **3** was dissolved in water (2 mL) and lithium hydroxide (50 mg, 1.19 mmol, 2.2 equiv.) was added before the reaction was stirred overnight at room temperature. The solution was adjusted to pH 7 with

## 7. Experimental

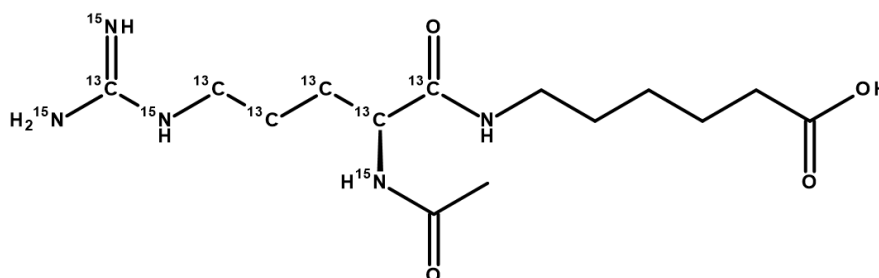
hydrochloric acid (conc. 37%) and subsequently concentrated *in vacuo*. The crude residue was taken onto the subsequent step without further purification. UPLC (HILIC, pH 3) 2.47 min. ESI-MS (pos. *m/z*) 227.2 (100% [M+H]<sup>+</sup>).

### Methyl 6-[[[(2S)-2-[<sup>15</sup>N]acetamido-5-[<sup>13</sup>C,<sup>15</sup>N<sub>3</sub>]guanidino-[1,2,3,4,5-<sup>13</sup>C<sub>5</sub>]pentanoyl]amino]hexanoate **6**



Crude (2S)-2-[<sup>15</sup>N]acetamido-5-[<sup>13</sup>C,<sup>15</sup>N<sub>3</sub>]guanidino-*N*-methyl-[1,2,3,4,5-<sup>13</sup>C<sub>5</sub>]pentanoic acid **5**, methyl 6-aminocaproate (90 mg, 0.495 mmol, 1 equiv.), 1-hydroxybenzotriazole (300 mg, 1.959 mmol, 4 equiv.) and *N,N*-diisopropylethylamine (0.45 mL, 2.6 mmol, 5 equiv.) were dissolved in *N,N*-dimethyl formamide (2 mL) at 0 °C in an ice/water bath. HBTU (225 mg, 0.593 mmol, 1.2 equiv.) was added and the reaction was stirred overnight whilst warming to room temperature. The desired product was purified directly from the reaction mixture by reverse-phase prep-HPLC over a 19 x 100 5 μm C18 column using a gradient of 10 - 25% solvent B (95% acetonitrile) in solvent A (10 mM ammonium bicarbonate, pH 10). The desired compound eluted at 7.1 min as confirmed by mass spectrometry. Fractions containing **6** were pooled and concentrated *in vacuo* to give the desired product as a white solid (85 mg, 44% over three steps). UPLC (HILIC, pH 3) 1.19 min. ESI-MS (pos. *m/z*) 354.2 (100% [M+H]<sup>+</sup>).

### 6-[[[(2S)-2-[<sup>15</sup>N]acetamido-5-[<sup>13</sup>C,<sup>15</sup>N<sub>3</sub>]guanidino-[1,2,3,4,5-<sup>13</sup>C<sub>5</sub>]pentanoyl]amino]hexanoic acid **7**



Methyl 6-[[[(2S)-2-[<sup>15</sup>N]acetamido-5-[<sup>13</sup>C,<sup>15</sup>N<sub>3</sub>]guanidino-[1,2,3,4,5-<sup>13</sup>C<sub>5</sub>]pentanoyl]oxyhexanoate **6** (85 mg, 0.218 mmol) was dissolved in water (2 mL) and lithium hydroxide (20 mg, 0.477 mmol, 2.2 equiv.) was added before the reaction was stirred overnight at room temperature. Following adjustment to pH 7 with hydrochloric acid (conc. 37%), the desired product was purified directly from the reaction mixture over a 19 x 150 mm 5 μm HILIC prep-HPLC column (Waters) using a

10 - 20% gradient of solvent A (100 mM ammonium formate, pH 3) in solvent B (95% acetonitrile). The desired compound eluted at 10.2 min as confirmed by mass spectrometry. Fractions containing **7** were pooled and concentrated *in vacuo* to give the desired product as a gummy solid (50 mg, 61%, formate salt). UPLC (HILIC, pH 3) 1.79 min. ESI-MS (pos. *m/z*) 340.2 (100% [M+H]<sup>+</sup>). TOF-MS (pos. *m/z*) [M+H]<sup>+</sup> calcd. for [<sup>13</sup>C]<sub>6</sub>C<sub>8</sub>H<sub>28</sub>[<sup>15</sup>N]<sub>4</sub>NO<sub>4</sub>: 340.2224; found: 340.2235. <sup>1</sup>H NMR (600 MHz, DMSO-d<sub>6</sub>) δ 9.89 (d, *J* = 90.5 Hz, 1H, H<sup>ε</sup>), 8.04 (q, *J* = 5.1 Hz, 1H, NH), 7.99 (dd, *J* = 92.0, 7.8 Hz, 1H, NH), 7.30 (d, *J* = 91.0 Hz, 4H, H<sup>n</sup>), 4.19 (d, *J* = 140.7 Hz, 1H, H<sup>α</sup>), 3.29 – 3.17 (m, 1H, *N*-CH<sub>2</sub>), 3.09 (d, *J* = 144.6 Hz, 1H, H<sup>δ'</sup>), 3.01 (d, *J* = 138.6 Hz, 1H, H<sup>δ''</sup>), 2.93 – 2.80 (m, 1H, *N*-CH<sub>2</sub>), 2.03 (t, *J* = 6.6 Hz, 2H, CH<sub>2</sub>CO<sub>2</sub>H), 1.84 (d, *J* = 1.3 Hz, 3H, CH<sub>3</sub>), 1.68 (d, *J* = 136.8 Hz, 1H, C<sup>β'</sup>), 1.64 – 1.17 (m, 5H, C<sup>β''</sup>+ C<sup>γ</sup> + CH<sub>2</sub>CH<sub>2</sub>CH<sub>2</sub>). <sup>13</sup>C NMR (151 MHz, DMSO-d<sub>6</sub>) δ 177.22 (CO<sub>2</sub>H), 171.89 (dd, *J* = 52.7, 2.2 Hz, C'), 169.50 (d, *J* = 13.4 Hz, C'), 157.81 (q, *J* = 20.1 Hz, C<sup>ξ</sup>), 52.40 (dddd, *J* = 51.8, 34.9, 11.5, 4.1 Hz, C<sup>α</sup>), 40.26 (ddd, *J* = 35.3, 9.7, 4.1 Hz, C<sup>δ</sup>), 38.60 (*N*-CH<sub>2</sub>), 36.26 (CH<sub>2</sub>CO<sub>2</sub>H), 30.26 (t, *J* = 35.0 Hz, C<sup>β</sup>), 29.00 (CH<sub>2</sub>), 26.35 (CH<sub>2</sub>), 25.67 (t, *J* = 35.3 Hz, C<sup>γ</sup>), 25.48 (CH<sub>2</sub>), 22.96 (dd, *J* = 9.0, 1.5 Hz, CH<sub>3</sub>).

## 7.4 NMR Spectroscopy

### 7.4.1 NMR Hardware

All NMR experiments were performed on the Bruker spectrometers set out below in Table 7.1. Unless stated otherwise, all NMR experiments were performed at 298 K. The deuterated solvent was used as the lock and the residual solvent as the internal reference in all cases.

Spectrometer	B <sub>0</sub> Field T ( <sup>1</sup> H MHz)	Probe	Location
Bruker AVIII	11.7 (500)	BBO Prodigy	UCL, London
Bruker AVI	14.1 (600)	TXO CryoProbe	UCL, London
Bruker AVIII	16.4 (700)	TCI CryoProbe	UCL, London
Bruker AVIIID	18.8 (800)	TCI CryoProbe	UCL, London
Bruker AVIIID	18.8 (800)	TCI CryoProbe	Francis Crick Institute, London
Bruker AVIIID	22.3 (950)	TCI CryoProbe	Francis Crick Institute, London
Bruker AVIII	9.4 (400)	DCH CryoProbe	UCB, Slough
Bruker AV4	14.1 (600)	QCI-F CryoProbe	UCB, Slough

**Table 7.1** NMR spectrometers used during this work. All probeheads were 5 mm and equipped with a z-gradient coil with a maximum nominal gradient strength of 53.5 G/cm.

### 7.4.2 Small Molecule NMR

Chemical shift information for each signal is given in units of parts per million (ppm) relative to tetramethylsilane (TMS) where δ<sub>H,C</sub> = 0.00 ppm. The number of protons (n) for a reported resonance signal are indicated as nH from their integral value and their multiplicity by the

## 7. Experimental

symbol in parentheses. Their coupling constants ( $J$ ) are determined by analysis using the MestreNova software (Version 14.1.1, Mestrelab Research, 2019) quoted to the nearest 0.1 Hz. Identical coupling constants are averaged in each spectrum and are reported to the nearest 0.1 Hz. Atom-specific chemical shift assignments were confirmed using standard two-dimensional NMR experiments including:  $^1\text{H}$ - $^{13}\text{C}$  HSQC,  $^1\text{H}$ - $^{13}\text{C}$  HMBC,  $^1\text{H}$ - $^1\text{H}$  COSY and  $^1\text{H}$ - $^1\text{H}$  NOESY.

### 7.4.3 Protein NMR

$^1\text{H}$  and  $^{13}\text{C}$  chemical shift information for each signal is given in units of parts per million (ppm) relative to tetramethylsilane (TMS) where  $\delta_{\text{H,C}} = 0.00$  ppm.  $^{15}\text{N}$  chemical shift information is given in units of parts per million (ppm) relative to liquid ammonia ( $\text{NH}_3$ ) where  $\delta_{\text{N}} = 0.00$  ppm. Backbone  $^1\text{H}$ ,  $^{15}\text{N}$ ,  $^{13}\text{C}'$  and  $^{13}\text{C}^\alpha$  chemical shift assignments for T4-lysozyme, Barnase and  $\alpha$ Synuclein were taken from literature sources and confirmed where appropriate using standard triple resonance NMR experiments: HNCO/HN(CA)CO and HNCACB/HN(CO)CACB. Arginine  $^{13}\text{C}^\zeta$  and  $^{15}\text{N}^\epsilon$  resonances were assigned by comparing the  $^{13}\text{C}^{\alpha-\delta}$  chemical shifts measured using CC(CO)NH and CCN $^\epsilon\text{C}^\zeta$  TOCSY experiments as described in Chapter 1. The  $^{15}\text{N}^\eta$  chemical shifts were assigned using the novel pulse sequence described in Chapter 2 (Figure 2.7). NMR data was processed using NMRPipe<sup>[247]</sup> and subsequently analysed using the Analysis module of the CCPNMR package.<sup>[248]</sup>

### 7.4.4 NMR Parameters

Selected acquisition parameters for the NMR spectra presented in this thesis are shown below in Table 7.2.

Figure	Sample	Conc. mM	B <sub>0</sub> Field T	Temp. K	Spectral Width ppm	Complex Points	d <sub>1</sub> sec	NS	Time hr
2.1	T4L99A pH 5.5	2.0	16.4	298	10 ( $^{15}\text{N}$ ) 11 ( $^{13}\text{C}$ )	48 ( $^{15}\text{N}$ ) 512 ( $^{13}\text{C}$ )	3	128	12
2.2	T4L99A pH 5.5	2.0	11.7	298	80 ( $^{15}\text{N}$ ) 16 ( $^1\text{H}$ )	512 ( $^{15}\text{N}$ ) 1024 ( $^1\text{H}$ )	1	4	1.3
2.3c	T4L99A pH 5.5	2.0	16.4	298	12 ( $^{15}\text{N}$ ) 11 ( $^{13}\text{C}$ )	48 ( $^{15}\text{N}$ ) 512 ( $^{13}\text{C}$ )	3	256	23
2.8a	<i>free arg. 1</i> pH 5.5	25	14.1	275	10 ( $^{15}\text{N}$ ) 20 ( $^{13}\text{C}$ )	32 ( $^{15}\text{N}$ ) 512 ( $^{13}\text{C}$ )	2	16	0.7
2.8b	<i>free arg. 1</i> pH 5.5	25	14.1	275	10 ( $^{15}\text{N}$ ) 20 ( $^{13}\text{C}$ )	32 ( $^{15}\text{N}$ ) 512 ( $^{13}\text{C}$ )	2	16	0.7
2.8c	<i>free arg. 1</i> pH 5.5	25	14.1	275	5 ( $^{15}\text{N}$ ) 5 ( $^{15}\text{N}$ ) 20 ( $^{13}\text{C}$ )	16 ( $^{15}\text{N}$ ) 16 ( $^{15}\text{N}$ ) 512 ( $^{13}\text{C}$ )	2	16	12
2.9	T4L99A pH 5.5	2.0	16.4	298	12 ( $^{15}\text{N}$ ) 11 ( $^{13}\text{C}$ )	48 ( $^{15}\text{N}$ ) 512 ( $^{13}\text{C}$ )	3	256	23

Figure	Sample	Conc. mM	B <sub>0</sub> Field T	Temp. K	Spectral Width ppm	Complex Points	d <sub>1</sub> sec	NS	Time hr
2.10b	T4L99A pH 5.5	2.0	11.7	298	10 ( <sup>15</sup> N) 10 ( <sup>15</sup> N) 40 ( <sup>13</sup> C)	32 ( <sup>15</sup> N) 32 ( <sup>15</sup> N) 512 ( <sup>13</sup> C)	3.5	16	71
2.11a,b	<i>free arg. 1</i> pH 5.5	25	14.1	274	10 ( <sup>15</sup> N) 20 ( <sup>13</sup> C)	32 ( <sup>15</sup> N) 512 ( <sup>13</sup> C)	2	8	0.3
2.11c,d	<i>free arg. 1</i> pH 5.5	25	14.1	308	10 ( <sup>15</sup> N) 20 ( <sup>13</sup> C)	32 ( <sup>15</sup> N) 512 ( <sup>13</sup> C)	2	8	0.3
3.3b	<i>free arg. 1</i> pH 5.5	25	14.1	298	10 ( <sup>15</sup> N) 20 ( <sup>13</sup> C)	48 ( <sup>15</sup> N) 512 ( <sup>13</sup> C)	2	16	1.0
3.5b	<i>free arg. 1</i> pH 5.5	25	14.1	298	10 ( <sup>15</sup> N) 20 ( <sup>13</sup> C)	8 ( $\tau_{\text{mix}}$ ) 48 ( <sup>15</sup> N) 512 ( <sup>13</sup> C)	2	16	9.0
3.6b	<i>free arg. 1</i> pH 5.5	25	14.1	298	5 ( <sup>15</sup> N) 5 ( <sup>15</sup> N) 20 ( <sup>13</sup> C)	4 ( $\tau_{\text{mix}}$ ) 16 ( <sup>15</sup> N) 16 ( <sup>15</sup> N) 512 ( <sup>13</sup> C)	2	8	22
3.8a	<i>free arg. 1</i> pH 5.5	25	11.7	298	5 ( <sup>15</sup> N) 20 ( <sup>13</sup> C)	64 ( <sup>15</sup> N) 512 ( <sup>13</sup> C)	1	8	0.3
3.8b	<i>free arg. 1</i> pH 5.5	25	11.7	298	5 ( <sup>15</sup> N) 20 ( <sup>13</sup> C)	64 ( <sup>15</sup> N) 512 ( <sup>13</sup> C)	1	8	0.3
3.8c	<i>free arg. 1</i> pH 5.5	25	11.7	298	5 ( <sup>15</sup> N) 20 ( <sup>13</sup> C)	64 ( <sup>15</sup> N) 512 ( <sup>13</sup> C)	1	8	0.3
3.19	T4WT pH 5.5	2.0	18.8	298	10 ( <sup>15</sup> N) 20 ( <sup>13</sup> C)	2 ( $\phi_3$ ) 10 ( $\tau_{\text{mix}}$ ) 48 ( <sup>15</sup> N) 512 ( <sup>13</sup> C)	1	80	64
3.21	T4WT pH 7.4	2.0	18.8	308	10 ( <sup>15</sup> N) 20 ( <sup>13</sup> C)	2 ( $\phi_3$ ) 10 ( $\tau_{\text{mix}}$ ) 48 ( <sup>15</sup> N) 512 ( <sup>13</sup> C)	1	80	64
3.22	T4WT pH 5.5	2.0	18.8	288	10 ( <sup>15</sup> N) 16 ( <sup>1</sup> H)	16 ( <sup>15</sup> N) 1024 ( <sup>1</sup> H)	1	8	0.1 <sup>a</sup>
4.1a	<i>free arg. 1</i> pH 5.5	25	14.1	298	10 ( <sup>15</sup> N) 20 ( <sup>13</sup> C)	64 ( <sup>15</sup> N) 512 ( <sup>13</sup> C)	2	4	0.3
4.1b	<i>free arg. 1</i> pH 5.5	25	14.1	298	10 ( <sup>15</sup> N) 20 ( <sup>13</sup> C)	64 ( <sup>15</sup> N) 512 ( <sup>13</sup> C)	2	4	0.3
4.1c	<i>free arg. 1</i> pH 5.5	25	14.1	298	10 ( <sup>15</sup> N) 20 ( <sup>13</sup> C)	64 ( <sup>15</sup> N) 512 ( <sup>13</sup> C)	2	16	1.3
4.1d	<i>free arg. 1</i> pH 5.5	25	14.1	298	10 ( <sup>15</sup> N) 10 ( <sup>15</sup> N) 20 ( <sup>13</sup> C)	30 ( <sup>15</sup> N) 30 ( <sup>15</sup> N) 512 ( <sup>13</sup> C)	2	16	19
4.3b	<i>free arg. 1</i> pH 5.5	25	14.1	298	10 ( <sup>15</sup> N) 20 ( <sup>13</sup> C)	2 ( $\phi_3$ ) 64 ( <sup>15</sup> N) 512 ( <sup>13</sup> C)	2	4	0.6
4.4b	<i>free arg. 1</i> pH 5.5	25	14.1	298	10 ( <sup>15</sup> N) 20 ( <sup>13</sup> C)	2 ( $\phi_3$ ) 64 ( <sup>15</sup> N) 512 ( <sup>13</sup> C)	2	64	10

## 7. Experimental

Figure	Sample	Conc. mM	B <sub>0</sub> Field T	Temp. K	Spectral Width ppm	Complex Points	d <sub>1</sub> sec	NS	Time hr
4.8	<i>complexed arg. 7</i>	25	14.1	298	10 ( <sup>15</sup> N) 20 ( <sup>13</sup> C)	64 (CEST) 14 ( <sup>15</sup> N) 512 ( <sup>13</sup> C)	2	8	10 <sup>b</sup>
4.11	Barnase pH 5.5	0.5	16.4	298	10 ( <sup>15</sup> N) 20 ( <sup>13</sup> C)	2 (Φ <sub>3</sub> ) 32 ( <sup>15</sup> N) 512 ( <sup>13</sup> C)	1.5	256	15
5.1a	T4WT pH 5.5	2.0	14.1	298	33 ( <sup>15</sup> N) 16 ( <sup>1</sup> H)	128 ( <sup>15</sup> N) 1024 ( <sup>1</sup> H)	1	2	0.2
5.1b	T4WT pH 5.5	2.0	14.1	298	33 ( <sup>15</sup> N) 20 ( <sup>13</sup> C)	2 (IPAP) 64 ( <sup>15</sup> N) 512 ( <sup>13</sup> C)	2	16	2.3
5.2a	αS pH 7.1	1.0	14.1	298	33 ( <sup>15</sup> N) 16 ( <sup>1</sup> H)	128 ( <sup>15</sup> N) 1024 ( <sup>1</sup> H)	1	2	0.2
5.2b	αS pH 7.1	1.0	14.1	298	33 ( <sup>15</sup> N) 20 ( <sup>13</sup> C)	2 (IPAP) 64 ( <sup>15</sup> N) 512 ( <sup>13</sup> C)	1.5	16	1.7
5.6	Ubq pH 7.0	1.0	11.7	298	35 ( <sup>15</sup> N) 24 ( <sup>13</sup> C)	64 ( <sup>15</sup> N) 512 ( <sup>13</sup> C)	1	16	0.7
5.8	Ubq pH 7.0	1.0	11.7	298	35 ( <sup>15</sup> N) 24 ( <sup>13</sup> C)	64 ( <sup>15</sup> N) 512 ( <sup>13</sup> C)	1	16	0.7
5.12	Ubq pH 7.0	1.0	11.7	298	35 ( <sup>15</sup> N) 24 ( <sup>13</sup> C)	64 ( <sup>15</sup> N) 512 ( <sup>13</sup> C)	1	16	0.7
5.16	αS pH 7.1	1.0	14.1	298	35 ( <sup>15</sup> N) 24 ( <sup>13</sup> C)	2 (IPAP) 2 (Φ <sub>3</sub> ) 8 (τ <sub>relax</sub> ) 128 ( <sup>15</sup> N) 512 ( <sup>13</sup> C)	2	4	27
5.17	αS, pH 7.3	0.6	14.1	288	33 ( <sup>15</sup> N) 24 ( <sup>13</sup> C)	2 (IPAP) 2 (Φ <sub>3</sub> ) 128 ( <sup>15</sup> N) 512 ( <sup>13</sup> C)	2.5	4	3.0
5.18	αS, pH 7.3	0.6	14.1	288	33 ( <sup>15</sup> N) 24 ( <sup>13</sup> C)	2 (IPAP) 2 (Φ <sub>3</sub> ) 10 (τ <sub>mix</sub> ) 128 ( <sup>15</sup> N) 512 ( <sup>13</sup> C)	1.5	8	45 <sup>c</sup>
5.19	αS, pH 7.1	1.0	22.3	298	30 ( <sup>15</sup> N) 16 ( <sup>1</sup> H)	2 (Φ <sub>3</sub> ) 10 (τ <sub>mix</sub> ) 219 ( <sup>15</sup> N) 2048 ( <sup>1</sup> H)	1	16	60

**Table 7.2** Acquisition parameters for NMR spectra presented in this work. <sup>a</sup> Back-to-back spectra were collected for a total of 16 hours. <sup>b</sup> Time taken for each MQ-CEST experiment. Each experiment was conducted using two CEST B<sub>1</sub> fields (10 Hz and 20 Hz) at each of the sample conditions described in Table 4.4. <sup>c</sup> Repeated in triplicate to provide the data displayed in Figure 5.18.

## 7.5 Pulse Sequences for Bruker Spectrometers

The following section provides the code required to implement the pulse sequences discussed in this thesis on Bruker spectrometers. Whilst each experiment has been thoroughly tested on at least one spectrometer listed in Table 7.1, none are designed to be compatible with the *getprosol* command in TopSpin. For this reason, the code is provided for information purposes only and no warranty is implied.

The RF pulses used in each sequence are identified as follows:

***p1*** is the hard (non-selective) 90° RF pulse on Channel 1

***p2*** is the hard (non-selective) 90° RF pulse on Channel 2

***p3*** is the hard (non-selective) 90° RF pulse on Channel 3

***p4*** is the hard (non-selective) 90° RF pulse on Channel 4

Similarly, for frequency selective RF-pulses:

***p11 (sp11)*** is the first frequency selective RF pulse used on Channel 1

***p12 (sp12)*** is the second frequency selective RF pulse used on Channel 1

***p21 (sp21)*** is the first frequency selective RF pulse used on Channel 2

Power levels are defined using a similar syntax:

***pl1*** is the power level for the hard 90° pulse on Channel 1 (*p1*)

***pl2*** is the power level for the hard 90° pulse on Channel 1 (*p2*)

***pl11*** is the power level for the first selective RF pulse on Channel 1 (*p11*)

Decoupling power on each channel is set using:

***pl19*** is the power level for CPD decoupling on Channel 1

***pl29*** is the power level for CPD decoupling on Channel 2

Where the phase of a pulse is not varied during the sequence, it is defined using the phase tables:

***ph10*** x (0°)

***ph11*** y (90°)

***ph12*** -x (180°)

***ph13*** -y (270°)

Otherwise, the usual phase tables (***ph1***, ***ph2***, ...) are used.

## 7. Experimental

To aid the reading of the pulse sequences, each RF pulse is assigned a human-readable moniker. For example, a pulse sequence involving non-selective  $^1\text{H}$  and  $^{15}\text{N}$  RF pulses on Channels 1 and 3 respectively, would contain the definitions (“pwh = p1” and “pwn = p3”) and the **pwh/pwn** notation would be used throughout the rest of the sequence.

### 7.5.1 Arginine $^{13}\text{C}^{\zeta}$ - $^{15}\text{N}^{\epsilon}$ HSQC

This pulse sequence allows the recording of two-dimensional  $^{13}\text{C}^{\zeta}$ - $^{15}\text{N}^{\epsilon}$  HSQC spectra on uniformly- $^{13}\text{C}$ ,  $^{15}\text{N}$ -labelled samples. It is a  $^{13}\text{C}$ -excited,  $^{13}\text{C}$ -detected triple-resonance experiment requiring the routing of  $^{13}\text{C}$ ,  $^1\text{H}$  and  $^{15}\text{N}$  to Channels 1, 2 and 3, respectively. Optional  $^2\text{H}$  decoupling during  $t_1$  can be switched on using the **-DD\_DEC** option and requires the routing of  $^2\text{H}$  to Channel 4. The carriers are set to approximately 156 ppm ( $^{13}\text{C}$ ), 84 ppm ( $^{15}\text{N}$ ) and 7 ppm ( $^1\text{H}/^2\text{H}$ ). The  $^1J_{\text{CN}}$  coupling constant (20 Hz) and  $^{13}\text{C}^{\delta}$  (40 ppm) and  $^{15}\text{N}^{\eta}$  (70 ppm) chemical shifts must be provided using **cnst2**, **cnst22** and **cnst32**. Two selective RF pulses ( $^{13}\text{C}^{\zeta}$  excitation,  $^{15}\text{N}^{\epsilon}$  refocussing) are used as well an adiabatic  $^{13}\text{C}$  chirp pulse. The shapes **Eburp-2** (1.5 ms), **Reburp** (4.5 ms) and **Crp80,0.5,20.1** (0.5 ms) are appropriate for a 16.4 T spectrometer.  $^1\text{H}$ ,  $^2\text{H}$  and  $^{15}\text{N}$  CPD decoupling uses the **WALTZ64**, **WALTZ16** and **GARP4** schemes at power levels corresponding to 70, 250 and 350  $\mu\text{s}$   $90^\circ$  pulses, respectively.

This pulse sequence can also be used to record  $^{13}\text{C}^{\zeta}$ - $^{15}\text{N}^{\eta}$  HSQC spectra by doubling the  $^1J_{\text{CN}}$  coupling constant **cnst2** and swapping the  $^{15}\text{N}$  carrier frequency with the  $^{15}\text{N}^{\eta}$  chemical shift **cnst32**.

```
;Filename: arg_czne_hsqc.hm
;2D CzNe HSQC spectrum (incl. optional 2H decoupling during t1)
;Cz -> Ne(t1) -> Cz(t2)

;$CLASS=HighRes
;$DIM=2D
;$TYPE=
;$SUBTYPE=
;$COMMENT=

#include <Avance.incl>
#include <Delay.incl>
#include <Grad.incl>

;DEFINE PULSES

define pulse pwc
    "pwc=p1"
    ;13C hard pulse at p11
define pulse pwc_sele
    "pwc_sele=p11"
    ;13C selective e-pulse at p111
define pulse pwc_chirp
    "pwc_chirp=p12"
    ;13C chirp pulse at p112

define pulse pwh
    "pwh=p2"
    ;1H hard pulse at p12

define pulse pwn
    "pwn=p3"
    ;15N hard pulse at p13
define pulse pwn_selr
    "pwn_selr=p31"
    ;15N selective r-pulse at p131

#ifdef D_DEC
```

```

define pulse pwd
    "pwd=p4" ;2H hard pulse at plw49
#endif

;DEFINE DELAYS

define delay taua
    "taua=1s/(cnst2*4)" ;1/4JCN

"d11= 30m" ;Delay for disk
"d12= 20u" ;Delay for power switching
"d16= 200u" ;Delay for gradient recovery

"in0=infl/2"

#ifdef HALFDWELL
    "d0=in0/2-0.5*pwd_chirp-0.63662*pwn"
#else
    "d0=in0-0.5*pwd_chirp-0.63662*pwn"
#endif /*HALFDWELL*/

;DEFINE OFFSETS

"cnst21=o1/bf1" ;Czeta
"cnst23=0.5*(cnst21+cnst22)" ;13C decoupling position
"cnst31=o3/bf3" ;Nepsilon
"cnst33=0.5*(cnst31+cnst32)" ;15N decoupling position

;DEFINE ZERO POWER ON ALL CHANNELS

"plw10=0"
"plw30=0"

;PULSE PROGRAM BEGINS

1 ze

    d11 LOCKDEC_ON ;lock decoupling on
    50u LOCKH_ON ;lock hold on
    d11 H2_PULSE ;switch 2H to pulse
    d12 pl29:f2 pl149:f4 ;power to decouple(1H, 2H)
#else
    d12 pl29:f2 ;power to decouple(1H)
#endif
2 d11 do:f2 do:f3 ;decoupling off

#ifdef D_DEC
    d11 H2_LOCK ;switch 2H to lock
    d1*0.34 ;recycle delay
    6m LOCKH_OFF ;lock hold off
    d1*0.66 ;recycle delay
    50u LOCKH_ON ;lock hold on
    d12 H2_PULSE ;switch 2H to pulse
#else
    d1
#endif

    ;purge equilibrium 15N magnetisation

#ifdef D_DEC
    50u UNBLKGRAMP ;gradient amp on
#else
    50u UNBLKGRAD ;gradient amp on
#endif

    30u fq=cnst33(bf ppm):f3 ;set 15N carrier
    d12 pl3:f3 ;power to high (15N)
    (pwn ph10):f3 ;90x
    2u
    p51:gpl ;cleaning gradient
    d16

;end purge block

d12 pl10:f1 pl30:f3 ;power to 0(13C, 15N)
30u fq=cnst21(bf ppm):f1 ;set 13C carrier, Czeta
30u fq=cnst31(bf ppm):f3 ;set 15N carrier, Nepsilon

;start INEPT

```

## 7. Experimental

```
(pwc_sele:sp11 ph1):f1 ;13C selective excitation

;start Ne selective block
"DELTA = taua-2u-p52-d16-0.5*larger(pwc*2,pwn_selr)"
DELTA
2u
p52:gp2
d16 pl1:f1 ;power to high (13C)
( center (pwc*2 ph10):f1 (pwn_selr:sp31 ph10):f3 )
2u
p52:gp2
d16
"DELTA = taua-2u-p52-d16-0.5*larger(pwc*2,pwn_selr)-0.6366*pwc"
DELTA
;end Ne selective block
(pwc ph11):f1 ;-2CxNz to 2CzNz

;end INEPT

30u fq=cnst23(bf ppm):f1 ;set 13C carrier to decouple
d12 pl10:f1 pl3:f3 ;power to 0(13C), high(15N)
2u
p53:gp3 ;cleaning gradient
d16

#ifdef D_DEC
(pwd ph11):f4 ;2H flanking pulse (90y)
4u cpd4:f4 ph10 ;2H decoupling on
#endif

4u cpd2:f2 ph10 ;1H decoupling on

(pwn ph2):f3 ;2CzNz to -2CzNy

;start t1 evolution period with 1H and 2H decoupling

d0 ;incremented delay, t1/2
(pwc_chirp:sp12 ph10):f1 ;13C decoupling pulse
d0 ;incremented delay, t1/2

;end t1 evolution period, start second INEPT

(pwn ph10):f3 ;-2CzNy to -2CzNz
4u do:f2 ;1H decoupling off

#ifdef D_DEC
4u do:f4 ;2H decoupling off
(pwd ph13):f4 ;2H flanking pulse (90-y)
#endif

30u fq=cnst21(bf ppm):f1 ;13C carrier returned to Czeta
d12 pl1:f1 pl30:f3 ;power to high(13C), 0(15N)
2u
p54:gp4 ;cleaning gradient
d16
(pwc ph10):f1 ;-2CzNz to 2CyNz

;start Ne selective block
"DELTA = taua-0.6366*pwc-2u-p55-d16-0.5*larger(pwc*2,pwn_selr)"
DELTA
2u
p55:gp5
d16
( center (pwc*2 ph10):f1 (pwn_selr:sp31 ph10):f3 )
2u
p55:gp5
d16
30u fq=cnst33(bf ppm):f3 ;set 15N carrier to decouple
d12 pl39:f3 ;power to decouple(15N)

#ifdef D_DEC
50u BLKGRAMP ;gradient amp off
#else
50u BLKGRAD ;gradient amp off
#endif

"DELTA = taua-0.5*larger(pwc,pwn_selr)-2u-p55-d16-30u-d12-50u"
DELTA
;end Ne selective block
```

```

;end second INEPT, acquire Cx magnetisation with 15N, 1H decoupling

go=2 ph31 cpd2:f2 cpd3:f3
d11 do:f2 do:f3 mc #0 to 2
    F1PH(calph(ph2,+90), caldel(d0,+in0))

#ifdef D_DEC
    d11 H2_LOCK ;switch H2 to lock
    d11 LOCKH_OFF ;lock hold off
    d11 LOCKDEC_OFF ;lock decoupling off
#endif

exit

;PHASE PROGRAMS

ph1= 0 2
ph2= 0 0 2 2
ph31= 0 2 2 0

ph10= 0
ph11= 1
ph12= 2
ph13= 3

;DEFINITIONS

;p11 : f1 channel - power level for hard pulse
;p12 : f2 channel - power level for hard pulse
;p13 : f3 channel - power level for hard pulse
;p129 : f2 channel - power level for CPD/BB decoupling
;p139 : f3 channel - power level for CPD/BB decoupling
;p149 : f4 channel - power level for CPD/BB decoupling
;sp11 : f1 channel - shaped pulse 90 degree (Czeta)
;spnam11 : Eburp2.1000
;sp12 : f1 channel - shaped pulse 180 degree (adiabatic)
;spnam12 : Crp80,0.5,20.1
;sp31 : f3 channel - shaped pulse 180 degree (Nepsilon)
;spnam31 : Reburp.1000
;p1 : f1 channel - 90 degree high power pulse
;p11 : f1 channel - 90 degree shaped pulse [1.5 ms at 16.4T]
;p12 : f1 channel - 180 degree shaped pulse [500 us at 16.4T]
;p3 : f3 channel - 90 degree high power pulse
;p31 : f3 channel - 180 degree shaped pulse [4.5 ms at 16.4T]
;p4 : f4 channel - 90 degree high power pulse
;p51 : homospoil/gradient pulse
;p52 : homospoil/gradient pulse
;p53 : homospoil/gradient pulse
;p54 : homospoil/gradient pulse
;p55 : homospoil/gradient pulse
;d0 : incremented delay
;d1 : relaxation delay
;taua : 1/(4JCN)
;d11 : delay for disk I/O [30 msec]
;d12 : delay for power switching [20 usec]
;d16 : delay for homospoil/gradient recovery
;cnst2 : J(CN) [20 Hz]
;cnst21 : Czeta chemical shift offset [= o1p, 156 ppm]
;cnst22 : Cdelta chemical shift offset [40 ppm]
;cnst31 : Nepsilon chemical shift offset [= o3p, 84 ppm]
;cnst32 : Neta chemical shift offset [70 ppm]
;o1p : Czeta chemical shift offset [156 ppm]
;o2p : Hepsilon/Heta chemical shift offset [7 ppm]
;o3p : Nepsilon chemical shift offset [71 ppm]
;o4p : Depsilon/Deta chemical shift offset [7 ppm]
;inf1 : 1/SW = 2 * DW
;in0 : 1/(2 * SW) = DW
;NS : 4 * n
;DS : 16
;td1 : number of experiments
;FnMODE : States-TPPI
;cpd2 : decoupling according to sequence defined by cpdprg2 (WALTZ64)
;pcpd2 : f2 channel - 90 degree pulse for decoupling [70 us]
;cpd3 : decoupling according to sequence defined by cpdprg3 (GARP4)
;pcpd3 : f3 channel - 90 degree pulse for decoupling [350 us]
;cpd4 : decoupling according to sequence defined by cpdprg3 (WALTZ16)
;pcpd4 : f4 channel - 90 degree pulse for decoupling [250 us]

;for z-only gradients:
;gpz1 : 37%

```

## 7. Experimental

```
;gpz2      : 11%
;gpz3      : 23%
;gpz4      : 31%
;gpz5      : 13%

;use gradient files:
;gpnam1    : SMSQ10.100
;gpnam2    : SMSQ10.100
;gpnam3    : SMSQ10.100
;gpnam4    : SMSQ10.100
;gpnam5    : SMSQ10.100

;preprocessor-flags-start
;HALFDWELL: for initial sampling delay of half a dwell-time with
;          option -DHALFDWELL (eda: ZGOPTNS)
;D_DEC     : for 2H decoupling during indirect chemical shift evolutions
;preprocessor-flags-end
```

### 7.5.2 Arginine $^{13}\text{C}^{\zeta}\text{-}^{15}\text{N}^{\eta}$ HDQC

This pulse sequence allows the recording of two-dimensional  $^{13}\text{C}^{\zeta}\text{-}^{15}\text{N}^{\eta}$  HDQC spectra on uniformly- $^{13}\text{C},^{15}\text{N}$ -labelled samples. It is a  $^{13}\text{C}$ -excited,  $^{13}\text{C}$ -detected triple-resonance experiment requiring the routing of  $^{13}\text{C}$ ,  $^1\text{H}$  and  $^{15}\text{N}$  to Channels 1, 2 and 3, respectively. Optional  $^2\text{H}$  decoupling during  $t_1$  can be switched on using the **-DD\_DEC** option and requires the routing of  $^2\text{H}$  to Channel 4. The carriers are set to approximately 156 ppm ( $^{13}\text{C}$ ), 70 ppm ( $^{15}\text{N}$ ) and 7 ppm ( $^1\text{H}/^2\text{H}$ ). The  $^1J_{\text{CN}}$  coupling constant (20 Hz) and  $^{13}\text{C}^{\delta}$  (40 ppm) and  $^{15}\text{N}^{\epsilon}$  (84 ppm) chemical shifts must be provided using **cnst2**, **cnst22** and **cnst32**. Two selective RF pulses ( $^{13}\text{C}^{\zeta}$  excitation,  $^{15}\text{N}^{\epsilon}$  refocussing) are used with the shapes **Eburp-2** (1.5 ms) and **Reburp** (4.5 ms) appropriate for a 16.4 T spectrometer.  $^1\text{H}$ ,  $^2\text{H}$  and  $^{15}\text{N}$  CPD decoupling uses the **WALTZ64**, **WALTZ16** and **GARP4** schemes at power levels corresponding to 70, 250 and 350  $\mu\text{s}$   $90^\circ$  pulses, respectively.

```
;Filename: arg_cznh_hdqc.hm
;2D CzNh HDQC spectrum (incl. optional 2H decoupling during t1)
;Cz -> Nh_DQ(t1) -> Cz(t2)

;$CLASS=HighRes
;$DIM=2D
;$TYPE=
;$SUBTYPE=
;$COMMENT=

#include <Avance.incl>
#include <Delay.incl>
#include <Grad.incl>

;DEFINE PULSES

define pulse pwc
    "pwc=p1"
;13C hard pulse at p11
define pulse pwc_sele
    "pwc_sele=p11"
;13C selective e-pulse at p11

define pulse pwh
    "pwh=p2"
;1H hard pulse at p12

define pulse pwn
    "pwn=p3"
;15N hard pulse at p13
define pulse pwn_selr
    "pwn_selr=p31"
;15N selective r-pulse at p131

#ifdef D_DEC
define pulse pwd
    "pwd=p4"
;2H hard pulse at plw49
#endif
```

```

;DEFINE DELAYS

define delay taua
    "taua=1s/(cnst2*4)"
                                ;1/4JCN

"d11= 30m"
                                ;Delay for disk
"d12= 20u"
                                ;Delay for power switching
"d16= 200u"
                                ;Delay for gradient recovery

"in0=in0/2"

#ifdef HALFDWELL
    "d0=in0/2-pwc-0.63662*pwn"
#else
    "d0=in0-pwc-0.63662*pwn"
#endif /*HALFDWELL*/

;DEFINE OFFSETS

"cnst21=o1/bf1"
                                ;Czeta
"cnst31=o3/bf3"
                                ;Neta
"cnst33=0.5*(cnst31+cnst32)"
                                ;15N decoupling position

;DEFINE ZERO POWER ON ALL CHANNELS

"plw10=0"
"plw30=0"

;PULSE PROGRAM BEGINS

1 ze

    d11 LOCKDEC_ON
                                ;lock decoupling on
    50u LOCKH_ON
                                ;lock hold on
    d11 H2_PULSE
                                ;switch 2H to pulse
    d12 p129:f2 p149:f4
                                ;power to decouple(1H, 2H)
#else
    d12 p129:f2
                                ;power to decouple(1H)
#endif
2 d11 do:f2 do:f3
                                ;decoupling off

#ifdef D_DEC
    d11 H2_LOCK
                                ;switch 2H to lock
    d1*0.34
                                ;recycle delay
    6m LOCKH_OFF
                                ;lock hold off
    d1*0.66
                                ;recycle delay
    50u LOCKH_ON
                                ;lock hold on
    d12 H2_PULSE
                                ;switch 2H to pulse
#else
    d1
#endif

    ;purge equilibrium 15N magnetisation

#ifdef D_DEC
    50u UNBLKGRAMP
                                ;gradient amp on
#else
    50u UNBLKGRAD
                                ;gradient amp on
#endif

    30u fq=cnst33(bf ppm):f3
                                ;set 15N carrier
    d12 p13:f3
                                ;power to high (15N)
    (pwn ph10):f3
                                ;90x
    2u
    p51:gpl
                                ;cleaning gradient
    d16

;end purge block

d12 p110:f1 p130:f3
                                ;power to 0(13C, 15N)
30u fq=cnst31(bf ppm):f3
                                ;set 15N carrier, Neta

;start INEPT

(pwc_sele:sp11 ph1):f1
                                ;13C selective excitation
                                ;start Nh selective block
"DELTA = taua-2u-p52-d16-0.5*larger(pwc*2,pwn_selr)"
DELTA
2u

```

## 7. Experimental

```
p52:gp2
d16 p11:f1 ;power to high (13C)
( center (pwc*2 ph10):f1 (pwn_selr:sp31 ph10):f3 )
2u
p52:gp2
d16
"DELTA = taua-2u-p52-d16-0.5*larger(pwc*2,pwn_selr)-0.6366*pwc"
DELTA
(pwc ph10):f1 ;end Neta selective block
;-4CzNh1zNh2z to -4CzNh1zNh2z
;end INEPT
d12 p13:f3 ;power to high(15N)
2u
p53:gp3 ;cleaning gradient
d16
#ifdef D_DEC
(pwd ph11):f4 ;2H flanking pulse (90y)
4u cpd4:f4 ph10 ;2H decoupling on
#endif
4u cpd2:f2 ph10 ;1H decoupling on
(pwn ph2):f3 ;-4CzNh1zNh2z to -4CzNh1yNh2y
;start t1 evolution period with 1H decoupling
d0 ;incremented delay, t1/2
(pwc*2 ph10):f1 ;13C decoupling pulse
d0 ;incremented delay, t1/2
;end t1 evolution period, start second INEPT
(pwn ph10):f3 ;-4CzNh1yNh2y to -4CzNh1zNh2z
4u do:f2 ;1H decoupling off
#ifdef D_DEC
4u do:f4 ;2H decoupling off
(pwd ph13):f4 ;2H flanking pulse (90-y)
#endif
d12 p130:f3 ;power to 0(15N)
2u
p54:gp4 ;cleaning gradient
d16
(pwc ph10):f1 ;-4CzNh1zNh2z to 4CyNh1zNh2z
;start Nh selective block
"DELTA = taua-0.6366*pwc-2u-p55-d16-0.5*larger(pwc*2,pwn_selr)"
DELTA
2u
p55:gp5
d16
( center (pwc*2 ph10):f1 (pwn_selr:sp31 ph10):f3 )
2u
p55:gp5
d16
30u fq=cnst33(bf ppm):f3 ;set 15N carrier to decouple
d12 p139:f3 ;power to decouple(15N)
#ifdef D_DEC
50u BLKGRAMP ;gradient amp off
#else
50u BLKGRAD ;gradient amp off
#endif
"DELTA = taua-0.5*larger(pwc,pwn_selr)-2u-p55-d16-30u-d12-50u"
DELTA
;end Nh selective block
;end second INEPT, acquire Cy magnetisation with 15N, 1H decoupling
go=2 ph31 cpd2:f2 cpd3:f3
d11 do:f2 do:f3 mc #0 to 2
F1PH(calph(ph2,+45), caldel(d0,+in0))
#ifdef D_DEC
d11 H2_LOCK ;switch H2 to lock
d11 LOCKH_OFF ;lock hold off
d11 LOCKDEC_OFF ;lock decoupling off
```

```

#endif

exit

;PHASE PROGRAMS

ph1= 0 2
ph2= 0 0 1 1 2 2 3 3
ph31= 0 2 2 0

ph10= 0
ph11= 1
ph12= 2
ph13= 3

;DEFINITIONS

;p11      : f1 channel - power level for hard pulse
;p12      : f2 channel - power level for hard pulse
;p13      : f3 channel - power level for hard pulse
;p129     : f2 channel - power level for CPD/BB decoupling
;p139     : f3 channel - power level for CPD/BB decoupling
;p149     : f4 channel - power level for CPD/BB decoupling
;sp11     : f1 channel - shaped pulse 90 degree (Czeta)
;spnam11  : Eburp2.1000
;sp31     : f3 channel - shaped pulse 180 degree (Neta)
;spnam31  : Reburp.1000
;p1       : f1 channel - 90 degree high power pulse
;p11      : f1 channel - 90 degree shaped pulse [1.5 ms at 16.4T]
;p3       : f3 channel - 90 degree high power pulse
;p31      : f3 channel - 180 degree shaped pulse [4.5 ms at 16.4T]
;p4       : f4 channel - 90 degree high power pulse
;p51      : homospoil/gradient pulse
;p52      : homospoil/gradient pulse
;p53      : homospoil/gradient pulse
;p54      : homospoil/gradient pulse
;p55      : homospoil/gradient pulse
;d0       : incremented delay
;d1       : relaxation delay
;taua     : 1/(4JCN)
;d11      : delay for disk I/O [30 msec]
;d12      : delay for power switching [20 usec]
;d16      : delay for homospoil/gradient recovery
;cnst2    : J(CN) [20 Hz]
;cnst21   : Czeta chemical shift offset [= o1p, 156 ppm]
;cnst31   : Neta chemical shift offset [= o3p, 70 ppm]
;cnst32   : Nepsilon chemical shift offset [84 ppm]
;o1p      : Czeta chemical shift offset [156 ppm]
;o2p      : Hepsilon/Heta chemical shift offset [7 ppm]
;o3p      : Neta chemical shift offset [70 ppm]
;o4p      : Depsilon/Deta chemical shift offset [7 ppm]
;inf1     : 1/SW = 2 * DW
;in0      : 1/(2 * SW) = DW
;NS       : 8 * n
;DS       : 16
;td1      : number of experiments
;FnMODE   : States-TPPI
;cpd2     : decoupling according to sequence defined by cpdprg2 (WALTZ64)
;pcpd2    : f2 channel - 90 degree pulse for decoupling [70 us]
;cpd3     : decoupling according to sequence defined by cpdprg3 (GARP4)
;pcpd3    : f3 channel - 90 degree pulse for decoupling [350 us]
;cpd4     : decoupling according to sequence defined by cpdprg3 (WALTZ16)
;pcpd4    : f4 channel - 90 degree pulse for decoupling [250 us]

;for z-only gradients:
;gpz1     : 37%
;gpz2     : 11%
;gpz3     : 23%
;gpz4     : 31%
;gpz5     : 13%

;use gradient files:
;gpnam1   : SMSQ10.100
;gpnam2   : SMSQ10.100
;gpnam3   : SMSQ10.100
;gpnam4   : SMSQ10.100
;gpnam5   : SMSQ10.100

;preprocessor-flags-start

```

## 7. Experimental

```
;HALFDWELL: for initial sampling delay of half a dwell-time with
;          option -DHALFDWELL (eda: ZGOTNS)
;D_DEC    : for 2H decoupling during indirect chemical shift evolutions
;preprocessor-flags-end
```

### 7.5.3 Arginine $^{13}\text{C}^{\zeta}$ - $^{15}\text{N}^{\epsilon}$ - $^{15}\text{N}^{\eta}$ Correlation

This pulse sequence allows the recording of three-dimensional  $^{13}\text{C}^{\zeta}$ - $^{15}\text{N}^{\epsilon}$ - $^{15}\text{N}^{\eta}$  spectra on uniformly- $^{13}\text{C}$ ,  $^{15}\text{N}$ -labelled samples. It is a  $^{13}\text{C}$ -excited,  $^{13}\text{C}$ -detected triple-resonance experiment requiring the routing of  $^{13}\text{C}$ ,  $^1\text{H}$  and  $^{15}\text{N}$  to Channels 1, 2 and 3, respectively. Optional  $^2\text{H}$  decoupling during  $t_1$  and  $t_2$  can be switched on using the **-DD\_DEC** option and requires the routing of  $^2\text{H}$  to Channel 4. The carriers are set to approximately 156 ppm ( $^{13}\text{C}$ ), 84 ppm ( $^{15}\text{N}$ ) and 7 ppm ( $^1\text{H}/^2\text{H}$ ). The  $^1J_{\text{CN}}$  coupling constant (20 Hz) and  $^{13}\text{C}^{\delta}$  (40 ppm) and  $^{15}\text{N}^{\eta}$  (70 ppm) chemical shifts must be provided using **cnst2**, **cnst22** and **cnst32**. Two selective RF pulses ( $^{13}\text{C}^{\zeta}$  excitation,  $^{15}\text{N}^{\epsilon}$  refocussing) are used as well an adiabatic  $^{13}\text{C}$  chirp pulse. The shapes **Eburp-2** (1.5 ms), **Reburp** (4.5 ms) and **Crp80,0.5,20.1** (0.5 ms) are appropriate for a 16.4 T spectrometer.  $^1\text{H}$ ,  $^2\text{H}$  and  $^{15}\text{N}$  CPD decoupling uses the **WALTZ64**, **WALTZ16** and **GARP4** schemes at power levels corresponding to 70, 250 and 350  $\mu\text{s}$   $90^\circ$  pulses, respectively.

```
;Filename: arg_cznenh_3d.hm
;3D CzNeNh spectrum (incl. optional 2H decoupling during t1,t2)
;Cz -> Ne(t1) -> Nh_DQ(t2) -> Cz(t3)

;$CLASS=HighRes
;$DIM=3D
;$TYPE=
;$SUBTYPE=
;$COMMENT=

#include <Avance.incl>
#include <Delay.incl>
#include <Grad.incl>

;DEFINE PULSES

define pulse pwc
    "pwc=p1"
    ;13C hard pulse at p11
define pulse pwc_sele
    "pwc_sele=p11"
    ;13C selective e-pulse at p111
define pulse pwc_chirp
    "pwc_chirp=p12"
    ;13C chirp pulse at p112

define pulse pwh
    "pwh=p2"
    ;1H hard pulse at p12

define pulse pwn
    "pwn=p3"
    ;15N hard pulse at p13
define pulse pwn_selr
    "pwn_selr=p31"
    ;15N selective r-pulse at p131

#ifdef D_DEC
define pulse pwd
    "pwd=p4"
    ;2H hard pulse at plw49
#endif

;DEFINE DELAYS

define delay taua
    "taua=1s/(cnst2*4)"
    ;1/4JCN

"d11= 30m"
    ;Delay for disk
"d12= 20u"
    ;Delay for power switching
"d16= 200u"
    ;Delay for gradient recovery
```

```

"in0=inf2/2"
"in10=inf1/2"

#ifdef HALFDWELL
    "d0=in0/2-0.5*pwd_chirp-0.63662*pwn"
    "d10=in10/2-pwd-0.63662*pwn"
#else
    "d0=in0-0.5*pwd_chirp-0.63662*pwn"
    "d10=in10-pwd-0.63662*pwn"
#endif /*HALFDWELL*/

;DEFINE OFFSETS

"cnst21=o1/bf1" ;Czeta
"cnst23=0.5*(cnst21+cnst22)" ;13C decoupling position
"cnst31=o3/bf3" ;Nepsilon
"cnst33=0.5*(cnst31+cnst32)" ;15N decoupling position

;DEFINE ZERO POWER ON ALL CHANNELS

"plw10=0"
"plw30=0"

;PULSE PROGRAM BEGINS

1 ze

    d11 LOCKDEC_ON ;lock decoupling on
    50u LOCKH_ON ;lock hold on
    d11 H2_PULSE ;switch 2H to pulse
    d12 pl29:f2 pl149:f4 ;power to decouple(1H, 2H)
#else
    d12 pl29:f2 ;power to decouple(1H)
#endif
2 d11 do:f2 do:f3 ;decoupling off

#ifdef D_DEC
    d11 H2_LOCK ;switch 2H to lock
    d1*0.34 ;recycle delay
    6m LOCKH_OFF ;lock hold off
    d1*0.66 ;recycle delay
    50u LOCKH_ON ;lock hold on
    d12 H2_PULSE ;switch 2H to pulse
#else
    d1
#endif

;purge equilibrium 15N magnetisation

#ifdef D_DEC
    50u UNBLKGRAMP ;gradient amp on
#else
    50u UNBLKGRAD ;gradient amp on
#endif

    30u fq=cnst33(bf ppm):f3 ;set 15N carrier
    d12 pl3:f3 ;power to high (15N)
    (pwn ph10):f3 ;90x
    2u
    p51:gp1 ;cleaning gradient
    d16

;end purge block

d12 pl10:f1 pl130:f3 ;power to 0(13C, 15N)
30u fq=cnst21(bf ppm):f1 ;set 13C carrier, Czeta
30u fq=cnst31(bf ppm):f3 ;set 15N carrier, Nepsilon

;start INEPT

(pwd_sele:sp11 ph10):f1 ;13C selective excitation
;start Ne selective block
"DELTA = taua-2u-p51-d16-0.5*larger(pwd*2,pwn_selr)"
DELTA
2u
p52:gp2
d16 pl1:f1 ;power to high (13C)
( center (pwd*2 ph10):f1 (pwn_selr:sp31 ph10):f3 )
2u

```

## 7. Experimental

```
p52:gp2
d16
"DELTA = taua-2u-p51-d16-0.5*larger(pwc*2,pwn_selr)-0.6366*pwc"
DELTA
                                ;end Ne selective block
(pwc ph11):f1                    ;2CxNez to -2CzNez
;end INEPT

30u fq=cnst23(bf ppm):f1         ;set 13C carrier to decouple
d12 pl10:f1 pl3:f3              ;power to 0(13C), high(15N)
2u
p53:gp3                          ;cleaning gradient
d16

#ifdef D_DEC
  (pwd ph11):f4                  ;2H flanking pulse (90y)
  4u cpd4:f4 ph10                ;2H decoupling on
#endif

4u cpd2:f2 ph10                  ;1H decoupling on

(pwn ph1):f3                     ;-2CzNez to 2CzNey

;start t1 evolution period with 1H and 2H decoupling

d0                                ;incremented delay, t1/2
(pwc_chirp:sp12 ph10):f1        ;13C decoupling pulse
d0                                ;incremented delay, t1/2

;end t1 evolution period, start second INEPT

(pwn ph10):f3                    ;2CzNey to 2CzNez
4u do:f2                          ;1H decoupling off

#ifdef D_DEC
  4u do:f4                        ;2H decoupling off
  (pwd ph13):f4                  ;2H flanking pulse (90-y)
#endif

30u fq=cnst21(bf ppm):f1         ;13C carrier returned to Czeta
30u fq=cnst33(bf ppm):f3        ;15N carrier to Ne + Nh
d12 pl1:f1 pl3:f3              ;power to high(13C, 15N)
2u
p54:gp4                          ;cleaning gradient
d16
(pwc ph10):f1                    ;2CzNez to -2CyNez
                                ;start non-selective block
"DELTA = taua-2u-p54-d16-larger(pwc,pwn)"
DELTA
2u
p55:gp5                          ;generates -4CxNh1zNh2z
d16
( center (pwc*2 ph10):f1 (pwn*2 ph10):f3 )
2u
p55:gp5
d16
"DELTA = taua-larger(pwc,pwn)-2u-p54-d16"
DELTA
                                ;end non-selective block
;end second INEPT

(pwc ph11):f1                    ;-4CxNh1zNh2z to -4CzNh1zNh2z
30u fq=cnst32(bf ppm):f3        ;set 15N carrier to Nh
2u
p56:gp6                          ;cleaning gradient
d16

#ifdef D_DEC
  (pwd ph11):f4                  ;2H flanking pulse (90y)
  4u cpd4:f4 ph10                ;2H decoupling on
#endif

4u cpd2:f2 ph10                  ;1H decoupling on

(pwn ph2):f3                     ;-4CzNh1zNh2z to 4CzNh1yNh2y

;start t2 evolution period with 1H and 2H decoupling
```

## 7. Experimental

```

d10 ;incremented delay, t2/2
(pwc*2 ph10):f1 ;13C decoupling pulse
d10 ;incremented delay, t2/2

;end t2 evolution period, start third INEPT

(pwn ph10):f3 ;4CzNh1yNh2y to 4CzNh1zNh2z
4u do:f2 ;1H decoupling off

#ifdef D_DEC
4u do:f4 ;2H decoupling off
(pwd ph13):f4 ;2H flanking pulse (90-y)
#endif

d12 pl30:f3 ;power to 0(15N)
2u
p57:gp7 ;cleaning gradient
d16
(pwc ph10):f1 ;4CzNh1zNh2z to -4CyNh1zNh2z
;start Nh selective block
"DELTA = taua-0.6366*pwc-2u-p57-d16-0.5*larger(pwc*2,pwn_selr)"
DELTA
2u
p58:gp8
d16
( center (pwc*2 ph10):f1 (pwn_selr:sp31 ph10):f3 )
2u
p58:gp8
d16
30u fq=cnst33 (bf ppm):f3 ;set 15N carrier to decouple
d12 pl39:f3 ;power to decouple(15N)

#ifdef D_DEC
50u BLKGRAMP ;gradient amp off
#else
50u BLKGRAD ;gradient amp off
#endif

"DELTA = taua-0.5*larger(pwc,pwn_selr)-2u-p57-d16-30u-d12-50u"
DELTA
;end Nh selective block

;end third INEPT, acquire Cx magnetisation with 15N, 1H decoupling

go=2 ph31 cpd2:f2 cpd3:f3
d11 do:f2 do:f3 mc #0 to 2
F1PH(calph(ph2,+45), caldel(d10,+in10))
F2PH(calph(ph1,+90), caldel(d0,+in0))

#ifdef D_DEC
d11 H2_LOCK ;switch H2 to lock
d11 LOCKH_OFF ;lock hold off
d11 LOCKDEC_OFF ;lock decoupling off
#endif

exit

;PHASE PROGRAMS

ph1= 0 2
ph2= 0 0 1 1 2 2 3 3
ph31= 0 2 2 0

ph10= 0
ph11= 1
ph12= 2
ph13= 3

;DEFINITIONS

;p11 : f1 channel - power level for hard pulse
;p12 : f2 channel - power level for hard pulse
;p13 : f3 channel - power level for hard pulse
;p14 : f4 channel - power level for hard pulse
;p129 : f2 channel - power level for CPD/BB decoupling
;p139 : f3 channel - power level for CPD/BB decoupling
;p149 : f4 channel - power level for CPD/BB decoupling
;sp11 : f1 channel - shaped pulse 90 degree (Czeta)
;sp12 : f1 channel - shaped pulse 180 degree (adiabatic)
;spnam11 : Eburp2.1000

```

## 7. Experimental

```
;spnam12 : Crp80,0.5,20.1
;sp31 : f3 channel - shaped pulse 180 degree
;spnam31 : Reburp.1000
;p1 : f1 channel - 90 degree high power pulse
;p11 : f1 channel - 90 degree shaped pulse [1.5 ms at 16.4T]
;p12 : f1 channel - shaped pulse 180 degree [500 us at 16.4T]
;p3 : f3 channel - 90 degree high power pulse
;p31 : f3 channel - 180 degree shaped pulse [4.5 ms at 16.4T]
;p4 : f4 channel - 90 degree high power pulse
;p51 : homospoil/gradient pulse
;p52 : homospoil/gradient pulse
;p53 : homospoil/gradient pulse
;p54 : homospoil/gradient pulse
;p55 : homospoil/gradient pulse
;p56 : homospoil/gradient pulse
;p57 : homospoil/gradient pulse
;p58 : homospoil/gradient pulse
;d0 : incremented delay (13C-15Ne)
;d10 : incremented delay (13C-15Nh DQ)
;d1 : relaxation delay
;taua : 1/(4JCN)
;d11 : delay for disk I/O [30 msec]
;d12 : delay for power switching [20 usec]
;d16 : delay for homospoil/gradient recovery
;cnst2 : J(NC) [20 Hz]
;cnst21 : Czeta chemical shift offset [= o1p, 156 ppm]
;cnst22 : Cdelta chemical shift offset [40 ppm]
;cnst31 : Nepsilon chemical shift offset [= o3p, 84ppm]
;cnst32 : Neta chemical shift offset [70 ppm]
;o1p : Czeta chemical shift offset [156 ppm]
;o2p : Hepsilon/Heta chemical shift offset [7 ppm]
;o3p : Nepsilon chemical shift offset [84 ppm]
;o4p : Depsilon/Deta chemical shift offset [7 ppm]
;inf1 : 1/SW(Nh) = 2 * DW(Nh)
;inf2 : 1/SW(Ne) = 2 * DW(Ne)
;in0 : 1/(2 * SW(Ne)) = DW(Ne)
;in10 : 1/(2 * SW(Nh)) = DW(Nh)
;NS : 8 * n
;DS : 16
;td1 : number of experiments (Ne)
;td2 : number of experiments (Nh)
;FnMODE : States-TPPI
;cpd2 : decoupling according to sequence defined by cpdprg2 (WALTZ64)
;pcpd2 : f2 channel - 90 degree pulse for decoupling [70 us]
;cpd3 : decoupling according to sequence defined by cpdprg3 (GARP4)
;pcpd3 : f3 channel - 90 degree pulse for decoupling [350 us]
;cpd4 : decoupling according to sequence defined by cpdprg3 (WALTZ16)
;pcpd4 : f4 channel - 90 degree pulse for decoupling [250 us]

;for z-only gradients:
;gpz1: 37%
;gpz2: 11%
;gpz3: 23%
;gpz4: 31%
;gpz5: 13%
;gpz6: 41%
;gpz7: 47%
;gpz8: 17%

;use gradient files:
;gpnam1: SMSQ10.100
;gpnam2: SMSQ10.100
;gpnam3: SMSQ10.100
;gpnam4: SMSQ10.100
;gpnam5: SMSQ10.100
;gpnam6: SMSQ10.100
;gpnam7: SMSQ10.100
;gpnam8: SMSQ10.100

;preprocessor-flags-start
;HALFDWELL: for initial sampling delay of half a dwell-time with
; option -DHALFDWELL (eda: ZGOPTNS)
;D_DEC : for 2H decoupling during indirect chemical shift evolutions
;preprocessor-flags-end
```

### 7.5.4 Arginine $^{15}\text{N}^\epsilon(^1\text{H}/^2\text{H})$ zz-Exchange (pseudo-3D)

This pulse sequence allows the recording of pseudo-three-dimensional  $^{13}\text{C}^\zeta\text{-}^{15}\text{N}^\epsilon$  spectra on uniformly- $^{13}\text{C},^{15}\text{N}$ -labelled samples prepared in mixed  $^1\text{H}_2\text{O}:\text{}^2\text{H}_2\text{O}$  buffers. It is essentially Experiment 7.5.1 with an additional mixing time inserted after the  $t_1$  evolution period to follow the hydrogen exchange process. It is a  $^{13}\text{C}$ -excited,  $^{13}\text{C}$ -detected quadruple-resonance experiment requiring the routing of  $^{13}\text{C}$ ,  $^1\text{H}$ ,  $^{15}\text{N}$  and  $^2\text{H}$  to Channels 1, 2, 3 and 4, respectively. The delays to be executed for the incremented mixing time,  $\tau_{\text{mix}}$ , are read from a **vdlist**. The carriers are set to approximately 156 ppm ( $^{13}\text{C}$ ), 84 ppm ( $^{15}\text{N}$ ) and 7 ppm ( $^1\text{H}/^2\text{H}$ ). The  $^1J_{\text{CN}}$  coupling constant (20 Hz) and  $^{13}\text{C}^\delta$  (40 ppm) and  $^{15}\text{N}^\eta$  (70 ppm) chemical shifts must be provided using **cnst2**, **cnst22** and **cnst32**. Two selective RF pulses ( $^{13}\text{C}^\zeta$  excitation,  $^{15}\text{N}^\epsilon$  refocussing) are used as well an adiabatic  $^{13}\text{C}$  chirp pulse. The shapes **Eburp-2** (1.5 ms), **Reburp** (4.5 ms) and **Crp80,0.5,20.1** (0.5 ms) are appropriate for a 16.4 T spectrometer.  $^1\text{H}$ ,  $^2\text{H}$  and  $^{15}\text{N}$  CPD decoupling uses the **WALTZ64**, **WALTZ16** and **GARP4** schemes at power levels corresponding to 70, 250 and 350  $\mu\text{s}$  90° pulses, respectively.

```
;Filename: arg_czne_zz_exchange_p3d.hm
;pseudo-3D zz-exchange
;Cz -> Ne(t1) -> 2CzNz(tmix) -> Cz(t2)

;$CLASS=HighRes
;$DIM=3D
;$TYPE=
;$SUBTYPE=
;$COMMENT=

#include <Avance.incl>
#include <Delay.incl>
#include <Grad.incl>

;DEFINE PULSES

define pulse pwc
    "pwc=p1" ;13C hard pulse at p11
define pulse pwc_sele
    "pwc_sele=p11" ;13C selective e-pulse at p111
define pulse pwc_chirp
    "pwc_chirp=p12" ;13C chirp pulse at p112

define pulse pwh
    "pwh=p2" ;1H hard pulse at p12

define pulse pwn
    "pwn=p3" ;15N hard pulse at p13
define pulse pwn_selr
    "pwn_selr=p31" ;15N selective r-pulse at p131

define pulse pwd
    "pwd=p4" ;2H hard pulse at plw49

;DEFINE DELAYS

define delay taua
    "taua=1s/(cnst2*4)" ;1/4JCN

define list<delay> vd_list=<$VDLIST> ;List for relaxation delay(s)
"l11=0"

"TAU=-4u-4u-pwd-30u-d12-2u-p54-d16"
"TAU=TAU"

"d11= 30m" ;Delay for disk
"d12= 20u" ;Delay for power switching
```

## 7. Experimental

```
"d16= 200u" ;Delay for gradient recovery

"in0=inf2/2"

#ifdef HALFDWELL
    "d0=in0/2-0.5*pwd_chirp-0.63662*pwn"
#else
    "d0=in0-0.5*pwd_chirp-0.63662*pwn"
#endif /*HALFDWELL*/

;DEFINE OFFSETS

"cnst21=o1/bf1" ;Czeta
"cnst23=0.5*(cnst21+cnst22)" ;13C decoupling position
"cnst31=o3/bf3" ;Nepsilon
"cnst33=0.5*(cnst31+cnst32)" ;15N decoupling position

;DEFINE ZERO POWER ON ALL CHANNELS

"plw10=0"
"plw30=0"

;PULSE PROGRAM BEGINS

aqseq 312

1 ze

    d11 LOCKDEC_ON ;lock decoupling on
    50u LOCKH_ON ;lock hold on
    d11 H2_PULSE ;switch 2H to pulse
    d12 pl29:f2 pl49:f4 ;power to decouple(1H, 2H)
2 d11 do:f2 do:f3 ;decoupling off
    d11 H2_LOCK ;switch 2H to lock
    d1*0.34 ;recycle delay
    6m LOCKH_OFF ;lock hold off
    d1*0.66 ;recycle delay
    50u LOCKH_ON ;lock hold on
    d12 H2_PULSE ;switch 2H to pulse

;purge equilibrium 15N magnetisation

50u UNBLKGRAMP ;gradient amp on
30u fq=cnst33(bf ppm):f3 ;set 15N carrier
d12 pl3:f3 ;power to high (15N)
(pwn ph10):f3 ;90x
2u
p51:gp1 ;cleaning gradient
d16

;end purge block

d12 pl10:f1 pl30:f3 ;power to 0(13C, 15N)
30u fq=cnst21(bf ppm):f1 ;set 13C carrier, Czeta
30u fq=cnst31(bf ppm):f3 ;set 15N carrier, Nepsilon

;start INEPT

(pwc_sel:sp11 ph1):f1 ;13C selective excitation
;start Ne selective block
"DELTA = taua-2u-p52-d16-0.5*larger(pwc*2,pwn_selr) "
DELTA
2u
p52:gp2
d16 pl1:f1 ;power to high (13C)
( center (pwc*2 ph10):f1 (pwn_selr:sp31 ph10):f3 )
2u
p52:gp2
d16
"DELTA = taua-2u-p52-d16-0.5*larger(pwc*2,pwn_selr)-0.6366*pwc"
DELTA
;end Ne selective block
(pwc ph11):f1 ;-2CxNz to 2CzNz

;end INEPT

30u fq=cnst23(bf ppm):f1 ;set 13C carrier to decouple
d12 pl10:f1 pl3:f3 ;power to 0(13C), high(15N)
2u
p53:gp3 ;cleaning gradient
```

```

d16
(pwd ph11):f4 ;2H flanking pulse (90y)
4u cpd4:f4 ph10 ;2H decoupling on
4u cpd2:f2 ph10 ;1H decoupling on
(pwn ph2):f3 ;2CzNz to -2CzNy

;start t1 evolution period with 1H and 2H decoupling

d0 ;incremented delay, t1/2
(pwc_chirp:sp12 ph10):f1 ;13C decoupling pulse
d0 ;incremented delay, t1/2

;end t1 evolution period, start zz-exchange mixing

(pwn ph10):f3 ;-2CzNy to -2CzNz
4u do:f2 ;1H decoupling off
4u do:f4 ;2H decoupling off
(pwd ph13):f4 ;2H flanking pulse (90-y)
30u fq=cnst21(bf ppm):f1 ;13C carrier returned to Czeta
d12 pl1:f1 pl30:f3 ;power to high(13C), 0(15N)
2u
p54:gp4 ;cleaning gradient
d16

"d2=vd_list[l111]-4u-4u-pwd-30u-d12-2u-p54-d16"
d2 ;delay for zz-exchange

;end zz-relaxation, start second INEPT

(pwc ph10):f1 ;-2CzNz to 2CzNz
;start Ne selective block
"DELTA = taua-0.6366*pwc-2u-p55-d16-0.5*larger(pwc*2,pwn_selr)"
DELTA
2u
p55:gp5
d16
( center (pwc*2 ph10):f1 (pwn_selr:sp31 ph10):f3 )
2u
p55:gp5
d16
30u fq=cnst33(bf ppm):f3 ;set 15N carrier to decouple
d12 pl39:f3 ;power to decouple(15N)
50u BLKGRAMP ;gradient amp off
"DELTA = taua-0.5*larger(pwc,pwn_selr)-2u-p55-d16-30u-d12-50u"
DELTA
;end Ne selective block

;end second INEPT, acquire Cx magnetisation with 15N, 1H decoupling

go=2 ph31 cpd2:f2 cpd3:f3
d11 do:f2 do:f3 mc #0 to 2
F2PH(calph(ph2,+90), caldel(d0,+in0))
F1QF(calclc(l11,1))

d11 H2_LOCK ;switch H2 to lock
d11 LOCKH_OFF ;lock hold off
d11 LOCKDEC_OFF ;lock decoupling off

exit

;PHASE PROGRAMS

ph1= 0 2
ph2= 0 0 2 2
ph31= 0 2 2 0

ph10= 0
ph11= 1
ph12= 2
ph13= 3

;DEFINITIONS

;p11 : f1 channel - power level for hard pulse
;p12 : f2 channel - power level for hard pulse
;p13 : f3 channel - power level for hard pulse
;p129 : f2 channel - power level for CPD/BB decoupling
;p139 : f3 channel - power level for CPD/BB decoupling
;p149 : f4 channel - power level for CPD/BB decoupling
;sp11 : f1 channel - shaped pulse 90 degree (Czeta)

```

## 7. Experimental

```
;spnam11 : Eburp2.1000
;sp12 : f1 channel - shaped pulse 180 degree (adiabatic)
;spnam12 : Crp80,0.5,20.1
;sp31 : f3 channel - shaped pulse 180 degree (Nepsilon)
;spnam31 : Reburp.1000
;p1 : f1 channel - 90 degree high power pulse
;p11 : f1 channel - 90 degree shaped pulse [1.5 ms at 16.4T]
;p12 : f1 channel - 180 degree shaped pulse [500 us at 16.4T]
;p3 : f3 channel - 90 degree high power pulse
;p31 : f3 channel - 180 degree shaped pulse [4.5 ms at 16.4T]
;p4 : f4 channel - 90 degree high power pulse
;p51 : homospoil/gradient pulse
;p52 : homospoil/gradient pulse
;p53 : homospoil/gradient pulse
;p54 : homospoil/gradient pulse
;p55 : homospoil/gradient pulse
;d0 : incremented delay
;d1 : relaxation delay
;taua : 1/(4JCN)
;d11 : delay for disk I/O [30 msec]
;d12 : delay for power switching [20 usec]
;d16 : delay for homospoil/gradient recovery
;cnst2 : J(CN) [20 Hz]
;cnst21 : Czeta chemical shift offset [= o1p, 156 ppm]
;cnst22 : Cdelta chemical shift offset [40 ppm]
;cnst31 : Nepsilon chemical shift offset [= o3p, 84 ppm]
;cnst32 : Neta chemical shift offset [70 ppm]
;o1p : Czeta chemical shift offset [156 ppm]
;o2p : Hepsilon/Heta chemical shift offset [7 ppm]
;o3p : Nepsilon chemical shift offset [71 ppm]
;o4p : Depsilon/Deta chemical shift offset [7 ppm]
;inf1 : 1/SW = 2 * DW
;in0 : 1/(2 * SW) = DW
;NS : 4 * n
;DS : 16
;td1 : number of experiments
;FnMODE : States-TPPI
;cpd2 : decoupling according to sequence defined by cpdprg2 (WALTZ64)
;pcpd2 : f2 channel - 90 degree pulse for decoupling [65 us]
;cpd3 : decoupling according to sequence defined by cpdprg3 (GARP4)
;pcpd3 : f3 channel - 90 degree pulse for decoupling [350 us]
;cpd4 : decoupling according to sequence defined by cpdprg3 (WALTZ16)
;pcpd4 : f4 channel - 90 degree pulse for decoupling [250 us]

;for z-only gradients:
;gpz1 : 37%
;gpz2 : 11%
;gpz3 : 23%
;gpz4 : 31%
;gpz5 : 13%

;use gradient files:
;gpnam1 : SMSQ10.100
;gpnam2 : SMSQ10.100
;gpnam3 : SMSQ10.100
;gpnam4 : SMSQ10.100
;gpnam5 : SMSQ10.100

;preprocessor-flags-start
;HALFDWELL: for initial sampling delay of half a dwell-time with
; option -DHALFDWELL (eda: ZGOPTNS)
;preprocessor-flags-end
```

### 7.5.5 Arginine $^{15}\text{N}^{\epsilon}(^1\text{H}/^2\text{H})$ zz-Exchange (pseudo-4D)

This pulse sequence allows the recording of pseudo-four-dimensional  $^{13}\text{C}^{\zeta}\text{-}^{15}\text{N}^{\epsilon}$  spectra on uniformly- $[^{13}\text{C}, ^{15}\text{N}]$ -labelled samples prepared in mixed  $^1\text{H}_2\text{O}:\text{}^2\text{H}_2\text{O}$  buffers. It is a  $^{13}\text{C}$ -excited,  $^{13}\text{C}$ -detected quadruple-resonance experiment requiring the routing of  $^{13}\text{C}$ ,  $^1\text{H}$ ,  $^{15}\text{N}$  and  $^2\text{H}$  to Channels 1, 2, 3 and 4, respectively. The delays to be executed for the incremented mixing time,  $\tau_{\text{mix}}$ , are read from a **vdlist**. The carriers are set to approximately 156 ppm ( $^{13}\text{C}$ ), 84 ppm ( $^{15}\text{N}$ )

and 7 ppm ( $^1\text{H}/^2\text{H}$ ). The  $^1J_{\text{CN}}$  coupling constant (20 Hz) and  $^{13}\text{C}^\delta$  (40 ppm) and  $^{15}\text{N}^\eta$  (70 ppm) chemical shifts must be provided using **cnst2**, **cnst22** and **cnst32**. Two selective RF pulses ( $^{13}\text{C}^\zeta$  excitation,  $^{15}\text{N}^\epsilon$  refocussing) are used as well an adiabatic  $^{13}\text{C}$  chirp pulse. The shapes **Eburp-2** (1.5 ms), **Reburp** (4.5 ms) and **Crp80,0.5,20.1** (0.5 ms) are appropriate for a 16.4 T spectrometer.  $^1\text{H}$ ,  $^2\text{H}$  and  $^{15}\text{N}$  CPD decoupling uses the **WALTZ64**, **WALTZ16** and **GARP4** schemes at power levels corresponding to 70, 250 and 350  $\mu\text{s}$   $90^\circ$  pulses, respectively.

```

;Filename: arg_czne_zz_exchange_p4d.hm
;pseudo-4D zz-exchange
;Cz -> Ne(t1) -> 2CzNz(tmix) -> Ne(t2) -> Cz(t3)

;CLASS=HighRes
;DIM=4D
;TYPE=
;SUBTYPE=
;COMMENT=

#include <Avance.incl>
#include <Delay.incl>
#include <Grad.incl>

;DEFINE PULSES

define pulse pwc
    "pwc=p1"
    ;13C hard pulse at p11
define pulse pwc_sele
    "pwc_sele=p11"
    ;13C selective e-pulse at p111
define pulse pwc_chirp
    "pwc_chirp=p12"
    ;13C chirp pulse at p112

define pulse pwh
    "pwh=p2"
    ;1H hard pulse at p12

define pulse pwn
    "pwn=p3"
    ;15N hard pulse at p13
define pulse pwn_selr
    "pwn_selr=p31"
    ;15N selective r-pulse at p131

define pulse pwd
    "pwd=p4"
    ;2H hard pulse at plw49

;DEFINE DELAYS

define delay taua
    "taua=1s/(cnst2*4)"
    ;1/4JCN

define list<delay> vd_list=<${VDLIST}>
    "l11=0"
    ;List for relaxation delay(s)

"TAU=-4u-4u-pwd-30u-d12-2u-p54-d16"
"TAU=TAU"

"d11= 30m"
"d12= 20u"
"d16= 200u"
;Delay for disk
;Delay for power switching
;Delay for gradient recovery

"in0=in1/2"
"in10=in2/2"

#ifdef HALFDWELL
    "d0=in0/2-0.5*pwc_chirp-0.63662*pwn"
    "d10=in10/2-0.5*pwc_chirp-0.63662*pwn"
#else
    "d0=in0-0.5*pwc_chirp-0.63662*pwn"
    "d10=in10-0.5*pwc_chirp-0.63662*pwn"
#endif /*HALFDWELL*/

;DEFINE OFFSETS

"cnst21=o1/bf1"
"cnst23=0.5*(cnst21+cnst22)"
"cnst31=o3/bf3"
"cnst33=0.5*(cnst31+cnst32)"
;Czeta
;13C decoupling position
;Nepsilon
;15N decoupling position

```

## 7. Experimental

```
;DEFINE ZERO POWER ON ALL CHANNELS

"plw10=0"
"plw30=0"

;PULSE PROGRAM BEGINS

1 ze

d11 LOCKDEC_ON ;lock decoupling on
50u LOCKH_ON ;lock hold on
d11 H2_PULSE ;switch 2H to pulse
d12 pl29:f2 pl49:f4 ;power to decouple(1H, 2H)
2 d11 do:f2 do:f3 ;decoupling off
d11 H2_LOCK ;switch 2H to lock
d1*0.34 ;recycle delay
6m LOCKH_OFF ;lock hold off
d1*0.66 ;recycle delay
50u LOCKH_ON ;lock hold on
d12 H2_PULSE ;switch 2H to pulse

;purge equilibrium 15N magnetisation

50u UNBLKGRAMP ;gradient amp on
30u fq=cnst33(bf ppm):f3 ;set 15N carrier
d12 pl3:f3 ;power to high (15N)
(pwn ph10):f3 ;90x
2u
p51:gp1 ;cleaning gradient
d16

;end purge block

d12 pl10:f1 pl30:f3 ;power to 0(13C, 15N)
30u fq=cnst21(bf ppm):f1 ;set 13C carrier, Czeta
30u fq=cnst31(bf ppm):f3 ;set 15N carrier, Nepsilon

;start INEPT

(pwc_sele:sp11 ph1):f1 ;13C selective excitation

;start Ne selective block
"DELTA = taua-2u-p52-d16-0.5*larger(pwc*2,pwn_selr)"
DELTA
2u
p52:gp2
d16 pl1:f1 ;power to high (13C)
( center (pwc*2 ph10):f1 (pwn_selr:sp31 ph10):f3 )
2u
p52:gp2
d16
"DELTA = taua-2u-p52-d16-0.5*larger(pwc*2,pwn_selr)-0.6366*pwc"
DELTA
(pwc ph11):f1 ;end Ne selective block
;-2CxNz to 2CzNz

;end INEPT

30u fq=cnst23(bf ppm):f1 ;set 13C carrier to decouple
d12 pl10:f1 pl3:f3 ;power to 0(13C), high(15N)
2u
p53:gp3 ;cleaning gradient
d16
(pwd ph11):f4 ;2H flanking pulse (90y)
4u cpd4:f4 ph10 ;2H decoupling on
4u cpd2:f2 ph10 ;1H decoupling on
(pwn ph2):f3 ;2CzNz to -2CzNy

;start t1 evolution period with 1H and 2H decoupling

d0 ;incremented delay, t1/2
(pwc_chirp:sp12 ph10):f1 ;13C decoupling pulse
d0 ;incremented delay, t1/2

;end t1 evolution period, start zz-exchange mixing

(pwn ph10):f3 ;-2CzNy to -2CzNz
4u do:f2 ;1H decoupling off
4u do:f4 ;2H decoupling off
```

## 7. Experimental

```

(pwd ph13):f4 ;2H flanking pulse (90-y)
2u
p54:gp4 ;cleaning gradient
d16

"d2=vd_list[l11]-4u-4u-pwd-2u-p54-d16-pwd-4u-4u"
d2 ;delay for zz-exchange

(pwd ph11):f4 ;2H flanking pulse (90y)
4u cpd4:f4 ph10 ;2H decoupling on
4u cpd2:f2 ph10 ;1H decoupling on
(pwn ph3):f3 ;2CzNz to -2CzNy

;end zz-exchange, start t2 evolution period with 1H and 2H decoupling

d10 ;incremented delay, t2/2
(pwc_chirp:sp12 ph10):f1 ;13C decoupling pulse
d10 ;incremented delay, t2/2

;end t2 evolution period, start second INEPT

(pwn ph10):f3 ;-2CzNy to -2CzNz
4u do:f2 ;1H decoupling off
4u do:f4 ;2H decoupling off
(pwd ph13):f4 ;2H flanking pulse (90-y)
30u fq=cnst21(bf ppm):f1 ;13C carrier returned to Czeta
d12 pl1:f1 pl130:f3 ;power to high(13C), 0(15N)
2u
p54:gp4 ;cleaning gradient
d16
(pwc ph10):f1 ;-2CzNz to 2CyNz
;start Ne selective block

"DELTA = taua-0.6366*pwc-2u-p55-d16-0.5*larger(pwc*2,pwn_selr)"
DELTA
2u
p55:gp5
d16
( center (pwc*2 ph10):f1 (pwn_selr:sp31 ph10):f3 )
2u
p55:gp5
d16
30u fq=cnst33(bf ppm):f3 ;set 15N carrier to decouple
d12 pl39:f3 ;power to decouple(15N)
50u BLKGRAMP ;gradient amp off
"DELTA = taua-0.5*larger(pwc,pwn_selr)-2u-p55-d16-30u-d12-50u"
DELTA
;end Ne selective block

;end second INEPT, acquire Cx magnetisation with 15N, 1H decoupling

go=2 ph31 cpd2:f2 cpd3:f3
d11 do:f2 do:f3 mc #0 to 2
F1QF(calclc(l11,1))
F2PH(calph(ph2,+90), caldel(d0,+in0))
F3PH(calph(ph3,+90), caldel(d10,+in10))

d11 H2_LOCK ;switch H2 to lock
d11 LOCKH_OFF ;lock hold off
d11 LOCKDEC_OFF ;lock decoupling off

exit

;PHASE PROGRAMS

ph1= 0 2
ph2= 0 0 2 2
ph3= 0 0 0 0 2 2 2 2
ph31= 0 2 2 0 2 0 0 2

ph10= 0
ph11= 1
ph12= 2
ph13= 3

;DEFINITIONS

;p11 : f1 channel - power level for hard pulse
;p12 : f2 channel - power level for hard pulse
;p13 : f3 channel - power level for hard pulse
;p129 : f2 channel - power level for CPD/BB decoupling

```

## 7. Experimental

```
;pl39 : f3 channel - power level for CPD/BB decoupling
;pl49 : f4 channel - power level for CPD/BB decoupling
;sp11 : f1 channel - shaped pulse 90 degree (Czeta)
;spnam11 : Eburp2.1000
;sp12 : f1 channel - shaped pulse 180 degree (adiabatic)
;spnam12 : Crp80,0.5,20.1
;sp31 : f3 channel - shaped pulse 180 degree (Nepsilon)
;spnam31 : Reburp.1000
;p1 : f1 channel - 90 degree high power pulse
;p11 : f1 channel - 90 degree shaped pulse [1.5 ms at 16.4T]
;p12 : f1 channel - 180 degree shaped pulse [500 us at 16.4T]
;p3 : f3 channel - 90 degree high power pulse
;p31 : f3 channel - 180 degree shaped pulse [4.5 ms at 16.4T]
;p4 : f4 channel - 90 degree high power pulse
;p51 : homospoil/gradient pulse
;p52 : homospoil/gradient pulse
;p53 : homospoil/gradient pulse
;p54 : homospoil/gradient pulse
;p55 : homospoil/gradient pulse
;d0 : incremented delay
;d1 : relaxation delay
;d2 : delay for H/D exchange
;taua : 1/(4JCN)
;d11 : delay for disk I/O [30 msec]
;d12 : delay for power switching [20 usec]
;d16 : delay for homospoil/gradient recovery
;cnst2 : J(CN) [20 Hz]
;cnst21 : Czeta chemical shift offset [= o1p, 156 ppm]
;cnst22 : Cdelta chemical shift offset [40 ppm]
;cnst31 : Nepsilon chemical shift offset [= o3p, 84 ppm]
;cnst32 : Neta chemical shift offset [70 ppm]
;o1p : Czeta chemical shift offset [156 ppm]
;o2p : Hepsilon/Heta chemical shift offset [7 ppm]
;o3p : Nepsilon chemical shift offset [84 ppm]
;o4p : Depsilon/Deta chemical shift offset [7 ppm]
;inf1 : 1/SW = 2 * DW
;in0 : 1/(2 * SW) = DW
;NS : 8 * n
;DS : 16
;td1 : number of experiments
;FnMODE : States-TPPI
;cpd2 : decoupling according to sequence defined by cpdprg2 (WALTZ64)
;pcpd2 : f2 channel - 90 degree pulse for decoupling [70 us]
;cpd3 : decoupling according to sequence defined by cpdprg3 (GARP4)
;pcpd3 : f3 channel - 90 degree pulse for decoupling [350 us]
;cpd4 : decoupling according to sequence defined by cpdprg3 (WALTZ16)
;pcpd4 : f4 channel - 90 degree pulse for decoupling [250 us]

;for z-only gradients:
;gpz1 : 37%
;gpz2 : 11%
;gpz3 : 23%
;gpz4 : 31%
;gpz5 : 13%

;use gradient files:
;gpnam1 : SMSQ10.100
;gpnam2 : SMSQ10.100
;gpnam3 : SMSQ10.100
;gpnam4 : SMSQ10.100
;gpnam5 : SMSQ10.100

;preprocessor-flags-start
;HALFDWELL: for initial sampling delay of half a dwell-time with
; option -DHALFDWELL (eda: ZGPTNS)
;preprocessor-flags-end
```

### 7.5.6 Arginine $^{13}\text{C}^{\zeta}\text{-}^{15}\text{N}^{\epsilon}$ PEP-HSQC

This pulse sequence allows the recording of two-dimensional  $^{13}\text{C}^{\zeta}\text{-}^{15}\text{N}^{\epsilon}$  HSQC spectra on uniformly- $^{13}\text{C}$ ,  $^{15}\text{N}$ -labelled samples using the PEP signal enhancement. It is a  $^{13}\text{C}$ -excited,  $^{13}\text{C}$ -detected triple-resonance experiment requiring the routing of  $^{13}\text{C}$ ,  $^1\text{H}$  and  $^{15}\text{N}$  to Channels 1, 2 and 3, respectively. The carriers are set to approximately 156 ppm ( $^{13}\text{C}$ ), 84 ppm ( $^{15}\text{N}$ ) and 7 ppm

( $^1\text{H}$ ). The  $^1J_{\text{CN}}$  coupling constant (20 Hz) and  $^{13}\text{C}^\delta$  (40 ppm) and  $^{15}\text{N}^\eta$  (70 ppm) chemical shifts must be provided using **cnst2**, **cnst21** and **cnst32**. Three selective RF pulses ( $^{13}\text{C}^\zeta$  excitation,  $^{15}\text{N}^\epsilon$  refocussing,  $^{13}\text{C}^\zeta$  refocussing) are used as well an adiabatic  $^{13}\text{C}$  chirp pulse. The shapes **Eburp-2** (1.5 ms), **Reburp** (4.5 ms), **Seducer** (0.3 ms) and **Crp80,0.5,20.1** (0.5 ms) are appropriate for a 16.4 T spectrometer.  $^1\text{H}$  and  $^{15}\text{N}$  CPD decoupling uses the **WALTZ64** and **GARP4** schemes at power levels corresponding to 70 and 350  $\mu\text{s}$   $90^\circ$  pulses, respectively.

This pulse sequence can also be used to record  $^{13}\text{C}^\zeta$ - $^{15}\text{N}^\eta$  HSQC spectra by doubling the  $^1J_{\text{CN}}$  coupling constant **cnst2** and swapping the  $^{15}\text{N}$  carrier frequency with the  $^{15}\text{N}^\eta$  chemical shift **cnst32**.

```
;Filename: arg_czne_hsqc_pep.hm
;2D CzNe PEP-HSQC spectrum
;Cz -> Ne(t1) -> Cz(t2)

;$CLASS=HighRes
;$DIM=2D
;$TYPE=
;$SUBTYPE=
;$COMMENT=

#include <Avance.incl>
#include <Delay.incl>
#include <Grad.incl>

;DEFINE PULSES

define pulse pwc
    "pwc=p1" ;13C hard pulse at p11
define pulse pwc_sele
    "pwc_sele=p11" ;13C selective e-pulse at p111
define pulse pwc_chirp
    "pwc_chirp=p12" ;13C chirp pulse at p112
define pulse pwc_seducer
    "pwc_seducer=p13" ;13C seducer pulse at p113

define pulse pwh
    "pwh=p2" ;1H hard pulse at p12

define pulse pwn
    "pwn=p3" ;15N hard pulse at p13
define pulse pwn_selr
    "pwn_selr=p31" ;15N selective r-pulse at p131

;DEFINE DELAYS

define delay taua
    "taua=1s/(cnst2*4)" ;1/4JCN

"d11= 30m" ;Delay for disk
"d12= 20u" ;Delay for power switching
"d16= 200u" ;Delay for gradient recovery

"in0=infl/2"

#ifdef HALFDWELL
    "d0=in0/2-0.5*pwc_chirp-0.63662*pwn"
#else
    "d0=in0-0.5*pwc_chirp-0.63662*pwn"
#endif /*HALFDWELL*/

;DEFINE OFFSETS

"cnst21=o1/bf1" ;Czeta
"cnst23=0.5*(cnst21+cnst22)" ;13C decoupling position
"cnst31=o3/bf3" ;Nepsilon
"cnst33=0.5*(cnst31+cnst32)" ;15N decoupling position
```

## 7. Experimental

```
;DEFINE ZERO POWER ON ALL CHANNELS

"plw10=0"
"plw30=0"

"l0=0"

;PULSE PROGRAM BEGINS

1 ze
  d12 pl29:f2 ;power to decouple(1H)
2 d11 do:f2 do:f3 ;decoupling off
  d1 ;recycle delay

;purge equilibrium 15N magnetisation

50u UNBLKGRAD ;gradient amp on
30u fq=cnst33(bf ppm):f3 ;set 15N carrier
d12 pl3:f3 ;power to high (15N)
(pwn ph10):f3 ;90x
2u
p51:gp1 ;cleaning gradient
d16

;end purge block

d12 pl10:f1 pl30:f3 ;power to 0(13C, 15N)
30u fq=cnst21(bf ppm):f1 ;set 13C carrier, Czeta
30u fq=cnst31(bf ppm):f3 ;set 15N carrier, Nepsilon

;start INEPT

(pwc_sele:sp11 ph1):f1 ;13C selective excitation

;start Ne selective block
"DELTA = taua-2u-p52-d16-0.5*larger(pwc*2,pwn_selr)"
DELTA
2u
p52:gp2
d16 pl1:f1 ;power to high (13C)
( center (pwc*2 ph10):f1 (pwn_selr:sp31 ph10):f3 )
2u
p52:gp2
d16
"DELTA = taua-2u-p52-d16-0.5*larger(pwc*2,pwn_selr)-0.6366*pwc"
DELTA

(pwc ph11):f1 ;end Ne selective block
;-2CxNz to 2CzNz

;end INEPT

d12 pl10:f1 pl3:f3 ;power to 0(13C), high(15N)
2u
p53:gp3 ;cleaning gradient
d16
4u cpd2:f2 ph10 ;1H decoupling on
(pwn ph2):f3 ;2CzNz to -2CzNy

;start t1 evolution period with 1H decoupling

d0 ;incremented delay, t1/2
(pwc_chirp:sp12 ph10):f1 ;13C decoupling pulse
"DELTA=d0-d12"
DELTA ;incremented delay, t1/2
d12 pl1:f1
;end t1 evolution period, start second INEPT

( ralign (pwn ph3):f3 (pwc ph3):f1 )

;start Ne selective PEP block
"DELTA = taua-0.6366*pwc-2u-p55-d16-0.5*larger(pwc*2,pwn_selr)"
DELTA
2u
p55:gp5
d16 pl10:f1 pl30:f3
( center (pwc_seducer:sp13 ph10):f1 (pwn_selr:sp31 ph10):f3 )
2u
p55:gp5
d16
d12 pl1:f1 pl3:f3
```

```

"DELTA = taua-0.5*larger(pwc,pwn_selr)-2u-p55-d16-d12-0.6366*larger(pwc,pwn) "
DELTA

if "10 %2 == 1"
{
  ( center (pwc ph4):f1 (pwn ph4):f3 ) ;-Cx/2CyNx to Cz/-2CyNz
}
else
{
  ( center (pwc ph5):f1 (pwn ph6):f3 ) ;-Cx/2CyNx to Cz/-2CyNz
}

"DELTA = taua-0.6366*larger(pwc,pwn)-d12-2u-p56-d16-0.5*larger(pwc*2,pwn_selr) "
DELTA do:f2
d12 pl30:f3
2u
p56:gp6
d16
( center (pwc*2 ph10):f1 (pwn_selr:sp31 ph10):f3 )
2u
p56:gp6
d16
30u fq=cnst33(bf ppm):f3 ;set 15N carrier to decouple
d12 pl39:f3 ;power to decouple(15N)
50u BLKGRAD ;gradient amp off
"DELTA = taua-0.5*larger(pwc*2,pwn_selr)-2u-p56-d16-30u-d12-50u-0.6366*pwc"
DELTA ;end Ne selective PEP block

(pwc ph7):f1

;end second INEPT, acquire C magnetisation with 15N, 1H decoupling

go=2 ph31 cpd2:f2 cpd3:f3
d11 do:f2 do:f3 mc #0 to 2
F1EA(calclc(10,1), caldel(d0,+in0))

exit

;PHASE PROGRAMS

ph1= 0 2
ph2= 0 0 2 2
ph3= 0 0 0 0 1 1 1 1
ph4= 1 1 1 1 0 0 0 0
ph5= 1 1 1 1 2 2 2 2
ph6= 3 3 3 3 0 0 0 0
ph7= 2 2 2 2 3 3 3 3
ph31= 0 2 2 0

ph10= 0
ph11= 1
ph12= 2
ph13= 3

;DEFINITIONS

;p11 : f1 channel - power level for hard pulse
;p12 : f2 channel - power level for hard pulse
;p13 : f3 channel - power level for hard pulse
;p129 : f2 channel - power level for CPD/BB decoupling
;p139 : f3 channel - power level for CPD/BB decoupling
;sp11 : f1 channel - shaped pulse 90 degree (Czeta)
;spnam11 : Eburp2.1000
;sp12 : f1 channel - shaped pulse 180 degree (adiabatic)
;spnam12 : Crp80,0.5,20.1
;sp13 : f1 channel - shaped pulse 180 degree (Czeta)
;spnam13 : Seduce.100
;sp31 : f3 channel - shaped pulse 180 degree (Nepsilon)
;spnam31 : Reburp.1000
;p1 : f1 channel - 90 degree high power pulse
;p11 : f1 channel - 90 degree shaped pulse [1.5 ms at 16.4T]
;p12 : f1 channel - 180 degree shaped pulse [500 us at 16.4T]
;p3 : f3 channel - 90 degree high power pulse
;p31 : f3 channel - 180 degree shaped pulse [4.5 ms at 16.4T]
;p51 : homospoil/gradient pulse
;p52 : homospoil/gradient pulse
;p53 : homospoil/gradient pulse
;p54 : homospoil/gradient pulse
;p55 : homospoil/gradient pulse

```

## 7. Experimental

```
;d0      : incremented delay
;d1      : relaxation delay
;taua    : 1/(4JCN)
;d11     : delay for disk I/O [30 msec]
;d12     : delay for power switching [20 usec]
;d16     : delay for homospoil/gradient recovery
;cnst2   : J(CN) [20 Hz]
;cnst21  : Czeta chemical shift offset [= o1p, 156 ppm]
;cnst22  : Cdelta chemical shift offset [40 ppm]
;cnst31  : Nepsilon chemical shift offset [= o3p, 84 ppm]
;cnst32  : Neta chemical shift offset [70 ppm]
;o1p     : Czeta chemical shift offset [156 ppm]
;o2p     : Hepsilon/Heta chemical shift offset [7 ppm]
;o3p     : Nepsilon chemical shift offset [84 ppm]
;inf1    : 1/SW = 2 * DW
;in0     : 1/(2 * SW) = DW
;NS      : 8 * n
;DS      : 16
;td1     : number of experiments
;FnMODE  : Echo-antiecho
;cpd2    : decoupling according to sequence defined by cpdprg2 (WALTZ64)
;pcpd2   : f2 channel - 90 degree pulse for decoupling [70 us]
;cpd3    : decoupling according to sequence defined by cpdprg3 (GARP4)
;pcpd3   : f3 channel - 90 degree pulse for decoupling [350 us]

;for z-only gradients:
;gpz1    : 37%
;gpz2    : 11%
;gpz3    : 23%
;gpz4    : 31%
;gpz5    : 13%

;use gradient files:
;gpnam1  : SMSQ10.100
;gpnam2  : SMSQ10.100
;gpnam3  : SMSQ10.100
;gpnam4  : SMSQ10.100
;gpnam5  : SMSQ10.100

;preprocessor-flags-start
;HALFDWELL: for initial sampling delay of half a dwell-time with
;          option -DHALFDWELL (eda: ZGOPTNS)
;preprocessor-flags-end
```

### 7.5.7 Selective $^{13}\text{C}^z$ Excitation

This pulse sequence allows the recording of one-dimensional  $^{13}\text{C}^z$  spectra using a selective  $90^\circ$  pulse. It is a  $^{13}\text{C}$ -excited,  $^{13}\text{C}$ -detected triple-resonance experiment requiring the routing of  $^{13}\text{C}$ ,  $^1\text{H}$  and  $^{15}\text{N}$  to Channels 1, 2 and 3, respectively. The carriers are set to approximately 156 ppm ( $^{13}\text{C}$ ), 77 ppm ( $^{15}\text{N}$ ) and 7 ppm ( $^1\text{H}$ ). Selective excitation is achieved using the **Eburp-2** shape with a duration of 1.5 ms appropriate for a 16.4 T spectrometer.  $^1\text{H}$  and  $^{15}\text{N}$  CPD decoupling uses the **WALTZ64** and **GARP4** schemes at power levels corresponding to 70 and 350  $\mu\text{s}$   $90^\circ$  pulses, respectively.

```
;Filename: arg_cz.hm
;1D Cz spectrum using selective pulse
;Cz(t1)

;$CLASS=HighRes
;$DIM=1D
;$TYPE=
;$SUBTYPE=
;$COMMENT=

#include <Avance.incl>
#include <Delay.incl>

;DEFINE PULSES
```

```

define pulse pwc_sele
    "pwc_sele=p11" ;13C selective e-pulse at p11

"d11= 30m" ;Delay for disk
"d12= 20u" ;Delay for power switching

;DEFINE ZERO POWER ON ALL CHANNELS

"plw10=0"

;PULSE PROGRAM BEGINS

1 ze
  d12 pl10:f1 pl29:f2 pl39:f3 ;power to decouple(1H,15N), 0 (13C)
2 d11 do:f2 do:f3 ;decoupling off
  dl ;recycle delay

  (pwc_sele:sp11 ph1):f1 ;13C selective excitation

;acquire 13C magnetisation with 15N, 1H decoupling

go=2 ph31 cpd2:f2 cpd3:f3
d11 do:f2 do:f3 mc #0 to 2 F0(zd)

exit

;PHASE PROGRAMS

ph1= 0 2 2 0 1 3 3 1
ph31= 0 2 2 0 1 3 3 1

;DEFINITIONS

;sp11 : f1 channel - shaped pulse 90 degree (Czeta)
;spnam11 : Eburp2.1000
;p11 : f1 channel - 90 degree shaped pulse [1.5 ms at 16.4T]
;d1 : relaxation delay
;d11 : delay for disk I/O [30 msec]
;d12 : delay for power switching [20 usec]
;o1p : Czeta chemical shift offset [156 ppm]
;o2p : Hepsilon/Heta chemical shift offset [7 ppm]
;o3p : Nepsilon/Neta chemical shift offset [77 ppm]
;NS : 1 * n
;DS : 16
;cpd2 : decoupling according to sequence defined by cpdprg2 (WALTZ64)
;pcpd2 : f2 channel - 90 degree pulse for decoupling [70 us]
;cpd3 : decoupling according to sequence defined by cpdprg3 (GARP4)
;pcpd3 : f3 channel - 90 degree pulse for decoupling [350 us]

```

### 7.5.8 HetCP $^{13}\text{C}^z$ Excitation

This pulse sequence allows the recording of one-dimensional  $^{13}\text{C}^z$  spectra using a HetCP transfer of magnetisation from the  $^1\text{H}^{\epsilon/\eta}$  nuclei. It is a  $^1\text{H}$ -excited,  $^{13}\text{C}$ -detected triple-resonance experiment requiring the routing of  $^{13}\text{C}$ ,  $^1\text{H}$  and  $^{15}\text{N}$  to Channels 1, 2 and 3, respectively. The carriers are set to approximately 156 ppm ( $^{13}\text{C}$ ), 77 ppm ( $^{15}\text{N}$ ) and 7 ppm ( $^1\text{H}$ ). HetCP transfers from  $^1\text{H}^{\epsilon/\eta}$  to  $^{15}\text{N}^{\epsilon/\eta}$  and from  $^{15}\text{N}^{\epsilon/\eta}$  to  $^{13}\text{C}^z$  are achieved using the **DIPSI-2** (62.5  $\mu\text{s}$ ) and **DIPSI-3** (140  $\mu\text{s}$ ) schemes, respectively.  $^1\text{H}$  and  $^{15}\text{N}$  CPD decoupling uses the **WALTZ64** and **GARP4** schemes at power levels corresponding to 70 and 350  $\mu\text{s}$  90° pulses, respectively.

```

;Filename: arg_cz_hetcp.hm
;1D Cz spectrum using hetcp transfers
;Heh -> Neh -> Cz(t1)

;$CLASS=HighRes
;$DIM=1D
;$TYPE=
;$SUBTYPE=
;$COMMENT=

```

## 7. Experimental

```
#include <Avance.incl>
#include <Delay.incl>
#include <Grad.incl>

;DEFINE PULSES

define pulse pwc
    "pwc=p1"
define pulse pwc_dip3
    "pwc_dip3=p11"

define pulse pwh
    "pwh=p2"
define pulse pwh_dip2
    "pwh_dip2=p21"

define pulse pwn
    "pwn=p3"
define pulse pwn_dip2
    "pwn_dip2=p31"
define pulse pwn_dip3
    "pwn_dip3=p32"

"d11= 30m"
"d12= 20u"
"d16= 200u"

;CALCULATE POWER LEVELS

"plw11=(p1/p11)*(p1/p11)*plw1"
"plw21=(p2/p21)*(p2/p21)*plw2"
"plw31=(p3/p31)*(p3/p31)*plw3"
"plw32=(p3/p33)*(p3/p32)*plw3"

;PULSE PROGRAM BEGINS

1 ze
2 d11 do:f2 do:f3
    d12 pl2:f2

    d1

    50u UNBLKGRAD

    (pwh ph1):f2
    d12 pl21:f2 pl31:f3

3 (pwh_dip2*3.556 ph10):f2 (pwn_dip2*3.556 ph10):f3
  (pwh_dip2*4.556 ph12):f2 (pwn_dip2*4.556 ph12):f3
  (pwh_dip2*3.222 ph10):f2 (pwn_dip2*3.222 ph10):f3
  (pwh_dip2*3.167 ph12):f2 (pwn_dip2*3.167 ph12):f3
  (pwh_dip2*0.333 ph10):f2 (pwn_dip2*0.333 ph10):f3
  (pwh_dip2*2.722 ph12):f2 (pwn_dip2*2.722 ph12):f3
  (pwh_dip2*4.167 ph10):f2 (pwn_dip2*4.167 ph10):f3
  (pwh_dip2*2.944 ph12):f2 (pwn_dip2*2.944 ph12):f3
  (pwh_dip2*4.111 ph10):f2 (pwn_dip2*4.111 ph10):f3

  (pwh_dip2*3.556 ph12):f2 (pwn_dip2*3.556 ph12):f3
  (pwh_dip2*4.556 ph10):f2 (pwn_dip2*4.556 ph10):f3
  (pwh_dip2*3.222 ph12):f2 (pwn_dip2*3.222 ph12):f3
  (pwh_dip2*3.167 ph10):f2 (pwn_dip2*3.167 ph10):f3
  (pwh_dip2*0.333 ph12):f2 (pwn_dip2*0.333 ph12):f3
  (pwh_dip2*2.722 ph10):f2 (pwn_dip2*2.722 ph10):f3
  (pwh_dip2*4.167 ph12):f2 (pwn_dip2*4.167 ph12):f3
  (pwh_dip2*2.944 ph10):f2 (pwn_dip2*2.944 ph10):f3
  (pwh_dip2*4.111 ph12):f2 (pwn_dip2*4.111 ph12):f3

  (pwh_dip2*3.556 ph12):f2 (pwn_dip2*3.556 ph12):f3
  (pwh_dip2*4.556 ph10):f2 (pwn_dip2*4.556 ph10):f3
  (pwh_dip2*3.222 ph12):f2 (pwn_dip2*3.222 ph12):f3
  (pwh_dip2*3.167 ph10):f2 (pwn_dip2*3.167 ph10):f3
  (pwh_dip2*0.333 ph12):f2 (pwn_dip2*0.333 ph12):f3
  (pwh_dip2*2.722 ph10):f2 (pwn_dip2*2.722 ph10):f3
  (pwh_dip2*4.167 ph12):f2 (pwn_dip2*4.167 ph12):f3
  (pwh_dip2*2.944 ph10):f2 (pwn_dip2*2.944 ph10):f3
  (pwh_dip2*4.111 ph12):f2 (pwn_dip2*4.111 ph12):f3

;13C hard pulse at pl1
;13C dipsi-3 pulse at pl11

;1H hard pulse at pl2
;1H dipsi-2 pulse at pl21

;15N hard pulse at pl3
;15N dipsi-2 pulse at pl31
;15N dipsi-3 pulse at pl32

;Delay for disk
;Delay for power switching
;Delay for gradient recovery

;decoupling off
;power to high(1H)

;recycle delay

;1H excitation
;power to dipsi2(1H,15N)

;begin DIPSI-2 on 1H and 15N
```

## 7. Experimental

```
(pwn_dip2*3.556 ph10):f2 (pwn_dip2*3.556 ph10):f3
(pwn_dip2*4.556 ph12):f2 (pwn_dip2*4.556 ph12):f3
(pwn_dip2*3.222 ph10):f2 (pwn_dip2*3.222 ph10):f3
(pwn_dip2*3.167 ph12):f2 (pwn_dip2*3.167 ph12):f3
(pwn_dip2*0.333 ph10):f2 (pwn_dip2*0.333 ph10):f3
(pwn_dip2*2.722 ph12):f2 (pwn_dip2*2.722 ph12):f3
(pwn_dip2*4.167 ph10):f2 (pwn_dip2*4.167 ph10):f3
(pwn_dip2*2.944 ph12):f2 (pwn_dip2*2.944 ph12):f3
(pwn_dip2*4.111 ph10):f2 (pwn_dip2*4.111 ph10):f3

;end DIPSI-2 on 1H and 15N

d12 pl3:f3 ;power to high(15N)
(pwn ph11):f3 ;store 15N

2u
p51:gp1 ;cleaning gradient
d16

(pwn ph11):f3 ;15N pulse

d12 pl11:f1 pl132:f3 ;power to dipsi3(13C,15N)

;begin DIPSI-3 on 13C and 15N

4 (pwn_dip3*2.722 ph12):f3 (pwn_dip3*2.722 ph12):f1
(pwn_dip3*4.389 ph10):f3 (pwn_dip3*4.389 ph10):f1
(pwn_dip3*2.778 ph12):f3 (pwn_dip3*2.778 ph12):f1
(pwn_dip3*3.056 ph10):f3 (pwn_dip3*3.056 ph10):f1
(pwn_dip3*0.333 ph12):f3 (pwn_dip3*0.333 ph12):f1
(pwn_dip3*2.556 ph10):f3 (pwn_dip3*2.556 ph10):f1
(pwn_dip3*4.000 ph12):f3 (pwn_dip3*4.000 ph12):f1
(pwn_dip3*2.722 ph10):f3 (pwn_dip3*2.722 ph10):f1
(pwn_dip3*4.111 ph12):f3 (pwn_dip3*4.111 ph12):f1
(pwn_dip3*3.778 ph10):f3 (pwn_dip3*3.778 ph10):f1
(pwn_dip3*3.889 ph12):f3 (pwn_dip3*3.889 ph12):f1
(pwn_dip3*2.889 ph10):f3 (pwn_dip3*2.889 ph10):f1
(pwn_dip3*3.000 ph12):f3 (pwn_dip3*3.000 ph12):f1
(pwn_dip3*0.333 ph10):f3 (pwn_dip3*0.333 ph10):f1
(pwn_dip3*2.500 ph12):f3 (pwn_dip3*2.500 ph12):f1
(pwn_dip3*4.056 ph10):f3 (pwn_dip3*4.056 ph10):f1
(pwn_dip3*2.833 ph12):f3 (pwn_dip3*2.833 ph12):f1
(pwn_dip3*4.389 ph10):f3 (pwn_dip3*4.389 ph10):f1

(pwn_dip3*2.722 ph10):f3 (pwn_dip3*2.722 ph10):f1
(pwn_dip3*4.389 ph12):f3 (pwn_dip3*4.389 ph12):f1
(pwn_dip3*2.778 ph10):f3 (pwn_dip3*2.778 ph10):f1
(pwn_dip3*3.056 ph12):f3 (pwn_dip3*3.056 ph12):f1
(pwn_dip3*0.333 ph10):f3 (pwn_dip3*0.333 ph10):f1
(pwn_dip3*2.556 ph12):f3 (pwn_dip3*2.556 ph12):f1
(pwn_dip3*4.000 ph10):f3 (pwn_dip3*4.000 ph10):f1
(pwn_dip3*2.722 ph12):f3 (pwn_dip3*2.722 ph12):f1
(pwn_dip3*4.111 ph10):f3 (pwn_dip3*4.111 ph10):f1
(pwn_dip3*3.778 ph12):f3 (pwn_dip3*3.778 ph12):f1
(pwn_dip3*3.889 ph10):f3 (pwn_dip3*3.889 ph10):f1
(pwn_dip3*2.889 ph12):f3 (pwn_dip3*2.889 ph12):f1
(pwn_dip3*3.000 ph10):f3 (pwn_dip3*3.000 ph10):f1
(pwn_dip3*0.333 ph12):f3 (pwn_dip3*0.333 ph12):f1
(pwn_dip3*2.500 ph10):f3 (pwn_dip3*2.500 ph10):f1
(pwn_dip3*4.056 ph12):f3 (pwn_dip3*4.056 ph12):f1
(pwn_dip3*2.833 ph10):f3 (pwn_dip3*2.833 ph10):f1
(pwn_dip3*4.389 ph12):f3 (pwn_dip3*4.389 ph12):f1

(pwn_dip3*2.722 ph10):f3 (pwn_dip3*2.722 ph10):f1
(pwn_dip3*4.389 ph12):f3 (pwn_dip3*4.389 ph12):f1
(pwn_dip3*2.778 ph10):f3 (pwn_dip3*2.778 ph10):f1
(pwn_dip3*3.056 ph12):f3 (pwn_dip3*3.056 ph12):f1
(pwn_dip3*0.333 ph10):f3 (pwn_dip3*0.333 ph10):f1
(pwn_dip3*2.556 ph12):f3 (pwn_dip3*2.556 ph12):f1
(pwn_dip3*4.000 ph10):f3 (pwn_dip3*4.000 ph10):f1
(pwn_dip3*2.722 ph12):f3 (pwn_dip3*2.722 ph12):f1
(pwn_dip3*4.111 ph10):f3 (pwn_dip3*4.111 ph10):f1
(pwn_dip3*3.778 ph12):f3 (pwn_dip3*3.778 ph12):f1
(pwn_dip3*3.889 ph10):f3 (pwn_dip3*3.889 ph10):f1
(pwn_dip3*2.889 ph12):f3 (pwn_dip3*2.889 ph12):f1
(pwn_dip3*3.000 ph10):f3 (pwn_dip3*3.000 ph10):f1
(pwn_dip3*0.333 ph12):f3 (pwn_dip3*0.333 ph12):f1
(pwn_dip3*2.500 ph10):f3 (pwn_dip3*2.500 ph10):f1
(pwn_dip3*4.056 ph12):f3 (pwn_dip3*4.056 ph12):f1
(pwn_dip3*2.833 ph10):f3 (pwn_dip3*2.833 ph10):f1
```

## 7. Experimental

```
(pwn_dip3*4.389 ph12):f3 (pwc_dip3*4.389 ph12):f1

(pwn_dip3*2.722 ph12):f3 (pwc_dip3*2.722 ph12):f1
(pwn_dip3*4.389 ph10):f3 (pwc_dip3*4.389 ph10):f1
(pwn_dip3*2.778 ph12):f3 (pwc_dip3*2.778 ph12):f1
(pwn_dip3*3.056 ph10):f3 (pwc_dip3*3.056 ph10):f1
(pwn_dip3*0.333 ph12):f3 (pwc_dip3*0.333 ph12):f1
(pwn_dip3*2.556 ph10):f3 (pwc_dip3*2.556 ph10):f1
(pwn_dip3*4.000 ph12):f3 (pwc_dip3*4.000 ph12):f1
(pwn_dip3*2.722 ph10):f3 (pwc_dip3*2.722 ph10):f1
(pwn_dip3*4.111 ph12):f3 (pwc_dip3*4.111 ph12):f1
(pwn_dip3*3.778 ph10):f3 (pwc_dip3*3.778 ph10):f1
(pwn_dip3*3.889 ph12):f3 (pwc_dip3*3.889 ph12):f1
(pwn_dip3*2.889 ph10):f3 (pwc_dip3*2.889 ph10):f1
(pwn_dip3*3.000 ph12):f3 (pwc_dip3*3.000 ph12):f1
(pwn_dip3*0.333 ph10):f3 (pwc_dip3*0.333 ph10):f1
(pwn_dip3*2.500 ph12):f3 (pwc_dip3*2.500 ph12):f1
(pwn_dip3*4.056 ph10):f3 (pwc_dip3*4.056 ph10):f1
(pwn_dip3*2.833 ph12):f3 (pwc_dip3*2.833 ph12):f1
(pwn_dip3*4.389 ph10):f3 (pwc_dip3*4.389 ph10):f1

;end DIPSI-3 on 15N and 13C

d12 pl1:f1 pl29:f2 pl39:f3 ;power high(13C), decouple(1H,15N)
(pwc ph11):f1 ;store 13C

2u
p52:gp2 ;cleaning gradient
d16 BLKGRAD

(pwc ph10):f1 ;13C read

;acquire 13C magnetisation with 15N, 1H decoupling

go=2 ph31 cpd2:f2 cpd3:f3
d11 do:f2 do:f3 mc #0 to 2 F0(zd)

exit

;PHASE PROGRAMS

ph1= 1 3
ph31= 2 0

ph10= 0
ph11= 1
ph12= 2
ph13= 3

;p11 : f1 channel - power level for hard pulse
;p111 : f1 channel - power level for dipsi-3
;p12 : f2 channel - power level for hard pulse
;p121 : f2 channel - power level for dipsi-2
;p129 : f2 channel - power level for CPD/BB decoupling
;p13 : f3 channel - power level for hard pulse
;p131 : f3 channel - power level for dipsi-2
;p132 : f3 channel - power level for dipsi-3
;p139 : f3 channel - power level for CPD/BB decoupling
;p1 : f1 channel - 90 degree high power pulse
;p11 : f1 channel - 90 degree dipsi-3 pulse [140 us]
;p2 : f2 channel - 90 degree high power pulse
;p21 : f2 channel - 90 degree dipsi-2 pulse [62.5 us]
;p3 : f3 channel - 90 degree high power pulse
;p31 : f3 channel - 90 degree dipsi-2 pulse [62.5 us]
;p32 : f3 channel - 90 degree dipsi-3 pulse [140 us]
;p51 : homospoil/gradient pulse
;p52 : homospoil/gradient pulse
;d1 : relaxation delay
;d11 : delay for disk I/O [30 msec]
;d12 : delay for power switching [20 usec]
;d16 : delay for homospoil/gradient recovery
;o1p : Czeta chemical shift offset [156 ppm]
;o2p : Hepsilon/Heta chemical shift offset [7 ppm]
;o3p : Nepsilon/Neta chemical shift offset [77 ppm]
;NS : 2 * n
;DS : 16
;cpd2 : decoupling according to sequence defined by cpdprg2 (WALTZ64)
;pcpd2 : f2 channel - 90 degree pulse for decoupling [70 us]
;cpd3 : decoupling according to sequence defined by cpdprg3 (GARP4)
;pcpd3 : f3 channel - 90 degree pulse for decoupling [350 us]
```

```

;for z-only gradients:
;gpz1   : 17%
;gpz2   : 11%

;use gradient files:
;gpnam1 : SMSQ10.100
;gpnam2 : SMSQ10.100

```

### 7.5.9 ASHDEX Experiment

This pulse sequence allows the recording of the pseudo-four-dimensional ASHDEX experiment on uniformly- $^{13}\text{C}$ ,  $^{15}\text{N}$ -labelled samples prepared in mixed  $^1\text{H}_2\text{O}:$  $^2\text{H}_2\text{O}$  buffers. It is a  $^1\text{H}$ -excited,  $^{13}\text{C}$ -detected quadruple-resonance experiment requiring the routing of  $^{13}\text{C}$ ,  $^1\text{H}$ ,  $^{15}\text{N}$  and  $^2\text{H}$  to Channels 1, 2, 3 and 4, respectively. The delays to be executed for the incremented mixing time,  $\tau_{\text{mix}}$ , are read from a **vdlist**. The carriers are set to approximately 156 ppm ( $^{13}\text{C}$ ), 84 ppm ( $^{15}\text{N}$ ) and 7 ppm ( $^1\text{H}/^2\text{H}$ ). The  $^1J_{\text{HN}}$  coupling constant (92 Hz),  $^1J_{\text{CN}}$  coupling constant (20 Hz) and  $^{13}\text{C}^\delta$  (40 ppm) and  $^{15}\text{N}^\eta$  (70 ppm) chemical shifts must be provided using **cnst2**, **cnst3**, **cnst11** and **cnst32**. Three selective RF pulses ( $^{13}\text{C}^\zeta$  refocussing,  $^{13}\text{C}^\delta$  refocussing,  $^{13}\text{C}^\zeta$  excitation and  $^{15}\text{N}^\epsilon$  refocussing) are used with the shapes **Seduce** (0.3 ms), **Seduce** (0.3 ms), **Eburp-2** (1.5 ms) and **Reburp** (3.75 ms) appropriate for a 18.8 T spectrometer.  $^1\text{H}$ ,  $^2\text{H}$  and  $^{15}\text{N}$  CPD decoupling uses the **WALTZ64**, **WALTZ16** and **GARP4** schemes at power levels corresponding to 70, 250 and 350  $\mu\text{s}$   $90^\circ$  pulses, respectively.

```

;Filename: arg_ashdex.hm
;pseudo-4D ASHDEX experiment
;He -> Ne -> Nz(tmix) -> sign-coding(phi3) -> Ne(t1) -> Cz(t2)

;$CLASS=HighRes
;$DIM=4D
;$TYPE=
;$SUBTYPE=
;$COMMENT=

#include <Avance.incl>
#include <Delay.incl>
#include <Grad.incl>

;DEFINE PULSES

define pulse pwc
    "pwc=p1" ;13C hard pulse at p11
define pulse pwc_selr1
    "pwc_selr1=p11" ;13Cz selective r-pulse at p11
define pulse pwc_selr2
    "pwc_selr2=p12" ;13Cd selective r-pulse at p112
define pulse pwc_sele
    "pwc_sele=p13" ;13Cz selective e-pulse at p113

define pulse pwh
    "pwh=p2" ;1H hard pulse at p12

define pulse pwn
    "pwn=p3" ;15N hard pulse at p13
define pulse pwn_selr
    "pwn_selr=p31" ;15N selective r-pulse at p131

define pulse pwd
    "pwd=p4" ;2H hard pulse at plw49

;DEFINE DELAYS

```

## 7. Experimental

```
define delay taua
    "taua=1s/(cnst2*4)" ;1/4JHN
define delay taub
    "taub=1s/(cnst3*4)" ;1/4JCN

"d11= 30m" ;Delay for disk
"d12= 2u" ;Delay for power switching
"d16= 200u" ;Delay for gradient recovery

define list<delay> vd_list=<{$VDLIST}> ;List for mixing time(s)
"l11=0"
"d2=vd_list[l11]"

;SEMI-CONSTANT TIME PARAMETERS

"cnst9=4*taub/inf1"
"cnst10=2/td1"

"d10=0"
"d20=0"
"d30=0"

"in10=inf1/2"
"in20=(inf1/2)-cnst10*taub"
"in30=cnst10*taub"

;DEFINE OFFSETS

"spoffs11=0" ;Czeta for seduce
"spoffs12=(cnst11*bf1)/1000000-o1" ;Cdelta for seduce
"spoffs13=0" ;Czeta for eburp2
"spoffs31=0" ;Nepsilon for reburp

;DEFINE ZERO POWER ON ALL CHANNELS USING SHAPED PULSES

"plw10=0"
"plw30=0"

;DEFINE CONSTANTS

"cnst31=o3/bf3" ;Nepsilon
"cnst33=0.5*(cnst31+cnst32)" ;15N decoupling position

;PULSE PROGRAM BEGINS

1 ze

    d11 LOCKDEC_ON ;lock decoupling on
    50u LOCKH_ON ;lock hold on
    d11 H2_PULSE ;switch 2H to pulse

2 d11 do:f2 do:f3 do:f4 ;decoupling off
  d12 pl10:f1 pl2:f2 pl3:f3 pl49:f4 ;set initial power levels

;purge 1H magnetisation before d1

50u UNBLKGRAMP ;gradient amp on
(pwh ph10):f2 ;90x
2u
p51:gp1 ;cleaning gradient
d16
50u BLKGRAMP ;gradient amp off

;end 1H purge, start d1

d11 H2_LOCK ;switch 2H to lock
d1*0.34 ;recycle delay
6m LOCKH_OFF ;lock hold off
d1*0.66 ;recycle delay
50u LOCKH_ON ;lock hold on
d12 H2_PULSE ;switch 2H to pulse

;start purge equilibrium 15N magnetisation

50u UNBLKGRAMP ;gradient amp on
d12 fq=cnst33(bf ppm):f3 ;set 15N carrier
(pwn ph10):f3 ;90x
2u
p51:gp1 ;cleaning gradient
d16
```

```

d12 fq=cnst31(bf ppm):f3 ;set 15N carrier, Ne

;end purge block, start HN INEPT (Non-selective)

(pwh ph10):f2
"DELTA = taua-0.6366*pwh-2u-p52-d16-0.5*larger(pwh*2,pwn*2)"
DELTA
2u
p52:gp2
d16
( center (pwh*2 ph10):f2 (pwn*2 ph10):f3 )
2u
p52:gp2
d16
"DELTA = taua-0.5*larger(pwc*2,pwn*2)-2u-p52-d16-0.6366*pwh"
DELTA
(pwh ph11):f2
(pwn ph10):f3

;refocus 2HzNy to Nx

"DELTA = taua-0.6366*pwn-2u-p53-d16-0.5*larger(pwh*2,pwn*2)"
DELTA
2u
p53:gp3
d16
( center (pwh*2 ph10):f2 (pwn*2 ph10):f3 )
2u
p53:gp3
d16
"DELTA = taua-0.5*larger(pwc*2,pwn*2)-2u-p53-d16-0.6366*pwn"
DELTA
(pwn ph1):f3 ;Nx to Nz
2u
p54:gp4 ;cleaning gradient
d16

;end INEPT, start relaxation delay for H/D exchange

"d2=vd_list[l11]"

if "d2<250m"
{
"DELTA=d2-2u-p54-d16-d12-pwd-d12"
DELTA ;relaxation delay
}
else
{
"DELTA=d2-2u-p54-d16-d12-50u-d11-50m-6m-50u-d12-50u-pwd-d12"
50u BLKGRAMP ;gradient amp off
d11 H2_LOCK ;switch 2H to lock
50m
6m LOCKH_OFF ;lock hold off
DELTA ;relaxation delay
50u LOCKH_ON ;lock hold on
d12 H2_PULSE ;switch 2H to pulse
50u UNBLKGRAMP ;gradient amp on
}

(pwd ph11):f4 ;2H flanking pulse (90y)
d12 cpd4:f4 ph10 ;2H decoupling on

(pwn ph2):f3 ;start sign-coding filter
"DELTA=2*taua-0.6366*pwn-larger(pwh,pwn)"
DELTA
(center (pwh ph10 pwh ph3):f2 (pwn*2 ph10):f3)
"DELTA=2*taua-larger(pwh,pwn)-d12-4u+0.6366*pwn"
DELTA ;end sign-coding
d12 p129:f2
4u cpd2:f2 ph10

;evolve Ny to 2CzNx during semi-constant time chemical shift evolution
d10
2u
(pwc_selr2:sp12 ph10):f1 ;Cdelta
2u
taub
2u
(pwc_selr1:sp11 ph10):f1 ;Czeta
2u

```

## 7. Experimental

```
d20
(pwn*2 ph10):f3
"DELTA=taub-d30"
DELTA
2u
(pwc_selr1:sp11 ph10):f1 ;Czeta
2u
2u
(pwc_selr2:sp12 ph10):f1 ;Cdelta
2u

(pwn ph10):f3 ;end t1

d12 do:f2 do:f4 ;1H, 2H decoupling off
(pwd ph13):f4 ;2H flanking pulse (90-y)
d12 pl30:f3 ;power to 0(15N)
2u
p55:gp5 ;cleaning gradient
d16
(pwc_sele:sp13 ph10):f1 ;2CzNz to 2CyNz, Czeta eburp2

;start Ne selective block
"DELTA = taub-0.6366*pwc-2u-p56-d16-0.5*larger(pwc*2,pwn_selr)"
DELTA
2u
p56:gp6
d16 pl1:f1 ;power to high (13C)
( center (pwc*2 ph10):f1 (pwn_selr:sp31 ph10):f3 )
2u
p56:gp6
d16
30u fq=cnst33(bf ppm):f3 ;set 15N carrier to decouple
d12 pl29:f2 pl39:f3 ;power to decouple(1H,15N)
50u BLKGRAMP ;gradient amp off
"DELTA = taub-0.5*larger(pwc,pwn_selr)-2u-p56-d16-30u-d12-50u"
DELTA ;end Ne selective block

;acquire Cx magnetisation with 15N, 1H decoupling

go=2 ph31 cpd2:f2 cpd3:f3
d11 do:f2 do:f3 mc #0 to 2
F3QF(calph(ph3,+180)) ;sign-coding
F2QF(calclc(l11,1)) ;t_relax
F1PH(calph(ph2,+90),\
caldel(d10,+in10) &\
caldel(d20,+in20) &\
caldel(d30,+in30)) ;15Ne chemical shift

d11 H2_LOCK ;switch H2 to lock
d11 LOCKH_OFF ;lock hold off
d11 LOCKDEC_OFF ;lock decoupling off

exit

;PHASE PROGRAMS

ph1= 1 3
ph2= 0 0 2 2
ph3= 0
ph31= 0 2 2 0

ph10= 0
ph11= 1
ph12= 2
ph13= 3

;DEFINITIONS

;p11 : f1 channel - power level for hard pulse
;p12 : f2 channel - power level for hard pulse
;p13 : f3 channel - power level for hard pulse
;p14 : f4 channel - power level for hard pulse
;p129 : f2 channel - power level for CPD/BB decoupling
;p139 : f3 channel - power level for CPD/BB decoupling
;p149 : f3 channel - power level for CPD/BB decoupling
;sp11 : f1 channel - shaped pulse 180 degree (Czeta)
;spnam11 : Seduce.100
;sp12 : f1 channel - shaped pulse 180 degree (Cdelta)
;spnam12 : Seduce.100
```

```

;sp13 : f1 channel - shaped pulse 90 degree (Czeta)
;spnam13 : Eburp2.1000
;sp31 : f3 channel - shaped pulse 180 degree (Nepsilon)
;spnam31 : Reburp.1000
;p1 : f1 channel - 90 degree high power pulse
;p11 : f1 channel - 180 degree shaped pulse [300 us at 18.8T]
;p12 : f1 channel - 180 degree shaped pulse [300 us at 18.8T]
;p13 : f1 channel - 90 degree shaped pulse [1.5 ms at 18.8T]
;p2 : f2 channel - 90 degree high power pulse
;p3 : f3 channel - 90 degree high power pulse
;p31 : f3 channel - 180 degree shaped pulse [3.75 ms at 18.8T]
;p4 : f4 channel - 90 degree high power pulse [250 us]
;p51 : homospoil pulse
;p52 : gradient pulse
;p53 : gradient pulse
;p54 : homospoil pulse
;p55 : homospoil pulse
;p56 : gradient pulse
;d1 : relaxation delay
;d2 : initial delay for HDX reaction
;l11 : counter for VD list
;d10 : incremented delay 1
;d20 : incremented delay 2
;d30 : incremented delay 3
;taua : 1/(4JHN)
;taub : 1/(4JCN)
;d11 : delay for disk I/O [30 ms]
;d12 : delay for power switching [2 us]
;d16 : delay for homospoil/gradient recovery
;cnst2 : J(HN) [92 Hz]
;cnst3 : J(CN) [20 Hz]
;cnst10 : semi-constant time factor (1 / (2*TD1))
;cnst11 : Cdelta chemical shift offset [40 ppm]
;cnst31 : Nepsilon chemical shift offset [= o3p, 84 ppm]
;cnst32 : Neta chemical shift offset [70 ppm]
;o1p : Czeta chemical shift offset [156 ppm]
;o2p : Hepsilon/Heta chemical shift offset [7 ppm]
;o3p : Nepsilon chemical shift offset [84 ppm]
;o4p : Depsilon/Deta chemical shift offset [7 ppm]
;inf1 : 1/SW = 2 * DW
;in10 : semi-constant time increment 1
;in20 : semi-constant time increment 2
;in30 : semi-constant time increment 3
;NS : 4 * n
;DS : 16
;td1 : number of experiments (15Ne chemical shift)
;td2 : number of experiments (mixing times) [8-12]
;td3 : number of experiment (sign-coding filter) [2]
;FnMODE : States-TPPI
;cpd2 : decoupling according to sequence defined by cpdprg2 (WALTZ64)
;pcpd2 : f2 channel - 90 degree pulse for decoupling [70 us]
;cpd3 : decoupling according to sequence defined by cpdprg3 (GARP4)
;pcpd3 : f3 channel - 90 degree pulse for decoupling [350 us]
;cpd4 : decoupling according to sequence defined by cpdprg3 (WALTZ16)
;pcpd4 : f4 channel - 90 degree pulse for decoupling [250 us]

;for z-only gradients:
;gpz1 : 47% (spoil)
;gpz2 : 11%
;gpz3 : 17%
;gpz4 : 41% (spoil)
;gpz5 : 31% (spoil)
;gpz6 : 23%

;use gradient files:
;gpnam1 : SMSQ10.100
;gpnam2 : SMSQ10.100
;gpnam3 : SMSQ10.100
;gpnam4 : SMSQ10.100
;gpnam5 : SMSQ10.100
;gpnam6 : SMSQ10.100

```

## 7. Experimental

### 7.5.10 Arginine $^{13}\text{C}^{\zeta}$ - $^{15}\text{N}^{\epsilon}$ HSQC (pseudo-3D)

This pulse sequence allows the recording of separate  $^{13}\text{C}^{\zeta}$ - $^{15}\text{N}^{\epsilon}$ ( $^1\text{H}$ ) and  $^{13}\text{C}^{\zeta}$ - $^{15}\text{N}^{\epsilon}$ ( $^2\text{H}$ ) HSQC spectra on uniformly- $^{13}\text{C}$ ,  $^{15}\text{N}$ -labelled samples prepared in mixed  $^1\text{H}_2\text{O}$ : $^2\text{H}_2\text{O}$  buffers using a sign-coding filter. It is a  $^{13}\text{C}$ -excited,  $^{13}\text{C}$ -detected quadruple-resonance experiment requiring the routing of  $^{13}\text{C}$ ,  $^1\text{H}$ ,  $^{15}\text{N}$  and  $^2\text{H}$  to Channels 1, 2, 3 and 4, respectively. The carriers are set to approximately 156 ppm ( $^{13}\text{C}$ ), 84 ppm ( $^{15}\text{N}$ ) and 7 ppm ( $^1\text{H}/^2\text{H}$ ). The  $^1J_{\text{CN}}$  coupling constant (20 Hz),  $^1J_{\text{HN}}$  coupling constant (92 Hz) and  $^{13}\text{C}^{\delta}$  (40 ppm) and  $^{15}\text{N}^{\eta}$  (70 ppm) chemical shifts must be provided using **cnst2**, **cnst3**, **cnst22** and **cnst32**. Two selective RF pulses ( $^{13}\text{C}^{\zeta}$  excitation,  $^{15}\text{N}^{\epsilon}$  refocussing) are used as well an adiabatic  $^{13}\text{C}$  chirp pulse. The shapes **Eburp-2** (1.5 ms), **Reburp** (4.5 ms) and **Crp80,0.5,20.1** (0.5 ms) are appropriate for a 16.4 T spectrometer.  $^1\text{H}$ ,  $^2\text{H}$  and  $^{15}\text{N}$  CPD decoupling uses the **WALTZ64**, **WALTZ16** and **GARP4** schemes at power levels corresponding to 70, 250 and 350  $\mu\text{s}$  90° pulses, respectively.

```
;Filename: arg_czne_hsqc_p3d.hm
;pseudo-3D CzNe(H/D) HSQC spectrum
;Cz -> Ne -> sign-coding(phi3) -> Ne(t1) -> Cz(t2)

;$CLASS=HighRes
;$DIM=3D
;$TYPE=
;$SUBTYPE=
;$COMMENT=

#include <Avance.incl>
#include <Delay.incl>
#include <Grad.incl>

;DEFINE PULSES

define pulse pwc
    "pwc=p1" ;13C hard pulse at p11
define pulse pwc_sele
    "pwc_sele=p11" ;13C selective e-pulse at p111
define pulse pwc_chirp
    "pwc_chirp=p12" ;13C chirp pulse at p112

define pulse pwh
    "pwh=p2" ;1H hard pulse at p12

define pulse pwn
    "pwn=p3" ;15N hard pulse at p13
define pulse pwn_selr
    "pwn_selr=p31" ;15N selective r-pulse at p131

define pulse pwd
    "pwd=p4" ;2H hard pulse at plw49

;DEFINE DELAYS

define delay taua
    "taua=1s/(cnst2*4)" ;1/4JCN
define delay taub
    "taub=1s/(cnst3*2)" ;1/2JHN

"d11= 30m" ;Delay for disk
"d12= 20u" ;Delay for power switching
"d16= 200u" ;Delay for gradient recovery

"in0=inf2/2"

#ifdef HALFDWELL
    "d0=in0/2-0.5*pwc_chirp-0.63662*pwn"
#else
```

```

    "d0=in0-0.5*pwd_chirp-0.63662*pwn"
#endif /*HALFDWELL*/

;DEFINE OFFSETS

"cnst21=o1/bf1" ;Czeta
"cnst23=0.5*(cnst21+cnst22)" ;13C decoupling position
"cnst31=o3/bf3" ;Nepsilon
"cnst33=0.5*(cnst31+cnst32)" ;15N decoupling position

;DEFINE ZERO POWER ON ALL CHANNELS

"plw10=0"
"plw30=0"

aqseq 312

;PULSE PROGRAM BEGINS

1 ze

    d11 LOCKDEC_ON ;lock decoupling on
    50u LOCKH_ON ;lock hold on
    d11 H2_PULSE ;switch 2H to pulse
    d12 pl49:f4 ;power to decouple(2H)
2 d11 do:f2 do:f3 ;decoupling off
    d11 H2_LOCK ;switch 2H to lock
    d1*0.34 ;recycle delay
    6m LOCKH_OFF ;lock hold off
    d1*0.66 ;recycle delay
    50u LOCKH_ON ;lock hold on
    d12 H2_PULSE ;switch 2H to pulse

;purge equilibrium 15N magnetisation

    50u UNBLKGRAMP ;gradient amp on
    30u fq=cnst33(bf ppm):f3 ;set 15N carrier
    d12 pl3:f3 ;power to high (15N)
    (pwn ph10):f3 ;90x
    2u
    p51:gp1 ;cleaning gradient
    d16

;end purge block

    d12 pl10:f1 pl30:f3 ;power to 0(13C, 15N)
    30u fq=cnst21(bf ppm):f1 ;set 13C carrier, Czeta
    30u fq=cnst31(bf ppm):f3 ;set 15N carrier, Nepsilon

;start INEPT

    (pwc_sele:sp11 ph1):f1 ;13C selective excitation
    ;start Ne selective block
"DELTA = taua-2u-p52-d16-0.5*larger(pwc*2,pwn_selr)"
DELTA
    2u
    p52:gp2
    d16 pl1:f1 ;power to high (13C)
    ( center (pwc*2 ph10):f1 (pwn_selr:sp31 ph10):f3 )
    2u
    p52:gp2
    d16
"DELTA = taua-2u-p52-d16-0.5*larger(pwc*2,pwn_selr)-0.6366*pwc"
DELTA

    ;end Ne selective block
    (pwc ph11):f1 ;-2CxNz to 2CzNz

;end INEPT

    30u fq=cnst23(bf ppm):f1 ;set 13C carrier to decouple
    d12 pl10:f1 pl2:f2 pl3:f3 ;power to 0(13C), high(1H,15N)
    2u
    p53:gp3 ;cleaning gradient
    d16
    (pwd ph11):f4 ;2H flanking pulse (90y)
    4u cpd4:f4 ph10 ;2H decoupling on

    (pwn ph2):f3 ;start sign-coding filter
"DELTA=taub-0.6366*pwn-larger(pwh,pwn)"
DELTA

```

## 7. Experimental

```
(center (pwh ph10 pwh ph3):f2 (pwn*2 ph10):f3)
"DELTA=taub-larger(pwh,pwn)-d12-4u"
DELTA                                     ;end sign-coding
d12 pl29:f2
4u cpd2:f2 ph10                           ;1H decoupling on

;start t1 evolution period with 1H and 2H decoupling

d0                                         ;incremented delay, t1/2
(pwc_chirp:sp12 ph10):f1                 ;13C decoupling pulse
d0                                         ;incremented delay, t1/2

;end t1 evolution period, start second INEPT

(pwn ph10):f3                             ;-2CzNy to -2CzNz
4u do:f2                                  ;1H decoupling off
4u do:f4                                  ;2H decoupling off
(pwd ph13):f4                             ;2H flanking pulse (90-y)
30u fq=cnst21(bf ppm):f1                 ;13C carrier returned to Czeta
d12 pl1:f1 pl30:f3                       ;power to high(13C), 0(15N)
2u
p54:gp4                                   ;cleaning gradient
d16
(pwc ph10):f1                             ;-2CzNz to 2CyNz

                                         ;start Ne selective block
"DELTA = taua-0.6366*pwc-2u-p55-d16-0.5*larger(pwc*2,pwn_selr)"
DELTA
2u
p55:gp5
d16
( center (pwc*2 ph10):f1 (pwn_selr:sp31 ph10):f3 )
2u
p55:gp5
d16
30u fq=cnst33(bf ppm):f3                 ;set 15N carrier to decouple
d12 pl39:f3                               ;power to decouple(15N)
50u BLKGRAMP                             ;gradient amp off
"DELTA = taua-0.5*larger(pwc,pwn_selr)-2u-p55-d16-30u-d12-50u"
DELTA                                     ;end Ne selective block

;end second INEPT, acquire Cx magnetisation with 15N, 1H decoupling

go=2 ph31 cpd2:f2 cpd3:f3
d11 do:f2 do:f3 mc #0 to 2
      F2PH(calph(ph2,+90), caldel(d0,+in0))
      F1QF(calph(ph3,+180))               ;sign-coding

d11 H2_LOCK                               ;switch H2 to lock
d11 LOCKH_OFF                             ;lock hold off
d11 LOCKDEC_OFF                           ;lock decoupling off

exit

;PHASE PROGRAMS

ph1= 0 2
ph2= 0 0 2 2
ph3= 2
ph31= 0 2 2 0

ph10= 0
ph11= 1
ph12= 2
ph13= 3

;DEFINITIONS

;p11      : f1 channel - power level for hard pulse
;p12      : f2 channel - power level for hard pulse
;p13      : f3 channel - power level for hard pulse
;p129     : f2 channel - power level for CPD/BB decoupling
;p139     : f3 channel - power level for CPD/BB decoupling
;p149     : f3 channel - power level for CPD/BB decoupling
;sp11     : f1 channel - shaped pulse 90 degree (Czeta)
;spnam11  : Eburp2.1000
;sp12     : f1 channel - shaped pulse 180 degree (adiabatic)
;spnam12  : Crp80,0.5,20.1
;sp31     : f3 channel - shaped pulse 180 degree (Nepsilon)
```

```

;spnam31 : Reburp.1000
;p1      : f1 channel - 90 degree high power pulse
;p11     : f1 channel - 90 degree shaped pulse [1.5 ms at 16.4T]
;p12     : f1 channel - 180 degree shaped pulse [500 us at 16.4T]
;p3      : f3 channel - 90 degree high power pulse
;p31     : f3 channel - 180 degree shaped pulse [4.5 ms at 16.4T]
;p4      : f4 channel - 90 degree high power pulse
;p51     : homospoil/gradient pulse
;p52     : homospoil/gradient pulse
;p53     : homospoil/gradient pulse
;p54     : homospoil/gradient pulse
;p55     : homospoil/gradient pulse
;d0      : incremented delay
;d1      : relaxation delay
;taua    : 1/(4JCN)
;taub    : 1/(2JHN)
;d11     : delay for disk I/O [30 msec]
;d12     : delay for power switching [20 usec]
;d16     : delay for homospoil/gradient recovery
;cnst2   : J(CN) [20 Hz]
;cnst3   : J(HN) [92 Hz]
;cnst21  : Czeta chemical shift offset [= o1p, 156 ppm]
;cnst22  : Cdelta chemical shift offset [40 ppm]
;cnst31  : Nepsilon chemical shift offset [= o3p, 84 ppm]
;cnst32  : Neta chemical shift offset [70 ppm]
;o1p     : Czeta chemical shift offset [156 ppm]
;o2p     : Hepsilon/Heta chemical shift offset [7 ppm]
;o3p     : Nepsilon chemical shift offset [70 ppm]
;o4p     : Depsilon/Deta chemical shift offset [7 ppm]
;inf1    : 1/SW = 2 * DW
;in0     : 1/(2 * SW) = DW
;NS      : 4 * n
;DS      : 16
;td1     : number of experiments
;FnMODE  : States-TPPI
;cpd2    : decoupling according to sequence defined by cpdprg2 (WALTZ64)
;pcpd2   : f2 channel - 90 degree pulse for decoupling [70 us]
;cpd3    : decoupling according to sequence defined by cpdprg3 (GARP4)
;pcpd3   : f3 channel - 90 degree pulse for decoupling [350 us]
;cpd4    : decoupling according to sequence defined by cpdprg3 (WALTZ16)
;pcpd4   : f4 channel - 90 degree pulse for decoupling [250 us]

;for z-only gradients:
;gpz1    : 37%
;gpz2    : 11%
;gpz3    : 23%
;gpz4    : 31%
;gpz5    : 13%

;use gradient files:
;gpnam1  : SMSQ10.100
;gpnam2  : SMSQ10.100
;gpnam3  : SMSQ10.100
;gpnam4  : SMSQ10.100
;gpnam5  : SMSQ10.100

;preprocessor-flags-start
;HALFDWELL: for initial sampling delay of half a dwell-time with
;          option -DHALFDWELL (eda: ZGOPTNS)
;preprocessor-flags-end

```

### 7.5.11 ( $^1\text{H}$ ) $^{13}\text{C}'$ - $^{15}\text{N}$ HSQC (coupled)

This pulse sequence allows the recording of two-dimensional  $^{13}\text{C}^\alpha$ -coupled ( $^1\text{H}$ ) $^{13}\text{C}'$ - $^{15}\text{N}$  HSQC spectra on uniformly- $^{13}\text{C}$ ,  $^{15}\text{N}$ -labelled samples. It is a  $^1\text{H}$ -excited,  $^{13}\text{C}$ -detected triple-resonance experiment requiring the routing of  $^{13}\text{C}$ ,  $^1\text{H}$  and  $^{15}\text{N}$  to Channels 1, 2 and 3, respectively. The carriers are set to approximately 173 ppm ( $^{13}\text{C}$ ), 118 ppm ( $^{15}\text{N}$ ) and 7 ppm ( $^1\text{H}$ ). The  $^1J_{\text{HN}}$  coupling constant (92 Hz),  $^1J_{\text{CN}}$  coupling constant (20 Hz) and  $^{13}\text{C}^\alpha$  (55 ppm) chemical shift must be provided using **cnst2**, **cnst3** and **cnst11**. Three selective RF pulses ( $^{13}\text{C}'$  refocussing,  $^{13}\text{C}^\alpha$

## 7. Experimental

refocussing,  $^{13}\text{C}$  excitation) are used with the shapes **Reburp** (1.25 ms), **Reburp** (0.75 ms) and **Eburp-2** (1.5 ms) appropriate for a 14.1 T spectrometer.  $^1\text{H}$  and  $^{15}\text{N}$  CPD decoupling uses the **WALTZ64** and **GARP4** schemes at power levels corresponding to 70 and 220  $\mu\text{s}$  90° pulses, respectively.

```
;Filename: HCON_coupled.hm
;2D (H)CON experiment with no Ca decoupling
;H -> N(t1) -> C'(t2)

;$CLASS=HighRes
;$DIM=2D
;$TYPE=
;$SUBTYPE=
;$COMMENT=

#include <Avance.incl>
#include <Delay.incl>
#include <Grad.incl>

;DEFINE PULSES

define pulse pwc_selr_CO
    "pwc_selr_CO=p11"
define pulse pwc_selr_Ca
    "pwc_selr_Ca=p12"
define pulse pwc_sele_CO
    "pwc_sele_CO=p13"

define pulse pwh
    "pwh=p2"

define pulse pwn
    "pwn=p3"

;DEFINE DELAYS

define delay taua
    "taua=1s/(cnst2*4)"
define delay taub
    "taub=1s/(cnst3*4)"

"d11= 30m"
"d12= 2u"
"d16= 200u"

;SEMI-CONSTANT TIME PARAMETERS

"cnst9=4*taub/inf1"
"cnst10=2/td1"

"d10=0"
"d20=0"
"d30=0"

"in10=inf1/2"
"in20=(inf1/2)-cnst10*taub"
"in30=cnst10*taub"

;DEFINE OFFSETS

"spoffs11=0"
"spoffs12=(cnst11*bf1)/1000000-o1"
"spoffs13=0"

;DEFINE ZERO POWER ON ALL CHANNELS USING SHAPED PULSES

"plw10=0"

;PULSE PROGRAM BEGINS

1 ze

2 d11 do:f2 do:f3

    d1
```

```

;start purge equilibrium 15N magnetisation

50u UNBLKGRAD ;gradient amp on
d12
(pwn ph10):f3 ;90x
2u
p51:gp1 ;cleaning gradient
d16

;end purge block, start HN INEPT (Non-selective)

(pwh ph10):f2
"DELTA = taua-0.6366*pwh-2u-p52-d16-0.5*larger(pwh*2,pwn*2)"
DELTA
2u
p52:gp2
d16
( center (pwh*2 ph10):f2 (pwn*2 ph10):f3 )
2u
p52:gp2
d16
"DELTA = taua-0.5*larger(pwh*2,pwn*2)-2u-p52-d16-0.6366*pwh"
DELTA
(pwh ph11):f2
2u
p57:gp7
d16
(pwn ph10):f3

;refocus 2HzNy to Nx

"DELTA = taua-0.6366*pwn-2u-p53-d16-0.5*larger(pwh*2,pwn*2)"
DELTA
2u
p53:gp3
d16
( center (pwh*2 ph10):f2 (pwn*2 ph10):f3 )
2u
p53:gp3
d16
"DELTA = taua-0.5*larger(pwh*2,pwn*2)-2u-p53-d16-0.6366*pwn"
DELTA
(pwn ph1):f3 ;Nx to Nz
2u
p54:gp4 ;cleaning gradient
d16

4u cpd2:f2 ph10 ;1H decoupling on

(pwn ph2):f3 ;Nz to Ny

;Ny to 2CzNx during semi-CT t1 period
d10
2u
(pwc_selr_Ca:sp12 ph10):f1
2u
taub
2u
(pwc_selr_CO:sp11 ph10):f1
2u
d20
(pwn*2 ph10):f3
"DELTA=taub-d30"
DELTA
2u
(pwc_selr_CO:sp11 ph10):f1
2u
2u
(pwc_selr_Ca:sp12 ph10):f1
2u

(pwn ph10):f3 ;end t1

4u do:f2 ;1H decoupling off

2u
p55:gp5 ;cleaning gradient
d16

;start CO selective INEPT block

```

## 7. Experimental

```
(pwc_sele_CO:sp13 ph10):f1 ;2CzNz to 2CyNz, CO pulse
"DELTA=taub*-2u-p56-d16-larger(pwc_selr_CO,pwn*2)*0.5"
DELTA
2u
p56:gp6
d16
( center (pwc_selr_CO:sp11 ph10):f1 (pwn*2 ph10):f3 )
2u
p56:gp6
d16
"DELTA=taub-larger(pwc_selr_CO,pwn*2)*0.5-2u-p56-d16-d12-50u"
DELTA
;end CO selective INEPT block

d12 p139:f3 ;power to decouple(15N)
50u BLKGRAMP ;gradient amp off

;acquire Cx magnetisation with 15N, 1H decoupling

go=2 ph31 cpd2:f2 cpd3:f3
d11 do:f2 do:f3 mc #0 to 2
    F1PH(caliph(ph2,+90),\
        caldel(d10,+in10) &\
        caldel(d20,+in20) &\
        caldel(d30,+in30)) ;15N chemical shift

exit

;PHASE PROGRAMS

ph1= 1 3
ph2= 1 1 3 3
ph3= 0
ph31= 2 0 0 2

ph10= 0
ph11= 1
ph12= 2
ph13= 3

;DEFINITIONS

;p11 : f1 channel - power level for hard pulse
;p12 : f2 channel - power level for hard pulse
;p13 : f3 channel - power level for hard pulse
;p129 : f2 channel - power level for CPD/BB decoupling
;p139 : f3 channel - power level for CPD/BB decoupling
;sp11 : f1 channel - shaped pulse 180 degree (CO)
;spnam11 : Reburp.1000 (CO)
;sp12 : f1 channel - shaped pulse 180 degree (Ca)
;spnam12 : Reburp.1000 (Ca)
;sp13 : f1 channel - shaped pulse 90 degree (CO)
;spnam13 : Eburp2.1000 (CO)
;p1 : f1 channel - 90 degree high power pulse
;p11 : f1 channel - 180 degree shaped pulse (CO)
;p12 : f1 channel - 180 degree shaped pulse (Ca)
;p13 : f1 channel - 90 degree shaped pulse (CO)
;p2 : f2 channel - 90 degree high power pulse
;p3 : f3 channel - 90 degree high power pulse
;p51 : homospoil pulse
;p52 : gradient pulse
;p53 : gradient pulse
;p54 : homospoil pulse
;p55 : homospoil pulse
;p56 : gradient pulse
;p57 : homospoil pulse
;d1 : relaxation delay
;d10 : incremented delay 1
;d20 : incremented delay 2
;d30 : incremented delay 3
;taua : 1/(4JHN)
;taub : 1/(4JCN)
;d11 : delay for disk I/O [30 ms]
;d12 : delay for power switching [2 us]
;d16 : delay for homospoil/gradient recovery [200 us]
;cnst2 : J(HN) [92 Hz]
;cnst3 : J(CN) [20 Hz]
;cnst9 : minimum number of experiments (TD1)
;cnst11 : Ca chemical shift offset [55 ppm]
```

```

;inf1      : 1/SW = 2 * DW
;in10     : semi-constant time increment 1
;in20     : semi-constant time increment 2
;in30     : semi-constant time increment 3
;NS       : 4 * n
;DS       : 16
;td1      : number of experiments (15Ne chemical shift)
;FnMODE   : States-TPPI
;cpd2     : decoupling according to sequence defined by cpdprg2 (WALTZ64)
;pcpd2    : f2 channel - 90 degree pulse for decoupling [70 us]
;cpd3     : decoupling according to sequence defined by cpdprg3 (GARP4)
;pcpd3    : f3 channel - 90 degree pulse for decoupling [220 us]

;for z-only gradients:
;gpz1     : 47% (spoil)
;gpz2     : 11%
;gpz3     : 17%
;gpz4     : 41% (spoil)
;gpz5     : 31% (spoil)
;gpz6     : 23%
;gpz7     : 13% (spoil)

;use gradient files:
;gpnam1   : SMSQ10.100
;gpnam2   : SMSQ10.100
;gpnam3   : SMSQ10.100
;gpnam4   : SMSQ10.100
;gpnam5   : SMSQ10.100
;gpnam6   : SMSQ10.100
;gpnam7   : SMSQ10.100

```

### 7.5.12 ( $^1\text{H}$ )- $^{13}\text{C}$ '- $^{15}\text{N}$ HSQC (BASH decoupled)

This pulse sequence allows the recording of two-dimensional ( $^1\text{H}$ )- $^{13}\text{C}$ '- $^{15}\text{N}$  HSQC spectra with BASH decoupling on uniformly- $^{13}\text{C}$ , $^{15}\text{N}$ -labelled samples. It is a  $^1\text{H}$ -excited,  $^{13}\text{C}$ -detected triple-resonance experiment requiring the routing of  $^{13}\text{C}$ ,  $^1\text{H}$  and  $^{15}\text{N}$  to Channels 1, 2 and 3, respectively. The carriers are set to approximately 173 ppm ( $^{13}\text{C}$ ), 118 ppm ( $^{15}\text{N}$ ) and 7 ppm ( $^1\text{H}$ ). The  $^1J_{\text{HN}}$  coupling constant (92 Hz),  $^1J_{\text{CN}}$  coupling constant (20 Hz) and  $^{13}\text{C}^\alpha$  (55 ppm) chemical shift must be provided using **cnst2**, **cnst3** and **cnst11**. Three selective RF pulses ( $^{13}\text{C}'$  refocussing,  $^{13}\text{C}^\alpha$  refocussing,  $^{13}\text{C}'$  excitation) are used with the shapes **Reburp** (1.25 ms), **Reburp** (0.75 ms) and **Eburp-2** (1.5 ms) appropriate for a 14.1 T spectrometer. An additional shaped RF pulse is required to invert both  $^{13}\text{C}'$  and  $^{13}\text{C}^\alpha$  simultaneously.  $^1\text{H}$  and  $^{15}\text{N}$  CPD decoupling uses the **WALTZ64** and **GARP4** schemes at power levels corresponding to 70 and 220  $\mu\text{s}$  90° pulses, respectively.

```

;Filename: HCON_bash.hm
;2D (H)CON experiment with BASH decoupling
;H -> N(t1) -> C'(t2)

;$CLASS=HighRes
;$DIM=2D
;$TYPE=
;$SUBTYPE=
;$COMMENT=

#include <Avance.incl>
#include <Delay.incl>
#include <Grad.incl>
#include <De.incl>

;DEFINE PULSES

define pulse pwc_selr_CO
    "pwc_selr_CO=p11"
    ;13CO selective r-pulse at p11

```

## 7. Experimental

```
define pulse pwc_selr_Ca
    "pwc_selr_Ca=p12" ;13Ca selective r-pulse at p112
define pulse pwc_sele_CO
    "pwc_sele_CO=p13" ;13CO selective e-pulse at p113
define pulse pwc_CO_Ca
    "pwc_CO_Ca=p14" ;13CO/Ca pulse at p114

define pulse pwh
    "pwh=p2" ;1H hard pulse at p12

define pulse pwn
    "pwn=p3" ;15N hard pulse at p13

"p59=300u" ;short gradient pulse

;DEFINE DELAYS

define delay taua
    "taua=1s/(cnst2*4)" ;1/4JHN
define delay taub
    "taub=1s/(cnst3*4)" ;1/4JCN

"d11= 30m" ;Delay for disk
"d12= 2u" ;Delay for power switching
"d16= 200u" ;Delay for gradient recovery

"d62=aq/(10*2)" ;data chunk
"d63=d62/2"

;SEMI-CONSTANT TIME PARAMETERS

"cnst9=4*taub/inf1"
"cnst10=2/td1"

"d10=0"
"d20=0"
"d30=0"

"in10=inf1/2"
"in20=(inf1/2)-cnst10*taub"
"in30=cnst10*taub"

;DEFINE OFFSETS

"spoffs11=0" ;CO
"spoffs12=(cnst11*bf1)/1000000-o1" ;Calpha
"spoffs13=0" ;CO

;DEFINE ZERO POWER ON ALL CHANNELS USING SHAPED PULSES

"plw10=0"

;PULSE PROGRAM BEGINS

dwellmode explicit

1 ze

2 d11 do:f2 do:f3 ;decoupling off

d1 ;recycle delay

;start purge equilibrium 15N magnetisation

50u UNBLKGRAD ;gradient amp on
d12
(pwn ph10):f3 ;90x
2u
p51:gp1 ;cleaning gradient
d16

;end purge block, start HN INEPT (Non-selective)

(pwh ph10):f2
"DELTA = taua-0.6366*pwh-2u-p52-d16-0.5*larger(pwh*2,pwn*2)"
DELTA
2u
p52:gp2
d16
( center (pwh*2 ph10):f2 (pwn*2 ph10):f3 )
```

```

2u
p52:gp2
d16
"DELTA = taua-0.5*larger(pwh*2,pwn*2)-2u-p52-d16-0.6366*pwh"
DELTA
(pwh ph11):f2
2u
p57:gp7
d16
(pwn ph10):f3

;refocus 2HzNy to Nx

"DELTA = taua-0.6366*pwn-2u-p53-d16-0.5*larger(pwh*2,pwn*2)"
DELTA
2u
p53:gp3
d16
( center (pwh*2 ph10):f2 (pwn*2 ph10):f3 )
2u
p53:gp3
d16
"DELTA = taua-0.5*larger(pwh*2,pwn*2)-2u-p53-d16-0.6366*pwn"
DELTA
(pwn ph1):f3 ;Nx to Nz
2u
p54:gp4 ;cleaning gradient
d16

4u cpd2:f2 ph10 ;1H decoupling on
(pwn ph2):f3 ;Nz to Ny

;Ny to 2CzNx during semi-CT t1 period
d10
2u
(pwc_selr_Ca:sp12 ph10):f1
2u
taub
2u
(pwc_selr_CO:sp11 ph10):f1
2u
d20
(pwn*2 ph10):f3
"DELTA=taub-d30"
DELTA
2u
(pwc_selr_CO:sp11 ph10):f1
2u
2u
(pwc_selr_Ca:sp12 ph10):f1
2u

(pwn ph10):f3 ;end t1

4u do:f2 ;1H decoupling off

2u
p55:gp5 ;cleaning gradient
d16 ;start CO selective INEPT block

(pwc_sele_CO:sp13 ph10):f1 ;2CzNz to 2CyNz, CO pulse
"DELTA=taub*-2u-p56-d16-larger(pwc_selr_CO,pwn*2)*0.5"
DELTA
2u
p56:gp6
d16
( center (pwc_selr_CO:sp11 ph10):f1 (pwn*2 ph10):f3 )
2u
p56:gp6
d16
"DELTA=taub-larger(pwc_selr_CO,pwn*2)*0.5-2u-p56-d16-d12-50u"
DELTA ;end CO selective INEPT block

d12 pl39:f3 ;power to decouple(15N)
50u BLKGRAMP ;gradient amp off

;acquire Cx magnetisation with 15N, 1H, 13Ca decoupling

```

## 7. Experimental

```
4u cpd2:f2 cpd3:f3 ;1H, 2H decoupling on

ACQ_START(ph30,ph31)

0.1u REC_UNBLK
0.05u DWL_CLK_ON
d63:r ;half-chunk
0.05u DWL_CLK_OFF
0.1u REC_BLK

4 p59:gp7
d16
4u
(pwc_CO_Ca:sp14 ph10):f1
4u
P59:gp7
d16

p59:gp8
d16
4u
(pwc_selr_CO:sp11 ph12):f1
4u
P59:gp8
d16

0.1u REC_UNBLK
0.05u DWL_CLK_ON
d62:r ;full chunk
0.05u DWL_CLK_OFF
0.1u REC_BLK

P59:gp7
d16
4u
(pwc_CO_Ca:sp14 ph10):f1
4u
P59:gp7
d16

p59:gp8
d16
4u
(pwc_selr_CO:sp11 ph12):f1
4u
P59:gp8
d16

0.1u REC_UNBLK
0.05u DWL_CLK_ON
d62:r ;full chunk
0.05u DWL_CLK_OFF
0.1u REC_BLK

lo to 4 times 10

d62

rcyc=2

d11 do:f2 do:f3 mc #0 to 2
    F1PH(calph(ph2,+90),\
        caldel(d10,+in10) &\
        caldel(d20,+in20) &\
        caldel(d30,+in30)) ;15N chemical shift

exit

;PHASE PROGRAMS

ph1= 1 3
ph2= 1 1 3 3
ph3= 0
ph31= 2 0 0 2

ph10= 0
ph11= 1
ph12= 2
ph13= 3
```

```

ph30=0

;DEFINITIONS

;p11      : f1 channel - power level for hard pulse
;p12      : f2 channel - power level for hard pulse
;p13      : f3 channel - power level for hard pulse
;p129     : f2 channel - power level for CPD/BB decoupling
;p139     : f3 channel - power level for CPD/BB decoupling
;sp11     : f1 channel - shaped pulse 180 degree (CO)
;spnam11  : Reburp.1000 (CO)
;sp12     : f1 channel - shaped pulse 180 degree (Ca)
;spnam12  : Reburp.1000 (Ca)
;sp13     : f1 channel - shaped pulse 90 degree (CO)
;spnam13  : Eburp2.1000 (CO)
;sp14     : f1 channel - shaped pulse 90 degree (CO)
;spnam14  : CaCOCa.hm (CO+Ca)
;p1       : f1 channel - 90 degree high power pulse
;p11      : f1 channel - 180 degree shaped pulse (CO)
;p12      : f1 channel - 180 degree shaped pulse (Ca)
;p13      : f1 channel - 90 degree shaped pulse (CO)
;p14      : f1 channel - 180 degree shaped pulse (CO+Ca)
;p2       : f2 channel - 90 degree high power pulse
;p3       : f3 channel - 90 degree high power pulse
;p51      : homospoil pulse
;p52      : gradient pulse
;p53      : gradient pulse
;p54      : homospoil pulse
;p55      : homospoil pulse
;p56      : gradient pulse
;p57      : homospoil pulse
;p59      : homospoil pulse
;d1       : relaxation delay
;d10      : incremented delay 1
;d20      : incremented delay 2
;d30      : incremented delay 3
;d62      : datachunk (<1/5J)
;d63      : half-chunk (d62/2)
;taua     : 1/(4JHN)
;taub     : 1/(4JCN)
;d11      : delay for disk I/O [30 ms]
;d12      : delay for power switching [2 us]
;d16      : delay for homospoil/gradient recovery [200 us]
;cnst2    : J(HN) [92 Hz]
;cnst3    : J(CN) [20 Hz]
;cnst9    : minimum number of experiments (TD1)
;cnst11   : Ca chemical shift offset [55 ppm]
;inf1     : 1/SW = 2 * DW
;in10     : semi-constant time increment 1
;in20     : semi-constant time increment 2
;in30     : semi-constant time increment 3
;NS       : 4 * n
;DS       : 16
;td1      : number of experiments (15Ne chemical shift)
;FnMODE   : States-TPPI
;cpd2     : decoupling according to sequence defined by cpdprg2 (WALTZ64)
;pcpd2    : f2 channel - 90 degree pulse for decoupling [70 us]
;cpd3     : decoupling according to sequence defined by cpdprg3 (GARP4)
;pcpd3    : f3 channel - 90 degree pulse for decoupling [220 us]

;for z-only gradients:
;gpz1     : 47% (spoil)
;gpz2     : 11%
;gpz3     : 17%
;gpz4     : 41% (spoil)
;gpz5     : 31% (spoil)
;gpz6     : 23%
;gpz7     : 13% (spoil)

;use gradient files:
;gpnam1   : SMSQ10.100
;gpnam2   : SMSQ10.100
;gpnam3   : SMSQ10.100
;gpnam4   : SMSQ10.100
;gpnam5   : SMSQ10.100
;gpnam6   : SMSQ10.100
;gpnam7   : SMSQ10.100

```

## 7. Experimental

### 7.5.13 ( $^1\text{H}$ )- $^{13}\text{C}$ '- $^{15}\text{N}$ HSQC (IPAP decoupled)

This pulse sequence allows the recording of two-dimensional ( $^1\text{H}$ )- $^{13}\text{C}$ '- $^{15}\text{N}$  HSQC spectra with IPAP decoupling on uniformly- $^{13}\text{C}$ , $^{15}\text{N}$ -labelled samples. The in-phase (IP) and anti-phase (AP) components are recorded as two planes of a pseudo-three-dimensional experiment. It is a  $^1\text{H}$ -excited,  $^{13}\text{C}$ -detected triple-resonance experiment requiring the routing of  $^{13}\text{C}$ ,  $^1\text{H}$  and  $^{15}\text{N}$  to Channels 1, 2 and 3, respectively. The carriers are set to approximately 173 ppm ( $^{13}\text{C}$ ), 118 ppm ( $^{15}\text{N}$ ) and 7 ppm ( $^1\text{H}$ ). The  $^1J_{\text{HN}}$  coupling constant (92 Hz),  $^1J_{\text{CN}}$  coupling constant (20 Hz),  $^1J_{\text{CC}}$  coupling constant (53 Hz) and  $^{13}\text{C}^\alpha$  (55 ppm) chemical shift must be provided using **cnst2**, **cnst3**, **cnst4** and **cnst11**. Three selective RF pulses ( $^{13}\text{C}'$  refocussing,  $^{13}\text{C}^\alpha$  refocussing,  $^{13}\text{C}'$  excitation) are used with the shapes **Reburp** (1.25 ms), **Reburp** (0.75 ms) and **Eburp-2** (1.5 ms) appropriate for a 14.1 T spectrometer.  $^1\text{H}$  and  $^{15}\text{N}$  CPD decoupling uses the **WALTZ64** and **GARP4** schemes at power levels corresponding to 70 and 220  $\mu\text{s}$   $90^\circ$  pulses, respectively.

```
;Filename: HCON_ipap.hm
;pseudo-3D (H)CON experiment with IPAP decoupling
;H -> N(t1) -> IPAP -> C'(t2)

;$CLASS=HighRes
;$DIM=3D
;$TYPE=
;$SUBTYPE=
;$COMMENT=

#include <Avance.incl>
#include <Delay.incl>
#include <Grad.incl>

;DEFINE PULSES

define pulse pwc_selr_CO
    "pwc_selr_CO=p11"                ;13CO selective r-pulse at p11
define pulse pwc_selr_Ca
    "pwc_selr_Ca=p12"                ;13Ca selective r-pulse at p12
define pulse pwc_sele_CO
    "pwc_sele_CO=p13"                ;13CO selective e-pulse at p13

define pulse pwh
    "pwh=p2"                          ;1H hard pulse at p12

define pulse pwn
    "pwn=p3"                          ;15N hard pulse at p13

;DEFINE DELAYS

define delay taua
    "taua=1s/(cnst2*4)"                ;1/4JHN
define delay taub
    "taub=1s/(cnst3*4)"                ;1/4JCN
define delay tauc
    "tauc=1s/(cnst4*4)"                ;1/4JCC

"d11= 30m"                            ;Delay for disk
"d12= 2u"                              ;Delay for power switching
"d16= 200u"                            ;Delay for gradient recovery

"l12=0"                                ;ipap flag

;SEMI-CONSTANT TIME PARAMETERS

"cnst9=4*taub/inf1"
"cnst10=2/td1"

"d10=0"
"d20=0"
```

```

"d30=0"

"in10=inf1/2"
"in20=(inf1/2)-cnst10*taub"
"in30=cnst10*taub"

;DEFINE OFFSETS

"spoffsl1=0" ;CO
"spoffsl2=(cnst11*bf1)/1000000-ol" ;Calpha
"spoffsl3=0" ;CO

;DEFINE ZERO POWER ON ALL CHANNELS USING SHAPED PULSES

"plw10=0"

;PULSE PROGRAM BEGINS

1 ze

2 d11 do:f2 do:f3 ;decoupling off

d1 ;recycle delay

;start purge equilibrium 15N magnetisation

50u UNBLKGRAD ;gradient amp on
d12
(pwn ph10):f3 ;90x
2u
p51:gp1 ;cleaning gradient
d16

;end purge block, start HN INEPT (Non-selective)

(pwh ph10):f2
"DELTA = taua-0.6366*pwh-2u-p52-d16-0.5*larger(pwh*2,pwn*2)"
DELTA
2u
p52:gp2
d16
( center (pwh*2 ph10):f2 (pwn*2 ph10):f3 )
2u
p52:gp2
d16
"DELTA = taua-0.5*larger(pwh*2,pwn*2)-2u-p52-d16-0.6366*pwh"
DELTA
(pwh ph11):f2
2u
p57:gp7
d16
(pwn ph10):f3

;refocus 2HzNy to Nx

"DELTA = taua-0.6366*pwn-2u-p53-d16-0.5*larger(pwh*2,pwn*2)"
DELTA
2u
p53:gp3
d16
( center (pwh*2 ph10):f2 (pwn*2 ph10):f3 )
2u
p53:gp3
d16
"DELTA = taua-0.5*larger(pwh*2,pwn*2)-2u-p53-d16-0.6366*pwn"
DELTA
(pwn ph1):f3 ;Nx to Nz
2u
p54:gp4 ;cleaning gradient
d16

4u cpd2:f2 ph10 ;1H decoupling on

(pwn ph2):f3 ;Nz to Ny

;Ny to 2CzNx during semi-CT t1 period
d10
2u
(pwc_selr_Ca:sp12 ph10):f1
2u

```

## 7. Experimental

```
taub
2u
(pwc_selr_CO:sp11 ph10):f1
2u
d20
(pwn*2 ph10):f3
"DELTA=taub-d30"
DELTA
2u
(pwc_selr_CO:sp11 ph10):f1
2u
2u
(pwc_selr_Ca:sp12 ph10):f1
2u

(pwn ph10):f3 ;end t1

4u do:f2 ;1H decoupling off

2u
p55:gp5 ;cleaning gradient
d16 ;start CO-N INEPT block (IPAP Ca)

if "112 %2 ==0" ;In-Phase spectrum
{

(pwc_sele_CO:sp13 ph10):f1 ;2CzNz to 2CyNz, CO pulse
"DELTA=taub*0.5-pwc_selr_Ca*0.5"
DELTA
(pwc_selr_Ca:sp12 ph10):f1 ;13Ca pulse
"DELTA=taub*0.5-pwc_selr_Ca*0.5-2u-p56-d16-larger(pwc_selr_CO,pwn*2)*0.5"
DELTA
2u
p56:gp6
d16
( center (pwc_selr_CO:sp11 ph10):f1 (pwn*2 ph10):f3 )
2u
p56:gp6
d16
"DELTA=taub*0.5-larger(pwc_selr_CO,pwn*2)*0.5-2u-p56-d16-pwc_selr_Ca*0.5"
DELTA
(pwc_selr_Ca:sp12 ph10):f1 ;13Ca pulse
"DELTA=taub*0.5-pwc_selr_Ca*0.5-0.1u-d12-50u"
DELTA
}
else ;Anti-Phase spectrum
{
(pwc_sele_CO:sp13 ph11):f1 ;2CzNz to 2CyNz, CO pulse
"DELTA=tauc"
DELTA
(pwc_selr_Ca:sp12 ph10):f1
"DELTA=taub-tauc-pwc_selr_Ca-2u-p56-d16-larger(pwc_selr_CO,pwn*2)*0.5"
DELTA
2u
p56:gp6
d16
( center (pwc_selr_CO:sp11 ph10):f1 (pwn*2 ph10):f3 )
2u
p56:gp6
d16
"DELTA=taub-larger(pwc_selr_CO,pwn*2)*0.5-2u-p56-d16-pwc_selr_Ca-0.1u-d12-50u"
DELTA
(pwc_selr_Ca:sp12 ph10):f1

}

0.1u ;end CO-N INEPT block

d12 pl39:f3 ;power to decouple(15N)
50u BLKGRAMP ;gradient amp off

;acquire Cx magnetisation with 15N, 1H decoupling

go=2 ph31 cpd2:f2 cpd3:f3
d11 do:f2 do:f3 mc #0 to 2
F2QF(calclc(112,1)) ;IPAP decoupling
F1PH(calph(ph2,+90),\
caldel(d10,+in10) &\
```

```

caldel(d20,+in20) &\
caldel(d30,+in30) ;15N chemical shift

exit

;PHASE PROGRAMS

ph1= 1 3
ph2= 1 1 3 3
ph3= 0
ph31= 2 0 0 2

ph10= 0
ph11= 1
ph12= 2
ph13= 3

;DEFINITIONS

;p11 : f1 channel - power level for hard pulse
;p12 : f2 channel - power level for hard pulse
;p13 : f3 channel - power level for hard pulse
;p129 : f2 channel - power level for CPD/BB decoupling
;p139 : f3 channel - power level for CPD/BB decoupling
;sp11 : f1 channel - shaped pulse 180 degree (CO)
;spnam11 : Reburp.1000 (CO)
;sp12 : f1 channel - shaped pulse 180 degree (Ca)
;spnam12 : Reburp.1000 (Ca)
;sp13 : f1 channel - shaped pulse 90 degree (CO)
;spnam13 : Eburp2.1000 (CO)
;p1 : f1 channel - 90 degree high power pulse
;p11 : f1 channel - 180 degree shaped pulse (CO)
;p12 : f1 channel - 180 degree shaped pulse (Ca)
;p13 : f1 channel - 90 degree shaped pulse (CO)
;p2 : f2 channel - 90 degree high power pulse
;p3 : f3 channel - 90 degree high power pulse
;p51 : homospoil pulse
;p52 : gradient pulse
;p53 : gradient pulse
;p54 : homospoil pulse
;p55 : homospoil pulse
;p56 : gradient pulse
;p57 : homospoil pulse
;d1 : relaxation delay
;d10 : incremented delay 1
;d20 : incremented delay 2
;d30 : incremented delay 3
;taua : 1/(4JHN)
;taub : 1/(4JCN)
;tauc : 1/(4JCC)
;d11 : delay for disk I/O [30 ms]
;d12 : delay for power switching [2 us]
;d16 : delay for homospoil/gradient recovery [200 us]
;cnst2 : J(HN) [92 Hz]
;cnst3 : J(CN) [20 Hz]
;cnst4 : J(CC) [53 Hz]
;cnst9 : minimum number of experiments (TD1)
;cnst11 : Ca chemical shift offset [55 ppm]
;inf1 : 1/SW = 2 * DW
;in10 : semi-constant time increment 1
;in20 : semi-constant time increment 2
;in30 : semi-constant time increment 3
;NS : 4 * n
;DS : 16
;td1 : number of experiments (15Ne chemical shift)
;FnMODE : States-TPPI
;cpd2 : decoupling according to sequence defined by cpdprg2 (WALTZ64)
;pcpd2 : f2 channel - 90 degree pulse for decoupling [70 us]
;cpd3 : decoupling according to sequence defined by cpdprg3 (GARP4)
;pcpd3 : f3 channel - 90 degree pulse for decoupling [220 us]

;for z-only gradients:
;gpz1 : 47% (spoil)
;gpz2 : 11%
;gpz3 : 17%
;gpz4 : 41% (spoil)
;gpz5 : 31% (spoil)
;gpz6 : 23%
;gpz7 : 13% (spoil)

```

## 7. Experimental

```
;use gradient files:
;gpnam1 : SMSQ10.100
;gpnam2 : SMSQ10.100
;gpnam3 : SMSQ10.100
;gpnam4 : SMSQ10.100
;gpnam5 : SMSQ10.100
;gpnam6 : SMSQ10.100
;gpnam7 : SMSQ10.100
```

### 7.5.14 CARBEX Experiment

This pulse sequence allows the recording of the pseudo-five-dimensional CARBEX experiment on uniformly- $^{13}\text{C}$ , $^{15}\text{N}$ -labelled samples prepared in mixed  $^1\text{H}_2\text{O}$ : $^2\text{H}_2\text{O}$  buffers. It is a  $^1\text{H}$ -excited,  $^{13}\text{C}$ -detected quadruple-resonance experiment requiring the routing of  $^{13}\text{C}$ ,  $^1\text{H}$ ,  $^{15}\text{N}$  and  $^2\text{H}$  to Channels 1, 2, 3 and 4, respectively. The delays to be executed for the incremented mixing time,  $\tau_{\text{mix}}$ , are read from a **vdlist**. The carriers are set to approximately 173 ppm ( $^{13}\text{C}$ ), 118 ppm ( $^{15}\text{N}$ ) and 7 ppm ( $^1\text{H}/^2\text{H}$ ). The  $^1J_{\text{HN}}$  coupling constant (92 Hz),  $^1J_{\text{CN}}$  coupling constant (20 Hz),  $^1J_{\text{CC}}$  coupling constant (53 Hz) and  $^{13}\text{C}^\alpha$  (55 ppm) chemical shift must be provided using **cnst2**, **cnst3**, **cnst4** and **cnst11**. Three selective RF pulses ( $^{13}\text{C}$  refocussing,  $^{13}\text{C}^\alpha$  refocussing,  $^{13}\text{C}$  excitation) are used with the shapes **Reburp** (1.25 ms), **Reburp** (0.75 ms) and **Eburp-2** (1.5 ms) appropriate for a 14.1 T spectrometer.  $^1\text{H}$ ,  $^2\text{H}$  and  $^{15}\text{N}$  CPD decoupling uses the **WALTZ64**, **WALTZ16** and **GARP4** schemes at power levels corresponding to 70, 250 and 220  $\mu\text{s}$   $90^\circ$  pulses, respectively.

```
;Filename: carbex_ipap.hm
;pseudo-5D CARBEX experiment with IPAP decoupling
;H -> N -> Nz(tmix) -> sign-coding(phi3) -> N(t1) -> IPAP -> C'(t2)

;$CLASS=HighRes
;$DIM=5D
;$TYPE=
;$SUBTYPE=
;$COMMENT=

#include <Avance.incl>
#include <Delay.incl>
#include <Grad.incl>

;DEFINE PULSES

define pulse pwc_selr_CO
    "pwc_selr_CO=p11" ;13CO selective r-pulse at p11
define pulse pwc_selr_Ca
    "pwc_selr_Ca=p12" ;13Ca selective r-pulse at p12
define pulse pwc_sele_CO
    "pwc_sele_CO=p13" ;13CO selective e-pulse at p13

define pulse pwh
    "pwh=p2" ;1H hard pulse at p12

define pulse pwn
    "pwn=p3" ;15N hard pulse at p13

define pulse pwd
    "pwd=p4" ;2H hard pulse at plw49

;DEFINE DELAYS

define delay taua
    "taua=1s/(cnst2*4)" ;1/4JHN
define delay taub
    "taub=1s/(cnst3*4)" ;1/4JCN
define delay tauc
    "tauc=1s/(cnst4*4)" ;1/4JCC
```

```

"d11= 30m" ;Delay for disk
"d12= 2u" ;Delay for power switching
"d16= 200u" ;Delay for gradient recovery

;SEMI-CONSTANT TIME PARAMETERS

"cnst9=4*taub/inf1"
"cnst10=2/td1"

"d10=0"
"d20=0"
"d30=0"

"in10=inf1/2"
"in20=(inf1/2)-cnst10*taub"
"in30=cnst10*taub"

;DEFINE OFFSETS

"spoffs1=0" ;CO
"spoffs2=(cnst11*bf1)/1000000-o1" ;Calpha
"spoffs3=0" ;CO

;DEFINE ZERO POWER ON ALL CHANNELS USING SHAPED PULSES

"plw10=0"

define list<delay> vd_list=< $VDLIST > ;List for mixing time(s)
"l11=0"
"d2=d2"

"l12=0" ;ipap flag

;PULSE PROGRAM BEGINS

1 ze

d11 LOCKDEC_ON ;lock decoupling on
50u LOCKH_ON ;lock hold on
d11 H2_PULSE ;switch 2H to pulse

2 d11 do:f2 do:f3 do:f4 ;decoupling off

;purge 1H magnetisation before d1

50u UNBLKGRAMP ;gradient amp on
d12 pl10:f1 pl2:f2 pl3:f3 pl49:f4 ;set initial power levels
(pwh ph10):f2 ;90x
2u
p51:gp1 ;cleaning gradient
d16
50u BLKGRAMP ;gradient amp off

;end 1H purge, start d1

d11 H2_LOCK ;switch 2H to lock
d1*0.34 ;recycle delay
6m LOCKH_OFF ;lock hold off
d1*0.66 ;recycle delay
50u LOCKH_ON ;lock hold on
d12 H2_PULSE ;switch 2H to pulse

;start purge equilibrium 15N magnetisation

50u UNBLKGRAMP ;gradient amp on
d12 ;
(pwn ph10):f3 ;90x
2u
p51:gp1 ;cleaning gradient
d16

;end purge block, start HN INEPT (Non-selective)

(pwh ph10):f2
"DELTA = taua-0.6366*pwh-2u-p52-d16-0.5*larger(pwh*2,pwn*2) "
DELTA
2u
p52:gp2
d16
( center (pwh*2 ph10):f2 (pwn*2 ph10):f3 )

```

## 7. Experimental

```
2u
p52:gp2
d16
"DELTA = taua-0.5*larger(pwh*2,pwn*2)-2u-p52-d16-0.6366*pwh"
DELTA
(pwh ph11):f2
2u
p57:gp7
d16
(pwn ph10):f3

;refocus 2HzNy to Nx

"DELTA = taua-0.6366*pwn-2u-p53-d16-0.5*larger(pwh*2,pwn*2) "
DELTA
2u
p53:gp3
d16
( center (pwh*2 ph10):f2 (pwn*2 ph10):f3 )
2u
p53:gp3
d16
"DELTA = taua-0.5*larger(pwh*2,pwn*2)-2u-p53-d16-0.6366*pwn"
DELTA
(pwn ph1):f3 ;Nx to Nz
2u
p54:gp4 ;cleaning gradient
d16

;end INEPT, start relaxation delay for H/D exchange

"d2=vd_list[l11]"

if "d2<250m"
{
"DELTA=d2-2u-p54-d16-pwd-d12"
DELTA ;mixing time
}
else
{
"DELTA=d2-2u-p54-d16-50u-d11-50m-6m-50u-d12-50u-pwd-d12"
50u BLKGRAMP ;gradient amp off
d11 H2_LOCK ;switch 2H to lock
50m
6m LOCKH_OFF ;lock hold off
DELTA ;relaxation delay
50u LOCKH_ON ;lock hold on
d12 H2_PULSE ;switch 2H to pulse
50u UNBLKGRAMP ;gradient amp on
}

(pwd ph11):f4 ;2H flanking pulse (90y)
d12 cpd4:f4 ph10 ;2H decoupling on

(pwn ph2):f3 ;start sign-coding filter
"DELTA=2*taua-0.6366*pwn-larger(pwh,pwn) "
DELTA
(center (pwh ph10 pwh ph3):f2 (pwn*2 ph10):f3)
"DELTA=2*taua-larger(pwh,pwn)-d12"
DELTA
d12 p129:f2
"DELTA=0.6366*pwn"
DELTA cpd2:f2 ph10 ;end sign-coding, 1H dec on

;Ny to 2CzNx during semi-CT t1 period
d10
2u
(pwc_selr_Ca:sp12 ph10):f1
2u
taub
2u
(pwc_selr_CO:sp11 ph10):f1
2u
d20
(pwn*2 ph10):f3
"DELTA=taub-d30"
DELTA
2u
(pwc_selr_CO:sp11 ph10):f1
2u
```

```

2u
(pwc_selr_Ca:sp12 ph10):f1
2u

(pwn ph10):f3 ;end t1

d12 do:f2 d12 do:f4 ;1H, 2H decoupling off
(pwd ph13):f4 ;2H flanking pulse (90-y)
2u
p55:gp5 ;cleaning gradient
d16 ;start CO-N INEPT block (IPAP Ca)

if "112 %2 ==0" ;In-Phase spectrum
{
(pwc_sele_CO:sp13 ph10):f1 ;2CzNz to 2CyNz, CO pulse
"DELTA=taub*0.5-pwc_selr_Ca*0.5"
DELTA
(pwc_selr_Ca:sp12 ph10):f1 ;13Ca pulse
"DELTA=taub*0.5-pwc_selr_Ca*0.5-2u-p56-d16-larger(pwc_selr_CO,pwn*2)*0.5"
DELTA
2u
p56:gp6
d16
( center (pwc_selr_CO:sp11 ph10):f1 (pwn*2 ph10):f3 )
2u
p56:gp6
d16
"DELTA=taub*0.5-larger(pwc_selr_CO,pwn*2)*0.5-2u-p56-d16-pwc_selr_Ca*0.5"
DELTA
(pwc_selr_Ca:sp12 ph10):f1 ;13Ca pulse
"DELTA=taub*0.5-pwc_selr_Ca*0.5-0.1u-d12-50u"
DELTA
}
else ;Anti-Phase spectrum
{
(pwc_sele_CO:sp13 ph11):f1 ;2CzNz to 2CyNz, CO pulse
"DELTA=tauc"
DELTA
(pwc_selr_Ca:sp12 ph10):f1
"DELTA=taub-tauc-pwc_selr_Ca-2u-p56-d16-larger(pwc_selr_CO,pwn*2)*0.5"
DELTA
2u
p56:gp6
d16
( center (pwc_selr_CO:sp11 ph10):f1 (pwn*2 ph10):f3 )
2u
p56:gp6
d16
"DELTA=taub-larger(pwc_selr_CO,pwn*2)*0.5-2u-p56-d16-pwc_selr_Ca-0.1u-d12-50u"
DELTA
(pwc_selr_Ca:sp12 ph10):f1
}

0.1u ;end CO-N INEPT block

d12 p139:f3 ;power to decouple(15N)
50u BLKGRAMP ;gradient amp off

;acquire Cx magnetisation with 15N, 1H decoupling

go=2 ph31 cpd2:f2 cpd3:f3
d11 do:f2 do:f3 mc #0 to 2
F4QF(calclc(l12,1)) ;IPAP decoupling
F3QF(calph(ph3,+180)) ;sign-coding
F2QF(calclc(l11,1)) ;t_mix
F1PH(calph(ph2,+90),\
caldel(d10,+in10) &\
caldel(d20,+in20) &\
caldel(d30,+in30)) ;15N chemical shift

d11 H2_LOCK ;switch H2 to lock
d11 LOCKH_OFF ;lock hold off
d11 LOCKDEC_OFF ;lock decoupling off

exit

```

## 7. Experimental

; PHASE PROGRAMS

ph1= 1 3  
ph2= 1 1 3 3  
ph3= 0  
ph31= 2 0 0 2

ph10= 0  
ph11= 1  
ph12= 2  
ph13= 3

; DEFINITIONS

;p11 : f1 channel - power level for hard pulse  
;p12 : f2 channel - power level for hard pulse  
;p13 : f3 channel - power level for hard pulse  
;p129 : f2 channel - power level for CPD/BB decoupling  
;p139 : f3 channel - power level for CPD/BB decoupling  
;p149 : f4 channel - power level for CPD/BB decoupling  
;sp11 : f1 channel - shaped pulse 180 degree (CO)  
;spnam11 : Reburp.1000 (CO)  
;sp12 : f1 channel - shaped pulse 180 degree (Ca)  
;spnam12 : Reburp.1000 (Ca)  
;sp13 : f1 channel - shaped pulse 90 degree (CO)  
;spnam13 : Eburp2.1000 (CO)  
;p1 : f1 channel - 90 degree high power pulse  
;p11 : f1 channel - 180 degree shaped pulse (CO)  
;p12 : f1 channel - 180 degree shaped pulse (Ca)  
;p13 : f1 channel - 90 degree shaped pulse (CO)  
;p2 : f2 channel - 90 degree high power pulse  
;p3 : f3 channel - 90 degree high power pulse  
;p4 : f4 channel - 90 degree high power pulse  
;p51 : homospoil pulse  
;p52 : gradient pulse  
;p53 : gradient pulse  
;p54 : homospoil pulse  
;p55 : homospoil pulse  
;p56 : gradient pulse  
;p57 : homospoil pulse  
;d1 : relaxation delay  
;d2 : initial delay for HDX reaction  
;d10 : incremented delay 1  
;d20 : incremented delay 2  
;d30 : incremented delay 3  
;l11 : counter for VD list  
;taua : 1/(4JHN)  
;taub : 1/(4JCN)  
;tauc : 1/(4JCC)  
;d11 : delay for disk I/O [30 ms]  
;d12 : delay for power switching [2 us]  
;d16 : delay for homospoil/gradient recovery [200 us]  
;cnst2 : J(HN) [92 Hz]  
;cnst3 : J(CN) [20 Hz]  
;cnst4 : J(CC) [53 Hz]  
;cnst9 : minimum number of experiments (TD1)  
;cnst11 : Ca chemical shift offset [55 ppm]  
;infl : 1/SW = 2 \* DW  
;in10 : semi-constant time increment 1  
;in20 : semi-constant time increment 2  
;in30 : semi-constant time increment 3  
;NS : 4 \* n  
;DS : 16  
;td1 : number of experiments (15Ne chemical shift)  
;td2 : number of experiments (mixing times) [8-12]  
;td3 : number of experiments (sign-coding filter) [2]  
;td4 : number of experiments (IPAP) [2]  
;FnMODE : States-TPPI  
;cpd2 : decoupling according to sequence defined by cpdprg2 (WALTZ64)  
;pcpd2 : f2 channel - 90 degree pulse for decoupling [70 us]  
;cpd3 : decoupling according to sequence defined by cpdprg3 (GARP4)  
;pcpd3 : f3 channel - 90 degree pulse for decoupling [220 us]  
;cpd4 : decoupling according to sequence defined by cpdprg4 (WALTZ16)  
;pcpd4 : f4 channel - 90 degree pulse for decoupling [250 us]  
;for z-only gradients:  
;gpz1 : 47% (spoil)  
;gpz2 : 11%  
;gpz3 : 17%  
;gpz4 : 41% (spoil)

```

;gpz5      : 31% (spoil)
;gpz6      : 23%
;gpz7      : 13% (spoil)

;use gradient files:
;gpnam1    : SMSQ10.100
;gpnam2    : SMSQ10.100
;gpnam3    : SMSQ10.100
;gpnam4    : SMSQ10.100
;gpnam5    : SMSQ10.100
;gpnam6    : SMSQ10.100
;gpnam7    : SMSQ10.100

```

### 7.5.15 $^{13}\text{C}'(^1\text{H}/^2\text{H}) T_1$ Measurement

This pulse sequence allows the measurement of the longitudinal relaxation times of  $^{13}\text{C}'$  in uniformly- $[^{13}\text{C},^{15}\text{N}]$ -labelled samples prepared in mixed  $^1\text{H}_2\text{O}:$  $^2\text{H}_2\text{O}$  buffers and is used as a *setup experiment* for a subsequent CARBEX acquisition. The delays to be executed for the incremented mixing time,  $\tau_{\text{relax}}$ , are read from a **vdlist**. It is a  $^{13}\text{C}$ -excited,  $^{13}\text{C}$ -detected quadruple-resonance experiment requiring the routing of  $^{13}\text{C}$ ,  $^1\text{H}$ ,  $^{15}\text{N}$  and  $^2\text{H}$  to Channels 1, 2, 3 and 4, respectively. The carriers are set to approximately 173 ppm ( $^{13}\text{C}$ ), 118 ppm ( $^{15}\text{N}$ ) and 7 ppm ( $^1\text{H}/^2\text{H}$ ). The  $^1J_{\text{HN}}$  coupling constant (92 Hz),  $^1J_{\text{CN}}$  coupling constant (20 Hz),  $^1J_{\text{CC}}$  coupling constant (53 Hz) and  $^{13}\text{C}^\alpha$  (55 ppm) chemical shift must be provided using **cnst2**, **cnst3**, **cnst4** and **cnst11**. Three selective RF pulses ( $^{13}\text{C}'$  refocussing,  $^{13}\text{C}^\alpha$  refocussing,  $^{13}\text{C}'$  excitation) are used with the shapes **Reburp** (1.25 ms), **Reburp** (0.75 ms) and **Eburp-2** (1.5 ms) appropriate for a 14.1 T spectrometer. An adiabatic  $^{13}\text{C}$  pulse is also used during the sequence (**Crp80,0.5,20.1**, 0.5 ms).  $^1\text{H}$ ,  $^2\text{H}$  and  $^{15}\text{N}$  CPD decoupling uses the **WALTZ64**, **WALTZ16** and **GARP4** schemes at power levels corresponding to 70, 250 and 220  $\mu\text{s}$   $90^\circ$  pulses, respectively.

```

;Filename: carbex_t1_ipap.hm
;pseudo-5D  $^{13}\text{C}'$  T1 measurement with IPAP decoupling
;C -> T1(trelax) -> N -> sign-coding(phi3) -> N(t1) -> IPAP -> C'(t2)

;$CLASS=HighRes
;$DIM=5D
;$TYPE=
;$SUBTYPE=
;$COMMENT=

#include <Avance.incl>
#include <Delay.incl>
#include <Grad.incl>

;DEFINE PULSES

define pulse pwc
    "pwc=p1" ;13C hard pulse at p11
define pulse pwc_selr_CO
    "pwc_selr_CO=p11" ;13CO selective r-pulse at p111
define pulse pwc_selr_Ca
    "pwc_selr_Ca=p12" ;13Ca selective r-pulse at p112
define pulse pwc_sele_CO
    "pwc_sele_CO=p13" ;13CO selective e-pulse at p113
define pulse pwc_chirp
    "pwc_chirp=p14" ;13C chirp pulse

define pulse pwh
    "pwh=p2" ;1H hard pulse at p12

define pulse pwn
    "pwn=p3" ;15N hard pulse at p13

```

## 7. Experimental

```
define pulse pwd
    "pwd=p4"
;2H hard pulse at plw49

;DEFINE DELAYS

define delay taua
    "taua=1s/(cnst2*4)"
;1/4JHN
define delay taub
    "taub=1s/(cnst3*4)"
;1/4JCN
define delay tauc
    "tauc=1s/(cnst4*4)"
;1/4JCC

"d11= 30m"
;Delay for disk
"d12= 2u"
;Delay for power switching
"d16= 200u"
;Delay for gradient recovery

define list<delay> vd_list=<{$VDLIST}>
;List for relaxation delay(s)
"l11=0"
"d2=vd_list[l11]"

;SEMI-CONSTANT TIME PARAMETERS

"cnst9=4*(taub/inf1)"
"cnst10=2/td1"

"d10=0"
"d20=0"
"d30=0"

"in10=inf1/2"
"in20=(inf1/2)-cnst10*taub"
"in30=cnst10*taub"

;DEFINE OFFSETS

"spoffs11=0"
;CO
"spoffs12=(cnst11*bf1)/1000000-o1"
;Calpha
"spoffs13=0"
;CO
"spoffs14=(cnst12*bf1)/1000000-o1"
;decoupling position

;DEFINE ZERO POWER ON ALL CHANNELS USING SHAPED PULSES

"plw10=0"

"l12=0"
;ipap flag

;PULSE PROGRAM BEGINS

1 ze

    d11 LOCKDEC_ON
;lock decoupling on
    50u LOCKH_ON
;lock hold on
    d11 H2_PULSE
;switch 2H to pulse

2 d11 do:f2 do:f3 do:f4
;decoupling off
    d12 pl1:f1 pl2:f2 pl3:f3 pl49:f4
;set initial power levels

;purge 13C magnetisation before d1

    50u UNBLKGRAMP
;gradient amp on
    (pwc ph10):f1
;90x
    2u
    p58:gp8
;cleaning gradient
    d16
    50u BLKGRAMP
;gradient amp off

;end 13CH purge, start d1

    d11 H2_LOCK
;switch 2H to lock
    d1*0.34
;recycle delay
    6m LOCKH_OFF
;lock hold off
    d1*0.66
;recycle delay
    50u LOCKH_ON
;lock hold on
    d12 H2_PULSE
;switch 2H to pulse

;start purge equilibrium 15N magnetisation

    50u UNBLKGRAMP
;gradient amp on
    d12
```

```

(pwn ph10):f3 ;90x
2u
p51:gp1 ;cleaning gradient
d16

;end purge block, start relaxation measurement

(pwc ph10):f1
(pwc ph1):f1

"d2=vd_list[l11]"
d2 ;relaxation delay

;end relaxation block, start CN INEPT

(pwc ph10):f1
"DELTA = taub-0.6366*pwc-2u-p52-d16-0.5*larger(pwc_selr_CO,pwn*2)"
DELTA
2u
p52:gp2
d16 p110:f1
( center (pwc_selr_CO:sp11 ph10):f1 (pwn*2 ph10):f3 )
2u
p52:gp2
d16 p11:f1
"DELTA = taub-0.5*larger(pwc_selr_CO,pwn*2)-2u-p52-d16-0.6366*pwc"
DELTA
(pwc ph11):f1 ;2COzNz

2u
p57:gp7 ;cleaning gradient
d16

(pwd ph11):f4 ;2H flanking pulse (90y)
d12 cpd4:f4 ph10 ;2H decoupling on

(pwn ph2):f3 ;start sign-coding filter
"DELTA=2*taua-0.6366*pwn-larger(pwh,pwn)"
DELTA
(center (pwh ph10 pwh ph3):f2 (pwn*2 ph10):f3)
"DELTA=2*taua-larger(pwh,pwn)-d12"
DELTA
d12 p110:f1 p129:f2
"DELTA=0.6366*pwn"
DELTA cpd2:f2 ph10 ;end sign-coding, 1H dec on

;start semi-constant time t1 period

d10
4u
(pwc_chirp:sp14 ph10):f1
4u
taub
d0 * 0.5
d20
(pwn*2 ph10):f3
"DELTA=taub-d30+(d0*0.5)"
DELTA
4u
(pwc_chirp:sp14 ph10):f1
4u

(pwn ph10):f3 ;end t1

d12 do:f2 d12 do:f4 ;1H, 2H decoupling off
(pwd ph13):f4 ;2H flanking pulse (90-y)
2u
p55:gp5 ;cleaning gradient
d16 ;start CO-N INEPT block (IPAP Ca)

if "l12 %2 ==0" ;In-Phase spectrum
{
(pwc_sele_CO:sp13 ph10):f1 ;2CzNz to 2CyNz, CO pulse
"DELTA=taub*0.5-pwc_selr_Ca*0.5"
DELTA
(pwc_selr_Ca:sp12 ph10):f1 ;13Ca pulse
"DELTA=taub*0.5-pwc_selr_Ca*0.5-2u-p56-d16-larger(pwc_selr_CO,pwn*2)*0.5"
DELTA
2u

```

## 7. Experimental

```
p56:gp6
d16
( center (pwc_selr_CO:sp11 ph10):f1 (pwn*2 ph10):f3 )
2u
p56:gp6
d16
"DELTA=taub*0.5-larger(pwc_selr_CO,pwn*2)*0.5-2u-p56-d16-pwc_selr_Ca*0.5"
DELTA
(pwc_selr_Ca:sp12 ph10):f1 ;13Ca pulse
"DELTA=taub*0.5-pwc_selr_Ca*0.5-0.1u-d12-50u"
DELTA
}
else ;Anti-Phase spectrum
{
(pwc_selr_CO:sp13 ph11):f1 ;2CzNz to 2CyNz, CO pulse
"DELTA=tauc"
DELTA
(pwc_selr_Ca:sp12 ph10):f1
"DELTA=taub-tauc-pwc_selr_Ca-2u-p56-d16-larger(pwc_selr_CO,pwn*2)*0.5"
DELTA
2u
p56:gp6
d16
( center (pwc_selr_CO:sp11 ph10):f1 (pwn*2 ph10):f3 )
2u
p56:gp6
d16
"DELTA=taub-larger(pwc_selr_CO,pwn*2)*0.5-2u-p56-d16-pwc_selr_Ca-0.1u-d12-50u"
DELTA
(pwc_selr_Ca:sp12 ph10):f1
}
0.1u ;end CO-N INEPT block

d12 pl39:f3 ;power to decouple(15N)
50u BLKGRAMP ;gradient amp off

;acquire Cx magnetisation with 15N, 1H decoupling

go=2 ph31 cpd2:f2 cpd3:f3
d11 do:f2 do:f3 mc #0 to 2
F4QF(calclc(l12,1)) ;IPAP decoupling
F3QF(calph(ph3,+180)) ;sign-coding
F2QF(calclc(l11,1)) ;t_relax
F1PH(calph(ph2,+90),\
caldel(d10,+in10) &\
caldel(d20,+in20) &\
caldel(d30,+in30) ) ;15N chemical shift

d11 H2_LOCK ;switch H2 to lock
d11 LOCKH_OFF ;lock hold off
d11 LOCKDEC_OFF ;lock decoupling off

exit

;PHASE PROGRAMS

ph1= 0 2
ph2= 0 0 2 2
ph3= 0
ph31= 0 2 2 0

ph10= 0
ph11= 1
ph12= 2
ph13= 3

;DEFINITIONS

;p11 : f1 channel - power level for hard pulse
;p12 : f2 channel - power level for hard pulse
;p13 : f3 channel - power level for hard pulse
;p129 : f2 channel - power level for CPD/BB decoupling
;p139 : f3 channel - power level for CPD/BB decoupling
;sp11 : f1 channel - shaped pulse 180 degree (CO)
;spnam11 : Reburp.1000 (CO)
;sp12 : f1 channel - shaped pulse 180 degree (Ca)
;spnam12 : Reburp.1000 (Ca)
;sp13 : f1 channel - shaped pulse 90 degree (CO)
;spnam13 : Eburp2.1000 (CO)
```

```

;p1      : f1 channel - 90 degree high power pulse
;p11     : f1 channel - 180 degree shaped pulse (CO)
;p12     : f1 channel - 180 degree shaped pulse (Ca)
;p13     : f1 channel - 90 degree shaped pulse (CO)
;p2      : f2 channel - 90 degree high power pulse
;p3      : f3 channel - 90 degree high power pulse
;p51     : homospoil pulse
;p52     : gradient pulse
;p53     : gradient pulse
;p54     : homospoil pulse
;p55     : homospoil pulse
;p56     : gradient pulse
;p57     : homospoil pulse
;d0      : 'extra' time due to longer 13C pulses in CARBEX experiment
;d1      : relaxation delay
;taua    : 1/(4JHN)
;taub    : 1/(4JCN)
;tauc    : 1/(4JCC)
;d11     : delay for disk I/O [30 ms]
;d12     : delay for power switching [2 us]
;d16     : delay for homospoil/gradient recovery [200 us]
;cnst2   : J(HN) [92 Hz]
;cnst3   : J(CN) [20 Hz]
;cnst4   : J(CC) [53 Hz]
;cnst9   : minimum number of experiments (TD1)
;cnst11  : Cdelta chemical shift offset [55 ppm]
;cnst12  : 13C decoupling position [119 ppm]
;inf2    : 1/SW = 2 * DW
;NS      : 4 * n
;DS      : 16
;td1     : number of experiments
;FnMODE  : States-TPPI
;cpd2    : decoupling according to sequence defined by cpdprg2 (WALTZ64)
;pcpd2   : f2 channel - 90 degree pulse for decoupling [70 us]
;cpd3    : decoupling according to sequence defined by cpdprg3 (GARP4)
;pcpd3   : f3 channel - 90 degree pulse for decoupling [220 us]
;cpd4    : decoupling according to sequence defined by cpdprg3 (WALTZ16)
;pcpd4   : f4 channel - 90 degree pulse for decoupling [250 us]

;for z-only gradients:
;gpz1    : 47% (spoil)
;gpz2    : 11%
;gpz3    : 17%
;gpz4    : 41% (spoil)
;gpz5    : 31% (spoil)
;gpz6    : 23%
;gpz7    : 13% (spoil)
;gpz8    : 27% (spoil)

;use gradient files:
;gpnam1  : SMSQ10.100
;gpnam2  : SMSQ10.100
;gpnam3  : SMSQ10.100
;gpnam4  : SMSQ10.100
;gpnam5  : SMSQ10.100
;gpnam6  : SMSQ10.100
;gpnam7  : SMSQ10.100
;gpnam8  : SMSQ10.100

```

### 7.5.16 Fractionation Factor Measurement

This pulse sequence allows the measurement of residue-specific fractionation factors in uniformly- $^{13}\text{C}$ ,  $^{15}\text{N}$ -labelled samples prepared in mixed  $^1\text{H}_2\text{O}$ : $^2\text{H}_2\text{O}$  buffers and is used as a *setup experiment* for a subsequent CARBEX acquisition. It is a  $^{13}\text{C}$ -excited,  $^{13}\text{C}$ -detected quadruple-resonance experiment requiring the routing of  $^{13}\text{C}$ ,  $^1\text{H}$ ,  $^{15}\text{N}$  and  $^2\text{H}$  to Channels 1, 2, 3 and 4, respectively. The carriers are set to approximately 173 ppm ( $^{13}\text{C}$ ), 118 ppm ( $^{15}\text{N}$ ) and 7 ppm ( $^1\text{H}/^2\text{H}$ ). The  $J_{\text{HN}}$  coupling constant (92 Hz),  $J_{\text{CN}}$  coupling constant (20 Hz),  $J_{\text{CC}}$  coupling constant (53 Hz) and  $^{13}\text{C}^\alpha$  (55 ppm) chemical shift must be provided using **cnst2**, **cnst3**, **cnst4** and **cnst11**.

## 7. Experimental

Three selective RF pulses ( $^{13}\text{C}'$  refocussing,  $^{13}\text{C}^\alpha$  refocussing,  $^{13}\text{C}'$  excitation) are used with the shapes **Reburp** (1.25 ms), **Reburp** (0.75 ms) and **Eburp-2** (1.5 ms) appropriate for a 14.1 T spectrometer. An adiabatic  $^{13}\text{C}$  pulse is also used during the sequence (**Crp80,0.5,20.1**, 0.5 ms).  $^1\text{H}$ ,  $^2\text{H}$  and  $^{15}\text{N}$  CPD decoupling uses the **WALTZ64**, **WALTZ16** and **GARP4** schemes at power levels corresponding to 70, 250 and 220  $\mu\text{s}$   $90^\circ$  pulses, respectively.

```
;Filename: carbex_ff_ipap.hm
;pseudo-4D fractionation factor experiment with IPAP decoupling
;C -> N -> sign-coding(phi3) -> N(t1) -> IPAP -> C'(t2)

;$CLASS=HighRes
;$DIM=4D
;$TYPE=
;$SUBTYPE=
;$COMMENT=

#include <Avance.incl>
#include <Delay.incl>
#include <Grad.incl>

;DEFINE PULSES

define pulse pwc
    "pwc=p1" ;13C hard pulse at p11
define pulse pwc_selr_CO
    "pwc_selr_CO=p11" ;13CO selective r-pulse at p111
define pulse pwc_selr_Ca
    "pwc_selr_Ca=p12" ;13Ca selective r-pulse at p112
define pulse pwc_sele_CO
    "pwc_sele_CO=p13" ;13CO selective e-pulse at p113
define pulse pwc_chirp
    "pwc_chirp=p14" ;13C chirp pulse

define pulse pwh
    "pwh=p2" ;1H hard pulse at p12

define pulse pwn
    "pwn=p3" ;15N hard pulse at p13

define pulse pwd
    "pwd=p4" ;2H hard pulse at plw49

;DEFINE DELAYS

define delay taua
    "taua=1s/(cnst2*4)" ;1/4JHN
define delay taub
    "taub=1s/(cnst3*4)" ;1/4JCN
define delay tauc
    "tauc=1s/(cnst4*4)" ;1/4JCC

"d11= 30m" ;Delay for disk
"d12= 2u" ;Delay for power switching
"d16= 200u" ;Delay for gradient recovery

;SEMI-CONSTANT TIME PARAMETERS

"cnst9=4*(taub/inf1)"
"cnst10=2/td1"

"d10=0"
"d20=0"
"d30=0"

"in10=inf1/2"
"in20=(inf1/2)-cnst10*taub"
"in30=cnst10*taub"

;DEFINE OFFSETS

"spoffs11=0" ;CO
"spoffs12=(cnst11*bf1)/1000000-o1" ;Calpha
"spoffs13=0" ;CO
"spoffs14=(cnst12*bf1)/1000000-o1" ;decoupling position
```

```

;DEFINE ZERO POWER ON ALL CHANNELS USING SHAPED PULSES

"plw10=0"

"l12=0" ;ipap flag

;PULSE PROGRAM BEGINS

1 ze

d11 LOCKDEC_ON ;lock decoupling on
50u LOCKH_ON ;lock hold on
d11 H2_PULSE ;switch 2H to pulse

2 d11 do:f2 do:f3 do:f4 ;decoupling off
d12 pl1:f1 pl2:f2 pl3:f3 pl49:f4 ;set initial power levels

d11 H2_LOCK ;switch 2H to lock
d1*0.34 ;recycle delay
6m LOCKH_OFF ;lock hold off
d1*0.66 ;recycle delay
50u LOCKH_ON ;lock hold on
d12 H2_PULSE ;switch 2H to pulse

;start purge equilibrium 15N magnetisation

50u UNBLKGRAMP ;gradient amp on
d12
(pwn ph10):f3 ;90x
2u
p51:gp1 ;cleaning gradient
d16

;end purge block, start CN INEPT

(pwc ph1):f1
"DELTA = taub-0.6366*pwc-2u-p52-d16-0.5*larger(pwc_selr_CO,pwn*2)"
DELTA
2u
p52:gp2
d16 pl10:f1
( center (pwc_selr_CO:sp11 ph10):f1 (pwn*2 ph10):f3 )
2u
p52:gp2
d16 pl1:f1
"DELTA = taub-0.5*larger(pwc_selr_CO,pwn*2)-2u-p52-d16-0.6366*pwc"
DELTA
(pwc ph11):f1 ;2COzNz

2u
p57:gp7 ;cleaning gradient
d16

(pwd ph11):f4 ;2H flanking pulse (90y)
d12 cpd4:f4 ph10 ;2H decoupling on

(pwn ph2):f3 ;start sign-coding filter
"DELTA=2*taua-0.6366*pwn-larger(pwh,pwn)"
DELTA
(center (pwh ph10 pwh ph3):f2 (pwn*2 ph10):f3)
"DELTA=2*taua-larger(pwh,pwn)-d12"
DELTA
d12 pl10:f1 pl29:f2
"DELTA=0.6366*pwn"
DELTA cpd2:f2 ph10 ;end sign-coding, 1H dec on

;start semi-constant time t1 period

d10
4u
(pwc_chirp:sp14 ph10):f1
4u
taub
d0 * 0.5
d20
(pwn*2 ph10):f3
"DELTA=taub-d30+(d0*0.5)"
DELTA
4u

```

## 7. Experimental

```
(pwc_chirp:sp14 ph10):f1
4u

(pwn ph10):f3 ;end t1

d12 do:f2 d12 do:f4 ;1H, 2H decoupling off
(pwd ph13):f4 ;2H flanking pulse (90-y)
2u
p55:gp5 ;cleaning gradient
d16 ;start CO-N INEPT block (IPAP Ca)

if "l12 %2 ==0" ;In-Phase spectrum
{
(pwc_sele_CO:sp13 ph10):f1 ;2CzNz to 2CyNz, CO pulse
"DELTA=taub*0.5-pwc_selr_Ca*0.5"
DELTA
(pwc_selr_Ca:sp12 ph10):f1 ;13Ca pulse
"DELTA=taub*0.5-pwc_selr_Ca*0.5-2u-p56-d16-larger(pwc_selr_CO,pwn*2)*0.5"
DELTA
2u
p56:gp6
d16
( center (pwc_selr_CO:sp11 ph10):f1 (pwn*2 ph10):f3 )
2u
p56:gp6
d16
"DELTA=taub*0.5-larger(pwc_selr_CO,pwn*2)*0.5-2u-p56-d16-pwc_selr_Ca*0.5"
DELTA
(pwc_selr_Ca:sp12 ph10):f1 ;13Ca pulse
"DELTA=taub*0.5-pwc_selr_Ca*0.5-0.1u-d12-50u"
DELTA
}
else ;Anti-Phase spectrum
{
(pwc_sele_CO:sp13 ph11):f1 ;2CzNz to 2CyNz, CO pulse
"DELTA=tauc"
DELTA
(pwc_selr_Ca:sp12 ph10):f1
"DELTA=taub-tauc-pwc_selr_Ca-2u-p56-d16-larger(pwc_selr_CO,pwn*2)*0.5"
DELTA
2u
p56:gp6
d16
( center (pwc_selr_CO:sp11 ph10):f1 (pwn*2 ph10):f3 )
2u
p56:gp6
d16
"DELTA=taub-larger(pwc_selr_CO,pwn*2)*0.5-2u-p56-d16-pwc_selr_Ca-0.1u-d12-50u"
DELTA
(pwc_selr_Ca:sp12 ph10):f1
}
0.1u ;end CO-N INEPT block

d12 pl39:f3 ;power to decouple(15N)
50u BLKGRAMP ;gradient amp off

;acquire Cx magnetisation with 15N, 1H decoupling

go=2 ph31 cpd2:f2 cpd3:f3
d11 do:f2 do:f3 mc #0 to 2
F3QF(calclc(l12,1)) ;IPAP decoupling
F2QF(calph(ph3,+180)) ;sign-coding
F1PH(calph(ph2,+90),\
caldel(d10,+in10) &\
caldel(d20,+in20) &\
caldel(d30,+in30) ) ;15N chemical shift

d11 H2_LOCK ;switch H2 to lock
d11 LOCKH_OFF ;lock hold off
d11 LOCKDEC_OFF ;lock decoupling off

exit

;PHASE PROGRAMS

ph1= 0 2
ph2= 0 0 2 2
ph3= 0
```

```

ph31= 0 2 2 0

ph10= 0
ph11= 1
ph12= 2
ph13= 3

;DEFINITIONS

;p11      : f1 channel - power level for hard pulse
;p12      : f2 channel - power level for hard pulse
;p13      : f3 channel - power level for hard pulse
;p129     : f2 channel - power level for CPD/BB decoupling
;p139     : f3 channel - power level for CPD/BB decoupling
;sp11     : f1 channel - shaped pulse 180 degree (CO)
;spnam11  : Reburp.1000 (CO)
;sp12     : f1 channel - shaped pulse 180 degree (Ca)
;spnam12  : Reburp.1000 (Ca)
;sp13     : f1 channel - shaped pulse 90 degree (CO)
;spnam13  : Eburp2.1000 (CO)
;p1       : f1 channel - 90 degree high power pulse
;p11      : f1 channel - 180 degree shaped pulse (CO)
;p12      : f1 channel - 180 degree shaped pulse (Ca)
;p13      : f1 channel - 90 degree shaped pulse (CO)
;p2       : f2 channel - 90 degree high power pulse
;p3       : f3 channel - 90 degree high power pulse
;p51      : homospoil pulse
;p52      : gradient pulse
;p53      : gradient pulse
;p54      : homospoil pulse
;p55      : homospoil pulse
;p56      : gradient pulse
;p57      : homospoil pulse
;d0       : 'extra' time due to longer 13C pulses in CARBEX experiment
;d1       : relaxation delay
;taua     : 1/(4JHN)
;taub     : 1/(4JCN)
;tauc     : 1/(4JCC)
;d11      : delay for disk I/O [30 ms]
;d12      : delay for power switching [2 us]
;d16      : delay for homospoil/gradient recovery [200 us]
;cnst2    : J(HN) [92 Hz]
;cnst3    : J(CN) [20 Hz]
;cnst4    : J(CC) [53 Hz]
;cnst9    : minimum number of experiments (TD1)
;cnst11   : Cdelta chemical shift offset [55 ppm]
;cnst12   : 13C decoupling position [119 ppm]
;inf2     : 1/SW = 2 * DW
;NS       : 4 * n
;DS       : 16
;td1      : number of experiments
;FnMODE   : States-TPPI
;cpd2     : decoupling according to sequence defined by cpdprg2 (WALTZ64)
;pcpd2    : f2 channel - 90 degree pulse for decoupling [70 us]
;cpd3     : decoupling according to sequence defined by cpdprg3 (GARP4)
;pcpd3    : f3 channel - 90 degree pulse for decoupling [220 us]
;cpd4     : decoupling according to sequence defined by cpdprg3 (WALTZ16)
;pcpd4    : f4 channel - 90 degree pulse for decoupling [250 us]

;for z-only gradients:
;gpz1     : 47% (spoil)
;gpz2     : 11%
;gpz3     : 17%
;gpz4     : 41% (spoil)
;gpz5     : 31% (spoil)
;gpz6     : 23%
;gpz7     : 13% (spoil)

;use gradient files:
;gpnam1   : SMSQ10.100
;gpnam2   : SMSQ10.100
;gpnam3   : SMSQ10.100
;gpnam4   : SMSQ10.100
;gpnam5   : SMSQ10.100
;gpnam6   : SMSQ10.100
;gpnam7   : SMSQ10.100

```

## 7.6 Data Processing Scripts

### 7.6.1 Conversion Script (nmrPipe) for ASHDEX Experiment

The pseudo-4D ASHDEX experiment results in a stack of FIDs in the order of acquisition:

$^{13}\text{C}(\text{F4})$ , Sign-coding(F3),  $\tau_{\text{mix}}(\text{F2})$  and  $^{15}\text{N}(\text{F1})$

During the conversion of the Bruker data into a format suitable for processing using the nmrPipe software package, the FIDs are re-ordered such that the first two dimensions are chemical shift:

$^{13}\text{C}(\text{F4})$ ,  $^{15}\text{N}(\text{F3})$ ,  $\tau_{\text{mix}}(\text{F2})$  and Sign-coding(F1)

```
=====
#!/bin/csh

#Script to convert Bruker data to nmrPipe format
#For HDX data recorded in a psuedo-4D manner using sequence: arg_ashdex.hm
#Assumes order of FIDs in ser file to be C13(X), Sign_Coding(Y), t_mix(Z), N15(A)

bruk2pipe -in ./ser \
  -bad 0.0 -ext -aswap -AMX -decim 5000 -dspfv 20 -grpdlly 67.9851226806641 \
  -xN 1024 -yN 2 -zN 10 -aN 96 \
  -xT 256 -yT 2 -zT 10 -aT 48 \
  -xMODE DQD -yMODE Real -zMODE Real -aMODE States-TPPI \
  -xSW 4000.000 -ySW 1 -zSW 1 -aSW 800.000 \
  -xOBS 201.223 -yOBS 10 -zOBS 10 -aOBS 81.089 \
  -xCAR 156.000 -yCAR 100 -zCAR 100 -aCAR 84.000 \
  -xLAB C13 -yLAB Sign_Coding -zLAB t_mix -aLAB N15 \
  -ndim 4 -yq2D States \
  -out ./bruker.fid -verb -ov

#Re-orders datafile to C13-N15-t_mix-Sign_Coding:

nmrPipe -in bruker.fid \
  | nmrPipe -fn TP -auto \
  | nmrPipe -fn ATP \
  | nmrPipe -fn TP -auto \
  | nmrPipe -ov -verb -out temp.fid \

mv temp.fid bruker.fid
=====
```

### 7.6.2 Processing Script (nmrPipe) for ASHDEX Experiment

After execution of the above Conversion Script, the following script is used to apply the usual NMR processing to the time-domain data. The script also handles the processing of the sign-coding filter and results in two pseudo-3D NMR spectra.

```
=====
#!/bin/csh

#For HDX data recorded in a psuedo-4D manner using sequence: arg_ashdex.hm
#Takes converted nmrPipe datafile from fid_hdx3d.com as input

#Output is two sepearate psuedo-3D spectra:
#CzNeH: Shows only Ne(H) signals. Intensity decays due to H/D exchange and relaxation
#CzNeD: Shows only Ne(D) signals. Intensity increases due to H/D exchange
# and decays due to relaxation

#Read in data and split into two psuedo-3D cubes

echo '##### Pre-processing #####'

nmrPipe -in bruker.fid \
```

```

| pipe2xyz -verb -out temp/temp%02d.fid

cd temp
foreach file ( temp*.fid )
  sethdr $file -yT 1 -aN 1
  xyz2pipe -in $file | nmrPipe -ov -out ${file:s/temp/fid/}
  sethdr ${file:s/temp/fid/} -ndim 3
#  rm $file
end
cd ../

#Take sum/difference
addNMR -in1 temp/fid01.fid -in2 temp/fid02.fid -out temp/CzNeD.fid
addNMR -sub -in1 temp/fid02.fid -in2 temp/fid01.fid -out temp/CzNeH.fid

echo 'Complete!'

#Process CzNeH spectrum

echo '##### Protonated spectrum processing #####'

nmrPipe      -in temp/CzNeH.fid                \
| nmrPipe    -fn GM -g1 0 -g2 25 -g3 0 -c 1.0   \
| nmrPipe    -fn ZF -zf 2 -auto                \
| nmrPipe    -fn FT -auto                    \
| nmrPipe    -fn PS -p0 -220.00 -p1 0.00 -di -verb \
| nmrPipe    -fn TP                          \
| nmrPipe    -fn GM -g1 -5 -g2 25 -g3 0 -c 1.0 \
| nmrPipe    -fn ZF -zf 4 -auto                \
| nmrPipe    -fn FT -alt                      \
| nmrPipe    -fn PS -p0 -3.00 -p1 180.00 -di -verb \
| nmrPipe    -fn TP                          \
| nmrPipe    -fn POLY -auto                   \
              -ov -out CzNeH.ft3

echo 'Complete!'

#Process CzNeD spectrum

echo '##### Deuterated spectrum processing #####'

nmrPipe      -in temp/CzNeD.fid                \
| nmrPipe    -fn GM -g1 0 -g2 25 -g3 0 -c 1.0   \
| nmrPipe    -fn ZF -zf 2 -auto                \
| nmrPipe    -fn FT -auto                    \
| nmrPipe    -fn PS -p0 -221.00 -p1 0.00 -di -verb \
| nmrPipe    -fn TP                          \
| nmrPipe    -fn GM -g1 -5 -g2 25 -g3 0 -c 1.0 \
| nmrPipe    -fn ZF -zf 4 -auto                \
| nmrPipe    -fn FT -alt                      \
| nmrPipe    -fn PS -p0 -4.00 -p1 180.00 -di -verb \
| nmrPipe    -fn TP                          \
| nmrPipe    -fn POLY -auto                   \
              -ov -out CzNeD.ft3

echo 'Complete!'

rm temp/*.fid
rmdir temp

echo 'CzNeH.ft3 stored'
echo 'CzNeD.ft3 stored'
=====

```

### 7.6.3 Conversion Script (nmrPipe) for CARBEX Experiment

The pseudo-5D CARBEX experiment results in a stack of FIDs in the order of acquisition:

$^{13}\text{C}(\text{F5})$ , IPAP(F4), Sign-coding(F3),  $\tau_{\text{mix}}(\text{F2})$  and  $^{15}\text{N}(\text{F1})$

During the conversion of the Bruker data into a format suitable for processing using the nmrPipe software package, the FIDs are re-ordered such that the first two dimensions are chemical shift:

## 7. Experimental

$^{13}\text{C}(\text{F5})$ ,  $^{15}\text{N}(\text{F4})$ , Sign-coding(F3),  $\tau_{\text{relax}}(\text{F2})$  and Sign-coding(F1)

Unfortunately, nmrPipe is unable to natively handle five separate dimensions so in the first instance the IPAP, Sign-coding and  $\tau_{\text{mix}}$  dimensions are treated together. The conversion script also handles the IPAP decoupling and the processing of Sign-coding filter. The output is two pseudo-3D time-domain datasets. Following the execution of this Conversion Script, a standard processing script can be applied to process the time-domain data.

```
=====
#!/bin/csh

# Script for pre-processing of pseudo-5D CARBEX data
# Writes out 2D planes
# Processes IPAP decoupling of Calpha
# Splits into NH/ND subspectra
# Recombines fids into two pseudo-3D files

mkdir all_planes
mkdir decoupled
mkdir NH
mkdir ND

#bruk2pipe conversion

printf "\n"
printf "bruk2pipe conversion....."

bruk2pipe -in ../ser \
  -bad 0.0 -ext -aswap -AMX -decim 5712 -dspfvfs 20 -grpdlly 67.9851226806641 \
  -xN 1024 -yN 40 -zN 256 \
  -xT 512 -yT 40 -zT 128 \
  -xMODE DQD -yMODE Real -zMODE States-TPPI \
  -xSW 3501.401 -ySW 1 -zSW 2000.000 \
  -xOBS 150.876 -yOBS 10 -zOBS 60.797 \
  -xCAR 174.000 -yCAR 100 -zCAR 119.000 \
  -xLAB C13 -yLAB IPAP_sign_relax -zLAB N15 \
  -ndim 3 \
  -out ./bruker.fid -ov

printf "complete!\n"

#Re-orders datafile:

printf "fid shuffle....."

nmrPipe -in bruker.fid \
  | nmrPipe -fn TP -auto \
  | nmrPipe -fn ZTP \
  | nmrPipe -fn TP -auto \
  | nmrPipe -ov -out temp.fid \

mv temp.fid bruker.fid

printf "complete!\n"

#write out all 13C/15N planes

printf "writing planes....."

nmrPipe -in bruker.fid \
  | pipe2xyz -out all_planes/temp%02d.fid

cd all_planes
foreach file ( temp*.fid )
  sethdr $file -zN 1
  sethdr $file -yT 1
  xyz2pipe -in $file | nmrPipe -ov -out ${file:s/temp/fid/}
  sethdr ${file:s/temp/fid/} -ndim 2
rm $file
end
cd ../

printf "complete!\n"
```

```

#IPAP virtual decoupling

printf "decoupling C alpha....."

@ a = 1
@ b = 2
@ c = 1

while ($a < 40)

    if ($a < 10) then
        set a = 0$a
    endif
    if ($b < 10) then
        set b = 0$b
    endif
    if ($c < 10) then
        set c = 0$c
    endif

addNMR -in1 ./all_planes/fid$a.fid -in2 ./all_planes/fid$b.fid -out ./all_planes/add.fid
addNMR -sub -in1 ./all_planes/fid$a.fid -in2 ./all_planes/fid$b.fid -out
./all_planes/sub.fid

nmrPipe -in ./all_planes/add.fid \
| nmrPipe -fn PS -ls -27.5Hz \
| nmrPipe -out ./all_planes/add_shift.fid -ov

nmrPipe -in ./all_planes/sub.fid \
| nmrPipe -fn PS -ls +27.5Hz \
| nmrPipe -out ./all_planes/sub_shift.fid -ov

addNMR -in1 ./all_planes/add_shift.fid -in2 ./all_planes/sub_shift.fid -out
./decoupled/fid$c.fid

rm all_planes/add.fid
rm all_planes/sub.fid
rm all_planes/add_shift.fid
rm all_planes/sub_shift.fid

    @ a = $a + 2
    @ b = $b + 2
    @ c = $c + 1
end

printf "complete!\n"

#split into NH/ND subspectra

printf "splitting NH/ND subspectra....."

@ a = 1
@ b = 2
@ c = 1

while ($a < 20)

    if ($a < 10) then
        set a = 0$a
    endif
    if ($b < 10) then
        set b = 0$b
    endif
    if ($c < 10) then
        set c = 0$c
    endif

addNMR -in1 ./decoupled/fid$a.fid -in2 ./decoupled/fid$b.fid -out ./ND/fid$c.fid
addNMR -sub -in1 ./decoupled/fid$b.fid -in2 ./decoupled/fid$a.fid -out ./NH/fid$c.fid

    @ a = $a + 2
    @ b = $b + 2
    @ c = $c + 1
end

printf "complete!\n"

#collect NH/ND data into two pseudo-3D files

```

## 7. Experimental

```
printf "collecting psuedo-3D data....."

foreach file ( NH/fid*.fid )
  sethdr $file -yT 10 -zN 10 -yLAB t_mix
  sethdr $file -ndim 3
end

xyz2pipe -in NH/fid%02d.fid -out fid01.fid

foreach file ( ND/fid*.fid )
  sethdr $file -yT 10 -zN 10 -yLAB t_mix
  sethdr $file -ndim 3
end

xyz2pipe -in ND/fid%02d.fid -out fid02.fid

printf "complete!\n"

rm all_planes -r
rm decoupled -r
rm NH -r
rm ND -r

printf "storing fid01.fid.....complete!\n"
printf "storing fid02.fid.....complete!\n"
printf "\n"
=====
```

### 7.6.4 Fitting Script (Python) for the Extraction of HX Rates

The following python script is used to extract the residue-specific hydrogen exchanges rates from the build-up/decay intensity data obtained using the ASHDEX or CARBEX experiments. The input is a text file containing the data in the following format:

```
MIXING_TIME_1    N(H)_INTENSITY_1    N(D)_INTENSITY_1
MIXING_TIME_2    N(H)_INTENSITY_2    N(D)_INTENSITY_2
MIXING_TIME_3    N(H)_INTENSITY_3    N(D)_INTENSITY_3
...              ...              ...
```

```
=====
#!/usr/bin/env python

import numpy as np
import matplotlib.pyplot as plt
from scipy.linalg import expm
import lmfit
import sys
import os

def eq(mixing_time, kAB, kBA, R1A, R1B, H_init, D_init):

    TimeListLength = len(mixing_time)

    time = mixing_time
    gamma = np.zeros( (3,3) )
    gamma2 = np.zeros( (3, 3), dtype=complex)
    gamma3 = np.zeros( (3, 3), dtype=complex)
    m0=np.array( [H_init, 0, D_init] )

    R2A = 0.0
    R2B = 0.0
    wH = 35 * np.pi * 2. / 2.
    wD = -35 * np.pi * 2. / 2.
    J = 92.0
    tau = 0.01086957

    gamma[0, 0] = -np.sqrt(R1A*R1A) - kAB
    gamma[2, 2] = -np.sqrt(R1B*R1B) - kBA
    gamma[0, 2] = kBA
    gamma[2, 0] = kAB

    gamma2[0, 0] = (1j * wH) - kAB - R2A
    gamma2[0, 1] = (1j * np.pi * J)
```

```

gamma2[0, 2] = kBA
gamma2[1, 0] = (1j * np.pi * J)
gamma2[1, 1] = (1j * wH) - kAB - R2A
gamma2[2, 0] = kAB
gamma2[2, 2] = (1j * wD) - kBA - R2B

gamma3[0, 0] = (1j * -wH) - kAB - R2A
gamma3[0, 1] = (1j * np.pi * -J)
gamma3[0, 2] = kBA
gamma3[1, 0] = (1j * np.pi * -J)
gamma3[1, 1] = (1j * -wH) - kAB - R2A
gamma3[2, 0] = kAB
gamma3[2, 2] = (1j * -wD) - kBA - R2B

mt = np.zeros((3, TimeListLength), dtype=complex)

for i in range(TimeListLength):
    mm=expm( gamma*time[i]).dot(m0)
    mm1 = expm(gamma2 * tau/2).dot(mm)
    mm2 = expm(gamma3 * tau/2).dot(mm1)

    #NH
    mt[0,i]=mm2[0]
    #ND
    mt[2,i]=mm2[2]

return np.real(mt[0,:]), np.real(mt[2,:])

def residual(params, NH_exp, ND_exp):
    NH_mod , ND_mod = eq(mixing_time-params['T0'], params['k1'],
                        params['k1']*params['klr'], params['R1'],
                        params['R1']*params['R1r'], params['IOH'], params['IOD'])
    NH_diffs = NH_exp - NH_mod
    ND_diffs = ND_exp - ND_mod

    diffs = np.concatenate([NH_diffs, ND_diffs])

    return diffs

def fit(NH_exp, ND_exp):
    H_init = NH[0]
    D_init = ND[0]

    params = lmfit.Parameters()
    params.add('k1', value=10.0, vary=True)
    params.add('klr', value= 1.00, vary=True)
    params.add('R1', value= 0.213, vary=True, min = 0.0)
    params.add('R1r', value= 0.25, vary=True, min = 0.0)
    params.add('IOH', value= H_init, vary=True)
    params.add('IOD', value= D_init, vary=True)
    params.add('T0', value= 0.0, vary=False)

    out = lmfit.minimize(residual, params, args=(NH_exp, ND_exp))
    print (lmfit.fit_report(out))

    return out

def read_in_data(file):
    mixing_time = []
    NH = []
    ND = []

    with open(file, 'r') as infile:
        for line in infile:
            if line.startswith('#'):
                continue
            i = line.split()
            mixing_time.append(float(i[0]))
            NH.append(float(i[1]))
            ND.append(float(i[2]))

    return np.array(mixing_time), np.array(NH), np.array(ND)

#####
mixing_time, NH, ND = read_in_data('input.txt')

```

## 7. Experimental

```
# normalize data
MaxVal=np.max( np.max( NH ) )
NH=100.*NH/MaxVal
ND=100.*ND/MaxVal

fitted_const = fit(NH, ND)

plt.scatter(mixing_time, NH)
plt.scatter(mixing_time, ND)

dict_ = fitted_const.params

model_range = np.linspace(mixing_time[0], mixing_time[-1:][0], 1001)
NH_fmod , ND_fmod = eq(model_range, dict_['k1'],
                      dict_['k1']*dict_['k1r'],
                      dict_['R1'], dict_['R1']*dict_['R1r'],
                      dict_['IOH'], dict_['IOD'])

plt.plot(model_range, NH_fmod)
plt.plot(model_range, ND_fmod)

plt.show()
=====
```

# 8

## References

- [1] A. C. Brown, T. R. Fraser, *J. Anat. Physiol.* **1868**, 2, 224–242.
- [2] R. Guha, *Methods Mol. Biol.* **2013**, 993, 81–94.
- [3] E. Fischer, *Berichte der Dtsch. Chem. Gesellschaft* **1894**, 27, 2985–2993.
- [4] D. E. Koshland, *Proc. Natl. Acad. Sci.* **1958**, 44, 98–104.
- [5] H. P. Erickson, *Biol. Proced. Online* **2009**, 11, 32–51.
- [6] I. I. Rabi, J. R. Zacharias, S. Millman, P. Kusch, *Phys. Rev.* **1938**, 53, 318.
- [7] F. Bloch, W. W. Hansen, M. Packard, *Phys. Rev.* **1946**, 69, 127–127.
- [8] F. Bloch, W. W. Hansen, M. Packard, *Phys. Rev.* **1946**, 70, 474–485.
- [9] E. M. Purcell, H. C. Torrey, R. V. Pound, *Phys. Rev.* **1946**, 69, 37–38.
- [10] R. R. Ernst, W. A. Anderson, *Rev. Sci. Instrum.* **1966**, 37, 93–102.
- [11] W. P. Aue, E. Bartholdi, R. R. Ernst, *J. Chem. Phys.* **1976**, 64, 2229–2246.
- [12] A. Kumar, R. R. Ernst, K. Wüthrich, *Biochem. Biophys. Res. Commun.* **1980**, 95, 1–6.
- [13] K. Wüthrich, G. Wider, G. Wagner, W. Braun, *J. Mol. Biol.* **1982**, 155, 311–319.
- [14] M. P. Williamson, T. F. Havel, K. Wüthrich, *J. Mol. Biol.* **1985**, 182, 295–315.
- [15] T. D. W. Claridge, *High-Resolution NMR Techniques in Organic Chemistry*, Elsevier, **2016**.
- [16] J. Cavanagh, W. J. Fairbrother, A. G. Palmer, M. Rance, N. J. Skelton, *Protein NMR Spectroscopy*, Elsevier, **2007**.
- [17] V. I. Bakhmutov, *Solid-State NMR in Materials Science*, CRC Press, **2016**.
- [18] A.-H. Emwas, K. Szczepski, B. G. Poulson, K. Chandra, R. T. McKay, M. Dhahri, F. Alahmari, L. Jaremko, J. I. Lachowicz, M. Jaremko, *Molecules* **2020**, 25:4597, 1–63.

## 8. References

- [19] Y. Shi, *Cell* **2014**, *159*, 995–1014.
- [20] K. Murata, M. Wolf, *Biochim. Biophys. Acta - Gen. Subj.* **2018**, *1862*, 324–334.
- [21] F. Lugauer, J. Wetzl, in *Med. Imaging Syst.*, Springer, Cham, **2018**, pp. 91–118.
- [22] *Nature* **1944**, *154*, 634–634.
- [23] *Nature* **1952**, *170*, 911–912.
- [24] R. R. Ernst, *Angew. Chemie Int. Ed. English* **1992**, *31*, 805–823.
- [25] K. Wüthrich, *Angew. Chemie Int. Ed.* **2003**, *42*, 3340–3363.
- [26] F. W. Wehrli, *Magn. Reson. Med.* **2004**, *51*, 1–3.
- [27] D. R. Lide, *CRC Handbook of Chemistry and Physics*, CRC Press, **2002**.
- [28] R. Verardi, N. J. Traaseth, L. R. Masterson, V. V. Vostrikov, G. Veglia, *Adv. Exp. Med. Biol.* **2012**, *992*, 35–62.
- [29] O. W. Sørensen, G. W. Eich, M. H. Levitt, G. Bodenhausen, R. R. Ernst, *Prog. Nucl. Magn. Reson. Spectrosc.* **1984**, *16*, 163–192.
- [30] M. Karplus, *J. Chem. Phys.* **1959**, *30*, 11–15.
- [31] M. Karplus, *J. Am. Chem. Soc.* **1963**, *85*, 2870–2871.
- [32] M. J. Minch, *Concepts Magn. Reson.* **1994**, *6*, 41–56.
- [33] A. C. Wang, A. Bax, *J. Am. Chem. Soc.* **1996**, *118*, 2483–2494.
- [34] A. G. Redfield, *Adv. Magn. Opt. Reson.* **1965**, *1*, 1–32.
- [35] I. Solomon, *Phys. Rev.* **1955**, *99*, 559–565.
- [36] A. Sekhar, L. E. Kay, *Annu. Rev. Biophys.* **2019**, *48*, 297–319.
- [37] M. Sattler, S. W. Fesik, *Structure* **1996**, *4*, 1245–1249.
- [38] E. L. Hahn, *Phys. Rev.* **1950**, *80*, 580–594.
- [39] I. M. Gelfand, M. Saul, in *Trigonometry*, Birkhäuser Boston, Boston, MA, **2001**, pp. 139–171.
- [40] G. A. Morris, R. Freeman, *J. Am. Chem. Soc.* **1979**, *101*, 760–762.
- [41] A. J. Shaka, J. Keeler, T. Frenkiel, R. Freeman, *J. Magn. Reson.* **1983**, *52*, 335–338.
- [42] A. . Shaka, J. Keeler, R. Freeman, *J. Magn. Reson.* **1983**, *53*, 313–340.

- [43] Z. Zhou, R. Kümmerle, X. Qiu, D. Redwine, R. Cong, A. Taha, D. Baugh, B. Winniford, *J. Magn. Reson.* **2007**, *187*, 225–233.
- [44] A. J. Shaka, P. B. Barker, R. Freeman, *J. Magn. Reson.* **1985**, *64*, 547–552.
- [45] G. Bodenhausen, D. J. Ruben, *Chem. Phys. Lett.* **1980**, *69*, 185–189.
- [46] A. Bax, M. Ikura, L. E. Kay, D. A. Torchia, R. Tschudin, *J. Magn. Reson.* **1990**, *86*, 304–318.
- [47] T. J. Norwood, J. Boyd, J. E. Heritage, N. Soffe, I. D. Campbell, *J. Magn. Reson.* **1990**, *87*, 488–501.
- [48] D. J. States, R. A. Haberkorn, D. J. Ruben, *J. Magn. Reson.* **1982**, *48*, 286–292.
- [49] D. Marion, K. Wüthrich, *Biochem. Biophys. Res. Commun.* **1983**, *113*, 967–974.
- [50] L. E. Kay, D. Marion, A. Bax, *J. Magn. Reson.* **1989**, *84*, 72–84.
- [51] A. L. Davis, J. Keeler, E. D. Laue, D. Moskau, *J. Magn. Reson.* **1992**, *98*, 207–216.
- [52] L. Mueller, *J. Am. Chem. Soc.* **1979**, *101*, 4481–4484.
- [53] K. Pervushin, R. Riek, G. Wider, K. Wuthrich, *Proc. Natl. Acad. Sci.* **1997**, *94*, 12366–12371.
- [54] M. Ikura, L. E. Kay, A. Bax, *Biochemistry* **1990**, *29*, 4659–4667.
- [55] L. E. Kay, M. Ikura, R. Tschudin, A. Bax, *J. Magn. Reson.* **1990**, *89*, 496–514.
- [56] M. Sattler, *Prog. Nucl. Magn. Reson. Spectrosc.* **1999**, *34*, 93–158.
- [57] R. Freeman, *Prog. Nucl. Magn. Reson. Spectrosc.* **1998**, *32*, 59–106.
- [58] L. Emsley, G. Bodenhausen, *Chem. Phys. Lett.* **1990**, *165*, 469–476.
- [59] E. Kupce, J. Boyd, I. D. Campbell, *J. Magn. Reson. Ser. B* **1995**, *106*, 300–303.
- [60] H. Geen, R. Freeman, *J. Magn. Reson.* **1991**, *93*, 93–141.
- [61] G. Bodenhausen, R. Freeman, D. L. Turner, *J. Magn. Reson.* **1977**, *27*, 511–514.
- [62] Y. Shen, F. Delaglio, G. Cornilescu, A. Bax, *J. Biomol. NMR* **2009**, *44*, 213–223.
- [63] Y. Shen, A. Bax, in *Artif. Neural Networks*, **2015**, pp. 17–32.
- [64] Y. Shen, O. Lange, F. Delaglio, P. Rossi, J. M. Aramini, G. Liu, A. Eletsy, Y. Wu, K. K. Singarapu, A. Lemak, A. Ignatchenko, C. H. Arrowsmith, T. Szyperski, G. T. Montelione, D. Baker, A. Bax, *Proc. Natl. Acad. Sci.* **2008**, *105*, 4685–4690.

## 8. References

- [65] Y. Shen, R. Vernon, D. Baker, A. Bax, *J. Biomol. NMR* **2009**, *43*, 63–78.
- [66] P. Güntert, L. Buchner, *J. Biomol. NMR* **2015**, *62*, 453–471.
- [67] E. Schmidt, P. Güntert, *J. Am. Chem. Soc.* **2012**, *134*, 12817–12829.
- [68] D. Ban, T. Sabo, C. Griesinger, D. Lee, *Molecules* **2013**, *18*, 11904–11937.
- [69] A. K. Mittermaier, L. E. Kay, *Trends Biochem. Sci.* **2009**, *34*, 601–611.
- [70] A. G. Palmer, F. Massi, *Chem. Rev.* **2006**, *106*, 1700–1719.
- [71] D. M. Korzhnev, L. E. Kay, *Acc. Chem. Res.* **2008**, *41*, 442–451.
- [72] R. W. Montalvao, A. Cavalli, X. Salvatella, T. L. Blundell, M. Vendruscolo, *J. Am. Chem. Soc.* **2008**, *130*, 15990–15996.
- [73] J. Orts, A. D. Gossert, *Methods* **2018**, *138–139*, 3–25.
- [74] D. Wishart, *Curr. Pharm. Biotechnol.* **2005**, *6*, 105–120.
- [75] J.-J. Shu, *Biosystems* **2017**, *151*, 21–26.
- [76] P. B. Crowley, A. Golovin, *Proteins Struct. Funct. Bioinforma.* **2005**, *59*, 231–239.
- [77] R. Rohs, X. Jin, S. M. West, R. Joshi, B. Honig, R. S. Mann, *Annu. Rev. Biochem.* **2010**, *79*, 233–269.
- [78] A. K. Casey, M. A. Hicks, J. L. Johnson, P. C. Babbitt, P. A. Frantom, *Biochemistry* **2014**, *53*, 2915–2925.
- [79] J. Friedt, F. M. V. Leavens, E. Mercier, H.-J. Wieden, U. Kothe, *Nucleic Acids Res.* **2014**, *42*, 3857–3870.
- [80] C. Zeymer, N. D. Werbeck, S. Zimmermann, J. Reinstein, D. F. Hansen, *Angew. Chemie Int. Ed.* **2016**, *55*, 11533–11537.
- [81] M. P. Goldschen-Ohm, D. A. Wagner, M. V. Jones, *Mol. Pharmacol.* **2011**, *80*, 647–656.
- [82] A. R. Gargaro, T. A. Frenkiel, P. M. Nieto, B. Birdsall, V. I. Polshakov, W. D. Morgan, J. Feeney, *Eur. J. Biochem.* **1996**, *238*, 435–439.
- [83] R. M. Vernon, P. A. Chong, B. Tsang, T. H. Kim, A. Bah, P. Farber, H. Lin, J. D. Forman-Kay, *Elife* **2018**, *7*:e67381, 1–48.
- [84] P. A. Chong, R. M. Vernon, J. D. Forman-Kay, *J. Mol. Biol.* **2018**, *430*, 4650–4665.
- [85] M. R. Sawaya, J. Kraut, *Biochemistry* **1997**, *36*, 586–603.

- [86] L. C. Tarshis, P. J. Proteau, B. A. Kellogg, J. C. Sacchettini, C. D. Poulter, *Proc. Natl. Acad. Sci.* **1996**, *93*, 15018–15023.
- [87] A. E. Eriksson, T. A. Jones, A. Liljas, *Proteins Struct. Funct. Genet.* **1988**, *4*, 274–282.
- [88] A. Cheng, S. M. Wong, Y. A. Yuan, *Cell Res.* **2009**, *19*, 187–195.
- [89] C. A. Fitch, G. Platzer, M. Okon, B. Garcia-Moreno E., L. P. McIntosh, *Protein Sci.* **2015**, *24*, 752–761.
- [90] M. J. Harms, J. L. Schlessman, G. R. Sue, B. Garcia-Moreno E., *Proc. Natl. Acad. Sci.* **2011**, *108*, 18954–18959.
- [91] N. D. Werbeck, J. Kirkpatrick, D. F. Hansen, *Angew. Chemie Int. Ed.* **2013**, *52*, 3145–3147.
- [92] Y. Yoshimura, N. A. Oktaviani, K. Yonezawa, H. Kamikubo, F. A. A. Mulder, *Angew. Chemie Int. Ed.* **2017**, *56*, 239–242.
- [93] R. B. Pritchard, D. F. Hansen, *Nat. Commun.* **2019**, *10*:1747, 1–7.
- [94] P. Carter, *Biochem. J.* **1986**, *237*, 1–7.
- [95] F. Castorena-Torres, K. Peñuelas-Urquides, M. B. de León, in *Polym. Chain React. Biomed. Appl.*, InTech, **2016**.
- [96] B. T. Farmer, R. A. Venters, L. D. Spicer, M. G. Wittekind, L. Müller, *J. Biomol. NMR* **1992**, *2*, 195–202.
- [97] S. Grzesiek, A. Bax, *J. Magn. Reson.* **1992**, *96*, 432–440.
- [98] A. Bax, M. Ikura, *J. Biomol. NMR* **1991**, *1*, 99–104.
- [99] D. R. Muhandiram, L. E. Kay, *J. Magn. Reson. Ser. B* **1994**, *103*, 203–216.
- [100] R. T. Clubb, V. Thanabal, G. Wagner, *J. Magn. Reson.* **1992**, *97*, 213–217.
- [101] S. Grzesiek, A. Bax, *J. Magn. Reson.* **1992**, *99*, 201–207.
- [102] M. Wittekind, L. Mueller, *J. Magn. Reson. Ser. B* **1993**, *101*, 201–205.
- [103] S. Grzesiek, A. Bax, *J. Am. Chem. Soc.* **1992**, *114*, 6291–6293.
- [104] T. Yamazaki, W. Lee, C. H. Arrowsmith, D. R. Muhandiram, L. E. Kay, *J. Am. Chem. Soc.* **1994**, *116*, 11655–11666.
- [105] G. T. Montelione, B. A. Lyons, S. D. Emerson, M. Tashiro, *J. Am. Chem. Soc.* **1992**, *114*,

## 8. References

- 10974–10975.
- [106] S. Grzesiek, J. Anglister, A. Bax, *J. Magn. Reson. Ser. B* **1993**, *101*, 114–119.
- [107] T. Yamazaki, S. M. Pascal, A. U. Singer, J. D. Forman-Kay, L. E. Kay, *J. Am. Chem. Soc.* **1995**, *117*, 3556–3564.
- [108] H. Vis, R. Boelens, M. Mariani, R. Stroop, C. E. Vorgias, K. S. Wilson, R. Kaptein, *Biochemistry* **1994**, *33*, 14858–14870.
- [109] T. Yamazaki, M. Yoshida, K. Nagayama, *Biochemistry* **1993**, *32*, 5656–5669.
- [110] G. D. Henry, B. D. Sykes, *J. Biomol. NMR* **1995**, *6*, 59–66.
- [111] S. M. Pascal, A. U. Singer, G. Gish, T. Yamazaki, S. E. Shoelson, T. Pawson, L. E. Kay, J. D. Forman-Kay, *Cell* **1994**, *77*, 461–72.
- [112] W. D. Morgan, B. Birdsall, P. M. Nieto, A. R. Gargaro, J. Feeney, *Biochemistry* **1999**, *38*, 2127–2134.
- [113] N. Trbovic, J.-H. Cho, R. Abel, R. A. Friesner, M. Rance, A. G. Palmer, *J. Am. Chem. Soc.* **2009**, *131*, 615–622.
- [114] J. Iwahara, G. M. Clore, *J. Biomol. NMR* **2006**, *36*, 251–257.
- [115] P. M. Nieto, B. Birdsall, W. D. Morgan, T. A. Frenkiel, A. R. Gargaro, J. Feeney, *FEBS Lett.* **1997**, *405*, 16–20.
- [116] M. Rabinovitz, A. Pines, *J. Am. Chem. Soc.* **1969**, *91*, 1585–1589.
- [117] I. R. Kleckner, M. P. Foster, *Biochim. Biophys. Acta - Proteins Proteomics* **2011**, *1814*, 942–968.
- [118] H. M. McConnell, *J. Chem. Phys.* **1958**, *28*, 430–431.
- [119] D. F. Hansen, J. J. Led, *J. Magn. Reson.* **2003**, *163*, 215–227.
- [120] A. G. Palmer, *J. Magn. Reson.* **2014**, *241*, 3–17.
- [121] P. J. Farber, A. Mittermaier, *Biophys. Rev.* **2015**, *7*, 191–200.
- [122] D. F. Hansen, P. Vallurupalli, L. E. Kay, *J. Phys. Chem. B* **2008**, *112*, 5898–5904.
- [123] A. Zhuravleva, V. Y. Orekhov, *J. Am. Chem. Soc.* **2008**, *130*, 3260–3261.
- [124] H. Y. Carr, E. M. Purcell, *Phys. Rev.* **1954**, *94*, 630–638.
- [125] T. Yuwen, P. Vallurupalli, L. E. Kay, *Angew. Chemie - Int. Ed.* **2016**, *55*, 11490–11494.

- [126] V. Y. Orekhov, D. M. Korzhnev, L. E. Kay, *J. Am. Chem. Soc.* **2004**, *126*, 1886–1891.
- [127] K. V. Pervushin, G. Wider, R. Riek, K. Wuthrich, *Proc. Natl. Acad. Sci.* **1999**, *96*, 9607–9612.
- [128] K. Gerecht, A. M. Figueiredo, D. F. Hansen, *Chem. Commun.* **2017**, *53*, 10062–10065.
- [129] A. Bax, R. Freeman, T. A. Frenkiel, M. H. Levitt, *J. Magn. Reson.* **1981**, *43*, 478–483.
- [130] H. W. Mackenzie, D. F. Hansen, *J. Biomol. NMR* **2017**, *69*, 123–132.
- [131] T. Hofmann, S. A. Samsonov, A. Pichert, K. Lemmnitzer, J. Schiller, D. Huster, M. T. Pisabarro, M. von Bergen, S. Kalkhof, *Methods* **2015**, *89*, 45–53.
- [132] S. W. Englander, N. R. Kallenbach, *Q. Rev. Biophys.* **1983**, *16*, 521–655.
- [133] C. Woodward, I. Simon, E. Tuchsén, *Mol. Cell. Biochem.* **1982**, *48*, 135–160.
- [134] A. Berger, K. Linderstrøm-Lang, *Arch. Biochem. Biophys.* **1957**, *69*, 106–118.
- [135] E. E. Benson, K. Linderstrøm-Lang, *Biochim. Biophys. Acta* **1959**, *32*, 579–581.
- [136] G. R. Masson, M. L. Jenkins, J. E. Burke, *Expert Opin. Drug Discov.* **2017**, *12*, 981–994.
- [137] F. Shu, V. Ramakrishnan, B. P. Schoenborn, *Proc. Natl. Acad. Sci.* **2000**, *97*, 3872–3877.
- [138] J. C.-H. Chen, B. L. Hanson, S. Z. Fisher, P. Langan, A. Y. Kovalevsky, *Proc. Natl. Acad. Sci.* **2012**, *109*, 15301–15306.
- [139] G. Veglia, A. Carolina Zeri, C. Ma, S. J. Opella, *Biophys. J.* **2002**, *82*, 2176–2183.
- [140] G. Khirich, M. J. Holliday, J. C. Lin, A. Nandy, *J. Phys. Chem. B* **2018**, *122*, 2368–2378.
- [141] J.-M. L. del Amo, U. Fink, B. Reif, *J. Biomol. NMR* **2010**, *48*, 203–212.
- [142] S. D. Kelly, K. D. Heaton, P. Brereton, *Rapid Commun. Mass Spectrom.* **2001**, *15*, 1283–1286.
- [143] A. Hvidt, K. Linderstrøm-Lang, *Biochim. Biophys. Acta* **1954**, *14*, 574–575.
- [144] S. W. Englander, L. Mayne, Y. Bai, T. R. Sosnick, *Protein Sci.* **1997**, *6*, 1101–1109.
- [145] A. Hvidt, K. Linderstrøm-Lang, *C. R. Trav. Lab. Carlsberg. Chim.* **1955**, *29*, 385–402.
- [146] A. Hvidt, S. O. Nielsen, **1966**, pp. 287–386.
- [147] S. W. Englander, T. R. Sosnick, J. J. Englander, L. Mayne, *Curr. Opin. Struct. Biol.* **1996**, *6*, 18–23.

## 8. References

- [148] A. C. LiWang, A. Bax, *J. Am. Chem. Soc.* **1996**, *118*, 12864–12865.
- [149] K. Linderstrøm-Lang, *Biochim. Biophys. Acta* **1955**, *18*, 308.
- [150] S. W. Englander, A. Poulsen, *Biopolymers* **1969**, *7*, 379–393.
- [151] L. Swint-Kruse, A. D. Robertson, *Biochemistry* **1996**, *35*, 171–180.
- [152] Y.-Z. Zhang, Protein and Peptide Structure and Interactions Studied by Hydrogen Exchange and NMR, Ph.D Thesis, University of Pennsylvania, USA, **1995**.
- [153] W. J. Albery, J. R. Knowles, *Biochemistry* **1976**, *15*, 5588–5600.
- [154] W. A. Houry, J. M. Sauder, H. Roder, H. A. Scheraga, *Proc. Natl. Acad. Sci. U. S. A.* **1998**, *95*, 4299–4302.
- [155] G. Wagner, K. Wüthrich, *J. Mol. Biol.* **1982**, *160*, 343–361.
- [156] Y. Bai, J. S. Milne, L. Mayne, S. W. Englander, *Proteins Struct. Funct. Genet.* **1993**, *17*, 75–86.
- [157] J. J. Skinner, W. K. Lim, S. Bédard, B. E. Black, S. W. Englander, *Protein Sci.* **2012**, *21*, 987–995.
- [158] S. M. Pascal, T. Yamazaki, A. U. Singer, L. E. Kay, J. D. Forman-Kay, *Biochemistry* **1995**, *34*, 11353–11362.
- [159] S. Grzesiek, A. Bax, *J. Biomol. NMR* **1993**, *3*, 627–638.
- [160] T.-L. Hwang, S. Mori, A. J. Shaka, P. C. M. van Zijl, *J. Am. Chem. Soc.* **1997**, *119*, 6203–6204.
- [161] T. L. Hwang, P. C. van Zijl, S. Mori, *J. Biomol. NMR* **1998**, *11*, 221–6.
- [162] V. Chevelkov, Y. Xue, D. Krishna Rao, J. D. Forman-Kay, N. R. Skrynnikov, *J. Biomol. NMR* **2010**, *46*, 227–244.
- [163] P. E. Hansen, *Magn. Reson. Chem.* **2000**, *38*, 1–10.
- [164] F. Kateb, P. Pelupessy, G. Bodenhausen, *J. Magn. Reson.* **2007**, *184*, 108–113.
- [165] T. Segawa, F. Kateb, L. Duma, G. Bodenhausen, P. Pelupessy, *ChemBioChem* **2008**, *9*, 537–542.
- [166] J. Jeener, B. H. Meier, P. Bachmann, R. R. Ernst, *J. Chem. Phys.* **1979**, *71*, 4546–4553.
- [167] B. Borden, J. Luscombe, in *Essent. Math. Phys. Sci. Vol. I Homog. Bound. Value Probl.*

*Fourier Methods, Spec. Funct.*, IOP Publishing, **2017**.

- [168] J. Cavanagh, M. Rance, *Annu. Reports NMR Spectrosc.* **1993**, *27*, 1–58.
- [169] A. G. Palmer, J. Cavanagh, P. E. Wright, M. Rance, *J. Magn. Reson.* **1991**, *93*, 151–170.
- [170] J. Cavanagh, A. G. Palmer, P. E. Wright, M. Rance, *J. Magn. Reson.* **1991**, *91*, 429–436.
- [171] A. G. Palmer, J. Cavanagh, R. A. Byrd, M. Rance, *J. Magn. Reson.* **1992**, *96*, 416–424.
- [172] J. Schleucher, M. Sattler, C. Griesinger, *Angew. Chemie Int. Ed. English* **1993**, *32*, 1489–1491.
- [173] M. Akke, P. A. Carr, A. G. Palmer, *J. Magn. Reson. Ser. B* **1994**, *104*, 298–302.
- [174] M. Rance, *Bull. Magn. Reson.* **1994**, *16*, 54–67.
- [175] T. Yuwen, N. R. Skrynnikov, *J. Biomol. NMR* **2014**, *58*, 175–192.
- [176] A. J. Shaka, C. J. Lee, A. Pines, *J. Magn. Reson.* **1988**, *77*, 274–293.
- [177] S. P. Rucker, A. J. Shaka, *Mol. Phys.* **1989**, *68*, 509–517.
- [178] M. Kadkhodaie, O. Rivas, M. Tan, A. Mohebbi, A. . Shaka, *J. Magn. Reson.* **1991**, *91*, 437–443.
- [179] D. P. Burum, R. R. Ernst, *J. Magn. Reson.* **1980**, *39*, 163–168.
- [180] J. Iwahara, Y.-S. Jung, G. M. Clore, *J. Am. Chem. Soc.* **2007**, *129*, 2971–2980.
- [181] S. Ehni, B. Luy, *J. Magn. Reson.* **2014**, *247*, 111–117.
- [182] A. Bax, A. F. Mehlkopf, J. Smidt, *J. Magn. Reson.* **1979**, *35*, 373–377.
- [183] A. Bax, R. Freeman, *J. Magn. Reson.* **1981**, *44*, 542–561.
- [184] M. Rance, G. Wagner, O. W. Sørensen, K. Wüthrich, R. . Ernst, *J. Magn. Reson.* **1984**, *59*, 250–261.
- [185] J. Santoro, G. C. King, *J. Magn. Reson.* **1992**, *97*, 202–207.
- [186] G. W. Vuister, A. Bax, *J. Magn. Reson.* **1992**, *98*, 428–435.
- [187] J. Xu, O. Millet, L. E. Kay, N. R. Skrynnikov, *J. Am. Chem. Soc.* **2005**, *127*, 3220–3229.
- [188] H. W. Mackenzie, D. F. Hansen, *ChemPhysChem* **2019**, *20*, 252–259.
- [189] G. Karunanithy, J. Reinstein, D. F. Hansen, *J. Phys. Chem. Lett.* **2020**, *11*, 5649–5654.
- [190] D. W. Heinz, W. A. Baase, F. W. Dahlquist, B. W. Matthews, *Nature* **1993**, *361*, 561–564.

## 8. References

- [191] J. H. Tomlinson, S. Ullah, P. E. Hansen, M. P. Williamson, *J. Am. Chem. Soc.* **2009**, *131*, 4674–4684.
- [192] M. P. Williamson, A. M. Hounslow, J. Ford, K. Fowler, M. Hebditch, P. E. Hansen, *Chem. Commun.* **2013**, *49*, 9824–9826.
- [193] S. Bolvig, P. Erik Hansen, *Curr. Org. Chem.* **2000**, *4*, 19–54.
- [194] L. Kozerski, B. Kwiecień, R. Kawęcki, Z. Urbańczyk-Lipkowska, W. Bocian, E. Bednarek, J. Sitkowski, J. Maurin, L. Pazderski, P. E. Hansen, *New J. Chem.* **2004**, *28*, 1562–1567.
- [195] J. G. Soñnicki, P. E. Hansen, *Tetrahedron Lett.* **2005**, *46*, 839–842.
- [196] P. E. Hansen, S. N. Ibsen, T. Kristensen, S. Bolvig, *Magn. Reson. Chem.* **1994**, *32*, 399–408.
- [197] M. Munch, A. E. Hansen, P. E. Hansen, T. D. Bouman, F. Abildgaard, J. J. Led, S. B. Christensen, *Acta Chem. Scand.* **1992**, *46*, 1065–1071.
- [198] P. E. Hansen, A. E. Hansen, A. Lycka, A. Buvári-Barcza, H. Møllendal, A. Sveiczler, Y. Stenstrøm, M. Trætteberg, A. Nasiri, T. Tsuda, *Acta Chem. Scand.* **1993**, *47*, 777–788.
- [199] J. Abildgaard, S. Bolvig, P. E. Hansen, *J. Am. Chem. Soc.* **1998**, *120*, 9063–9069.
- [200] A. Lycka, P. E. Hansen, *Magn. Reson. Chem.* **1985**, *23*, 973–976.
- [201] J. Abildgaard, P. E. Hansen, M. N. Manalo, A. LiWang, *J. Biomol. NMR* **2009**, *44*, 119–126.
- [202] Y. Zhao, D. G. Truhlar, *Theor. Chem. Acc.* **2008**, *120*, 215–241.
- [203] R. Krishnan, J. S. Binkley, R. Seeger, J. A. Pople, *J. Chem. Phys.* **1980**, *72*, 650–654.
- [204] E. Fischer, A. Speier, *Berichte der Dtsch. Chem. Gesellschaft* **1895**, *28*, 3252–3258.
- [205] K. Basu, S. Chakraborty, A. K. Sarkar, C. Saha, *J. Chem. Sci.* **2013**, *125*, 607–613.
- [206] F. Machetti, I. Bucelli, G. Indiani, A. Guarna, *Comptes Rendus Chim.* **2003**, *6*, 631–633.
- [207] A. J. Alpert, *J. Chromatogr. A* **1990**, *499*, 177–196.
- [208] B. Dayal, G. Salen, B. Toome, G. S. Tint, S. Shefer, J. Padia, *Steroids* **1990**, *55*, 233–237.
- [209] L. A. Carpino, *J. Am. Chem. Soc.* **1993**, *115*, 4397–4398.
- [210] P. Vallurupalli, G. Bouvignies, L. E. Kay, *J. Am. Chem. Soc.* **2012**, *134*, 8148–8161.
- [211] P. Vallurupalli, A. Sekhar, T. Yuwen, L. E. Kay, *J. Biomol. NMR* **2017**, *67*, 243–271.

- [212] J. Hunger, R. Buchner, M. E. Kandil, E. F. May, K. N. Marsh, G. Hefter, *J. Chem. Eng. Data* **2010**, *55*, 2055–2065.
- [213] D. G. Archer, P. Wang, *J. Phys. Chem. Ref. Data* **1990**, *19*, 371–411.
- [214] G. Ritzoulis, N. Papadopoulos, D. Jannakoudakis, *J. Chem. Eng. Data* **1986**, *31*, 146–148.
- [215] F. I. Mopsik, *J. Res. Natl. Bur. Stand. Sect. A Phys. Chem.* **1967**, *71A*, 287.
- [216] J. W. Williams, I. J. Krcma, *J. Am. Chem. Soc.* **1927**, *49*, 1676–1686.
- [217] C. Martin, V. Richard, M. Salem, R. Hartley, Y. Mauguén, *Acta Crystallogr. Sect. D Biol. Crystallogr.* **1999**, *55*, 386–398.
- [218] W. Bermel, I. Bertini, L. Duma, I. C. Felli, L. Emsley, R. Pierattelli, P. R. Vasos, *Angew. Chemie Int. Ed.* **2005**, *44*, 3089–3092.
- [219] P. E. Wright, H. J. Dyson, *Nat. Rev. Mol. Cell Biol.* **2015**, *16*, 18–29.
- [220] S. Gil, T. Hošek, Z. Solyom, R. Kümmerle, B. Brutscher, R. Pierattelli, I. C. Felli, *Angew. Chemie Int. Ed.* **2013**, *52*, 11808–11812.
- [221] N. N. Naseri, H. Wang, J. Guo, M. Sharma, W. Luo, *Neurosci. Lett.* **2019**, *705*, 183–194.
- [222] C. R. Fields, N. Bengoa-Vergniory, R. Wade-Martins, *Front. Mol. Neurosci.* **2019**, *12*:299, 1–14.
- [223] J.-H. Na, W.-K. Lee, Y. Yu, *Int. J. Mol. Sci.* **2018**, *19*, 381.
- [224] D. S. Wishart, B. D. Sykes, F. M. Richards, *FEBS Lett.* **1991**, *293*, 72–80.
- [225] D. Braun, G. Wider, K. Wuethrich, *J. Am. Chem. Soc.* **1994**, *116*, 8466–8469.
- [226] D. S. Wishart, C. G. Bigam, A. Holm, R. S. Hodges, B. D. Sykes, *J. Biomol. NMR* **1995**, *5*, 67–81.
- [227] J. Yao, H. J. Dyson, P. E. Wright, *FEBS Lett.* **1997**, *419*, 285–289.
- [228] F. Avbelj, D. Kocjan, R. L. Baldwin, *Proc. Natl. Acad. Sci.* **2004**, *101*, 17394–17397.
- [229] J. A. Vila, Y. A. Arnautova, H. A. Scheraga, *Proc. Natl. Acad. Sci.* **2008**, *105*, 1891–1896.
- [230] W. Bermel, I. Bertini, I. C. Felli, R. Kümmerle, R. Pierattelli, *J. Magn. Reson.* **2006**, *178*, 56–64.
- [231] E. C. Cook, G. A. Usher, S. A. Showalter, *Methods Enzymol.* **2018**, *611*, 81–100.
- [232] I. C. Felli, R. Pierattelli, *J. Magn. Reson.* **2014**, *241*, 115–125.

## 8. References

- [233] E. B. Gibbs, R. W. Kriwacki, *Methods* **2018**, *138–139*, 39–46.
- [234] K. Takeuchi, H. Arthanari, I. Shimada, G. Wagner, *J. Biomol. NMR* **2015**, *63*, 323–331.
- [235] S. Chhabra, P. Fischer, K. Takeuchi, A. Dubey, J. J. Ziarek, A. Boeszoermyeni, D. Mathieu, W. Bermel, N. E. Davey, G. Wagner, H. Arthanari, *Proc. Natl. Acad. Sci.* **2018**, *115*, E1710–E1719.
- [236] W. Bermel, I. Bertini, I. C. Felli, Y.-M. Lee, C. Luchinat, R. Pierattelli, *J. Am. Chem. Soc.* **2006**, *128*, 3918–3919.
- [237] J. Ying, F. Li, J. H. Lee, A. Bax, *J. Biomol. NMR* **2014**, *60*, 15–21.
- [238] J. Ying, J. Roche, A. Bax, *J. Magn. Reson.* **2014**, *241*, 97–102.
- [239] N. Khaneja, T. Reiss, C. Kehlet, T. Schulte-Herbrüggen, S. J. Glaser, *J. Magn. Reson.* **2005**, *172*, 296–305.
- [240] F. Bloch, A. Siegert, *Phys. Rev.* **1940**, *57*, 522–527.
- [241] M. Ottiger, F. Delaglio, A. Bax, *J. Magn. Reson.* **1998**, *131*, 373–378.
- [242] J. Lautenschläger, A. D. Stephens, G. Fusco, F. Ströhl, N. Curry, M. Zacharopoulou, C. H. Michel, R. Laine, N. Nespovitaya, M. Fantham, D. Pinotsi, W. Zago, P. Fraser, A. Tandon, P. St George-Hyslop, E. Rees, J. J. Phillips, A. De Simone, C. F. Kaminski, G. S. K. Schierle, *Nat. Commun.* **2018**, *9*, 712.
- [243] M. Foroozandeh, P. Singh, *Automatica* **2021**, *129*, 109611.
- [244] J. R. J. Yong, M. Foroozandeh, *Anal. Chem.* **2021**, *93*, 10735–10739.
- [245] F. A. A. Mulder, B. Hon, D. R. Muhandiram, F. W. Dahlquist, L. E. Kay, *Biochemistry* **2000**, *39*, 12614–12622.
- [246] L. Kang, K.-P. Wu, M. Vendruscolo, J. Baum, *J. Am. Chem. Soc.* **2011**, *133*, 13465–13470.
- [247] F. Delaglio, S. Grzesiek, G. Vuister, G. Zhu, J. Pfeifer, A. Bax, *J. Biomol. NMR* **1995**, *6*, 277–293.
- [248] W. F. Vranken, W. Boucher, T. J. Stevens, R. H. Fogh, A. Pajon, M. Llinas, E. L. Ulrich, J. L. Markley, J. Ionides, E. D. Laue, *Proteins Struct. Funct. Bioinforma.* **2005**, *59*, 687–696.